

Post-Earthquake Assessment of Reinforced Concrete Frames

Cal F. Bearman

A thesis submitted in partial fulfillment of the
requirements for the degree of

Master of Science in Civil Engineering

University of Washington

2012

Committee:

Laura Lowes

Marc Eberhard

John Stanton

Program Authorized to Offer Degree:
Department of Civil and Environmental Engineering

Table of Contents

List of Figures	v
List of Tables.....	xi
Chapter 1: Introduction	1
1.1 Background and Motivation.....	1
1.2 Research Objectives.....	2
1.3 Thesis Organization	3
Chapter 2: Literature Review	5
2.1 Introduction.....	5
2.2 Damage Identification.....	5
2.2.1 Individual Test Programs	6
2.3 Observed Damage	7
2.4 Drift Capacity Models.....	9
2.5 Reinforced Concrete Modeling	12
2.5.1 Element Modeling	12
2.5.2 Effective Stiffness Models	21
2.5.3 Building Modeling.....	23
2.6 Nonlinear Structural Analysis Techniques.....	28
Chapter 3: Damage Progression in RC Columns Subjected to Earthquake Loading.....	31
3.1 Introduction.....	31
3.2 Response Modes	31
3.3 Damage Progression.....	32
3.3.1 Axial Load Effect	33
3.3.2 Damage Progression and Load-Displacement Response	33
3.3.3 Flexural Damage Progression.....	40
3.3.4 Shear Damage Progression.....	47
3.3.5 Loss of Load Carrying Capacity.....	58
3.3.6 Bi-Directional Loading Effect.....	58
3.4 Drift Corresponding to Damage States	59
3.4.1 Drift as the Selected Engineering Demand Parameter	59
3.4.2 Drift at Proposed Damage States from Bae (2005) and Sezen (2002)	59
3.4.3 Drift at Database and ATC-58 Damage States.....	60

3.5	Drift at Loss of Capacity Based on Capacity Models	67
3.5.1	Drift Model Review.....	67
3.6	Proposed Drifts for Onset of Damage	70
3.6.1	Drift Comparison for Flexure-Critical Columns	70
3.6.2	Proposed Drifts at Damage States for Flexure-Critical Columns.....	72
3.6.3	Drift Comparison for Shear-Critical Columns	73
3.6.4	Proposed Drifts at Damage States for Shear-Critical Columns.....	75
3.7	Residual Drift.....	75
3.7.1	PEER Structural Performance Database Data Acquisition	76
3.7.2	Residual Drift Results.....	77
3.8	Summary and Conclusions.....	84
3.8.1	Summary.....	84
3.8.2	Conclusions	84
Chapter 4:	Element Modeling and Analysis Validation.....	85
4.1	Introduction.....	85
4.2	Beam-Column Element Modeling	85
4.2.1	OpenSees Element Formulation	85
4.2.2	General Modeling Considerations	90
4.3	Beam-Column Element Modeling Validation Results.....	90
4.3.1	ACI Special Moment Frames	90
4.3.2	ACI Intermediate Moment Frames.....	94
4.3.3	ACI Ordinary Moment Frames.....	97
4.3.4	Beam-Column Modeling Results	100
4.4	Shear Failure Modeling.....	102
4.5	Shear Failure Validation Results.....	105
4.5.1	Shear and Flexure-Shear-Critical Columns	105
4.5.2	Shear and Flexure-Shear-Critical Column Modeling Statistics.....	106
4.6	Joint Element Modeling	109
4.6.1	Joint Modeling Techniques	109
4.7	Beam-Column Joint Modeling Validation Results	116
4.7.1	Older RC Interior Joints	116
4.7.2	Older RC Exterior Joints	120
4.7.3	Older Beam-Column Joint Modeling Results	121

4.8	Full Frame Model Validation.....	123
4.8.1	Experimental Summary	123
4.8.2	Modeling Summary	124
4.9	Summary and Conclusions.....	125
4.9.1	Summary.....	125
4.9.2	Conclusions	126
Chapter 5: Simulation of the Earthquake Response of Reinforced Concrete Frames and Assessment of Frame Performance		127
5.1	Introduction.....	127
5.2	Reinforced Concrete Frame Selection.....	127
5.3	Frame Design	130
5.3.1	SMF Design by Haselton (2006).....	131
5.3.2	OMF Designs by Liel (2008).....	133
5.4	Frame Nonlinear Analysis Models.....	134
5.4.1	Modeling Deficiencies.....	137
5.5	Full Frame Simulation.....	138
5.5.1	Data Recorded During Simulations.....	138
5.5.2	Monotonic Pushover Analysis.....	139
5.5.3	Pushover Results	139
5.5.4	Dynamic Time-History Analysis.....	150
5.5.5	Ground Motion Selection	150
5.5.6	Ground Motion Scaling	153
5.5.7	Foreshock-Aftershock Pair Explanation.....	158
5.5.8	Dynamic Results.....	159
5.6	Summary	175
Chapter 6: Summary and Conclusions		177
6.1	Summary	177
6.2	Conclusions.....	178
6.2.1	Column Damage Progression	178
6.2.2	Pushover Analysis	178
6.2.3	Foreshock-Aftershock Pair Analysis	179
6.3	Recommendations for Future Research	180
List of References.....		181

Appendix A : Database Damage Data	190
A.1 Introduction	190
A.2 Database Data	190
Appendix B : Database Modified Damage Data	200
B.1 Introduction	200
Appendix C : Element Sub-Assemblage Information	208
C.1 Introduction	208
C.2 SMF Column Simulation Plots	208
C.3 IMF Column Simulation Plots	213
C.4 OMF Column Simulation Plots	219
C.5 Shear Failure Simulation Plots	221
C.6 Older RC Interior Joint Simulation Plots	224
C.7 Older RC Exterior Joint Simulation Plots	228
C.8 Joint Experimental Observations and Analysis Discussion	234
Appendix D : Stanford Design Documentation	256
D.1 Introduction	256
D.2 Process for Obtaining Designs not Completed by Haselton and Liel	256
D.3 Frame Design Information	259
Appendix E : Ground Motions	269
E.1 Introduction	269
E.2 Ground Motions	269
E.3 Ground Motion Scaling Factors	272
E.4 Ground Motion Pairs	278
Appendix F : Building Pushover Data	283
F.1 Introduction	283
Appendix G : Cyclic Analysis Data	304
G.1 Introduction	304
G.2 Roof Drift Response	304
G.3 Probabilities for Frames	307
Appendix H : Additional Database Data	319

List of Figures

Figure 1.1 Proposed framework	2
Figure 2.1 Altoontash joint formulation (2004)	17
Figure 2.2 Lowes et al. joint formulation (2003)	18
Figure 2.3 Nomenclature for flat slab structures (Luo and Durrani 1995).....	20
Figure 2.4 Technique to determine effective stiffness	21
Figure 2.5 Effective stiffness models	23
Figure 2.6 Van Nuys building floor plan (Paspuleti 2002)	25
Figure 2.7 Van Nuys building elevation (Paspuleti 2002)	25
Figure 2.8 Benchmark building plan and elevation.....	27
Figure 2.9 Benchmark building elevation with modeling techniques	28
Figure 3.1 Load Drift History.....	34
Figure 3.2 (F4) Concrete Spalling on Flexural and Side Faces	34
Figure 3.3 (F5) Concrete Spalling Exposing Longitudinal Steel	34
Figure 3.4 (F6 & F7) Longitudinal Bar Buckling and Crushing of Core Concrete.....	34
Figure 3.5 (F8) Longitudinal Bar Fracture	34
Figure 3.6 Load Drift History.....	35
Figure 3.7 (F4) Concrete Spalling on Flexural and Side Faces	35
Figure 3.8 (F5) Concrete Spalling Exposing Longitudinal Steel	35
Figure 3.9 (F6 & F7) Longitudinal Bar Buckling and Crushing of Core Concrete.....	35
Figure 3.10 (F8) Longitudinal Bar Fracture	35
Figure 3.11 Load Drift History.....	36
Figure 3.12 (F2 & F4) Longitudinal Cracking and Concrete Spalling on Flexural and Side Faces.....	36
Figure 3.13 (F5) Concrete Spalling Exposing Longitudinal Steel	36
Figure 3.14 (F6 & F7) Longitudinal Bar Buckling and Crushing of Core Concrete.....	36
Figure 3.15 Load Drift History.....	37
Figure 3.16 (F1 & F2) Flexural and Longitudinal Cracking	37
Figure 3.17 (F3) Shear Cracking	37
Figure 3.18 (F4) Concrete Spalling on Flexural and Side Faces	37
Figure 3.19 (F5) Concrete Spalling Exposing Longitudinal Steel	37
Figure 3.20 (F6 & F7) Longitudinal Bar Buckling and Crushing of Core Concrete.....	37
Figure 3.21 (F8) Longitudinal Bar Fracture	37

Figure 3.22 Load Drift History.....	38
Figure 3.23 (S1 & S2) Flexural and Shear Cracking.....	38
Figure 3.24 (S3.0 & S3.1) Widening and Localization of Shear Cracking and Longitudinal Cracking on Side Face	38
Figures 3.25 and 3.26 (S3.2) Concrete Spalling on Side Faces.....	38
Figure 3.27 (S3.3) Longitudinal Bar Buckling.....	38
Figure 3.28 Load Drift History.....	39
Figures 3.29 and 3.30 (S1 & S2) Flexural and Shear Cracking	39
Figure 3.31 (S3.1) Widening and Localization of Longitudinal Cracking on Side Face	39
Figure 3.32 (S3.2) Concrete Spalling on Side Face After Load Reversal.....	39
Figure 3.33 (S3.3 & S3.4) Longitudinal Bar Buckling and Core Crushing After Loss of Load Carrying Capacity.....	39
Figure 3.34 Longitudinal cracking on flexural faces: experimental damage (Bae 2005).....	41
Figure 3.35 Longitudinal cracking: earthquake damage (PEER).....	42
Figure 3.36 Shear cracking on side faces: experimental damage (Bae 2005)	42
Figures 3.37, 3.38, and 3.39 Concrete spalling on flexural and side face: experimental damage (Bae 2005).....	43
Figure 3.40 Concrete spalling on flexural and side face: earthquake damage (PEER)	43
Figures 3.41, 3.42, and 3.43 Concrete spalling exposing longitudinal steel: experimental damage (Bae 2005).....	44
Figures 3.44, 3.45, and 3.46 Concrete spalling exposing longitudinal steel: earthquake damage (PEER).....	44
Figures 3.47, 3.48, and 3.49 Longitudinal bar buckling: experimental damage (Bae 2005).....	45
Figure 3.50 Longitudinal bar buckling: earthquake damage (PEER).....	45
Figures 3.51, 3.52, and 3.53 Crushing of core concrete: experimental damage (Bae 2005)	46
Figure 3.54 Crushing of core concrete: earthquake damage (PEER)	46
Figures 3.55 and 3.56 Longitudinal bar fracture: experimental damage (Bae 2005)	47
Figure 3.57 Flexural cracking and longitudinal cracking: experimental damage (Sezen 2002)	48
Figures 3.58 and 3.59 Flexural and longitudinal cracking: earthquake damage (Eberhard, et al. 2010)	49
Figures 3.60, 3.61, and 3.62 Shear cracking on side faces: experimental damage (Sezen 2002).....	49
Figures 3.63 and 3.64 Shear cracking on side faces: earthquake damage (Sedra, et al. 2010)	50
Figures 3.65 and 3.66 Shear cracking on side faces: earthquake damage (Eberhard, et al. 2010).....	50

Figures 3.67 and 3.68 Widening and localization of shear cracks: experimental damage (Sezen 2002)	51
Figures 3.69 and 3.70 Widening and localization of shear cracks: earthquake damage (Sedra, et al. 2010)	52
Figures 3.71 and 3.72 Widening and localization of shear cracks: earthquake damage (Eberhard, et al. 2010)	52
Figure 3.73 Widening and localization of shear cracks: earthquake damage (PEER)	52
Figures 3.74 and 3.75 Longitudinal cracking on side faces: experimental damage (Sezen 2002)	53
Figures 3.76 (Sedra, et al. 2010) and 3.77 (PEER) Longitudinal cracking on side faces: earthquake damage	53
Figures 3.78 and 3.79 Concrete spalling on side faces: experimental damage (Sezen 2002)	54
Figures 3.80, 3.81, 3.82, and 3.83 Concrete spalling on side faces: earthquake damage (PEER)	54
Figures 3.84, 3.85, and 3.86 Concrete spalling on side faces: earthquake damage (Eberhard, et al. 2010)	55
Figures 3.87, 3.88, 3.89, 3.90, and 3.91 Longitudinal bar buckling: experimental damage (Sezen 2002)	55
Figures 3.92, 3.93, 3.94, 3.95, and 3.96 Longitudinal bar buckling: earthquake damage (PEER)	56
Figures 3.97 and 3.98 Longitudinal bar buckling: earthquake damage (Sedra, et al. 2010)	56
Figure 3.99 Crushing of core concrete: experimental damage (Sezen 2002)	57
Figures 3.100, 3.101, and 3.102 Crushing of core concrete: earthquake damage (PEER)	57
Figure 3.103 Flexure-critical low axial load Bae data compared to Database data	64
Figure 3.104 Flexure-critical low axial load Bae data compared to ATC-58 data	64
Figure 3.105 Shear-critical low axial load Sezen data compared to Database data	65
Figure 3.106 Shear-critical low axial load Sezen data compared to ATC-58 data	65
Figure 3.107 Shear-critical high axial load Sezen data compared to Database data	66
Figure 3.108 Shear-critical high axial load Sezen data compared to ATC-58 data	66
Figure 3.109 Predicted response for a pre-1976 column	69
Figure 3.110 Plot of load-displacement history and unloading slopes	76
Figure 3.111 Maximum and residual drift from damage data and load-displacement history	77
Figure 3.112 Residual Drift vs. Maximum Drift for columns with low axial loads	78
Figure 3.113 Residual Drift vs. Maximum Drift for columns with high axial loads	78
Figure 3.114 Residual Drift vs. Damage State for columns with low axial loads	79
Figure 3.115 Residual Drift vs. Damage State for columns with high axial loads	79

Figure 3.116 Bilinear line fit for columns with low axial loads.....	80
Figure 3.117 Bilinear line fit for columns with high axial loads.....	81
Figure 3.118 Residual Drift Ratios vs. Flexural Damage States for columns with low axial loads....	82
Figure 3.119 Residual Drift Ratios vs. Flexural Damage States for columns with high axial loads....	83
Figure 4.1 Typical cross-section discretization	87
Figure 4.2 Concrete stress-strain relationship defined by Saatcioglu and Razvi.....	88
Figures 4.3 and 4.4 Example SMF force-displacement plots with good modeling accuracy.....	92
Figures 4.5 and 4.6 Example SMF force-displacement plots with poor modeling accuracy	93
Figures 4.7 and 4.8 Example IMF force-displacement plots with good modeling accuracy	95
Figures 4.9 and 4.10 Example IMF force-displacement plots with poor modeling accuracy	96
Figures 4.11 and 4.12 Example OMF force-displacement plots with good modeling accuracy	98
Figures 4.13 and 4.14 Example OMF force-displacement plots with poor modeling accuracy.....	99
Figure 4.15 Shear Spring Backbone Curve	103
Figure 4.16 Shear column formulation.....	104
Figures 4.17 (a) Shear Spring model with good modeling accuracy and (b) No Spring model.....	106
Figures 4.18 (a) Shear Spring model with poor modeling accuracy and (b) No Spring model	106
Figure 4.19 ASCE 41 rigid offset recommendations	110
Figure 4.20 Schematic of beam-column elements framing into a rigid joint	110
Figure 4.21 Interior joint modeling schematic	112
Figure 4.22 Steel reinforcement layout showing insignificant beam bottom bar embedment	113
Figure 4.23 Assumed depth used to define concrete stress-displacement relationship (Berry and Eberhard 2007).....	115
Figure 4.24 Exterior joint modeling schematic	116
Figures 4.25 and 4.26 Example interior joint plots with good modeling accuracy	118
Figures 4.27 and 4.28 Example interior joint plots with poor modeling accuracy.....	119
Figure 4.29 Pantelides 1 experiment and model results	120
Figure 4.30 Aycardi Exterior experiment and model results.....	121
Figure 4.31 Experimental and analytical floor displacements from 1/3 scale structure.....	125
Figure 5.1 Illustration of the gravity/lateral tributary areas for a space frame and perimeter frame..	130
Figure 5.2 MCE ground motion spectrum at the high seismic California site	132
Figure 5.3 Design documentation for SMF4-1.2-00	132
Figure 5.4 Design documentation for OMF4-1.2-00.....	133
Figure 5.5 Frame model components	134

Figure 5.6 Perimeter frame loading.....	135
Figure 5.7 Space frame loading.....	136
Figure 5.8 P- Δ column formulation.....	137
Figure 5.9 Pushover load pattern.....	139
Figure 5.10 Pushover response for the 4-Story SMFs.....	141
Figure 5.11 Drift profiles for 4-Story SMFs: (a) at maximum base shear and (b) at failure.....	141
Figure 5.12 Pushover response for the 12-Story SMFs.....	142
Figure 5.13 Drift profiles for 12-Story SMFs: (a) at maximum base shear and (b) at failure.....	142
Figure 5.14 Pushover response for the 4-Story OMFs.....	144
Figure 5.15 Drift profiles for 4-Story OMFs: (a) at maximum base shear and (b) at failure.....	144
Figure 5.16 Pushover response for the 12-Story OMFs.....	145
Figure 5.17 Drift profiles for 12-Story OMFs: (a) at maximum base shear and (b) at failure.....	145
Figure 5.18 Plot of Moment vs. Curvature (Paspuleti 2002).....	147
Figure 5.19 Ductility demand legend for pushover results.....	148
Figure 5.20 SMF4-1.2-00: Pushover Curve with Curvature Ductility Points.....	148
Figure 5.21 SMF4-1.2-00: Drift and Curvature Ductility Plots.....	148
Figure 5.22 OMF4-1.2-00: Pushover Curve with Curvature Ductility Points.....	149
Figure 5.23 OMF4-1.2-00: Drift and Curvature Ductility Plots.....	149
Figure 5.24 SET 1A Spectra.....	151
Figure 5.25 SET 1B Spectra.....	152
Figure 5.26 SET 2 Spectra.....	153
Figure 5.27 Example of scaling to a specific period.....	154
Figure 5.28 Example spectrum scaling.....	156
Figure 5.29 Set 1A average spectra.....	156
Figure 5.30 Set 1B average spectra.....	157
Figure 5.31 Set 2 average spectra.....	157
Figure 5.32 Foreshock-Aftershock ground motion pair.....	159
Figure 5.33 Roof drift response for SMF4-1.2-00 when excited by moderate GM 111 and GM 83.....	160
Figure 5.34 Second floor column drift responses for foreshock.....	161
Figure 5.35 Second floor column drift responses for foreshock-aftershock pair.....	162
Figure 5.36 SMF4-1.2-00 probability of damage states given the foreshock intensity.....	166
Figure 5.37 OMF4-1.2-00 probability of damage states given the foreshock intensity.....	166
Figure 5.38 SMF4-1.2-00 probability of damage states give the foreshock damage state.....	168

Figure 5.39 OMF4-1.2-00 probability of damage states given the foreshock damage state	168
Figure 5.40 Comparison of results for (a) SMF4-1.2-00 and (b) SMF4-1.2-0J	170
Figure 5.41 Comparison of results for (a) SMF4-1.2-00 and (b) SMF12-1.2-00.....	171
Figure 5.42 Comparison of results for (a) SMF12-1.2-00 and (b) SMF12-WS-00.....	171
Figure 5.43 Comparison of results for (a) SMF4-1.2-00 and (b) OMF4-1.2-00	172
Figure 5.44 Comparison of results for (a) OMF4-1.2-00 and (b) OMF4-1.2-0J	172
Figure 5.45 Comparison of results for (a) OMF4-1.2-00 and (b) OMF4-1.2-SJ.....	173
Figure 5.46 Comparison of results for (a) OMF4-1.2-00 and (b) OMF4-0.8-00	173
Figure 5.47 Comparison of results for (a) OMF4-1.2-00 and (b) OMF4-2.0-00	174
Figure 5.48 Comparison of results for (a) OMF4-1.2-00 and (b) OMF12-1.2-00	174
Figure 5.49 Comparison of results for (a) OMF12-1.2-00 and (b) OMF12-WS-00	175

List of Tables

Table 2.1 ATC-58 damage states for columns	8
Table 2.2 Damage state comparison.....	9
Table 3.1 Flexural damage progression and description	40
Table 3.2 Shear damage progression and description	48
Table 3.3 Drift at Flexural Damage States for Bae Specimens	60
Table 3.4 Drift at Shear Damage States for Sezen Specimens	60
Table 3.5 Damage Data: Flexure-Critical Columns	62
Table 3.6 Damage Data: Shear-Critical Columns	62
Table 3.7 ASCE41-06 column parameters	68
Table 3.8 Pre-1976 Column Properties	68
Table 3.9 Predicted drift for pre 1976 column (Shear-Critical)	69
Table 3.10 Flexure-Critical Columns with low axial loads: median drifts.....	70
Table 3.11 Flexure-Critical Columns with high axial loads: median drifts	71
Table 3.12 Proposed drift at onset of flexural damage states	73
Table 3.13 Shear-Critical Columns with low axial loads: median drifts.....	74
Table 3.14 Shear-Critical Columns with high axial loads: median drifts.....	74
Table 3.15 Proposed Drift at onset of Shear Damage States.....	75
Table 3.16 Residual drift data	80
Table 3.17 Residual drift data using bilinear technique	81
Table 3.18 Residual ratio data	83
Table 4.1 Raw data from experimental tests and analytical models.....	101
Table 4.2 Statistical data from experimental tests and analytical models	102
Table 4.3 Raw Data from Experimental Tests and Analytical Models	108
Table 4.4 Statistical data from experimental tests and analytical models	108
Table 4.5 Average bond strengths	114
Table 4.6 Raw data from experimental tests and analytical models.....	122
Table 4.7 Statistical data from experimental tests and analytical models	123
Table 4.8 Initial testing program for 1/3 scale structure.....	124
Table 5.1 Information for RC frame parameter study	129
Table 5.2 Design assumptions used by Haselton	131
Table 5.3 4-Story SMF pushover results.....	143

Table 5.4 12-Story SMF pushover results	143
Table 5.5 4-Story OMF pushover results	146
Table 5.6 12-Story OMF pushover results	146
Table 5.7 Pushover failure mechanism results	150
Table 5.8 Ground motion summary	153
Table 5.9 Frame periods for ground motion scaling purposes	155
Table 5.10 Full suite of foreshock-aftershock simulations.....	158
Table 5.11 Reduced set of damage states for use in building analysis: flexure-critical columns with low axial loads.....	163
Table 5.12 Reduced set of damage states for use in building analysis: flexure-critical columns with high axial loads.....	163
Table 5.13 Reduced set of damage states for use in building analysis: shear-critical columns with low axial loads.....	164
Table 5.14 Reduced set of damage states for use in building analysis: shear-critical columns with high axial loads.....	164

Acknowledgments

This research would not have been possible without the guidance of Professor Laura Lowes. The rest of the research team (Jong-Su Jeon, Dr. Reginald DesRoches, Stephanie German, and Dr. Ioannis Brilakis) at Georgia Institute of Technology also deserve credit for making my portion of the research possible. Thanks also must go to Dr. Marc Eberhard and Dr. John Stanton for providing their input serving on my committee.

Thank you to the National Science Foundation for providing funding for this research.

Without the support of my family back in Indiana and friends here at the UW, I would not have been able to make it through graduate school.

Chapter 1: Introduction

1.1 Background and Motivation

The February 2011 Christchurch earthquake was a devastating event that caused major damage in and around the city of Christchurch. In the weeks following this and any major earthquake, assessing the structural integrity of damaged buildings and infrastructure is exceedingly important. The aftermath of recent earthquakes around the world has shown that it can take weeks or even months to inspect and grant access to damaged buildings. Prior to access being granted to structurally sound buildings, families may be displaced from homes and businesses are without facilities.

The research presented here contributes to a collaborative research project conducted by faculty and students at the University of Washington and Georgia Tech and funded by the National Science Foundation (NSF) with the goal of developing a semi-automated procedure for post-earthquake inspection and assessment of reinforced concrete (RC) buildings. Currently, buildings are evaluated by certified on-site building inspectors using guidelines from ATC-20 (1991). This process is subjective, time consuming, and costly.

The proposed technique, Figure 1.1, will utilize a hard-hat mounted camera taking video as an inspector walks through a damaged RC building. The images will be transmitted via a hand-held PDA to an off-site computer to be analyzed. Image analysis will characterize building component damage and quantify the severity and distribution of damage within the structure. Damage data will then be used to query a database of results of numerical simulations of undamaged and damaged structures to estimate the condition of the building. This information is then used by an on-site inspector to make a faster, less subjective decision about the building's structural integrity. Throughout this document the goals of the UW-GA Tech Project will be tied to the work presented in this document. The overall project will be referred to as the UW-GA Tech Project.

In RC frames, gravity loads are carried by columns; thus, column failure is a primary cause of collapse for older RC frame buildings and assessing the structural integrity of RC columns after a seismic event is critical to evaluating the collapse risk of a damaged structure. The research presented here seeks to use data from previous experimental tests of concrete columns to establish a link between observed damage and the structural performance state of the column and to develop fragility functions characterizing the collapse risk of a damaged structure subjected to an aftershock of variable intensity. These research results will be combined with results of research addressing image processing and with other fragility functions to achieve the overall objectives of the UW-GA Tech Project described above.

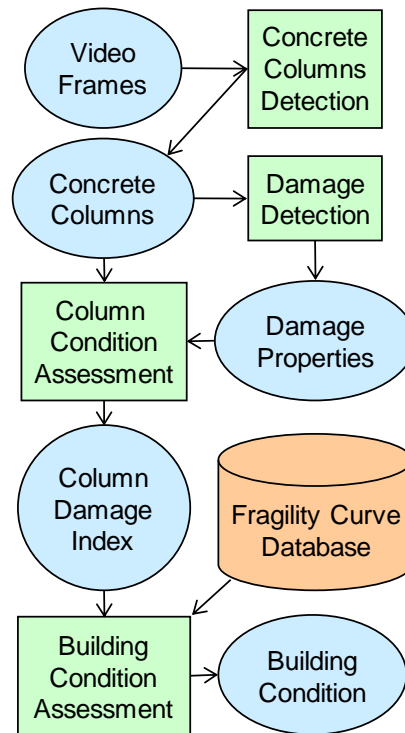


Figure 1.1 Proposed framework

1.2 Research Objectives

The objectives of the current study are to link observed damage with structural performance for RC columns, link damage states with engineering demand parameters, and determine the likelihood a damaged structure will reach a particular damage state in an aftershock. It is expected that images of component damage, data characterizing the severity of damage, and estimates of the collapse risk posed by the damaged building will enable a qualified inspector to provide an offsite assessment of the structure. The ability to have offsite assessment of structural safety will greatly reduce the time required to inspect the building inventory after an earthquake and thereby speed recovery.

Structural performance and engineering demand parameters were linked for two different column response modes: flexure and shear. For each response mode a series of damage states were established that represent progressively more severe damage and less residual capacity. A damage state was defined by observed damage and the range of story drifts for which this damage state has been observed to occur. The observed damage was described by the orientation, spacing, and width of concrete cracks; the location, extent, and depth of concrete spalling; and the location and extent of longitudinal reinforcement buckling. The results of previous experimental tests were used to establish the damage characteristics and the link between damage and engineering demand parameters.

Analysis results were used to develop fragilities defining the likelihood a previously damaged structure will develop a particular damage state as a result of an aftershock. Specifically an idealized RC frame was subjected to a series of random pairs of earthquake records where the pair of records was intended to represent the main earthquake and the aftershock. The damage state of the structural components following the first earthquake determines the damage state of the structure after the main earthquake and the damage state of the structural components following the second earthquake establishes the damage state of the structure after the aftershock. These data were used to develop fragilities defining the likelihood a damaged structure will reach a particular damage state, including the “collapse” damage state in an aftershock. Multiple RC frame heights and designs were considered. The results of previous tests were used to validate numerical models

1.3 Thesis Organization

Research activities and results are presented as follows:

Chapter 2 presents a review of previous research pertinent to the current study. Previous experimental investigations of RC columns, from which the progression of damage and demand at a damage state were determined, are summarized. Data from these tests were used also to validate numerical models. Additionally, previous research addressing elastic effective stiffness of columns and numerical modeling of RC frames was reviewed. Finally, previous research that addresses analyses of RC frames to establish performance and collapse risk are reviewed.

Chapter 3 establishes damage states for flexure-critical and shear-critical columns with both low and high axial loads. This chapter discusses the effects of bi-directional loading on the damage progression and the loss of load-carrying capacity in RC columns. Correlating drift, the EDP chosen for this research effort, with each damage state was also accomplished. Multiple sources were used to propose drifts that correspond to RC column damage states. Finally, experimental data characterizing residual drifts, unloading stiffness, and secant stiffness for RC columns subjected to cyclic loading in the laboratory are reviewed.

Chapter 4 addresses modeling of RC frames. Material models, beam-column element models, and joint models are presented. A preferred set of models was established and these models are validated through comparisons of simulated and observed results.

Chapter 5 describes the full-frame nonlinear modeling activities and results. A discussion of the frame design and modeling assumptions was provided. Pushover and dynamic analysis under pairs of earthquake ground motions are described and the results of the analytical parameter study are discussed. The results predicting the probability of a damage state occurring based on an initial seismic event and a

second event are presented. Finally, fragilities describing the likelihood of a damaged frame achieving a particular damage state are presented.

Chapter 6 summarizes the research effort, provides conclusions, and makes recommendations for future work.

Additional information about the RC column damage states, modeling results, frame designs, and ground motions used for the dynamic simulations was provided in appendices at the end of this document.

Chapter 2: Literature Review

2.1 Introduction

This chapter reviews literature addressing the seismic response of reinforced concrete columns and frames. Included in this literature review is the column database used to correlate damage with demand, work done on predicting damage, and modeling techniques for inelastic analysis of RC frames.

2.2 Damage Identification

The first objective of this study was to link observed damage with structural performance for RC columns. A review of past experimental tests was conducted to establish a detailed characterization of damage in RC building columns. Older and modern columns must be considered to have potentially unique damage states due to the potential of having unique failure mechanisms. Experiments performed on rectangular columns were pertinent to this study, as building columns are typically rectangular. Establishing an image set of the damage states was deemed important for the purpose of testing the machine vision algorithms used to detect structural component damage in RC elements. Images of experimental tests also provide useful information regarding the damage state description.

The review focused on the UW/PEER Structural Performance Database (Berry, Parrish and Eberhard 2005), which has been referred to as the Database throughout the document, to identify experimental investigations with image sets. The Database has a comprehensive user's manual (Berry, Parrish and Eberhard 2005) that describes the included data. The results of cyclic lateral-load tests for RC columns compiled by researchers at the National Institute of Standards and Technology and the University of Washington are available in the Database. Column geometry, material properties, axial load, force-displacement history, and displacement at various damage observations are included. The Database includes data from tests for 306 rectangular reinforced columns and 177 spiral reinforced columns. The 177 spiral reinforced columns were not considered to be representative of building columns due their geometry and were not used in this work. One or more references are provided for each test specimen. Recent research conducted on RC columns, not in the Database, was also reviewed.

Many of the tests in the Database were performed before digital photography was commonly employed in the lab. This caused difficulties in finding high quality images corresponding to damage states. The initial database review identified tests that had reported damage data and occurred after 1993 in hopes of finding tests with high-resolution digital images. Five flexure-critical, one shear-critical, and three flexure-shear-critical columns in seven test programs occurred after 1993. Only one report (Sezen 2002) from the Database was available with a high-quality image set. Further investigation identified a

research program (Bae 2005) that tested five full-scale columns in 2005 that were not included in the Database. The six test programs that did not provide high-quality images were not used to characterize damage states. The Sezen and Bae reports are summarized in the following section.

2.2.1 Individual Test Programs

Sezen (2002)

The primary goal of the Sezen study was to determine the principal causes of shear failure and axial load collapse of lightly reinforced columns. Four square columns, 18 inches, were tested. The columns were 116 inches long and tested under a double cantilever configuration. The double cantilever configuration represented a full column bent in double curvature. The first specimen was used as a reference specimen. It was subjected to an axial load of 15% of its nominal axial strength. The second specimen was identical to the first except for the axial load which was 60% of its nominal strength. The third specimen had a varying axial load and the fourth specimen was subjected to 15% of its nominal strength, but it was loaded laterally in a monotonic fashion. For specimens 1 through 3 the lateral loading was applied in three cycles at incremental deflections until loss of lateral and axial load-carrying capacity were observed.

The columns responded in a similar fashion at small displacements. Horizontal cracks were prevalent at the ends of the columns. As the lateral deformations increased shear cracking occurred. Some spalling occurred at the tops and bottoms of the specimens. The four columns were categorized as being shear-critical by Sezen. A complete description of the damage progression can be found in Section 3.3.4 along with images from the report.

Bae (2005)

One of the primary goals of the Bae study was to investigate the impact of span-to-depth ratio and axial load on ductility and drift-capacity. A second objective was to develop a model for estimating deformation capacity. Five full-scale square columns, 4 at 24 inches and 1 at 17 inches, were tested. The columns were 104-inches long and tested in a cantilever configuration. The test specimens represented half of a column bent in double curvature. The testing procedure was initiated by applying a constant axial load. Three of the columns were subjected to an axial load of 50% of their nominal axial strength, and two of the columns were subjected to 20% of their nominal strength. The columns were then subjected to three cycles of progressively larger lateral displacements. During the first displacement cycle, approximately 75% of the column shear strength was applied. The resulting load-displacement curve was used to determine a yield displacement, Δ_y . The displacement cycles were increased, Δ_y , $2\Delta_y$, $3\Delta_y$, etc., until loss of lateral and axial load-carrying capacity were observed.

Similar results were obtained at the initial drift levels. The first flexural cracking occurred approximately six inches from the bottom of the columns. Longitudinal cracking occurred at $2\Delta_y$, and spalling occurred on the front and back faces in the following cycles. At $3\Delta_y$ the side cover spalled, and by $4\Delta_y$ the front and back cover had completely spalled to at least 30 inches from the base of the column. The three columns tested under high axial load ($0.5P_0$) experienced a sudden failure from $6\Delta_y$ to $8\Delta_y$ due to excessive core concrete damage. The other two columns did not experience axial load loss until displacements of $8\Delta_y$ and $10\Delta_y$. The five columns were categorized as being flexure-critical by Bae. A complete description of the damage progression can be found in section 3.3.3 along with images from the report.

2.3 Observed Damage

An objective of the current study was to link damage states with engineering demand parameters. Two sources of damage state data linked to drift, an EDP, are the Database and the ATC-58 report developed by Lowes et al. (2010). Chapter 3 presents the Database data and uses the ATC-58 document to develop the damage progression.

The Database includes damage data for column tests for which damage was documented by the researcher. The maximum displacement sustained by the test specimen prior to the onset of a particular damage state was included in the dataset. The damage states included in the Database are the onset of spalling, onset of significant spalling, onset of bar buckling, longitudinal bar fracture, transverse reinforcement fracture, and loss of axial load-carrying capacity. The onset of spalling was defined as the first observation of spalling. The onset of significant spalling was defined by the observation of “significant spalling” or “considerable spalling.” If spall heights were recorded or easily determined, significant spalling was defined as a spall height equal to at least 10% of the cross-section depth. Onset of bar buckling was defined as the observation of the first sign of bar buckling. Longitudinal bar fracture was defined as the first observed longitudinal bar fracture. Transverse reinforcement fracture was defined as the observation of the first sign of transverse reinforcement fracturing or the untying of transverse reinforcement. Loss of axial load-carrying capacity was defined as the observation of the loss of axial load-carrying capacity.

The ATC-58 report also provides damage categories for RC components. The goal of the report was to link demand with damage and ultimately with repair method and cost. Fragility functions are presented defining the likelihood that an RC frame will achieve a particular damage state. This damage state corresponds to a repair method. The report uses the Database to supplement the damage data taken from a literature review of reinforced concrete joints. Six damage states were defined to characterize the

damage progression. The report uses damage states that correlate well with a repair technique. Each of the six states corresponded to a repair activity.

The ATC-58 damage states are damage to finishes, concrete cracking, moderate concrete cracking, concrete spalling, concrete crushing, and steel yielding, buckling, or fracture. The damage states are described in further detail in the second column of Table 2.1. The first column in Table 2.1 identifies the naming convention of the damage states in the ATC-58 document.

Table 2.1 ATC-58 damage states for columns

Damage State	Frame Damage Characteristics
C	Damage to finishes: Cosmetic finishes exhibit damage but residual concrete crack widths are too narrow to require repair. Hairline cracking of concrete. Longitudinal reinforcement yields.
0	Concrete Cracking: Residual crack widths that require epoxy injection. Residual concrete crack widths exceed 0.02 in. Yielding of longitudinal reinforcement.
1	Moderate Concrete Cracking: Residual crack widths that require epoxy injection. Residual concrete crack widths exceed 0.06 in.
2	Concrete Spalling: Spalling of cover concrete that exposes transverse but not longitudinal reinforcing steel.
3	Concrete Crushing: Spalling of cover concrete exposes longitudinal reinforcement. Strength loss initiates in laboratory.
4	Steel yielding, buckling, and fracture: Reinforcing steel experiences severe inelastic deformation and requires replacement. Longitudinal steel exhibits severe inelastic strain, buckling, or fracture.

The ATC-58 damage states focus on the early stages in the progression of damage. The first three damage states cover the progression of cracking. The Database does not focus on the initial damage progression due to the difficulty in identifying the initial cracking in reinforced concrete test reports. There was some compatibility between the damage states used to develop the ATC-58 report and those provided in the Database. Table 2.2 indicates the damage states used from the Database in the ATC-58 report. The first three ATC-58 damage states do not have a corresponding Database damage state. The final three Database damage states do not have a corresponding ATC-58 damage state.

Table 2.2 Damage state comparison

PEER Structural Performance Database	Damage States						
		Onset of Spalling	Significant Concrete Spalling	Long Bar Buckling	Long Bar Fracture,	Spiral Fracture,	Axial Capacity Loss
ATC-58	C,0,1	2	3	4			

2.4 Drift Capacity Models

An objective of this research was the prediction of collapse risk of RC frames. Previous research to develop models defining the drift at which a column loses lateral and axial load-carrying capacity can be used to predict the risk of collapse. Three papers documenting four drift-capacity models are summarized in this section. The summaries include a brief description of the models, characteristics of the empirical data set, and the proposed equation defining drift-capacity. Drift capacity, as described above, may refer to the drift at which lateral load-carrying capacity is lost or the drift at which axial load-carrying capacity is lost. The numerical models presented below define one or the other.

“Drift Capacity of Reinforced Concrete Columns with Light Transverse Reinforcement” (Elwood and Moehle 2005)

This paper presents an empirical drift-capacity model for loss of lateral load-carrying capacity due to shear failure for shear-critical columns. An experimental database consisting of 50 rectangular reinforced concrete column tests was compiled to calibrate the model. The proposed empirical drift-capacity model was based on observations from the database. It was observed that drift was affected by maximum shear stress, transverse reinforcement ratio, and the axial load ratio. The following expression is the equation used to estimate drift at shear failure:

$$\frac{\Delta_s}{L} = \frac{3}{100} + 4\rho'' - \frac{1}{500} \frac{v}{\sqrt{f'_c}} - \frac{1}{40} \frac{P}{A_g f'_c} \geq \frac{1}{100} \quad (2.1)$$

where Δ_s = displacement at shear failure (20% loss in peak shear), L = clear height of the column, ρ'' = transverse reinforcement ratio, v = maximum nominal shear stress, f'_c = concrete compressive strength, P = axial load, and A_g = gross cross-sectional area of the column.

- **Prediction of Model:** The model predicts the drift at shear failure in rectangular reinforced concrete columns. Shear failure was defined as the displacement, Δ_s , when shear resistance dropped below 80% of the maximum recorded shear.
- **Characteristics of Empirical Data Set:** The columns used for this research were intended to be representative of shear-critical columns from older reinforced concrete buildings. The columns in the

database met the following criteria where d is the depth to the centerline of the outermost tension reinforcement, s is the spacing of transverse reinforcement, ρ_l is the longitudinal reinforcement ratio, ρ'' is the transverse reinforcement ratio, A_g is the gross area of the column, f'_c is the compressive strength of the concrete, and P is the axial load:

- Transverse reinforcement spacing to depth ratio: $2.0 \leq \frac{s}{d} \leq 4.0$
- Longitudinal reinforcement ratio: $0.01 \leq \rho_l \leq 0.04$
- Transverse reinforcement ratio: $0.0010 \leq \rho'' \leq 0.0065$
- Axial load ratio: $0.0 \leq \frac{P}{A_g f'_c} \leq 0.6$

“An Axial Capacity Model for Shear-Damaged Columns” (Elwood and Moehle 2004)

This paper presents a model predicting the drift at loss of axial load-carrying capacity for a shear-critical column. The model was developed using data from a small number of tests: twelve rectangular reinforced concrete columns tested by Sezen (2002) and Lynn (2001). The following expression is the equation used to estimate drift at loss of axial load-carrying capacity:

$$\frac{\Delta_a}{L} = \frac{4}{100} \frac{1 + (\tan\theta)^2}{\tan\theta + P \left(\frac{s}{A_{st} f_{yt} d_c \tan\theta} \right)} \quad (2.2)$$

where Δ_a = displacement at axial failure, L = clear height of the column, θ = angle from horizontal of the critical shear failure plane, P = axial load, A_{st} = area of transverse reinforcement, f_{yt} = yield strength of transverse reinforcement, and d_c = depth of core concrete.

- **Prediction of Model:** The model predicts the drift at axial failure in shear-critical rectangular reinforced concrete columns.
- **Characteristics of Empirical Data Set:** The columns used for this research were intended to be representative of shear-critical columns from reinforced concrete buildings. The columns in the data set met the following criteria. The notation is the same as the previous model.
 - Transverse reinforcement spacing to depth ratio: $2.0 \leq \frac{s}{d} \leq 4.0$
 - Longitudinal reinforcement ratio: $0.02 \leq \rho_l \leq 0.03$
 - Transverse reinforcement ratio: $0.0025 \leq \rho'' \leq 0.0065$
 - Axial load ratio: $0.12 \leq \frac{P}{A_g f'_c} \leq 0.6$

“Classification and Seismic Safety Evaluation of Existing Reinforced Concrete Columns” (Zhu, Elwood and Haukaas 2007)

This paper presents probabilistic drift-capacity models. The first model predicts the drift at 20% loss in lateral load-carrying capacity. The second model predicts the drift at loss of axial capacity for shear-critical columns.

The classification of columns as shear-critical or flexure-critical was also discussed. To categorize the columns a two-zone column classification method was used. The three column parameters used to identify the failure mechanism were plastic shear demand to shear strength ratio (V_p/V_n), the aspect ratio (a/d , where a is the shear span and d is the depth to the centerline of the outermost tension reinforcement), and the transverse reinforcement ratio (ρ''). To develop the models, columns from the Database were used based on the characteristics of the empirical data set shown below.

$$\delta_{ss} = 2.02\rho'' - 0.025\frac{s}{d} + 0.013\frac{a}{d} - 0.031\frac{P}{A_g f'_c} \quad (2.3)$$

$$\delta_{as} = 0.184 e^{-1.45\mu} \quad \text{where } \mu = \frac{\frac{P}{A_{st} f_{yt} d_{c/s}} - 1}{\frac{P}{A_{st} f_{yt} d_{c/s}} \frac{1}{\tan \alpha} + \tan \alpha} \quad \text{and } \alpha = 65^\circ \quad (2.4)$$

where δ_{ss} = drift at lateral failure for shear-critical columns, ρ'' = transverse reinforcement ratio, s = transverse reinforcement spacing, d = depth to the centerline of the outermost tension reinforcement, a = shear span, f'_c = concrete compressive strength, P = axial load, A_g = gross cross-sectional area of the column, δ_{sf} = drift at lateral failure for flexure-critical columns, ρ'' = transverse reinforcement ratio, ρ_l = longitudinal reinforcement ratio, f_{yt} = yield strength of transverse reinforcement, δ_{as} = drift at axial failure for shear-critical columns, d_c = depth of core concrete, and A_{st} = area of transverse reinforcement.

- **Predictions of Models:** The models predict drift at shear and axial failure in rectangular reinforced concrete columns. Shear failure was defined as the displacement, Δ_s , when shear resistance dropped below 80% of the maximum recorded shear. The axial failure model should not be applied to shear-dominated columns.
- **Characteristics of Empirical Data Set:** The columns used for this research were intended to represent older columns in reinforced concrete buildings. The columns in the data set met the following criteria. The notation is the same as the previous model.
 - Transverse reinforcement spacing to depth ratio: $0.1 \leq \frac{s}{d} \leq 1.2$
 - Longitudinal reinforcement ratio: $0.012 \leq \rho_l \leq 0.033$
 - Transverse reinforcement ratio: $0.0006 \leq \rho'' \leq 0.022$
 - Axial load ratio: $0.0 \leq \frac{P}{A_g f'_c} \leq 0.8$

2.5 Reinforced Concrete Modeling

To accomplish the objective of predicting the likelihood a damaged structure will reach a particular damage state in an aftershock, RC modeling and analysis techniques must be used to simulate the response of frames. A literature review was conducted to identify reinforced concrete modeling techniques. The review covers element modeling, code based modeling, and past research on full frame modeling.

The analysis platform selected for this study was the Open System for Earthquake Engineering Simulation, OpenSees. OpenSees is an open source, object-oriented software framework. It provides a platform for simulating the response of structural systems subjected to different types of loads, including earthquake loading (OpenSeesWiki 2011). OpenSees elements and materials can be used to create a previously proposed model. The element modeling discussion below will discuss the applicability and availability of element formulations in OpenSees.

2.5.1 Element Modeling

This research intends to simulate the response of a range of RC frames. Special moment frames per current ACI provisions and frames with detailing that was representative of older frames in zones of high seismicity are included in the modeling effort. Thus, simulating the flexural response of beams and columns, shear failure of columns, and joint failure was required to capture the response of the set of frames. A review of element formulations used to simulate these response modes and studies using the formulations are presented below.

2.5.1.1 Beam-Column Models

OpenSees provides three beam-column element formulations that allow for simulation of nonlinear material response. One method was to model columns using lumped plasticity in which the nonlinear behavior is focused at the ends of an elastic element. The other two modeling techniques simulating nonlinear response are distributed plasticity formulations based on finite-element methods. Two simplified element formulations do not account for material nonlinearity. They are the simple elastic model and effective stiffness model. These models are incapable of capturing the degrading behavior of beam-column elements as they approach failure, and have not been considered further in this research effort.

- Lumped Plasticity Element Formulation

All members (beams and columns) are modeled using a force-based element formulation in which nonlinear behavior occurs in plastic hinge regions at the ends of the element. A fiber

section is utilized to define the inelastic moment-curvature response of the plastic hinge regions. One-dimensional concrete and steel material models are also used to develop element cross section response. A plastic hinge integration scheme based on a modified Gauss-Radau quadrature scheme was developed by Scott and Fenves (2006) to overcome the strain-softening issues that arise with Gauss-Lobatto integration.

OpenSees implements the **beam with hinges element** (BWH) by dividing it into three pieces: two inelastic hinges at the ends and an elastic center region. The BWH element localizes the integration points in the hinge. The inelastic hinges are defined by assigning a fiber section; the elastic section is assigned using the dimensions of the member cross section and concrete modulus of elasticity. Plastic hinge length must also be defined.

– Nonlinear Force-Based Element Formulation

All members (beams and columns) are modeled using a **force-based beam-column element** formulation in which nonlinear behavior is allowed to spread along the length of the element. A linear moment distribution is assumed over the length of the elements. The deformation is defined by the curvatures developing at integration points along the length of the element. An integration scheme is applied to represent the distributed plasticity in the elements. Multiple numerical integration options have been discussed in previous research. The Gauss-Lobatto integration is the most common approach for evaluating the response of force-based elements because it places an integration point at each end of the element (Neuenhofer and Filippou 1997). A fiber section is utilized to define the inelastic moment-curvature response of the element.

OpenSees implements the **force-based beam-column element** by assigning a fiber section to the element and defining the number of integration points along the length of the element.

– Nonlinear Displacement-Based Element Formulation

All members (beams and columns) are modeled using a **displacement-based beam-column element** formulation in which nonlinear behavior is allowed to spread along the length of the element. To approximate nonlinear element response, constant axial deformation and linear curvature distribution are enforced along the element length. The Gauss-Lobatto quadrature rule is the default integration scheme for displacement-based elements. A fiber section is utilized to define the inelastic moment-curvature response of the element.

OpenSees implements the **displacement-based beam-column element** by assigning a fiber section to the element and defining the number of integration points along the length of the element.

The lumped plasticity element formulation was well suited for the current study. It concentrates the inelastic response at the ends of elements. This matches the degrading behavior of RC elements as discussed in Chapter 3. The OpenSees lumped plasticity element requires a plastic hinge length definition. Plastic hinge length models have been developed by many researchers. Two simple approaches were developed by Corley (1966) and Mattock (1967). Corley's equation for l_p , the plastic hinge length, is the following expression.

$$l_p = \frac{d}{2} + 0.2 \frac{z}{\sqrt{d}} \quad (2.5)$$

Mattock's equation for l_p is the following equation.

$$l_p = \frac{d}{2} + 0.05z \quad (2.6)$$

Both these equations depend on d , the effective depth of the member, and z , the distance from the critical section to the point of contra-flexure. Park et al. (1982) suggested simply using $0.5H$ as the plastic hinge length for RC columns; where h is the depth of the member. Priestley and Park (1987) proposed the following equation.

$$l_p = 0.08L + 6d_b \quad (2.7)$$

Paulay and Priestley (1992) subsequently refined the above equation to account for different grades of longitudinal reinforcement. The revised equation is given in the following expression.

$$l_p = 0.08L + 0.15d_b f_y \quad (f_y \text{ in ksi}) \quad (2.8)$$

Both these equations depend on L , the distance from the critical section to the point of contra-flexure, and d_b , the diameter of the longitudinal reinforcing bars. The proposed equations for plastic hinge length predict lengths equal to approximately half the depth of the member. The OpenSees models use a plastic hinge length of $0.5H$ where H is the element depth. The suggestion by Park et al. of simply using $0.5H$ was based on standard steel and concrete material strengths and was deemed sufficient for the purposes of this research. The lumped plasticity element with a plastic hinge length of half the depth of the member has been used in all the models presented in Chapter 4 and Chapter 5.

2.5.1.2 Shear Failure Models

To simulate shear failure, one technique is to use a shear strength prediction model. When the predicted shear strength is exceeded by the shear demand on the column it fails in a brittle manner. The

brittle failure is characterized by the column losing its lateral load-carrying capacity. In previous studies completed by Pincheira and Jirsa (1992), Paspuleti (2002), and Theiss (2005) this type of shear modeling was used. Using this approach has limitations and assumes that columns have no lateral stiffness after elements reach their shear capacity.

Shear springs are also a popular technique for modeling the shear response of reinforced concrete columns. In a study performed by Barin and Pincheira (2002) a shear force versus shear strain relationship was defined. The shear data used in the study was input in a Drain-2D model. This model did not fail in a completely brittle manner and retained some residual shear strength after reaching a user defined shear spring deformation.

The Pincheira et al. study (1999) developed a similar column element that incorporated nonlinear shear and rotational springs in series. One negative to this solution is the use of a positive slope on the descending branch of the backbone curve which does not exist. This results in a force unbalance which is applied in the next time step. This procedure may not represent the true characteristics of a softening structure and can be computationally demanding. A similar technique was used by Marini and Spacone (2006). The shear response is modeled using a nonlinear shear stress versus shear strain, $V-\gamma$, relationship. Their proposed technique allows for a brittle or slightly ductile shear failure to be modeled by specifying the points on the envelope curve for the shear response. Some residual shear strength is left after the peak shear strength has been reached.

The shear modeling techniques discussed above initiate shear strength degradation based on the shear force exceeding the specified shear strength. The shear strength degradation during inelastic flexural deformations is not accounted for using these modeling methods; shear failure may not be accurately predicted for columns that experience flexural yielding prior to shear failure.

The shear spring models discussed above concentrate the flexural deformations in the beam-column element and the shear deformations are modeled by the shear spring. When the shear strength is less than the flexural yield strength of the column the models are able to capture the degrading shear behavior. When the shear strength is estimated to be greater than the flexural yield strength the models fail to capture shear degradation. This is not a realistic response for columns which yield in flexure close to their shear strengths. A model that alleviates this issue has been proposed by Elwood (2004). It identifies a shear failure based on both the column shear demand and deformation of the column. The total deformation involves coupling the shear spring and beam-column element. A new uniaxial material model was developed to perform this function. The material model, called limit state material, traces the behavior of the beam-column element and changes the backbone of the material model to include strength degradation once the response of the beam-column element exceeds a predefined limit state surface.

The limit state material model can be used to model any failure mode that triggers a sudden change in component behavior, i.e. shear and axial failure in a RC column. The material model can be used to define the force-displacement response of a shear spring in series with a beam-column element. The material model tracks the beam-column element response. After the shear limit curve is reached on the total response backbone, the response changes to represent a shear failure. The same procedure can be modified to incorporate an axial spring into the column model. The axial capacity model assumes that shear failure has already occurred using a limit state material for shear response. There are downsides to this modeling approach. Owing to the significant change in the response of the structure once a limit curve is reached, the limit state failure model is particularly sensitive to any variability in the limit curves. Limited experimental studies on the response of RC columns after shear and axial failure make it difficult to accurately model the limit curves. Probabilistic models for the limit curves can help to identify the variability associated with modeling different RC columns in building frames.

An extension of Elwood's work has been presented by LeBorgne (2012). A model capable of estimating the lateral strength degrading behavior of RC columns prone to shear failure was developed. The model triggers shear failure when either a shear capacity or plastic hinge rotation capacity is reached. This model monitors the difference in rotation between user defined nodes and triggers degrading behavior in a shear spring. LeBorgne developed the model to take in user defined column parameters using the OpenSees platform.

The LeBorgne model was selected to be used for this research effort. A pilot study, using the technique presented by LeBorgne, was conducted using experimental data from columns with shear failures from the Database. The element formulation did not provide converged solutions for the modeled columns. The failure of the LeBorgne model prompted the use of a simple shear spring, such as the one implemented by Barin and Pincheira. A more detailed discussion of the modeling techniques used for this shear spring formulation is found in Section 4.4.

2.5.1.3 Joint Models

The seismic response of RC beam-column joints is complex and depends on a number of design parameters. Simulating the strength, stiffness, drift-capacity, and failure of joints requires a model complex enough to account for multiple response mechanisms, yet simple enough to guarantee computational efficiency. A literature review was completed by Theiss (2005) that detailed the approaches used to model RC joints. This review will be used as the basis of the review that follows.

The most simple frame models do not account explicitly for joint action. These models assume joints to be completely rigid or flexible. The rigid joints are modeled using rigid offsets equal to the frame

member depth at each beam-column connection. Flexible joints are modeled with the beam-column elements running to the centerline dimensions of the intersection locations. This modeling technique provides the simplest way to model RC frames but fails to simulate the seismic response of the joints.

Many relatively simple models that account for joint action have been proposed for use in full frame seismic simulation. The simple approaches generally require user input, accounting for experimental data, to calibrate the models. These approaches range in sophistication from a zero-length rotational spring element to finite-area super-elements with multiple zero-area rotational springs.

A simple model was developed by Biddah and Ghobarah (1999). Their model implemented one rotational spring for joint shear and one rotational spring for bond slip. Hysteretic models are used for the bond slip spring and the softened truss theory was used to calibrate the shear spring. The marginal increases in modeling accuracy were outweighed by the complex calibration procedures.

The work mentioned above was used by Altoontash (2004) and Lowes et al. (2003) as the basis for the development of beam-column joint models for the OpenSees platform. Altoontash developed a versatile model that has relatively good computational efficiency. Five components, one shear-panel and four joint interface rotations, of joint response are explicitly modeled and make it possible to achieve one of the three primary joint response mechanisms. The model formulation can be seen in Figure 2.1. Different models could be used to simulate the response of the five components. This allows the joint damage to be defined as a function of deformation history, number of load cycles, energy dissipation, or a combination of these parameters.

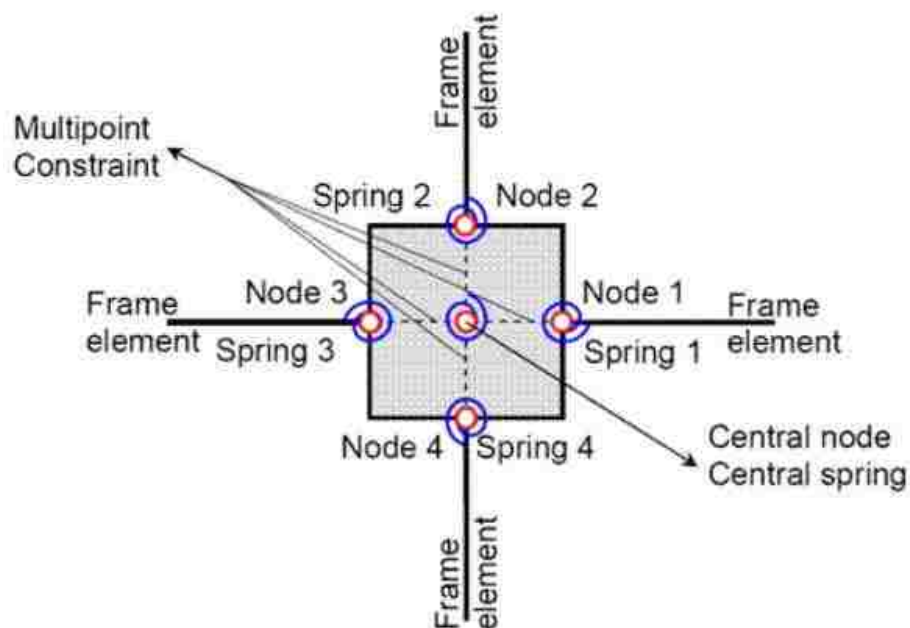


Figure 2.1 Altoontash joint formulation (2004)

The Lowes et al. model implemented a finite area super-element that required relatively few user assumptions. This method accounts explicitly for the primary joint response mechanisms. A shear-panel, eight bar slip, and four interface shear components make up the element and can be seen in Figure 2.2. Each of the components requires a 1D load-deformation response history. Constitutive models were developed to aid in the calibration of the rotational springs. This modeling technique was intended to balance the accuracy of more complex joint models with the computational efficiency of the simple models discussed previously.

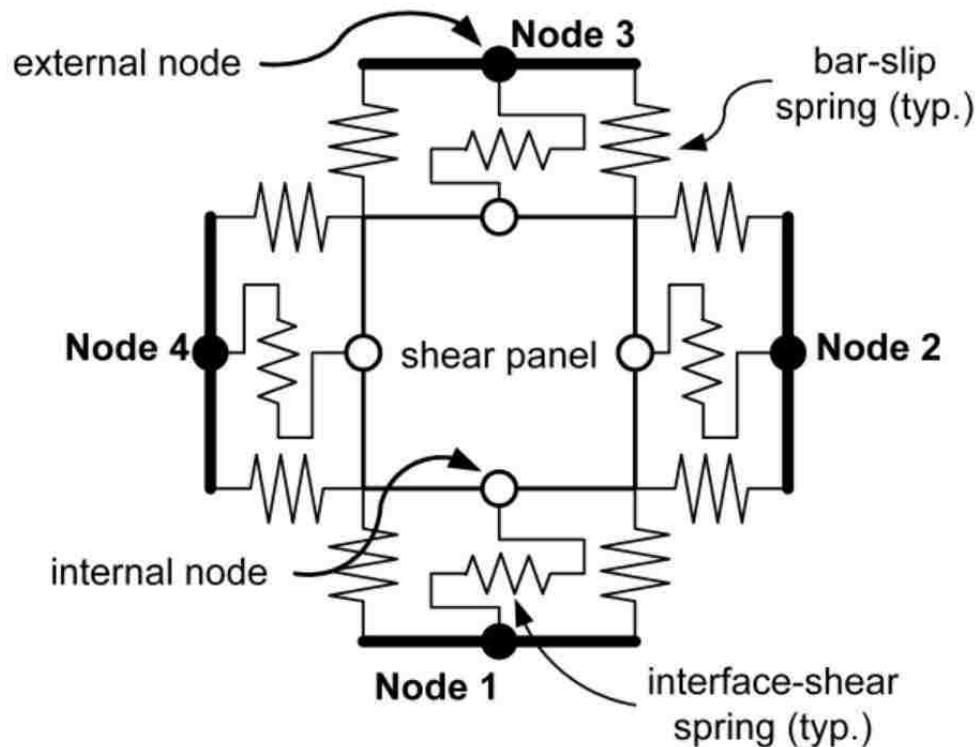


Figure 2.2 Lowes et al. joint formulation (2003)

The Lowes et al. model was selected to be used for this research effort. A pilot study was conducted using experimental data from joints with older RC detailing. This study used Lowes's proposed modeling technique. The recently updated version of OpenSees was not compatible with this element formulation and during dynamic analyses the simulation was unable to find a converged solution. Due to this issue a joint formulation was implemented that had a nonlinear rotational spring at the center of the joint. The rotational spring followed a constitutive relationship developed by Anderson (2003). The joint model also utilized an OpenSees zero-length section that captured the bar slip response of poorly developed longitudinal reinforcement at exterior joints. A more detailed discussion of the modeling techniques used for this joint formulation is found in Section 4.6.

2.5.1.4 Slab Modeling

Slab modeling in slab-column frames is often done by using an equivalent beam representing the portion of the flat slab that contributes to the flexural response. Pan and Moehle (1988) and Luo and Durrani (1995) have shown that lateral loading of a column in a slab-column frame causes a rotation pattern across the slab. The maximum value of the variable rotation occurs near the column and the minimum values occur at the slab centerlines. The equivalent slab-beam is defined as the width that provides the same column displacement as the original slab based on a uniform rotation across its width. The effective width factor is defined as the ratio of the width of the “equivalent” slab to the distance between the columns in the direction perpendicular to the modeling direction.

A study performed by Luo and Durrani (1995) suggested an analytical model for computing the effective slab width using experimental results from forty interior RC beam-column connection tests. A modification factor, χ , is included in the model that is applied to a simplified version of Pecknold's formula. The modification factor was introduced to account for cracking due to gravity loads in an elastic analysis. The following formula is the simplified version of Pecknold's formula for computing the effective slab width ratio, α_i . The terms in the expression are illustrated in Figure 2.3 and the expression is valid for $0.5 \leq c_1/c_2 \leq 2.0$ and $0.5 \leq l_1/l_2 \leq 2.0$.

$$\alpha_i = \frac{1.02 \left(\frac{c_1}{c_2}\right)}{0.05 + 0.002 \left(\frac{l_1}{l_2}\right)^4 - 2 \left(\frac{c_1}{l_1}\right)^3 - 2.8 \left(\frac{c_1}{l_1}\right)^2 + 1.1 \left(\frac{c_1}{l_1}\right)} \quad (2.9)$$

The modification factor developed by Luo and Durrani is defined as follows:

$$\chi = \left(1 - 0.4 \frac{V_g}{4A_c \sqrt{f'_c}}\right) \quad (2.10)$$

where, V_g = direct shear force due to gravity load only

A_c = area of slab critical section (ACI-318-08 2008)

f'_c = compressive strength of concrete

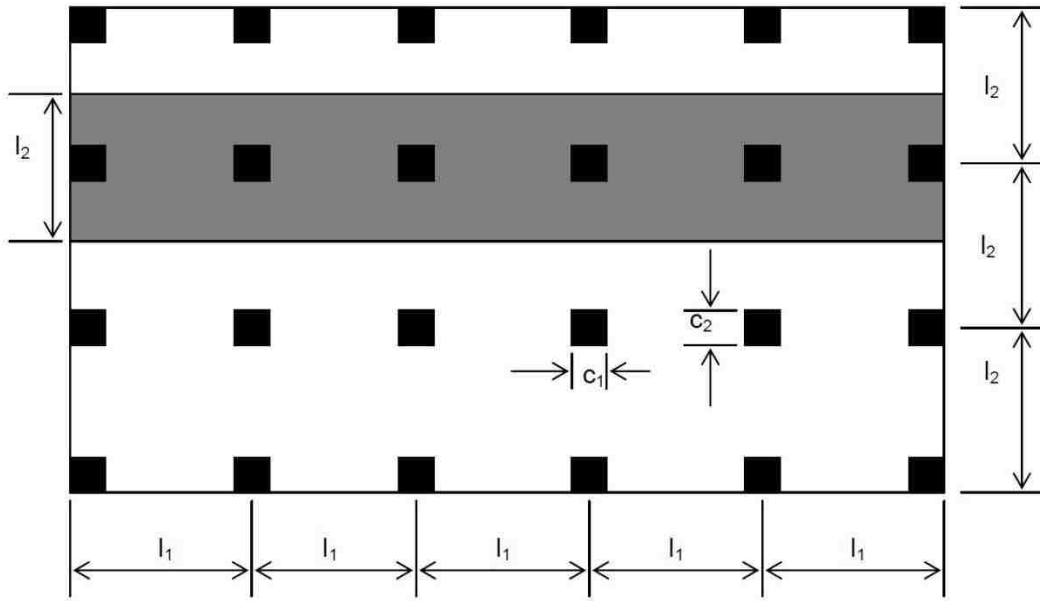


Figure 2.3 Nomenclature for flat slab structures (Luo and Durrani 1995)

The effective moment of inertia, I_e , can be reasonably predicted by the ACI code equation 9-7 (ACI-318-95 1995) according to Luo and Durrani.

Pan and Moehle (1988) tested four RC flat plate slabs under biaxial lateral loading and noted that the slab effective stiffness factor underestimates slab stiffness at low drifts and overestimates the slab stiffness at high drifts. They suggested modifying the elastic equivalent slab width factor by a coefficient of 0.33 for the effective width of cracked slabs.

ASCE 41-06: Seismic Rehabilitation of Existing Buildings (2007) suggest the following formulas for the calculation of the effective width factors for an interior and exterior bay based on Hwang and Moehle's work (2000).

$$\text{Interior Bays: } \alpha = 2c_1 + l_1/3 \quad (2.11)$$

$$\text{Exterior Bays: } \alpha = c_1 + l_1/6 \quad (2.12)$$

where, α is the effective slab width, c_1 , and l_1 can be found in Figure 2.3. To account for cracking, the slab width values should be reduced by an effective stiffness factor (β). ASCE 41-06 recommends the following equation be used for the effective stiffness factor based on Hwang and Moehle's research (2000).

$$\beta = 4c_1/l_1 \geq 1/3 \quad (2.13)$$

After the review of the literature on effective slab width the ASCE 41-06 recommendations for slab effective width factors accounting for the slab's contribution to frame response were chosen for this research effort.

2.5.2 Effective Stiffness Models

A literature review was conducted to identify stiffness models. One paper and four structural codes propose models for effective stiffness. This portion of the literature review was conducted to identify a modeling technique that could be used to reduce the stiffness of the elastic section of the BWH element in OpenSees.

A research effort conducted by Elwood and Eberhard (2009) presented a three-component model that accounts for the effects of flexure, bar slip, and shear deformations. The effective stiffness of 221 rectangular columns were estimated using data from the PEER Database. Figure 2.4 shows the technique used to determine the effective stiffness of each column. A moment-curvature analysis was performed to determine the force at first yield. The calculated effective stiffness were used to evaluate existing models and the proposed model.

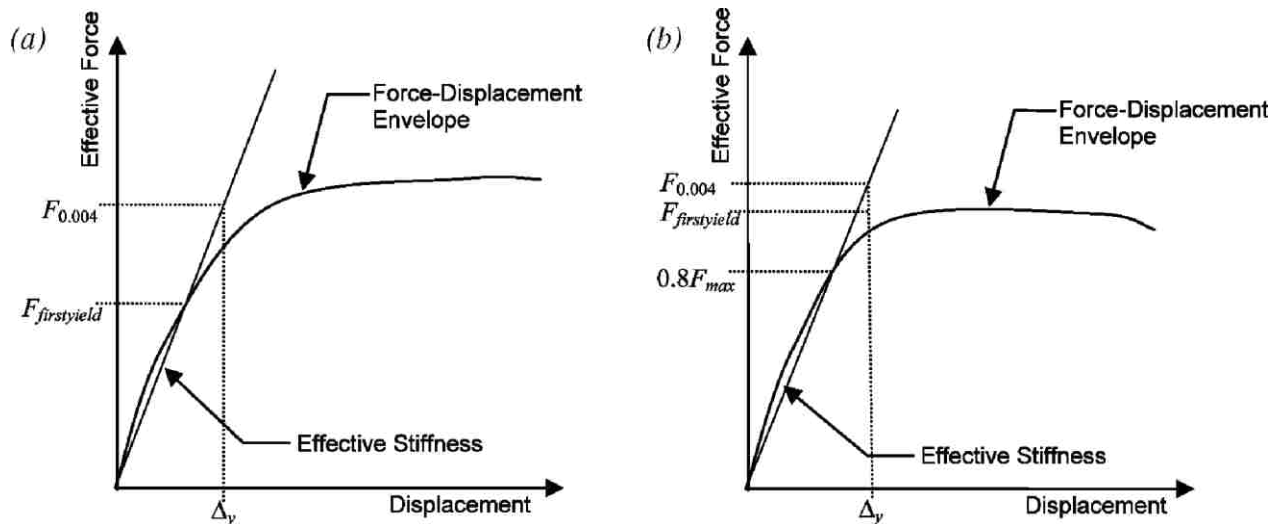


Figure 2.4 Technique to determine effective stiffness

The three-component model considers the displacement contributed by flexure, shear, and bar slip. The proposed model reproduces the trends observed from the calculated stiffness. The paper simplifies the three-component model for design purposes. It uses an approximation to moment-curvature analysis and accounts for bar slip in terms of span-to-depth ratio and axial load ratio. The model was adopted by ASCE 41-06 and has been discussed later in this section.

Due to the impracticality of evaluating properties at multiple cross sections, average values for the effective stiffness of reinforced concrete members are proposed by Paulay and Priestley (1992). An effective moment of inertia is recommended. The recommended effective stiffness is based on the gravity load placed on the column. The recommended effective stiffness for columns with axial loads greater than $0.5f_c'A_g$ is $0.8E_cI_g$. The recommended effective stiffness for columns with axial loads less than $-0.05f_c'A_g$ is $0.4E_cI_g$ (negative axial load means tension). The recommended effective stiffness for columns with axial loads equal to $0.2f_c'A_g$ is $0.6E_cI_g$. Linear interpolation is used to determine the effective stiffness of columns with axial loads in between these values. Their proposed model has been plotted in Figure 2.5 and is labeled PP 92.

The models implemented in many structural codes are similar to one another. In chapter 8 of ACI 318-08 three options for determining approximate member stiffness when considering lateral deflections are implemented. The first defines a difference between flexural and compression members. Flexural members ($P < 0.1f_c'A_g$) have a reduced stiffness of $0.35EI_g$, and compression members ($P \geq 0.1f_c'A_g$) are reduced to $0.7EI_g$. The second method the ACI code allows is $0.5EI_g$ for all members. The third option is to perform “a more detailed analysis considering the reduced stiffness of all members under the loading conditions.” FEMA 356 allows for interpolation between effective stiffness for low and high axial loads. For columns with compression due to gravity loads $\leq 0.3f_c'A_g$ the effective stiffness is $0.5E_cI_g$ and the effective stiffness of columns with gravity loads $\geq 0.5f_c'A_g$ is $0.7E_cI_g$. Linear interpolation can be used to determine the effective stiffness for columns with loads between 0.3 and 0.5 of the axial capacity. Modifications were implemented in ASCE 41 Supplement 1 to better predict the effective stiffness in columns with low axial loads. For columns with compression due to gravity loads $\leq 0.1f_c'A_g$ the effective stiffness is $0.3E_cI_g$ and the effective stiffness of columns with gravity loads $\geq 0.5f_c'A_g$ is $0.7E_cI_g$. Linear interpolation can be used to determine the effective stiffness for columns with loads between 0.1 and 0.5 of their axial capacity. The four code and standard models are plotted in Figure 2.5.

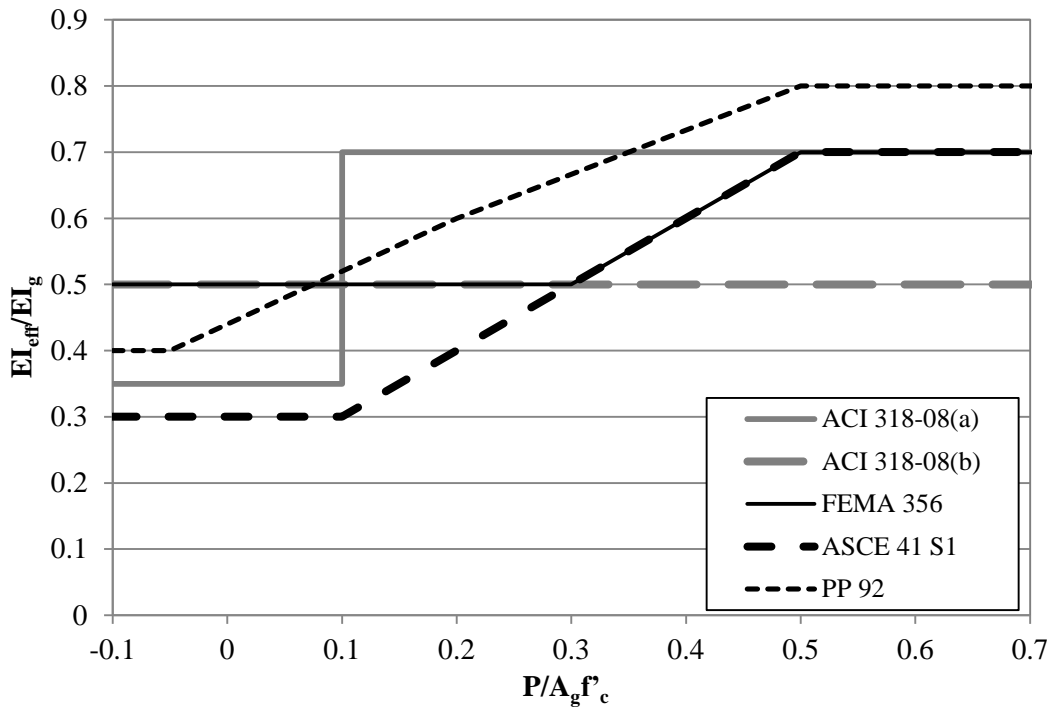


Figure 2.5 Effective stiffness models

2.5.3 Building Modeling

To meet the UW-GA Tech Project objectives, full frame analysis must be performed to establish a set of fragilities for mainshock damaged structures. This study considered previous research on full frames in order to determine how best to combine the element modeling formulations discussed previously. Potential pitfalls of building simulation were identified by reviewing work performed in past research studies. Another reason for the building modeling review was to identify a set of RC frames that were designed to meet current design code provisions for highly seismic regions and a set of RC frames that were designed prior to the implementation of ductile detailing requirements.

“Evaluating Current Procedures and Modeling for Seismic Performance of Reinforced Concrete Buildings” (Goel, et al. 2000)

The Van Nuys building has been instrumented since its construction in 1966 and records are available for three earthquakes (1971 San Fernando, 1989 Whittier, and 1994 Northridge), after the last of which shear failures were observed in the columns of the south face of the fourth floor. The structure has a rectangular floor plan that is uniform from the base to the roof of the structure. As a regular structure with structural and nonstructural details that are typical of building construction prior to the 1970’s, this building offered an ideal opportunity to compare analytical response with recorded response.

The scope of this research project involved performing two and three-dimensional analyses of the building with the intent of modeling the observed damage and recorded structural response. The analyses included both structural and nonstructural elements. The nonlinearity of both structural and nonstructural elements was modeled.

The structure was analyzed in the longitudinal direction. Rigid diaphragms were assumed to tie the four vertical plains in the out of plain direction together. ATC 40 and FEMA 273 were used to modify the strength and stiffness of the beams and columns. The column bases were assumed to be fixed (no foundation modeling was included). Mass was assigned to the nodes at beam-column intersections for dynamic analysis. Lumped plasticity elements were used throughout the structure. Both monotonic pushover and nonlinear dynamic analysis were performed. Drain-2DX was used to complete the nonlinear dynamic time-history analysis.

“Seismic Analysis of an Older Reinforced Concrete Frame Structure” (Paspuleti 2002)

The study investigated techniques used to model an existing RC structure, the Van Nuys building. The seven story reinforced concrete structure suffered significant damage during the Northridge earthquake. The focus of the study is the effectiveness of the applied inelastic modeling assumptions in predicting the actual building response. A parameter study was also completed to determine the variability of the simulated response when model parameters were changed.

The building was modeled in the longitudinal direction. Both an exterior and interior frame were included in the model Rigid diaphragms were assumed to tie the four vertical frames together in the out of plane direction. Mass was assigned to the frame at the beam-column intersecting nodes. The baseline model had Lumped plasticity elements and rigid joint offsets. Distributed plasticity elements were used in one of the parameter models. Another parameter model considered the beam-column joints to be completely flexible. A splice failure model was included in the baseline model. A post processing technique was used to incorporate shear failure modeling. Columns were assumed to be fixed at the base and no additional foundation modeling was included. The baseline model did not include second order P- Δ effects, but one of the parameter models did consider these effects. OpenSees was used in this study to perform the pushover and dynamic analysis performed.

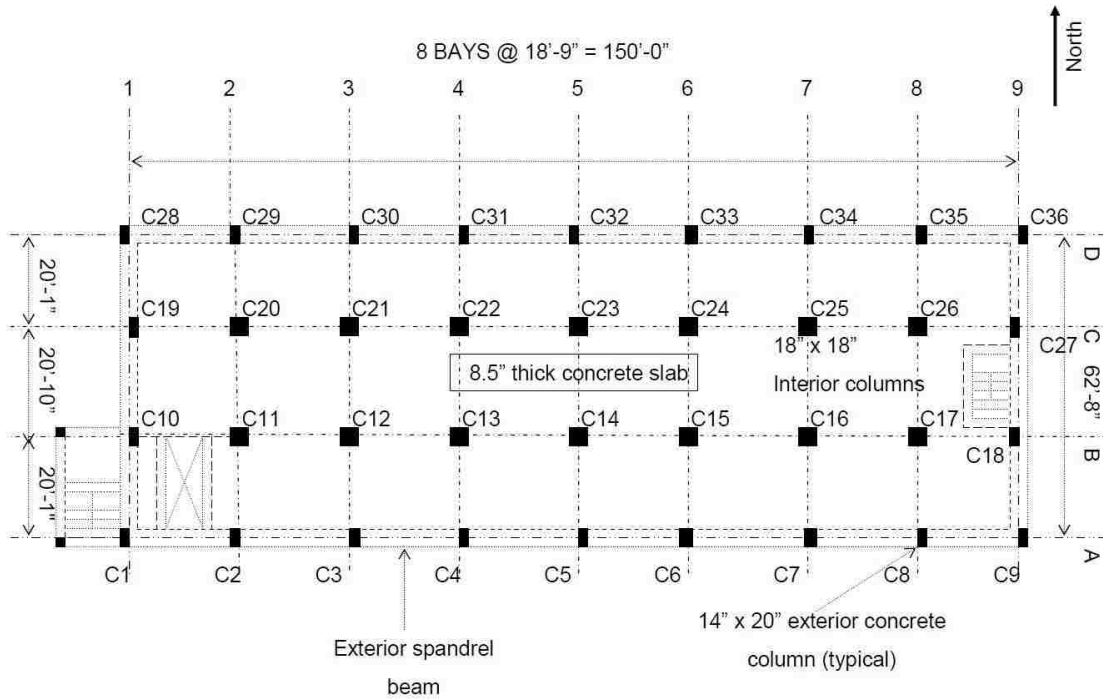


Figure 2.6 Van Nuys building floor plan (Paspuleti 2002)

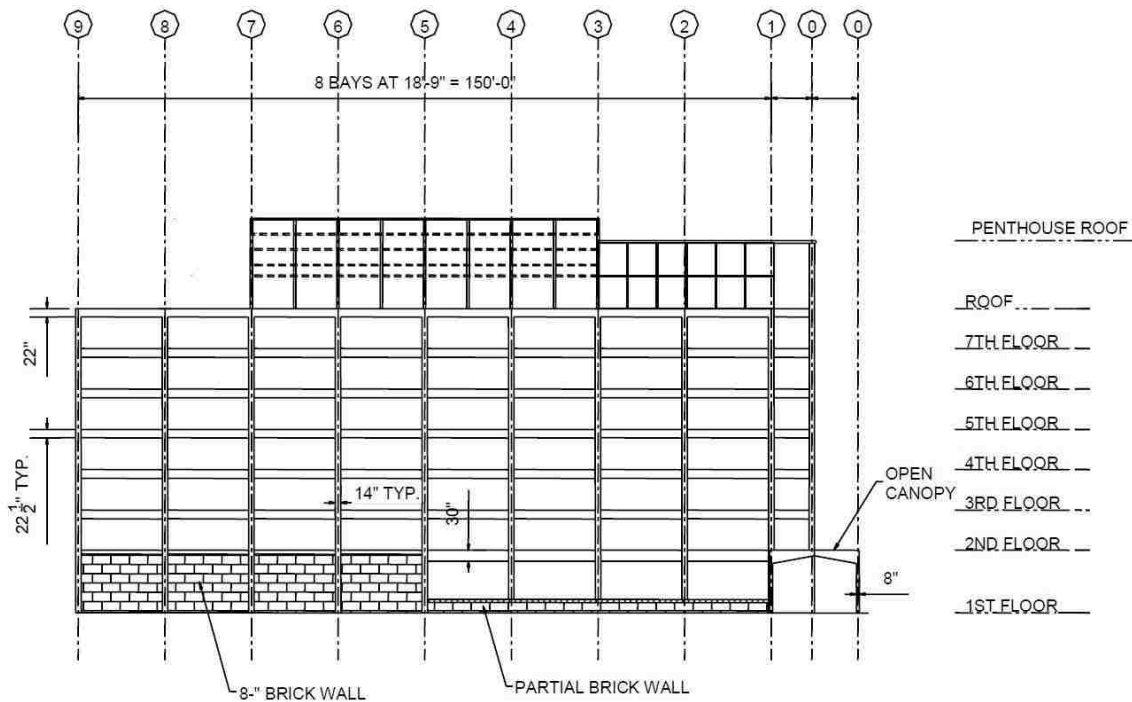


Figure 2.7 Van Nuys building elevation (Paspuleti 2002)

“Modeling the Earthquake Response of Older Reinforced Concrete Beam-Column Building Joints” (Theiss 2005)

The study investigated techniques used to model joints in an existing RC structure. Research conducted by Paspuleti (2002) was used as the starting point for this study. The focus of the study is the effectiveness of the applied inelastic joint modeling assumptions in predicting building response. The initial model used was essentially a duplicate of the baseline model used by Paspuleti. A parameter study was then conducted in which the joint modeling technique was modified.

The same basic modeling techniques as discussed in the Paspuleti summary were used by Theiss. The modifications made for the joint parameter study were discussed previously in Section 2.5.1.3. The building response was documented for each joint model used and compared to the response the actual structure saw during the Northridge earthquake.

“Influence of Modeling Parameters and Assumption on the Seismic Response of an Existing RC Building” (Barin and Pincheira 2002)

This study focuses on the influence of modeling assumptions when a seven story RC frame model undergoes nonlinear static and dynamic analyses. The same structure, the Van Nuys building, modeled by Paspuleti (2002) and Theiss (2005) was used in this study. The goal of the research effort was to validate current modeling practices used for RC structures.

The building was analyzed in the longitudinal direction. Exterior and interior frames were included in the model. Concentrated springs were used at the ends of an elastic sub element to capture the inelastic action. Rigid diaphragms were assumed to tie the four out of plain frames together. Lumped masses at the beam-column intersections were applied for dynamic analysis. Both elastic and inelastic shear deformations were considered. Beam-column joints were considered to be rigid and infinitely strong. Foundation modeling was not done for this study. Second order deflections and moments due to P- Δ effects were not considered. The analysis platform used was Drain-2DX.

“Evaluation of the Seismic Performance of a Code-Conforming Reinforced-Concrete Frame Building: From Seismic Hazard to Collapse Safety and Economic Losses” (Goulet, et al. 2007)

A seismic performance assessment was completed for a reinforced concrete moment-frame building designed per current building code provisions. The performance was quantified in terms of economic losses and collapse safety. The assessment includes site-specific seismic hazard analyses, nonlinear dynamic structural response simulations to collapse, damage analyses, and loss estimation.

A four-story reinforced concrete benchmark building was designed according to the 2003 International Building Code. To represent the current design practices eight variations of the RC frame were designed. The different frames had variations in the structural system, beam strength, strong-column weak-beam ratios, and other items.

The analysis was performed using OpenSees. Static pushover analyses were performed to establish the load-displacement relationship for the eight buildings. Nonlinear dynamic analyses were performed for the eight designs using ground motion suites intended to evoke pre-collapse responses. Collapse simulation was also performed using incremental dynamic analyses.

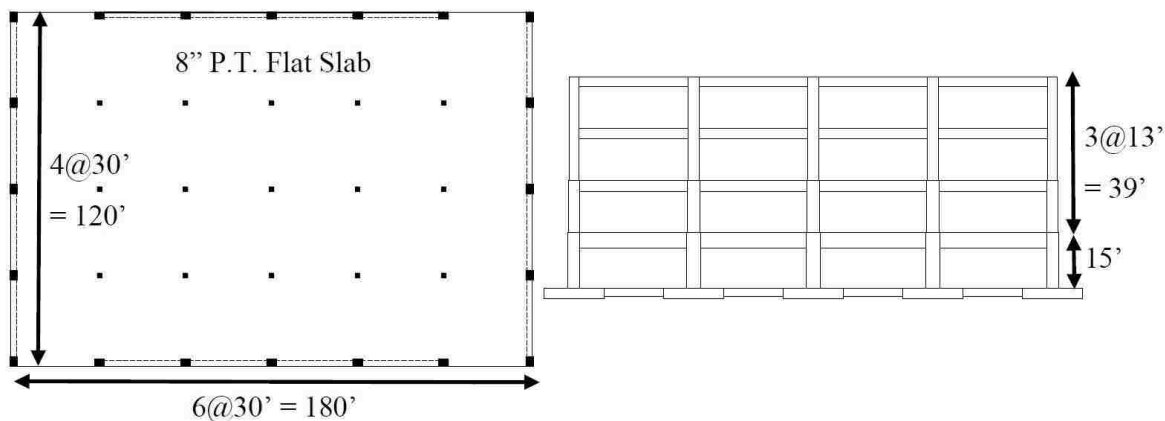


Figure 2.8 Benchmark building plan and elevation

“Assessing Seismic Collapse Safety of Modern Reinforced Concrete Moment Frame” Buildings
(C. B. Haselton 2006)

The two primary objectives of this thesis were to contribute to the development of methods and tools required for performing collapse assessment and assess the collapse risk of reinforced concrete special moment frame buildings designed according to modern building code requirements. Chapter 6 of the thesis identifies the reinforced concrete buildings modeled. It lays out how the models were created and the analysis techniques that were used to assess the collapse performance.

The archetypical building design used in Chapter 6 was composed of a matrix of 30 buildings. The differences in the 30 buildings consist of varying building height (six heights were used from 1 to 20 stories), two bay widths (20' and 30'), different lateral load resisting systems (perimeter and space frames), and a range of strength and stiffness values over the building height. A benchmark frame is shown in Figure 2.9. ASCE7-02 seismic provisions were used to meet code requirements. OpenSees was used to perform static pushover analysis, nonlinear dynamic analysis prior to collapse, and nonlinear dynamic analysis causing collapse. The frame's beam-column elements were modeled using a plastic hinge model.

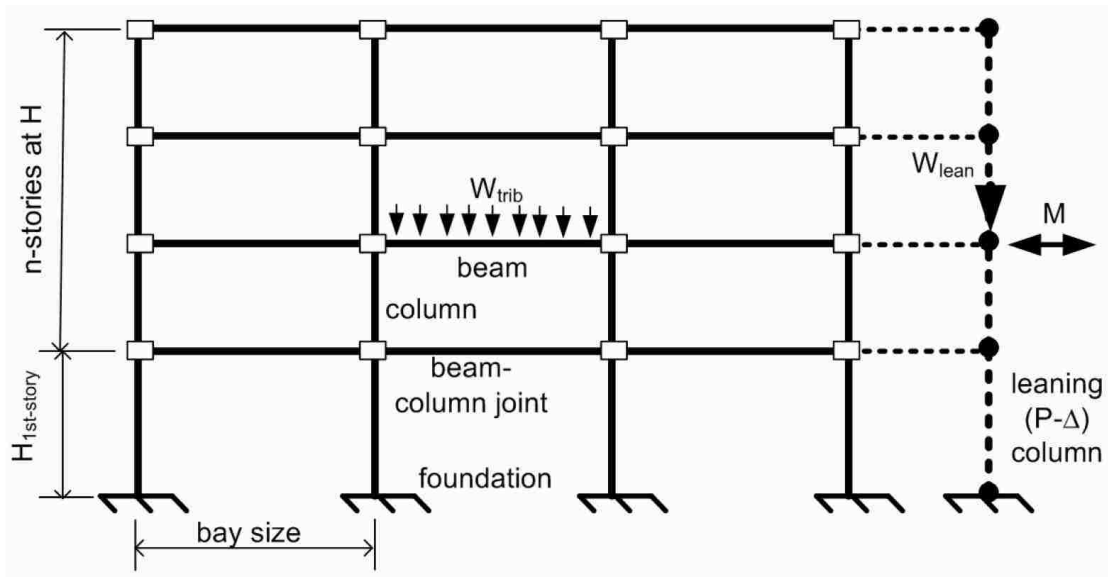


Figure 2.9 Benchmark building elevation with modeling techniques

“Assessing the Collapse Risk of California’s Existing Reinforced Concrete Frame Structures: Metrics for Seismic Safety Decision” (Liel 2008)

The primary objective of this thesis was to assess the collapse risk of California’s reinforced concrete frames designed and constructed prior to the 1970s. Chapter 3 of the thesis identifies the reinforced concrete buildings modeled. It lays out how the models were created and the analysis techniques that were used to assess the collapse performance.

A range of archetype structures were considered in Chapter 3. The differences in the buildings consist of varying building height (four heights were used from 2 to 12 stories), different lateral load resisting systems (perimeter and space frames), and a range of strength and stiffness values over the building height. The same frame layout was used in Liel’s work as Haselton used, shown in Figure 2.9. The 1967 UBC was used to satisfy dated code requirements. OpenSees was used to perform static pushover analysis, nonlinear dynamic analysis prior to collapse, and nonlinear dynamic analysis causing collapse. The frame’s beam-column elements were modeled using a plastic hinge model.

2.6 Nonlinear Structural Analysis Techniques

A literature review was conducted to identify potential dynamic analysis techniques. The UW-GA Tech Project objectives call for a suite of fragilities that identify the probability a foreshock damaged structure is more severely damaged, potentially to a collapse state, during an aftershock. The review covers incremental dynamic analysis (IDA), mainshock analysis, and mainshock-aftershock analysis. The

three papers that considered mainshock-aftershock pairs are summarized below. These papers present techniques used to simulate a mainshock damaged structure.

“Dynamic Versus Static Computations of Residual Capacity of a Mainshock-Damaged Building to Withstand an Aftershock” (Luco, Bazzurro and Cornell 2004)

The primary objectives of this paper are to compute the residual capacity of a mainshock damaged case-study structure, to compare dynamic and static analysis techniques, and to use the dynamic approach to calibrate the less accurate static approach. The case study building was a three story steel moment resisting frame. A set of damage states was identified to determine the residual capacity of the structure. The damage states ranged from the onset of damage to complete collapse.

The analysis procedure used for the nonlinear dynamic analysis was to subject the structure to an incremental dynamic analysis, IDA, using 30 ground motions. Following the mainshock IDA the structures were subjected to an aftershock IDA. The spectral acceleration capacity of the mainshock damaged structure after the aftershock was identified for all 900 combinations of mainshock-aftershock pairs.

The static pushover analysis process was much less computationally intensive. An initial static pushover was conducted to simulate the mainshock response. A second static pushover was conducted to simulate the aftershock. The results of both techniques were used to calibrate the static approach to predict the residual capacity of a structure.

“Developing Fragilities for Mainshock-Damaged Structures Through Incremental Dynamic Analysis” (Ryu, et al. 2011)

This paper presented a technique for developing aftershock fragilities. A sequence of IDAs for mainshock and aftershock ground motions was used to establish the fragility functions. The seismic response of a mainshock-damaged building was estimated by performing nonlinear time-history analysis with a sequence of mainshock and aftershock ground. Back-to-back dynamic analyses were performed for a number of levels of mainshock damage states, and a number of sequences of mainshock and aftershock ground motions. With estimated seismic responses from the back-to-back dynamic analyses, various damage state transition probabilities were computed. A damage state transition probability is the probability of exceeding a higher damage state from an aftershock given a damage state due to a mainshock. The building analyzed for this research effort was modeled using a single degree of freedom (SDOF) system.

“Comparison of Mainshock and Aftershock Fragility Curves Developed for New Zealand and US Buildings” (Uma, Ryu, et al. 2011)

The primary objective of this paper is to compute the fragility functions that express the relationship between ground motion intensity and damage potential. A set of mainshocks and aftershocks were used to compute the fragility functions. Structures typical of New Zealand and US practices were considered in the modeling effort. A set of damage states was identified for the computation of the fragility curves. The damage states ranged from slight damage to collapse.

The mainshock fragility curves were computed using the technique presented by Ryu et al. (2011). The time-history analyses utilized a pinching hysteretic model in order to simulate stiffness and strength degradation.

Chapter 3: Damage Progression in RC Columns Subjected to Earthquake Loading

3.1 Introduction

The UW-GA Tech Project aims to detect damage, identify damage properties, and make a condition assessment of the damaged component. A critical step in the process of using image data to assess collapse risk is the use of damage data to establish the current damage state and response mechanism of a building component. From these, the failure mode and drift capacity the component will likely exhibit under subsequent earthquake loading can be established. Chapter 3 presents the results of research activities to establish damage states for the response modes typically exhibited by RC building columns. To determine the prior displacement demand and current capacity a detailed description of the damaged column was critical. The differences in the damage patterns for shear-critical and flexure-critical columns will be used to determine the response category of the damaged column.

Reinforced concrete columns with different geometries, material strengths, and design details develop different damage patterns, response mechanisms, and failure modes when subjected to earthquake loading. In this study, damage characteristics, such as the extent and severity of concrete cracking or spalling, were used to define damage states. The results of previous experimental studies were used to determine a series of damage states that characterize the progression of damage for columns exhibiting different response mechanisms and failure modes. Capturing the loss of capacity through visual damage data is critical to the UW-GA Tech Project. Damage states that correspond to capacity loss were identified in this chapter.

The axial load on columns plays a role on column behavior. The effect of axial load does not change the progression of damage, but it does have an effect on the displacement capacity a column has. This is shown in Section 3.3.2 through the assessment of load-displacement plots corresponding to damage states and data from the Database supports this as shown in Section 3.4. The effects of bi-directional loading will also be discussed.

3.2 Response Modes

When reinforced concrete columns are subjected to axial load and cyclic lateral loading they exhibit three primary failure modes: flexure, shear, or flexure-shear (Camarillo 2003). A flexural failure occurs when the full flexural capacity of the column is achieved and the maximum shear force developed in the column is significantly below the shear strength. Flexural failure is characterized by horizontal cracking, spalling of cover concrete, and ultimately buckling and fracture of longitudinal reinforcement.

This failure mode is more likely to occur in buildings designed after 1976 due to the implementation of ductile detailing requirements in the 1976 Uniform Building Code due to the non-ductile damage caused by the 1971 San Fernando Earthquake. A shear failure is likely to occur if the shear demand associated with flexural yielding of the column greatly exceeds the shear capacity. Shear failure is characterized by development of distributed diagonal shear cracking that ultimately localizes in one or two cracks prior to yielding of the longitudinal steel in flexure (Zhu, Elwood and Haukaas 2007). This failure mode occurs predominantly in reinforced concrete structures constructed prior to the 1976 Uniform Building Code was implemented.

3.3 Damage Progression

The following sections outline the damage progression that occurs in a flexure-critical and a shear-critical column. The damage states presented in the following sections were the result of analysis of the progression of damage observed in dissertations completed by Bae (2005) and Sezen (2002). As discussed in Chapter 2, the Bae and Sezen research provided images that could be used to describe damage states and correlate drift data to the damage description. Bae provides damage and image data for columns exhibiting flexural response. Sezen provides similar data for shear-critical columns. The progression of damage was determined using the images provided in the Bae and Sezen reports and textual descriptions of the damage provided in other reports included in the Database (Saatcioglu and Grira 1999, Mo and Wang 2000, Sugano 1996, Lynn 2001).

The flexure-shear response mode has been left out of the damage progression discussion. This response mode presents the same damage patterns as a column responding in flexure through the cracking stage and then behaves as a shear-critical column.

Given the objective of the UW-GA Tech Project, it was desirable to have a large set of images that are representative of each damage state. Thus, images from studies were supplemented with images from the National Information Service for Earthquake Engineering's Earthquake Engineering Online Archive (PEER 2011), the Network for Earthquake Engineering Simulation, NEES (Sedra, et al. 2010), the *Mw 7.0 Haiti Earthquake of January 12, 2010: USGS/EERI Advance Reconnaissance Team Report* (Eberhard, et al. 2010), and laboratory test programs.

It should be noted that the descriptions of damage and of damaged columns were developed using data primarily from tests in which columns were subjected to unidirectional lateral loading. A discussion of the effects of bi-directional loading is provided following the damage descriptions in Section 3.3.6. The effect of axial load on the column damage is presented in Section 3.3.1.

3.3.1 Axial Load Effect

The axial load placed on a column has an effect on the progression of damage in a reinforced concrete column that has a flexural failure mechanism. The order that the damage occurs was the same, but the drift-capacity was changed with varying axial loads. Crack sizes may be affected by axial load. A high axial load will tend to keep flexural crack widths and inclined shear crack widths narrow at low lateral displacement amplitudes (Atalay and Penzien 1975).

Typically higher axial loads on a column will reduce the drift a flexure-critical column achieves prior to a damage state. Higher axial loads tend to cause concrete spalling, longitudinal bar buckling, and both the loss of lateral and axial load carrying capacity to occur at smaller lateral displacements. These trends are shown in Section 3.3.2 in the presentation of the load-displacement response for the Bae specimens. They will also be considered in the presentation of the Database data in Section 3.4.

The axial load placed on a column effects the progression of damage in a reinforced concrete column that exhibits a shear failure mode. Shear critical columns respond in a non-ductile manner. The non-ductile response was magnified when the axial load was increased. Columns with low axial loads may show the damage progression described in section 3.3.4. Columns with high axial loads tend to have a more rapid damage progression due to the non-ductile nature of shear failure. These trends are shown in Section 3.3.2 in the presentation of the load-displacement response for the Sezen specimens. They will also be considered in the presentation of the Database data in Section 3.4.

The axial load on columns can be considered a high axial load if the stress is equal to or greater than $0.5f_c A_g$. This value was obtained from ASCE 41 (2007) as a critically high value of axial load. The Database reports used to support the damage progression identified columns tested under loads less than $0.5f_c A_g$ as being low axial loads (Saatcioglu and Grira 1999, Mo and Wang 2000, Sugano 1996, Lynn 2001, Sezen 2002, Bae 2005). From this point on in the report low axial load will be defined as any load that is less than $0.5f_c A_g$ and a high axial load will be defined as a load equal to or greater than $0.5f_c A_g$.

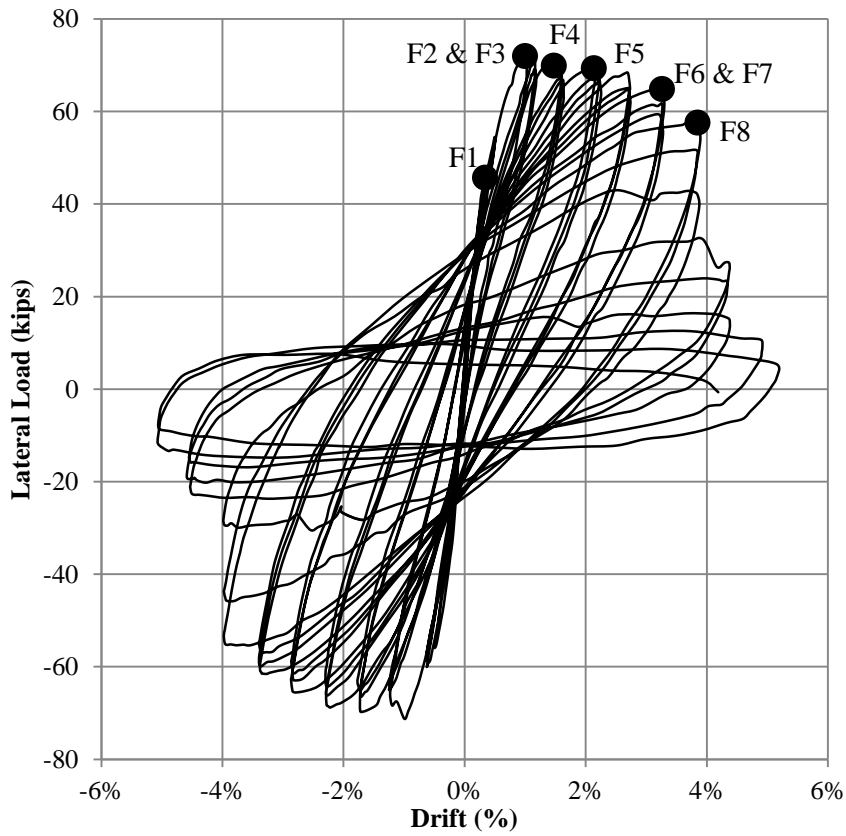
3.3.2 Damage Progression and Load-Displacement Response

Figure 3.1 through Figure 3.33 show what is considered to be the typical load displacement response and damage properties for six columns tested in the laboratory exhibiting flexure and shear response under low and high axial load. For each column a plot of the experimental load-displacement response is provided with the onset of the damage states developed as part of this research effort identified; also for each column a series of images is provided that show the damage state of the column. Table 3.1 and Table 3.2 list the damage states and damage characteristics associated with each damage state. Sections 3.3.3 and 3.3.4 provide a more detailed description of the damage states.

Flexure-Critical Column: Low Axial Load ($0.2f_c A_g$)

Test Name: S24-4UT

Source: (Bae 2005)



No Image for (F1, F2, or F3) Flexural, Longitudinal, and Shear Cracking

Figure 3.1 Load Drift History

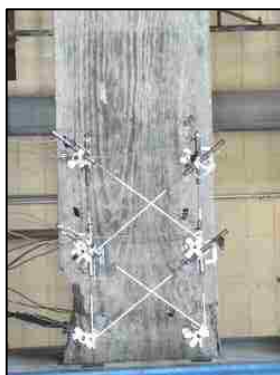


Figure 3.2 (F4) Concrete Spalling on Flexural and Side Faces

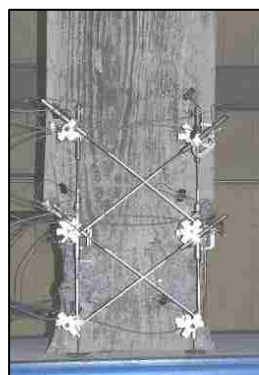


Figure 3.3 (F5) Concrete Spalling Exposing Longitudinal Steel

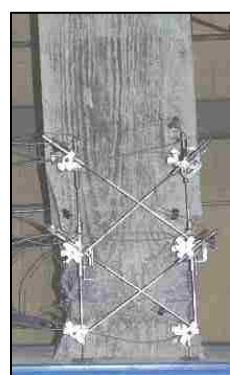


Figure 3.4 (F6 & F7) Longitudinal Bar Buckling and Crushing of Core Concrete

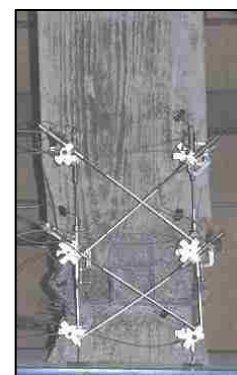
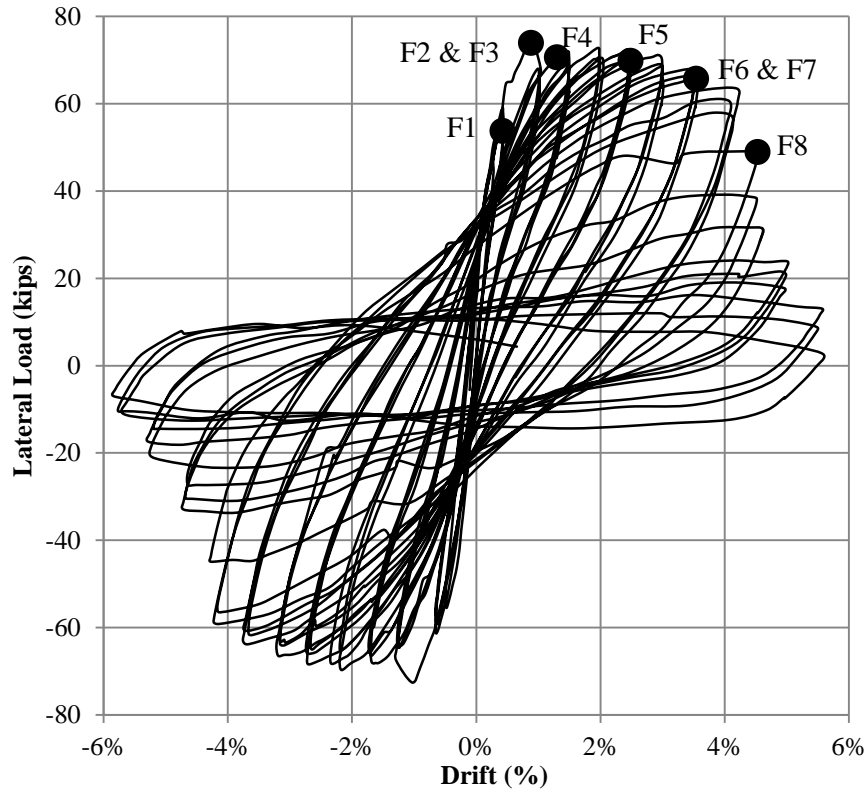


Figure 3.5 (F8) Longitudinal Bar Fracture

Flexure-Critical Column: Low Axial Load ($0.2f_c A_g$)

Test Name: S24-5UT

Source: (Bae 2005)



No Image for (F1, F2, or F3) Flexural, Longitudinal, and Shear Cracking

Figure 3.6 Load Drift History

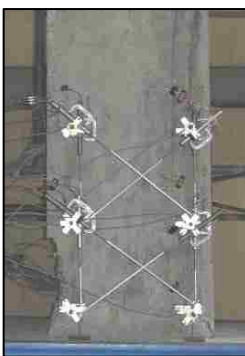


Figure 3.7 (F4) Concrete Spalling on Flexural and Side Faces

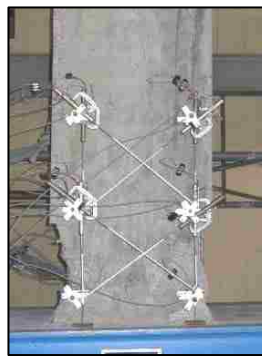


Figure 3.8 (F5) Concrete Spalling Exposing Longitudinal Steel

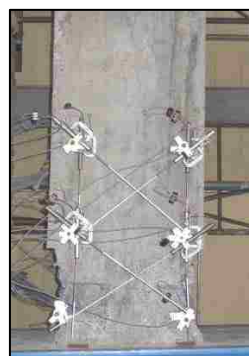


Figure 3.9 (F6 & F7) Longitudinal Bar Buckling and Crushing of Core Concrete

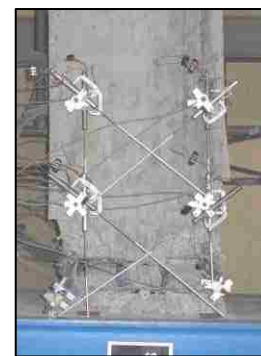
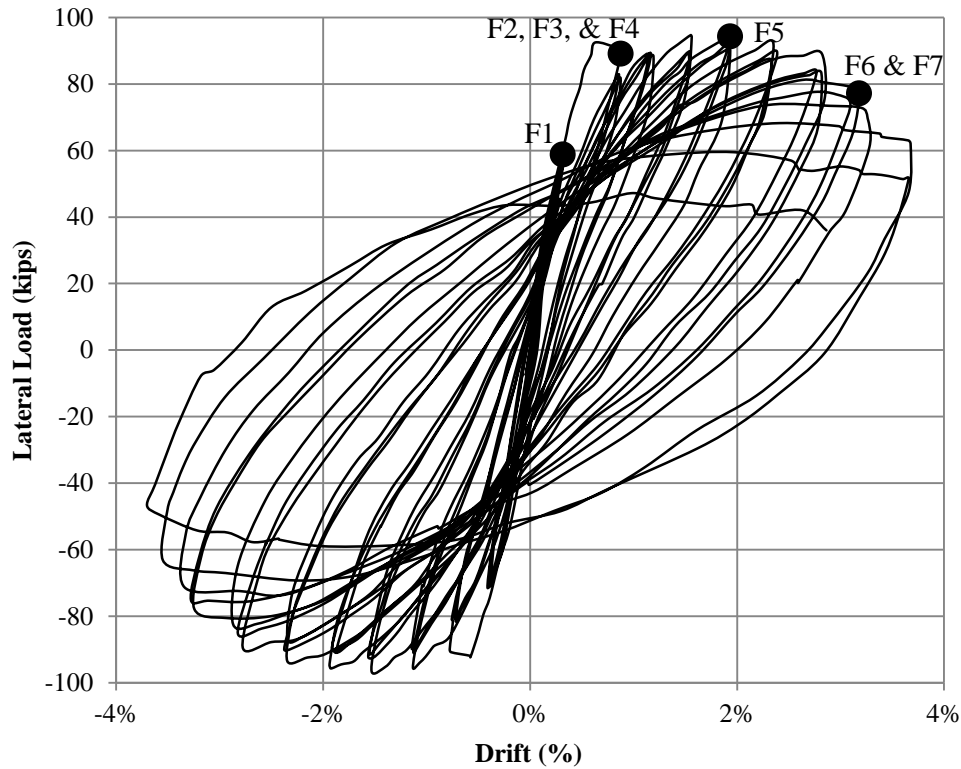


Figure 3.10 (F8) Longitudinal Bar Fracture

Flexure-Critical Column: High Axial Load ($0.5f_c A_g$)

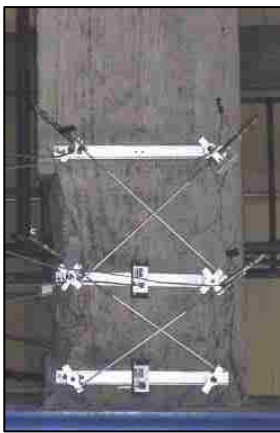
Test Name: S24-2UT

Source: (Bae 2005)



No Image for
(F1 or F3)
Flexural and
Shear Cracking

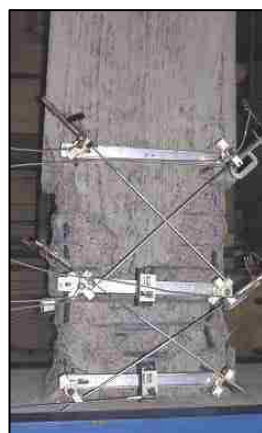
Figure 3.11 Load Drift History



**Figure 3.12 (F2 & F4)
Longitudinal Cracking and
Concrete Spalling on Flexural
and Side Faces**



**Figure 3.13 (F5)
Concrete Spalling
Exposing Longitudinal
Steel**



**Figure 3.14 (F6 & F7)
Longitudinal Bar Buckling
and Crushing of Core
Concrete**

No Image for
(F8)
Longitudinal
Bar Fracture

Flexure-Critical Column: High Axial Load ($0.5f_c A_g$)

Test Name: S17-3UT

Source: (Bae 2005)

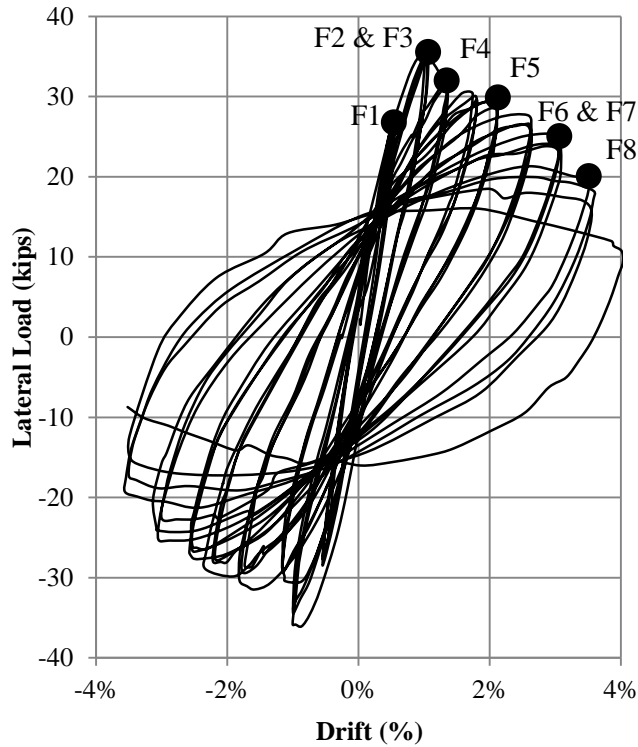


Figure 3.15 Load Drift History



Figure 3.16 (F1 & F2) Flexural and Longitudinal Cracking

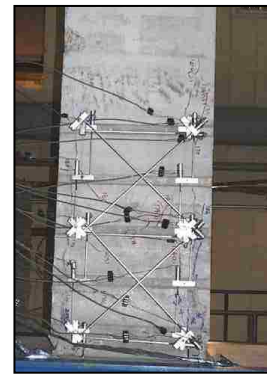


Figure 3.17 (F3) Shear Cracking



Figure 3.18 (F4) Concrete Spalling on Flexural and Side Faces

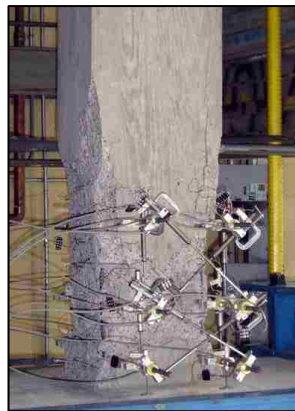


Figure 3.19 (F5) Concrete Spalling Exposing Longitudinal Steel



Figure 3.20 (F6 & F7) Longitudinal Bar Buckling and Crushing of Core Concrete



Figure 3.21 (F8) Longitudinal Bar Fracture

Shear-Critical Column: Low Axial Load ($0.15f_c A_g$)

Test Name: Specimen 1

Source: (Sezen 2002)

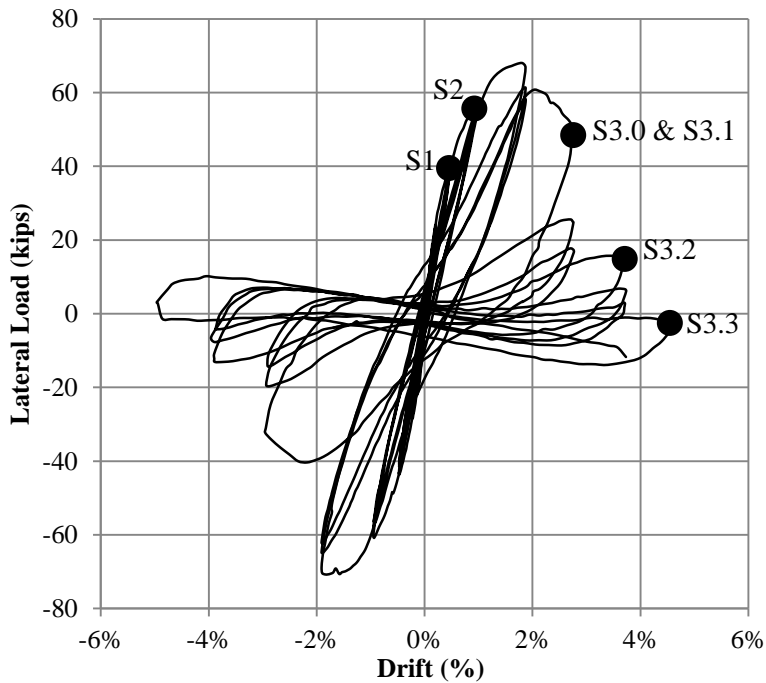


Figure 3.22 Load Drift History



Figure 3.23 (S1 & S2) Flexural and Shear Cracking



Figure 3.24 (S3.0 & S3.1) Widening and Localization of Shear Cracking and Longitudinal Cracking on Side Face



Figure 3.25 and 3.26 (S3.2) Concrete Spalling on Side Faces



Figure 3.27 (S3.3) Longitudinal Bar Buckling

Shear-Critical Column: High Axial Load ($0.6f_c A_g$)

Test Name: Specimen 2

Source: (Sezen 2002)

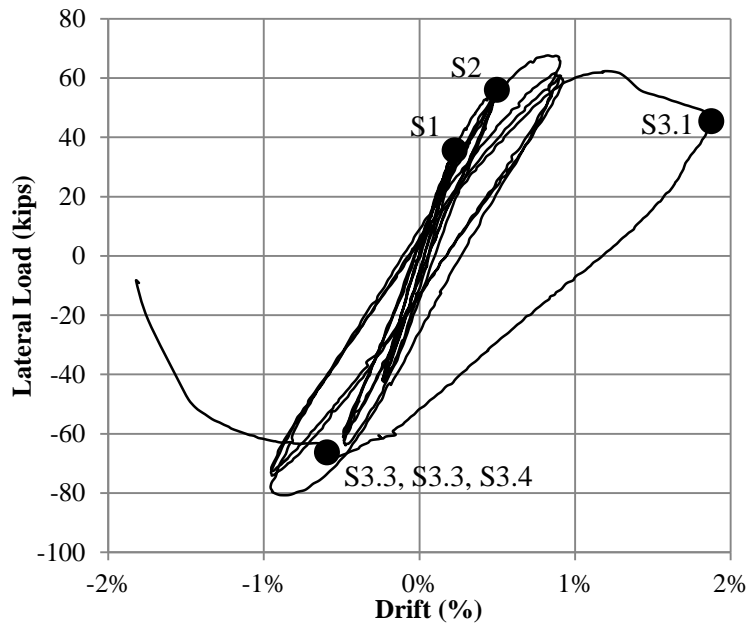
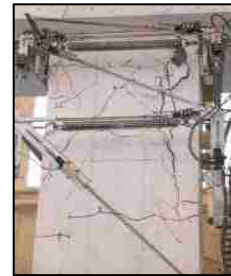


Figure 3.28 Load Drift History



**Figures 3.29 and 3.30 (S1 & S2)
Flexural and Shear Cracking**



**Figure 3.31 (S3.1) Widening and
Localization of Longitudinal
Cracking on Side Face**



**Figure 3.32 (S3.2)
Concrete Spalling on Side
Face After Load Reversal**



**Figure 3.33 (S3.3 & S3.4)
Longitudinal Bar Buckling and
Core Crushing After Loss of Load
Carrying Capacity**

3.3.3 Flexural Damage Progression

The following section identifies the damage progression typical of a flexure-critical column. Table 3.1 includes the order of the onset of damage and a detailed description of the appearance of a damage state. A discussion on each damage state follows the table. The progression of damage was determined using the images provided in the Bae report (2005), textual descriptions of the damage provided in other reports included in the Database (Saatcioglu and Grira 1999) (Mo and Wang 2000) (Sugano 1996). These damage states were determined using data from column tests in which a flexure critical column was tested.

Table 3.1 Flexural damage progression and description

Damage State	Flexure-Critical Damage Description (FC)
F1: Flexural Cracking	<ul style="list-style-type: none"> - Top and bottom 1/3 of column - Perpendicular to column axis - Span width of column - Uniformly spaced - Initially hairline cracks (<0.005 in.) - Prior to spalling \approx 0.1 in. at peak displacement (HAL) - Prior to spalling \approx 0.2 in. at peak displacement (LAL)
F2: Longitudinal Cracking	<ul style="list-style-type: none"> - Top and bottom 1/3 of column - Parallel to column axis - Prior to spalling \approx 0.15 in. at peak displacement
F3: Shear Cracking	<ul style="list-style-type: none"> - Top and bottom 1/3 of column - At 35° to 65° angle from horizontal - Initially hairline cracks (<0.005 in.) - Prior to spalling \approx 0.02 in. at peak displacement (HAL) - Prior to spalling \approx 0.04 in. at peak displacement (LAL)
F4: Initial Concrete Spalling	<ul style="list-style-type: none"> - Initially occurs in top and bottom 1/4 of column faces - Complete spalling \approx b from ends prior to failure
F5: Concrete Spalling Exposing Longitudinal Steel	<ul style="list-style-type: none"> - Initially exposed at \approx b/2 from ends - Exposed length \approx b
F6: Longitudinal Bar Buckling	<ul style="list-style-type: none"> - Initially occurs at \approx b/2 from ends - Total buckling length prior to fracture \approx b/2
F7: Crushing of Core Concrete	<ul style="list-style-type: none"> - Same location as bar buckling
F8: Longitudinal Bar Fracture	<ul style="list-style-type: none"> - Same location as bar buckling

b is the column width

F1. Flexural Cracking

The onset of flexural cracking occurs in reinforced concrete columns when lateral loads are applied to a structure. The horizontal forces induce bending stresses. Bending in a rectangular column causes one face to be placed in tension and the opposite face to be placed in compression. The flexural tension face is the location where initial cracking takes place. Flexural cracking occurs when the concrete tensile stress due to flexural tension exceeds the tensile strength.

Flexural cracks develop perpendicular to flexural tension stresses (perpendicular to the column axis). These cracks tend to span the width of the column on the flexural face. Load reversals cause

cracking on both flexural column faces. Initially the cracks close when the column is returned to zero lateral load.

The flexural cracks open and close with each load cycle. The onset of cracking occurs prior to the column reaching the nominal yield displacement. The initial cracking is located in the top and bottom thirds of the column. As the lateral load demand increases, the number and size of cracks increases and residual cracking is observed once the column is returned to zero lateral load. As lateral load demand increases further, residual crack width increases.

F2. Longitudinal Cracking on Flexural Faces

In columns exhibiting flexural response, longitudinal cracks may develop in flexural compression zones (Bae 2005, Watson 1989). These longitudinal cracks form parallel to the compressive stress caused by bending of the column, and thus parallel to the column axis. Higher axial loads cause larger compressive strains, which lead to more substantial longitudinal cracking (A. T. Council 1999).

Typically longitudinal cracks initiate near the column-beam interface and propagate toward mid height of the column. They will remain relatively short, typically extending no more than a third of the column height. These longitudinal cracks occur at the location of longitudinal steel. Longitudinal splitting cracks resulting from compressive loading of concrete cover may appear similar to splitting cracks associated with bond failure. Longitudinal cracks may not be observed in the field due to the cracking being closely followed by spalling at the crack locations.

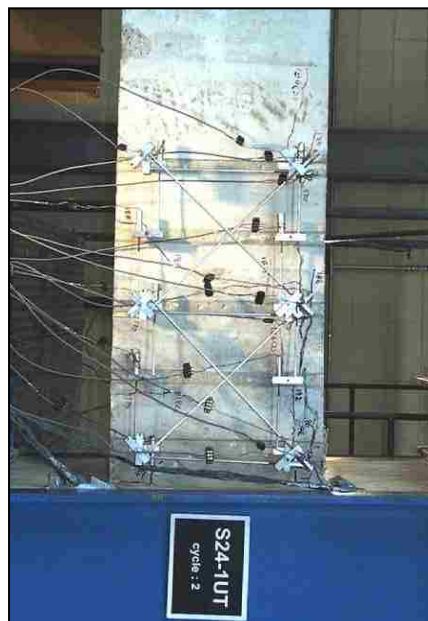


Figure 3.34 Longitudinal cracking on flexural faces: experimental damage (Bae 2005)



Figure 3.35 Longitudinal cracking: earthquake damage (PEER)

F3. Shear Cracking on Side Faces

Shear cracks result from principal diagonal tension stresses corresponding to applied shear forces. Shear cracks are initially narrow and remain narrow under increased lateral loading for columns exhibiting a flexural response. The cracks propagate from the flexural faces of the column and cross the sides of the column. Shear cracks are typically oriented at an angle of 35 to 65 degrees from the horizontal; the angle of cracking depends on the axial load and the geometry of the column.

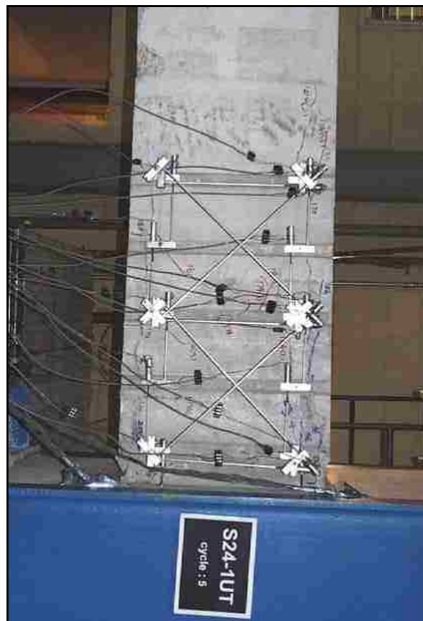
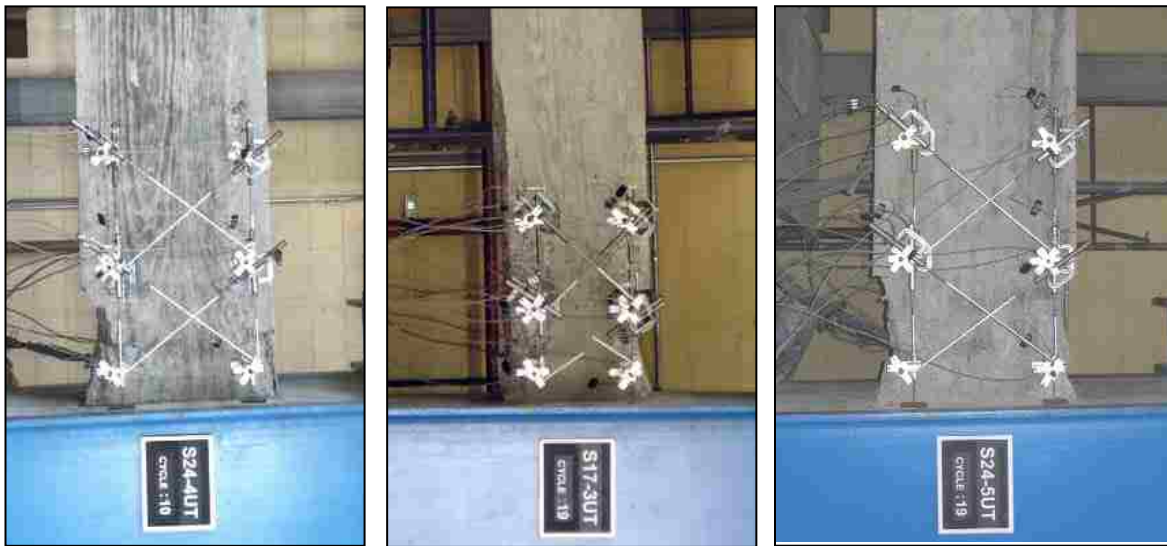


Figure 3.36 Shear cracking on side faces: experimental damage (Bae 2005)

F4. Concrete Spalling on Flexural Face and Side Face

Spalling on the flexural face occurs at the same location as the longitudinal cracking. As lateral load increases, compressive stresses and strains increase first causing longitudinal cracking and then spalling of cover concrete. The spalling will be located at the top and bottom fourth of the flexural faces of the column.

Increasing demands will result in spalling of cover concrete on the column side faces parallel to the loading direction. Upon load reversal, spalling may extend over all of the column faces. Spalling on the side faces typically extends over the top and bottom fifth of the column.



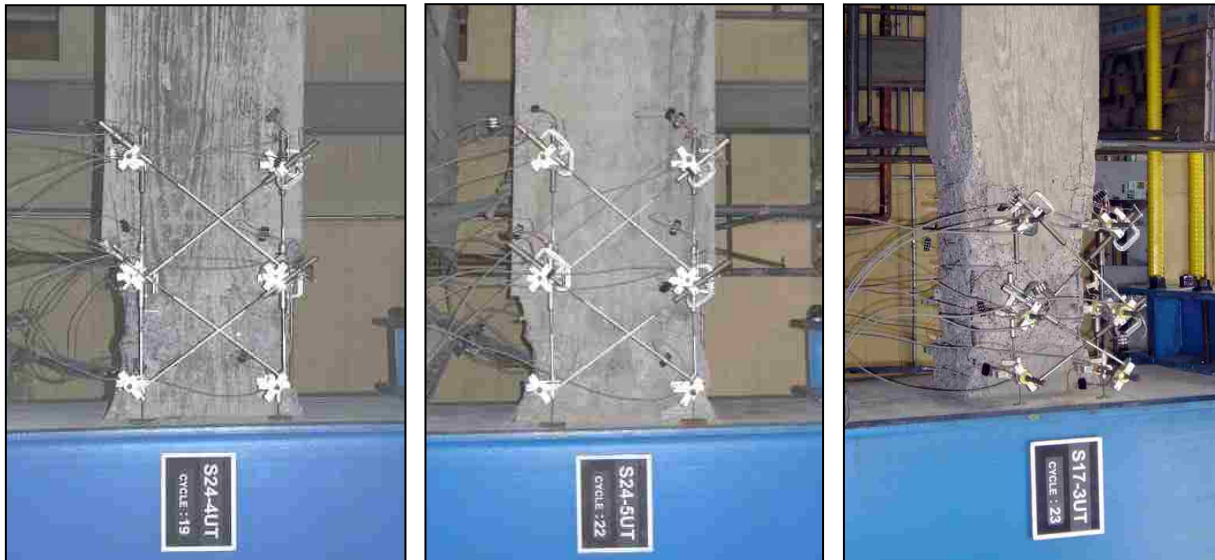
Figures 3.37, 3.38, and 3.39 Concrete spalling on flexural and side face: experimental damage (Bae 2005)



Figure 3.40 Concrete spalling on flexural and side face: earthquake damage (PEER)

F5. Concrete Spalling Exposing Longitudinal Steel

Increased demand will result in spalling that exposes longitudinal steel. Typically bars on the flexural faces of the column will be exposed first; bars on the sides of the column may be exposed as demand increases. Typically exposed reinforcing steel is observed within the top and bottom fifth of the column.



Figures 3.41, 3.42, and 3.43 Concrete spalling exposing longitudinal steel: experimental damage (Bae 2005)

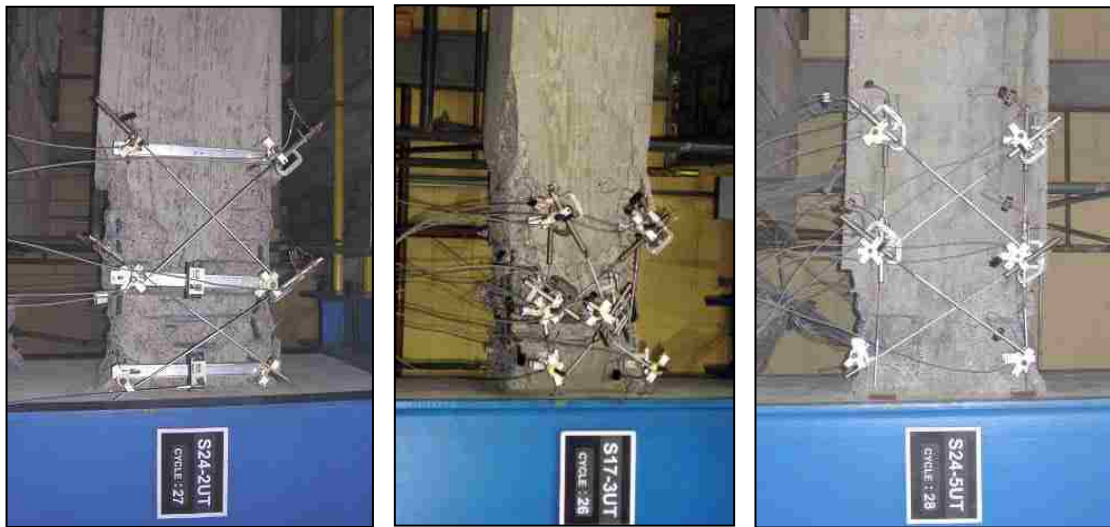


Figures 3.44, 3.45, and 3.46 Concrete spalling exposing longitudinal steel: earthquake damage (PEER)

F6. Longitudinal Bar Buckling

Prior to spalling the bars are surrounded by concrete and transverse reinforcement. The longitudinal bars that have yielded in tension, due to flexural demands, buckle once concrete has exposed enough longitudinal bar length to reach a critical buckling load.

Bar buckling in flexure-critical columns typically occurs over short lengths. Transverse reinforcement is usually spaced tightly in flexural critical columns and effectively braces the longitudinal bars against buckling. Depending on the spacing and stiffness of the transverse reinforcement, buckling may occur between ties or over several tie spaces. Buckling of the longitudinal bars is marked by the longitudinal bar curving outward from the column. Lateral and axial load-carrying capacity are often significantly reduced once bar buckling occurs.



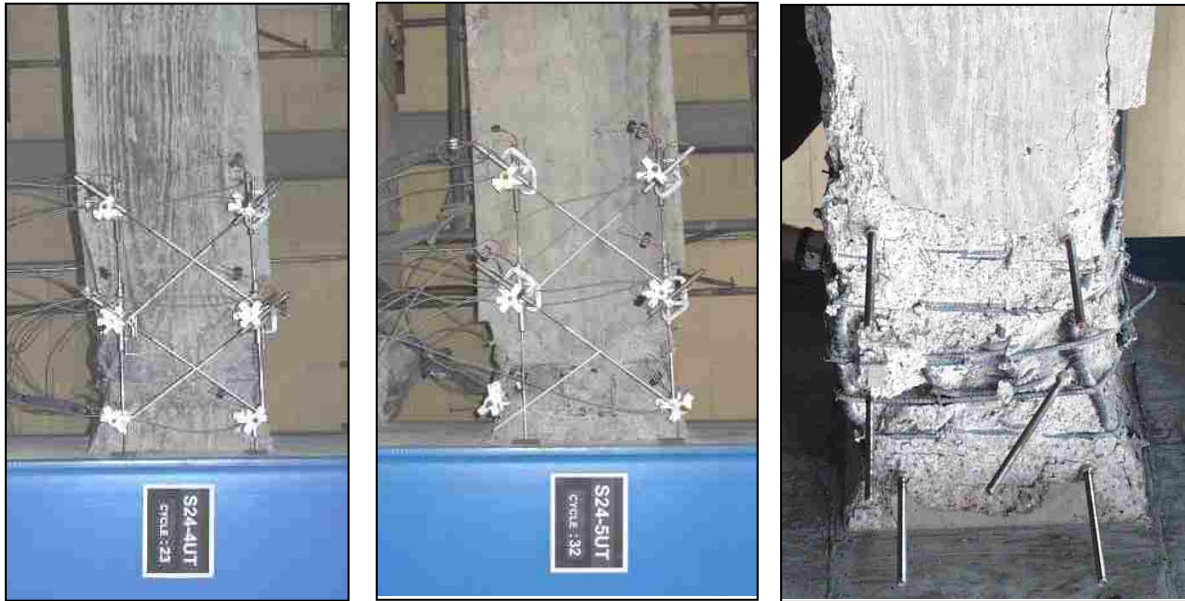
Figures 3.47, 3.48, and 3.49 Longitudinal bar buckling: experimental damage (Bae 2005)



Figure 3.50 Longitudinal bar buckling: earthquake damage (PEER)

F7. Crushing of Core Concrete

Yielding of transverse reinforcement, often due to buckling of longitudinal steel, eliminates confinement of core concrete and allows for crushing of core concrete. Lateral load-carrying capacity is often significantly reduced when the core concrete begins to crush. Axial load-carrying capacity is lost when extensive bar buckling and crushing of the core concrete has occurred.



Figures 3.51, 3.52, and 3.53 Crushing of core concrete: experimental damage (Bae 2005)



Figure 3.54 Crushing of core concrete: earthquake damage (PEER)

F8. Longitudinal Bar Fracture

Longitudinal bar fracture occurs after longitudinal bar buckling. Once the cycle is reversed and the bar is straightened again a large tensile strain occurs on the inside of the bend. A crack may occur during the cycles after buckling. That crack is likely to propagate through the bar's cross section and fracture in subsequent cycles. Lateral load-carrying capacity is significantly reduced when bar fracture occurs.



Figures 3.55 and 3.56 Longitudinal bar fracture: experimental damage (Bae 2005)

3.3.4 Shear Damage Progression

Columns that exhibit shear-controlled failure initially respond to low level lateral loads in flexure and exhibit flexural damage patterns including development of flexural cracks, residual flexural cracks, and longitudinal cracking. The damage progression and description is presented in Table 3.2. A discussion on each damage state follows the table. The progression of damage was determined using the images provided in the Sezen report (2002), textual descriptions of the damage provided in other reports included in the Database (Lynn 2001). These damage states were determined using data from column tests in which a shear critical column was tested.

Table 3.2 Shear damage progression and description

Damage State	Shear-Critical Damage Description (SC)
S1: Flexural Cracking and Longitudinal Cracking	<ul style="list-style-type: none"> - Same as FC HAL for F1 and F2 except as noted - Flexural cracks prior to S3 \approx 0.05 in. - Longitudinal cracks prior to S3 \approx 0.1 in.
S2: Shear Cracking	<ul style="list-style-type: none"> - Same as FC HAL for F3 except as noted - May occur at any height
S3.0: Widening and Localization of Shear Cracks	<ul style="list-style-type: none"> - May occur at any height - At 35° to 65° angle from horizontal - Prior to spalling \approx 0.3 in. residual (HAL) - Prior to spalling \approx 0.5 in. residual (LAL)
S3.1: Widening and Localization of Longitudinal Cracking on Side Faces	<ul style="list-style-type: none"> - May run the entire height of the column - Meet localized shear cracks near edge - Prior to spalling \approx 0.5 in. residual
S3.2: Concrete Spalling on Side Faces	<ul style="list-style-type: none"> - Possible spall shapes <ul style="list-style-type: none"> o Triangle where shear and longitudinal cracks meet o Parallelogram encompassing primary shear cracks - Edges of spall are at 35° to 65° angle from horizontal - May occur at any height
S3.3: Longitudinal Bar Buckling	<ul style="list-style-type: none"> - May occur at any height
S3.4: Crushing of Core Concrete	<ul style="list-style-type: none"> - Typically occurs with Bar Buckling - May occur at any height

S1. Flexural Cracking and Longitudinal Cracking

The description of flexural cracks, residual flexural cracks, and longitudinal cracks are identical to that of flexure-critical columns as presented in the section on flexural damage.



Figure 3.57 Flexural cracking and longitudinal cracking: experimental damage (Sezen 2002)

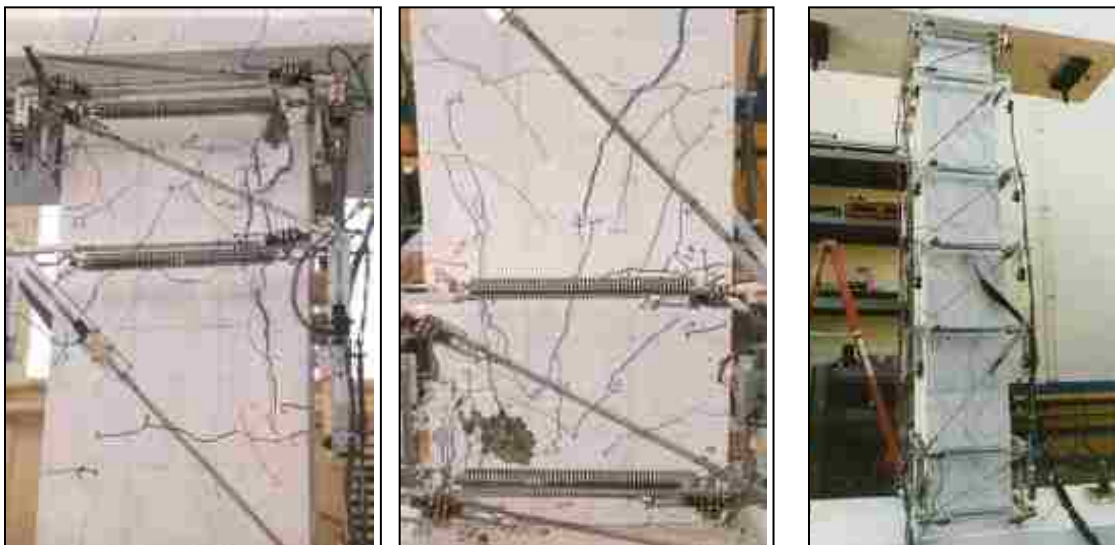


Figures 3.58 and 3.59 Flexural and longitudinal cracking: earthquake damage (Eberhard, et al. 2010)

S2. Shear Cracking on Side Faces

The description of shear cracking is very similar for a shear and flexure-critical column; it has been included here to identify the differences in the two response modes. Shear cracks result from principal diagonal tension stresses corresponding to applied shear forces. The cracks propagate from the flexural faces of the column and cross the sides of the column. Shear cracks are typically oriented at an angle of 35 to 65 degrees from the horizontal; the angle of cracking depends on the axial load and the geometry of the column.

For shear-critical columns shear cracks may form at any location along the column's height. As the displacement demand increases the width of shear cracks will increase.



Figures 3.60, 3.61, and 3.62 Shear cracking on side faces: experimental damage (Sezen 2002)



Figures 3.63 and 3.64 Shear cracking on side faces: earthquake damage (Sedra, et al. 2010)



Figures 3.65 and 3.66 Shear cracking on side faces: earthquake damage (Eberhard, et al. 2010)

S3. Damage Associated with Failure

The following five damage categories are associated with a brittle shear failure mechanism in a column. Review of data from previous experimental tests (Sezen 2002) indicates that these damage states typically occur suddenly and approximately simultaneously once earthquake shear demand exceeds capacity. A review of images from the National Information Service for Earthquake Engineering's online archive (<http://nisee.berkeley.edu/elibrary/>) suggests that because damage states occur approximately simultaneously, only the final damage state may be observed in the field following an earthquake. The damage states listed below were from a review of images of laboratory tests of shear-critical columns.

After the initial cracking occurs, columns with low axial loads can progress through the S3 damage states. This is possible in the laboratory setting because the column is able to carry the applied low axial load as an experimental test is carried out. Once the first S3 damage state occurs the column is likely to have lost its lateral load-carrying capacity but the test can continue until the column can no longer carry axial load. This makes it possible to achieve larger displacements in low axially loaded shear-critical columns.

Shear-critical columns loaded with high axial loads fail in a more brittle manner than those with low axial loads. Once the first S3 damage state occurs it is likely that the column has failed both laterally and axially. The sudden simultaneous failure occurs once the shear demand exceeds capacity.

S3.0 Widening and Localization of Shear Cracks

Prior to failure, shear cracking localizes with one or two wide shear cracks. The wide shear cracks have the same orientation as the initial shear cracking. In the field, one or two wide shear cracks indicate shear failure of the column.



Figures 3.67 and 3.68 Widening and localization of shear cracks: experimental damage (Sezen 2002)



Figures 3.69 and 3.70 Widening and localization of shear cracks: earthquake damage (Sedra, et al. 2010)



Figures 3.71 and 3.72 Widening and localization of shear cracks: earthquake damage (Eberhard, et al. 2010)



Figure 3.73 Widening and localization of shear cracks: earthquake damage (PEER)

S3.1 Longitudinal Cracking on Side Faces

Prior to failure shear cracks propagate towards the edge of the side face and turn vertical. The longitudinal cracking aligns with the location of the longitudinal steel at the edges of the column. Longitudinal cracks are likely to run the length of the column prior to failure. If the displacement demand increases rapidly, longitudinal cracking typically is not evident. Images from laboratory tests show longitudinal cracking; images of columns in the field infrequently show longitudinal cracking.



Figures 3.74 and 3.75 Longitudinal cracking on side faces: experimental damage (Sezen 2002)



Figures 3.76 (Sedra, et al. 2010) and 3.77 (PEER) Longitudinal cracking on side faces: earthquake damage

S3.2 Concrete Spalling on Side Faces

Side face concrete in the vicinity of dominant shear cracks and longitudinal cracks may spall. The region of spalled concrete typically consists of a triangle bounded by longitudinal and diagonal cracks or a parallelogram encompassing the primary diagonal cracks. Laboratory testing has shown that the onset of concrete spalling occurs simultaneously with the loss of lateral load-carrying capacity.



Figures 3.78 and 3.79 Concrete spalling on side faces: experimental damage (Sezen 2002)



Figures 3.80, 3.81, 3.82, and 3.83 Concrete spalling on side faces: earthquake damage (PEER)



Figures 3.84, 3.85, and 3.86 Concrete spalling on side faces: earthquake damage (Eberhard, et al. 2010)

S3.3 Longitudinal Bar Buckling

Longitudinal bar buckling typically occurs simultaneously with concrete spalling. Prior to spalling the bars are surrounded by concrete and transverse reinforcement. Significant spalling and bar buckling are followed closely by the loss of lateral load-carrying capacity.



Figures 3.87, 3.88, 3.89, 3.90, and 3.91 Longitudinal bar buckling: experimental damage (Sezen 2002)



Figures 3.92, 3.93, 3.94, 3.95, and 3.96 Longitudinal bar buckling: earthquake damage (PEER)



Figures 3.97 and 3.98 Longitudinal bar buckling: earthquake damage (Sedra, et al. 2010)

S3.4 Crushing of Core Concrete

Longitudinal bar buckling is typically accompanied by yielding of transverse reinforcement. The yielding of transverse reinforcement allows for crushing of the core concrete. The axial load-carrying capacity is lost once core crushing occurs.



Figure 3.99 Crushing of core concrete: experimental damage (Sezen 2002)



Figures 3.100, 3.101, and 3.102 Crushing of core concrete: earthquake damage (PEER)

3.3.5 Loss of Load Carrying Capacity

Two more critical damage states occur during the progression of damage. These two damage states represent the loss of load-carrying capacity for a column. Both the loss of lateral and axial load-carrying capacity are significant damage states for a column. Identifying the damage that corresponds to the loss of load-carrying capacity was crucial to the project.

Typically the loss of lateral load carrying capacity is documented when a load cycle to a displacement demand in excess of previous displacement demands drops below 80% of the maximum strength exhibited by the component. This definition was used in the current study. If multiple columns in a story of a building lose lateral load carrying capacity the building could be expected to have a high risk of collapse due to development of a side-sway mechanism under earthquake loading. This is because low lateral stiffness could be expected to result in large story drifts under earthquake loading and, as a result, large $P-\Delta$ moment demands in excess of column capacity. Because the columns designated as lateral load resisting components also carry gravity loads, loss of column axial load carrying capacity also increases the likelihood of structural collapse.

Damage states that typically correspond to the loss of lateral load carrying capacity for flexure-critical columns are bar buckling and core crushing. For flexure-critical columns the axial loads do not affect the damage states corresponding to the loss of lateral load carrying capacity. The non-ductile nature of shear-critical columns affects the progression of failure based on the axial load. Shear-critical columns loaded with low axial loads are expected to lose lateral load carrying capacity once shear cracks have widened and become localized. A high axial load on a shear-critical column may cause any of the S3 damage states to correspond to the loss of lateral load carrying capacity. The loss of axial load carrying capacity typically occurs after longitudinal reinforcement has fractured for flexure-critical columns. This damage is independent of the level of axial load. Loss of axial load carrying capacity typically is dependent on the axial load for shear-critical columns. A high axial load on a shear-critical column may cause any of the S3 damage states to correspond to the imminent loss of axial load carrying capacity.

3.3.6 Bi-Directional Loading Effect

Reinforced concrete columns experience bi-directional loading when subjected to earthquake ground motions. Columns loaded bi-directionally show the same damage patterns, but the damage occurs on all four sides of the columns. The same progression of damage occurs for both flexure and shear responses.

Damage identification will be effected early on in the damage progression by bi-directional loading. The initial cracking could potentially be effected due to the development of flexural and shear

cracking on all column faces. The horizontal flexural cracks and the angled shear cracks will run into and over one another. As mentioned previously, both flexure and shear-critical columns respond in similar ways to low levels of applied lateral loading. This leads to the conclusion that the initial crack patterns occurring due to bi-directional loading will not present additional difficulties in damage identification.

3.4 Drift Corresponding to Damage States

To enable assessment of the likelihood that the damaged structure will achieve a particular damage state, including collapse, in an aftershock or subsequent earthquake, it was necessary to link damage states with an engineering demand parameter (EDP) that can be determined from analysis. For the current study story drift was chosen as the EDP. Section 3.4.1 discusses the choice of drift as an EDP. Sections 3.4.1 through 3.6.4 present damage state data that corresponds to the EDP data as determined from Bae, Sezen, the Database, ATC-58, and proposed models. The objective of Section 3.4 was to compare the Bae and Sezen data with a wide range of column data in order to propose drifts that identify when a damage state occurs. The proposed drifts presented at the end of this section have been used in Chapter 5 to determine the damage in frames subjected to earthquake ground motions.

The effect of axial load was also considered when correlating damage data to drift data. As discussed in Section 3.3.1, the axial load typically affects the drift a column is able to achieve prior to a damage state occurring.

3.4.1 Drift as the Selected Engineering Demand Parameter

Drift was chosen as the EDP for this study. Story drift is a widely accepted EDP that corresponds to damage states (Elwood and Moehle 2004, Elwood and Moehle 2005, Pagni and Lowes 2006, Brown and Lowes 2007). The Database includes damage data for column tests for which damage was documented by the researcher. The maximum displacement sustained by the test specimen prior to the onset of a particular damage state is included in the dataset. The displacement data were converted to story drifts using the lengths of the columns which were taken from the Database. Drift data can easily be documented during analysis of frame models.

3.4.2 Drift at Proposed Damage States from Bae (2005) and Sezen (2002)

Data from multiple test programs were used to establish the damage states presented in Section 3.3; however, the primary sources were the tests performed by Bae (2005) and Sezen (2002). The data presented in Table 3.3 identify the median drifts at the onset of each flexural damage state as determined from the column tests with a low and high axial load (two columns at each axial load level) by Bae. Table

3.4 lists the drift at the onset of shear damage states for the columns tested by Sezen with low and high axial load (one column at each axial load level).

Table 3.3 Drift at Flexural Damage States for Bae Specimens

Flexural Damage States	Drift at Onset of Damage State	
	Low Axial Load	High Axial Load
F1 Flexural Cracking	0.25%	0.50%
F2 Longitudinal Cracking on Flexural Faces	1.00%	1.00%
F3 Shear Cracking on Side Faces	1.00%	1.00%
F4 Concrete Spalling on Flexural Face and Side Face	1.50%	1.00%
F5 Concrete Spalling Exposing Longitudinal Steel	2.00%	2.00%
F6 Longitudinal Bar Buckling	3.50%	3.00%
F7 Crushing of Core Concrete	3.50%	3.00%
F8 Longitudinal Bar Fracture	4.25%	3.50%
F9 Loss of Lateral Load-Carrying Capacity	3.75%	2.75%
F10 Loss of Axial Load-Carrying Capacity	5.00%	3.75%

Table 3.4 Drift at Shear Damage States for Sezen Specimens

Shear Damage States	Drift at Onset of Damage State	
	Low Axial Load	High Axial Load
S1 Flexural and Longitudinal Cracking	<0.25%	<0.25%
S2 Shear Cracking on Side Faces	<0.5%	<0.5%
S3.0 Widening and Localization of Shear Cracks	2.5%	1.75%
S3.1 Longitudinal Cracking on Side Faces	2.5%	1.75%
S3.2 Concrete Spalling on Side Faces	2.5%	1.75%
S3.3 Longitudinal Bar Buckling	4.5%	1.75%
S3.4 Crushing of Core Concrete	4.5%	1.75%
S3.5 Loss of Lateral Load-Carrying Capacity	2.5%	1.75%
S3.6 Loss of Axial Load-Carrying Capacity	4.5%	1.75%

3.4.3 Drift at Database and ATC-58 Damage States

The drift at onset of the proposed damage states as determined from column tests included in the Database are listed in Table 3.5 and Table 3.6. Data for individual tests are provided in Appendix A. The Database includes the displacement at onset of a relatively few damage states (spalling, significant spalling, bar buckling, longitudinal bar fracture, and loss of axial load-carrying capacity); thus, for tests which damage data were provided in the Database, original reports were reviewed to retrieve additional damage data. These data are also included in Appendix A. Data taken directly from the Database are labeled with an * in Table 3.5 and Table 3.6.

The Database damage states match the damage states identified in the damage progression for a flexure-critical column in Section 3.3. F4 corresponds to the onset of spalling, F5 corresponds to the

significant spalling, F6 corresponds to bar buckling, F8 corresponds to longitudinal bar fracture, and F10 corresponds to loss of axial load-carrying capacity. The damage states in Table 3.5 will be labeled the same way as Table 3.3. The Database damage states also match the damage states identified in the damage progression for a shear-critical column in Section 3.3 relatively well. S3.2 corresponds to onset of spalling, S3.3 corresponds to bar buckling, and S3.6 corresponds to loss of axial load-carrying capacity.

The Database can be used to identify the drift at which a column tested losses lateral load-carrying capacity. Camarillo (2003) identified the 80% effective force using an automated algorithm for the rectangular columns. The displacements identified by Camarillo were used to determine the drifts at which the columns lost their lateral load-carrying capacities.

The drift at onset of the proposed damage states as presented in the ATC-58 report are listed in Table 3.5 and Table 3.6. The ATC-58 includes the drift at onset of a relatively few damage states (0-concrete cracking, 1-concrete cracking, 2-concrete spalling, 3-concrete crushing, 4-steel buckling). These damage states correspond to the damage states identified in the damage progression for a flexure-critical column in Section 3.3. F1 corresponds to 0-concrete cracking, F5 corresponds to 2-concrete spalling, F6 corresponds to 4-steel buckling, and F6 corresponds to 3-concretete crushing. The ATC-58 damage states also correspond to the damage states identified in the damage progression for a shear-critical column in Section 3.3. S1 corresponds to 0-concrete cracking, S3.2 corresponds to 2-concrete spalling, and S3.3 corresponds to 3-concrete crushing.

Data from two types of experimental tests were used to develop fragility functions: frame subassemblage tests and cantilever column tests. Data from cantilever column tests were used to develop fragility functions for nine categories of frames. These include frame categories identified in ACI 318 as well as categories developed for frame component categories identified in ASCE 41-06. The frame type that corresponded to flexure critical columns with low axial loads was labeled ACI Special Moment Frames (SMF-CY) in the ATC-58. The frame type corresponding to shear critical columns with low axial loads was labeled ACI Ordinary Moment Frames Controlled by Shear Response of Columns with Moderate Axial Loads (OMF-CYSM/ASCE5) and the frame type corresponding to shear-critical columns with high axial loads was labeled ACI Ordinary Moment Frames Controlled by Shear Response of Columns with High Axial Loads (OMF-CYSH/ASCE6).

Table 3.5 Damage Data: Flexure-Critical Columns

Low Axial Load						
Damage States	Database Data			ATC-58 Data		
	No. of Tests	Median Drift (%)	Stand. Dev.	No. of Tests	Median Drift (%)	Stand. Dev.
F1 Flexural Cracking *	20	0.31	0.05	47	1.61	0.42
F2 Longitudinal Cracking on Flexural Faces *	12	1.13	0.15			
F3 Shear Cracking on Side Faces *	11	0.94	0.28			
F4 Concrete Spalling on Flexural Face and Side Face	89	1.43	0.64			
F5 Concrete Spalling Exposing Longitudinal Steel	31	2.14	0.57	16	2.89	0.46
F6 Longitudinal Bar Buckling	56	4.71	0.79	7	4.62	1.07
F7 Crushing of Core Concrete				6	4.58	0.82
F8 Longitudinal Bar Fracture	20	6.22	0.62			
F9 Loss of Lateral Load-Carrying Capacity	145	4.04	0.85			
F10 Loss of Axial Load-Carrying Capacity	11	6.07	0.95			
High Axial Load						
Damage States	Database Data			ATC-58 Data		
	No. of Tests	Median Drift (%)	Stand. Dev.	No. of Tests	Median Drift (%)	Stand. Dev.
F1 Flexural Cracking *	6	0.52	0.16			
F2 Longitudinal Cracking on Flexural Faces *	5	0.77	0.21			
F4 Concrete Spalling on Flexural Face and Side Face	19	0.77	0.35			
F5 Concrete Spalling Exposing Longitudinal Steel	1	1.09				
F6 Longitudinal Bar Buckling	8	3.53	1.06			
F9 Loss of Lateral Load-Carrying Capacity	21	2.18	0.77			
F10 Loss of Axial Load-Carrying Capacity	2	4.44	0.21			

* Database data identified through a review of the literature in the Database

Table 3.6 Damage Data: Shear-Critical Columns

Low Axial Load						
Damage States	Database Data			ATC-58 Data		
	No. of Tests	Median Drift (%)	Stand. Dev.	No. of Tests	Median Drift (%)	Stand. Dev.
S1 Flexural and Longitudinal Cracking *				5	1.42	0.52
S2 Shear Cracking on Side Faces *	5	1.10	0.56			
S3.0 Widening and Localization of Shear Cracks *	5	1.42	0.69			
S3.2 Concrete Spalling on Side Faces	1	2.49		3	1.59	0.63
S3.3 Longitudinal Bar Buckling	2	2.07	0.00	4	2.44	0.41
S3.5 Loss of Lateral Load-Carrying Capacity	24	1.81	0.62			
S3.6 Loss of Axial Load-Carrying Capacity	4	2.07	0.51			
High Axial Load						
Damage States	Database Data			ATC-58 Data		
	No. of Tests	Median Drift (%)	Stand. Dev.	No. of Tests	Median Drift (%)	Stand. Dev.
S1 Flexural and Longitudinal Cracking *				10	0.19	0.14
S3.2 Concrete Spalling on Side Faces				2	1.37	0.43
S3.3 Longitudinal Bar Buckling				10	0.71	0.57
S3.5 Loss of Lateral Load-Carrying Capacity	3	2.16	0.73			

* Database data identified through a review of the literature in the Database

Comparing the Bae and Sezen data to the data in Table 3.5 and Table 3.6 has been done in the fragilities in Figure 3.103 through Figure 3.108. The following two equations, presented by Porter et al. (2007), identify the function used to create the fragilities. $F_{dm}(edp)$ denotes the fragility for damage state dm , defined as the probability that the component reaches or exceeds damage state dm , given a particular EDP.

$$F_{dm}(edp) \equiv P[DM \geq dm | EDP = edp] \quad (3.1)$$

$$F_{dm}(edp) = \phi\left(\frac{\ln(edp/x_m)}{\beta}\right) \quad (3.2)$$

where ϕ denotes the standard normal cumulative distribution function, x_m denotes the median value of the distribution, and β is the standard deviation. The lognormal distribution has been used because it fits structural component failure data (Pagni and Lowes 2006).

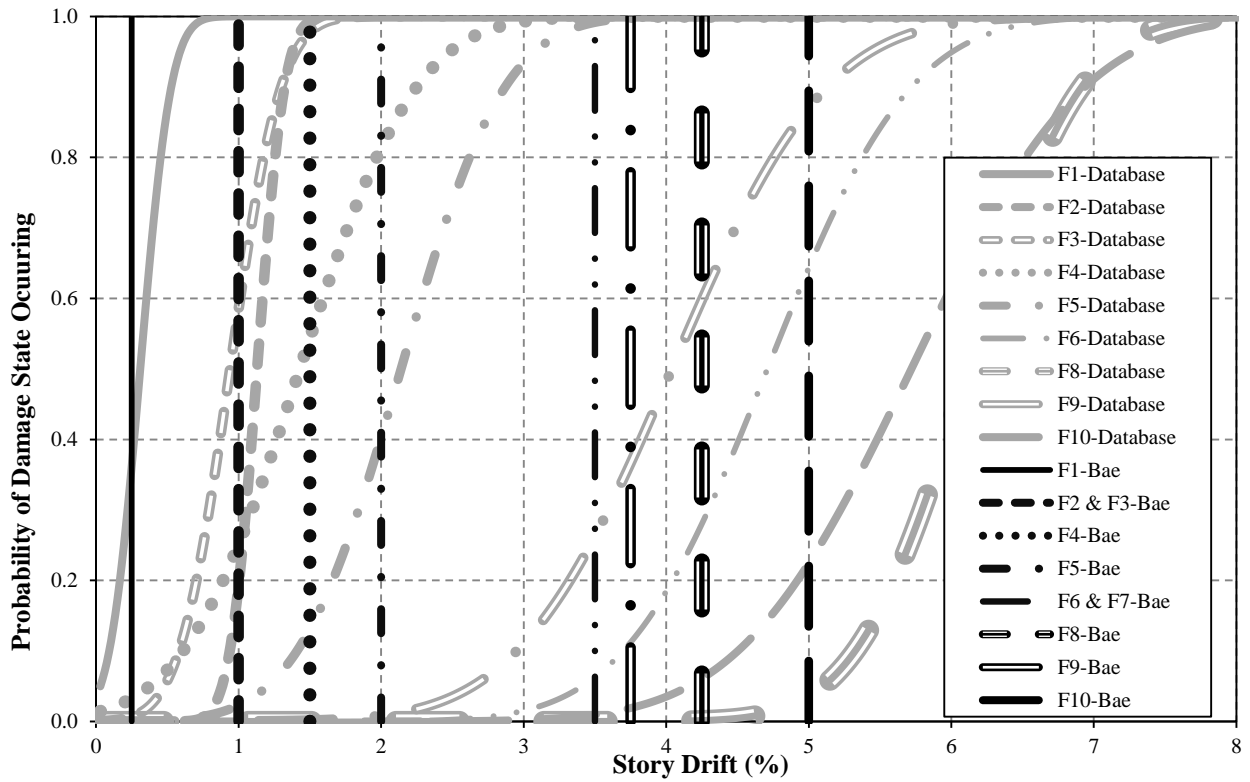


Figure 3.103 Flexure-critical low axial load Bae data compared to Database data

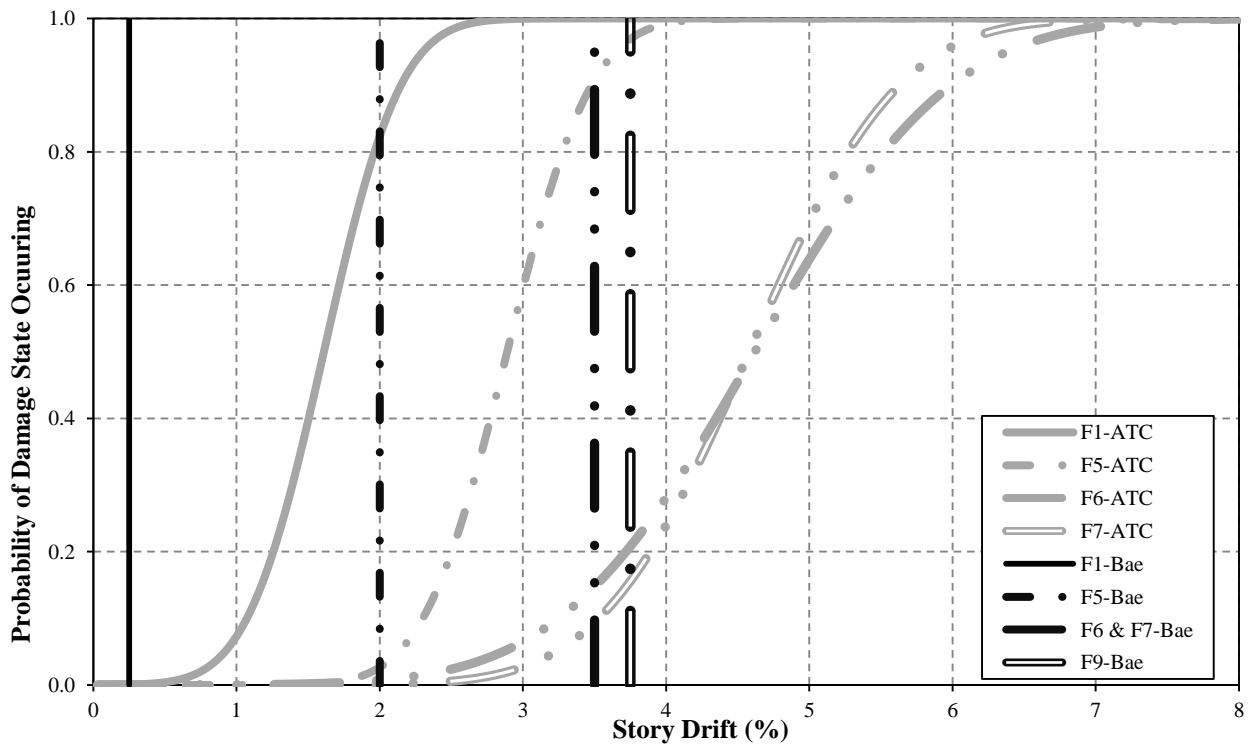


Figure 3.104 Flexure-critical low axial load Bae data compared to ATC-58 data

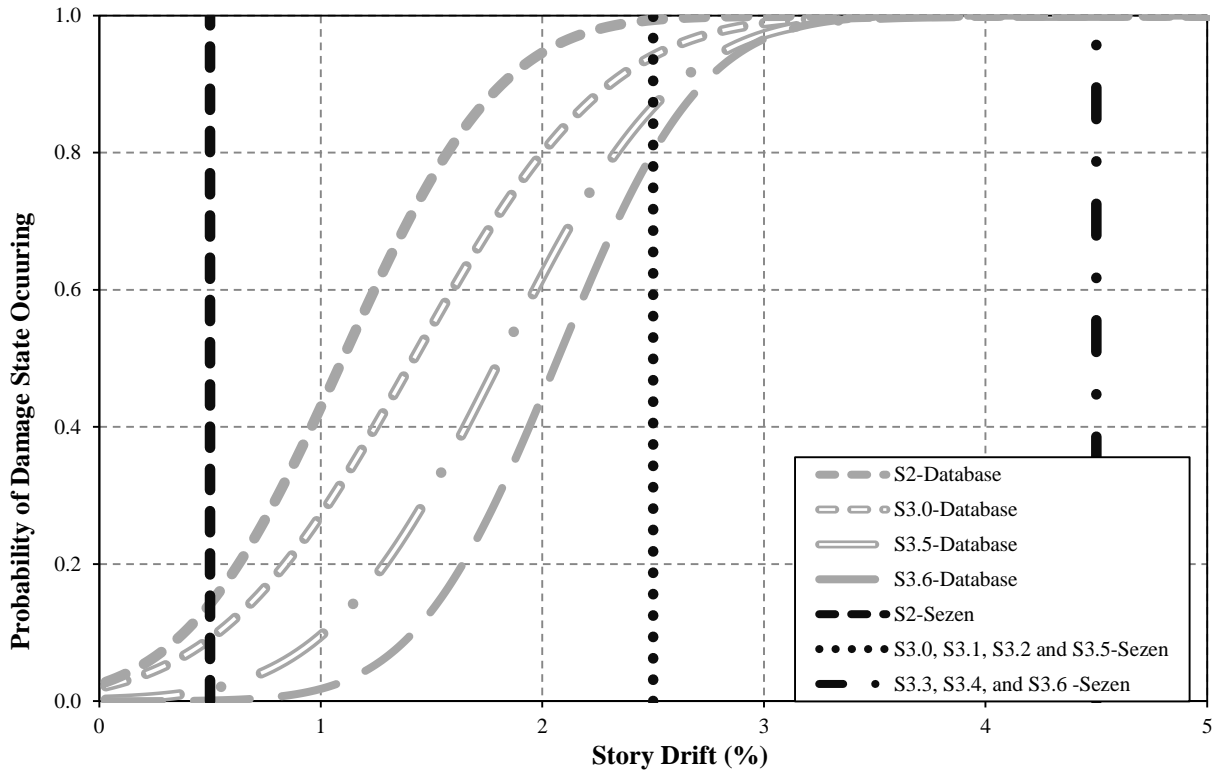


Figure 3.105 Shear-critical low axial load Sezen data compared to Database data

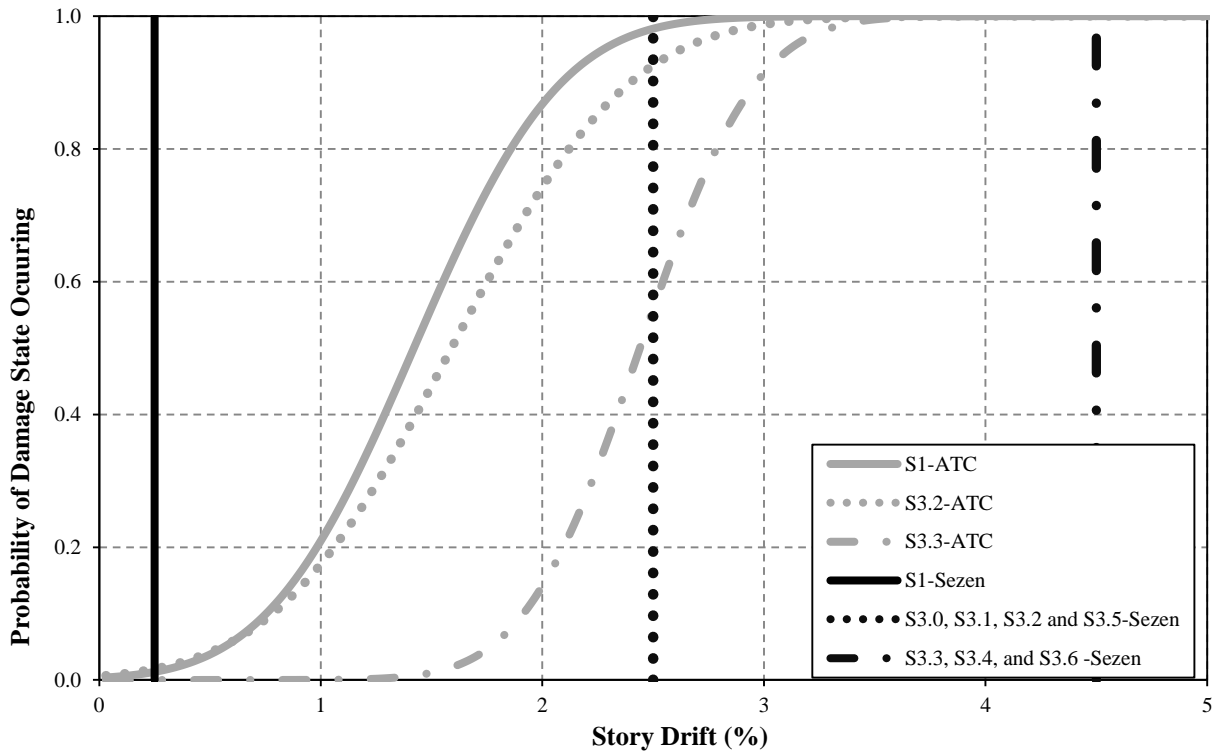


Figure 3.106 Shear-critical low axial load Sezen data compared to ATC-58 data

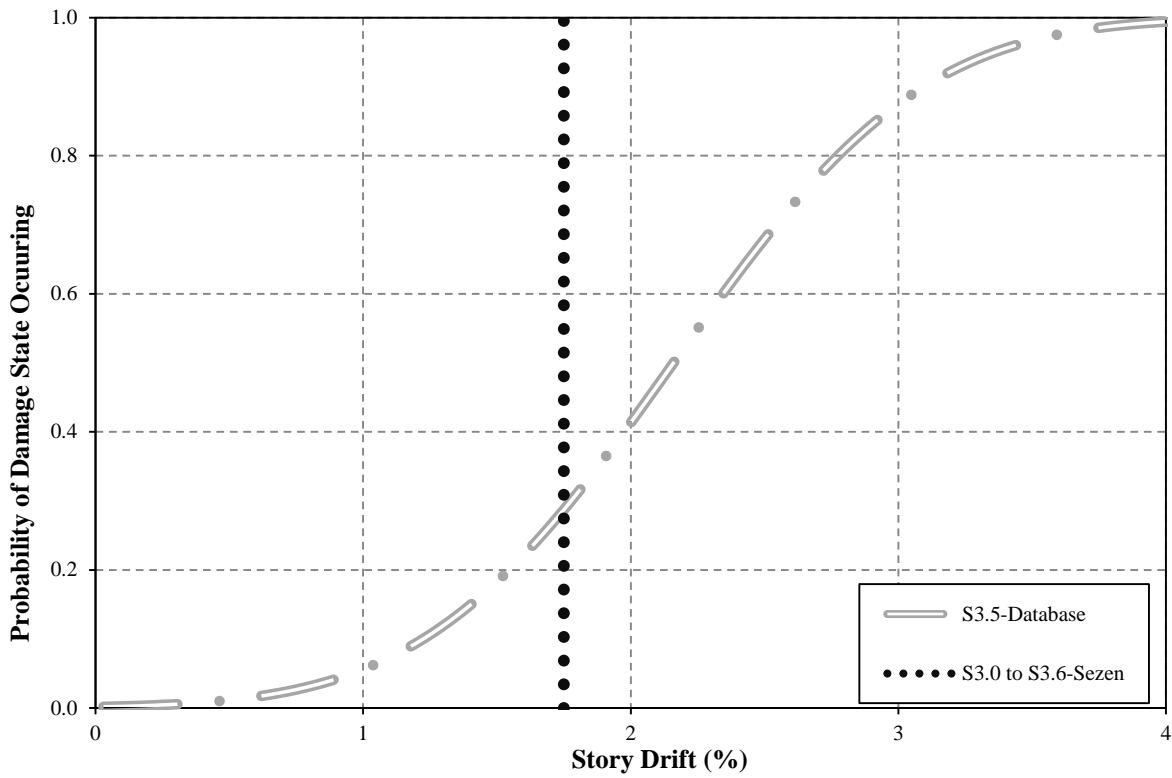


Figure 3.107 Shear-critical high axial load Sezen data compared to Database data

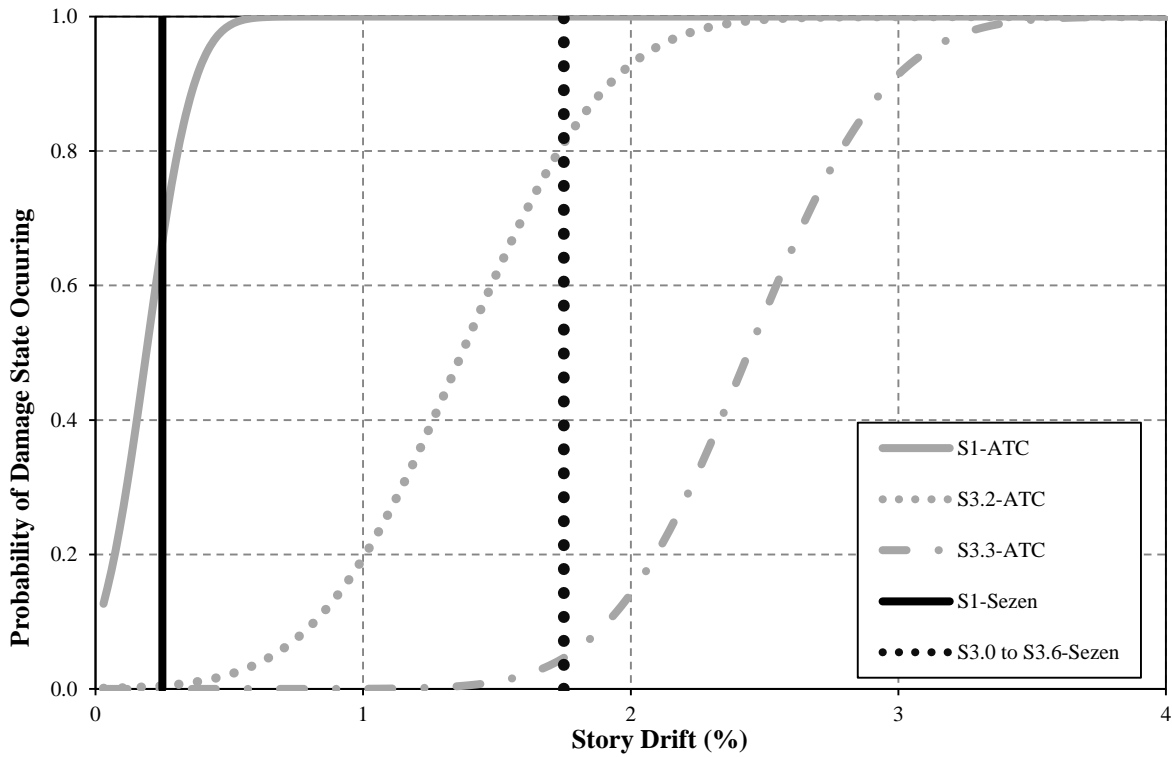


Figure 3.108 Shear-critical high axial load Sezen data compared to ATC-58 data

3.5 Drift at Loss of Capacity Based on Capacity Models

Section 2.4 presents previously proposed models predicting drift at the onset of loss of lateral load carrying capacity and loss of axial load carrying capacity. These models define drift at the onset of the capacity loss as a function of demand (shear and axial load) as well as column geometry. These models have been proposed for shear critical columns. The objective of this section was to use the models to provide a better prediction for the crucial capacity loss damage states for a typical shear critical column. A shear-critical column that is representative of a pre-1976 column has been presented in the following sections and used to predict the drift capacity at the loss of lateral and axial load carrying capacity using the models.

3.5.1 Drift Model Review

The models presented in Section 2.4 are labeled as equation 2.1 through equation 2.4. Equation 2.1 predicts the drift at loss of lateral load carrying capacity as a function of the transverse reinforcement ratio, maximum nominal shear stress, concrete compressive strength, and axial load ratio. Equation 2.2 predicts the drift at loss of axial load carrying capacity as a function of the angle of the shear plane, axial load, area of transverse reinforcement, yield strength of the transverse reinforcement, and depth of the concrete core. Equation 2.3 predicts the drift at loss of lateral load carrying capacity as a function of the longitudinal reinforcement ratio, transverse reinforcement spacing, depth of the cross section, shear span, and axial load ratio. Equation 2.4 predicts the drift at loss of axial load carrying capacity as a function of the same parameters used in equation 2.2.

3.5.1.1 Modeling Parameters

The design parameters used to define the representative shear-critical column come from ASCE/SEI 41-06, *Seismic Rehabilitation of Existing Buildings* (2007). Table 6-8 in ASCE 41-06 provides column parameters that will be used in the models to predict drift. Four categories were selected from the table to use in the models. The three parameters identified in Table 6-8 were axial load ratio, transverse reinforcement ratio, and shear demand ratio. Column category 1 provides the best case scenario for a column that will undergo seismic loading. It has a low axial load ratio, high transverse reinforcement ratio, and low shear demand. The worst case scenario presented in the ASCE 41-06 is labeled as category 4. With its low transverse reinforcement ratio, high axial load ratio, and high shear demand ratio, it was expected to have the smallest drift-capacity. Column categories 2 and 3 are representative of columns that have a high axial load ratio and a high transverse reinforcement ratio or a low axial load ratio and a low transverse reinforcement ratio respectively. These column categories provide a way to compare the

different parameters in the response of the models. Column categories 1 and 2 have been identified as representing columns likely to be flexure-critical. Column categories 3 and 4 are likely to be shear-critical.

Table 3.7 ASCE41-06 column parameters

Column Category	$\frac{P}{A_g f'_c}$	$\rho'' = \frac{A_{st}}{bs}$	$\frac{V}{bd\sqrt{f'_c}}$
1	0.1	0.006	3
2	0.6	0.006	6
3	0.1	0.0005	3
4	0.6	0.0005	6

The parameters in Table 3.7 were used to calculate the predicted drifts. Only equation 2.1 used all three parameters in Table 3.7 explicitly. This caused the need to consider typical dimensions and reinforcement properties. Dimensions and reinforcement data for the representative column was selected from previous experimental research by Lynn et al (1996). The prototype pre-1976 column details came from surveys of existing reinforced concrete buildings built prior to 1976 performed by Lynn. Table 3.8 shows the properties of a pre-1976 square column that were used to supplement the design parameters in Table 3.7.

Table 3.8 Pre-1976 Column Properties

b (in) = 18	b is the width
s (in) = 18	s is the transverse steel spacing
$\rho_l = 0.02$	ρ_l is the longitudinal reinforcement ratio
d (in) = 16.2	d is the distance from extreme compression concrete to center of tension steel
d_c (in) = 14.4	d_c is the concrete core dimension
f'_c (psi) = 4000	f'_c is the concrete compressive strength
f_{yt} (ksi) = 60	f_{yt} is the transverse reinforcement yield strength
a (in) = 58	a is the shear span of the column
d_b (in) = 1.27	d_b is the diameter of a longitudinal bar

3.5.1.2 Drift Capacity

Figure 3.109 shows the plot of the two predicted drifts at which lateral load-carrying capacity is reduced by 20% and the two predicted drifts at which axial load carrying capacity is lost for the pre-1976 column. Column category 1 in Table 3.7 is the least likely to have a shear-critical response. This explains the predicted drift at axial failure of 15% and 8% for equations 2.4 and 2.2 respectively. Shear failures in columns occur at much smaller drifts than those predicted for column category 1. Column category 2 is

less likely to be shear-critical than categories 3 and 4 from Table 3.7 due to the high transverse reinforcement ratio.

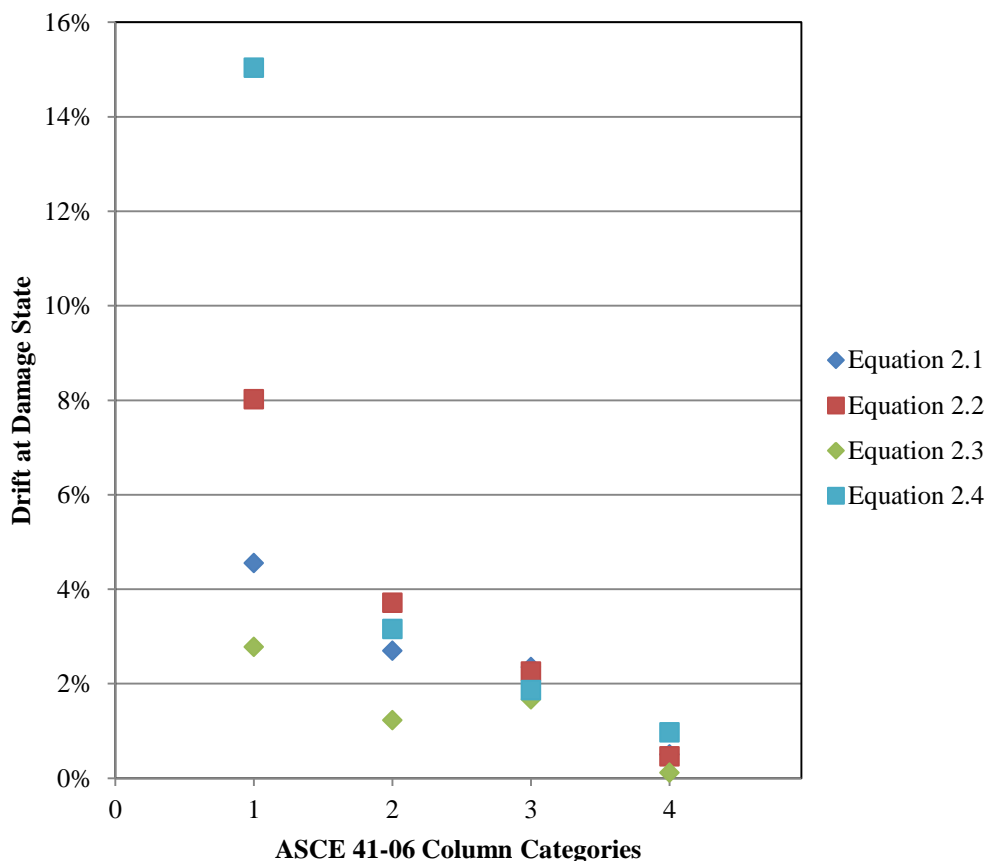


Figure 3.109 Predicted response for a pre-1976 column

Table 3.9 shows the applicable results that were plotted in Figure 3.109. Only the predicted drifts from the pertinent ASCE 41-06 column categories are shown in the table. For the drifts computed using the pre 1976 column properties, only column categories 3 and 4 are representative of shear-critical columns.

Table 3.9 Predicted drift for pre 1976 column (Shear-Critical)

Model Used	Damage State	ASCE Column Category	
		3	4
Equation 2.1	Lateral Load	2.35%	0.50%
Equation 2.3	Failure	1.67%	0.12%
Equation 2.2	Axial Load	2.26%	0.46%
Equation 2.4	Failure	1.86%	0.97%

3.6 Proposed Drifts for Onset of Damage

This section's objective was to consider the drift and damage state data presented previously in Chapter 3 and propose a set of drifts that could be expected to be observed in flexure-critical columns and shear-critical columns. The Database data will be the primary source for the proposed drifts at the onset of damage. Where the Database is lacking sufficient data, the other sources, including the Bae, Sezen, ATC-58, and shear-critical column models have been used. Table 3.10, Table 3.11, Table 3.13, and Table 3.14 presents the full set of data to be used to make conclusions on proposed drifts.

3.6.1 Drift Comparison for Flexure-Critical Columns

The flexure-critical columns with low axial loads have been considered first. Table 3.10 presents the Bae data, Database data, and ATC-58 data for a flexure-critical column with low axial load. The data has been discussed below the table.

Table 3.10 Flexure-Critical Columns with low axial loads: median drifts

Flexural Damage States	Bae Data	Database Data	ATC-58 Data
F1 Flexural Cracking	0.25%	0.31%	1.61%
F2 Longitudinal Cracking	1.00%	1.13%	
F3 Shear Cracking	1.00%	0.94%	
F4 Concrete Spalling	1.50%	1.43%	
F5 Significant Spalling	2.00%	2.14%	2.89%
F6 Bar Buckling	3.50%	4.71%	4.62%
F7 Core Crushing	3.50%		4.58%
F8 Bar Fracture	4.25%	6.22%	
F9 Loss of Lateral Capacity	3.75%	4.04%	
F10 Loss of Axial Capacity	5.00%	6.07%	

A comparison of the median drift values from the Database to the other data points in Table 3.10 shows that the Bae columns have similar drifts to the Database up to the bar buckling damage state. The Database flexural damage states F6, F8, F9, and F10 occur at larger median drift values than the Bae damage. The ATC-58 confirms the data for damage state F6. The ATC-58 data does present significantly larger drifts for the F1 damage state. The increased flexibility included in the A potential reason for the ATC-58 F1 damage state being large is due to the ATC-58 damage state, 0-concrete cracking, used for F1 was identified as having residual concrete cracking. The Database and Bae data likely were recorded when cracks first formed when the specimen was being held at a peak displacement. This difference could be significant; thus, the Database data has been used for damage state F1.

Another intriguing issue was the drifts at which longitudinal cracking and shear cracking occur. Based on the full data set it appears that longitudinal cracking occurs at a larger drift than shear cracking.

In the progression identified in the Bae tests, these two damage states occurred at the same drift level. After reviewing the tests in which the cracking data came from, only three column tests had data for both the F2 and F3 damage states. The three tests all reported the same displacement for both damage states. This indicates that if both these damage states are present in a column, they likely occurred at the same drift.

An additional unsuspected result came from the data presented in Table 3.10. The median Database drift at which the loss of axial load-carrying capacity occurred was less than the median drift at which longitudinal bar fracture occurred. This was a surprise because in a cyclic lateral load test, once the specimen loses the ability to carry axial load the test is typically terminated. This makes it impossible to see a damage state occur at a drift further than the test was concluded.

Upon review of the tests that the F8 and F10 data came from, only two tests had data for both damage states. One test reported longitudinal bar fracture and axial capacity loss at the same drift (6.13%) and the other test reported bar fracture (3.78%) prior to axial failure (4.63%). These two test specimens follow the expected progression of damage. This indicates the tests reporting loss of axial capacity were inherently weaker than the columns reporting longitudinal bar fracture. Despite the 20 columns with data for longitudinal bar fracture, it must be concluded that bar fracture will occur prior to axial capacity loss in order to be conservative when predicting the drift for the F8 damage state.

The proposed drifts for a flexure-critical column with low axial load to be used for identifying damage states during the analysis work will be presented in Table 3.12 along with the drifts for a flexure-critical column with high axial load. Table 3.11 presents the Bae data and Database data for a flexure-critical column with high axial load. The data has been discussed below the table.

Table 3.11 Flexure-Critical Columns with high axial loads: median drifts

Flexural Damage States	Bae Data	Database Data
F1 Flexural Cracking	0.50%	0.52%
F2 Longitudinal Cracking	1.00%	0.77%
F3 Shear Cracking	1.00%	
F4 Concrete Spalling	1.00%	0.77%
F5 Significant Spalling	2.00%	1.09%
F6 Bar Buckling	3.00%	3.53%
F7 Core Crushing	3.00%	
F8 Bar Fracture	3.50%	
F9 Loss of Lateral Capacity	2.75%	2.18%
F10 Loss of Axial Capacity	3.75%	4.44%

A comparison of the median drift values from the Database to the Bae data points in Table 3.11 shows that the Bae columns have similar drifts up to the significant spalling damage state. The flexural damage states F9 and F10 warrant further discussion.

There were only two data points for damage state F10, axial capacity loss. They both came from the same test program completed by Paultre et al. (2001). The two reported drifts were 4.30% and 4.60%. The small standard deviation provided a small range for another data point to fall inside. The loss of lateral capacity had enough data points to use the Database data. The high drifts achieved by the two Bae specimens are attributed to them having the lower limit of axial load ratio being placed on them. The Database considered columns with any level of axial load greater than or equal to $0.5f_c A_g$.

There were no reports including information on shear cracking or bar fracture. This lack of data for columns with high axial loads was partially due to there being only 23 columns with high axial load, of the 195 flexure-critical columns, in the Database that reported damage data of any kind. Another reason for the lack of data for shear cracking and longitudinal bar fracture is that these two damage states are less likely to occur in column specimens with high axial loads. Only one of the Bae specimens exhibited longitudinal bar fracture prior to the loss of axial capacity. If a column exhibits bar fracture it is likely to have a low axial load placed on it.

A final finding from the high axial load data was that longitudinal cracking, shear cracking, and initial spalling will typically occur at the same drift level. This was mentioned in the flexural damage progression discussed in section 3.3.3. If shear cracks occur without spalling, the column was likely to have a low axial load placed on it.

3.6.2 Proposed Drifts at Damage States for Flexure-Critical Columns

Table 3.12 shows the proposed drifts at each damage state for flexure-critical columns. The proposed drifts in Table 3.12 come from the data discussed in section 3.6.1. These drifts will be used later in the analysis section of this study when considering story drift data.

Table 3.12 Proposed drift at onset of flexural damage states

Flexural Damage States	Drift at Onset of Damage State	
	Low Axial Load	High Axial Load
F1 Flexural Cracking	0.3%	0.5%
F2 Longitudinal Cracking on Flexural Faces	1.0%	0.75%
F3 Shear Cracking on Side Faces	1.0%	0.75%
F4 Concrete Spalling on Flexural Face and Side Face	1.5%	0.75%
F5 Concrete Spalling Exposing Longitudinal Steel	2.0%	1.0%
F6 Longitudinal Bar Buckling	4.5%	3.0%
F7 Crushing of Core Concrete	4.5%	3.0%
F8 Longitudinal Bar Fracture	6.0%	3.5%
F9 Loss of Lateral Load-Carrying Capacity	4.0%	2.0%
F10 Loss of Axial Load-Carrying Capacity	6.0%	4.5%

Some of the high axial load drifts in Table 3.12 come from a very small data set or no data at all. The F5 damage state had only one reported drift. It was just slightly larger than the median value for F4. This makes sense when considering the effects of placing a high axial load on columns. The higher the axial load, the more explosive spalling will be. Another issue was the longitudinal bar fracture damage state for high axial loads. The high axial load inhibits the fracture of longitudinal reinforcement. There were not tests in the Database that reported longitudinal bar buckling for columns with a high axial load. To be somewhat conservative, the drift at which the bar fracture damage state occurred in the Bae test was chosen. It was only half a percent larger than the longitudinal bar buckling damage state and was a full percent smaller than the loss of axial load-carrying capacity.

As discussed in Section 3.3.5 the loss of lateral load carrying capacity corresponds to visible damage states. The proposed drifts have identified that a column was likely to have lost 20% of its lateral load carrying capacity prior to longitudinal bar buckling and core crushing. The axial capacity loss corresponds to the fracture of a longitudinal bar.

3.6.3 Drift Comparison for Shear-Critical Columns

The shear-critical columns with low axial loads have been considered first. Table 3.13 presents the Sezen data, Database data, ATC-58 data, and the data points from the drift capacity models for a shear-critical column with low axial load. The data has been discussed below the table.

Table 3.13 Shear-Critical Columns with low axial loads: median drifts

Shear Damage States	Sezen Data	Database Data	ATC-58 Data	Equation 2.1	Equation 2.2	Equation 2.3	Equation 2.4
S1 Flexural Cracking	0.25%		1.42%				
S2 Shear Cracking	0.50%	1.10%					
S3.0 Shear Crack Growth	2.50%	1.42%					
S3.1 Longitudinal Cracking	2.50%						
S3.2 Concrete Spalling	2.50%	2.49%	1.59%				
S3.3 Bar Buckling	4.50%	2.07%	2.44%				
S3.4 Core Crushing	4.50%						
S3.5 Loss of Lateral Capacity	2.50%	1.81%		2.35%		1.67%	
S3.6 Loss of Axial Capacity	4.50%	2.07%			2.26%		1.86%

A quick comparison of the median drift values from the Database to the other data points in Table 3.13 shows there was a wide range of drifts associated with damage. The major difficulty was that there are very few data points that come from the Database. This causes the median values for damage states S3.3 and S3.2 to be in reverse order of what would be expected. The proposed drifts at the onset of damage states for shear-critical columns with low axial loads are shown in Table 3.15 and primarily come from the Sezen Data.

Table 3.14 Shear-Critical Columns with high axial loads: median drifts

Shear Damage States	Sezen Data	Database Data	ATC-58 Data	Equation 2.1	Equation 2.2	Equation 2.3	Equation 2.4
S1 Flexural Cracking	0.25%		0.19%				
S2 Shear Cracking	0.50%						
S3.0 Shear Crack Growth	1.75%						
S3.1 Longitudinal Cracking	1.75%						
S3.2 Concrete Spalling	1.75%		1.37%				
S3.3 Bar Buckling	1.75%		0.71%				
S3.4 Core Crushing	1.75%						
S3.5 Loss of Lateral Capacity	1.75%	2.16%		0.50%		0.12%	
S3.6 Loss of Axial Capacity	1.75%				0.46%		0.97%

A comparison of the median drift values from the Database to the other data points in Table 3.14 shows there was a wide range of drifts associated with damage. The major difficulty was having no data from the Database. The drift capacity equations for the shear critical column have predicted small drift values. This was due to having the worst case scenario for the ASCE 41-06 design parameters. The axial load was high and the shear stress demand was high. This causes the proposed equations to predict essentially no capacity. Shear-critical columns with high axial loads should be approached with caution. The proposed drifts at the onset of damage states for shear-critical columns with high axial loads are shown in Table 3.15 and primarily come from the Sezen data.

3.6.4 Proposed Drifts at Damage States for Shear-Critical Columns

Table 3.15 shows the proposed drifts at each damage state for shear-critical columns. The proposed drifts in Table 3.15 come from the data presented in Section 3.6.3. These drifts will be used in the analysis section of Chapter 5 when considering story drift data.

Table 3.15 Proposed Drift at onset of Shear Damage States

Shear Damage States	Drift at Onset of Damage State	
	Low Axial Load	High Axial Load
S1 Flexural and Longitudinal Cracking	0.25%	0.25%
S2 Shear Cracking on Side Faces	0.50%	0.50%
S3.0 Widening and Localization of Shear Cracks	2.0%	1.75%
S3.1 Longitudinal Cracking on Side Faces	2.5%	1.75%
S3.2 Concrete Spalling on Side Faces	2.5%	1.75%
S3.3 Longitudinal Bar Buckling	2.5%	1.75%
S3.4 Crushing of Core Concrete	2.5%	1.75%
S3.5 Loss of Lateral Load-Carrying Capacity	2.5%	1.75%
S3.6 Loss of Axial Load-Carrying Capacity	4.5%	1.75%

The drifts in Table 3.15 primarily come from a conservative approach considering the Sezen data. There were very few reports containing damage data in the Database. This led to using what little data was provided by the Database to alter the Sezen data where required.

As discussed in Section 3.3.5 the loss of lateral load carrying capacity corresponds to visible damage states. The proposed drifts have identified that a column is likely to have lost 20% of its lateral load carrying capacity at the same drift level as the S3 damage states occur. The axial capacity loss corresponds to the S3 damage states for shear-critical columns with high axial loads, while a shear-critical column with a low axial load can withstand a greater drift than the visual S3 damage states.

3.7 Residual Drift

Recent advances in post-earthquake assessment techniques have highlighted the importance of considering residual deformations as a damage indicator. Using the maximum deformation and residual deformation as complimentary damage indicators has been proposed by multiple research teams including Yazgan and Dazio (2008), Uma et al. (2006), Christopoulos et al. (2003), and Ruiz-Garcia and Miranda (2006). Mackie and Stojadinovic (2004) have proposed that residual displacement is a better demand parameter for predicting the loss of load-carrying capacity in bridge columns than the more commonly used earthquake intensity level. The amplitude of residual deformations plays a role in assessing a building's structural integrity and helps determine the economic feasibility of repairing the structure.

Residual drifts have been identified as increasingly important parameters in assessing residual capacity of an earthquake damaged structure.

3.7.1 PEER Structural Performance Database Data Acquisition

Data from the Database were used to compute the residual drifts associated with each of the damage states described above. The load-displacement data for individual column tests were retrieved from the Database. Data were grouped based on axial load and response mode of the columns. A series of MATLAB functions were written to identify peak displacements and the drop at zero load following unloading from a peak displacement. Figure 3.110 shows displacement peaks (*) and residual displacements at zero force (x) following unloading from a peak for a typical force-displacement history.

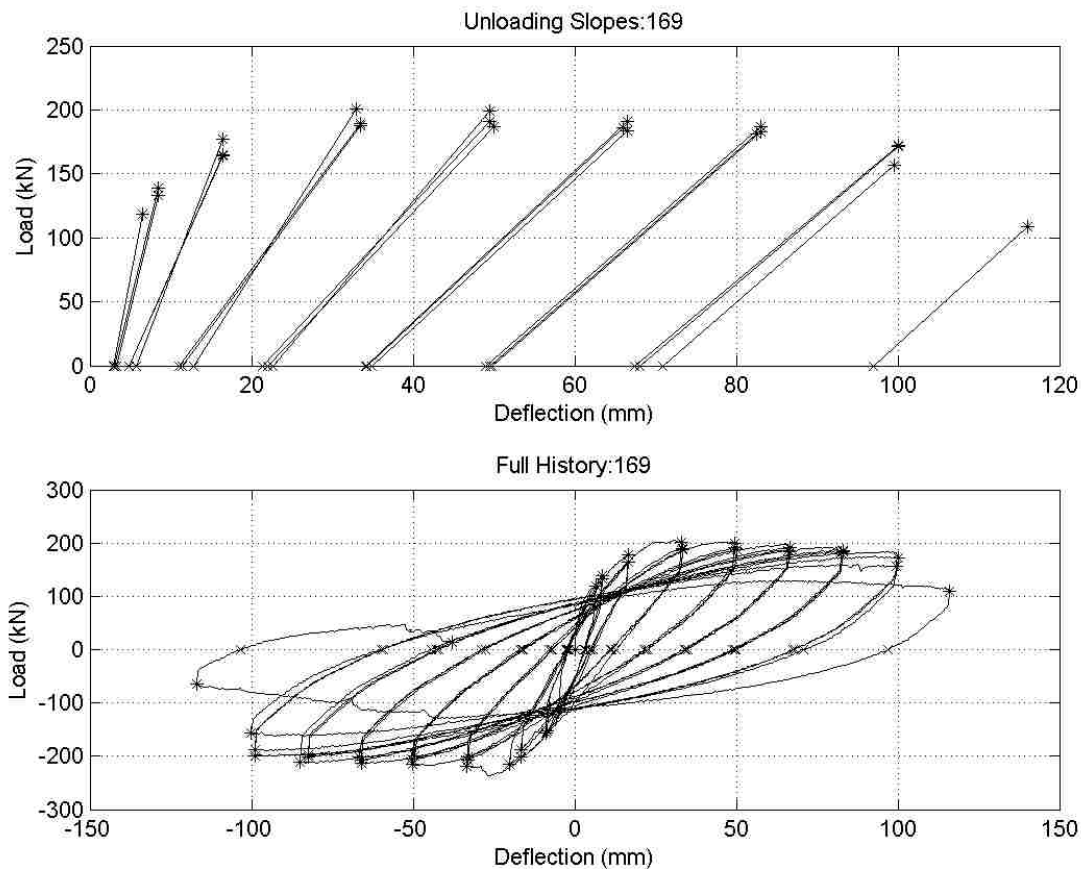


Figure 3.110 Plot of load-displacement history and unloading slopes

For each column and each damage state for which drift data was available the residual drift following unloading from the maximum displacement at which the onset of the damage state was identified in the Database, was determined. In some cases, the drift at which the damage state was defined to occur was slightly larger than the maximum displacement for a series of displacement cycles and

significantly smaller than the maximum drift demand imposed for the next series of displacement cycles. In this case, the residual drift was computed using the load-displacement data for the set of smaller displacement cycles.

The displacement portion of the load-displacement histories were converted to drift values by dividing the displacements by the length of the columns. The Database accounts for different test configurations and makes it possible to convert to drifts by dividing the damage displacements by the column lengths provided in the Database. The maximum drift and the residual drift, as seen in Figure 3.111, were recorded for each reported damage state.

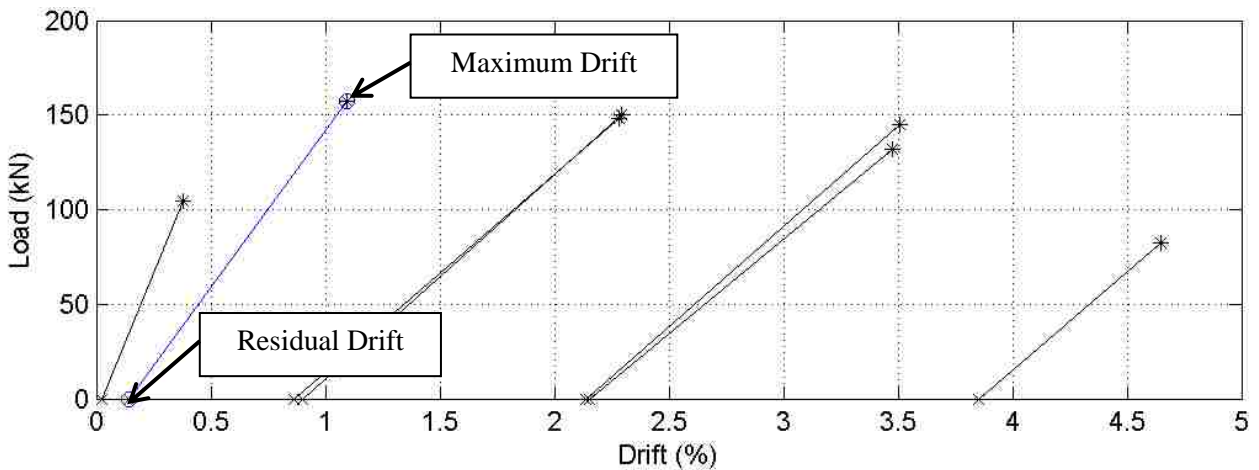


Figure 3.111 Maximum and residual drift from damage data and load-displacement history

3.7.2 Residual Drift Results

The residual drift data were plotted against the corresponding maximum drifts in Figure 3.112 and Figure 3.113. Table 3.16 presents statistics for the data. The plots in general show an increase in residual drift with increasing maximum drift as the damage in the columns progress. The two data sets plotted in Figure 3.112 and Figure 3.113 have bilinear trends that have been fitted with two line segments in Figure 3.116 and Figure 3.117. The bilinear models were determined by fitting one line to the data for damage states F1, F2, and F3. A second line was fitted to the data for damage states F4, F5, F6, F8, F9, and F10. The two line segments have can be used to predict residual drift based on the maximum drift. The data for this technique have been presented in Table 3.17. The resulting medians in Table 3.17 compare well with the Median residual drifts in Table 3.16. There are different counts in the two tables because the equation based results account for all the Database data while Table 3.16 just accounts for columns with full load displacement histories. Figure 3.114 and Figure 3.115 present the residual drift data plotted against the corresponding damages states.

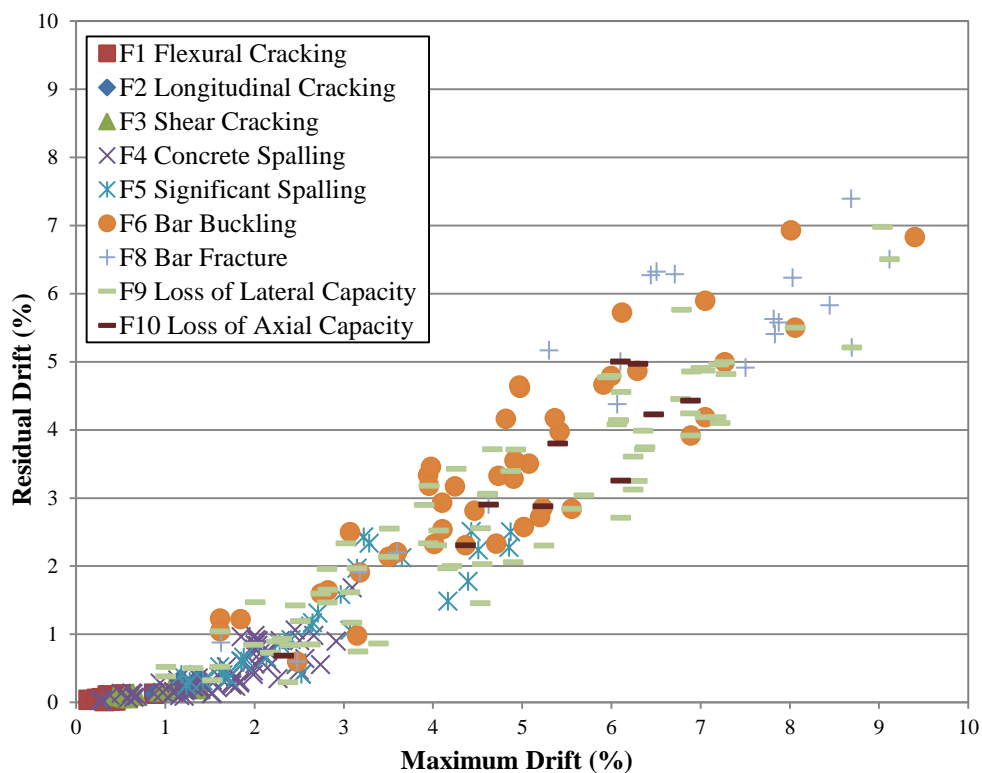


Figure 3.112 Residual Drift vs. Maximum Drift for columns with low axial loads

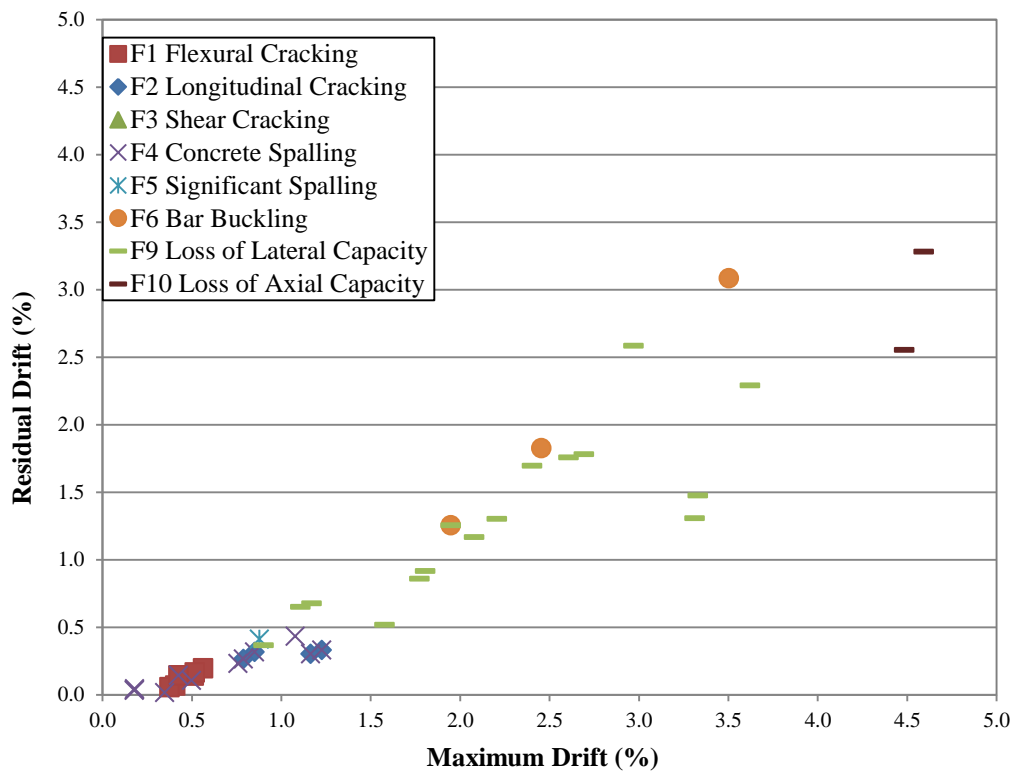


Figure 3.113 Residual Drift vs. Maximum Drift for columns with high axial loads

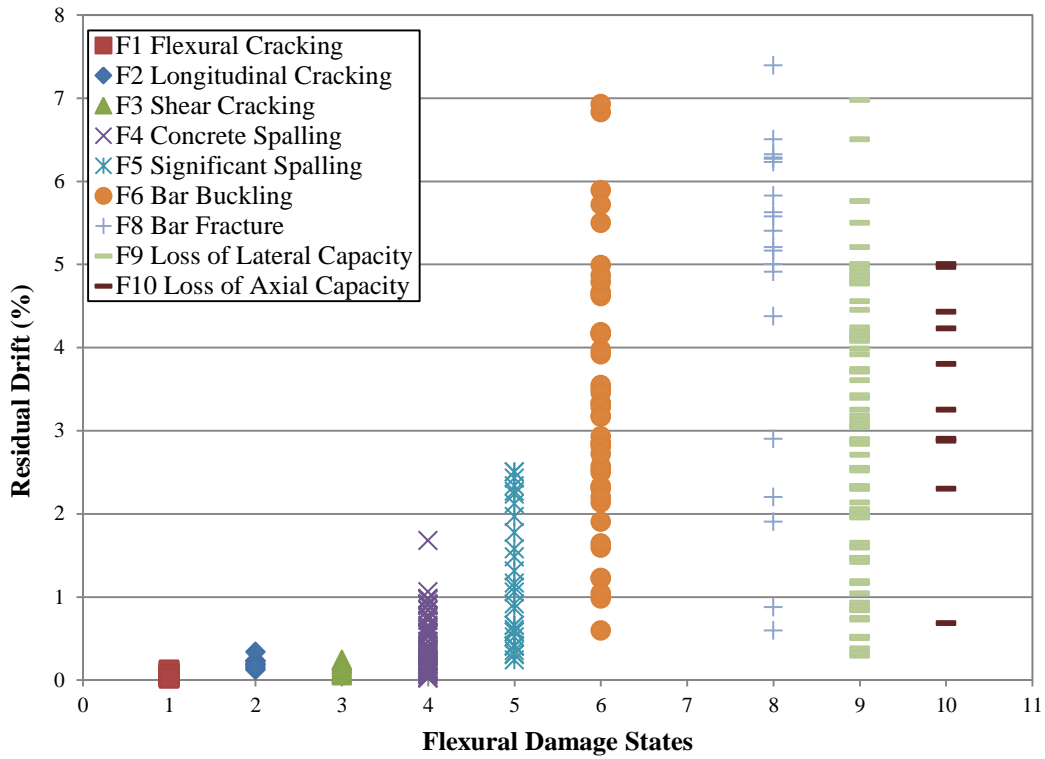


Figure 3.114 Residual Drift vs. Damage State for columns with low axial loads

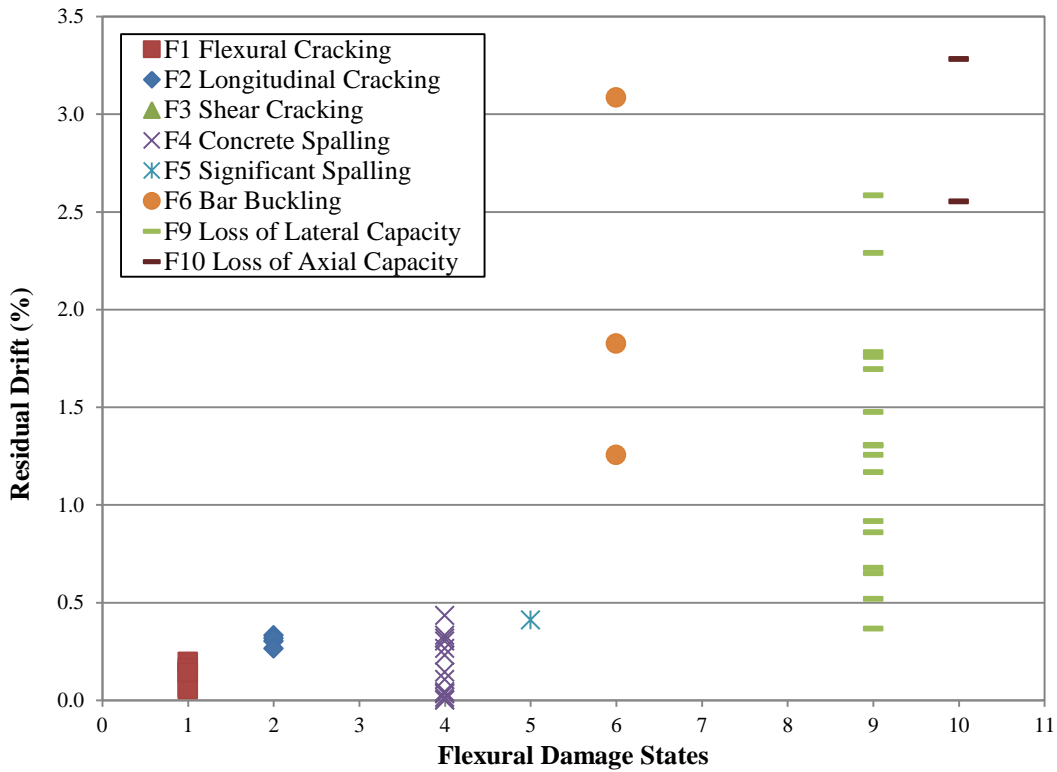


Figure 3.115 Residual Drift vs. Damage State for columns with high axial loads

Table 3.16 Residual drift data

Flexure Damage States	Residual Drift					
	Low Axial Load			High Axial Load		
	Count	Median	COV	Count	Median	COV
F1 Flexural Cracking	20	0.06	0.60	6	0.14	0.43
F2 Longitudinal Cracking	11	0.19	0.34	4	0.31	0.19
F3 Shear Cracking	11	0.16	0.44	0		
F4 Concrete Spalling	74	0.32	0.77	12	0.19	0.76
F5 Significant Spalling	30	0.99	0.66	1	0.41	
F6 Bar Buckling	45	3.18	0.46	3	1.83	0.46
F8 Bar Fracture	20	5.31	0.42	0		
F9 Loss of Lateral Capacity	83	2.88	0.56	16	1.28	0.49
F10 Loss of Axial Capacity	10	3.53	0.39	2	2.92	0.18

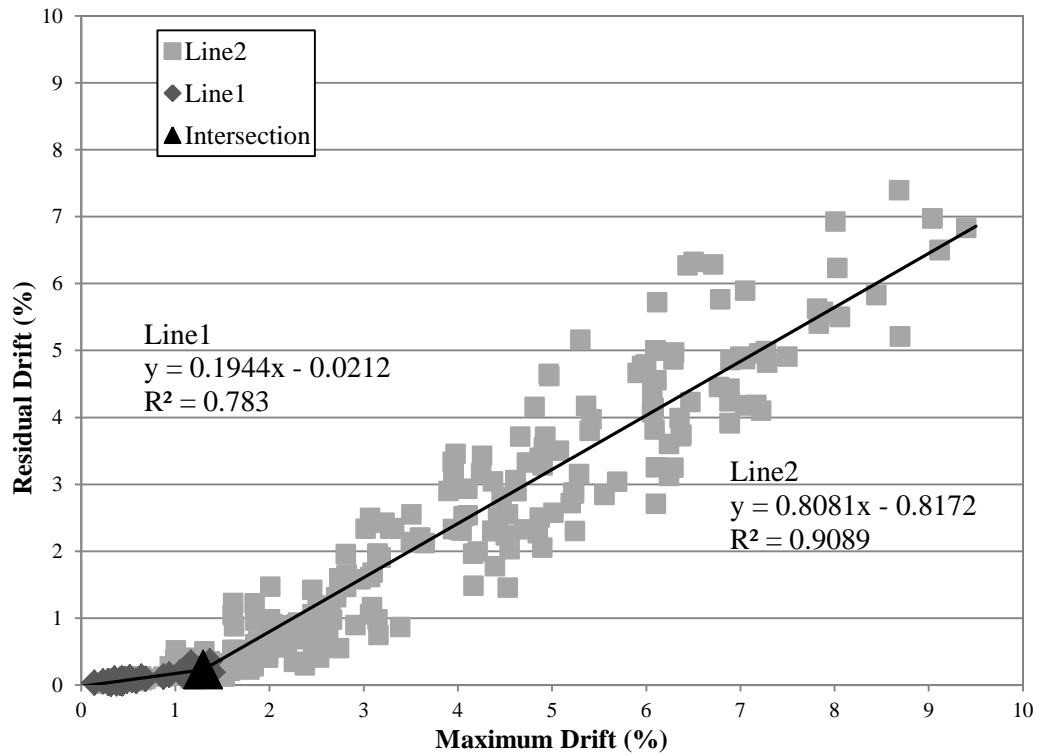


Figure 3.116 Bilinear line fit for columns with low axial loads

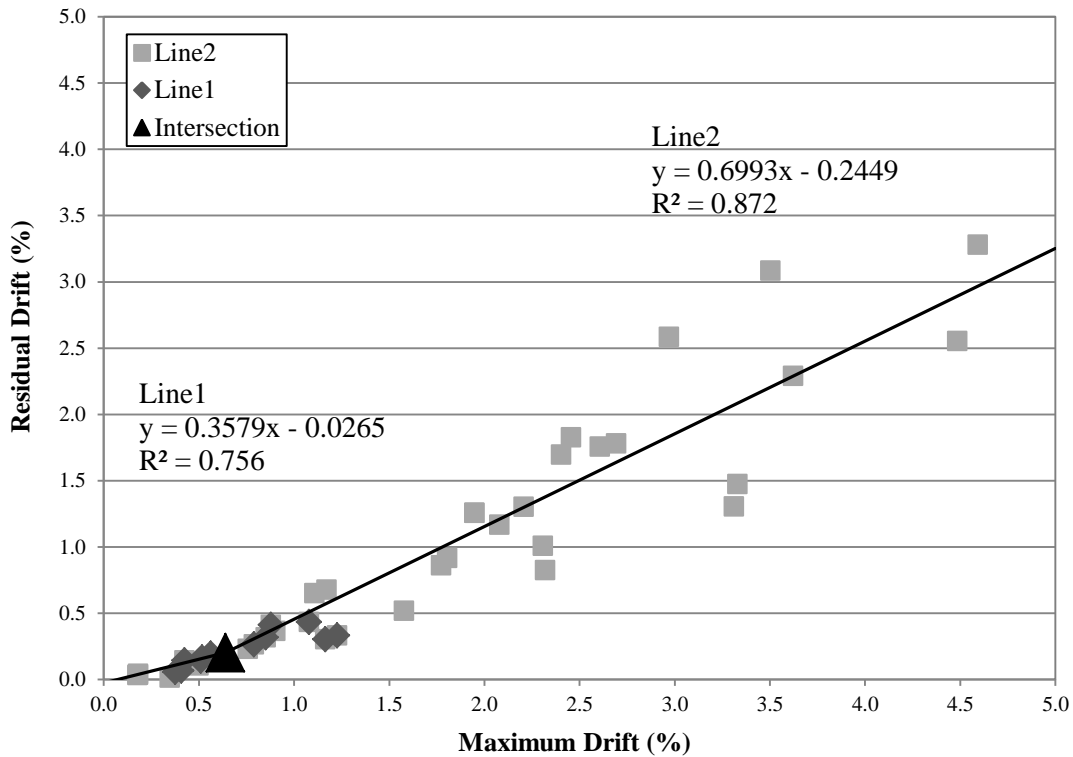


Figure 3.117 Bilinear line fit for columns with high axial loads

Table 3.17 Residual drift data using bilinear technique

Flexure Damage States	Residual Drift					
	Low Axial Load			High Axial Load		
	Count	Median	COV	Count	Median	COV
F1 Flexural Cracking	20	0.04	0.27	6	0.16	0.38
F2 Longitudinal Cracking	12	0.20	0.17	5	0.29	0.37
F3 Shear Cracking	11	0.16	0.36	0		
F4 Concrete Spalling	89	0.33	1.22	19	0.29	0.66
F5 Significant Spalling	31	0.91	0.71	1	0.37	
F6 Bar Buckling	56	2.99	0.46	8	2.22	0.34
F8 Bar Fracture	20	5.33	0.44	0		
F9 Loss of Lateral Capacity	140	2.47	0.59	21	1.28	0.41
F10 Loss of Axial Capacity	11	4.13	0.35	2	2.86	0.05

Residual drift data were evaluated also on the basis of the residual drift ratio defined as

$$\gamma = \frac{\Delta_r}{\Delta_m} \quad (3.3)$$

where Δ_r = residual drift demand and Δ_m = maximum drift demand. Figure 3.118 and Figure 3.119 present the residual ratio data plotted against the corresponding damage states. The median values for the residual

ratios are presented in Table 3.18 along with the coefficients of variation. The residual ratios were fairly consistent until damage state F5 was reached. The residual ratio then plateaus from damage state F6 to damage state F10. The F9 damage state falls in between the F5 and F6 damage states. This was the expected behavior as discussed previously in this chapter. The loss of lateral load carrying capacity was likely to occur after significant spalling and just prior to bar buckling.

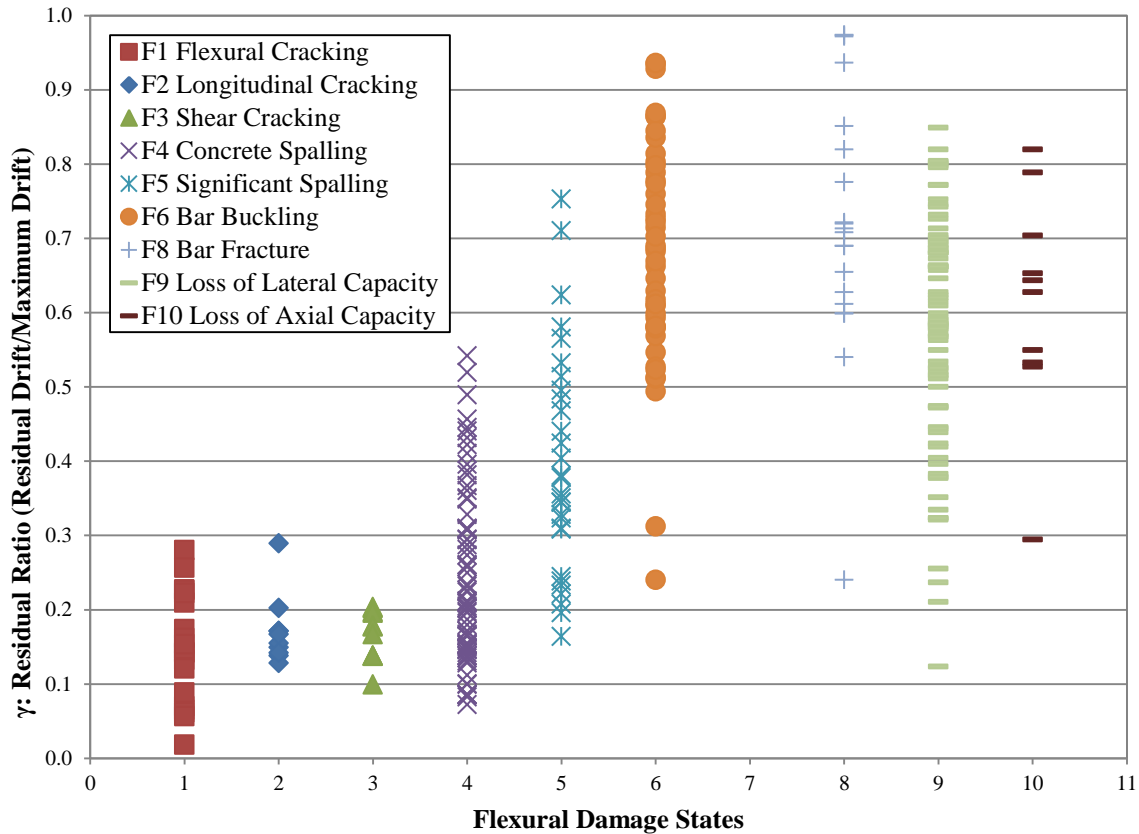


Figure 3.118 Residual Drift Ratios vs. Flexural Damage States for columns with low axial loads

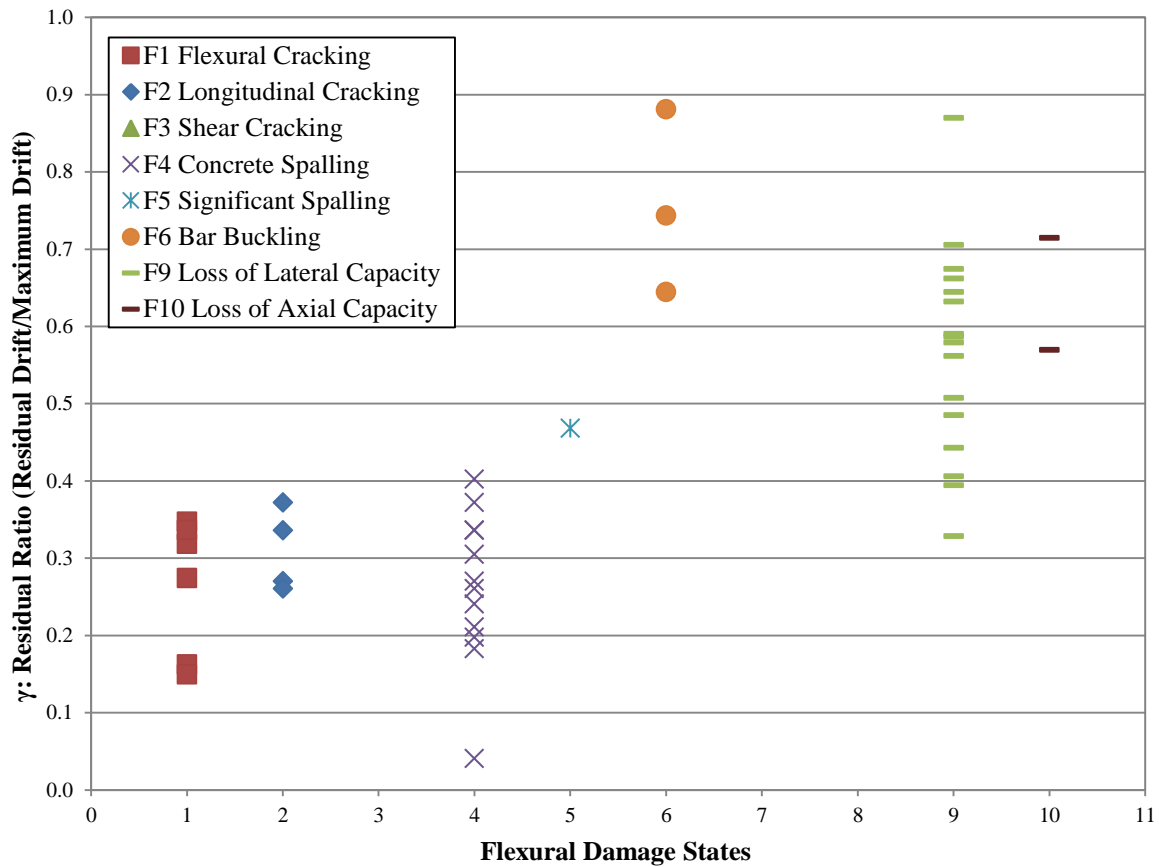


Figure 3.119 Residual Drift Ratios vs. Flexural Damage States for columns with high axial loads

Table 3.18 Residual ratio data

Flexure Damage States	γ : Residual Ratio			
	Low Axial Load		High Axial Load	
	Median	COV	Median	COV
F1 Flexural Cracking	14%	0.50	30%	0.33
F2 Longitudinal Cracking	17%	0.29	30%	0.19
F3 Shear Cracking	18%	0.21		
F4 Concrete Spalling	21%	0.49	27%	0.38
F5 Significant Spalling	37%	0.38	47%	
F6 Bar Buckling	69%	0.22	74%	0.16
F8 Bar Fracture	71%	0.24		
F9 Loss of Lateral Capacity	59%	0.27	58%	0.24
F10 Loss of Axial Capacity	64%	0.25	64%	0.16

3.8 Summary and Conclusions

3.8.1 Summary

Reinforced concrete columns with different geometries, material strengths, and design details develop different damage patterns, response mechanisms, and failure modes when subjected to earthquake loading. In this chapter, damage characteristics, such as the extent and severity of concrete cracking or spalling, were used to define damage states. The results of previous experimental studies were used to determine a series of damage states that characterize the progression of damage for columns exhibiting different response mechanisms and failure modes. Capturing the loss of capacity through visual damage data is critical to the UW-GA Tech Project. Damage states that correspond to capacity loss were identified in this chapter.

3.8.2 Conclusions

The response of a flexure-critical column is well defined. A significant amount of experimental data is available for flexure-critical columns. Thus, the proposed drifts at which damage states occur are well documented. Shear critical columns have not been as thoroughly tested. A lack of damage data makes it difficult to propose drifts at which damage will occur.

Predicting the likelihood of collapse in the event of an aftershock depends on the response of the columns. This is an issue because the initial damage states occurring in flexure and shear-critical columns is nearly identical. Once a shear-critical column is identified from images, it is likely that the structure has already lost a significant amount of lateral load-carrying capacity. The location of damage is the primary indicator of a shear failure. Damage is more likely to occur over the length of the column in a shear-critical column while in a flexure-critical column the damage will occur at the ends of the element.

Chapter 4: Element Modeling and Analysis Validation

4.1 Introduction

The objective of the UW-GA Tech Project is to develop an automated evaluation procedure for post-earthquake inspection of RC frame buildings. To do this a suite of RC frame structures must be modeled and analyzed. To ensure accurate simulation of frame response, component models were validated by comparing simulated and observed response for components and subassemblies tested in the laboratory. The range of beam-column response modes expected in the buildings to be simulated, were considered in these validation studies. This included flexural response of columns with low and high axial loads, detailing that could be expected to result in flexural response of columns with low and high axial loads, detailing that could be expected to result in flexural response with low and high ductility and transverse reinforcement ratios that could be expected to result in a non-ductile shear failure. This included beam-column joint subassemblies in which joint failure resulted in non-ductile response. Validation of models for accurate simulation of the response of low axial load was considered adequate for simulation of beam flexural response. The OpenSees analysis platform was used for all simulations.

4.2 Beam-Column Element Modeling

To verify the modeling techniques provide accurate element results for a wide range of beam and column designs, columns in special moment frames (SMF), intermediate moment frames (IMF), and ordinary moment frames (OMF) were modeled, where frame classification was based on ACI 318-08 (2008). The column selection will be discussed prior to the presentation of the results in Section 4.3.1, Section 4.3.2, and Section 4.3.3. A model of the column tested in the lab was created in OpenSees and subjected to the load applied in the lab. The modeled cyclic load-displacement history was compared with the experimental test results. The modeling techniques used to simulate the flexural response of beams and columns and an assessment of the accuracy of the technique are presented in the following sections.

4.2.1 OpenSees Element Formulation

As discussed in Section 2.5.1, the OpenSees BWH element was an ideal choice for modeling reinforced concrete beam-columns. Severe earthquakes cause inelastic flexural deformation typically concentrated at the ends of the element, this region is often referred to as the plastic hinge.

In this study all members (beams & columns) were modeled using the force-based BWH element formulation. OpenSees implements the BWH element by dividing it into three pieces: two inelastic hinges at the ends and an elastic center region. The BWH element localizes the integration points in the hinge. A

fiber section was utilized to define the inelastic moment-curvature and axial force-deflection response of the region at the element ends. One-dimensional concrete and steel material models were used to develop element cross-section response. The plastic hinge length and stiffness of the section between the plastic hinges must also be defined in OpenSees.

4.2.1.1 Effective Stiffness

As discussed in Section 2.5.1, the BWH element has an elastic center section. Definition of the flexural stiffness of the portion between the plastic-hinges requires a modification factor to account for concrete cracking. Despite the fact that significant inelastic action does not occur in this region of the beam or column, concrete will crack under service-level loading and under earthquake loading, and use of the gross-section stiffness results in an overly stiff prediction of response.

Many “effective stiffness” prediction models have been proposed as part of past research studies, design codes (e.g. ACI 318-11), and standards (e.g. ASCE 41-06). These efforts can be referenced in Section 2.5.2. For the current study, the research results from Elwood and Eberhard (2009), which were incorporated in ASCE 41-06 (2007) provisions, were used. These results were developed using data from experimental tests of square columns and provide accurate simulation of column stiffness at the first yield of the longitudinal reinforcement. The recommendations in ASCE 41-06 were applied to the elastic properties of the BWH element used in the OpenSees models. The modification factors for flexural stiffness depend on the axial load applied to the column. For columns with axial loads $\leq 0.1A_g f'_c$ the factor is 0.3. For columns with axial loads $\geq 0.5A_g f'_c$ the factor is 0.7. Linear interpolation between 0.3 and 0.7 provides the factors for columns with axial loads between $0.1A_g f'_c$ and $0.5A_g f'_c$. The factor for all beams is 0.3.

4.2.1.2 Hinge Length

Plastic hinge length models were discussed in Section 2.5.1. The selected hinge length was half the element depth. The OpenSees models use a plastic hinge length of $0.5H$ where H is the element depth. The suggestion by Park et al. (1982) to use $0.5H$ was based on standard steel and concrete material strengths and was deemed sufficient for the purposes of this research.

4.2.1.3 Cross-Section Discretization

The BWH element requires a section model to define the moment-curvature and axial load-deflection response of the plastic hinges. In the current study, a fiber-type section model was used. In a fiber-type section model, the RC section is discretized into concrete and steel fibers. A study was conducted to determine the number of fibers required to accurately simulate the moment-curvature

response of RC sections. It was determined that twenty fibers in both directions provided accurate results. Each fiber was assigned a 1D material model: unconfined concrete, confined concrete, and reinforcing steel. A typical column cross section can be seen in Figure 4.1.

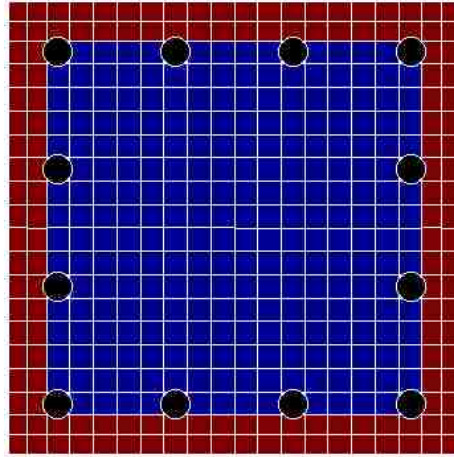


Figure 4.1 Typical cross-section discretization

4.2.1.4 Material Models

OpenSees has multiple concrete models that can be used to simulate the concrete stress-strain relationship. Two of the models are named **Concrete01** and **Concrete02**. These models define the same compressive response; a parabolic stress-strain response to the point of maximum compressive strength and linear post-peak response to a residual compressive strength. The difference between these material models is the tensile response. **Concrete01** has zero tensile strength. **Concrete02** defines a brittle response under tensile loading with a linear post-peak response to zero tensile strength. The concrete response of these two materials under compressive loading is defined by the concrete compressive strength, the compressive strain at which compressive strength is developed, the residual concrete strength, and the compressive strain at which residual compressive strength is developed. The tensile response of **Concrete02** is defined by the tensile strength and the tension softening stiffness. In the current study **Concrete02** is used to account for the limited tensile strength that concrete has.

The concrete in beam-column elements can be categorized as being unconfined or confined. The response of unconfined concrete is different than confined concrete. Concrete that is confined by lateral reinforcement will have increased ductility and strength that is not present when there is insufficient lateral reinforcement to provide confinement. Unconfined concrete fails in a brittle manner. Both confined and unconfined concrete can be modeled using **Concrete02**. The four parameters, concrete compressive strength, the compressive strain at which compressive strength is developed, the residual

concrete strength, and the compressive strain at which residual compressive strength is developed, will all need modifications to be used for confined concrete.

Many reinforced concrete material models have been proposed by researchers to account for the effects of confinement. One of the first models, developed by Kent and Park (1971), ignored any increase in strength due to confinement. This model was modified by Park, Priestley, and Gill (1982). The modified model includes the effect of confinement on concrete strength. A more complicated model was proposed by Mander, Priestley, and Park (1988). This model utilizes an energy balance technique that is still debated today. The model used for the OpenSees models is one proposed by Saatcioglu and Razvi (1992). This model is shown in Figure 4.2 and was used to define the confined **Concrete02** material.

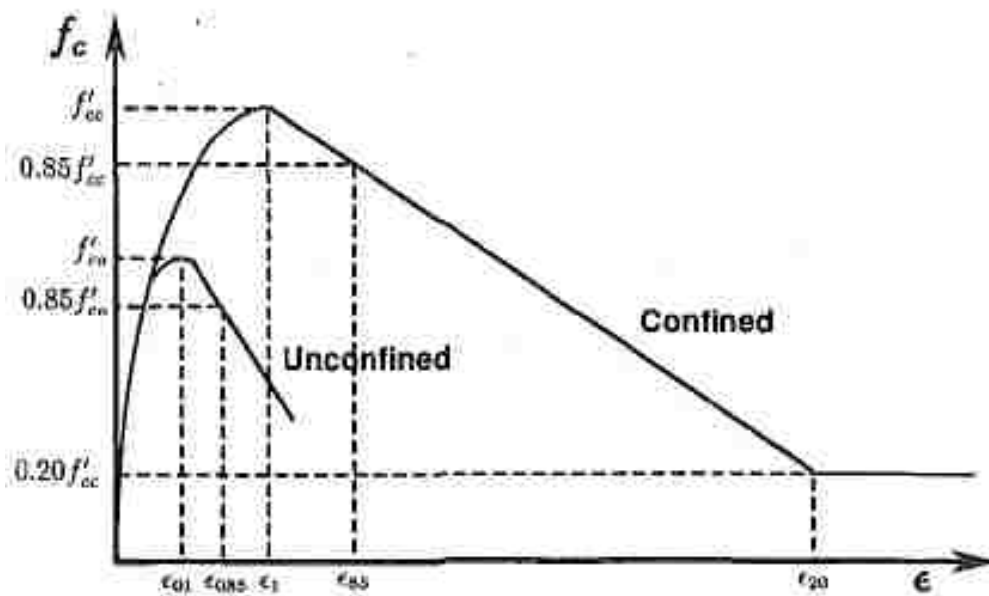


Figure 4.2 Concrete stress-strain relationship defined by Saatcioglu and Razvi

The Saatcioglu and Razvi model accounts for increased strength and ductility in confined concrete by using the transverse reinforcement layout, transverse reinforcement spacing, and transverse reinforcement yield strength. The equations used to compute the increased compressive strength are shown below.

$$f'_{cc} = f'_{co} + k_1 f_{le} \quad \text{where} \quad (4.1)$$

$$f_{le} = k_2 f_l \quad \text{and} \quad (4.2)$$

$$f_l = \frac{\sum A_s f_{yt} \sin \alpha}{s b_c} \quad \text{and} \quad (4.3)$$

$$k_1 = 6.7 (f_{le})^{-0.17} \quad \text{and} \quad (4.4)$$

$$k_2 = 0.26 \sqrt{\left(\frac{b_c}{s}\right) \left(\frac{b_c}{s_l}\right) \left(\frac{1}{f_l}\right)} \leq 1.0 \quad \text{and} \quad (4.5)$$

where f'_{cc} = confined concrete strength, f'_{co} = unconfined concrete strength, k_1 = lateral pressure coefficient, f_l = uniform confining pressure, b_c = core dimension, s = transverse steel spacing, s_l = lateral spacing of longitudinal steel, A_s = area of transverse steel, f_{yt} = yield strength of transverse steel, $\alpha = 90^\circ$ for rectangular transverse steel. In the above equations the values of f'_{co} , A_s , f_{yt} , s , b_c , and s_l were taken from the column Database. The equations used to define the strain at the increased compressive strength are shown below.

$$\varepsilon_1 = \varepsilon_{01} (1 + 5K) \quad \text{where} \quad (4.6)$$

$$K = \frac{k_1 f_{le}}{f'_{co}} \quad (4.7)$$

The equations used to define the confined residual strain, ε_{20} , are shown below.

$$\varepsilon_{85} = 260 \rho \varepsilon_1 \quad \text{where} \quad (4.8)$$

$$\rho = \frac{\sum A_s}{2 s b_c} \quad (4.9)$$

The value of ε_{85} is used to create the linear unloading path to ε_{20} .

OpenSees has multiple steel models that can be used to simulate the steel stress-strain relationship: **Steel01**, **Steel02**, and **Reinforcing Steel**. **Steel01** defines a classic 1D plasticity formulation with linear isotropic hardening. Response is defined by the steel yield strength, initial elastic modulus, and the strain hardening ratio. **Steel02** uses the same envelope as **Steel01** with Menegotto-Pinto (1973) curves to describe the unload-reload response. **Steel02** provides a better representation of the Bauschinger effect. The **Steel02** model requires definition of three parameters that define the transition from elastic to plastic branches. The OpenSeesWiki (2011) provides recommended values for parameters because of the improved simulation of the Bauschinger effect. **Reinforcing Steel** defines a bilinear plasticity formulation in which the yield plateau is defined and strain hardening is incorporated. Response is defined by the steel yield strength, initial elastic modulus, steel ultimate strength, tangent at initial strain hardening, strain corresponding to initial strain hardening, and strain at peak stress. The increased complexity of Reinforcing Steel made it impractical for this research effort due the lack of available data in the

Database. In the current study **Steel02** was used to model the longitudinal steel in the beam-column elements.

To define the steel material model, values for the elastic modulus, yield stress, ultimate stress, and strain at ultimate stress were used. The Database did not include the strain at ultimate strength, so the original research documentation was used to find the strain data. The strain hardening ratio was computed using the yield stress, yield strain, ultimate stress, and strain at ultimate stress.

4.2.2 General Modeling Considerations

The columns in the Database include the results of cyclic quasi-static tests. The tests employed multiple test set ups, but data were processed by Berry et al. (2005) to represent that of a cantilever column. Data processing accounted for the effects of moment due to P- Δ and the applied axial load.

In OpenSees the models were treated as cantilever columns with a fixed base and free end. The axial load was applied vertically at the top of the columns and the **PDelta** transformation was used to account for second-order P- Δ effects. The cyclic loading was completed using displacement control in the models. The applied horizontal force and displacement at the top of the column was recorded as each model was analyzed.

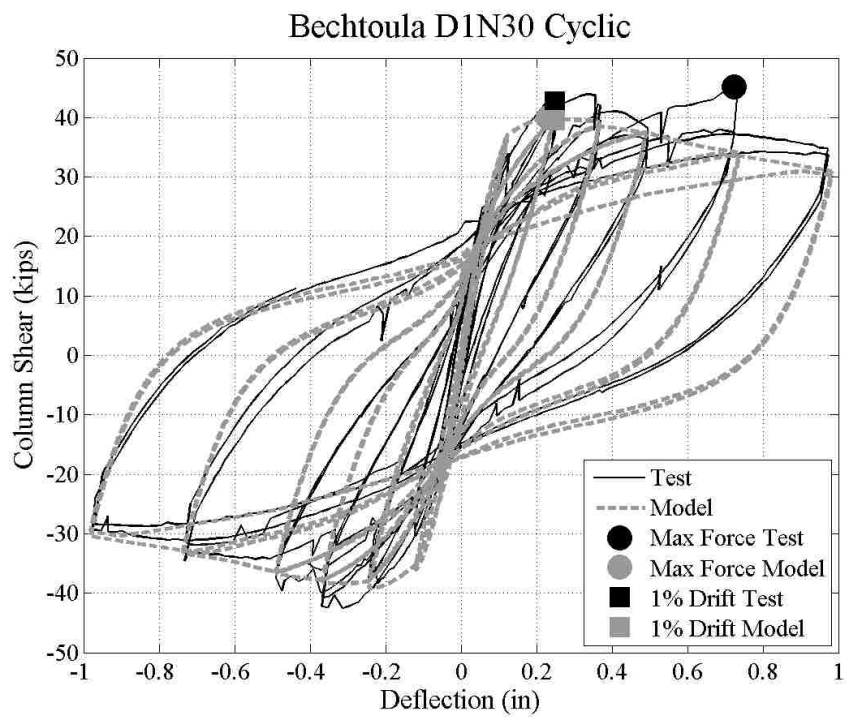
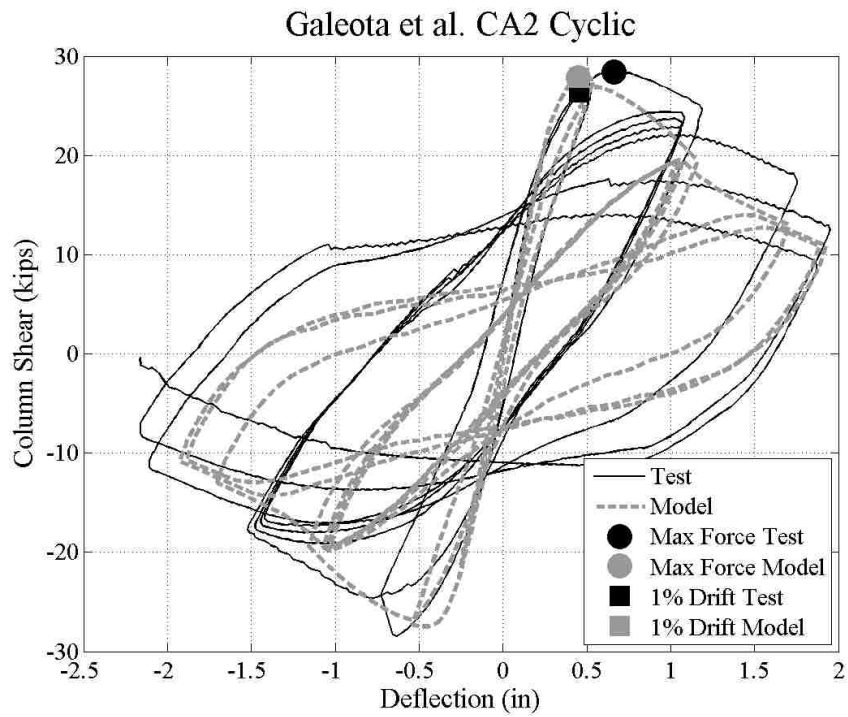
4.3 Beam-Column Element Modeling Validation Results

For each column a moment-curvature, monotonic pushover, and cyclic lateral load analysis were performed. The results from the moment-curvature analysis and the monotonic pushover analysis were used to verify that the modeling parameters were being implemented properly in the OpenSees models. Steel and concrete material response was also recorded for the monotonic pushover analysis; these data were used if peculiarities were identified in the pushover results. The cyclic analysis results were compared with the experimental test results. The cyclic material response of a longitudinal reinforcing bar, an extreme concrete fiber, and an extreme concrete core fiber were also tracked and visually inspected to ensure proper cyclic behavior. To quantify the accuracy with which the model simulated response the maximum lateral force the column resisted, the drift at that maximum force, the lateral force being resisted at 1% drift, and the deflection at which the column lost its lateral load-carrying capacity as simulated and as measured in the lab were compared. These statistics will be presented in the following sections and discussed in Section 4.3.4.

4.3.1 ACI Special Moment Frames

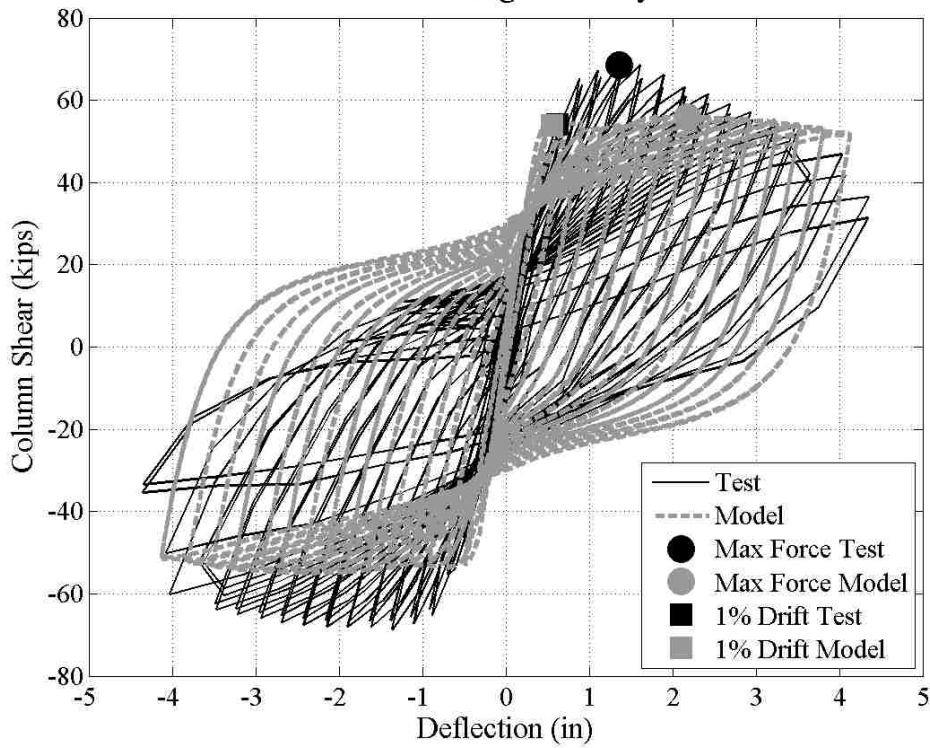
There were 47 columns from the Database that met the ACI 318 requirements for SMF. All but one of these columns was tested with a low axial load (Axial Load $\leq 0.5f_c A_g$). The one column with a

high axial load ratio ($0.6 f_c A_g$) was modeled. To validate the general beam-column element modeling techniques, eight of the 47 columns with axial load ratios ranging from 0.11 to 0.60 were modeled. Data required to determine the steel strain hardening ratio was only available for three of the eight columns in the Database. An OpenSees recommended value of 0.01 was used for the strain hardening ratio in place of test data. The axial load ratios and the columns with strain hardening ratio data are identified in Table 4.1. Figure 4.3 through Figure 4.6 show the simulated and experimental force-displacement results for two cases that represent the most accurate simulation of response and for two cases that represent the least accurate simulation of response. Similar figures are provided in Appendix C for all eight columns. Results for SMF, IMF, and OMF are discussed in Section 4.3.4.

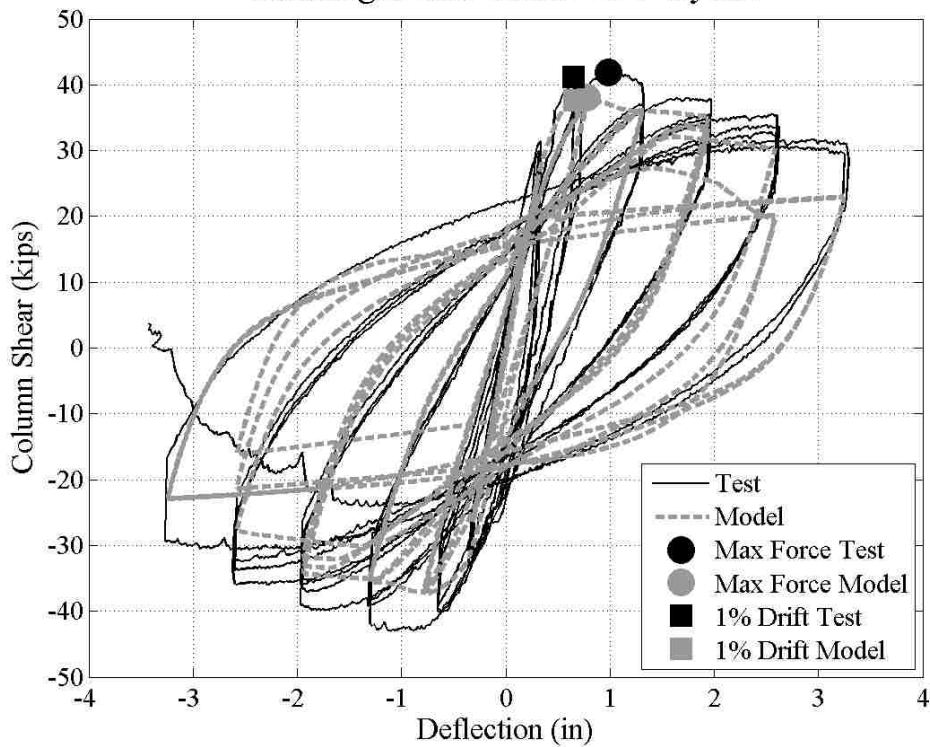


Figures 4.3 and 4.4 Example SMF force-displacement plots with good modeling accuracy

Mo and Wang C1-3 Cyclic



Saatcioglu and Grira BG-2 Cyclic

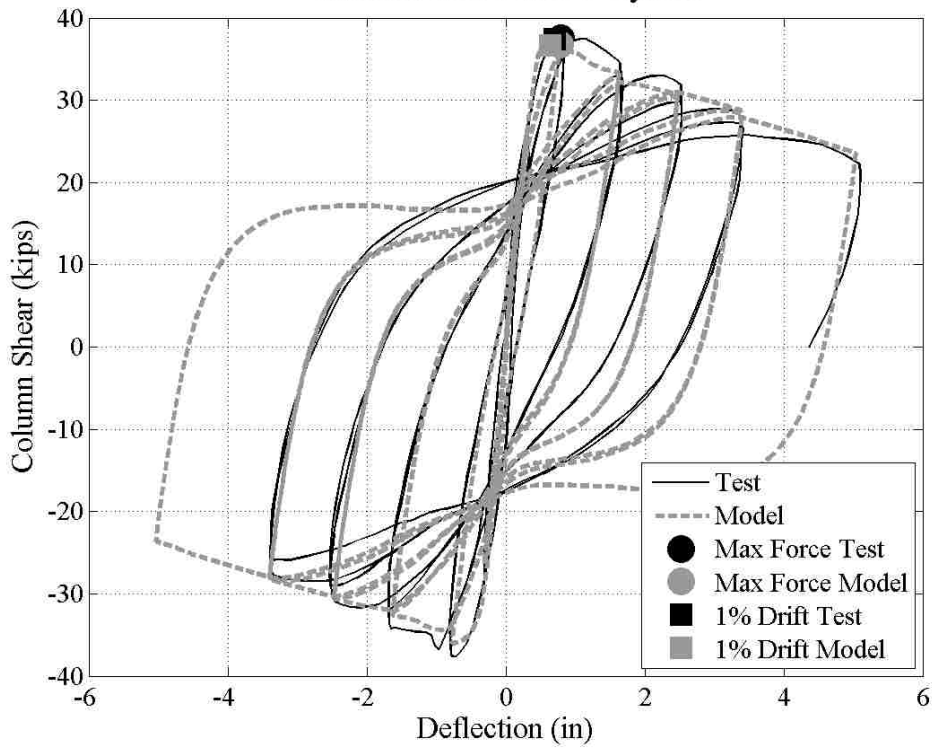


Figures 4.5 and 4.6 Example SMF force-displacement plots with poor modeling accuracy

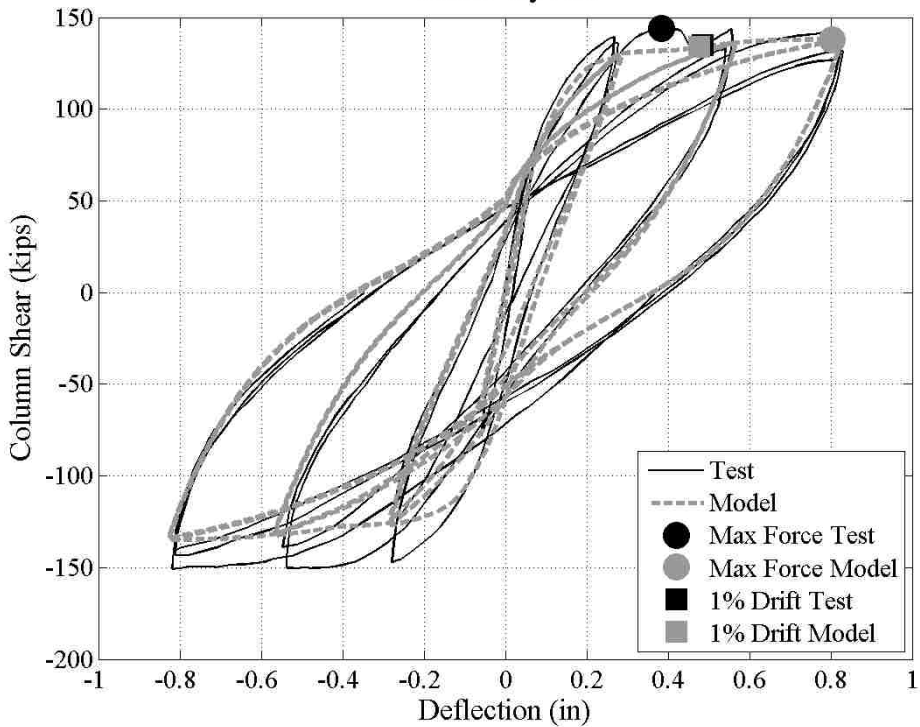
4.3.2 ACI Intermediate Moment Frames

There were 74 columns from the Database that met the ACI 318 requirements for IMF. All but five of these columns was tested with a low axial load ($\text{Axial Load} \leq 0.5f_c A_g$). Four of the five columns with a high axial load ratio were modeled. To validate the general beam-column element modeling techniques, thirteen of the 74 columns with axial load ratios ranging from 0.20 to 0.60 were modeled. Data required to determine the steel strain hardening ratio was only available for eight of the thirteen columns in the Database. An OpenSees recommended value of 0.01 was used for the strain hardening ratio in place of test data. The axial load ratios and the columns with strain hardening ratio data are identified in Table 4.1. Figure 4.7 through Figure 4.10 show the simulated and experimental force-displacement results for two cases that represent the most accurate simulation of response and for two cases that represent the least accurate simulation of response. Similar figures are provided in Appendix C for all thirteen columns. Results for SMF, IMF, and OMF are discussed in Section 4.3.4.

Tanaka and Park 1 Cyclic

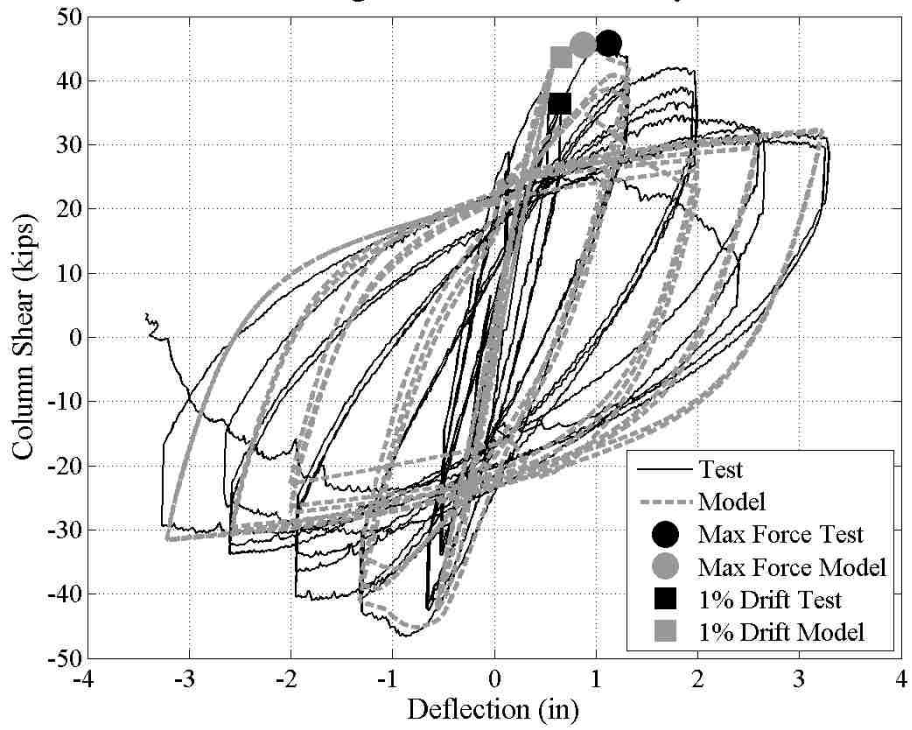


Gill 3 Cyclic

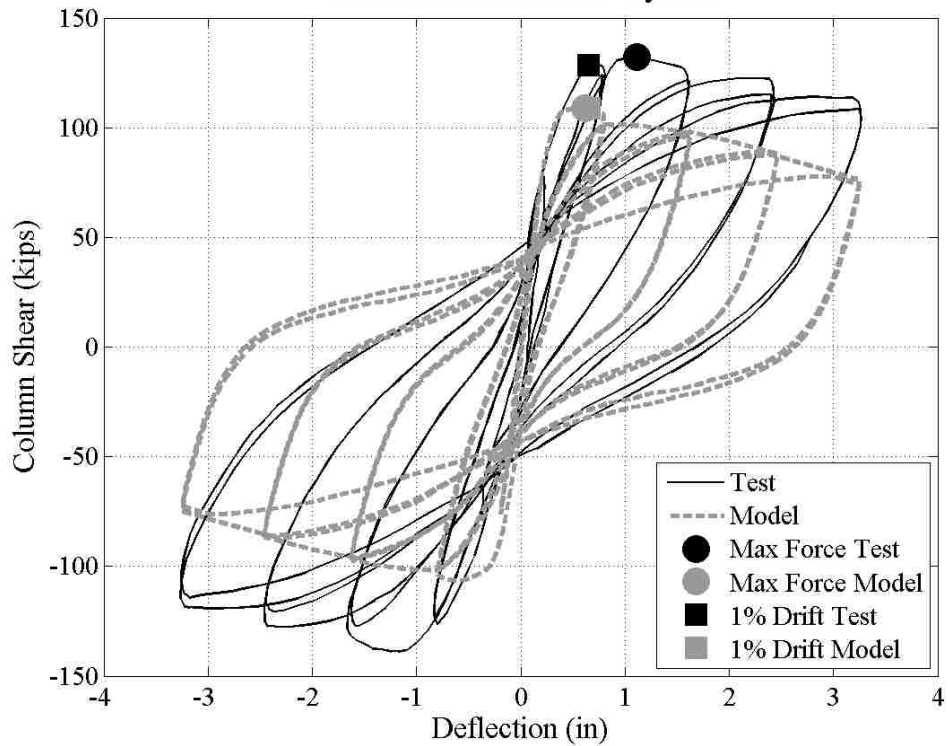


Figures 4.7 and 4.8 Example IMF force-displacement plots with good modeling accuracy

Saatcioglu and Grira BG-4 Cyclic



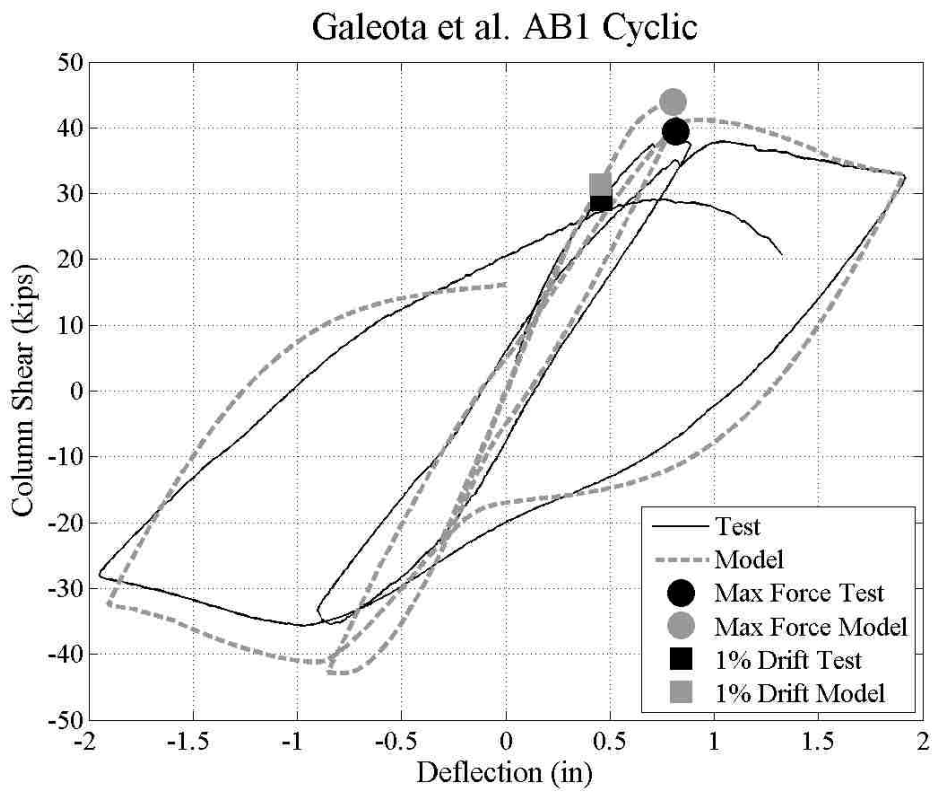
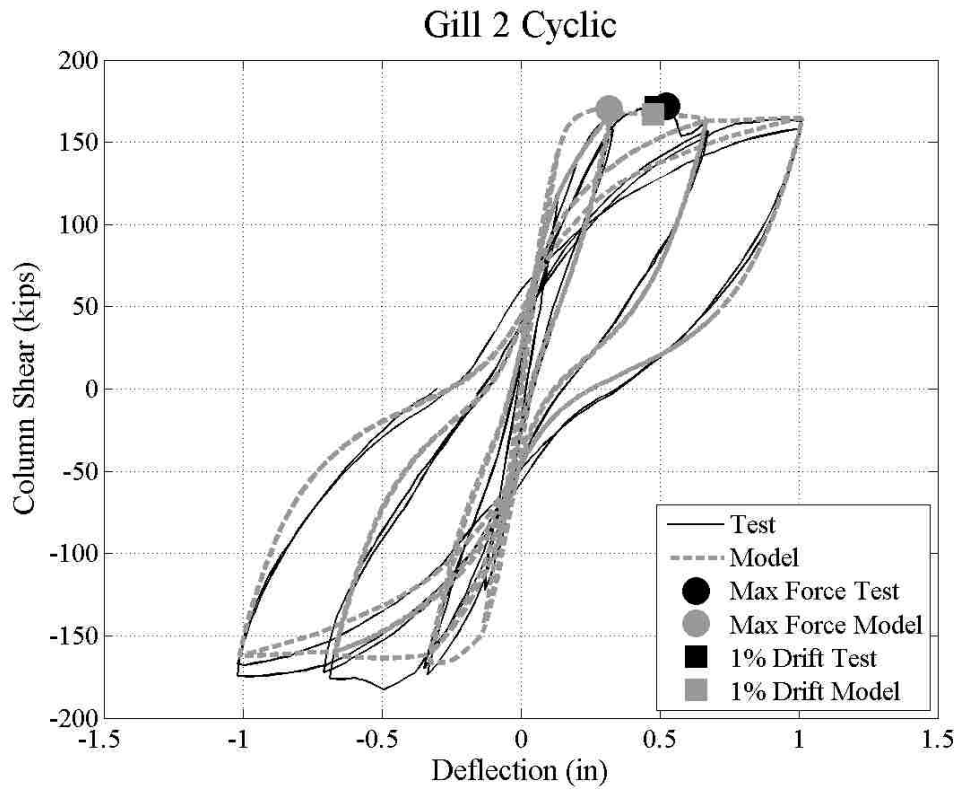
Tanaka and Park 7 Cyclic



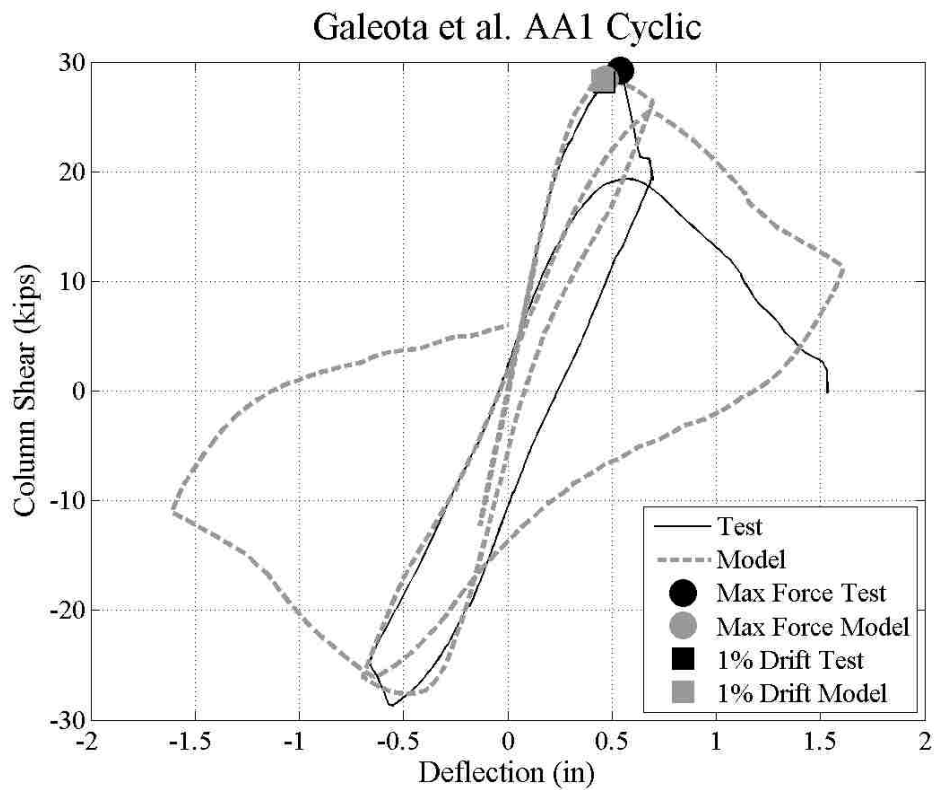
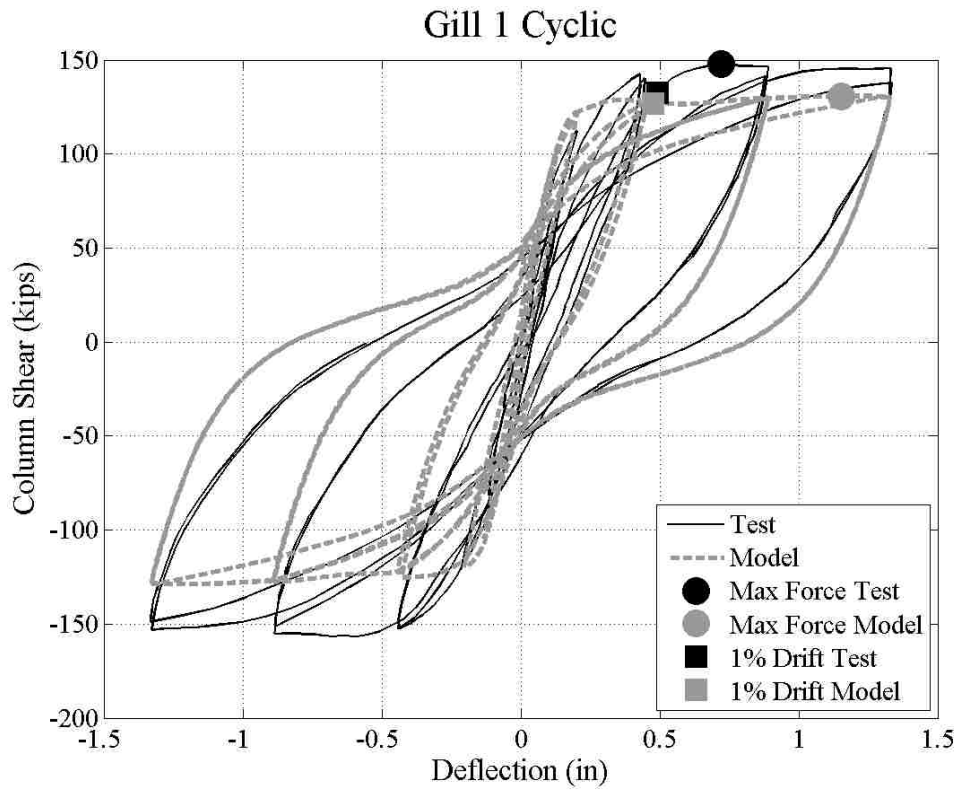
Figures 4.9 and 4.10 Example IMF force-displacement plots with poor modeling accuracy

4.3.3 ACI Ordinary Moment Frames

There were 24 columns from the Database that met the ACI 318 requirements for IMF. All of these columns were tested with a low axial load (Axial Load $\leq 0.5f_c A_g$). To validate the general beam-column element modeling techniques, four of the 24 columns with axial load ratios ranging from 0.20 to 0.30 were modeled. Data required to determine the steel strain hardening ratio was available for all four of the columns. The axial load ratios and the columns with strain hardening ratio data are identified in Table 4.1. Figure 4.11 through Figure 4.14 show the simulated and experimental force-displacement results for two cases that represent the most accurate simulation of response and for two cases that represent the least accurate simulation of response. The same figures are provided in Appendix C. Results for SMF, IMF, and OMF are discussed in Section 4.3.4.



Figures 4.11 and 4.12 Example OMF force-displacement plots with good modeling accuracy



Figures 4.13 and 4.14 Example OMF force-displacement plots with poor modeling accuracy

4.3.4 Beam-Column Modeling Results

Analysis results were evaluated qualitatively by comparing the simulated and experimental force-displacement responses and quantitatively by comparing the recorded data in Table 4.2. The maximum lateral force was plotted on the force-displacement plots for both the experimental tests and analytical models. The displacement at which the maximum force occurred was also used for comparison purposes. The force at 1% drift was also documented and compared in Table 4.1. The final point that was used to compare the test to the model was the deflection at which the column lost its lateral load-carrying capacity, as was previously defined in section 3.3.5. The results from all three frame types are shown in Table 4.1 and Table 4.2.

From visual inspection of Figure 4.3 through Figure 4.14 the general behavior of the models follows the behavior of the experiments. The initial stiffness of the simulated response was acceptable. Residual drifts are predicted to be slightly larger than experimental results as the deflection increases. This was the case for both the models with the best accuracy and poorest accuracy. Despite the relative inaccuracy in capturing the unloading response the plots support the modeling technique used. The statistics presented in Table 4.2 also support the modeling decisions. The ratios comparing the recorded data from the experimental and simulated response are generally near one. Thus, it was concluded that the modeling techniques implemented in the beam-column modeling results sufficiently captured the response of beam-column elements.

Table 4.1 Raw data from experimental tests and analytical models

Specimen Name	ACI Frame	Axial Ratio	Test		Model		Test	Model	Test	Model
			Max Lateral Force (kip)	Disp at Max Lat Force (in)	Max Lateral Force (kip)	Disp at Max Lat Force (in)	Lateral Force at 1% Drift (kip)	Lateral Force at 1% Drift (kip)	Disp at 80% Lat Force (in)	Disp at 80% Lat Force (in)
Mo and Wang 2000, C1-1	SMF	0.11	56.2	1.34	51.7	3.52	45.1	48.5	3.33	NA
Mo and Wang 2000, C1-2	SMF	0.16	60.2	1.41	54.0	2.70	54.9	52.1	3.70	NA
Mo and Wang 2000, C1-3	SMF	0.22	68.6	1.36	55.9	2.18	54.0	53.9	3.23	NA
Bechtoula et al. 2002, D1N30	SMF	0.30	45.2	0.72	40.0	0.23	42.6	39.5	0.87	0.89
Saatcioglu and Grira 1999, BG-2	SMF	0.43	41.9	0.98	38.1	0.77	41.2	37.7	2.84	2.50
Galeota et al. 1996, CA1	SMF	0.20	22.7	0.63	24.2	0.53	20.8	24.0	0.90	1.27
Galeota et al. 1996, CA2	SMF	0.30	28.4	0.66	27.9	0.45	26.4	27.9	1.29	0.98
Galeota et al. 1996, CA3	SMF	0.20	29.6	0.62	24.4	0.53	27.3	24.1	1.00	1.24
Bechtoula et al. 2002, D1N60	SMF	0.60	41.7	0.21	42.8	0.19	40.0	40.1	0.55	0.34
Gill et al. 1979, No. 3	IMF	0.42	144.2	0.38	137.9	0.80	135.1	133.9	NA	NA
Tanaka and Park 1990, No. 1	IMF	0.20	37.5	0.80	36.8	0.77	37.4	36.7	3.08	3.18
Tanaka and Park 1990, No. 7	IMF	0.30	132.2	1.12	109.1	0.62	128.4	108.8	3.50	2.50
Bayrak and Sheikh 1996, AS-2HT	IMF	0.36	33.5	0.39	33.3	1.04	31.0	29.0	1.93	1.73
Saatcioglu and Grira 1999, BG-4	IMF	0.46	45.8	1.12	45.6	0.87	36.5	43.6	2.30	1.58
Galeota et al. 1996, CB1	IMF	0.20	38.6	0.99	44.8	0.91	28.4	31.3	2.75	2.04
Galeota et al. 1996, CB2	IMF	0.20	37.5	0.79	44.8	0.91	28.6	31.3	2.24	1.89
Galeota et al. 1996, CB3	IMF	0.30	38.3	1.18	47.2	0.80	28.7	36.3	2.34	1.50
Galeota et al. 1996, CB4	IMF	0.30	38.7	1.12	47.1	0.76	30.7	36.3	2.03	1.47
Gill et al. 1979, No. 4	IMF	0.60	156.6	0.62	155.8	0.61	149.2	152.3	NA	NA
Watson and Park 1989, No. 5	IMF	0.50	65.6	0.73	61.7	0.59	64.7	61.6	1.44	1.08
Watson and Park 1989, No. 6	IMF	0.50	66.3	0.67	60.4	0.52	66.3	54.9	0.99	0.70
Bayrak and Sheikh 1996, AS-3HT	IMF	0.50	32.3	0.26	33.9	0.91	31.8	31.4	1.28	1.29
Gill et al. 1979, No. 1	OMF	0.26	147.7	0.72	130.8	1.15	132.5	127.0	NA	NA
Gill et al. 1979, No. 2	OMF	0.21	171.8	0.53	170.1	0.32	171.3	167.1	NA	NA
Galeota et al. 1996, AA1	OMF	0.30	29.3	0.54	28.4	0.47	28.1	28.4	0.60	0.88
Galeota et al. 1996, AB1	OMF	0.20	39.4	0.81	43.9	0.80	29.1	31.4	1.90	1.65

* Grey table entries had strain hardening data available, for other specimens a strain hardening ratio of 0.01 was used

Table 4.2 Statistical data from experimental tests and analytical models

Specimen Name	ACI Frame	Axial Ratio	Max Force Ratio: T/M	Disp at Max Force Ratio: T/M	Force at 1% Ratio: T/M	Disp at 80% Ratio: T/M
Mo and Wang 2000, C1-1	SMF	0.11	1.09	0.38	0.93	NA
Mo and Wang 2000, C1-2	SMF	0.16	1.11	0.52	1.05	NA
Mo and Wang 2000, C1-3	SMF	0.22	1.23	0.62	1.00	NA
Bechtoula et al. 2002, D1N30	SMF	0.30	1.13	3.13	1.08	0.98
Saatcioglu and Grira 1999, BG-2	SMF	0.43	1.10	1.28	1.09	1.13
Galeota et al. 1996, CA1	SMF	0.20	0.94	1.19	0.87	0.71
Galeota et al. 1996, CA2	SMF	0.30	1.02	1.47	0.95	1.32
Galeota et al. 1996, CA3	SMF	0.20	1.21	1.16	1.13	0.81
Bechtoula et al. 2002, D1N60	SMF	0.60	0.98	1.15	1.00	1.63
Gill et al. 1979, No. 3	IMF	0.42	1.05	0.48	1.01	NA
Tanaka and Park 1990, No. 1	IMF	0.20	1.02	1.03	1.02	0.97
Tanaka and Park 1990, No. 7	IMF	0.30	1.21	1.81	1.18	1.40
Bayrak and Sheikh 1996, AS-2HT	IMF	0.36	1.01	0.37	1.07	1.12
Saatcioglu and Grira 1999, BG-4	IMF	0.46	1.01	1.28	0.84	1.46
Galeota et al. 1996, CB1	IMF	0.20	0.86	1.09	0.91	1.35
Galeota et al. 1996, CB2	IMF	0.20	0.84	0.87	0.91	1.18
Galeota et al. 1996, CB3	IMF	0.30	0.81	1.47	0.79	1.56
Galeota et al. 1996, CB4	IMF	0.30	0.82	1.47	0.85	1.38
Gill et al. 1979, No. 4	IMF	0.60	1.00	1.00	0.98	NA
Watson and Park 1989, No. 5	IMF	0.50	1.06	1.24	1.05	1.33
Watson and Park 1989, No. 6	IMF	0.50	1.10	1.28	1.21	1.41
Bayrak and Sheikh 1996, AS-3HT	IMF	0.50	0.95	0.29	1.01	0.99
Gill et al. 1979, No. 1	OMF	0.26	1.13	0.63	1.04	NA
Gill et al. 1979, No. 2	OMF	0.21	1.01	1.66	1.03	NA
Galeota et al. 1996, AA1	OMF	0.30	1.03	1.16	0.99	0.68
Galeota et al. 1996, AB1	OMF	0.20	0.90	1.01	0.92	1.16

Steel strain hardening ratio data included

SMF	Mean	1.09	1.21	1.01	1.10
	Median	1.10	1.16	1.00	1.06
	ST. DEV.	0.09	0.77	0.08	0.31
	COV	0.09	0.63	0.08	0.28
IMF	Mean	0.98	1.05	0.99	1.29
	Median	1.01	1.09	1.01	1.35
	ST. DEV.	0.11	0.44	0.12	0.18
	COV	0.12	0.41	0.12	0.14
OMF	Mean	1.02	1.11	1.00	0.92
	Median	1.02	1.09	1.01	0.92
	ST. DEV.	0.08	0.37	0.05	0.24
	COV	0.08	0.33	0.05	0.26

4.4 Shear Failure Modeling

To capture the shear response of older RC columns, a shear spring implementation was used in this work. The ACI 318 shear strength equation was used to identify when shear failure has occurred (2008). Once the shear force has been reached, shear failure was triggered. Once failure has been identified, a zero-length shear spring connected in series with the beam-column flexural elements changes its constitutive properties to include pinching, strength degradation, and stiffness degradation. The model was developed to capture the response of shear-critical RC columns. The nominal ACI shear strength equation is shown below.

$$V_n = V_c + V_s \quad (4.10)$$

V_c is the concrete component and V_s is the transverse reinforcement's contribution to the columns shear strength. The concrete component is computed using the following equation.

$$V_c = 2 \left(1 + \frac{N_u}{2000A_g} \right) \lambda \sqrt{f'_c} b_w d \quad (4.11)$$

where N_u = axial load in pounds, A_g = gross area of the concrete cross section in square inches, λ = lightweight concrete modification factor, f'_c = concrete compressive strength in pounds per square inch, b = column depth, and d = distance from the extreme compression fiber to the centroid of the longitudinal tension reinforcement. The transverse reinforcement component is computed using the following equation.

$$V_s = \frac{A_v f_{yt} d}{s} \quad (4.12)$$

where A_v = area of transverse reinforcement within the spacing distance s , f_{yt} = yield strength of the transverse steel, and d is the same variable as before.

A uniaxial material constitutive relationship must be defined for the shear spring. The constitutive material was linear elastic until the nominal shear strength was reached. The material then degrades linearly to the residual shear strength. The residual strength was defined as 20 percent of the nominal shear strength to alleviate convergence issues in OpenSees. The initial stiffness of the spring was defined by multiplying the concrete shear area, A_{cv} , by the shear modulus, G , and dividing by the length of the column, L_c . The trilinear backbone can be seen in Figure 4.15.

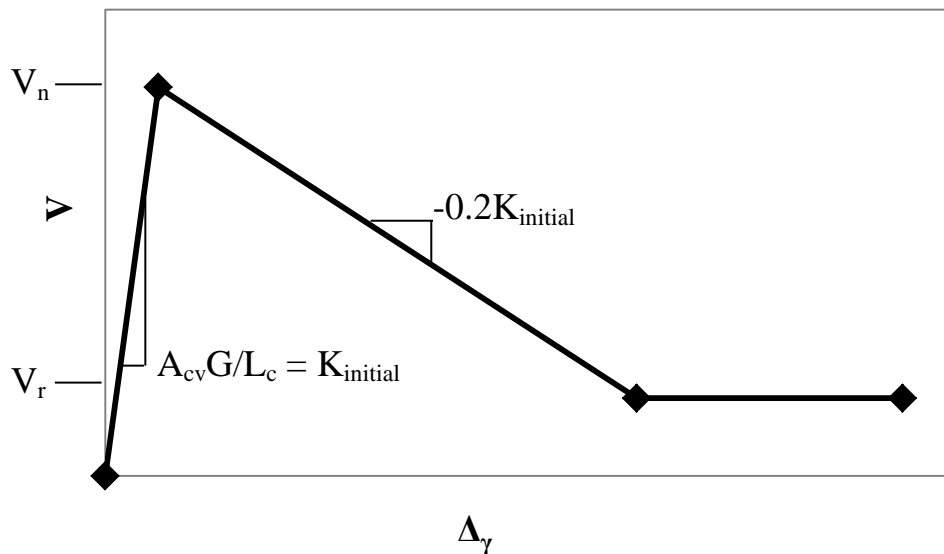


Figure 4.15 Shear Spring Backbone Curve

The constitutive relationship was modeled in OpenSees using a **zeroLength** element at the center of the joint. The two nodes connected by the **zeroLength** element were also tied together using the **EqualDOF** command. This keeps the two nodes from moving independently in the plane of the model. The element formulation is shown in Figure 4.16.

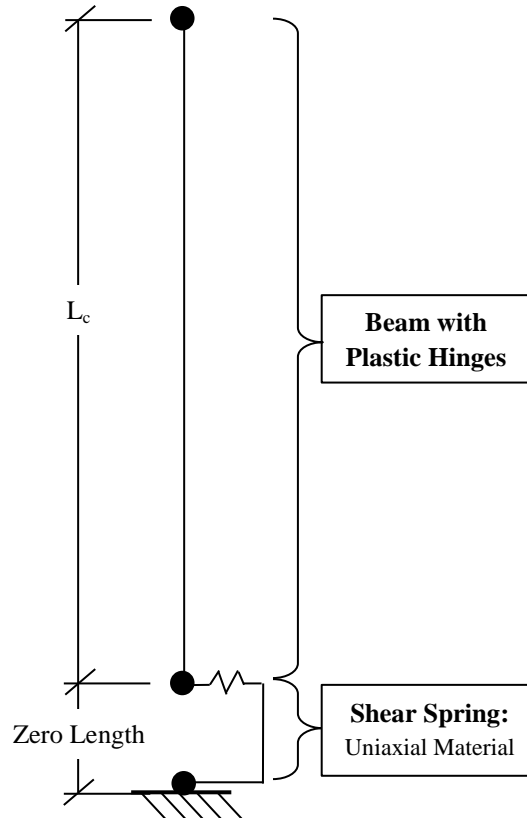


Figure 4.16 Shear column formulation

The limitation to this model formulation was the accuracy of predicting the shear capacity of a RC column. The ACI shear strength equation can be somewhat unconservative due to its inclusion of a concrete component. This concrete shear strength can be significantly reduced during cyclic loadings once cracking and spalling occur. The shear spring may remain on the linear elastic portion of its backbone curve if the column never reaches the nominal shear capacity. During the modeling validation this was observed, and the columns that did not reach the nominal ACI shear strengths are identified in Table 4.3.

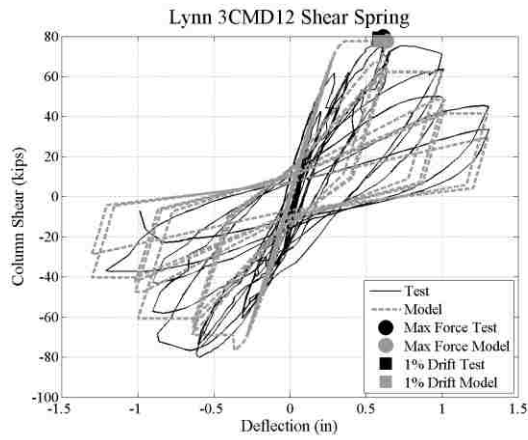
4.5 Shear Failure Validation Results

A moment-curvature, monotonic pushover, and cyclic analysis were performed on the columns that were modeled. Only columns identified in the Database as having a flexure-shear or shear failure were modeled using the shear spring. The results from the moment-curvature analysis and the monotonic pushover were used to ensure the modeling parameters were being implemented properly in the OpenSees models. The lateral load applied to the columns and the column drift were recorded. The shear spring response was also recorded. The cyclic model drift and column force results were plotted with the cyclic experimental test results.

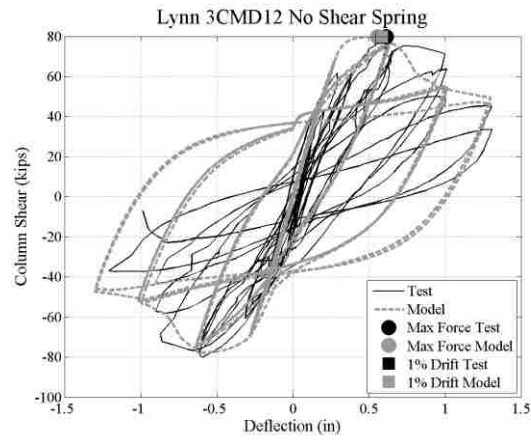
To determine how well the model was predicting behavior data was recorded for the maximum lateral force the column resisted, the drift at that maximum force, the lateral force being resisted at 1% drift, and the deflection at which the column lost its lateral load-carrying capacity. These statistics will be presented in Table 4.3 and Table 4.4 and discussed in the following sections.

4.5.1 Shear and Flexure-Shear-Critical Columns

There were 40 and 36 columns from the Database that had a shear and flexure-shear failure mechanism respectively. To validate the general beam-column element modeling techniques, columns tested under a range of axial loads were selected for modeling. A total of nine columns were modeled that had a shear or flexure-shear failure mechanism. These columns were also modeled without a shear spring. The axial load ratios are identified in Table 4.3. The following figures show the force-displacement results from both the experimental tests and the analyzed models. Two of the figures represent the most accurate shear models compared the corresponding model without a shear spring. Two of the figures represent the least accurate models. The same figures for all the modeled columns can be found in Appendix C.

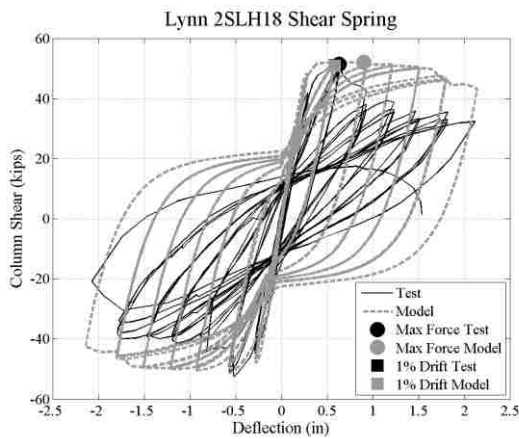


(a)

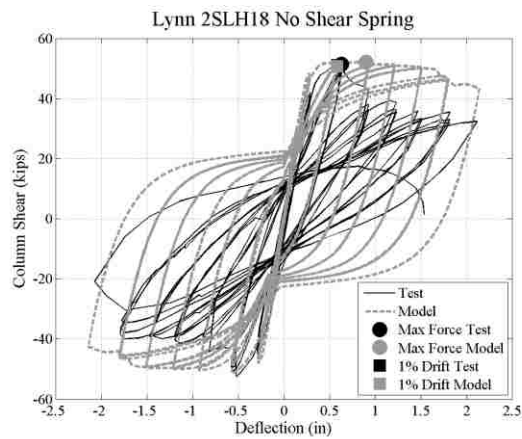


(b)

Figures 4.17 (a) Shear Spring model with good modeling accuracy and (b) No Spring model



(a)



(b)

Figures 4.18 (a) Shear Spring model with poor modeling accuracy and (b) No Spring model

4.5.2 Shear and Flexure-Shear-Critical Column Modeling Statistics

Analysis results were evaluated qualitatively by comparing the simulated and experimental force-displacement responses and quantitatively by comparing the recorded data in Table 4.4. The modeling statistics include three points from the load displacement history. The maximum lateral force was plotted on the force-displacement plots for both the experimental tests and analytical models. The displacement at which the maximum force occurred was also used for comparison purposes. The force at 1% drift was also documented and compared in Table 4.3. The final point that was used to compare the test to the model was the deflection at which the column lost its lateral load-carrying capacity, as was previously defined in Section 3.3.5. The results from the models with a shear spring and without a shear spring are shown in Table 4.3 and Table 4.4.

From visual inspection of Figures 4.17 and Figures 4.18 the behavior of the model with the shear spring follows the behavior of the experiment if the predicted nominal ACI 318 shear force was reached. The initial stiffness of the simulated response was acceptable. The simulated pinching behavior matched the experimental behavior well when the shear spring was activated. The pinching of the hysteretic behavior caused simulated residual deflections to be more accurate.

When the nominal ACI 318 shear force was not reached in the simulation, the behavior did not capture the drop in load carrying capacity associated with a shear failure. The shear spring remained elastic and the simulated response was the same as if there was no shear spring. This was not ideal for capturing the response of shear-critical columns. Due to the difficulties in implementing a more complex model discussed in Section 2.5.1, this shear model was implemented in the frame models.

Table 4.3 Raw Data from Experimental Tests and Analytical Models

Specimen Name	Shear Spring	ACI V_n	Axial Ratio	Test		Model		Test	Model	Test	Model
				Max Lat Force (kip)	Disp at Max Lat Force (in)	Max Lat Force (kip)	Disp at Max Lat Force (in)	Lat Force at 1% Drift (kip)	Lat Force at 1% Drift (kip)	Disp at 80% Lat Force (in)	Disp at 80% Lat Force (in)
Arakawa et al. 1989, OA2	Yes	Yes	0.18	29.4	0.07	13.3	0.05	28.5	12.2	0.11	0.14
Arakawa et al. 1989, OA5		Yes	0.45	30.1	0.03	17.2	0.03	23.8	15.4	0.07	0.14
Lynn et al. 1998, 3CLH18		Yes	0.09	62.3	0.61	56.7	0.57	62.3	47.3	0.61	0.92
Lynn et al. 1998, 2CLH18		No	0.07	54.1	1.11	52.1	0.90	50.6	50.9	1.51	1.91
Lynn et al. 1998, 3CMH18		Yes	0.26	73.7	0.53	69.5	0.28	71.3	69.2	0.61	0.67
Lynn et al. 1998, 3CMD12		Yes	0.26	79.8	0.61	77.6	0.64	79.4	77.6	1.01	1.05
Lynn et al. 1998, 2SLH18		No	0.07	51.5	0.63	52.1	0.90	51.0	50.9	0.95	2.31
Sezen and Moehle No. 1		Yes	0.15	68.0	1.05	66.7	0.51	56.7	63.4	1.50	1.09
Sezen and Moehle No. 4		Yes	0.15	66.2	1.19	67.3	3.08	54.8	67.3	1.70	3.35
Arakawa et al. 1989, OA2	No	NA	0.18	29.4	0.07	37.0	0.10	28.5	36.9	0.11	NA
Arakawa et al. 1989, OA5		NA	0.45	30.1	0.03	42.2	0.05	23.8	40.5	0.07	NA
Lynn et al. 1998, 3CLH18		NA	0.09	62.3	0.61	60.5	0.57	62.3	58.9	0.61	NA
Lynn et al. 1998, 2CLH18		NA	0.07	54.1	1.11	52.1	0.90	50.6	50.8	1.51	1.91
Lynn et al. 1998, 3CMH18		NA	0.26	73.7	0.53	80.1	0.53	71.3	79.8	0.61	0.75
Lynn et al. 1998, 3CMD12		NA	0.26	79.8	0.61	79.8	0.56	79.4	79.8	1.01	0.78
Lynn et al. 1998, 2SLH18		NA	0.07	51.5	0.63	52.1	0.90	51.0	50.8	0.95	2.31
Sezen and Moehle No. 1		NA	0.15	68.0	1.05	69.8	1.05	56.7	67.9	1.50	1.05
Sezen and Moehle No. 4		NA	0.15	66.2	1.19	71.8	0.75	54.8	70.5	1.70	1.07

Table 4.4 Statistical data from experimental tests and analytical models

Specimen Name	Shear Spring	ACI V_n	Axial Ratio	Max Force Ratio: T/M	Disp at Max Force Ratio: T/M	Force at 1% Ratio: T/M	Disp at 80% Ratio: T/M
Arakawa et al. 1989, OA2	Yes	Yes	0.18	2.21	1.44	2.33	0.82
Arakawa et al. 1989, OA5		Yes	0.45	1.75	1.00	1.55	0.52
Lynn et al. 1998, 3CLH18		Yes	0.09	1.10	1.06	1.32	0.66
Lynn et al. 1998, 2CLH18		No	0.07	1.04	1.24	0.99	0.79
Lynn et al. 1998, 3CMH18		Yes	0.26	1.06	1.87	1.03	0.91
Lynn et al. 1998, 3CMD12		Yes	0.26	1.03	0.96	1.02	0.96
Lynn et al. 1998, 2SLH18		No	0.07	0.99	0.70	1.00	0.41
Sezen and Moehle No. 1		Yes	0.15	1.02	2.06	0.89	1.38
Sezen and Moehle No. 4		Yes	0.15	0.98	0.39	0.81	0.51
Arakawa et al. 1989, OA2	No	NA	0.18	0.79	0.71	0.77	NA
Arakawa et al. 1989, OA5		NA	0.45	0.71	0.56	0.59	NA
Lynn et al. 1998, 3CLH18		NA	0.09	1.03	1.06	1.06	NA
Lynn et al. 1998, 2CLH18		NA	0.07	1.04	1.24	1.00	0.79
Lynn et al. 1998, 3CMH18		NA	0.26	0.92	1.00	0.89	0.81
Lynn et al. 1998, 3CMD12		NA	0.26	1.00	1.10	0.99	1.29
Lynn et al. 1998, 2SLH18		NA	0.07	0.99	0.70	1.00	0.41
Sezen and Moehle No. 1		NA	0.15	0.97	1.00	0.84	1.43
Sezen and Moehle No. 4		NA	0.15	0.92	1.57	0.78	1.59

Shear Model	Mean	1.24	1.19	1.22	0.77
	Median	1.04	1.06	1.02	0.79
	St. Dev.	0.41	0.50	0.45	0.28
	COV	0.33	0.42	0.37	0.36
No Shear Model	Mean	0.93	0.99	0.88	1.05
	Median	0.97	1.00	0.89	1.05
	St. Dev.	0.10	0.29	0.14	0.41
	COV	0.11	0.29	0.16	0.39

4.6 Joint Element Modeling

The results of previous research indicate that joint stiffness and strength loss can have a significant impact on frame response (Mosier 2000). To validate joint modeling techniques, simulations and measured response histories were compared for frame subassemblies intended to be representative of Pre-1976 RC frames. Research programs conducted by Walker (2001) and Alire (2002) at the University of Washington provided experimental data for cruciform-T shaped interior joints. Research conducted by Pantelides et al. (2002) at the University of Utah provided experimental results for exterior joints. The joint elements were then modeled using OpenSees. The modeled cyclic load-displacement history was then compared to the experimental test results.

Joint modeling for modern RC frames (SMF) and older RC frames (OMF) can be treated differently. Modern codes have been developed with the intention that yielding and failure occurs in beam elements in RC frames. Significant changes in design codes have caused joint reinforcement detailing to be drastically different in new construction than in buildings built prior to 1976. The transverse reinforcement provides sufficient confinement so that the joint's strength and stiffness degradation are minimal. Thus, this research effort did not evaluate any SMF subassemblies and the modeling technique used to simulate ductile response will be presented.

4.6.1 Joint Modeling Techniques

The techniques used for modeling the beam and column elements that frame into the joints were the same techniques used in Section 4.2. OpenSees provides multiple ways to model RC joints. The simplest modeling method is to utilize a rigid joint offset. Research has been conducted by Birely et al. (2012) that indicate the best modeling practice is to use rigid offsets that are six tenths the length of the joint for both column and beam offsets. ASCE 41 (2007) also makes recommendations, which are shown in Figure 4.19, on rigid offsets for joint modeling that are based on the strong-column weak-beam (SCWB) ratio for a joint. For joints with SCWB ratios greater than 1.2 only the columns are modeled with rigid offsets. For joints with SCWB ratios less than 0.8 only the beams are modeled with rigid offsets. For joints with SCWB ratios in between 0.8 and 1.2 both the columns and beams are modeled with rigid offsets that are half the length of the joint.

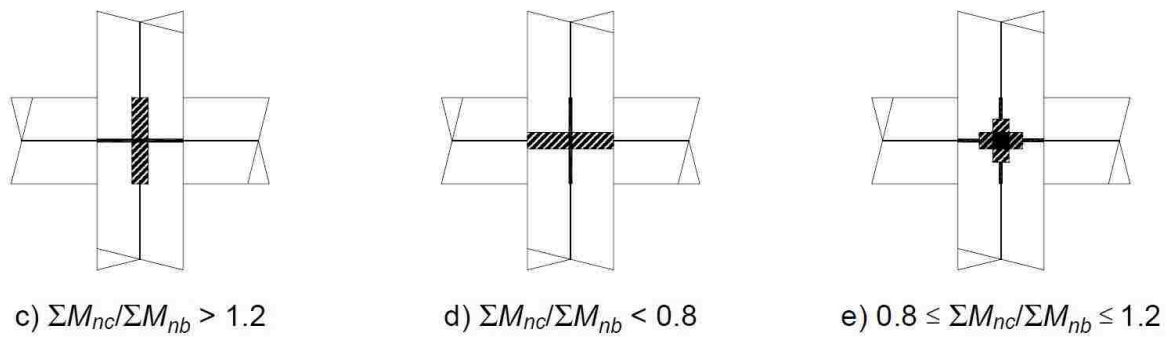


Figure 4.19 ASCE 41 rigid offset recommendations

The rigid offset technique implements beam-column elements modeled to the centerline of the joint. A simple command allows for the elements to terminate at the edge of the joint. This provides a rigid joint zone, as shown in Figure 4.20, which does not deform or degrade. It eliminates any joint shear action and does not include the response seen in actual experimental results. Practicing engineers have typically ignored joint deformations in seismic analyses by using rigid offsets. This has necessitated more complex joint models.

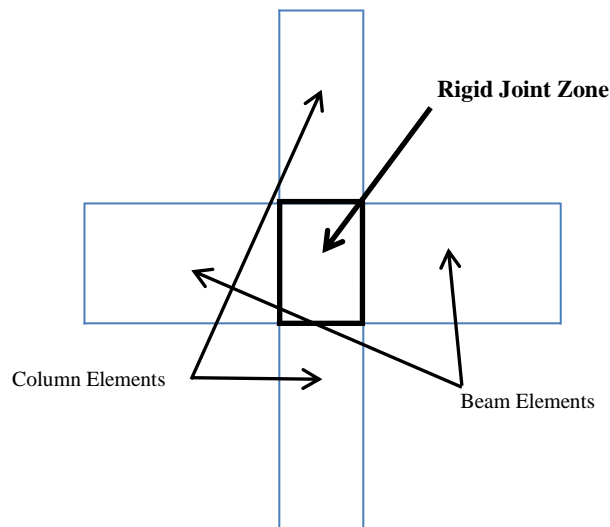


Figure 4.20 Schematic of beam-column elements framing into a rigid joint

Experimental results (Walker 2001, Alire 2002, and Lowes and Moehle 1999) and damage observed following earthquakes (EERI 1994) indicate that under earthquake loading strength and stiffness loss occurs due to joint damage in frames designed prior to 1976. This degradation can have serious implications on the response of structures that rely on RC frames for their seismic resistance. Implementing a model that accounts for the joint behavior was deemed necessary to capture the response of RC frames. To capture the joint response the modeling techniques for OMF and SMF were different.

4.6.1.1 SMF Joint Modeling

This research effort did not model or simulate any SMF subassemblies, based on the conclusion that modern designs have sufficient ductility to avoid strength and stiffness degradation of the joints. The SMF joints were modeled using Birely et al.'s rigid offset findings for ACI 318-08 compliant frames (2012). The proposed rigid offset value of three-fifths the joint dimensions for both the columns and beams will be used to model the joints. The offset combination provided good accuracy and precision based on sub-assembly models. The modeling work performed for the work was done using linear-elastic beam-column elements. These elements were used so the research could focus on modeling the joint behavior accurately. Applying the research findings should provide a more accurate model than using fully rigid joints.

4.6.1.2 Interior OMF and Pre-1976 Joint Modeling

In modern OMFs and pre-1976 frames, joints are likely to have insufficient confinement and limited transverse reinforcement. Joints with minimal to no transverse reinforcement have been shown to exhibit strength and stiffness loss under earthquake loading. Simulating this behavior is critical to simulating frame response (Altoontash 2004). A review of previous research addressing simulation of the nonlinear response of RC beam-column joints resulted in preferred modeling approach in which a joint spring was used to model the shear stress-strain response of the joint panel.

The interior joints were modeled using a simple technique that accounts for joint degradation. A joint spring was used to model the shear stress-strain response of the joint. The spring was modeled using the approach presented by Anderson et al. (2007). Their model provided a constitutive relationship between shear stress and strain in poorly detailed joints. The model accounted for strength and shear modulus degradation explicitly. The OpenSees **Pinching4** uniaxial material was used to model the shear stress-strain relationship. A **zeroLength** element at the center of the joint was assigned the Anderson material model. Figure 4.21 shows the OpenSees model for a frame subassembly. The joint spring is labeled at the center of the subassembly. The two nodes connected by the **zeroLength** element were also tied together using the **EqualDOF** command. This kept the two nodes from moving independently in the plane of the model. The joint spring must also be tied to the beams and columns. This was accomplished using rigid elements. The **elasticBeamColumn** element was used for the rigid link.

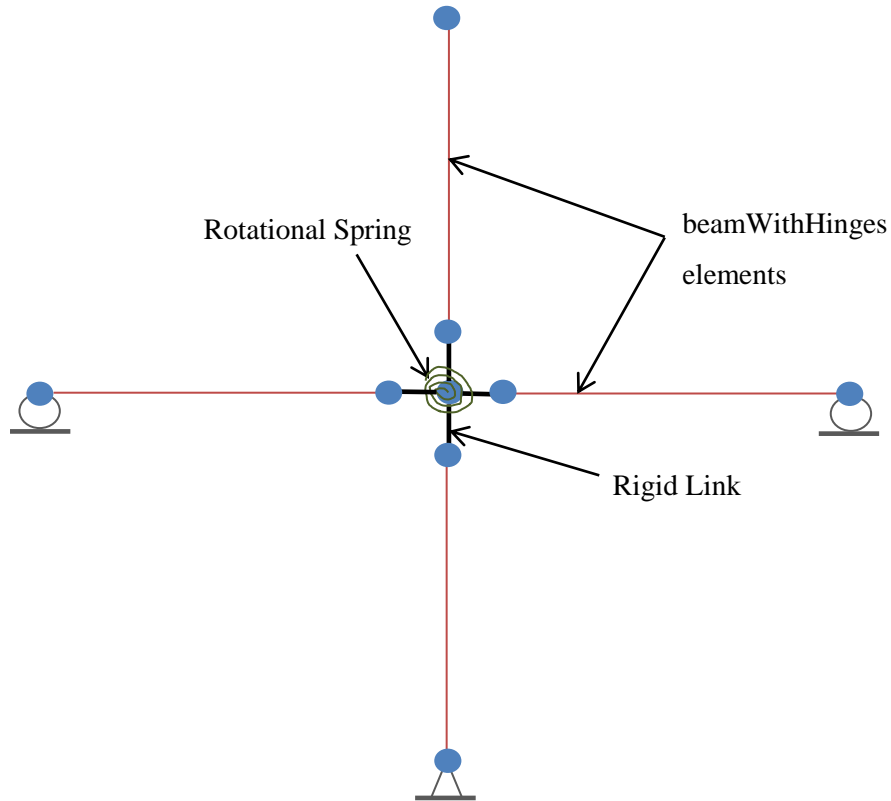


Figure 4.21 Interior joint modeling schematic

4.6.1.3 Exterior OMF and Pre-1976 Joint Modeling

The reinforcement in exterior joints in OMF and pre-1976 frames was sized for compression due to gravity loading. Thus, insufficient embedment of the beam's bottom bars in exterior joints typically results in loss of stiffness and strength under earthquake loading (Pantelides, et al. 2002). Figure 4.22 represents a joint tested by Aycardi et al. (1992) that identifies the insufficient embedment. To accurately simulate exterior joints the bar slip must be accounted for. A review of previous research addressing simulation of the nonlinear response of RC beam-column joints resulted in a modeling approach in which a joint spring was used to model the shear stress-strain response of the joint panel and a bond slip spring was used to model the potential embedment failure.

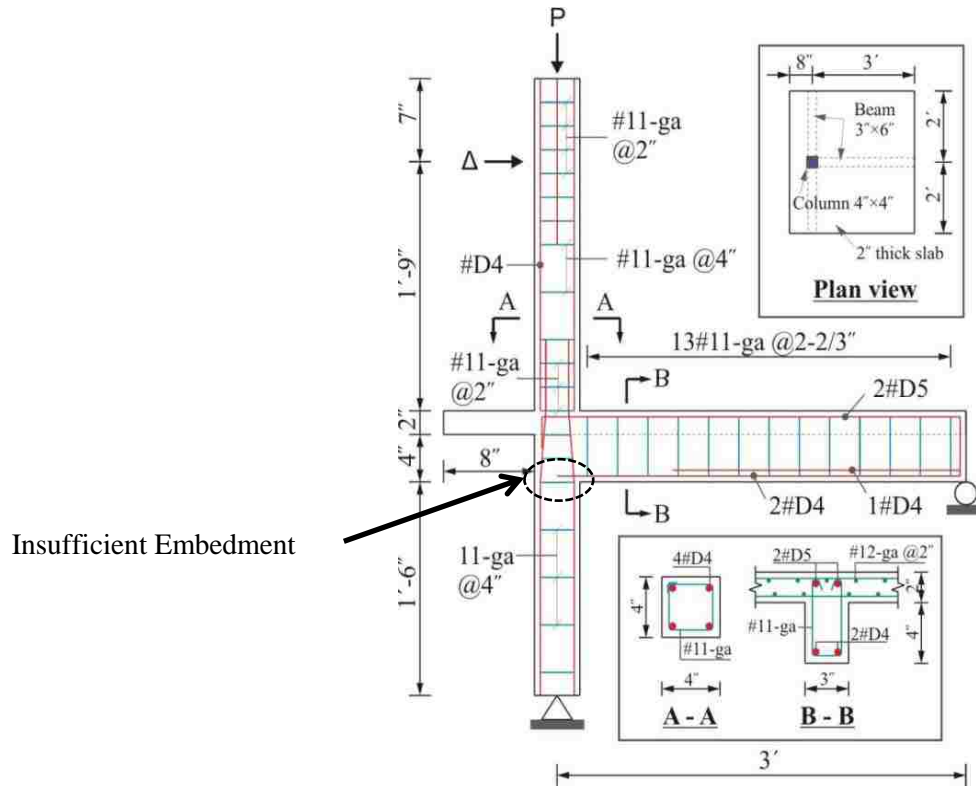


Figure 4.22 Steel reinforcement layout showing insignificant beam bottom bar embedment

To implement the bar slip spring, a **zeroLengthSection** element was placed at the interface between the beam and the joint, as seen in Figure 4.24. The two nodes connected by the **zeroLengthSection** element were also tied together using the **EqualDOF** command. Only the vertical displacement degree of freedom was tied for the two nodes, which allows for the nodes to interact axially and rotationally. The **zeroLengthSection** requires a stress-slip relationship for the materials that make up the fiber section. In this way, the fiber section represents force versus elongation and moment rotation. A similar approach was used by Berry and Eberhard (2007) to simulate bar slip for a reinforced concrete column to footing connection.

The steel response was defined based on the procedure described by Lowes and Altoontash (2003). Using the joint geometry and material properties the steel stress-slip response was defined using the **Pinching4** material in OpenSees. The backbone of the response was defined using the yield stress of a lower beam bar framing into an exterior joint. The ultimate stress was also used to define a point using the following equations:

$$\text{if } f_s < f_y \text{ slip} = 2 \frac{\tau_E l_{fs}^2}{E d_b} \quad (4.13)$$

$$\text{if } f_s \geq f_y \text{ slip} = 2 \frac{\tau_E l_e^2}{E d_b} + \frac{f_y}{E} l_y + 2 \frac{\tau_Y l_y^2}{E_h d_b} \quad (4.14)$$

$$\text{with } l_{fs} = \frac{f_s A_B}{\tau_{ET} \pi d_b} \quad (4.15)$$

$$\text{and } l_e = \frac{f_y A_B}{\tau_{ET} \pi d_b} \quad (4.16)$$

$$\text{and } l_y = \frac{f_s - f_y A_B}{\tau_{YT} \pi d_b} \quad (4.17)$$

where f_s = bar stress, f_y = steel yield strength, E = steel elastic modulus, E_h = steel hardening modulus, A_b = nominal bar area, and d_b = nominal bar diameter. The average bond strengths τ_{ET} and τ_{YT} are defined based on experimental tests performed by other researchers referenced in the Lowes and Altoontash paper (2003).

Table 4.5 Average bond strengths

Bar Stress, f_s (f_y = tensile yield strength)	Average Bond Strength, psi (f_c in psi)
Tension, $f_s < f_y$	$\tau_{ET} = 21\sqrt{f_c}$
Tension, $f_s > f_y$	$\tau_{YT} = 4.8\sqrt{f_c}$ to $0.6\sqrt{f_c}$
Compression, $-f_s < f_y$	$\tau_{EC} = 26\sqrt{f_c}$
Compression, $-f_s > f_y$	$\tau_{YC} = 43\sqrt{f_c}$

The summation of l_e and l_y provided a check on the required embedment length. When the required embedment surpassed the actual embedment the stress was capped even if the ultimate stress had not been attained. Once the slip corresponding to the ultimate stress had occurred the final point of the backbone was defined.

The concrete response was defined using the procedure proposed by Berry and Eberhard (2007). The compressive stress-displacement relationship of the concrete was calculated from the stress-strain relationship by assuming an effective depth over which the compressive strains act, and multiplying the strains by the assumed depth (d_{comp}) to obtain a displacement. The assumed depth is illustrated in the Figure 4.23.

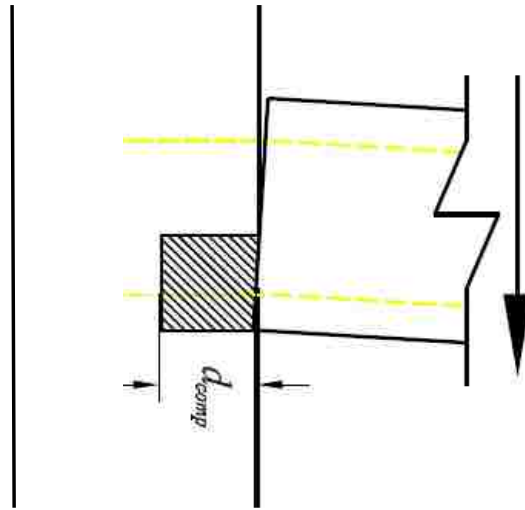


Figure 4.23 Assumed depth used to define concrete stress-displacement relationship (Berry and Eberhard 2007)

The **Concrete02** material was used to define the concrete response. The depth used for d_{comp} was twenty percent of the column depth. This produced a response of concrete stress versus deformation which could be used in the fiber section zero length spring.

The beam section used in the **zeroLengthSection** element was defined in the same manner as the section used for the **beamWithHinges** beam element. The bar slip material as defined above was only used for the bottom beam bars. The top reinforcing bars and slab steel were assigned a **uniaxialMaterialElastic** material with high stiffness. The concrete was assigned the concrete response as described above. A diagram of an exterior joint modeled using this technique can be seen in Figure 4.24.

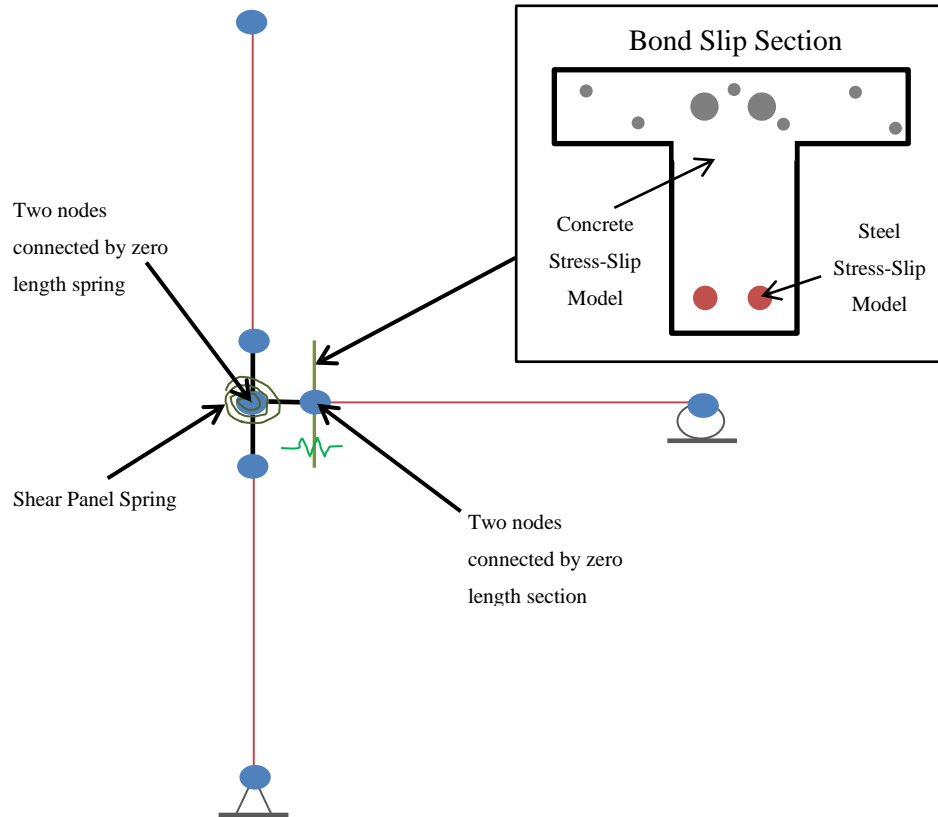


Figure 4.24 Exterior joint modeling schematic

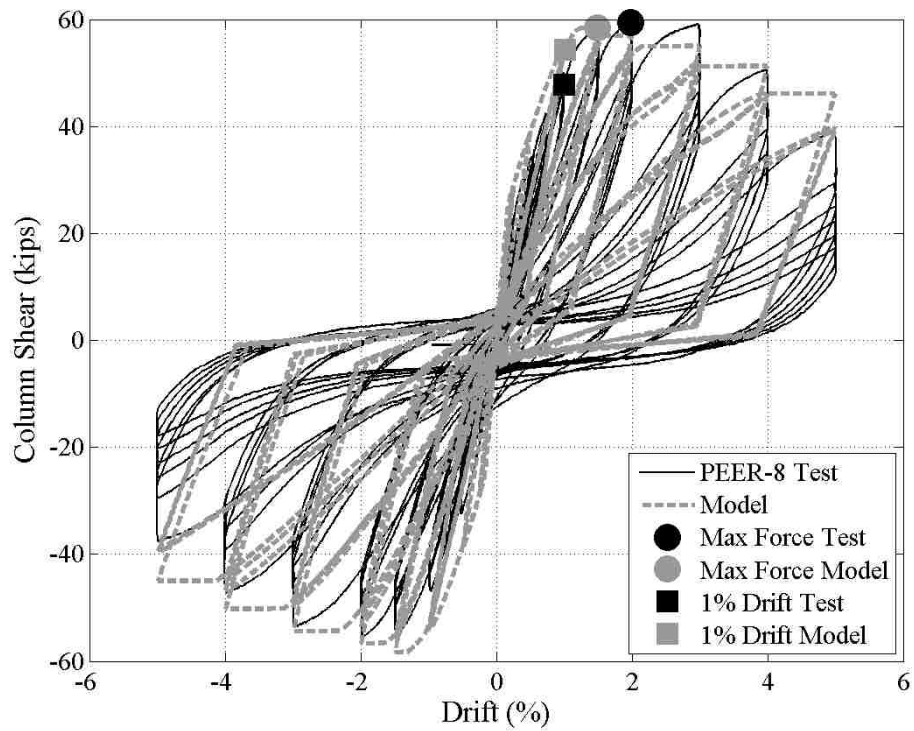
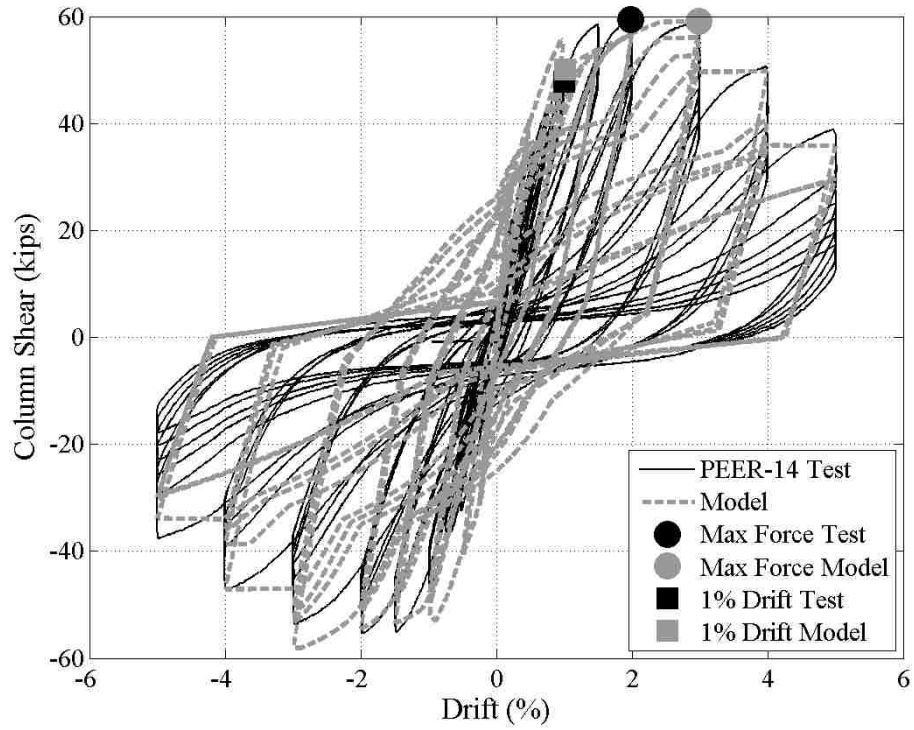
4.7 Beam-Column Joint Modeling Validation Results

To validate the proposed joint modeling techniques, OpenSees models were created of a series of interior and exterior joint subassemblies representative of pre-1976 frames tested in the laboratory. The models were subjected to the cyclic displacement histories imposed in the laboratory. The simulated and measured responses were compared. The models were evaluated by qualitatively comparing simulated joint, beam, and column response to the observed response in the laboratory. The proposed modeling procedures were quantitatively validated by comparing maximum lateral force the column resisted, the drift at that maximum force, the lateral force being resisted at 1% drift, and the deflection at which the column lost its lateral load-carrying capacity. Simulated and measured response values are provided in Section 4.7.3.

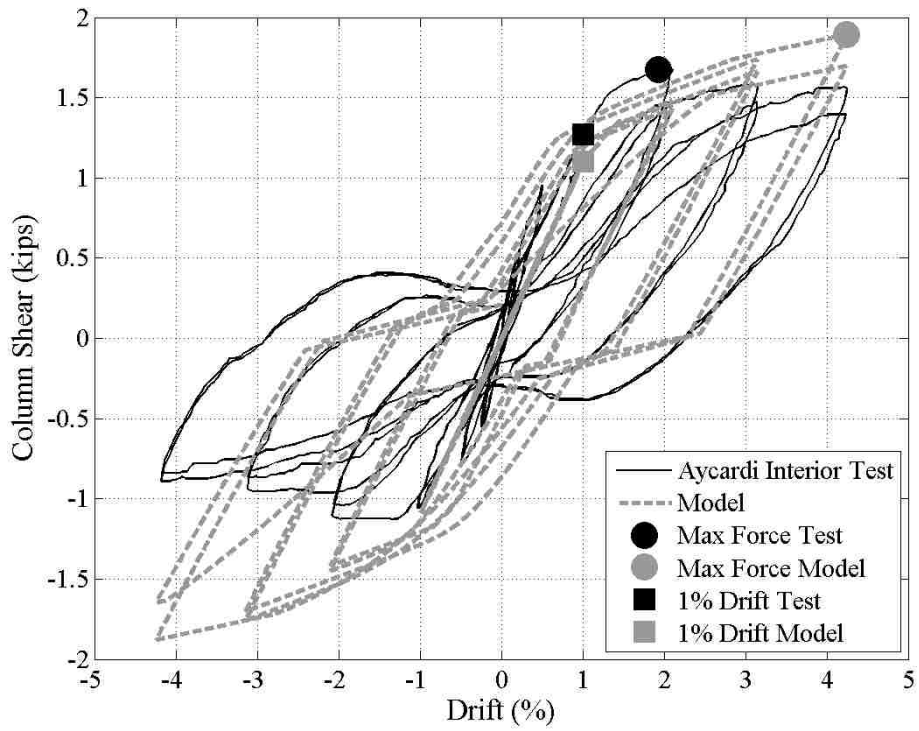
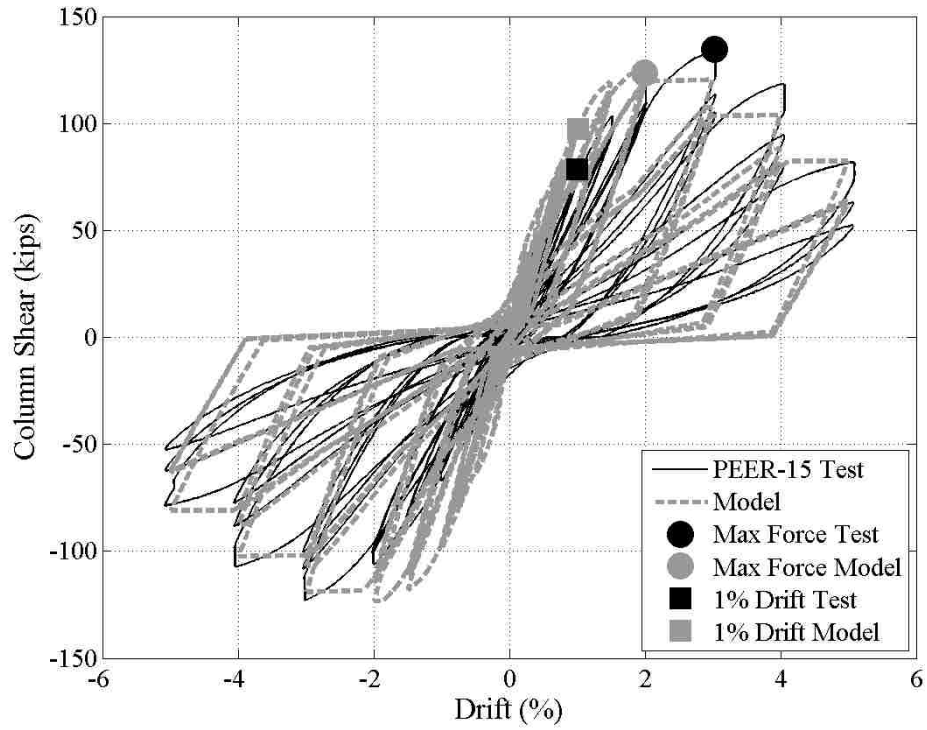
4.7.1 Older RC Interior Joints

The experimental investigations performed by Walker (2001) and Alire (2002) at the University of Washington were used to verify the interior joint modeling procedure. The experimental test matrix included 11 interior joints with non-ductile detailing. The tests were designed to study the influence of

joint shear stress demand and displacement history on joint performance. Six joints with varying joint shear stress demands were modeled. These six joints were selected because of the standard displacement history applied to the columns. The five joints not modeled had asymmetric displacement histories or displacement histories in which the joint was cycled 30 times at constant displacement amplitude. An interior joint sub-assembly test performed by Aycardi et al. (1992) was also used to verify the technique. An interior joint from a scaled three story structure was tested by Aycardi et al. prior to testing the full structure on a shake table. Figure 4.25 through Figure 4.28 show the simulated and experimental force-displacement results for two cases that represent the most accurate simulation of response and for two cases that represent the least accurate simulation of response. Similar figures are provided in Appendix C for all seven joints. A more comprehensive discussion on the model validation can be found in Appendix C. Results for interior and exterior joints are discussed in Section 4.7.3.



Figures 4.25 and 4.26 Example interior joint plots with good modeling accuracy



Figures 4.27 and 4.28 Example interior joint plots with poor modeling accuracy

4.7.2 Older RC Exterior Joints

The experimental investigations performed by Pantelides et al. (2002) at the University of Utah were used to verify the exterior joint modeling procedure. The experimental test matrix included six exterior joints with non-ductile detailing. The tests were designed to study the influence of joint reinforcement detailing on joint performance. All six joints were modeled. An exterior joint sub-assembly test performed by Aycardi et al. (1992) was also used to verify the technique. An interior joint from a scaled three story structure was tested by Aycardi et al. prior to testing the full structure on a shake table. Figure 4.29 and Figure 4.30 show the simulated and experimental force-displacement results for the two cases that experimental data was available. Figures are provided in Appendix C that present a side by side comparison of the simulated and experimental results for all seven joints. A more comprehensive discussion on the model validation can also be found in Appendix C. Results for interior and exterior joints are discussed in Section Older Beam-Column Joint Modeling 4.7.3.

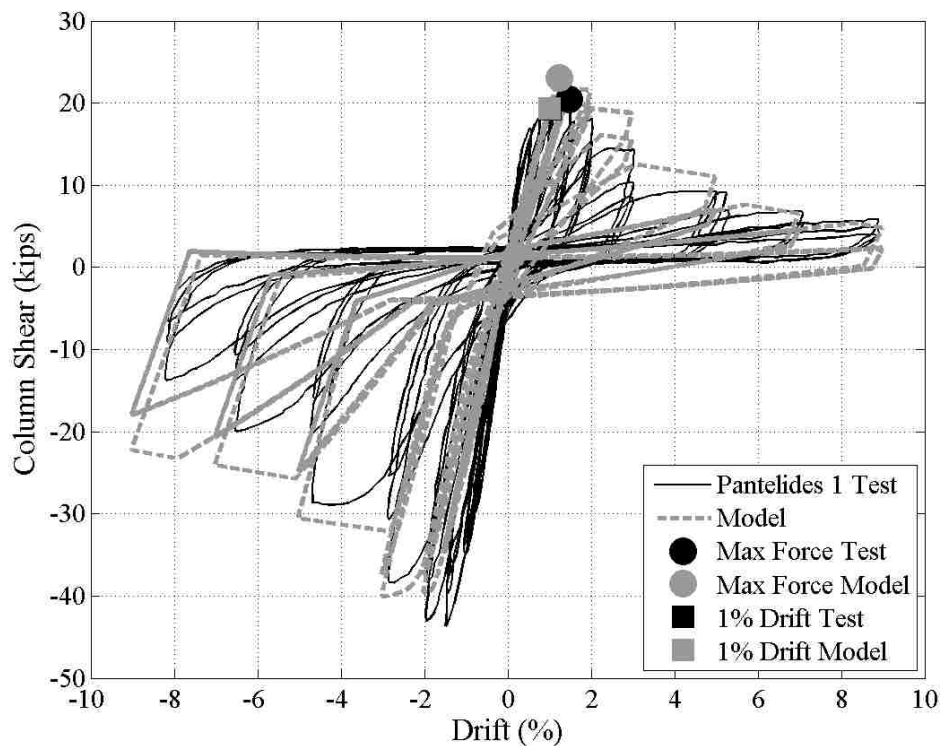


Figure 4.29 Pantelides 1 experiment and model results

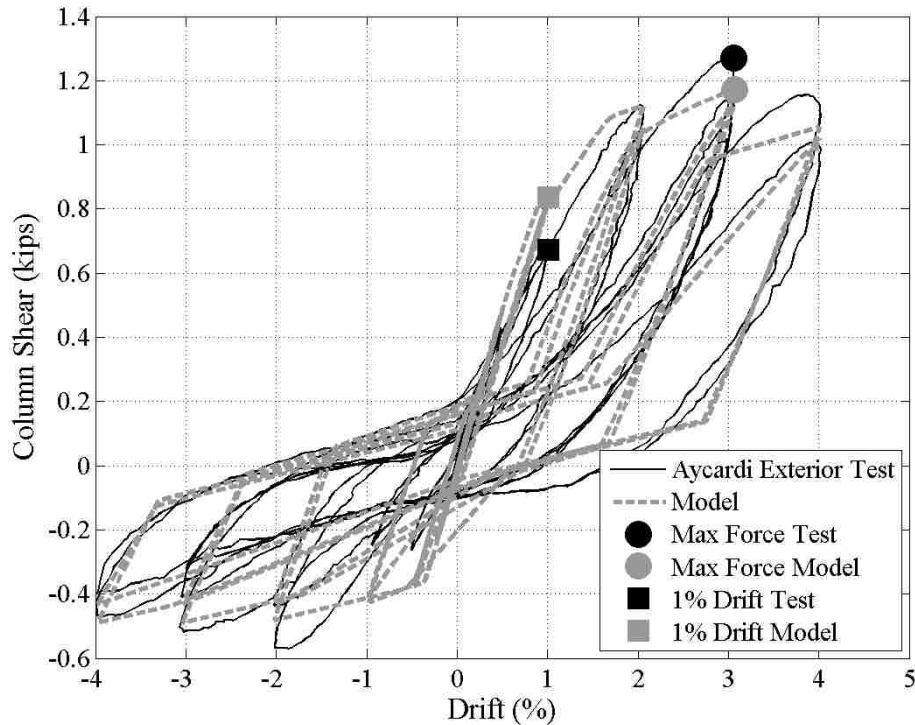


Figure 4.30 Aycardi Exterior experiment and model results

4.7.3 Older Beam-Column Joint Modeling Results

Analysis results were evaluated qualitatively by comparing the simulated and experimental force-displacement responses and quantitatively by comparing the recorded data in Table 4.7. The maximum lateral force was plotted on the force-displacement plots for both the experimental tests and analytical models. The displacement at which the maximum force occurred was also used for comparison purposes. The force at 1% drift was also documented. The final point that was used to compare the test to the model was the deflection at which the column lost its lateral load-carrying capacity, as was previously defined in section 3.3.5. The results from interior and exterior joints are shown in Table 4.6 and Table 4.7.

From visual inspection of Figure 4.25 through Figure 4.30 the general behavior of the models follows the behavior of the experiments. The poor simulated response shown in Figure 4.28 was due to significant column yielding. The joint response did not degrade as the inelastic action occurred in the column elements. The response did not show the pinching behavior that the other joints showed because the pinching behavior occurs when the joint degrades. This was the only joint modeled that had severe inelastic action occurring away from the joint. The initial stiffness of the simulated response of the exterior joints was not as accurate as the interior joints. The simulated response of the Pantelides joints under predicted the initial stiffness while the Aycardi joint over predicted the initial stiffness. If the poor

simulated response of the Aycardi interior joint shown in Figure 4.28 is not considered, the figures support the modeling technique used. A more thorough qualitative discussion on the joint modeling behavior is presented in Appendix C.

The statistics presented in Table 4.7 also support the modeling decisions. The ratios comparing the recorded data from the experimental and simulated response were generally near one. Thus, it was concluded that the modeling techniques implemented in the beam-column modeling results sufficiently captured the response of pre-1976 joints.

Table 4.6 Raw data from experimental tests and analytical models

Specimen Name	Frame Type	Test		Model		Test	Model	Test	Model
		Max Lateral Force (kip)	Drift at Max Lat Force (%)	Max Lateral Force (kip)	Drift at Max Lat Force (%)	Lateral Force at 1% Drift (kip)	Lateral Force at 1% Drift (kip)	Drift at 80% Lat Force (%)	Drift at 80% Lat Force (%)
Walker 2001, PEER14	Interior	59.5	1.98	59.1	3.00	47.8	50.1	4.20	4.15
Walker 2001, PEER22	Interior	80.8	2.92	78.5	1.50	58.4	70.1	4.05	4.72
Alire 2002, PEER8	Interior	59.5	1.98	58.5	1.50	47.8	54.3	4.32	4.80
Alire 2002, PEER9	Interior	93.4	3.06	84.8	1.20	76.6	78.6	4.74	4.21
Alire 2002, PEER15	Interior	134.6	3.03	123.6	2.00	78.4	97.5	4.36	4.23
Alire 2002, PEER41	Interior	126.0	2.00	136.9	1.50	96.1	99.1	3.78	3.39
Aycardi et al. 1992	Interior	1.7	1.93	1.7	2.10	1.3	1.2	NA	NA
Aycardi et al. 1992	Exterior	1.3	3.06	1.2	3.07	0.7	0.8	NA	NA
Pantelides 2002, 1	Exterior	20.5	1.47	23.1	1.23	19.3	19.4	2.57	3.01
Pantelides 2002, 2	Exterior	27.9	1.45	31.9	1.95	25.1	23.1	2.78	3.35
Pantelides 2002, 3	Exterior	42.3	2.09	42.8	1.97	32.7	24.0	4.48	4.78
Pantelides 2002, 4	Exterior	45.9	1.95	44.2	2.51	33.2	25.9	4.08	4.07
Pantelides 2002, 5	Exterior	44.1	2.81	41.0	2.97	28.2	21.5	4.11	5.21
Pantelides 2002, 6	Exterior	44.8	2.96	42.0	2.02	30.7	22.6	4.23	4.30

Table 4.7 Statistical data from experimental tests and analytical models

Specimen Name	Frame Type	Max Force Ratio: T/M	Drift at Max Force Ratio: T/M	Force at 1% Ratio: T/M	Drift at 80% Ratio: T/M
Walker 2001, PEER14	Interior	1.01	0.66	0.95	1.01
Walker 2001, PEER22	Interior	1.03	1.95	0.83	0.86
Alire 2002, PEER8	Interior	1.02	1.32	0.88	0.90
Alire 2002, PEER9	Interior	1.10	2.55	0.97	1.13
Alire 2002, PEER15	Interior	1.09	1.52	0.80	1.03
Alire 2002, PEER41	Interior	0.92	1.33	0.97	1.12
Aycardi et al. 1992	Interior	0.88	0.46	1.15	NA
Aycardi et al. 1992	Exterior	1.09	1.00	0.80	NA
Pantelides 2002, 1	Exterior	0.89	1.20	1.00	0.85
Pantelides 2002, 2	Exterior	0.87	0.74	1.09	0.83
Pantelides 2002, 3	Exterior	0.99	1.06	1.36	0.94
Pantelides 2002, 4	Exterior	1.04	0.78	1.28	1.00
Pantelides 2002, 5	Exterior	1.07	0.95	1.31	0.79
Pantelides 2002, 6	Exterior	1.07	1.47	1.36	0.98
Older RC Interior Joints	Mean	1.03	1.55	0.90	1.01
	Median	1.02	1.42	0.92	1.02
	ST. DEV.	0.06	0.58	0.07	0.10
	COV	0.06	0.38	0.07	0.10
Older RC Exterior Joints	Mean	0.96	1.00	1.06	0.87
	Median	0.94	1.03	1.04	0.85
	ST. DEV.	0.09	0.16	0.20	0.05
	COV	0.09	0.16	0.19	0.05

4.8 Full Frame Model Validation

To further validate the proposed modeling procedures simulated and measured response were compared for an RC frame subjected to shake table testing.

4.8.1 Experimental Summary

A 1/3-scale frame structure (3 bays and 3 stories) experimental investigation was performed by Bracci et al. (1992) in conjunction with the two experimental joint tests performed by Aycardi et al. (1992) included in the joint sub-assembly modeling section. The frame was designed for gravity and wind using the non-seismic detailing provisions of ACI 318-89 (1989). It was intended to be representative of a typical office building in the Eastern or Central United States.

The experimental investigation performed a set of initial tests outlined in Table 4.8. To identify the undamaged structure's dynamic characteristics, including the natural frequencies, modal shapes, equivalent damping ratios, stiffness matrix, and modal participation factors.

A very low level of excitation was achieved by striking the structure with an impact hammer to calculate story transfer functions. In the pull-back test, the structure was statically loaded by applying a horizontal tensile force to the center of each bay. The displacements were measured and a flexibility matrix was computed. The snap-back test consisted of applying the same loading to the structure as in the pull-back test, quickly releasing, and allowing the structure to vibrate freely. Accelerometer data were recorded for the snap-back tests. The white noise test was the last of the initial tests performed. This test was used to calibrate the shake table. A wide banded frequency response with accelerations not greater than 0.002 g was used for the white noise tests.

Table 4.8 Initial testing program for 1/3 scale structure

Test #	Description
1	Impact Hammer Test
2	Pull-Back Test
3	Snap-Back Test
4	Compensated White Noise

After the initial dynamic properties were identified, a minor earthquake ground motion was used to excite the structure. The Taft N21E ground motion was used and scaled to a peak ground acceleration of 0.05 g. This minor motion was used to investigate the pre-yield behavior of the structure. Next, the Taft N21E ground motion was scaled to a peak ground acceleration of 0.2g. This moderate motion was used to investigate the inelastic behavior of the structure. Damage was evaluated after the earthquake motion was applied, and many gauges were used to capture the frames response.

4.8.2 Modeling Summary

The OpenSees model used the older RC joint sub-assembly technique and the beam-column elements were implemented as discussed in Section 4.2. The gravity loads and masses were assigned at the joint nodes based on a tributary area. The frame model was subjected to the final motion used for the final shake table test. The minor Taft N21E ground motion was not considered in the analysis of the frame. The experimental investigation showed that the frame elements remained in the elastic range during this motion and experienced no visual damage; thus, it was deemed unnecessary to subject the model to a ground motion that would cause no damage.

Data was obtained for the story displacement levels from the experimental investigation. This provided a comparison for the modeled response shown in Figure 4.31. The analytical model matched the experimental displacements extremely well. The model captured the location of the inelastic action based on a qualitative comparison of plots in the report by Bracci et al. (1992) and plots of the simulated element behavior.

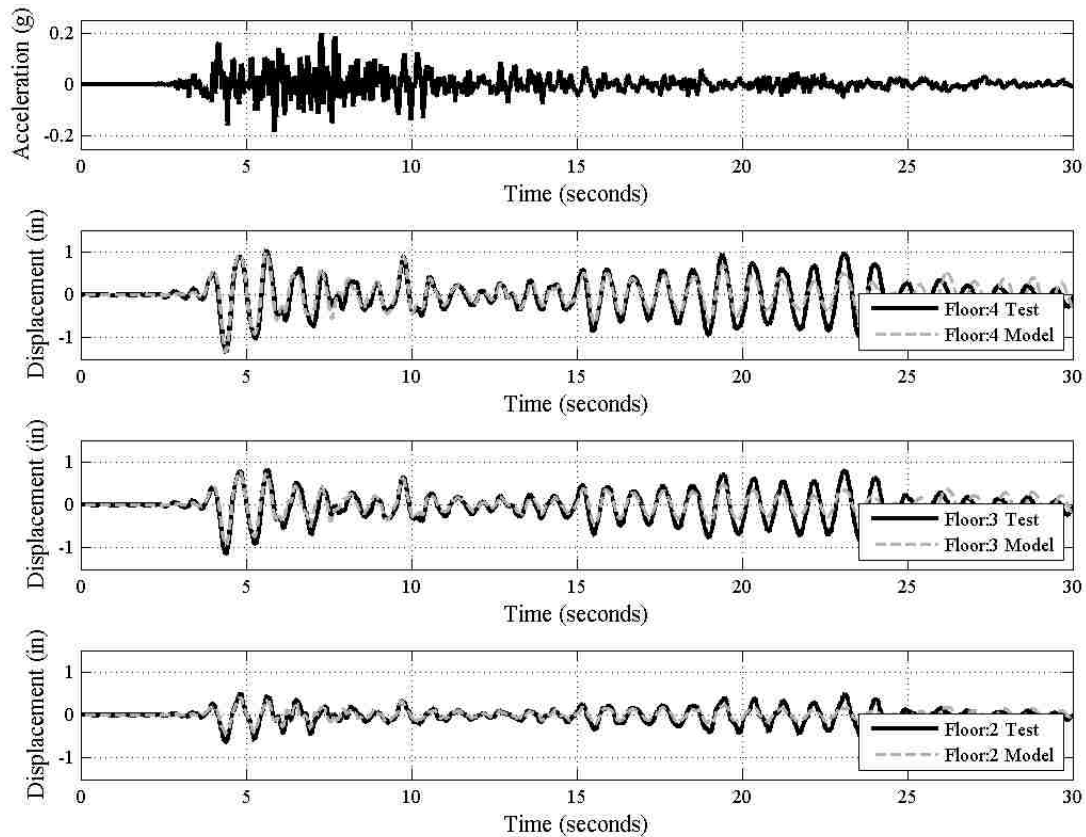


Figure 4.31 Experimental and analytical floor displacements from 1/3 scale structure

4.9 Summary and Conclusions

4.9.1 Summary

As part of the UW-GA Tech Project, nonlinear analysis will be used to assess the potential for earthquake damaged structures to sustain further damage, including collapse, under subsequent earthquake loading. To assess the accuracy with which RC frame response was simulated, the results of previous research were employed to establish preferred modeling approaches within the OpenSees analysis platform. For beams and columns, the preferred modeling approach consisted of a nonlinear force-based lumped plasticity element. Columns identified as having a shear or flexure-shear failure included a shear spring. For beam-column-joints, the preferred modeling approach consisted of a zero length rotational spring at the center of the joint for interior joints with minimal joint transverse reinforcement and a zero length rotational spring in combination with a bar slip spring for exterior joints with minimal joint transverse reinforcement. These modeling approaches were used to simulate the response of column and beam-column joint subassemblies tested in the laboratory under cyclic, quasi-static loading and simulated and measured response histories were compared. Additionally, the proposed

modeling approaches were used to simulate the response of a 1/3-scale multi-story, multi-bay frame subjected to dynamic loading and simulated and measured response was compared.

4.9.2 Conclusions

The modeling approaches discussed in this chapter have done a satisfactory job capturing the inelastic response of beams, columns, and joints. Chapter 5 explains how the modeling approaches were implemented in full-frame analyses.

Columns modeled meeting ACI 318 SMF, IMF, and OMF requirements performed equally well. The axial load level did not affect the model performance. The models captured the hysteretic response of the experimental tests performed in the laboratory. One weakness of the selected model was the unloading stiffness and residual displacement observed at zero load. The model tended to under predict the unloading stiffness, causing the residual displacement to be greater than the experimental response.

Seven of the nine columns modeled using the preferred shear spring implementation captured the degrading behavior of shear critical columns tested in the lab. The weakness of the shear spring model was that it relies on the ACI-318 nominal shear strength equation to predict the capacity of a column. When the nominal shear strength was not reached, the rate of strength and stiffness degradation was not captured accurately. The two columns that failed to activate the nonlinear behavior of the shear spring behaved in a ductile manner.

Models for interior and exterior joints with minimal transverse reinforcement performed well. The experimental hysteretic behavior was simulated accurately in all but one of the modeled joints. The pinching behavior of non-ductile joints was captured by the model. Maximum strengths and rate of degradation were accurately predicted.

Chapter 5: Simulation of the Earthquake Response of Reinforced Concrete Frames and Assessment of Frame Performance

5.1 Introduction

The objective of the UW-GA Tech Project is to develop an automated evaluation procedure for post-earthquake inspection of RC frame buildings. The final step in this process is the development of fragility functions that define the likelihood that an RC frame with a given level of damage due to mainshock earthquake loading, will reach a new damage state due to additional earthquake loading from an aftershock or subsequent event of known intensity. Obviously, the likelihood of subsequent damage is highly dependent on the frame design; if more information about the frame design is available, the uncertainty associated with prediction of aftershock performance can be reduced. To generate fragility functions defining damage probability, it is necessary to simulate the response of damaged structures subjected to various levels of earthquake loading. Chapter 5 presents the results of analyses of SMF and OMF RC frames of various heights subjected to earthquake motions of various intensities as well as the probability that these frames will reach a particular damage state when undamaged and subjected to an earthquake of a given hazard level and when damaged and subjected to an earthquake of a given hazard level.

5.2 Reinforced Concrete Frame Selection

A series of RC frames was selected for analysis that was considered to span a moderate range of building heights and design requirements. The frames used in this study were designed for research studies conducted by Haselton (2006) and Liel (2008) at Stanford University. Both studies considered a range of RC frame heights and design parameters. Haselton designed a series of frames according to current design provisions: to the ASCE 7-02 (ASCE-02 2002) and ACI 318-05 (ACI-318-05 2005). Haselton frames meet ACI 318-05 requirements for special moment frame (SMF) (e.g. strength, stiffness, capacity design, detailing for special moment frames). These frames represent modern construction and could be expected to respond in a ductile fashion to earthquake loading. The SMFs were designed for a high seismic Los Angeles site with soil class S_d that is located in the transition region of the 2003 IBC design maps (Haselton and Deierlein 2007). The Liel frames were designed to be representative of non-ductile reinforced concrete frame structures constructed in California prior to 1976. These designs meet the requirements of the 1967 Uniform Building Code (ICBO 1967). The Liel frames are representative of ACI 318-05's ordinary moment frames (OMF) designed per ACI 318-05. The OMFs were designed for

the highest seismic zone in the 1967 UBC, Zone 3. A more detailed discussion on their design considerations and assumptions can be found in Section 5.3.

To capture some variation in design of RC structures, several of the Haselton and Liel designs were used in this study. The design parameters identified by previous researchers (Haselton, et al. 2007) as having significant impact on earthquake response and deemed important for this study included the building height, the ratio of column to beam flexural strength, and weak-story effects. The building height was important to this study because of the wide range of heights of concrete frame structures that have built in the past. Buildings of different heights potentially exhibit different collapse mechanisms (Haselton and Deierlein 2007). The strong column weak beam (SCWB) design ratio plays a role in the location of damage in a structure. The ratio is defined by ACI 318-05 (2005) as the sum of nominal column flexural strengths framing into a joint divided by the sum of nominal beam flexural strengths framing into the same joint. Based on findings by Haselton (2006), the SCWB ratio was the most important of three design criteria on the collapse safety of RC structures. When the SCWB was increased from the ACI 318-05 code required value of 1.2, the collapse mechanism begins to involve more stories. The increased column strength moves hinging from the columns to the beams and eliminates the potential for a weak-story collapse. Based on evidence from previous earthquakes weak-story collapses are prevalent in older RC structures (PEER 2011). This was the reason for implementing designs that have a weak-story intentionally included.

To capture variation in the modeling assumptions discussed in Chapter 4, the Haselton and Liel designs were modeled using the different techniques presented in Chapter 4. The objective of including modeling variables is to assess the impact of these modeling assumptions (i.e. flexible versus rigid joint) and failure mode (nonlinear joint and column shear) on performance. Also, as there is uncertainty in the non-ductile shear strength and joint strength mechanisms that control response if they develop, the true probability of frame response is probably a combination of the results with and without these models.

The designs to be modeled are shown in Table 5.1. Five SMFs are included in the table. These five frames are Haselton designs meeting ACI-318 requirements for special moment frames. The SCWB ratio has not been varied for the SMFs due to the modern design requirements. Due to the expected ductility of a SMF, shear failure modeling will not be considered in these frames. Only the 12-story frame has been considered with a weak-story design. Based on the findings of Haselton and Deierlein (2007) the 4-story baseline designs experience weak-story collapse mechanisms in 31% of the collapse simulations performed for their research, while the 12-story baseline designs only experienced weak-story collapse mechanisms in 9% of their collapse simulations. When the weak-story was introduced, the probability of

a weak-story mechanism rose to 49%. Thus, the 4-story baseline exhibits the potential for a weak-story mechanism without introducing a weak-story into the design.

Table 5.1 Information for RC frame parameter study

Report ID	Stories	ACI Designation	Frame Type	Design Case	Shear Failure Modeling	Joint Modeling	
SMF4-1.2-00	4	SMF	Perimeter	Baseline	No	Rigid	
SMF4-1.2-0J	4		Perimeter	Baseline	No	SMF Model	
SMF12-1.2-00	12		Perimeter	Baseline	No	Rigid	
SMF12-1.2-0J	12		Perimeter	Baseline	No	SMF Model	
SMF12-WS-00	12		Perimeter	WS	No	Rigid	
OMF4-1.2-00	4	OMF	Space	Baseline	No	Rigid	
OMF4-1.2-0J	4		Space	Baseline	No	OMF Model	
OMF4-1.2-SJ	4		Space	Baseline	Yes	OMF Model	
OMF4-0.8-00	4		Space	SCWB 0.8	No	Rigid	
OMF4-2.0-00	4		Space	SCWB 2.0	No	Rigid	
OMF12-1.2-00	12		Space	Baseline	No	Rigid	
OMF12-1.2-0J	12		Space	Baseline	No	OMF Model	
OMF12-1.2-SJ	12		Space	Baseline	Yes	OMF Model	
OMF12-0.8-00	12		Space	SCWB 0.8	No	Rigid	
OMF12-2.0-00	12		Space	SCWB 2.0	No	Rigid	
OMF12-WS-00	12		Space	WS	No	Rigid	
Legend and Notes:							
Baseline - Baseline design with SCWB of ≥ 1.2							
SCWB 0.8 - Strong-Column Weak-Beam ratio of ≈ 0.8							
SCWB 2.0 - Strong-Column Weak-Beam ratio of ≈ 2.0							
WS - Weak-Story							

The frame type was also included in the modeling considerations. Perimeter frames were modeled for the SMFs because they are more common in current design practice. A perimeter frame resists lateral loads through frames at the perimeter of the building. Interior columns are designed to carry only gravity loads. A space frame resists lateral loads through frames at every grid line of columns. The difference in the space frame and perimeter frame tributary areas for gravity and lateral loads can be seen in Figure 5.1. Space frame structures are more typical of older RC frame structures, especially office buildings (Liel 2008).

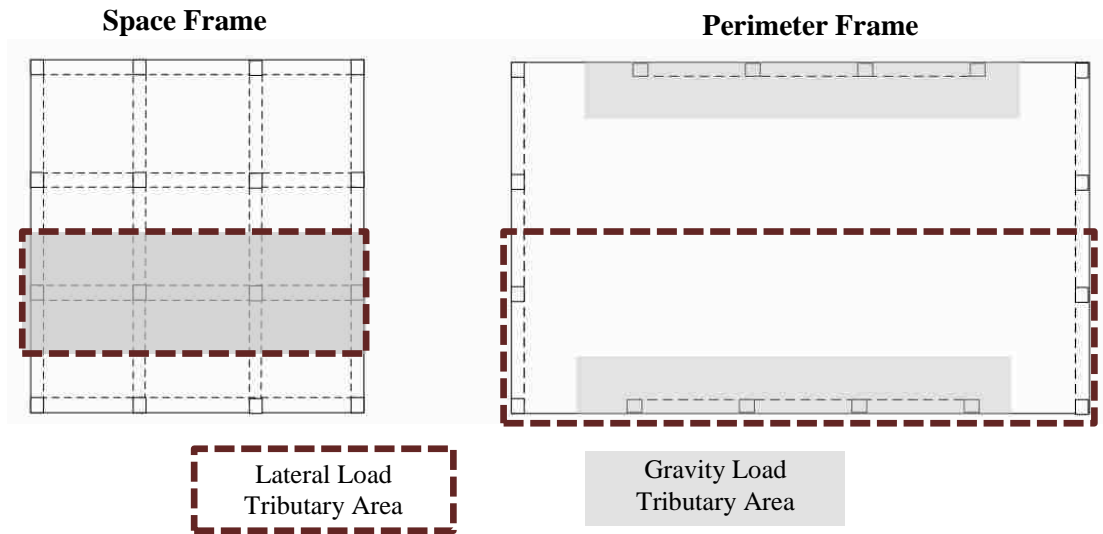


Figure 5.1 Illustration of the gravity/lateral tributary areas for a space frame and perimeter frame

The inclusion of shear modeling was necessary because the lumped plasticity beam-column elements are incapable of simulating the behavior associated with shear failure in the RC columns. This failure mechanism has been discussed in Section 3.3. Brittle shear failures tend to be more common in frames with short (captive) columns (Liel 2008). The designs created by Liel have taller story heights and are not likely to be shear-critical. However, they are expected to yield in flexure prior to experiencing a shear failure (Liel 2008).

Joint modeling was also considered in Table 5.1. As discussed in Section 4.4 two unique modeling techniques were used to capture the joint behavior of SMFs and OMFs. The basic models will use the rigid offset formulation and are labeled Rigid in Table 5.1. The rigid joint models provide the simplest modeling technique and allow for assessment of the impact on performance of joint flexibility and strength. The joint modeling technique labeled SMF Model and OMF Model in Table 5.1 were discussed in Section 4.6.1.

The frames will be identified using the Report ID in column one of Table 5.1 throughout the rest of the document. The naming convention identifies the ACI frame designation (SMF or OMF), frame type (Perimeter or Space), design case (SCWB ratio of 1.2, 0.8, or 2.0 and weak story), and modeling considerations (shear failure and joint failure).

5.3 Frame Design

The frame designs used in this work were done by Haselton (2006) and Liel (2008). The following sections describe these designs as described by Haselton and Liel. Each of the SMF buildings

were designed for the provisions of the 2003 IBC (2003), ASCE7-02 (2002), and the ACI 318-02 (2002). Each of the OMF buildings was designed for the provisions of the 1967 UBC (1967).

5.3.1 SMF Design by Haselton (2006)

The Haselton designs were done in consultation with practicing engineers. This was done to ensure consistency with the current design practice used in industry. The general design assumptions used in SMF design are presented in Table 5.2.

Table 5.2 Design assumptions used by Haselton

Design Parameter	Design Assumptions
Member Stiffness:	
Beams	$0.5EI_g$ (FEMA 356)
Columns	$0.7EI_g$ for All Axial Load Levels (Practitioner Rec.)
Slab Consideration	Slab Not Included in Stiffness/Strength Design
Joint Stiffness	Elastic Joint Stiffness
Expected Design Conservatism:	
Applied to Element Flexural and Shear Strength Design	1.15 of Required Strength
Applied to Joint Strength Design	1.0 of Required Strength
Applied to Strong-Column Weak-Beam Design	Use Expected Ratio of 1.3 Instead of 1.2

Additional design assumptions were used and are laid out in the following design guidelines:

- A 6” step size was used when reducing the sizes of beams and columns over the height of the building; element sizes were kept constant until a 6” step was possible.
- Beam concrete strength of $f'_c = 5$ ksi was used.
- The designs were started using $f'_c = 5$ ksi for the concrete strength. The column concrete strength was increased if required, up to $f'_c = 7$ ksi to help satisfy joint shear design requirements. The $f'_c = 7$ ksi maximum was chosen to avoid concrete placement coordination difficulties with lower strength beam and slab concrete.

The building site factored into the design considerations. The buildings were designed for a high seismic site in California (soil class S_d , $S_{ms} = 1.5g$, and $S_{ml} = 0.9g$). The maximum considered earthquake (MCE) used for the designs is shown in Figure 5.2. The designs were created using the ASCE 7 design provisions that include a $2/3$ factor on the MCE spectra.

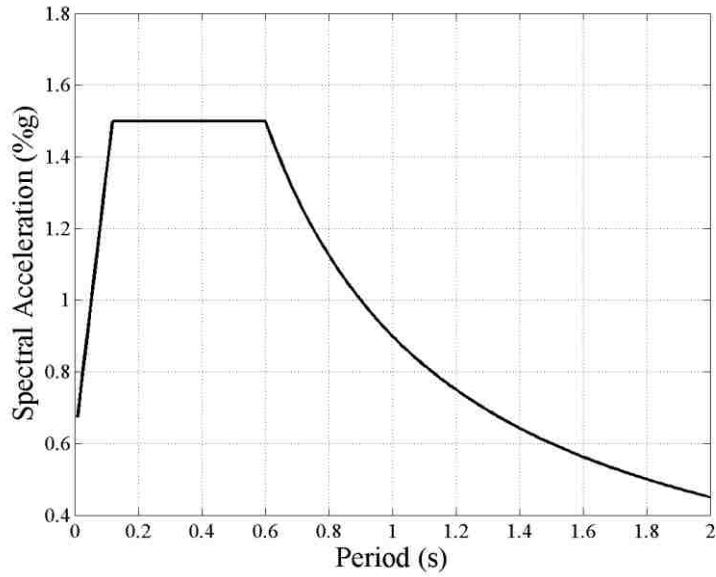


Figure 5.2 MCE ground motion spectrum at the high seismic California site

An example design of the SMFs is shown below in Figure 5.3. All the designs used can be found in Appendix D.

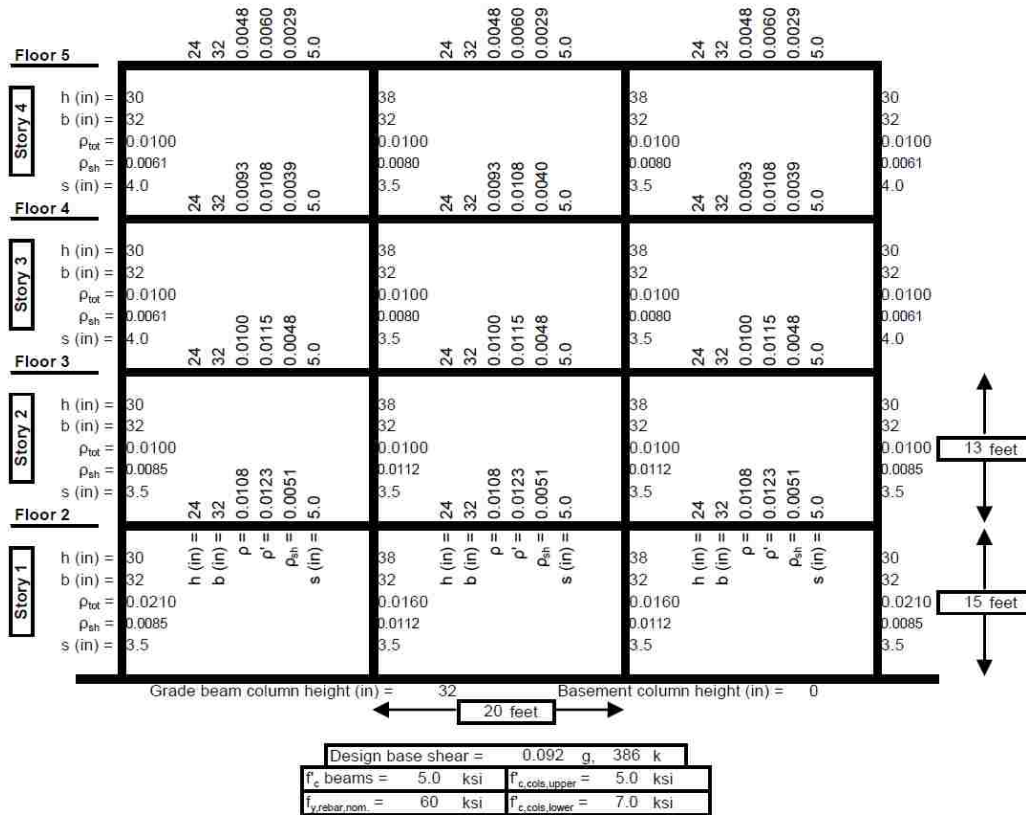


Figure 5.3 Design documentation for SMF4-1.2-00

5.3.2 OMF Designs by Liel (2008)

The frames designed by Liel were representative of California seismic designs between 1950 and 1975 (Liel 2008). The 1967 UBC equivalent static force procedure was used to determine the required base shear for each structure using seismic zone 3. Each structure was designed with the standard level of detailing which meant the system’s ductility and redundancy factor, K, was one. Story drifts were limited to 2% to reflect conventional practice. Code-defined load combinations were used, but wind loads were not considered. The beam and column elements were designed to have the same flexural over strength. Each element was designed to be 15% stronger than the minimum code design. Each structure was designed using ultimate strength design. Material strengths were held the same for all designs. The concrete strength was 4 ksi and both the longitudinal and transverse steel yield strengths were 60 ksi. A 6” step size was used when reducing the sizes of beams and columns over the height of the building; element sizes were kept constant until a 6” step was possible. An example design of the OMFs is shown below in Figure 5.4. All the designs used can be seen in Appendix D.

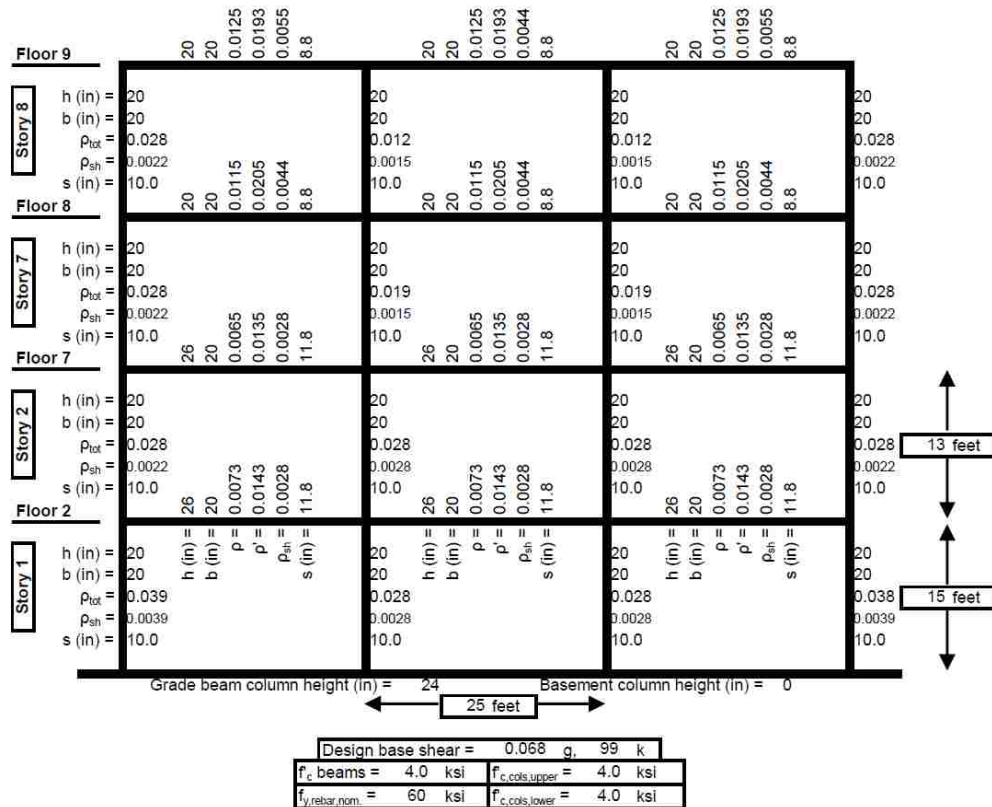


Figure 5.4 Design documentation for OMF4-1.2-00

5.4 Frame Nonlinear Analysis Models

Structural performance was assessed using story drifts determined from nonlinear analysis. Thus, for each building design, it was necessary to create a nonlinear model in OpenSees. A 2D, three-bay frame was modeled for each design using OpenSees. Only the lateral resisting system was modeled for simplicity reasons. A reference four-story frame can be seen in Figure 5.5.

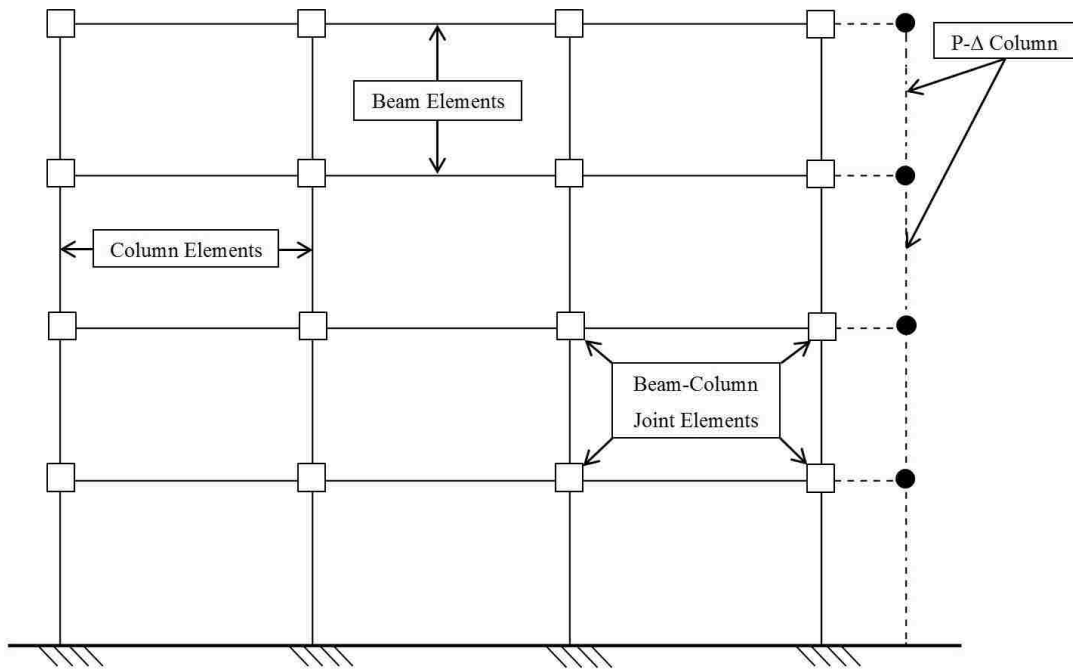


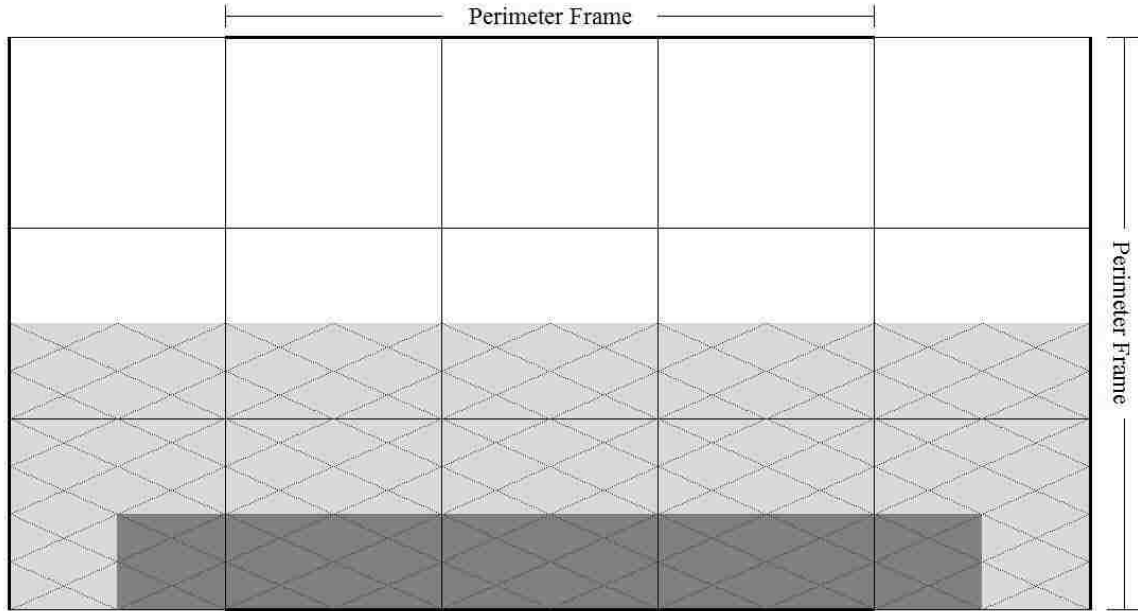
Figure 5.5 Frame model components

The beam and column elements were modeled in the same manner as discussed previously in Section 4.3. The only difference in modeling technique between the beams and columns was the geometric transformation used in OpenSees. The columns utilize a P-Delta transformation which accounts for the effects of gravity on column elements once displacements occur in a structure. Beams were not affected by P-Delta loads. Thus, the beams have a linear transformation.

The beam-column joint elements identified in Figure 5.5 were modeled as discussed in Section 4.6.1. The joint modeling technique depends on the frame being modeled. Table 5.1 identifies which joint modeling technique was applied to the frame.

The assignment of both vertical loads and mass was done at the nodes where beams and columns formed a joint. The gravity load was assigned based on a tributary area as seen in Figure 5.1 for each column. The only gravity load on the perimeter frames came from the immediate tributary area that is closest to the frame. The rest of half the plan view of the frame was assigned to the P- Δ column. In the

mass assignment all the mass (half the plan view of the frame) was assigned to the perimeter frame. Figure 5.6 and Figure 5.7 show the tributary areas assigned as mass and gravity load to perimeter and space frames respectively.




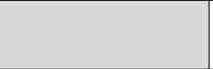

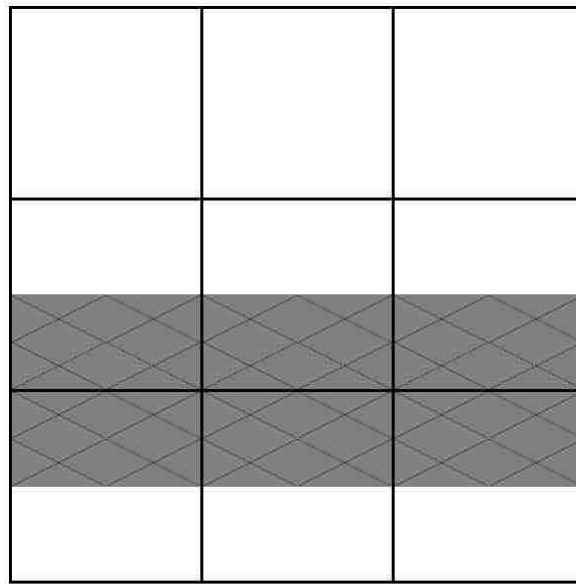
Perimeter Frame Loading		Pdelta Column Loading	
	Gravity Area Applied to Frame		Gravity Area Applied to P-Δ
Perimeter Frame Mass			
	Lateral Area (Mass to Frame)		

Figure 5.6 Perimeter frame loading



Space Frame Loading	
	Gravity Area Applied to Frame
Space Frame Mass	
	Lateral Area (Mass to Frame)

Figure 5.7 Space frame loading

The same dead and live loads that Haselton applied during his work were applied to the frames in this study. Haselton referenced work performed by Ellingwood (1980) on the expected dead and live loads to be applied during analysis. Ellingwood called for a dead load of 1.05 times the nominal load, which was taken as 175 psf. The live load assigned to the frames was 12 psf. Mass was assigned using the same tributary areas. Only the dead load contributed to the mass.

The P- Δ column shown in Figure 5.5 accounts for gravity load that was applied to the non-seismic portion of a perimeter frame. Figure 5.1 shows the tributary areas for both a space and perimeter frame. The gravity area that was directly applied to the frame to be analyzed does not account for the portion of the frame that was not carrying lateral load. This portion of the gravity load also will try to pull the structure over when P- Δ effects are considered.

The P- Δ column was loaded with vertical point loads at each floor that were equivalent to the tributary gravity loads not directly applied to the perimeter frame. No mass was assigned to the column because the tributary area for the lateral loads has already been accounted for and applied to the perimeter frame. A breakdown of the components that make up the P- Δ column can be seen in Figure 5.8.

The truss elements connecting the perimeter frame to the P- Δ column act only axially and were pinned at both ends. The elastic column elements have moments of inertia and areas approximately two orders of magnitude greater than the columns in the frame to represent the effect of all the gravity columns. Zero-length elements connect the columns to the truss elements. They act as rotational springs and were assigned an extremely small stiffness value so the column does not carry any moment. The base of the column was pinned.

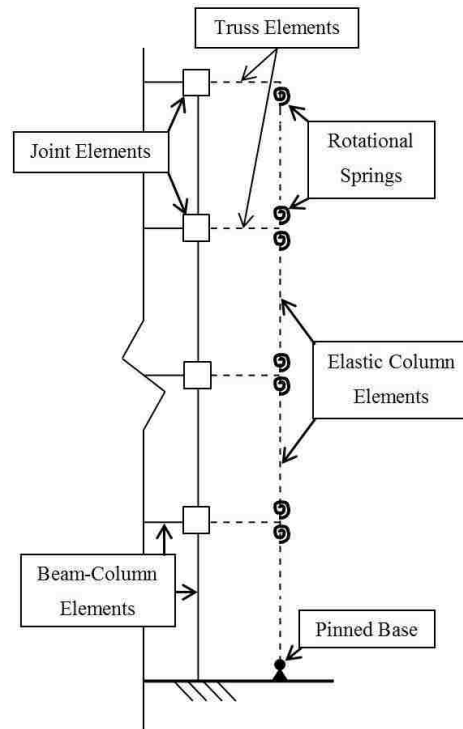


Figure 5.8 P- Δ column formulation

Another modeling decision made was to use an expected material strength for steel instead of the nominal strength used in design. This was done by Haselton and Liel in their work. An expected rebar yield strength of 67 kips per square inch was used for each frame (Melchers 1999). The concrete material strength was used as indicated in the Haselton and Liel designs.

5.4.1 Modeling Deficiencies

The nonlinear models developed for this study were idealizations of a structures actual geometry, loading, and dynamic behavior. The model was only a representation of the real structure and deficiencies exist in the modeling techniques. These deficiencies have been listed below and may limit the application of the results.

1. The 3D structure was idealized as a 2D planar system. The impact on response of bidirectional loading, torsion effects, floor diaphragm flexibility were not considered.
2. Nonstructural components were not included in the model. Previous research suggests partitions will contribute some strength and stiffness to the system, which can affect dynamic response (Yakut 2004).
3. Perimeter frame models do not include the gravity system; the gravity system can add stiffness and strength.
4. Soil-structure interaction was not considered; it may play a role depending on site geology.

5.4.1.1 Failure Modes Not Modeled

1. Failure of short and inadequately confined lap splices, found commonly in older RC frames, were not modeled.
2. Punching shear at slab-column connections in the gravity frame was not considered for perimeter frames.
3. Foundation failure was not considered.

5.5 Full Frame Simulation

This research effort required accurate frame modeling. To ensure an accurate full frame model was developed, pushover simulations were performed on each of the frames identified in Table 5.1. The pushover analyses were used to identify the deformation capacity, lateral strength, and potential failure mechanisms of the structures.

The primary analysis technique used for this research effort was nonlinear dynamic time-history analysis. This was accomplished by subjecting the frames to ground motions and documenting the response. A foreshock-aftershock pair was used to predict the response of a damaged structure.

5.5.1 Data Recorded During Simulations

During each nonlinear simulation the story drifts, roof drift, and section moment-curvatures have been recorded. The story drifts will be used to determine the damage states of the columns. These drift levels can be used in the analysis process to establish the foreshock damage classification. They will also be used once the aftershock has been applied to the structure to develop fragility curves for the damage states. The individual element section response has been used to identify the yielding mechanism of the frames during the pushover analyses.

5.5.2 Monotonic Pushover Analysis

Monotonic pushover analyses were performed to investigate the general load-deflection relationship for the models. Both a monotonic pushover and a cyclic pushover were completed. All the pushover analyses were performed using a static lateral force distribution. The primary load pattern for all the frame models used a force distribution derived from the equivalent lateral force procedures in the seismic design provisions of ASCE-05 (2005). The general load pattern can be seen in Figure 5.9.

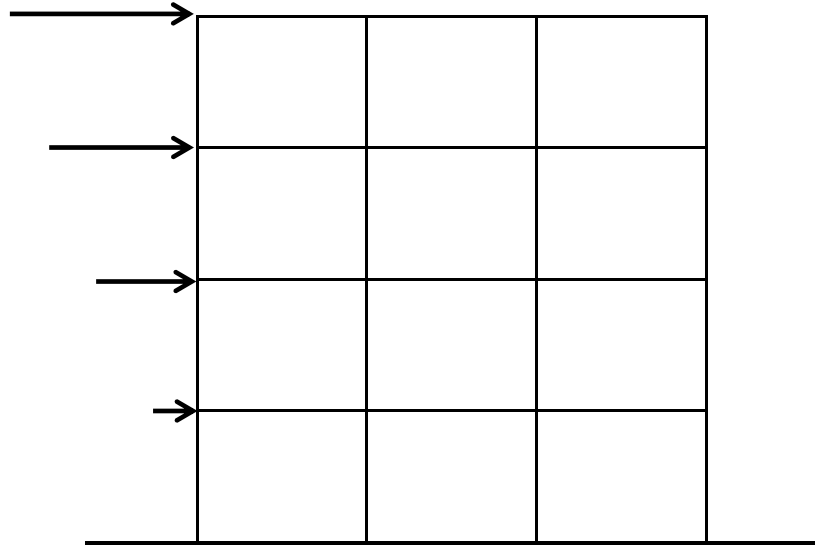


Figure 5.9 Pushover load pattern

The pushover analyses were used to validate the modeling procedure. Moment-curvature results were monitored at the ends of each element to understand the response of the structure when the pushover analyses were performed. Both the story drifts and moment-curvature responses were used to identify the failure mechanisms for each of the frames identified in Table 5.1.

5.5.3 Pushover Results

The results of the pushover simulations have been presented in Figure 5.10 through Figure 5.16. The data in the figures show roof drift versus base shear. These figures illustrate the trends in the overall response of the building that arise from including the simulation of inelastic joint behavior, varying the column to beam strength ratio, and introducing a weak-story. These trends have been quantified in Table 5.3, Table 5.4, Table 5.5, and Table 5.6. In these tables the maximum base shear, the roof drift at the point of maximum base shear, and the roof drift at a 20% drop of strength from the maximum base shear have been identified for the pushover tests.

5.5.3.1 Impact of Model Parameters

Figure 5.10 and Figure 5.12 show the results for the modeled SMFs. The results show the pushover curves, which indicate the frame base shear and the roof drift as the structure is pushed over. Figure 5.11 and Figure 5.13 show the drift profiles over the height of the SMF frames. The drift profiles at the maximum base shear and the frame failure point have been plotted. The failure point has been defined when the frame base shear drops by 20% or at a roof drift of 5% if the 20% reduction does not happen. The following bulleted list addresses the impact of the modeling and design variables in the SMF pushover results.

- SMF4-1.2-00 had greater initial stiffness, higher maximum base shear, and lower drift at maximum base shear than SMF4-1.2-0J
- SMF12-1.2-00 had greater initial stiffness, higher maximum base shear, and lower drift at maximum base shear than SMF12-1.2-0J
- SMF12-WS-00 had nearly identical performance to SMF12-1.2-00. The weak-story introduction had very little effect because Frame SMF12-1.2-00 had a 1st story mechanism; thus, making the columns stronger in the upper stories only made Frame SMF12-WS-00 slightly more brittle as the increase in the first story degradation was minimal.

These trends have been quantified in Table 5.3 and Table 5.4.

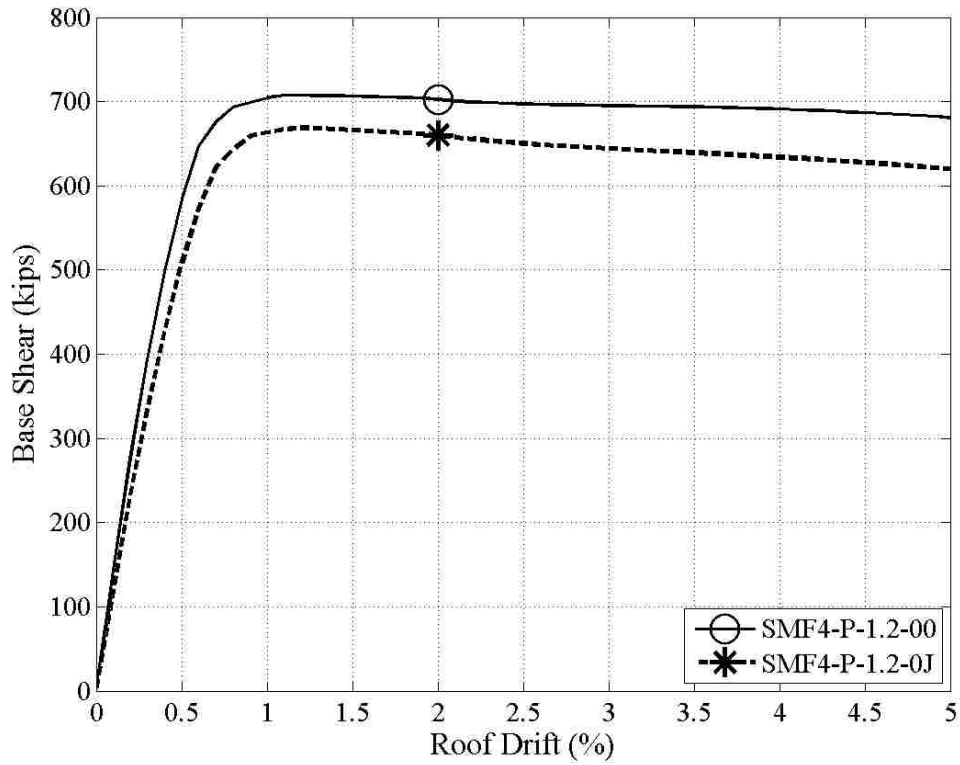


Figure 5.10 Pushover response for the 4-Story SMFs

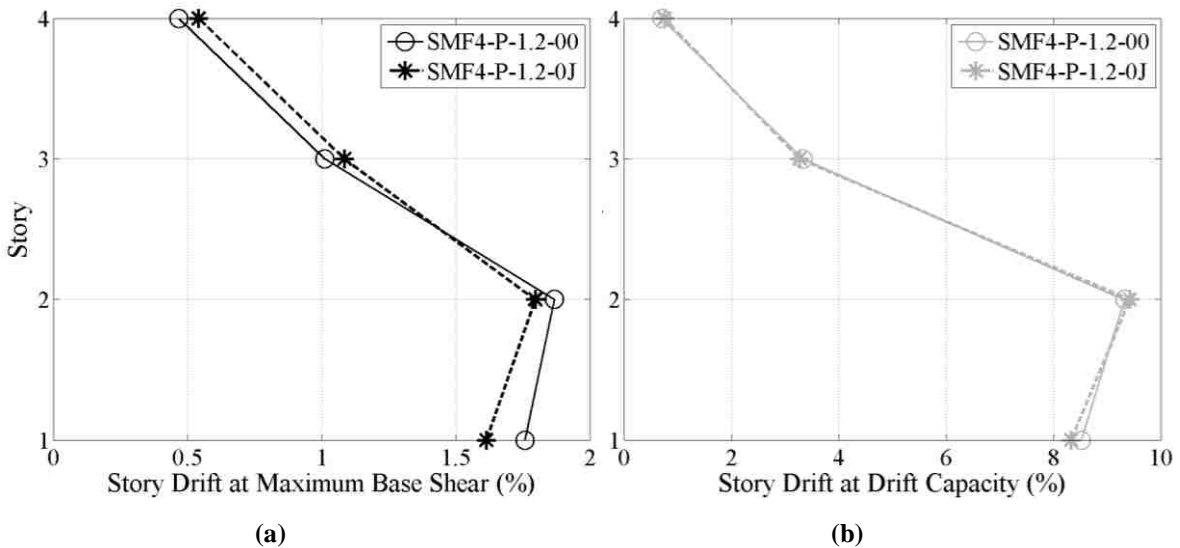


Figure 5.11 Drift profiles for 4-Story SMFs: (a) at maximum base shear and (b) at failure

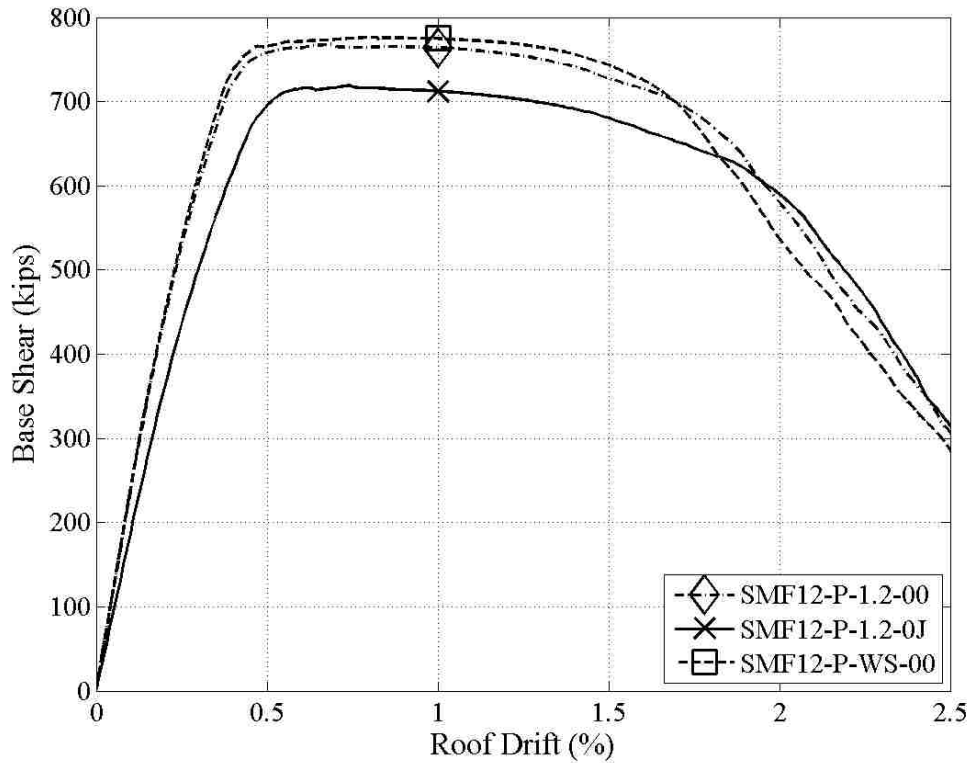


Figure 5.12 Pushover response for the 12-Story SMFs

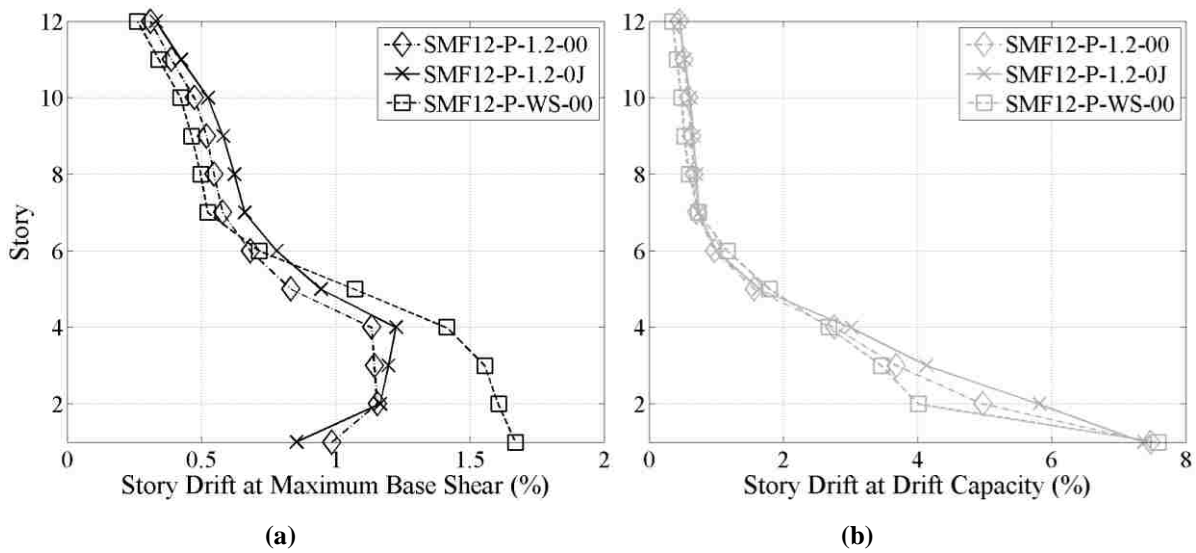


Figure 5.13 Drift profiles for 12-Story SMFs: (a) at maximum base shear and (b) at failure

Table 5.3 4-Story SMF pushover results

Report ID	Maximum Base Shear (kips)	Drift at Maximum Base Shear (%)	Drift at 80% of Maximum Base Shear (%)
SMF4-1.2-00	707	1.20	NA
SMF4-1.2-0J	669	1.20	NA

Table 5.4 12-Story SMF pushover results

Report ID	Maximum Base Shear (kips)	Drift at Maximum Base Shear (%)	Drift at 80% of Maximum Base Shear (%)
SMF12-1.2-00	768	0.69	1.92
SMF12-1.2-0J	719	0.74	2.04
SMF12-WS-00	776	0.82	1.85

Figure 5.14 and Figure 5.16 show the results for the OMFs. Figure 5.15 and Figure 5.17 show the drift profiles over the height of the SMF frames. The drift profiles at the maximum base shear and the frame failure point have been plotted. The following bulleted list addresses the impact of the modeling and design variables in the SMF pushover results.

- OMF4-1.2-00 had greater initial stiffness, higher maximum base shear, and lower drift at maximum base shear than OMF4-1.2-0J
- OMF12-1.2-00 had greater initial stiffness, higher maximum base shear, and lower drift at maximum base shear than OMF12-1.2-0J
- OMF4-1.2-SJ and OMF12-1.2-SJ followed the same pushover curve as OMF4-1.2-0J and OMF12-1.2-0J, respectively, until the ACI nominal shear strengths were reached at 4% roof drift and 1.5% roof drift for OMF4-1.2-SJ and OMF12-1.2-SJ, respectively.
- OMF4-1.2-00 had greater initial stiffness, higher maximum base shear, and lower drift at maximum base shear than OMF4-1.2-0J
- OMF4-1.2-0J had more ductility than OMF4-1.2-00, due to the spread of inelastic action into the joints.
- OMF12-1.2-0J had more ductility than OMF12-1.2-00, due to the spread of inelastic action into the joints.

- OMF4-0.8-00 and OMF12-0.8-00 were the most brittle of the 4-story and 12-story OMFs, respectively. This was due to the weak column-strong beam design.
- OMF4-2.0-00 and OMF12-2.0-00 were the most ductile of the 4-story and 12-story OMFs, respectively. This was due to the strong column-weak beam design. The increased ductility and base shear capacity was a product of a strong column-weak beam failure mechanism.
- OMF12-WS-00 was the only frame that had a 1st story failure mechanism as expected.

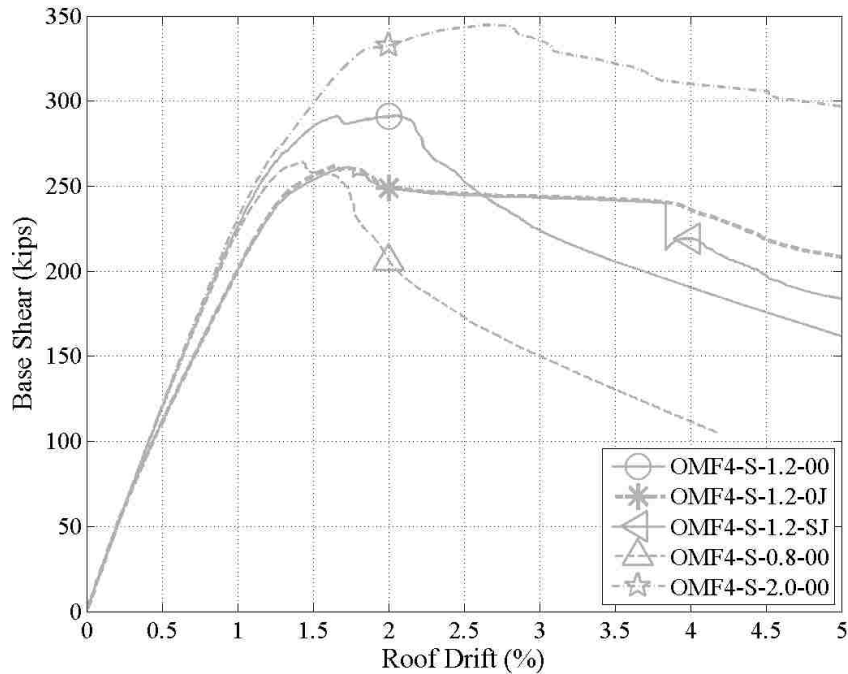


Figure 5.14 Pushover response for the 4-Story OMFs

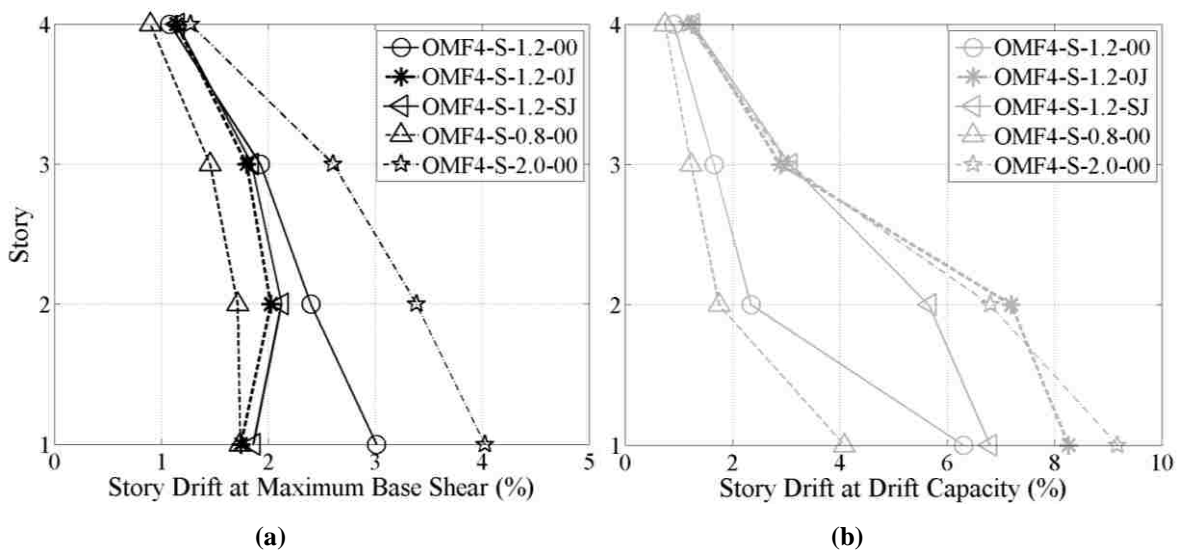


Figure 5.15 Drift profiles for 4-Story OMFs: (a) at maximum base shear and (b) at failure

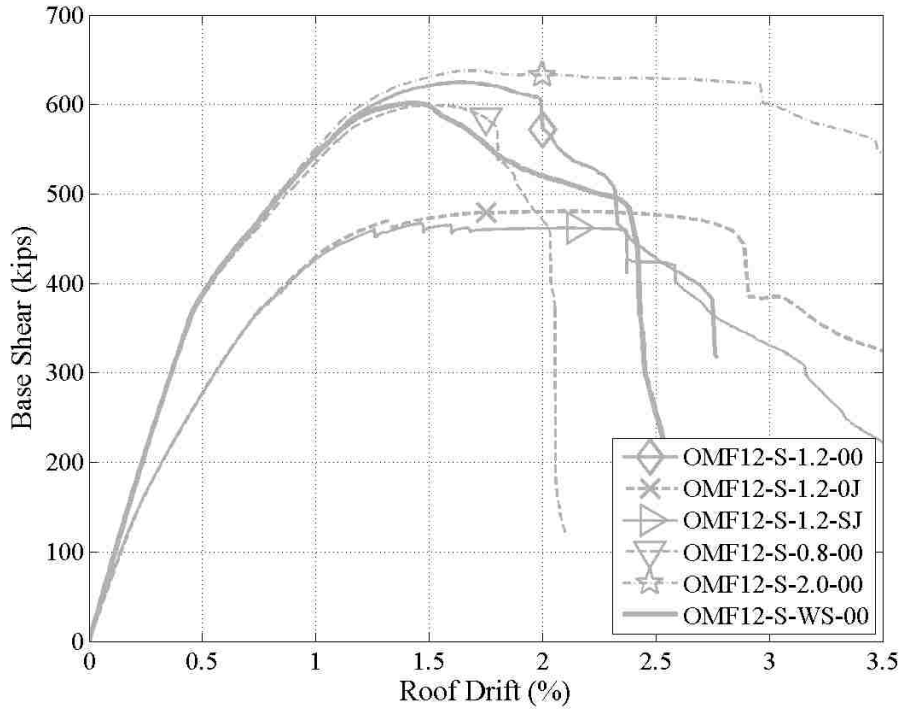


Figure 5.16 Pushover response for the 12-Story OMFs

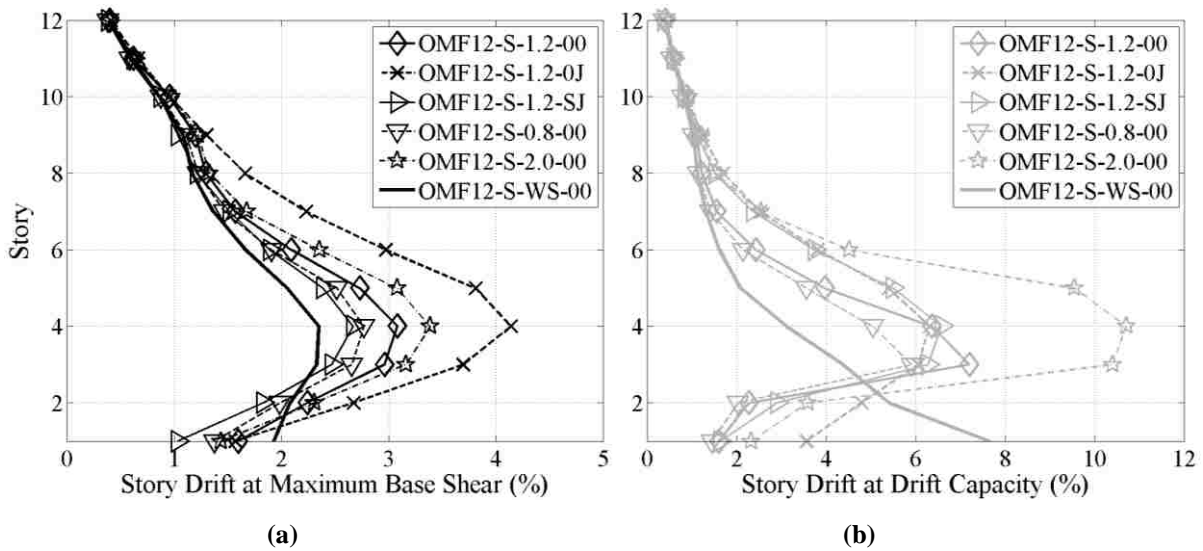


Figure 5.17 Drift profiles for 12-Story OMFs: (a) at maximum base shear and (b) at failure

Table 5.5 4-Story OMF pushover results

Report ID	Maximum Base Shear (kips)	Drift at Maximum Base Shear (%)	Drift at 80% of Maximum Base Shear (%)
OMF4-1.2-00	291	2.05	2.83
OMF4-1.2-0J	262	1.66	4.91
OMF4-1.2-SJ	261	1.73	4.21
OMF4-0.8-00	264	1.42	1.97
OMF4-2.0-00	345	2.70	5.00

Table 5.6 12-Story OMF pushover results

Report ID	Maximum Base Shear (kips)	Drift at Maximum Base Shear (%)	Drift at 80% of Maximum Base Shear (%)
OMF12-1.2-00	625	1.64	2.32
OMF12-1.2-0J	480	2.13	3.05
OMF12-1.2-SJ	467	1.46	2.72
OMF12-0.8-00	599	1.49	1.97
OMF12-2.0-00	637	1.73	3.82
OMF12-WS-00	601	1.43	2.38

5.5.3.2 Curvature Demand Under Pushover Loading

The curvature ductility, μ , at beam and column member ends due to pushover loading can be used to identify the progression of inelastic action of an RC frame. Curvature ductility demands can be determined using the OpenSees output by recording the member section responses. Curvature ductility demand was defined as,

$$\mu = \frac{\phi_{max}}{\phi_{yield}} \quad (5.1)$$

where ϕ_y was computed from the moment curvature relations for the sections by drawing a horizontal line at the point of maximum moment and then drawing a line passing through the origin with the initial slope to intersect the horizontal line at ϕ_y and M_y as shown in Figure 5.18. M_y is the moment at which the first instance of longitudinal steel yields.

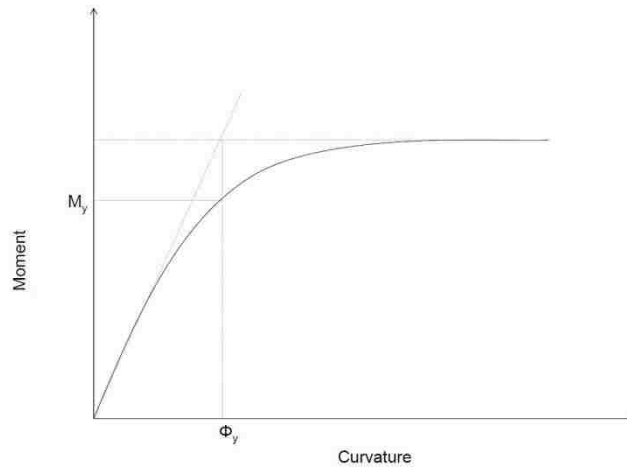


Figure 5.18 Plot of Moment vs. Curvature (Paspuleti 2002)

Figure 5.20 and Figure 5.22 show the pushover curve for the four-story SMF and OMF respectively. The pushover curve includes points in which the curvature ductilities at the member ends have been computed. Figure 5.21 and Figure 5.23 show simulated curvature ductility demand and story drifts at the points indicated on the pushover curves. These figures show the progression of inelastic action and the failure mechanism for the frames. Using these plots allows for a better understanding of the pushover results shown in Figure 5.10, Figure 5.12, Figure 5.14, and Figure 5.16.

SMF4-1.2-00 has a more ductile failure progression than OMF4-1.2-00. A two story failure mechanism occurs in SMF4-1.2-00. OMF4-1.2-00 has a first story failure mechanism. Similar comparisons and failure mechanisms have been identified using the figures in Appendix F and have been presented in Table 5.7.



Figure 5.19 Ductility demand legend for pushover results

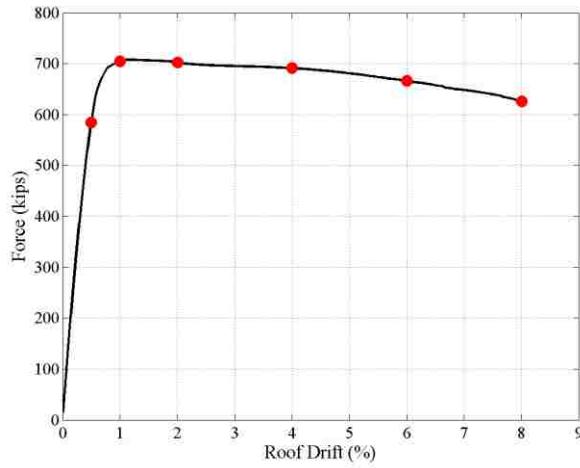


Figure 5.20 SMF4-1.2-00: Pushover Curve with Curvature Ductility Points

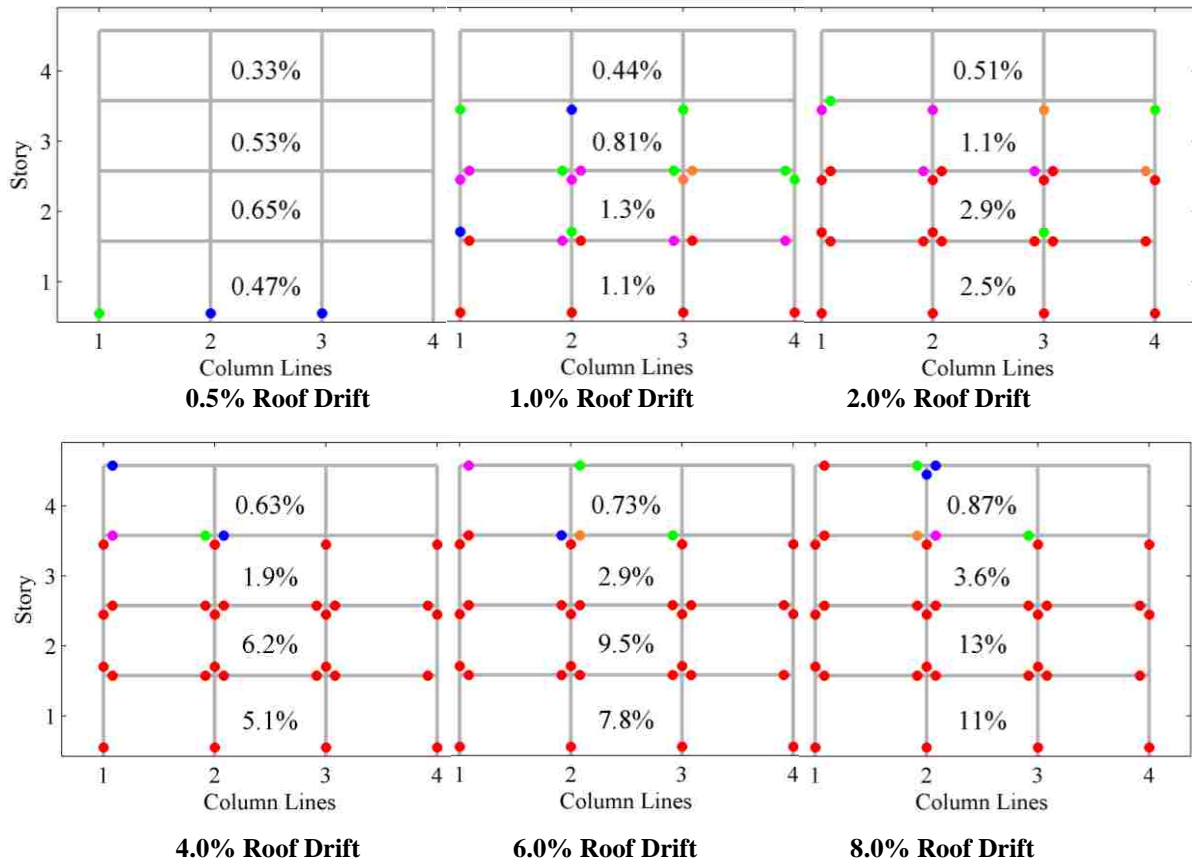


Figure 5.21 SMF4-1.2-00: Drift and Curvature Ductility Plots

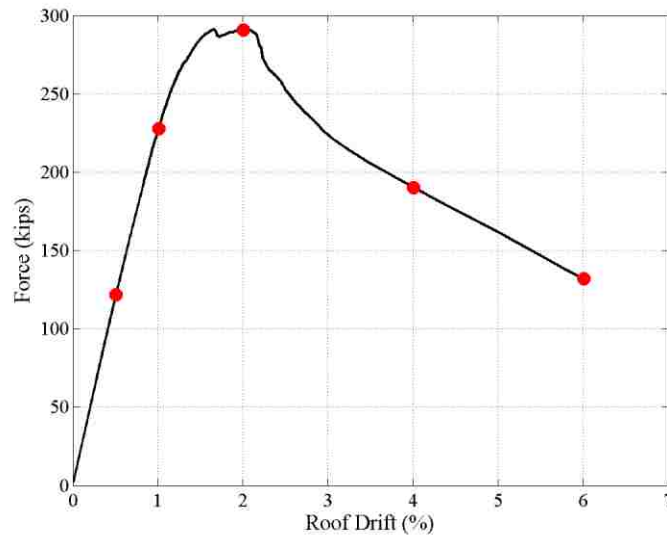


Figure 5.22 OMF4-1.2-00: Pushover Curve with Curvature Ductility Points

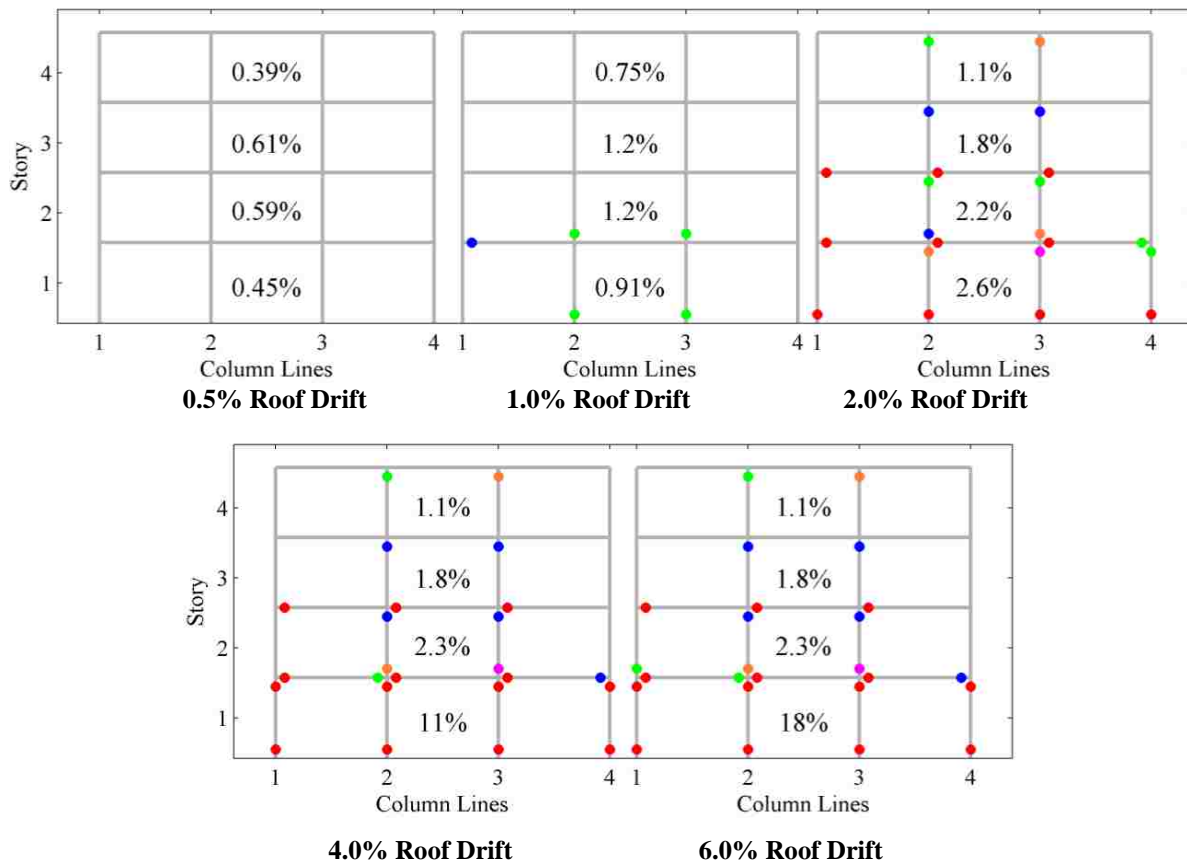


Figure 5.23 OMF4-1.2-00: Drift and Curvature Ductility Plots

Table 5.7 Pushover failure mechanism results

Report ID	Drift Capacity	Maximum Story Drift at Drift Capacity	Number of Stories Involved in Failure Mechanism	Floors Where Failure Mechanism Occurred
SMF4-1.2-00	5.00	9.33	2	1,2
SMF4-1.2-0J	5.00	9.42	2	1,2
SMF12-1.2-00	1.92	7.48	1	1
SMF12-1.2-0J	2.04	7.38	1	1
SMF12-WS-00	1.85	7.59	1	1
OMF4-1.2-00	2.83	6.31	1	1
OMF4-1.2-0J	4.91	8.26	2	1,2
OMF4-1.2-SJ	4.21	6.80	2	1,2
OMF4-0.8-00	1.97	4.10	1	1
OMF4-2.0-00	5.00	9.18	1	1
OMF12-1.2-00	2.32	7.20	2	3,4
OMF12-1.2-0J	3.05	6.31	4	1,2,3,4
OMF12-1.2-SJ	2.72	6.59	3	3,4,5
OMF12-0.8-00	1.97	5.91	1	3
OMF12-2.0-00	3.82	10.71	3	3,4,5
OMF12-WS-00	2.38	7.67	1	1

5.5.4 Dynamic Time-History Analysis

Frame models were subjected to a foreshock-aftershock pair to assess foreshock induced damage and subsequent aftershock induced damage. A suite of ground motions was selected and scaled to represent a relatively weak, moderate, and severe seismic event. The ground motion selection and scaling procedures are described in Sections 5.5.5 and 5.5.6, respectively. Then, motions of all intensity levels were randomly combined to generate a suite of foreshock-aftershock pairs. Thus, a foreshock-aftershock pair could be a severe earthquake followed by a weak intensity earthquake or vice versa.

5.5.5 Ground Motion Selection

To assess the performance of the RC frames for earthquake loading, one or more suites of earthquake ground motions was required. Because the objectives of this study were to assess the performance of typical RC structures subjected to earthquake motions, it was desirable that the motions represent a range of fault mechanisms, intensity levels, and source distances. The suite of motions developed for the PEER report by Baker et al. (2011) met these criteria and was chosen for the current study.

The first 40 ground motions was labeled SET 1A and was intended to represent a moderately large broad-band ground motion at a small distance on a soil site. The ground motions were selected so that their horizontal response spectra match the median and log standard deviations predicted for a magnitude 7 strike-slip earthquake at a distance of 10 km. The ground motions were selected to match the target earthquake at periods between 0 and 5 seconds. The acceleration spectra for the 40 ground motions in SET 1A can be seen plotted along with the average of the 40 spectra, MCE spectrum (2% in 50 years), 10% probability in 50 years spectrum, and the 50% in 50 year spectrum for the Los Angeles site considered for the frame designs in Figure 5.24.

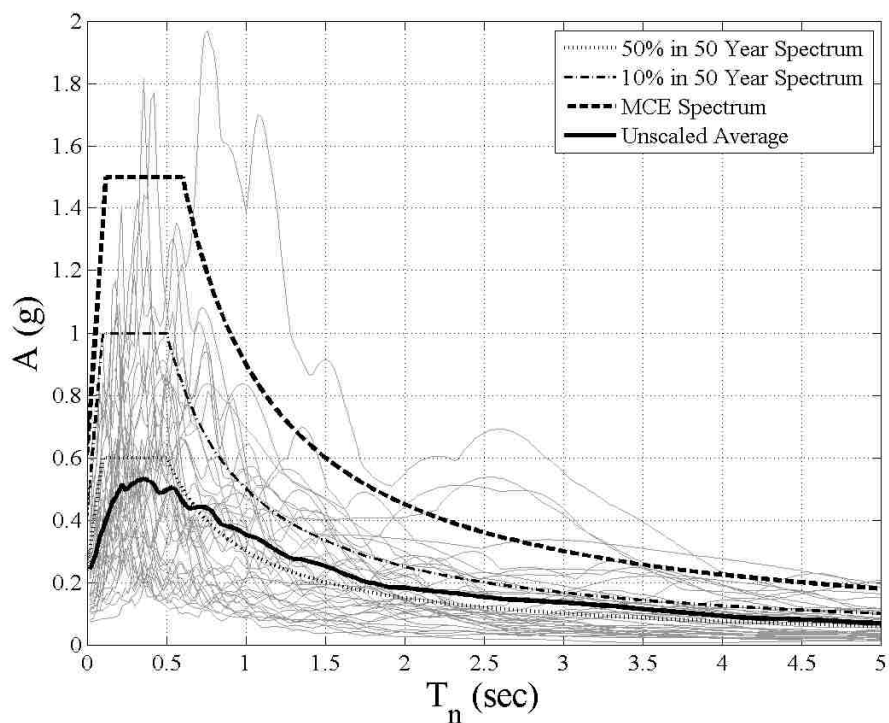


Figure 5.24 SET 1A Spectra

The second 40 ground motions were labeled SET 1B and were intended to represent a smaller broad-band earthquake at a moderate distance on a soil site. The ground motions were selected so that their horizontal response spectra match the median and log standard deviations predicted for a magnitude 6 strike-slip earthquake at a distance of 25 km. The acceleration spectra for the 40 ground motions in SET 1B can be seen plotted along with the average of the 40 spectra, MCE spectrum, and 10% probability in 50 year spectrum for the Los Angeles site considered for the frame designs in Figure 5.25.

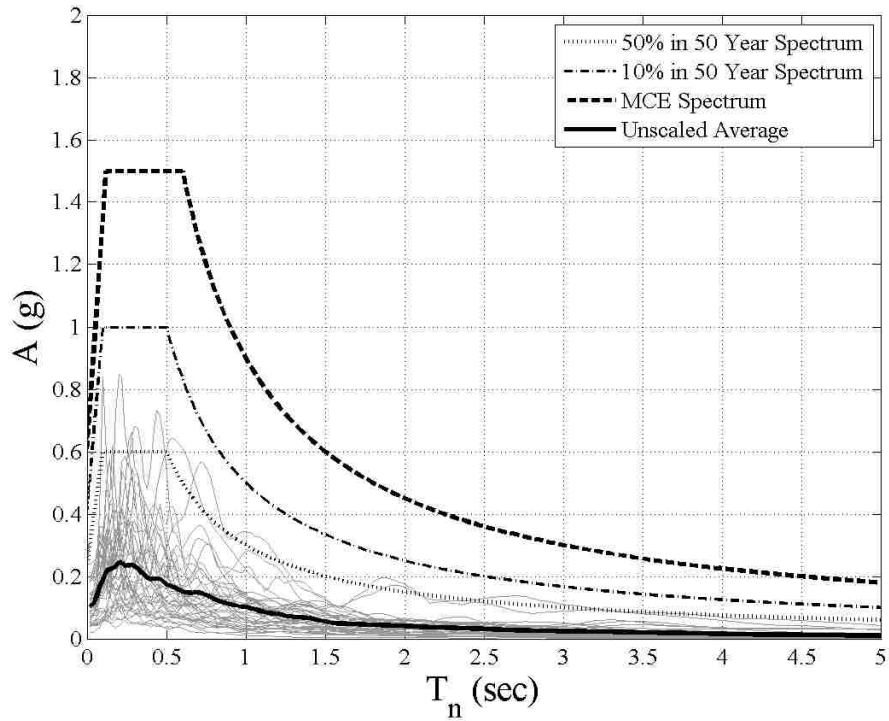


Figure 5.25 SET 1B Spectra

The third 40 ground motions were labeled SET 2 and were intended to represent a moderately large broad-band ground motion at a small distance on a rock site. The ground motions were selected so that their horizontal response spectra match the median and log standard deviations predicted for a magnitude 7 strike-slip earthquake at a distance of 10 km. The acceleration spectra for the 40 ground motions in SET 2 can be seen plotted along with the average of the 40 spectra, MCE spectrum, and 10% probability in 50 year spectrum for the Los Angeles site considered for the frame designs in Figure 5.26.

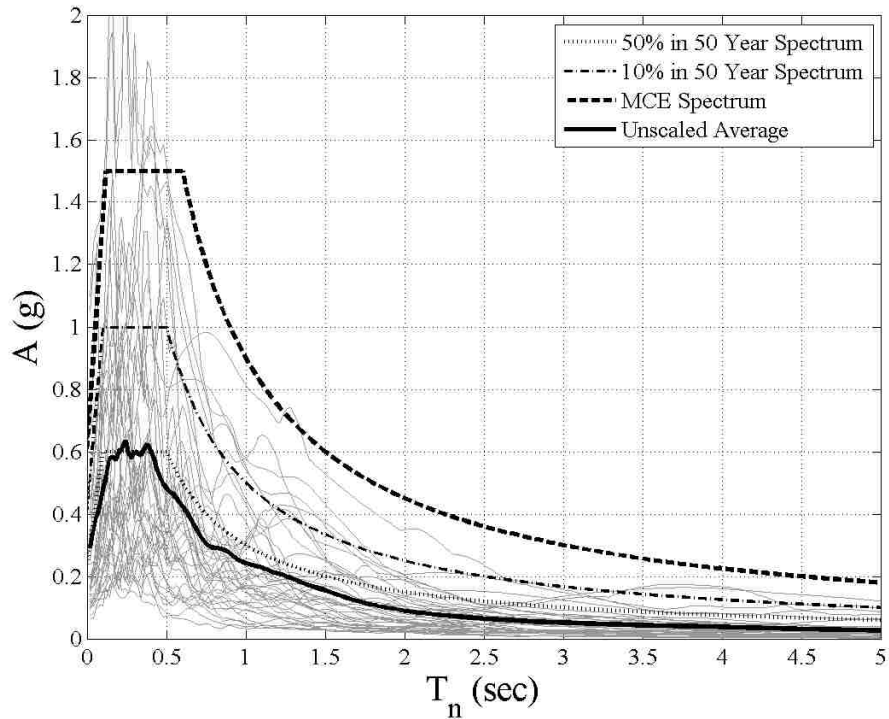


Figure 5.26 SET 2 Spectra

Table 5.8 Ground motion summary

Name	# of GMs	Magnitude	Distance	Site Type	Fault Type	Scaling
SET #1A	40	7	10	Soil	Strike-Slip	No
SET #1B	40	6	25	Soil	Strike-Slip	No
SET #2	40	7	10	Rock	Strike-Slip	No

Table 5.8 compares the different sets of ground motions that were used for the time-history analysis in this report. A more thorough discussion of the ground motion selection procedure can be found in the PEER report by Baker et al. (2011), and the ground motions that make up the three sets can be found in Appendix E.

5.5.6 Ground Motion Scaling

In the first phase of the project, the objective was to assess the performance of a damaged building subjected to an earthquake of a given hazard level. To achieve this objective, it was necessary to scale the motions to represent a specific hazard level. Often, suites of earthquake motions are scaled to a given hazard level by scaling the motions such that the spectral acceleration at the fundamental period of the structure equals the spectral acceleration for the equal hazard spectrum, as in Figure 5.27. This

approach is questionable if the period of the structure changes substantially or higher modes affect response.

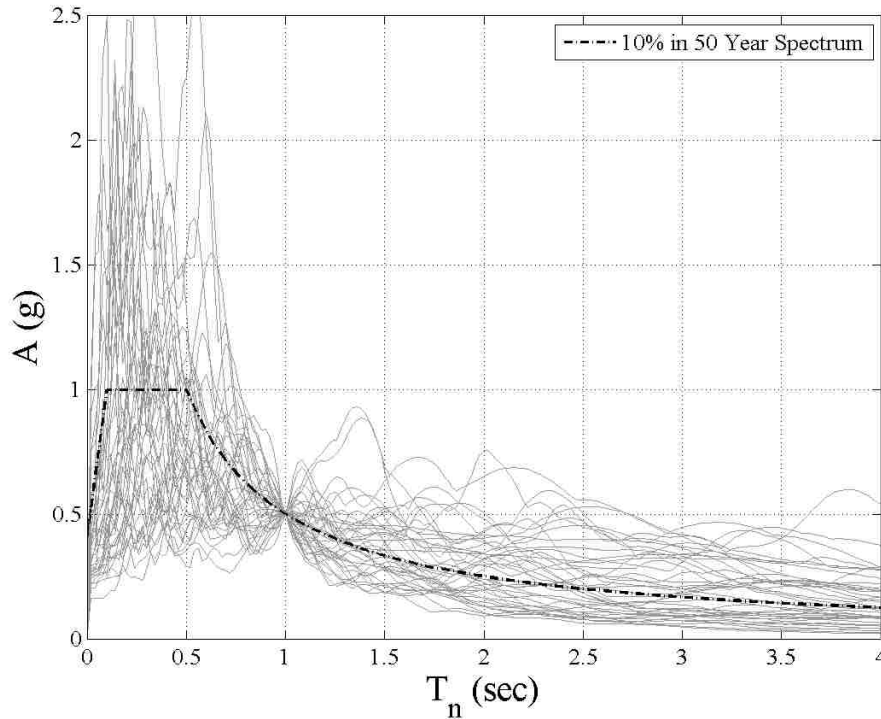


Figure 5.27 Example of scaling to a specific period

For this research effort each motion was scaled to “best fit” the hazard spectrum over the period range of 0.5 to 3.5 seconds. These periods were selected based on an initial set of nonlinear time-history analyses performed on Frames SMF4-1.2-00, SMF12-1.2-00, OMF4-1.2-00, and OMF12-1.2-00. An initial average scaling factor was applied to 10 ground motion records to acquire weak (50% in 50 year) and severe (MCE) events. The frames fundamental periods were considered prior to dynamic analysis, after the 10 weak foreshocks, and after the 10 severe aftershocks. The resulting periods can be seen in Table 5.9. The smallest and largest values have been shaded and were used to choose 0.5 and 3.5 seconds as the bounding periods for scaling the spectra.

Table 5.9 Frame periods for ground motion scaling purposes

Frame ID	Undamaged Structure Period (s)	Weak Foreshock Damaged Structure Minimum Period (s)	Severe Aftershock Damaged Structure Maximum Period (s)
SMF4-1.2-00	0.82	1.14	1.53
SMF12-1.2-00	1.74	2.53	3.26
OMF4-1.2-00	1.56	1.58	2.12
OMF12-1.2-00	2.32	2.32	3.31

To obtain suites of motions for assessment of seismic performance, the same procedure was used to determine scaling factors for the weak (50% in 50 year), moderate (10% in 50 year), and severe (2% in 50 year) procedure. Points on the earthquake hazard spectrum from 0.5 to 3.5 seconds were compared with the ground motion spectra. MATLAB was used to determine the scaling factor, α . The function took in the array of MCE spectrum values, MCE_{array} , and the array of spectrum values, EQ_{array} , from the individual records. It then iterates to find α using the following equation, which makes the summation show below equal to zero.

$$\sum MCE_{array} - \alpha * EQ_{array} \quad (5.2)$$

Each scale factor was then applied to the acceleration record used to create the original spectrum. The individual scaling factors have been provided in Appendix E. Figure 5.28 shows the original record, the 2% in 50 year hazard spectrum (MCE), and the ground motion scaled to provide a best-fit to this spectrum from 0.5 to 3.5 seconds. The averages of the scaled spectra for the three sets have been plotted in Figure 5.29, Figure 5.30, and Figure 5.31.

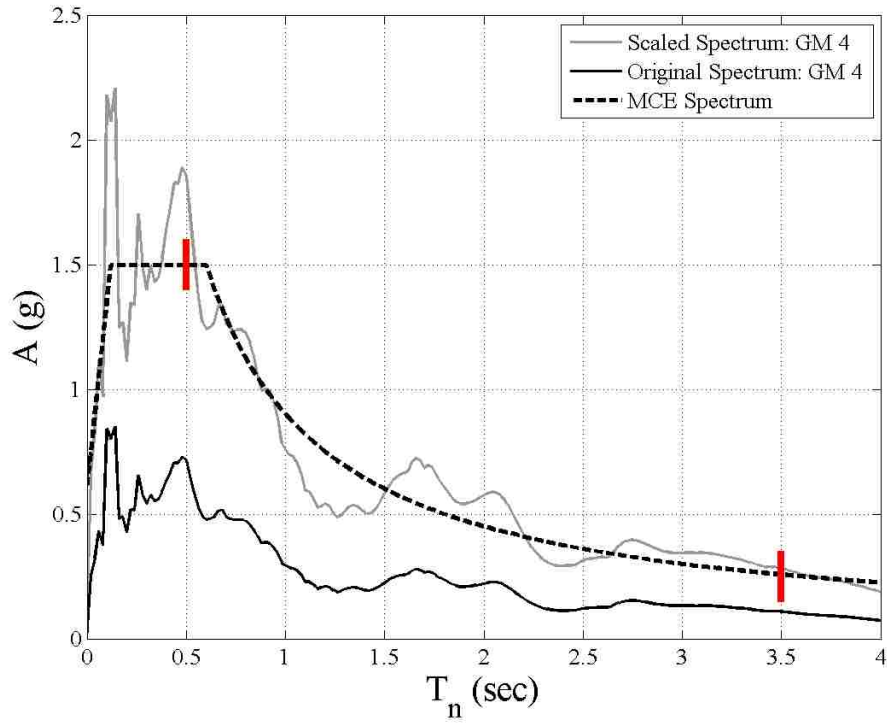


Figure 5.28 Example spectrum scaling

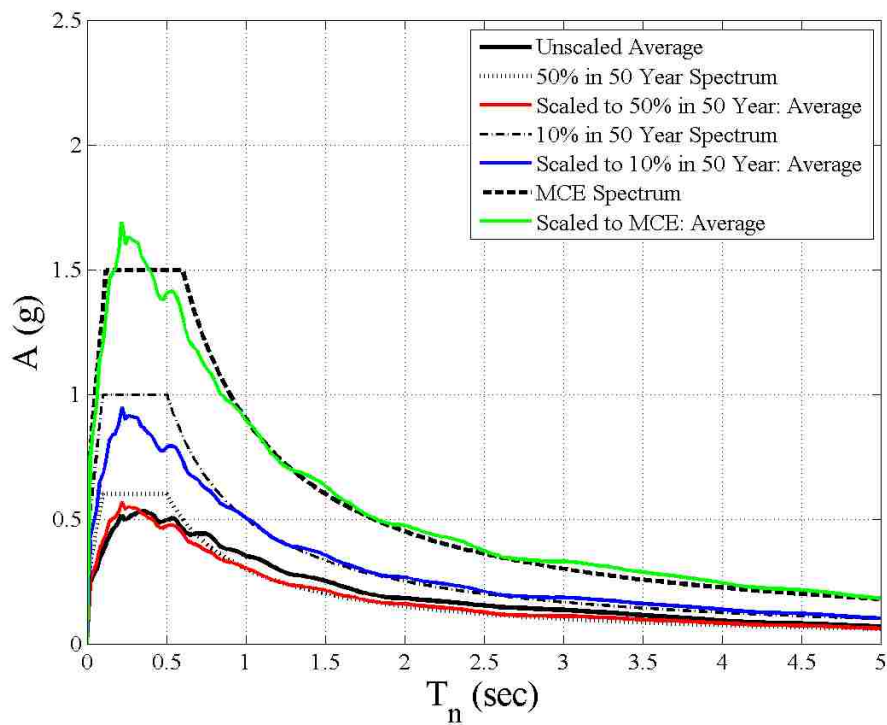


Figure 5.29 Set 1A average spectra

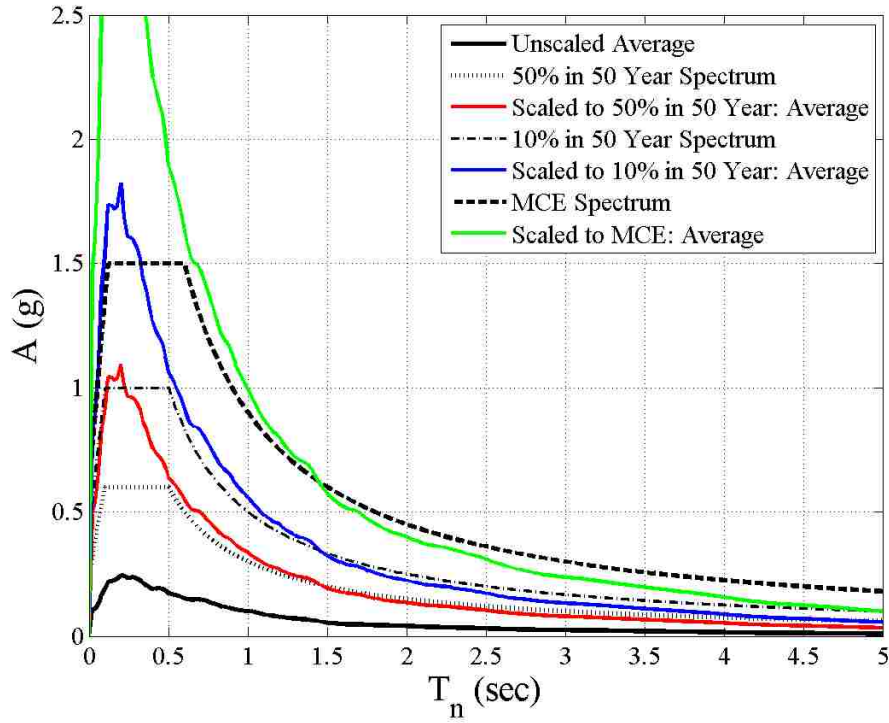


Figure 5.30 Set 1B average spectra

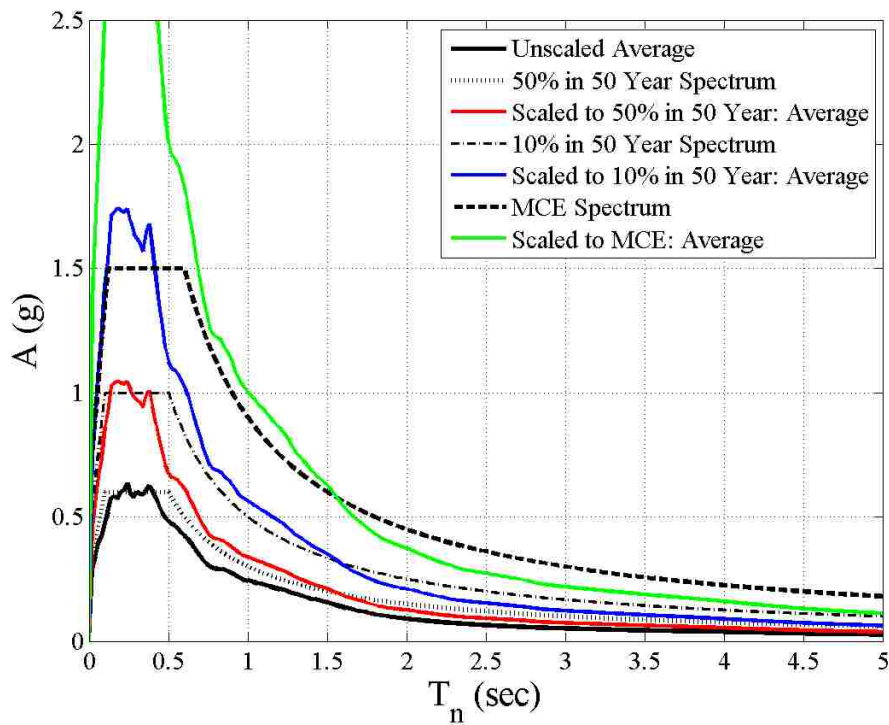


Figure 5.31 Set 2 average spectra

5.5.7 Foreshock-Aftershock Pair Explanation

To investigate the effects of damage on the performance of a damaged RC structure in a subsequent event, response under a foreshock and an aftershock must be simulated. The foreshock was used to cause the initial damage to the structure. The aftershock was used to determine what affect the damage caused by the foreshock had on the structural response.

Full frame nonlinear dynamic analyses take a significant amount of computational effort. One hundred randomly selected foreshocks and aftershocks were selected using MATLAB. The selected foreshocks were a different random set than the aftershocks. A table showing the 100 earthquakes selected for the foreshocks and aftershocks is included in Appendix E.

The foreshocks and aftershocks were scaled appropriately as described in the previous section. Table 5.10 identifies the full suite of foreshock-aftershock pairs used for the analyses on each frame (Table 5.1). This comprised 100 nonlinear time-history analyses for each of the un-shaded boxes in Table 5.10. Thus, 1200 total simulations were run for each frame. Moderate is in bold because a sample moderate foreshock-aftershock pair has been plotted in Figure 5.32.

Table 5.10 Full suite of foreshock-aftershock simulations

		Foreshock			
		None	Weak	Moderate	Severe
Aftershock	Weak	Weak	Weak	Weak	Weak
	Moderate	Moderate	Moderate	Moderate	Moderate
	Severe	Severe	Severe	Severe	Severe

Another issue that had to be accounted for was getting the frames to stop vibrating at the end of the foreshock. In a real world situation the structure will come to rest after an earthquake occurs. For the simulation purposes, it was easier to run the two ground motions in a back to back fashion. Twenty seconds of zero acceleration were added at the end of each record, allowing them to vibrate freely for that time. This ensured the structure was at rest when the second earthquake began. A plot of a moderate foreshock and moderate aftershock pair is shown in Figure 5.32. The full suite of pairs is plotted for the same two ground motions in Appendix E for comparison purposes.

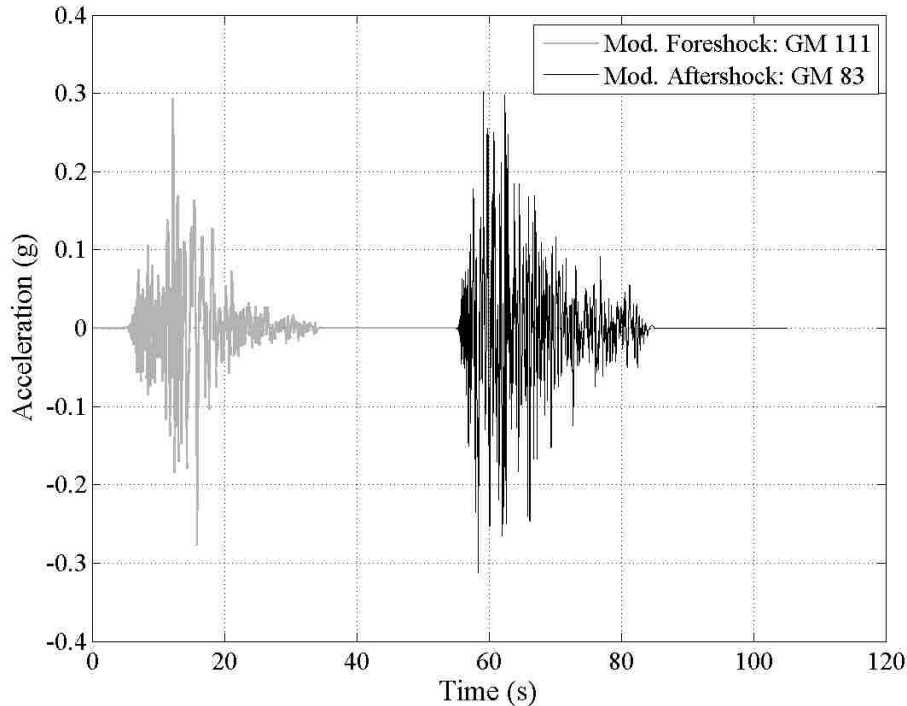


Figure 5.32 Foreshock-Aftershock ground motion pair

5.5.8 Dynamic Results

The results of the dynamic simulations were used to identify the probability of damage and collapse in an aftershock based on the damage occurring during a foreshock. To describe the effect of foreshocks on structures, nonlinear time-history simulations were performed for each frame. The story drift of each column was recorded during the nonlinear time-history simulations, so the damage state could be predicted; the data were then processed to determine the maximum drift experienced by a column in the foreshock. These data were used to determine the original damage state. The original damage state information was stored and used to categorize the aftershock results. The aftershock results consider both the scaling of the ground motion and the original damage state (i.e. post foreshock damage state).

A plot of the roof drift versus time is shown in Figure 5.33. This response corresponds to the roof drift for SMF4-1.2-00 being excited by the ground motion shown in Figure 5.32. The full suite of roof drift responses is plotted for the same two ground motions in Appendix G for comparison purposes.

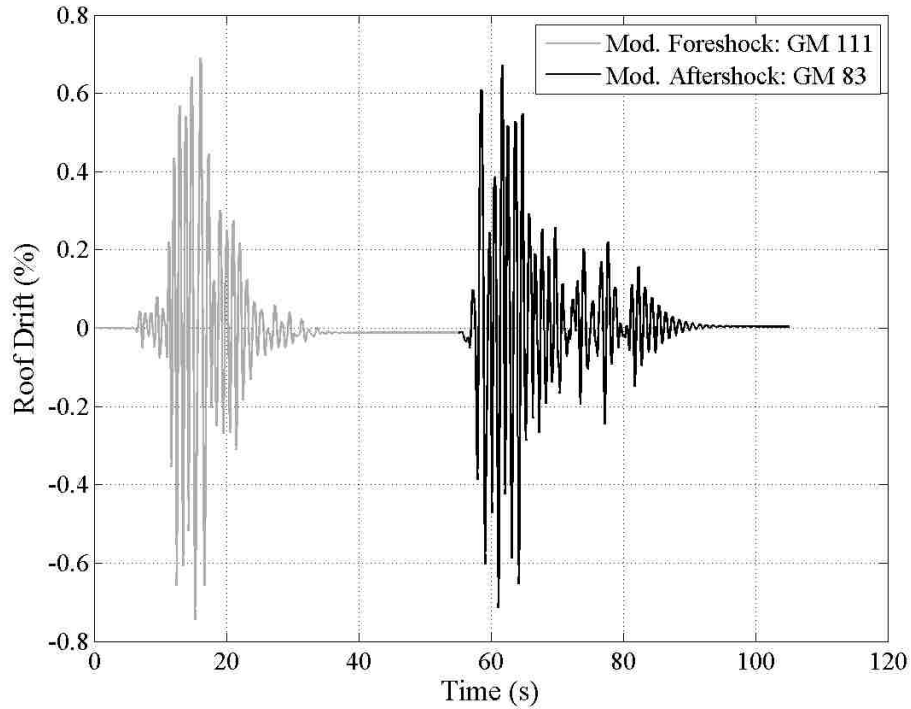


Figure 5.33 Roof drift response for SMF4-1.2-00 when excited by moderate GM 111 and GM 83

Figure 5.34 shows the second floor column drifts of SMF4-1.2-00 when the foreshock in Figure 5.32 was used to excite the structure. Only the second floor column responses have been plotted here due to the repetitive nature of these plots. The circles indicate the maximum drifts. The largest of the sixteen column drifts in the four-story frames was used to identify the damage state for the foreshock damaged frame.

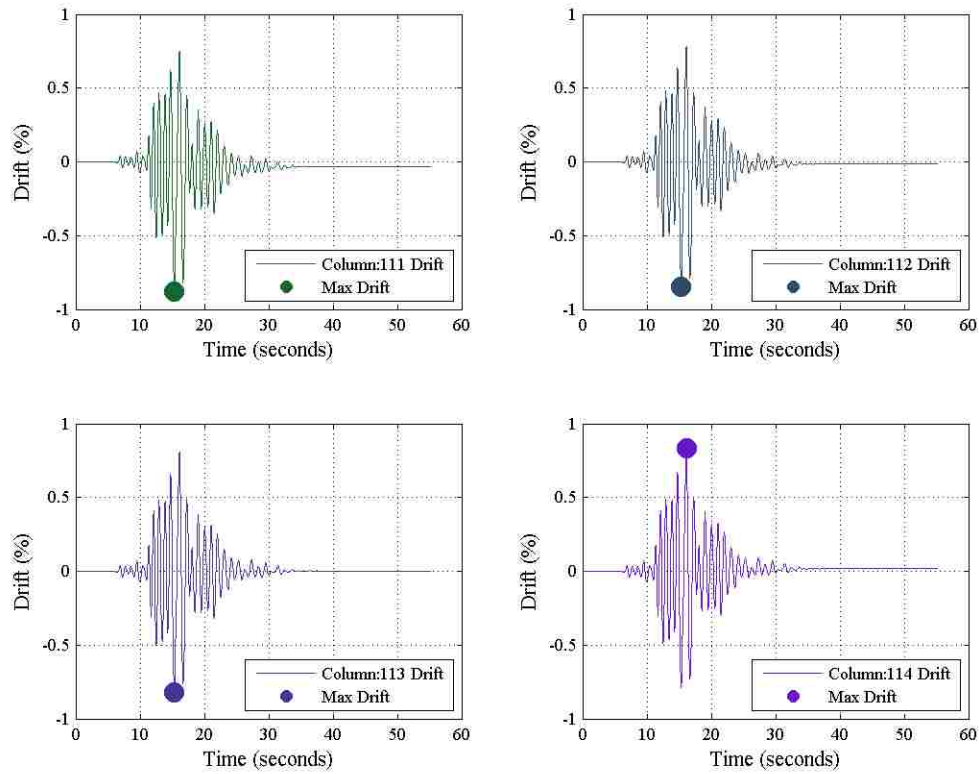


Figure 5.34 Second floor column drift responses for foreshock

Figure 5.35 shows the foreshock-aftershock response of the second floor columns of SMF4-1.2-00. The circles indicate the maximum drifts. The largest of the sixteen column drifts in the four-story frames was used to identify the damage state for the aftershock damaged frame.

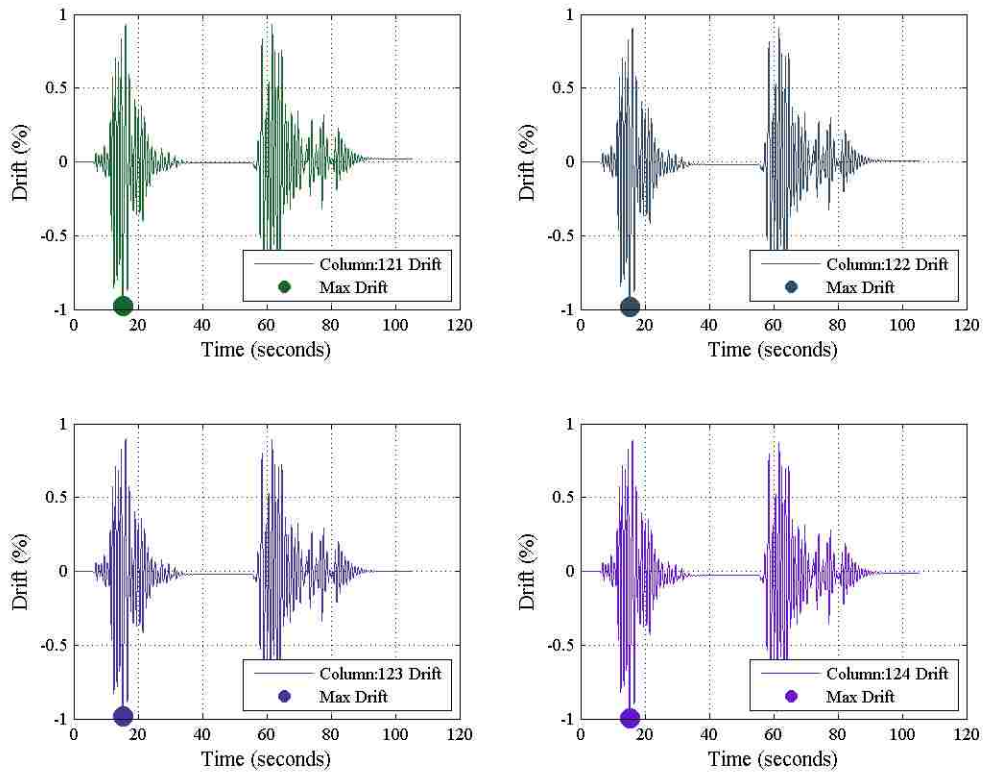


Figure 5.35 Second floor column drift responses for foreshock-aftershock pair

The drifts used to determine onset of damage states for the SMFs are based on the work presented in Section 3.6 and come from Table 3.12. Six damage states were used for damage categorization in the frames when considering low axial load and can be seen in Table 5.11. There are two reasons for reducing the number of damage states from those presented in Chapter 3. First, initial cracking damage states, F1-F3, have been identified as cosmetic damage that does not affect structural integrity (Berry and Eberhard 2003). Thus, the initial cracking damage states were combined into DS1 for damage state identification following frame analysis. Second, for the final damage states, observed damage (e.g. F6 longitudinal bar buckling, F7 crushing of core concrete, and F8 Longitudinal Bar Fracture) are linked with unobservable damage states (e.g. F9 Loss of Lateral Load-Carrying Capacity and F10 Loss of Axial Load-Carrying Capacity). Thus, DS4 was established as one damage state for F6, F7, and F9 as the experimental data indicate that loss of lateral load-carrying capacity is due to bar buckling and core crushing. Similarly, DS5 was established as one damage state for F8 and F10 as the experimental data indicate that loss of axial load-carrying capacity is imminent once longitudinal bar fracture has occurred.

Table 5.11 Reduced set of damage states for use in building analysis: flexure-critical columns with low axial loads

Damage State		Drift
DS0	No Damage	< 0.3
DS1	Cracking	0.3 - 1.5
DS2	Onset of Spalling	1.5 - 2.0
DS3	Spalling Exposing Steel	2.0 - 4.0
DS4	Bar Buckling/Core Crushing/Lateral Failure	4.0 - 6.0
DS5	Bar Fracture/Axial Failure/Potential Collapse	> 6.0

Five damage states were used for damage categorization in the frames when considering high axial load and can be seen in Table 5.12. The F4 damage state, onset of spalling, was included in DS1 as the data for flexure-critical columns with high axial loads indicated that this damage state occurs at the same drift demand as the cracking damage states. The same reasoning was used to establish DS3 and DS4 for the high axial loads as was used for low axial loads.

Table 5.12 Reduced set of damage states for use in building analysis: flexure-critical columns with high axial loads

Damage State		Drift
DS0	No Damage	< 0.5
DS1	Cracking and Onset of Spalling	0.5 - 1.0
DS2	Spalling Exposing Steel	1.0 - 2.0
DS3	Bar Buckling/Core Crushing/Lateral Failure	2.0 - 3.5
DS4	Bar Fracture/Axial Failure/Potential Collapse	> 3.5

The drifts used to determine onset of damage states for the OMFs are based on the work presented in Section 3.6 and come from Table 3.15. Six damage states were used for damage categorization in the frames when considering low axial load and can be seen in Table 5.13. The number of damage states was reduced because many of the severe damage states occur at the same drift level. This is indicative of and reflects the fact that shear failure is a non-ductile phenomenon. Thus, the observable severe damage states of localized longitudinal cracking (S3.1), concrete spalling (S3.2), bar buckling (S3.3), and core crushing (S3.4) were combined with the unobservable loss of lateral load-carrying capacity (S3.5) damage state.

Table 5.13 Reduced set of damage states for use in building analysis: shear-critical columns with low axial loads

Damage State		Drift
DS0	No Damage	< 0.25
DS1	Flexural Cracking	0.25 - 0.5
DS2	Shear Cracking	0.5 - 2.0
DS3	Shear Crack Widening	2.0 - 2.5
DS4	Spalling/Bar Buckling/Lateral Failure	2.5 - 4.5
DS5	Axial Failure/Potential Collapse	> 4.5

Four damage states were used for damage categorization in the frames when considering low axial load and can be seen in Table 5.14. The number of damage states was reduced because all of the severe damage states occur at the same drift level. The observable severe damage states of localized shear cracks (S3.0), localized longitudinal cracking (S3.1), concrete spalling (S3.2), bar buckling (S3.3), and core crushing (S3.4) were combined with the unobservable loss of lateral load-carrying capacity (S3.5) and loss of axial-load carrying capacity (S3.6) damage states.

Table 5.14 Reduced set of damage states for use in building analysis: shear-critical columns with high axial loads

Damage State		Drift
DS0	No Damage	< 0.25
DS1	Flexural Cracking	0.25 - 0.5
DS2	Shear Cracking	0.5 - 1.75
DS3	S3.0 - S3.4 Damage/Lateral Failure/ Axial Failure/Potential Collapse	> 1.75

Based on the nonlinear time-history results, the column axial loads remained at less than $0.4f_c A_g$. This was less than the previously high axial load limit of $0.5f_c A_g$. Thus, the low axial load damage state drifts in Table 5.11 and Table 5.13 were used to analyze the SMFs and OMFs.

Figure 5.36 through Figure 5.39 show the results of analyses of the reference 4-story frames, 4SMF-1.2-00 (Figure 5.36 and Figure 5.38) and 4OMF-1.2-00 (Figure 5.37 and Figure 5.39), subjected to 100 foreshock ground motions and 300 foreshock-aftershock pairs of ground motions. The top subplot of Figure 5.36 and Figure 5.37 shows the probability of a damage state occurring given the intensity of the foreshock, $P[DS|IM]$. Earthquake intensity is characterized as weak (50% probability of occurring in 50 years), moderate (10% probability of occurring in 50 years), and severe (2% probability of occurring in 50 years). The three subplots below show the probability that an aftershock of a specified intensity level (Weak, Moderate, Severe) will result in a damage state given the foreshock intensity level, $P[DS|FS_{intensity}]$. Note that because different ground motions were included in the set of foreshock motions

and set of aftershock motions, the probabilities in the top plot are slightly different than those for the “None” foreshock in the bottom three plots.

The results represented in both Figure 5.36 and Figure 5.37 show the same trend: an aftershock results in an increase in the damage state of the frame only if the intensity of the aftershock is equal to or greater than the intensity of the foreshock. This is observed by comparing the damage state probabilities for the b) Weak Aftershock subplot with the probabilities for the a) Foreshock subplot in Figure 5.36. In these subplots, the probabilities for each damage state for frames subjected to moderate or severe foreshocks are the same; thus, a weak aftershock has no effect on the damage state of a frame subjected to a moderate or severe aftershock. In these subplots, frames subjected to a weak-weak pair of motions show a slightly higher probability of being in a higher damage state and slightly lower probability of being in a lower damage state than do the frames subjected to just the weak foreshock. This results from frames that were in the DS0 after the weak foreshock reaching DS1 due to the weak aftershock. Similar trends are observed if the a) Foreshock and c) Moderate Aftershock or a) Foreshock and d) Severe Aftershock plots are compared. In considering the data in the d) Severe Aftershock subplot, it can be seen that the severity of the foreshock, and thus the severity of the damage due to the foreshock, does have some impact on the damage state resulting from a more severe aftershock. For any damage state in the d) Severe Aftershock subplots, probabilities for low damage states are higher for low intensity foreshocks and lower for high intensity foreshocks while for high damage states probabilities are lower for low intensity foreshocks and higher for high intensity foreshocks. Similar trends are observed for the data presented in the b) Weak Aftershock and c) Moderate Aftershock subplots.

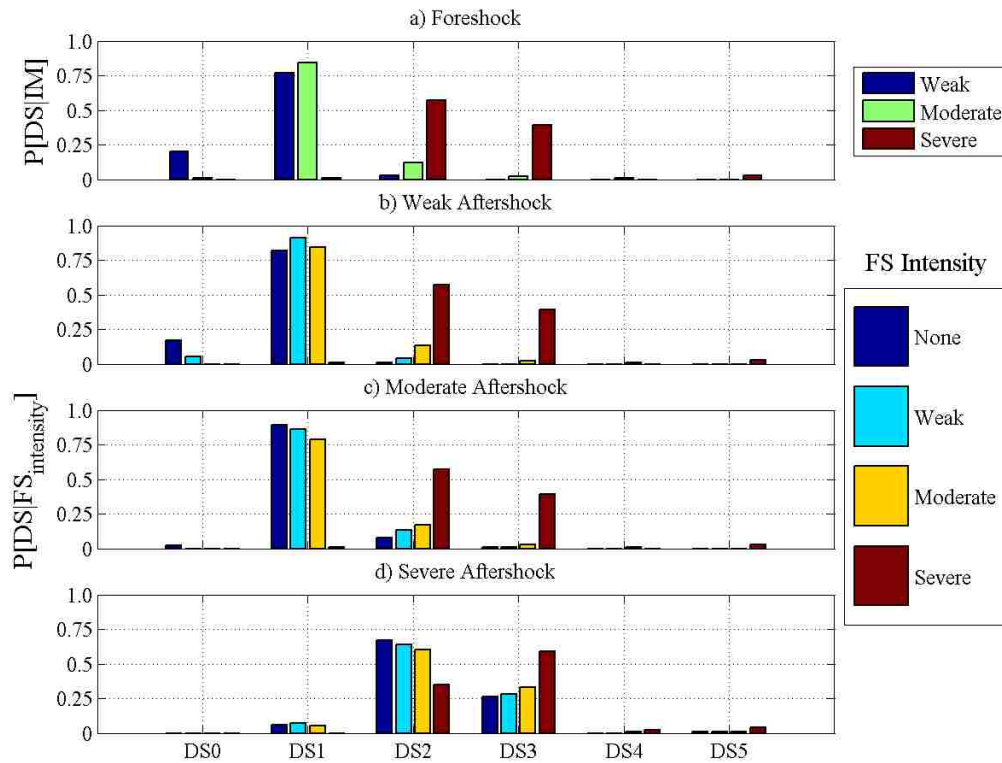


Figure 5.36 SMF4-1.2-00 probability of damage states given the foreshock intensity

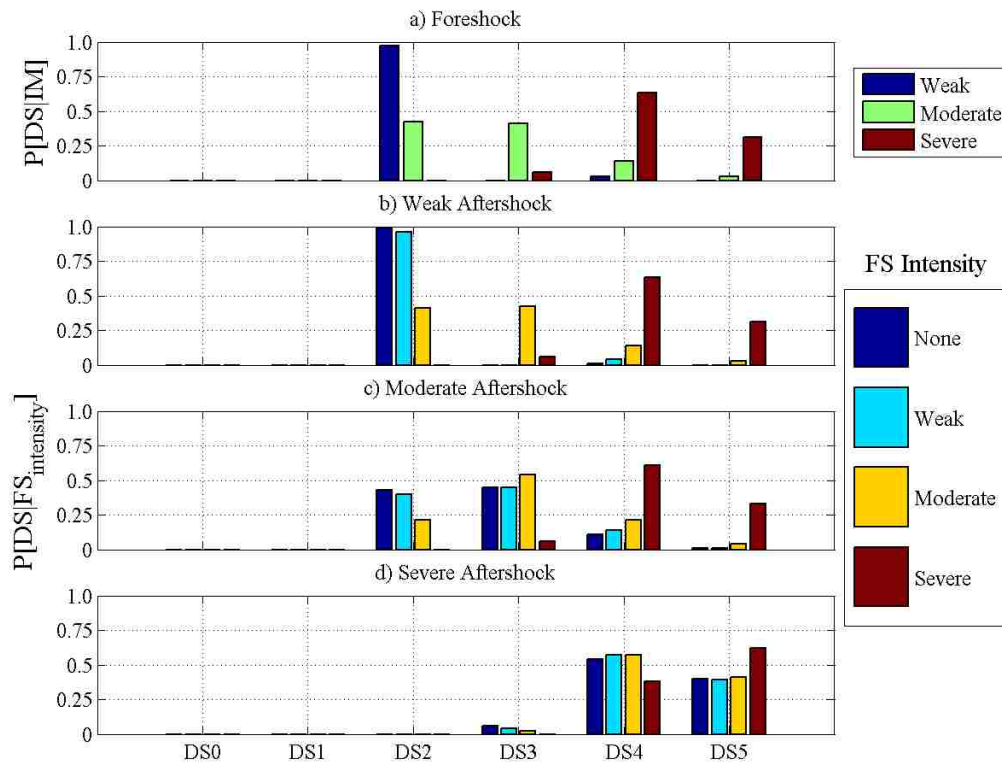


Figure 5.37 OMF4-1.2-00 probability of damage states given the foreshock intensity

Figure 5.38 and Figure 5.39 present the analysis data for the reference frames in a different way. These figures again show probability of a damage state given the intensity of the foreshock in subplot a) Foreshock. However, in Figure 5.38 and Figure 5.39, subplots b) Weak Aftershock, c) Moderate Aftershock, and d) Severe Aftershock show the probability that an aftershock of a specified intensity will result in a damage state given the damage state of the frame after the foreshock and before the aftershock, $P[DS|FS_{DS}]$. Subplots b) Weak Aftershock through d) Severe Aftershock do not include data for a frame not subjected to a foreshock. The data in Figure 5.38 and Figure 5.39 show the same trend observed in Figure 5.36 and Figure 5.37: the final damage state of the structure is determined primarily by the maximum intensity event, foreshock or aftershock. The damage state of the frame following the foreshock and before the aftershock has a small impact on the final damage state, if the frame is subjected to an event of equal or greater severity. The damage state of the frame following the foreshock and before the aftershock is the final damage state if the frame is subjected to an aftershock less severe than the foreshock. The data in Figure 5.38 and Figure 5.39 support these conclusions. The data in Figure 5.38 show a 76%, 80%, and 1% chance that DS1 will be caused by the weak, moderate, and severe events, respectively. Thus, considering 300 models of the SMF4 reference frame, subjected to 300 foreshock motions, 175 of 300 frames were in DS1 following the foreshock. Considering these frames in Figure 5.38 b) Weak Aftershock, c) Moderate Aftershock, and d) Severe Aftershock shows how these 175 frames performed when subjected to different intensity aftershocks (DS1 data is represented using light blue). The data in subplot b) Weak Aftershock show that more than 99% of the frames in DS1 after the foreshock stay in DS1. Note that they are joined by 75% of the frames that were in DS0 after the foreshock. The data in subplot d) Severe Aftershock show that 90% of the frames in DS1 after the foreshock were in DS2-DS5 after the severe aftershocks. The high probability of exceeding the initial damage state was expected. The weak and moderate foreshocks resulted in frames in DS1, since the intensity of the severe aftershock exceeded these foreshock intensities, the frames accumulated additional damage. For the frames in DS1 following the foreshock, the damage state probabilities in subplot d) Severe Aftershock are almost the same as those for the severe foreshock in subplot a) Foreshock. Thus, the damage caused by the less severe foreshock had minimal impact on the damage resulting from the more severe aftershock.

The results for SMF4-1.2-00 and OMF4-1.2-00 are representative of all frames. The damage state after the foreshock has limited impact on the damage state after the foreshock-aftershock pair. If the initial damage state is less than or equal to the minimum that which would develop if the frame were subjected only to the aftershock, then the final damage state is as if there was no foreshock. If the initial damage state is greater than that which would develop if the frame were subjected only to the aftershock,

then the damage state will not increase. There is only an increase in the damage state if the intensity of the aftershock meets or exceeds the intensity of the foreshock.

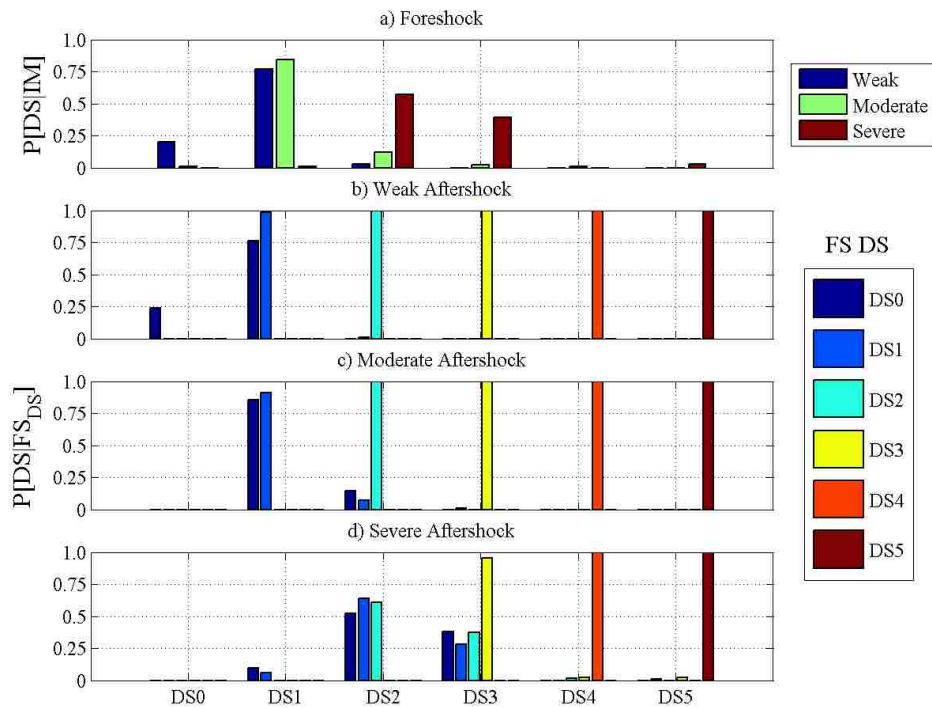


Figure 5.38 SMF4-1.2-00 probability of damage states give the foreshock damage state

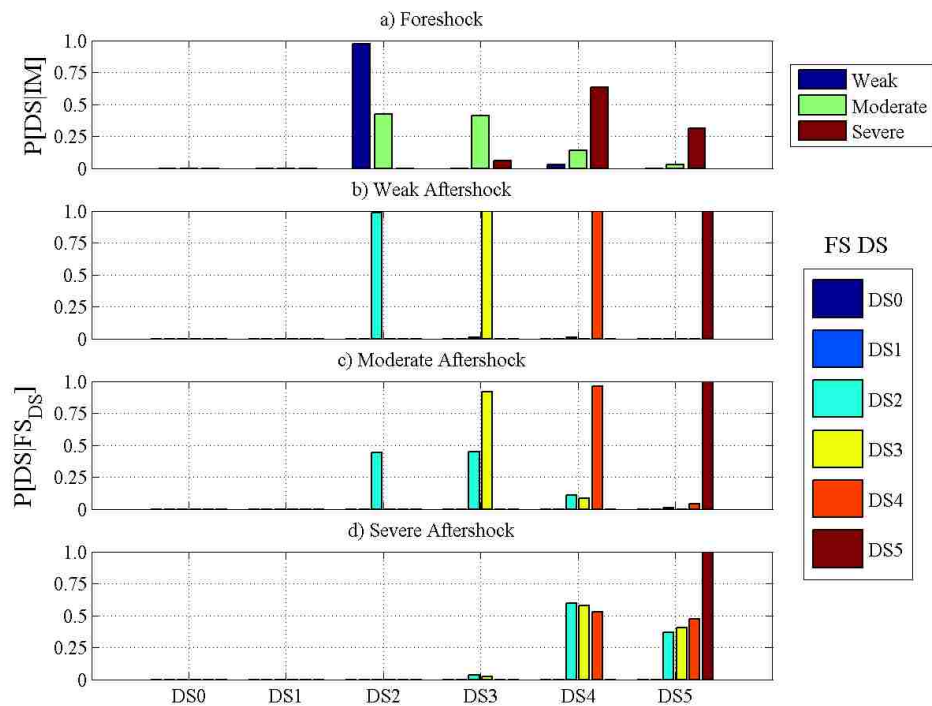


Figure 5.39 OMF4-1.2-00 probability of damage states given the foreshock damage state

The impact of the design parameters (i.e. building height, SCWB ratio, and weak-story) and modeling variability (i.e. joint flexibility, joint failure, and shear failure) on performance is shown by the data in Figure 5.40 through Figure 5.49, which compare the results for the reference frames with those for frames with different design or modeling characteristics. In Figure 5.40 through Figure 5.49, results for the reference frame are presented in subplot a) while those for a frame or frame model that differs from the reference frame are presented in subplot b). Plots of the probability of a given damage state given the foreshock damage state are used for the comparisons. The following bulleted list presents the key findings from Figure 5.40 through Figure 5.49.

- The data in Figure 5.40 show that for SMFs, simulating joint flexibility has no impact on performance during a foreshock or aftershock.
- The data in Figure 5.41 show that for SMFs, as the height of the structure is increased to 12 stories, the frame responds in the same way during the weak and moderate foreshocks and has less damage when subjected to the severe events. The reduction in damage under severe loading is attributed to the period increase in the 12-story frames. The aftershocks do not change the response of a SMF as the height of the structure is increased.
- The data in Figure 5.42 show that for SMFs, the introduction of a weak-story has no effect on the outcome of the response of the SMFs. This is attributed to the two frames having the same one-story mechanism identified during the pushover analysis.
- The data in Figure 5.43 show that in comparison with SMFs, OMFs develop more severe damage due to foreshock and foreshock-aftershock loading.
- The data in Figure 5.44 show that for OMFs, failure of beam-column joints has no impact on performance for weak or severe events but results in slightly more damage for moderate events. This is true for foreshocks and aftershocks.
- The data in Figure 5.45 show for OMFs, the simulation of both beam-column joint failure and column shear failure increases the severity of damage for foreshock and aftershock hazard levels.
- The data in Figure 5.46 and Figure 5.47 show for OMFs, reducing the ratio of column to beam flexural strength increases damage, while increasing the ratio of column to beam flexural strength reduces damage for both the foreshock and aftershock response.
- The data in Figure 5.48 show for OMFs, frame height affects the level of damage when the frames are subjected to moderate and severe events. The 12-story OMF exhibited less damage than the 4-story OMF.

- The data in Figure 5.49 show for OMFs, the introduction of a weak-story produced less damage during the weak and severe foreshocks and aftershocks.

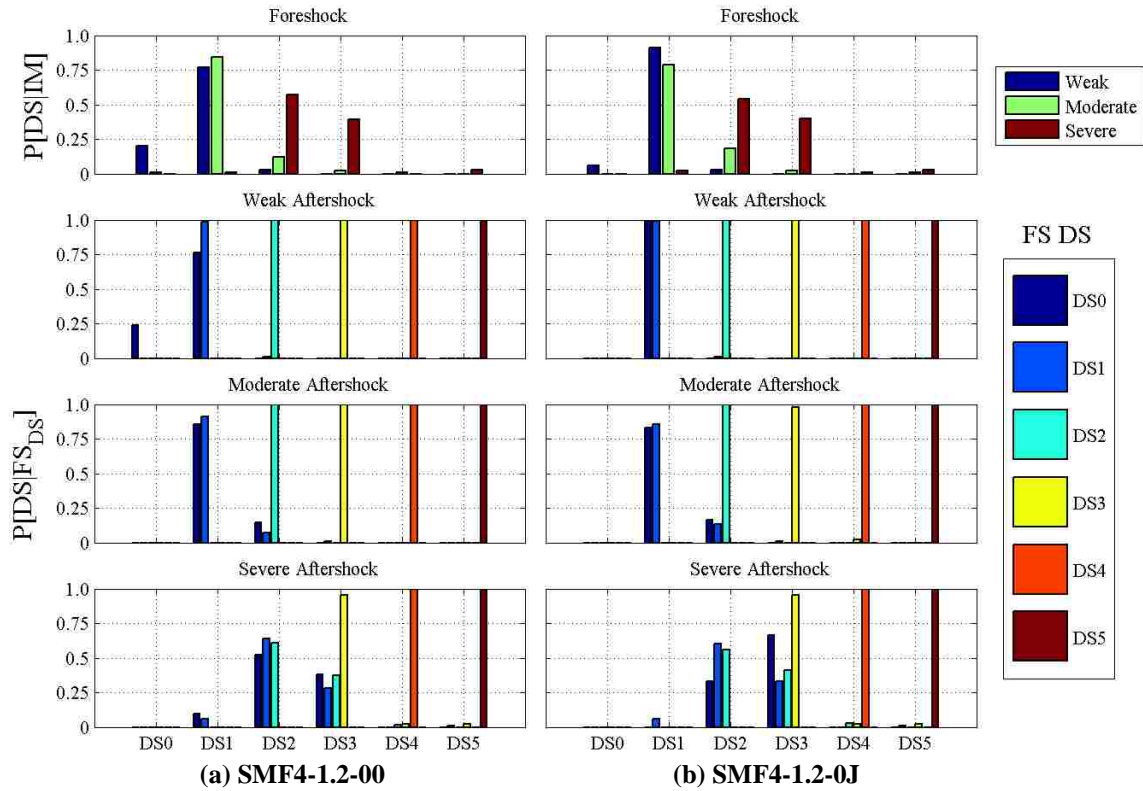


Figure 5.40 Comparison of results for (a) SMF4-1.2-00 and (b) SMF4-1.2-0J

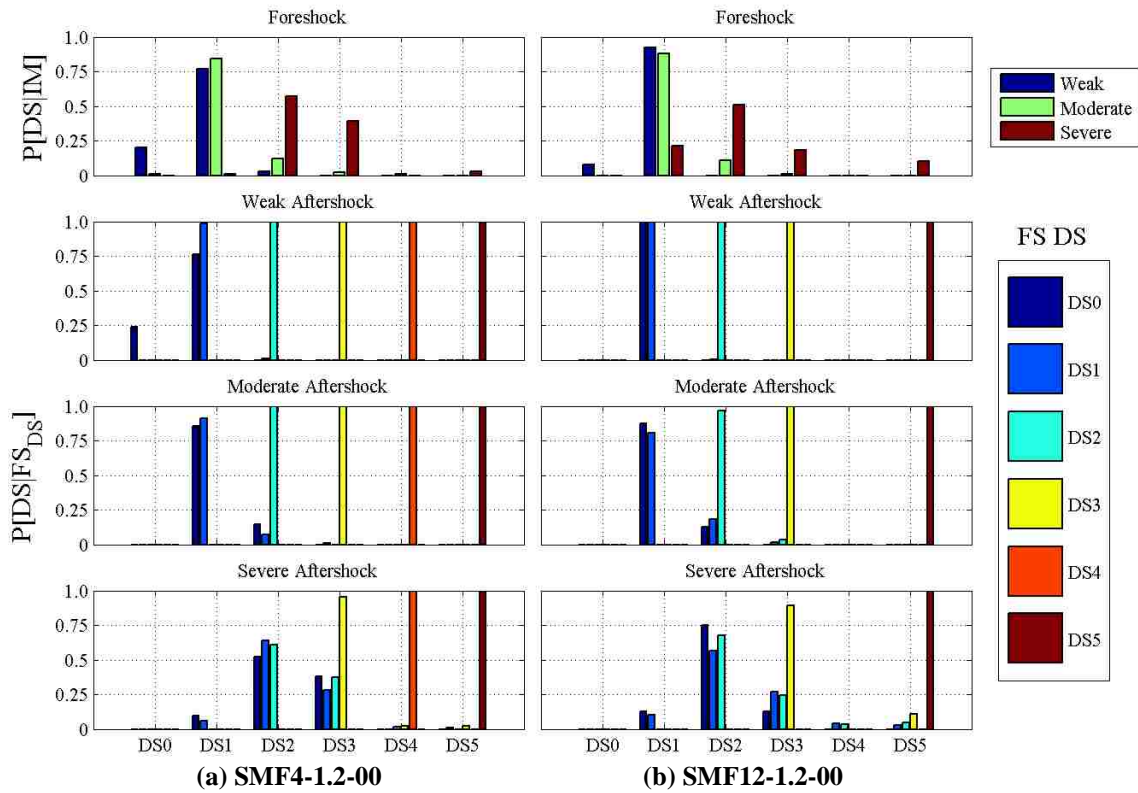


Figure 5.41 Comparison of results for (a) SMF4-1.2-00 and (b) SMF12-1.2-00

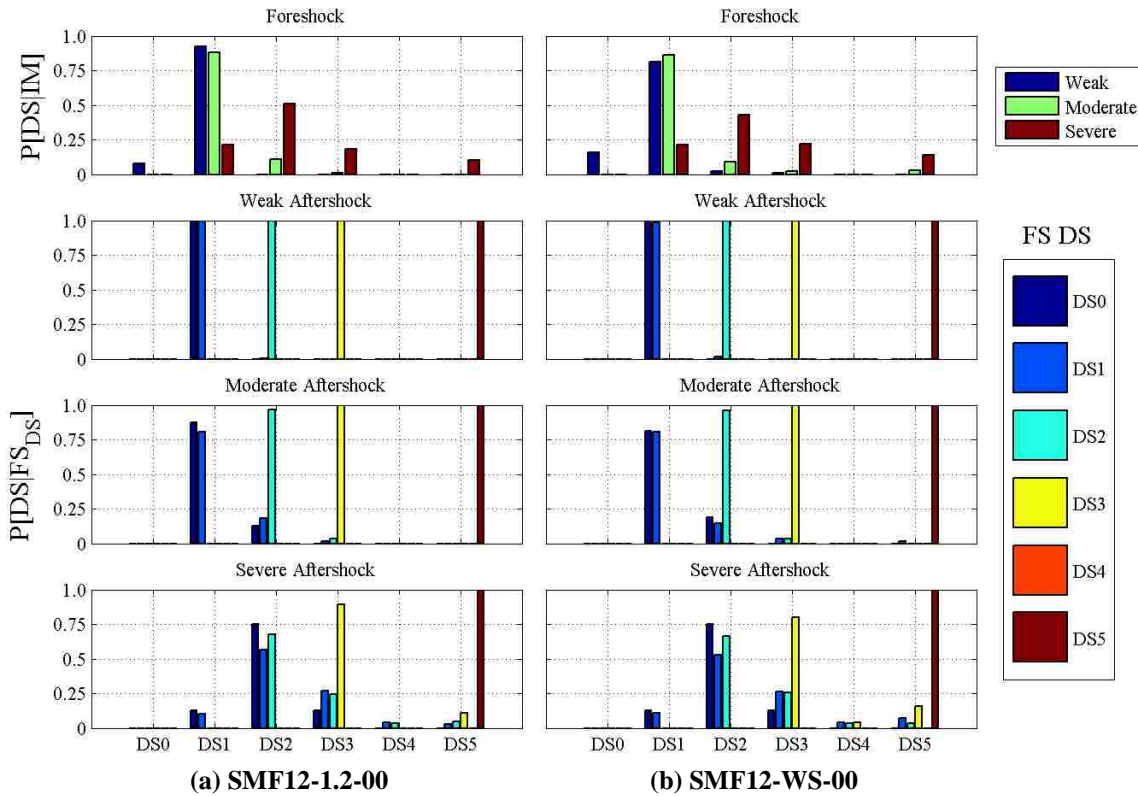


Figure 5.42 Comparison of results for (a) SMF12-1.2-00 and (b) SMF12-WS-00

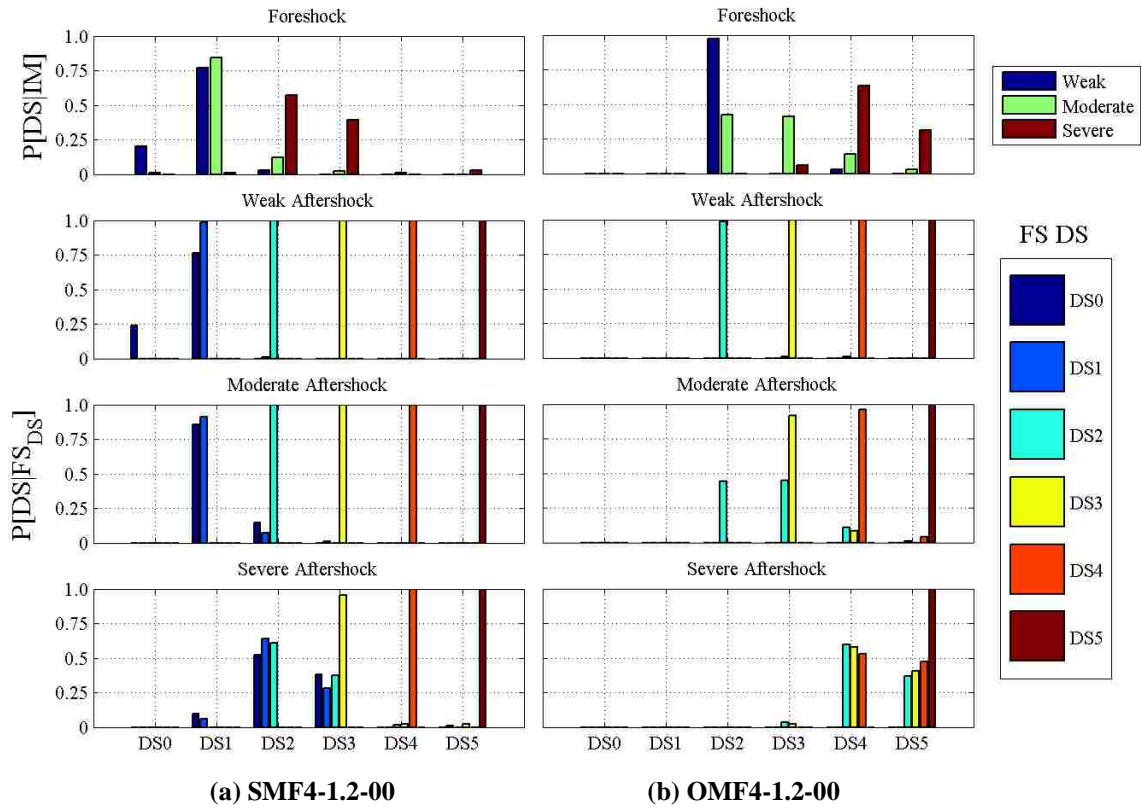


Figure 5.43 Comparison of results for (a) SMF4-1.2-00 and (b) OMF4-1.2-00

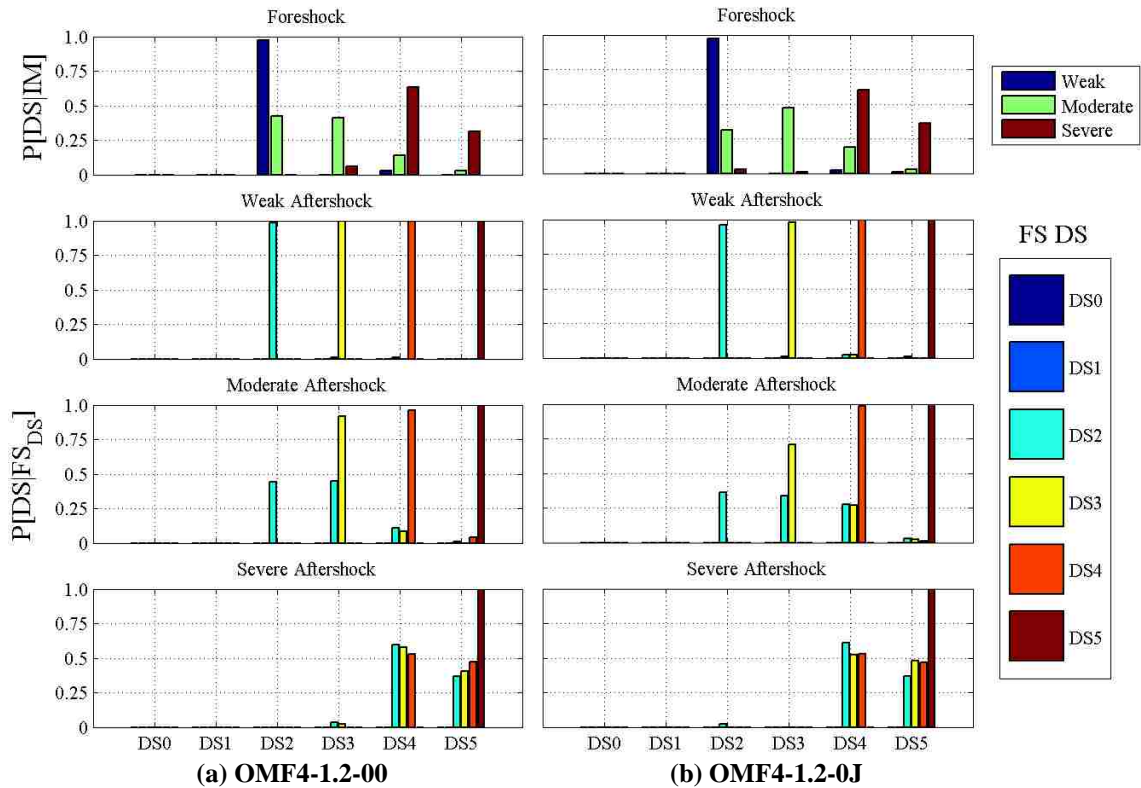


Figure 5.44 Comparison of results for (a) OMF4-1.2-00 and (b) OMF4-1.2-0J

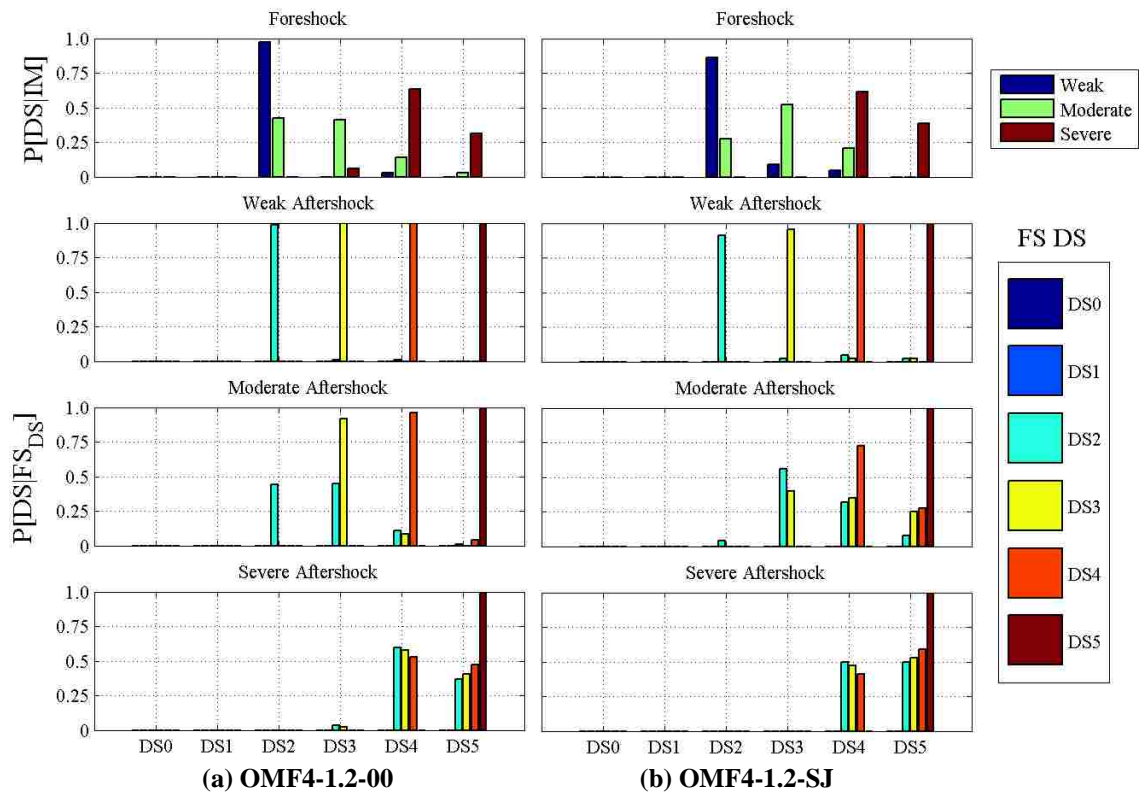


Figure 5.45 Comparison of results for (a) OMF4-1.2-00 and (b) OMF4-1.2-SJ

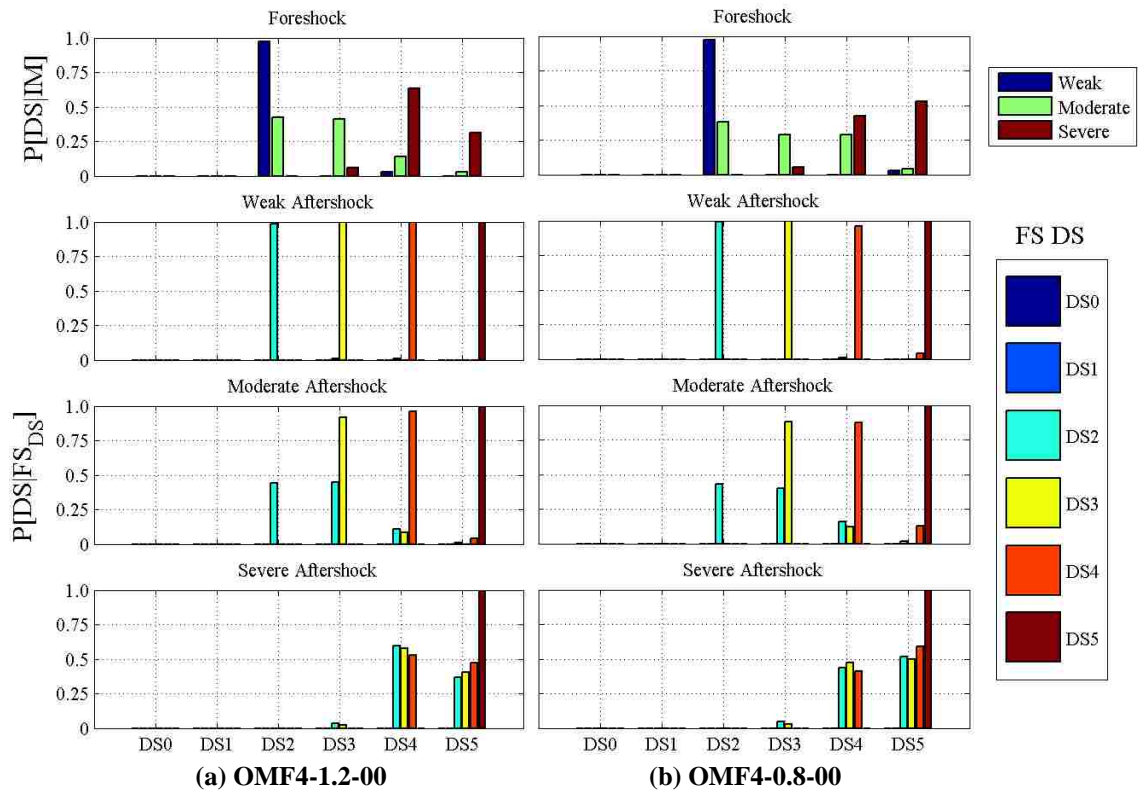


Figure 5.46 Comparison of results for (a) OMF4-1.2-00 and (b) OMF4-0.8-00

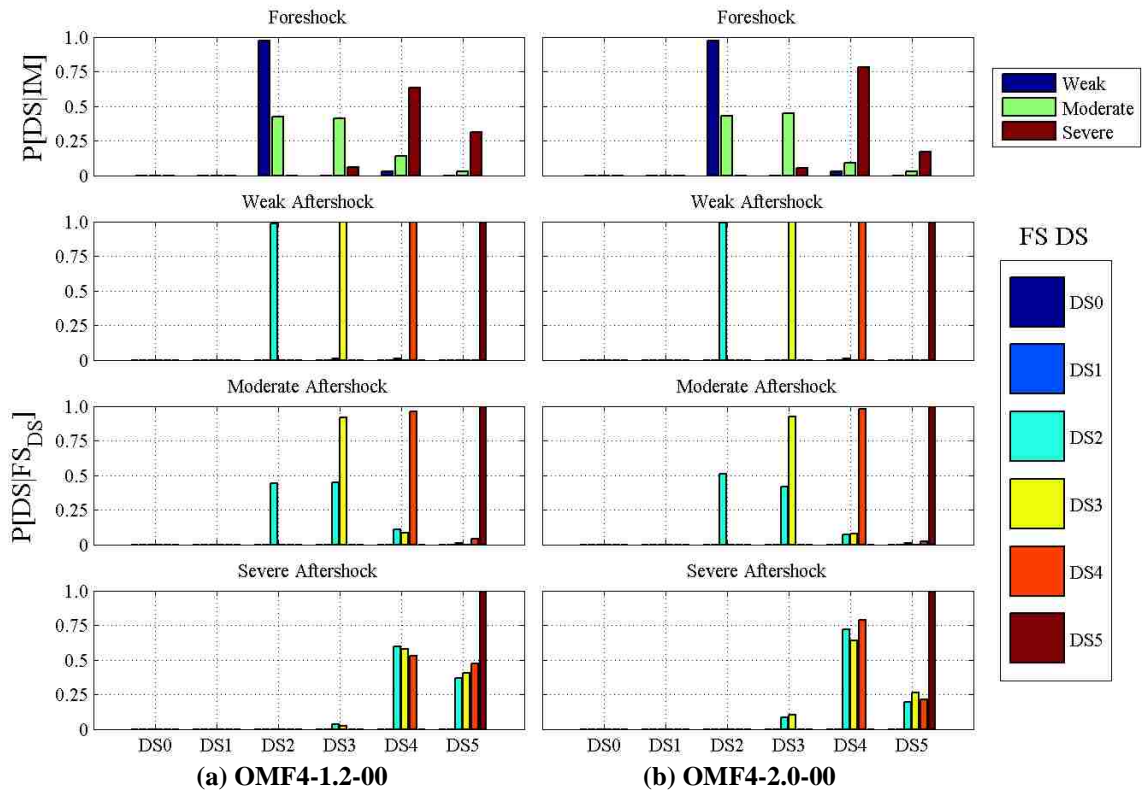


Figure 5.47 Comparison of results for (a) OMF4-1.2-00 and (b) OMF4-2.0-00

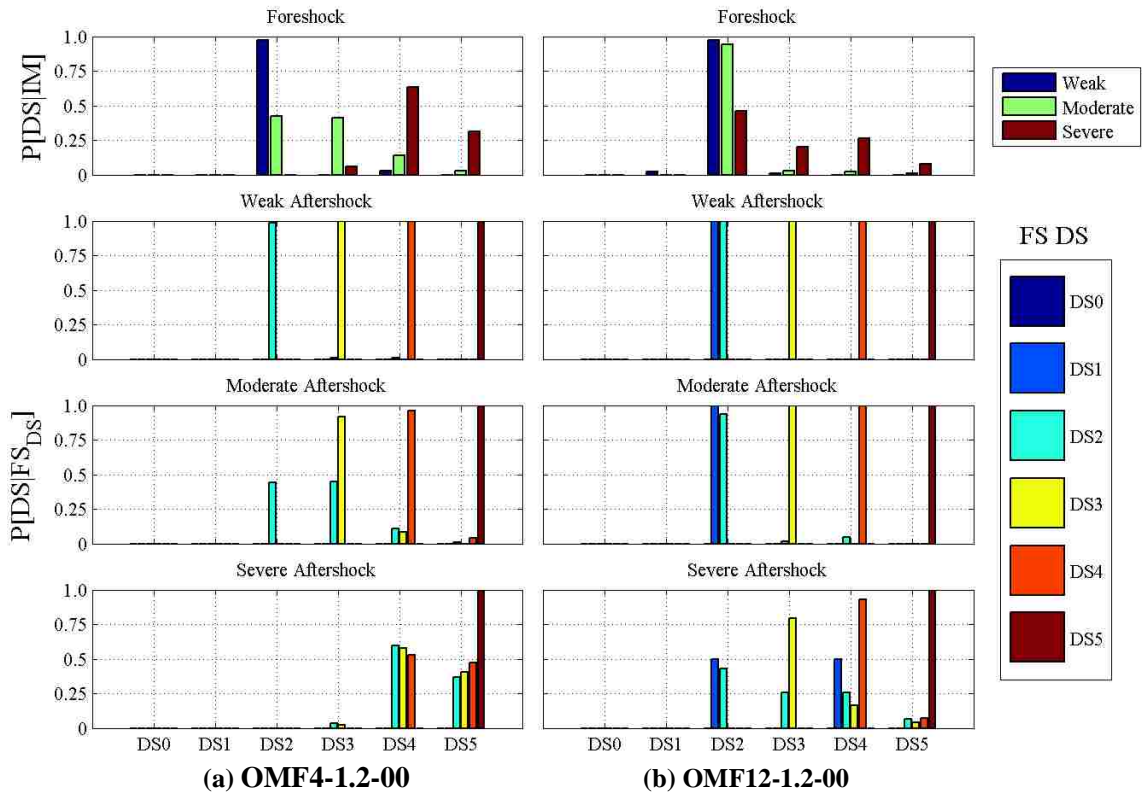


Figure 5.48 Comparison of results for (a) OMF4-1.2-00 and (b) OMF12-1.2-00

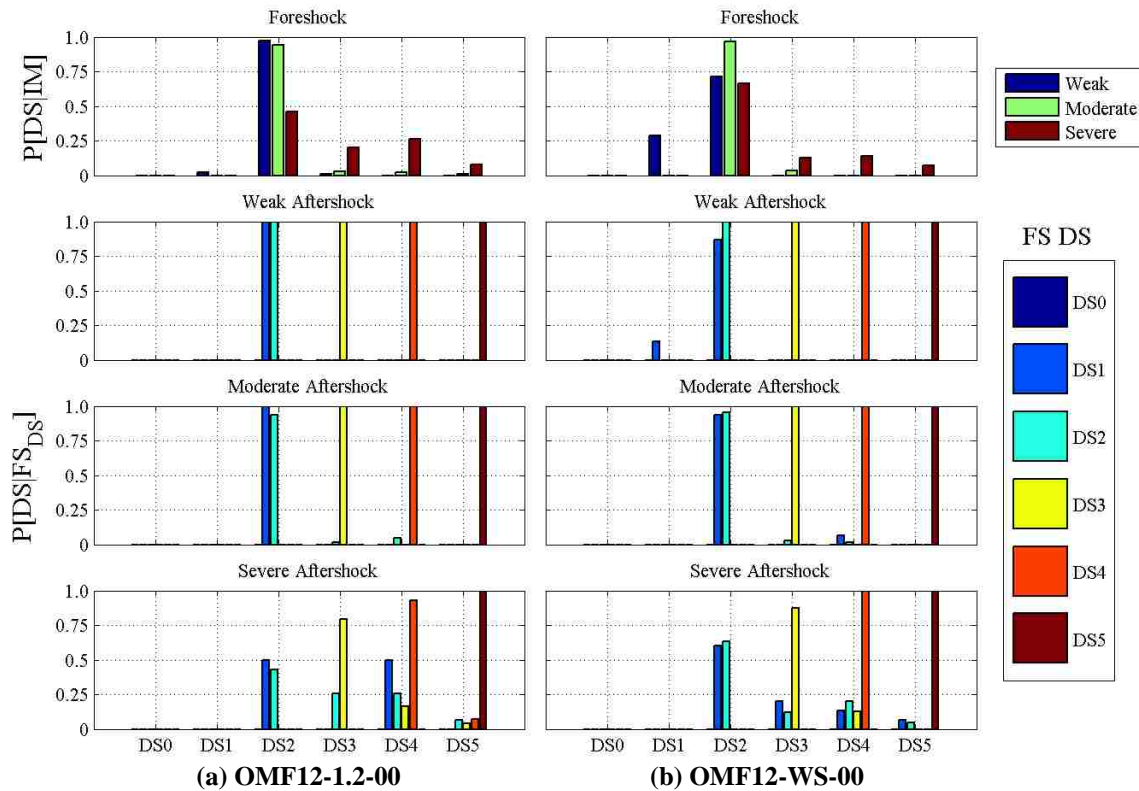


Figure 5.49 Comparison of results for (a) OMF12-1.2-00 and (b) OMF12-WS-00

5.6 Summary

As part of the UW-GA Tech Project, nonlinear analysis was used to assess the potential for a set of RC frame structures, damaged due to a foreshock, to sustain further damage, including collapse, under subsequent earthquake loading. The set of RC frame structures selected for this work included 4-story and 12-story SMF and OMF frames of variable design; frame performance was assessed using nonlinear pushover and dynamic time-history analysis, and the impact of modeling variability was considered. The results of pushover simulations were used to identify failure mechanisms for the set of frames. The results of time-history analyses were used to investigate the potential for a structure damaged during an initial earthquake to be more severely damaged during a subsequent event. Earthquake records were scaled to three intensity levels and randomly combined to subject the set of frames to foreshock–aftershock pairs. Story drift levels were used to determine the damage state of the structure after the foreshock and again after the aftershock. Results of these analyses are presented and indicate general trends in the behavior of RC frame structures.

The results of pushover analyses support the following conclusions:

- The joint modeling techniques used for the SMFs had minimal impact on response.

- Introducing a weak-story will have no impact on a frame if the frame already has a one-story failure mechanism where the weak-story has been included.
- For OMFs, simulating joint failure changed the failure mechanism from a one-story to a multiple-story mechanism for both the four-story and twelve-story frames.

The results of simulations in which RC frames were subjected to foreshock-aftershock pairs of ground motions support the following conclusions:

- The damage state resulting from the foreshock has an insignificant impact on the damage state resulting from the foreshock-aftershock pair for all the frames analyzed.
- The final damage state is dependent on the greater of the two intensity levels of the foreshock-aftershock pair. Frames only exhibited an increase in damage if the intensity of the aftershock equaled or exceeded the intensity of the foreshock.
- All SMFs behaved similarly with regard to level of damage observed during both foreshock and aftershock.
- The OMF design parameters and modeling variability effected the level of damage seen for foreshock and aftershocks.

Chapter 6: Summary and Conclusions

6.1 Summary

The research presented here contributes to a multi-investigator collaborative NSF funded research project to develop a semi-automated post-earthquake evaluation of RC frame buildings. Under the proposed framework, the visible damage (cracks, spalling, etc.) developed in columns of an RC frame subjected to earthquake loading is observed using video cameras and identified, characterized, and quantified using automated image processing techniques. The damage data are used to establish the performance state, including the response mechanism and expected failure mechanism. The performance states of the building columns are aggregated to establish the performance state and expected failure mechanism of the building. The post-earthquake damage state of the building is used to query pre-defined fragility curves that define the likelihood an RC frame will exhibit a particular damage state if subjected to an earthquake of a given intensity. In combination with the earthquake hazard at the site, this can be used to quantify the collapse risk posed by the structure.

The objectives of the work presented here were to i) characterize damage progression for RC columns exhibiting flexure and shear response modes and establish a series of discrete damage states that link damage states with drift demand, ii) develop a procedure for modeling the response of existing RC buildings subjected to earthquake loading to enable calculation of drift demands, from which column and building damage states can be established, iv) employ this modeling technique to determine the drift demands, and thus damage states, for existing RC frames subjected to a mainshock earthquake and a mainshock followed by an aftershock, and v) employ these modeling techniques to investigate the impact of design characteristics, response modes, and modeling decisions on earthquake performance.

Historical experimental investigations were reviewed to establish the progression of damage of RC columns under cyclic lateral loads. These data were used to define discrete damage states characterizing the extent of concrete and reinforcement damage in terms of cracking, spalling, buckling, fracture, and loss of lateral and axial load-carrying capacity and to link damage states with drift demand.

To ensure accurate simulation of frame response, component models were validated by comparing simulated and observed response for components and subassemblies tested in the laboratory. OpenSees simulations used a fiber model, shear strength model, and joint models per Birely (2012) and Anderson (2007) to account for the inelastic response of RC elements. Additionally, the proposed modeling approaches were used to simulate the response of a 1/3-scale multi-story, multi-bay frame subjected to dynamic loading.

To assess earthquake response of RC frames, analyses were carried out on four-story and twelve-story RC frames subjected to foreshock and foreshock-aftershock loading. The frame designs came from work performed at Stanford University by Haselton (2006) and Liel (2008). Both current design practices and pre-1976 design practices were considered. The different column and joint modeling approaches were paired in such a way that the effects of the different modeling approaches could be considered.

The foreshock-aftershock analysis procedure was accomplished by subjecting the modeled frames to a pair of ground motions. Each ground motion was scaled to three hazard levels (50% in 50 year event, 10% in 50 year event, and 2% in 50 year event) associated with the designed frames location. The simulated column drifts were used to determine the damage state after the foreshock and aftershock.

6.2 Conclusions

The results of this study support the following conclusions:

6.2.1 Column Damage Progression

Progression of damage for columns responding in flexure is well defined. Numerous lab tests of flexure-critical columns have been conducted and many of these tests included data linking damage with drift demand. Thus, it is possible to define a series of progressively severe damage states and define the drift at onset of these damage states with a relatively low level of uncertainty. Experimental testing of shear-critical columns is much more limited. It is still possible to define a series of damage states that characterize progressive damage; however, the level of uncertainty in the limited drift data makes it difficult to define drifts at the onset of these damage states.

An objective of the UW-GA Tech Project is to use image data to determine the likelihood that columns and the structure will reach a specific performance state in an aftershock. The likelihood of severe damage and collapse is highly dependent on the column response mode: flexure or shear. This is troublesome because the initial damage states for columns responding in flexure and shear are nearly identical.

6.2.2 Pushover Analysis

The results of the pushover analyses show that the joint modeling techniques used for the SMFs had minimal impact on response. Introducing a weak-story will have no impact on a frame if the frame already has a one-story failure mechanism.

The results for the pushover analyses show that joint modeling techniques and frame design characteristics do affect performance for OMF. Introducing the joint model changed the failure type from a one-story mechanism to a multi-story mechanism for both the four-story and twelve-story frames. This

introduced a limited amount of ductility into the system for the frame with the joint model. Reducing the strong column weak beam ratio to introduce weak columns reduced the strength and ductility of the frames. Increasing the strong column weak beam ratio increased the strength and ductility of the frame. Introducing a weak-story into the twelve-story frame caused the frame to respond in a more brittle manner because it moved the failure mechanism to the first story.

6.2.3 Foreshock-Aftershock Pair Analysis

Nonlinear dynamic analyses using foreshock-aftershock ground motion pairs provided data quantifying the probability an RC frame structure subjected to an earthquake would achieve a given performance state, including collapse, in the event of an aftershock. The damage caused by a foreshock has minimal impact on the final damage state of the RC frames when subjected to a weak (50% in 50 year event), moderate (10% in 50 year event), and severe (2% in 50 year event) aftershock. If the damage state following the foreshock is less than or equal to the damage state that would develop if the frame was subjected to aftershock, then the damage state before the aftershock has no impact on the damage state after the aftershock. If the damage state following the foreshock is greater than that which would develop if the frame was subjected to the aftershock, then the damage state will not increase after the aftershock. The aftershock will result in increased damage if the intensity of the aftershock is greater than or equal to the intensity of the foreshock. The relative intensity of the aftershock when compared to the foreshock controls the response of the frames modeled for this study.

Introducing nonlinear action to joints of a SMF did not change the performance of the four-story or twelve-story frames during aftershocks. The effect of introducing a weak-story in a SMF had no effect on the outcome of the analyses due to the failure mechanism identified during the pushover analysis.

For OMFs, varying modeling decisions and frame design characteristics did affect response of the four-story OMF. The development of a joint failure, shear failure, or reducing the ratio of column to beam flexural strength increased the probability of a more severe damage state occurring as a result of a foreshock and an aftershock. Increasing the strong column to weak beam ratio delays the progression of damage during a seismic event. The predicted damage states after an aftershock for the twelve-story OMF were only affected by the addition of joint failure and shear failure. The addition of a weak-story and adjusting the ratio of column to beam flexural strength had no effect on the outcome of the twelve-story OMF.

6.3 Recommendations for Future Research

The objectives of the research presented here were to investigate the damage progression observed during earthquake excitation of reinforced concrete columns and to accurately model the response of frames during dynamic analysis under pairs of earthquake ground motions. With respect to the assessment of post-earthquake vulnerability, the following research areas could be pursued to expand on the results of this research.

1. Create fragilities for earthquake damaged structures using incremental dynamic analysis. This would provide data for a wide range of ground motion intensity levels.
2. Investigate the effect of using cyclic pushovers to simulate damage from mainshocks to reduce the computational intensity of the analyses.
3. Consider performance and collapse potential due to factors other than column damage. Damage is unlikely to be solely concentrated in columns during earthquake excitation of RC frames.
4. Consider the 3D response of more complex RC buildings. The current research effort did not account for bidirectional loading or torsional effects. Other considerations for future work are modeling the soil-structure interaction and nonstructural elements that provide additional strength and stiffness.

List of References

- ACI-318-02. *Building Code Requirements for Structural Concrete and Commentary*. Farmington Hills, Michigan: American Concrete Institute, 2002.
- ACI-318-05. *Building Code Requirements for Structural Concrete and Commentary*. Farmington Hills, Michigan: American Concrete Institute, 2005.
- ACI-318-08. *Building Code Requirements for Structural Concrete and Commentary*. Farmington Hills, Michigan: American Concrete Institute, 2008.
- ACI-318-89. *Building Code Requirements for Structural Concrete and Commentary*. Farmington Hills, Michigan: American Concrete Institute, 1989.
- ACI-318-95. *Building Code Requirements for Structural Concrete and Commentary*. Farmington Hills, Michigan: American Concrete Institute, 1995.
- Alath, S., and S. K. Kunnath. "Modeling Inelastic Shear Deformation in Reinforced Concrete Beam-Column Joints." *Engineering Mechanics: Proceedings of 10th Conference*. Boulder, CO: American Society of Civil Engineers, 1995. 822-825.
- Alire, D. *Seismic Evaluation of Existing Unconfined Reinforced Concrete Beam-Column Joints*. Masters Thesis, Seattle, WA: University of Washington: Department of Civil and Environmental Engineering, 2002.
- Altoontash, A. *Simulation and Damage Models for Performance Assessment of Reinforced Concrete Beam-Column Joints*. PhD Thesis, Paolo Alto, CA: Stanford University, 2004.
- Anderson, J. C., and W. H. Townsend. "Models for Reinforced Concrete Frames with Degrading Stiffness." *Journal of the Structural Division*, 1977: 1433-1449.
- Anderson, M. *Analytical Modeling of Existing Reinforced Concrete Beam-Column Joints*. Masters Thesis, Seattle, WA: University of Washington: Department of Civil and Environmental Engineering, 2003.
- Anderson, M., D. Lehman, and J. Stanton. "A Cyclic Shear Stress-Strain Model for Joints Without Transverse Reinforcement." *Engineering Structures*, 2007: 941-954.
- ASCE-02. *ASCE 7-02: Minimum Design Loads for Buildings and Other Structures*. Reston, VA: American Society of Civil Engineers, 2002.
- ASCE-05. *ASCE 7-05: Minimum Design Loads for Buildings and Other Structures*. Reston, VA: American Society of Civil Engineers, 2005.
- ASCE-41-06. *Seismic Rehabilitation of Existing Buildings*. Reston, VA: American Society of Civil Engineers, 2007.

- Atalay, M. B., and J. Penzien. *The Seismic Behavior of Critical Regions of Reinforced Concrete Components as Influenced by Moment, Shear, and Axial Force*. Berkley, CA: Earthquake Engineering Research Center, 1975, 234.
- ATC-20. *Procedures for Postearthquake Safety Evaluation of Buildings*. Applied Technology Council, 1991.
- Aycardi, L. E., J. B. Mander, and A. M. Reinhorn. *Seismic Resistance of Reinforced Concrete Frame Structures Designed Only for Gravity Loads - Part II: Experimental Performance of Subassemblages*. Technical Report NCEER-92-0028, Buffalo, NY: National Center for Earthquake Engineering Research, 1992.
- Bae, S. *Seismic Performance of Full-Scale Reinforced Concrete Columns*. Ph.D. Thesis, Austin, TX: The University of Texas at Austin, 2005, 312.
- Baker, J. W., T. Lin, S. K. Shahi, and N. Jayaram. *New Ground Motion Selection Procedures and Selection Motions for the PEER Transportation Research Program*. PEER Report 2011/03, Berkeley, CA: Pacific Earthquake Engineering Research Center, 2011.
- Barin, B., and J. A. Pincheira. *Influence of Modeling Parameters and Assumptions on the Seismic Response of an Existing RC Building*. Madison, WI: University of Wisconsin-Madison: Department of Civil and Environmental Engineering, 2002.
- Berry, M., and M. Eberhard. *Performance Modeling Strategies for Modern Reinforced Concrete Bridge Columns*. PEER Report 2007/07, Berkley, CA: Pacific Earthquake Engineering Research Center, 2007.
- Berry, M., and M. Eberhard. *Performance Models for Flexural Damage in Reinforced Concrete Columns*. PEER Report 2003/18, Berkley, CA: Pacific Earthquake Engineering Research Center, 2003, 158.
- Berry, M., and M. Eberhard. "Practical Performance Model for Bar Buckling." *Journal of Structural Engineering*, 2005: 1060-1070.
- Berry, M., M. Parrish, and M. Eberhard. *PEER Structural Performance Database*. Berkeley, California: Pacific Engineering Research Center, 2005.
- Berry, M., M. Parrish, and M. Eberhard. *PEER Structural Performance Database User's Manual*. Berkeley, California: Pacific Engineering Research Center, 2005, 38.
- Biddah, A., and A. Ghobarah. "Modeling of Shear Deformations and Bond Slip in Reinforced Concrete Joints." *Structural Engineering and Mechanics*, 1999: 413-432.
- Birely, A. C., L. N. Lowes, and D. L. Lehman. "Linear Analysis of Concrete Frames Considering Joint Flexibility." *ACI Structural Journal*, 2012: 381-392.

- Bracci, J. M., A. M. Reinhorn, and J. B. Mander. *Seismic Resistance of Reinforced Concrete Frame Structures Designed Only for Gravity Loads - Part I: Design and Properties of a 1/3 Scale Model Structure*. Technical Report NCEER-92-0027, Buffalo, NY: National Center for Earthquake Engineering Research, 1992.
- Bracci, J. M., and A. M., Mander, J. B. Reinhorn. *Seismic Resistance of Reinforced Concrete Frame Structures Designed Only for Gravity Loads: Part III - Experimental Performance and Analytical Study of a Model*. Technical Report NCEER-92-0029, Buffalo, NY: National Center for Earthquake Engineering Research, 1992.
- Brown, P. C. *Probabilistic Earthquake Damage Prediction for Reinforced Concrete Building Components*. Masters Thesis, Seattle, WA: University of Washington: Department of Civil and Environmental Engineering, 2008.
- Brown, P. C., and L. N. Lowes. "Fragility Functions for Modern Reinforced-Concrete Beam-Column Joints." *Earthquake Spectra*, 2007: 263-289.
- Camarillo, H. R. "Evaluation of Shear Strength Methodologies for Reinforced Concrete Columns." MS Thesis, Dept. of Civil and Environmental Engineering, Univ. of Washington, Seattle, WA, 2003, 137.
- Celik, O. C. *Probabilistic Assessment of Non-Ductile Reinforced Concrete Frames Susceptible to Mid-America Ground Motions*. PhD Thesis, Atlanta, GA: Georgia Institute of Technology, 2007.
- Christopoulos, C., S. Pampanin, and N. Priestley. "Performance-Based Seismic Response of Frame Structures Including Residual Deformations. Part I: Single Degree of Freedom Systems." *Journal of Earthquake Engineering*, 2003: 97-118.
- Coleman, J., and E. Spacone. "Localization Issues in Force-Based Frame Elements." *Journal of Structural Engineering*, 2001: 1257-1265.
- Corley, W. G. "Rotational Capacity of Reinforced Concrete Beams." *Journal of the Structural Division*, 1966: 121-146.
- Council, Applied Technology. *Evaluation of FEMA 306: Earthquake Damaged Concrete and Masonry Wall Buildings: Basic Procedures Manual*. 1999.
- Council, International Code. *2003 International Building Code*. Falls Church, VA, 2003.
- Eberhard, M. O., S. Baldrige, J. Marshall, W. Mooney, and G. J. Rix. *The Mw 7.0 Haiti Earthquake of January 12, 2010: USGS/EERI Advance Reconnaissance Team Report*. U.S. Geological Survey Open-File Report, 2010, 58.
- EERI. *Northridge Earthquake January 17, 1994 Preliminary Reconnaissance Report*. Oakland, CA: Ed. J.F. Hall, 1994.

- Ellingwood, B., T. V. Galambos, J. G. MacGregor, and C. A. Cornell. *Development of a Probability Based Load Criterion for American National Standard A58*. Washington, DC: National Bureau of Standards, 1980.
- Elwood, K. J. "Modelling Failures in Existing Reinforced Concrete Columns." *Canadian Journal of Civil Engineering*, 2004: 846-859.
- Elwood, K. J., and J. P. Moehle. "An Axial Capacity Model for Shear-Damaged Columns." 2004.
- Elwood, K. J., and J. P. Moehle. "Drift Capacity of Reinforced Concrete Columns with Light Transverse Reinforcement." *Earthquake Spectra*, 2005: 20.
- Elwood, K. J., and M. O. Eberhard. "Effective Stiffness of Reinforced Concrete Columns." *ACI Structural Journal*, 2009: 476-484.
- Federal Emergency Management Agency. *Prestandard and Commentary for the Seismic Rehabilitation of Buildings: FEMA 356*. Reston, VA: American Society of Civil Engineers, 2000.
- FEMA. *Handbook for the Seismic Evaluation of Buildings - A Prestandard*. Federal Emergency Management Agency, 1998.
- Goel, R. K., A. C. Lynn, V. V. May, S. S. Rihal, and D. C. Weggel. "Evaluating Current Procedures and Modeling for Seismic Performance of Reinforced Concrete Buildings." *12th World Conference for Earthquake Engineering*. 2000. 2060-2068.
- Goulet, C. A., et al. "Evaluation of the Seismic Performance of a Code-Conforming Reinforced-Concrete Frame Building: From Seismic Hazard to Collapse Safety and Economic Losses." *Earthquake Engineering and Structural Dynamics*, 2007: 1973-1997.
- Haselton, C. B. *Assessing Seismic Collapse Safety of Modern Reinforced Concrete Moment Frame Buildings*. PhD Thesis, Stanford University, Palo Alto, CA: Stanford University, 2006, 281.
- Haselton, C. B., A. B. Liel, B. S. Dean, J. H. Chou, and G. G. Deierlein. "Seismic Collapse Safety and Behavior of Modern Reinforced Concrete Moment Frame Buildings." n.d.
- Haselton, C. B., and G. G. Deierlein. "Assessing Seismic Collapse Safety of Modern Reinforced Concrete Frame Buildings." Blume Center Technical Report No. 156, 2007.
- Haselton, C. B., et al. *An Assessment to Benchmark the Seismic Performance of a Code-Conforming Reinforced Concrete Moment-Frame Building*. PEER Rep. 2007/12, Berkeley, CA: Pacific Earthquake Engineering Research Center, 2007.
- Hwang, S. J., and J. P. Moehle. "Models for Laterally Loaded Slab-Column Frames." *ACI Structural Journal*, 2000: 345-353.
- Ibarra, L. F., R. A. Medina, and H. Krawinkler. "Hysteretic Models that Incorporate Strength and Stiffness Deterioration." *Earthquake Engineering and Structural Dynamics*, 2005: 1489-1511.

- ICBO. *Uniform Building Code*. Pasadena, CA: International Conference of Building Officials, 1967.
- Karsan, I. D., and J. O. Jirsa. "Behavior of Concrete Under Compressive Loading." *Journal of Structural Division*, 1969.
- Kent, C., and R. Park. "Flexural Members with Confined Concrete." *Journal of the Structural Division*, 1971: 1969-1990.
- Khuntia, M., and S.K. Ghosh. "Flexural Stiffness of Reinforced Concrete Columns and Beams: Analytical Approach." *ACI Structural Journal*, 2004: 351-363.
- Kisseberth, N. *Workspace*. 2010. <https://nees.org/resources/workspace>.
- LeBorgne, M. R. *Modeling the Post Shear Failure Behavior of Reinforced Concrete Columns*. PhD Thesis, Austin, TX: The University of Texas at Austin, 2012.
- Liel, A. B. "Assessing the Collapse Risk of California's Existing Reinforced Concrete Frame Structures: Metrics for Seismic Safety Decisions." PhD Thesis, Stanford University, 2008, 293.
- Lowes, L. N., and A. Altoontash. "Modeling Reinforced-Concrete Beam-Column Joints Subjected to Cyclic Loading." *Journal of Structural Engineering*, 2003: 1686-1697.
- Lowes, L. N., and J.P. Moehle. "Evaluation and Retrofit of Beam-Column T-Joints in Older Reinforced Concrete Bridge Structures." *ACI Structural Journal*, 1999: 519-532.
- Lowes, L. N., N. Mitra, and A. Altoontash. *A Beam-Column Joint Model for Simulating the Earthquake Response of Reinforced Concrete Frames*. PEER Report 2003/10, Berkeley, CA: Pacific Earthquake Engineering Research Center, 2003.
- Lowes, L., J. Li, and ATC 58 SPP Team. *Fragility Functions for Reinforced Concrete Moment Frames*. Applied Technology Council, 2010.
- Luco, N., M. C. Gerstberger, S. R. Uma, H. Ryu, A. B. Liel, and M. Raghunandan. "A Methodology for Post-Mainshock Probabilistic Assessment of Building Collapse Risk." *Ninth Pacific Conference on Earthquake Engineering*. Auckland, New Zealand, 2011.
- Luco, N., P. Bazzurro, and C. A. Cornell. "Dynamic Versus Static Computation of the Residual Capacity of a Mainshock-Damaged Building to Withstand an Aftershock." *13th World Conference on Earthquake Engineering*. Vancouver, B.C., 2004.
- Luo, Y. H., and A. J. Durrani. "Equivalent Beam Model for Flat-Slab Buildings - Part I: Interior Connections." *ACI Structural Journal*, 1995: 115-124.
- Lynn, A. C., J. P. Moehle, S. A. Mahin, and W. T. Holmes. "Seismic Evaluation of Existing Reinforced Concrete Building Columns." *Earthquake Spectra*, 1996.
- Lynn, A. "Seismic Evaluation of Existing Reinforced Concrete Building Columns." Ph.D. Thesis, Dept. of Civil and Environmental Engineering, Univ. of California at Berkeley, Berkeley, CA, 2001, 284.

- Mackie, K., and B Stojadinovic. "Residual Displacement and Post Earthquake Capacity of Highway Bridges." *The 13th World Conference on Earthquake Engineering*. Vancouver, B.C.: WCEE, 2004.
- Mander, J. B., M. J. N. Priestley, and R. Park. "Theoretical Stress-Strain Model for Confined Concrete." *Journal of Structural Engineering*, 1988: 1804-1826.
- Marini, A., and E. Spacone. "Analysis of Reinforced Concrete Elements Including Shear Effects." *ACI Structural Journal*, 2006: 645-655.
- Mattock, A. H. "Rotational Capacity of Hinging Regions in Reinforced Concrete Beams." *Journal of the Structural Division*, 1967: 519-522.
- Mehanny, S.S.F., H. Kuramoto, and G.G. Deierlein. "Stiffness Modeling of Reinforced concrete Beam-Columns for Frame Analysis." *ACI Structural Journal*, 2001: 215-225.
- Melchers, R. E. *Structural Reliability Analysis and Prediction*. New York: John Wiley and Sons Inc., 1999.
- Menegotto, M., and P. Pinto. "Method of Analysis for Cyclically Loaded R.C. Plane Frames Including Changes in Geometry and Non-Elastic Behavior of Elements Under Combined Normal Force and Bending." *IABSE Symposium on the Resistance and Ultimate Deformability of Structures Acted Upon by Well-defined Loads*. Lisbon, 1973.
- Mitra, N., and L. N. Lowes. "Evaluation, Calibration, and Verification of a Reinforced Concrete Beam-Column Joint Model." *Journal of Structural Engineering*, 2007: 105-120.
- Mo, Y. L., and S. J. Wang. "Seismic Behavior of RC Columns with Various Tie Configurations." *Journal of Structural Engineering* Vol. 126, no. 10 (October 2000): 1122-1130.
- Mosier, W. G. *Seismic Assessment of Reinforced Concrete Beam-Column Joints*. Master Thesis, Seattle, WA: University of Washington: Department of Civil and Environmental Engineering, 2000.
- Neuenhofer, A., and F. C. Filippou. "Evaluation of Nonlinear Frame Finite-Element Models." *Journal of Structural Engineering*, 1997: 958-966.
- Nielson, B. G., and R. DesRoches. "Seismic Fragility Methodology for Highway Bridges Using a Component Level Approach." *Earthquake Engineering and Structural Dynamics*, 2006: 823-839.
- OpenSees. *Open System for Earthquake Engineering Simulation (OpenSees)*. PEER, Berkeley: University of California. n.d. <http://www.opensees.berkeley.edu>.
- OpenSeesWiki*. April 21, 2011. http://opensees.berkeley.edu/wiki/index.php/Main_Page (accessed September 20, 2011).
- Otani, S. "Inelastic Analysis of Reinforced-Concrete Frame Structures." *Journal of the Structural Division*, 1974: 1422-1449.

- Pagni, C. A. *Modeling of Structural Damage of Older Reinforced Concrete Components*. Masters Thesis, Seattle, WA: University of Washington: Department of Civil and Environmental Engineering, 2003.
- Pagni, C. A., and L. N. Lowes. "Fragility Functions for Older Reinforced Concrete Beam-Column Joints." *Earthquake Spectra*, 2006: 215-238.
- Pagni, C., and L. Lowes. *Predicting Earthquake Damage in Older Reinforced Concrete Beam-Column Joints*. PEER Report 2003/17, Berkeley, CA: Pacific Earthquake Engineering Research Center, 2004.
- Pampanin, S., C. Christopoulos, and N. Priestley. "Performance-Based Seismic Response of Frame Structures Including Residual Deformations. Part II: Multi-Degree of Freedom Systems." *Journal of Earthquake Engineering*, 2003: 119-147.
- Pan, A. A., and J.P. Moehle. *Reinforced Concrete Flat Plates Under Lateral Loading: An Experimental Study Including Biaxial Effects*. Report No. UCB/EERRC88/16, Berkeley, CA: College of Engineering, University of California at Berkeley, 1988.
- Pantelides, C. P., J. Hansen, J. Nadeau, and L. D. Reaveley. *Assessment of Reinforced Concrete Building Exterior Joints with Substandard Details*. PEER Report 2002/18, Berkeley, CA: Pacific Earthquake Engineering Research Center, 2002.
- Park, R., M. J. N. Priestley, and W. D. Gill. "Ductility of Square Confined Concrete Columns." *Journal of Structural Division*, 1982: 929-950.
- Paspuleti, C. *Seismic Analysis of an Older Reinforced Concrete Frame Structure*. Masters Thesis, Seattle, WA: University of Washington: Department of Civil and Environmental Engineering, 2002.
- Paulay, T., and M. J. N. Priestley. *Seismic Design of Reinforced Concrete and Masonry Buildings*. New York: John Wiley & Sons Inc., 1992.
- Paultre, P., F. Legeron, and D. Mongeau. "Influence of Concrete Strength and Transverse Reinforcement Yield Strength on Behavior of High Strength Concrete Columns." *ACI Structural Journal*, 2001: 490-501.
- Pecknold, D. A. "Slab Width for Equivalent Frame Analysis." *ACI Journal*, 1975: 135-137.
- PEER. *NISEE Earthquake Engineering Online Archive*. 2011. <http://nisee.berkeley.edu/elibrary/> (accessed 2011).
- Pincheira, J. A., and J. O. Jirsa. "Seismic Strengthening of Reinforced Concrete Frames Using Post-Tensioned Bracing Systems." Phil M. Ferguson Structural Engineering Lab Report N. 92-3, University of Texas at Austin, Austin, TX, 1992.

- Pincheira, J. A., F. S. Dotwiala, and J. T. D'Souza. "Seismic Analysis of Older Reinforced Concrete Columns." *Earthquake Spectra*, 1999: 245-272.
- Popovics, S. "A Numerical Approach to the Complete Stress-Strain Curve of Concrete." *Cement and Concrete Research*, 1973: 583-599.
- Porter, K., R. Kennedy, and R. Bachman. "Creating Fragility Functions for Performance-Based Earthquake Engineering." *Earthquake Spectra*, 2007: 471-489.
- Priestley, M. J. N., and R. Park. "Strength and Ductility of Concrete Bridge Columns Under Seismic Loading." *ACI Structural Journal*, 1987: 61-76.
- Ramanathan, K., R. DesRoches, and J. E. Padgett. "Analytical Fragility Curves for Multispan Continuous Steel Girder Bridges in Moderate Seismic Zones." *Transportation Research Record*, 2010: 173-182.
- Ruiz-Garcia, J., and E. Miranda. "Evaluation of Residual Drift Demands in Regular Multi-Story Frames for Performance Based Assessment." *Earthquake Engineering and Structural Journal*, 2006: 1609-1629.
- Ruiz-Garcia, J., and E. Miranda. "Probabilistic Estimation of Residual Drift Demands for Seismic Assessment of Multi-Story Framed Buildings." *Engineering Structures*, 2010: 11-20.
- Ruiz-Garcia, J., and E. Miranda. "Residual Displacement Ratios for Assessment of Existing Structures." *Earthquake Engineering and Structural Dynamics*, 2005: 315-336.
- Ryu, H., N. Luco, S. R. Uma, and A. B. Liel. "Developing Fragilities for Mainshock-Damaged Structures Through Incremental Dynamic Analysis." *Ninth Pacific Conference on Earthquake Engineering*. Auckland, New Zealand, 2011.
- Saatcioglu, M., and M. Grira. "Confinement of Reinforced Concrete Columns with Welded Reinforcement Grids." *ACI Structural Journal*, January-February 1999: 11.
- Saatcioglu, M., and S. R. Razvi. "Strength and Ductility of Confined Concrete." *Journal of Structural Engineering*, 1992: 1590-1606.
- Scott, M. H., and G. L. Fenves. "Plastic Hinge Integration Methods for Force-Based Beam-Column Elements." *Journal of Structural Engineering*, 2006: 244-252.
- Sedra, N., et al. *The Haiti Earthquake Database*. 2010. <http://nees.org/resources/1797> (accessed 2011).
- Sezen, H. *Seismic Behavior and Modeling of Reinforced Concrete Building Columns*. Ph.D. Thesis, Berkley, CA: The University of California, 2002, 345.
- Soesianawati, M. T. *Limited Ductility Design of Reinforced Concrete Columns*. PhD Thsesis, Christchurch, New Zealand: University of Canterbury, 1986.

- Sugano, S. "Seismic Behavior of Reinforced Concrete Columns Which Used Ultra-High-Strength Concrete." *Eleventh World Conference on Earthquake Engineering*. Acapulco, Mexico, 1996. 1-8.
- Takeda, T., M. A. Sozen, and N. N. Nielsen. "Reinforced Concrete Response to Simulated Earthquakes." *Journal of the Structural Division*, December 1970: 2557-2573.
- Talacian, S., T. Haukaas, and K. J. Elwood. "Probabilistic Models For Seismic Damage and Subsequent Losses." *Proceedings of the 9th U.S. National and 10th Canadian Conference on Earthquake Engineering*. Toronto, 2010. 10.
- Theiss, A. G. *Modeling the Earthquake Response of Older Reinforced Concrete Beam-Column Building Joints*. Masters Thesis, Seattle, WA: University of Washington: Department of Civil and Environmental Engineering, 2005.
- Uma, S. R., H. Ryu, N. Luco, A. B. Liel, and M. Raghunandan. "Comparison of Main-Shock and Aftershock Fragility Curves Developed for New Zealand and US Buildings." *Ninth Pacific Conference on Earthquake Engineering*. Auckland, New Zealand, 2011.
- Uma, S. R., S. Pampanin, and C. Christopoulos. "A Probabilistic Framework for Performance-Based Seismic Assessment of Structures Considering Residual Deformations." *First European Conference on Earthquake engineering and Seismology*. Geneva, 2006. 1-10.
- Walker, S. *Seismic Performance of Existing Reinforced Concrete Beam-Column Joints*. Masters Thesis, Seattle, WA: University of Washington: Department of Civil and Environmental Engineering, 2001.
- Watson, S. "Design of Reinforced Concrete Frames of Limited Ductility." PhD Thesis, University of Canterbury, Christchurch, 1989, 232.
- Yakut, Ahmet. "Preliminary Seismic Performance Assessment Procedure for Existing RC Buildings." *Engineering Structures*, 2004: 1447-1461.
- Yazgan, U., and A. Dazio. "Utilization of Residual Displacements in the Post-Earthquake Assessment." *The 14th World Conference on Earthquake Engineering*. Beijing, China: WCEE, 2008.
- Zhu, L., K. J. Elwood, and T. Haukaas. "Classification and Seismic Safety Evaluation of Existing Reinforced Concrete Columns." *Journal of Structural Engineering*, 2007: 1316-1330.
- Zhu, L., K. J. Elwood, T. Haukaas, and P. Gardoni. "Application of a Probabilistic Drift Capacity Model for Shear-Critical Columns." *ACI Special Publication*, 2006: 81-102.

Appendix A: Database Damage Data

A.1 Introduction

This appendix identifies the columns in the Database that included experimental data at the onset of damage states. The data included in the Database are horizontal displacements of the columns in millimeters.

The tables in this appendix include a column identifying the axial load ratio. This column was used to categorize columns as columns with high axial loads or low axial loads. The columns are also categorized based on their failure mode.

The cracking and lateral capacity loss data in each table does not come directly from the Database. The cracking data was identified by a review of the reports identified by the Database. The loss of lateral load-carrying capacity is another damage state that the Database can be used to acquire. Camarillo (2003) identified the 80% effective force using an automated algorithm for the rectangular columns with load displacement histories that had a 20% reduction in capacity. The displacements identified by Camarillo were used to determine the drifts at which the columns lost their lateral load-carrying capacities. The number of tests that have data for each damage state are shown in Table A.1.

Appendix Table A.1 Number of PEER Database columns with damage data

	Flexural Cracking	Longitudinal Cracking	Shear Cracking	Onset of Spalling	Significant Concrete Spalling	Longitudinal Bar Buckling	Longitudinal Bar Fracture	Axial Capacity Loss	Lateral Capacity Loss
Flexure LAL	20	12	11	89	31	56	20	11	145
Flexure HAL	6	5	0	19	1	8	0	2	21
	Shear Cracking	Widening of Shear Cracks	Longitudinal Cracking	Onset of Spalling	Significant Concrete Spalling	Longitudinal Bar Buckling	Longitudinal Bar Fracture	Axial Capacity Loss	Lateral Capacity Loss
F-S LAL	1	2	1	2	1	4	1	4	21
F-S HAL	0	0	0	2	0	1	0	1	7
Shear LAL	5	5	1	1	0	2	0	4	24
Shear HAL	0	0	0	0	0	0	0	0	3

A.2 Database Data

There are 173 tests in Appendix Table A.2, 23 tests in Appendix Table A.3, 23 tests in Appendix Table A.4, 7 tests in Appendix Table A.5, 25 tests in Appendix Table A.6, and 3 tests in Appendix Table A.7.

Appendix Table A.2 Flexural Failure Mode with low axial loads

Test Number	Test Name	Axial Load Ratio	Flexural Cracking	Longitudinal Cracking	Shear Cracking	Onset of Spalling	Significant Concrete Spalling	Longitudinal Bar Buckling	Longitudinal Bar Fracture	Axial Capacity Loss	Lateral Capacity Loss
1	Gill et al. 1979, No. 1	0.26	3.0		6.0	11.5	22.5				
2	Gill et al. 1979, No. 2	0.21	4.0		8.0	8.0	17.0				
3	Gill et al. 1979, No. 3	0.42	3.0		7.0	7.0	14.0				
5	Ang et al. 1981, No. 3	0.38	5.0		10.0	10.0	20.0	50.0	50.0		
6	Ang et al. 1981, No. 4	0.21	7.0		18.0	19.0	20.0	58.0	58.0		
7	Soesianawati et al. 1986, No. 1	0.10	5.0		18.0	39.2	58.8	78.4	98.0	98.0	98.1
8	Soesianawati et al. 1986, No. 2	0.30	5.0		17.0	34.2	34.2	68.4	85.5		68.7
9	Soesianawati et al. 1986, No. 3	0.30	5.0	15.0	15.0	30.6	30.6	44.9			46.2
10	Soesianawati et al. 1986, No. 4	0.30	5.0		10.0	16.4	24.6	44.0			43.9
11	Zahn et al. 1986, No. 7	0.22	5.0	20.0	20.0	22.0		75.4			118.2
12	Zahn et al. 1986, No. 8	0.39	5.0	18.0	18.0	17.0		64.7			
18	Tanaka and Park 1990, No. 1	0.20	5.0	20.0		20.0	40.0	120.0			
19	Tanaka and Park 1990, No. 2	0.20	4.5	18.0		18.0	34.0	87.2			
20	Tanaka and Park 1990, No. 3	0.20	4.0	16.0		16.0	34.0	59.0			57.2
21	Tanaka and Park 1990, No. 4	0.20	4.0	16.0		16.0	32.0	80.0			
22	Tanaka and Park 1990, No. 5	0.10	5.5	22.0		22.0	46.0	73.8			
23	Tanaka and Park 1990, No. 6	0.10	4.8	19.0		19.0	32.0	67.2			
24	Tanaka and Park 1990, No. 7	0.30	4.8	19.0		19.0	29.0	82.4			
25	Tanaka and Park 1990, No. 8	0.30	3.3	13.0		13.0	25.0	78.0			
26	Park and Paulay 1990, No. 9	0.10	7.0	18.9				84.0			
32	Ohno and Nishioka 1984, L3	0.03									73.0
48	Kanda et al. 1988, 85STC-1	0.11									34.6
49	Kanda et al. 1988, 85STC-2	0.11									34.6
50	Kanda et al. 1988, 85STC-3	0.11									34.6
56	Muguruma et al. 1989, AL-1	0.40									21.4
66	Sakai et al. 1990, B1	0.35									10.2
67	Sakai et al. 1990, B2	0.35									20.1
68	Sakai et al. 1990, B3	0.35									10.1
69	Sakai et al. 1990, B4	0.35									10.1
70	Sakai et al. 1990, B5	0.35									9.5
71	Sakai et al. 1990, B6	0.35									10.1
72	Sakai et al. 1990, B7	0.35									5.1
89	Atalay and Penzien 1975, No. 2S1	0.09				20.3					

Table A.2 Continued

Test Number	Test Name	Axial Load Ratio	Flexural Cracking	Longitudinal Cracking	Shear Cracking	Onset of Spalling	Significant Concrete Spalling	Longitudinal Bar Buckling	Longitudinal Bar Fracture	Axial Capacity Loss	Lateral Capacity Loss
90	Atalay and Penzien 1975, No. 3S1	0.10				40.7					
91	Atalay and Penzien 1975, No. 4S1	0.10				20.3					
92	Atalay and Penzien 1975, No. 5S1	0.20				25.4					
93	Atalay and Penzien 1975, No. 6S1	0.18				30.5		40.6	40.7		
94	Atalay and Penzien 1975, No. 9	0.26				10.2					42.2
95	Atalay and Penzien 1975, No. 10	0.27				20.3					40.1
96	Atalay and Penzien 1975, No. 11	0.28				15.3					37.7
97	Atalay and Penzien 1975, No. 12	0.27				15.3					42.7
102	Azizinamini et al. 1988, NC-2	0.21				25.1					66.6
103	Azizinamini et al. 1988, NC-4	0.31				15.3					38.6
104	Saatcioglu and Ozcebe 1989, U1	0.00									48.7
105	Saatcioglu and Ozcebe 1989, U3	0.14									51.1
106	Saatcioglu and Ozcebe 1989, U4	0.15									89.9
107	Saatcioglu and Ozcebe 1989, U6	0.13									89.8
108	Saatcioglu and Ozcebe 1989, U7	0.13									88.0
109	Galeota et al. 1996, AA1	0.30									15.9
110	Galeota et al. 1996, AA2	0.30									17.2
111	Galeota et al. 1996, AA3	0.20									20.8
112	Galeota et al. 1996, AA4	0.20									16.0
113	Galeota et al. 1996, BA1	0.20									26.7
114	Galeota et al. 1996, BA2	0.30									36.4
115	Galeota et al. 1996, BA3	0.30									21.9
116	Galeota et al. 1996, BA4	0.20									41.0
117	Galeota et al. 1996, CA1	0.20									67.0
118	Galeota et al. 1996, CA2	0.30									53.5
119	Galeota et al. 1996, CA3	0.20									37.1
120	Galeota et al. 1996, CA4	0.30									40.5
122	Galeota et al. 1996, AB2	0.30									45.8
123	Galeota et al. 1996, AB3	0.30									42.7
124	Galeota et al. 1996, AB4	0.20									46.3
126	Galeota et al. 1996, BB1	0.20									58.0
127	Galeota et al. 1996, BB4	0.30									71.8
128	Galeota et al. 1996, BB4B	0.30									75.3

Table A.2 Continued

Test Number	Test Name	Axial Load Ratio	Flexural Cracking	Longitudinal Cracking	Shear Cracking	Onset of Spalling	Significant Concrete Spalling	Longitudinal Bar Buckling	Longitudinal Bar Fracture	Axial Capacity Loss	Lateral Capacity Loss
133	Wehbe et al. 1998, A1	0.10				47.0		122.0		163.0	122.1
134	Wehbe et al. 1998, A2	0.24				40.0		102.0		121.0	102.3
135	Wehbe et al. 1998, B1	0.09				47.0				185.0	160.8
136	Wehbe et al. 1998, B2	0.23						128.0		150.0	129.8
145	Xiao and Martirosyan 1998, HC4-8L19-T10-0.1P	0.10						47.0		47.0	47.8
146	Xiao and Martirosyan 1998, HC4-8L19-T10-0.2P	0.20						40.0			40.9
147	Xiao and Martirosyan 1998, HC4-8L16-T10-0.1P	0.10						37.0			37.6
148	Xiao and Martirosyan 1998, HC4-8L16-T10-0.2P	0.19						35.0			35.0
154	Sugano 1996, UC15L	0.35				1.3					20.4
155	Sugano 1996, UC20L	0.35				1.4					28.3
156	Nosho et al. 1996, No. 1	0.34				21.3	37.0		37.3		34.4
158	Bayrak and Sheikh 1996, AS-2HT	0.36				9.0		73.0			63.4
161	Bayrak and Sheikh 1996, AS-5HT	0.45				5.0		32.0			
162	Bayrak and Sheikh 1996, AS-6HT	0.46				8.0		56.0			55.7
163	Bayrak and Sheikh 1996, AS-7HT	0.45				4.0		34.0			23.1
164	Bayrak and Sheikh 1996, ES-8HT	0.47				7.0		29.7			25.0
165	Saatcioglu and Grira 1999, BG-1	0.43				32.9					41.0
166	Saatcioglu and Grira 1999, BG-2	0.43				32.9		82.3			66.5
167	Saatcioglu and Grira 1999, BG-3	0.20				32.9					116.0
168	Saatcioglu and Grira 1999, BG-4	0.46				32.9		65.8			50.5
169	Saatcioglu and Grira 1999, BG-5	0.46				32.9		115.2			100.0
170	Saatcioglu and Grira 1999, BG-6	0.46				32.9					100.0
171	Saatcioglu and Grira 1999, BG-7	0.46				32.9					100.0
172	Saatcioglu and Grira 1999, BG-8	0.23				32.9		115.2			118.0
173	Saatcioglu and Grira 1999, BG-9	0.46				32.9		65.8			116.0
174	Saatcioglu and Grira 1999, BG-10	0.46				32.9					99.5
175	Matamoros et al. 1999,C10-05N	0.05									38.6
176	Matamoros et al. 1999,C10-05S	0.05									38.1
177	Matamoros et al. 1999,C10-10N	0.10									44.5
178	Matamoros et al. 1999,C10-10S	0.10									44.7
179	Matamoros et al. 1999,C10-20N	0.21									38.4
180	Matamoros et al. 1999,C10-20S	0.21									38.1
181	Matamoros et al. 1999,C5-00N	0.00									38.9

Table A.2 Continued

Test Number	Test Name	Axial Load Ratio	Flexural Cracking	Longitudinal Cracking	Shear Cracking	Onset of Spalling	Significant Concrete Spalling	Longitudinal Bar Buckling	Longitudinal Bar Fracture	Axial Capacity Loss	Lateral Capacity Loss
182	Matamoros et al. 1999,C5-00S	0.00									38.9
183	Matamoros et al. 1999,C5-20N	0.14									32.3
184	Matamoros et al. 1999,C5-20S	0.14									32.0
185	Matamoros et al. 1999,C5-40N	0.36									26.4
186	Matamoros et al. 1999,C5-40S	0.36									25.4
187	Mo and Wang 2000,C1-1	0.11				42.5	69.5				88.4
188	Mo and Wang 2000,C1-2	0.16				37.0	63.0		104.0		96.6
189	Mo and Wang 2000,C1-3	0.22				36.0	62.0		111.0		88.1
190	Mo and Wang 2000,C2-1	0.11				37.0	63.0		113.0		98.0
191	Mo and Wang 2000,C2-2	0.16				35.0	68.0		110.0		94.9
192	Mo and Wang 2000,C2-3	0.21				38.0	58.0		109.0		77.0
201	Thomsen and Wallace 1994, A1	0.00				35.8					
202	Thomsen and Wallace 1994, A3	0.20				14.9	14.9	47.8			20.2
203	Thomsen and Wallace 1994, B1	0.00				35.8					
204	Thomsen and Wallace 1994, B2	0.10				17.9	17.9				14.6
205	Thomsen and Wallace 1994, B3	0.20				11.9					13.8
206	Thomsen and Wallace 1994, C1	0.00				35.8					
207	Thomsen and Wallace 1994, C2	0.10				17.9	23.9				29.8
208	Thomsen and Wallace 1994, C3	0.20				14.9	14.9				19.1
209	Thomsen and Wallace 1994, D1	0.20				14.9	17.9	29.0	47.8		18.9
210	Thomsen and Wallace 1994, D2	0.20				11.9	17.9	29.0	47.8		11.9
211	Thomsen and Wallace 1994, D3	0.20				11.9	11.9	29.0	47.8		12.1
215	Paultre & Legeron, 2000, No. 1006015	0.14				34.0			182.0		182.8
216	Paultre & Legeron, 2000, No. 1006025	0.28				31.1			178.0		144.5
217	Paultre & Legeron, 2000, No. 1006040	0.39				27.4				126.0	63.2
218	Paultre & Legeron, 2000, No. 10013015	0.14				30.4			122.0		91.1
219	Paultre & Legeron, 2000, No. 10013025	0.26				28.8			75.5	92.5	48.3
220	Paultre & Legeron, 2000, No. 10013040	0.37				24.8				46.6	29.9
221	Paultre et al., 2001, No. 806040	0.40				26.5			208.3		174.4
222	Paultre et al., 2001, No. 1206040	0.41				24.7				122.1	122.1
223	Paultre et al., 2001, No. 1005540	0.35				26.4			143.9		98.0
224	Paultre et al., 2001, No. 1008040	0.37				28.5				108.0	52.6
227	Pujol 2002, No. 10-2-3N	0.09									21.9

Table A.2 Continued

Test Number	Test Name	Axial Load Ratio	Flexural Cracking	Longitudinal Cracking	Shear Cracking	Onset of Spalling	Significant Concrete Spalling	Longitudinal Bar Buckling	Longitudinal Bar Fracture	Axial Capacity Loss	Lateral Capacity Loss
228	Pujol 2002, No. 10-2-3S	0.09									20.9
229	Pujol 2002, No. 10-3-1.5N	0.09									27.9
230	Pujol 2002, No. 10-3-1.5S	0.09									28.8
231	Pujol 2002, No. 10-3-3N	0.10									21.5
232	Pujol 2002, No. 10-3-3S	0.10									21.6
233	Pujol 2002, No. 10-3-2.25N	0.10									21.0
234	Pujol 2002, No. 10-3-2.25S	0.10									22.1
237	Pujol 2002, No. 20-3-3N	0.16									22.9
238	Pujol 2002, No. 20-3-3S	0.16									23.0
239	Pujol 2002, No. 10-2-2.25N	0.08									22.0
240	Pujol 2002, No. 10-2-2.25S	0.08									21.7
241	Pujol 2002, No. 10-1-2.25N	0.08									22.1
242	Pujol 2002, No. 10-1-2.25S	0.08									21.5
243	Bechtoula, Kono, Arai and Watanabe, 2002, D1N30	0.30									24.8
248	Takemura and Kawashima, 1997, Test 1 (JSCE-4)	0.03									43.7
249	Takemura and Kawashima, 1997, Test 2 (JSCE-5)	0.03									48.5
250	Takemura and Kawashima, 1997, Test 3 (JSCE-6)	0.03									74.2
251	Takemura and Kawashima, 1997, Test 4 (JSCE-7)	0.03									101.4
252	Takemura and Kawashima, 1997, Test 5 (JSCE-8)	0.03									84.5
254	Xiao & Yun 2002, No. FHC1-0.2	0.20						142.2			
255	Xiao & Yun 2002, No. FHC2-0.34	0.33						71.1			
256	Xiao & Yun 2002, No. FHC3-0.22	0.22						106.7			
257	Xiao & Yun 2002, No. FHC4-0.33	0.32						71.1			
258	Xiao & Yun 2002, No. FHC5-0.2	0.20						106.7			105.3
259	Xiao & Yun 2002, No. FHC6-0.2	0.20						106.7			
260	Bayrak & Sheikh, 2002, No. RS-9HT	0.34				17.0		98.4			85.0
263	Bayrak & Sheikh, 2002, No. RS-12HT	0.34				17.0		63.1			46.9
264	Bayrak & Sheikh, 2002, No. RS-13HT	0.35				13.0		68.6			56.2
265	Bayrak & Sheikh, 2002, No. RS-14HT	0.46				25.8		46.7			41.2
266	Bayrak & Sheikh, 2002, No. RS-15HT	0.36				31.7		88.9			69.3
267	Bayrak & Sheikh, 2002, No. RS-16HT	0.37				26.4		59.8			41.1
268	Bayrak & Sheikh, 2002, No. RS-17HT	0.34				22.2		80.2			62.1
271	Bayrak & Sheikh, 2002, No. RS-20HT	0.34				23.7		49.3			45.6

Table A.2 Continued

Test Number	Test Name	Axial Load Ratio	Flexural Cracking	Longitudinal Cracking	Shear Cracking	Onset of Spalling	Significant Concrete Spalling	Longitudinal Bar Buckling	Longitudinal Bar Fracture	Axial Capacity Loss	Lateral Capacity Loss
272	Bayrak & Sheikh, 2002, No. WRS-21HT	0.47				19.9		50.1			46.3
273	Bayrak & Sheikh, 2002, No. WRS-22HT	0.31				29.1		95.7			86.4
274	Bayrak & Sheikh, 2002, No. WRS-23HT	0.33				24.4		92.2			88.7
285	Saatcioglu and Ozcebe 1989, U2	0.16									42.0
286	Esaki, 1996 H-2-1/5	0.20									10.1
287	Esaki, 1996 HT-2-1/5	0.20									11.8
288	Esaki, 1996 H-2-1/3	0.33									8.0
289	Esaki, 1996 HT-2-1/3	0.33									10.0

Appendix Table A.3 Flexural Failure Mode with high axial loads

Test Number	Test Name	Axial Load Ratio	Flexural Cracking	Longitudinal Cracking	Shear Cracking	Onset of Spalling	Significant Concrete Spalling	Longitudinal Bar Buckling	Longitudinal Bar Fracture	Axial Capacity Loss	Lateral Capacity Loss
4	Gill et al. 1979, No. 4	0.60	5.0			5.0	10.5				
13	Watson and Park 1989, No. 5	0.50	5.0	18.5		18.5					38.9
14	Watson and Park 1989, No. 6	0.50	5.0	18.5		18.5					26.8
15	Watson and Park 1989, No. 7	0.70	10.0	12.3		12.3					18.7
16	Watson and Park 1989, No. 8	0.70	10.0	12.3		12.3					17.2
17	Watson and Park 1989, No. 9	0.70	10.0	12.3		12.3					43.9
43	Zhou et al. 1987, No. 214-08	0.80									6.5
58	Muguruma et al. 1989, AL-2	0.63									10.9
151	Sugano 1996, UC10H	0.60				0.6					4.1
152	Sugano 1996, UC15H	0.60				0.7					8.2
153	Sugano 1996, UC20H	0.60				0.8					16.3
157	Bayrak and Sheikh 1996, ES-1HT	0.50				7.0		37.0			32.2
159	Bayrak and Sheikh 1996, AS-3HT	0.50				7.0		48.0			34.1
160	Bayrak and Sheikh 1996, AS-4HT	0.50				9.0		64.5			51.6
225	Paultre et al., 2001, No. 1005552	0.53				19.9				91.8	66.4
226	Paultre et al., 2001, No. 1006052	0.51				22.5				85.9	66.1
244	Bechtoula, Kono, Arai and Watanabe, 2002, D1N60	0.60									18.7
246	Bechtoula, Kono, Arai and Watanabe, 2002, L1N60	0.57									31.3
261	Bayrak & Sheikh, 2002, No. RS-10HT	0.50				12.5		65.9			42.2

Table A.3 Continued

Test Number	Test Name	Axial Load Ratio	Flexural Cracking	Longitudinal Cracking	Shear Cracking	Onset of Spalling	Significant Concrete Spalling	Longitudinal Bar Buckling	Longitudinal Bar Fracture	Axial Capacity Loss	Lateral Capacity Loss
262	Bayrak & Sheikh, 2002, No. RS-11HT	0.51				15.6		87.8			
269	Bayrak & Sheikh, 2002, No. RS-18HT	0.50				20.0		48.9			26.9
270	Bayrak & Sheikh, 2002, No. RS-19HT	0.53				13.8		93.5			50.9
275	Bayrak & Sheikh, 2002, No. WRS-24HT	0.50				17.5		65.6			33.4

Appendix Table A.4 Flexure-Shear Failure Mode with low axial loads

Test Number	Test Name	Axial Load Ratio	Shear Cracking	Widening of Shear Cracks	Longitudinal Cracking	Onset of Spalling	Significant Concrete Spalling	Longitudinal Bar Buckling	Longitudinal Bar Fracture	Axial Capacity Loss	Lateral Capacity Loss
29	Nagasaka 1982, HPRC19-32	0.35									4.4
33	Ohue et al. 1985, 2D16RS	0.14									15.3
34	Ohue et al. 1985, 4D13RS	0.15									7.1
64	Ono et al. 1989, CA025C	0.26				3.0					7.6
74	Wight and Sozen 1973, No. 40.033a(East)	0.12									31.8
75	Wight and Sozen 1973, No. 40.033a(West)	0.12									31.3
76	Wight and Sozen 1973, No. 40.048(East)	0.15									42.8
77	Wight and Sozen 1973, No. 40.048(West)	0.15									48.1
78	Wight and Sozen 1973, No. 40.033(East)	0.11									45.6
79	Wight and Sozen 1973, No. 40.033(West)	0.11									49.0
81	Wight and Sozen 1973, No. 25.033(West)	0.07									42.1
82	Wight and Sozen 1973, No. 40.067(East)	0.11									60.1
83	Wight and Sozen 1973, No. 40.067(West)	0.11									60.3
86	Wight and Sozen 1973, No. 40.092(East)	0.11									52.1
87	Wight and Sozen 1973, No. 40.092(West)	0.11									53.8
138	Lynn et al. 1998, 2CLH18	0.07					38.0	38.0		46.0	38.3
139	Lynn et al. 1998, 2CMH18	0.28		15.0						15.0	15.3
143	Lynn et al. 1996, 2SLH18	0.07								53.0	
144	Lynn et al. 1996, 3SMD12	0.28	7.5	15.0	15.0			31.0		31.0	
149	Xiao and Martirosyan 1998, HC4-8L16-T6-0	0.10									32.5
150	Xiao and Martirosyan 1998, HC4-8L16-T6-0	0.19							22.0		21.6
212	Sezen and Moehle No. 1	0.15				55.9		139.7			37.7
214	Sezen and Moehle No. 4	0.15						139.7			51.4

Appendix Table A.5 Flexure-Shear Failure Mode with high axial loads

Test Number	Test Name	Axial Load Ratio	Shear Cracking	Widening of Shear Cracks	Longitudinal Cracking	Onset of Spalling	Significant Concrete Spalling	Longitudinal Bar Buckling	Longitudinal Bar Fracture	Axial Capacity Loss	Lateral Capacity Loss
42	Zhou et al. 1987, No. 204-08	0.80									3.3
44	Zhou et al. 1987, No. 223-09	0.90									12.1
45	Zhou et al. 1987, No. 302-07	0.70									7.0
46	Zhou et al. 1987, No. 312-07	0.70									6.9
65	Ono et al. 1989, CA060C	0.62				1.5					4.5
73	Amitsu et al. 1991, CB060C	0.74									2.8
213	Sezen and Moehe No. 2	0.60				27.9		55.9		55.9	19.6

Appendix Table A.6 Shear Failure Mode with low axial loads

Test Number	Test Name	Axial Load Ratio	Shear Cracking	Widening of Shear Cracks	Longitudinal Cracking	Onset of Spalling	Significant Concrete Spalling	Longitudinal Bar Buckling	Longitudinal Bar Fracture	Axial Capacity Loss	Lateral Capacity Loss
28	Nagasaka 1982, HPRC10-63	0.17									4.7
38	Imai and Yamamoto 1986, No. 1	0.07									18.6
54	Arakawa et al. 1989, OA2	0.18									2.9
55	Arakawa et al. 1989, OA5	0.45									1.9
80	Wight and Sozen 1973, No. 25.033(East)	0.07									31.5
98	Umehara and Jirsa 1982, CUS	0.16	5.0								5.0
99	Umehara and Jirsa 1982, CUW	0.16	8.5	17.0	17.0						8.6
100	Umehara and Jirsa 1982, 2CUS	0.27	5.1	10.2							4.7
101	Bett et al. 1985, No. 1-1	0.10				11.4					9.2
137	Lynn et al. 1998, 3CLH18	0.09		15.0						30.5	15.4
140	Lynn et al. 1998, 3CMH18	0.26		15.0				30.5		30.5	15.3
141	Lynn et al. 1998, 3CMD12	0.26	7.5					30.5		30.5	25.7
142	Lynn et al. 1996, 3SLH18	0.09	7.5	15.0						45.5	
199	Aboutaha et al. 1999, SC3	0.00									23.8
200	Aboutaha et al. 1999, SC9	0.00									10.8
276	Xiao et al, 1994, R1A	0.05									17.3
277	Xiao et al, 1994, R3A	0.06									12.3
278	Xiao et al, 1994, R5A	0.06									8.8
279	Ramirez & Jirsa, 1980, 00-U	0.00									17.0
280	Ramirez & Jirsa, 1980, 120C-U	0.19									15.3

Table A.6 Continued

Test Number	Test Name	Axial Load Ratio	Shear Cracking	Widening of Shear Cracks	Longitudinal Cracking	Onset of Spalling	Significant Concrete Spalling	Longitudinal Bar Buckling	Longitudinal Bar Fracture	Axial Capacity Loss	Lateral Capacity Loss
281	Wight and Sozen 1973, No. 00.033(East)	0.00									26.3
282	Wight and Sozen 1973, No. 00.033(West)	0.00									48.2
290	Iwasaki, 1985, P-18	0.00									24.8
291	Iwasaki, 1985, P-21	0.00									25.1
292	Iwasaki, 1985, P-25	0.00									38.2

Appendix Table A.7 Shear Failure Mode with high axial loads

Test Number	Test Name	Axial Load Ratio	Shear Cracking	Widening of Shear Cracks	Longitudinal Cracking	Onset of Spalling	Significant Concrete Spalling	Longitudinal Bar Buckling	Longitudinal Bar Fracture	Axial Capacity Loss	Lateral Capacity Loss
39	Zhou et al. 1987, No. 104-08	0.80									1.7
40	Zhou et al. 1987, No. 114-08	0.80									3.5
41	Zhou et al. 1987, No. 124-08	0.80									6.4

Appendix B: Database Modified Damage Data

B.1 Introduction

This appendix has the modified damage data used to identify residual drifts once a damage state occurred. The same column tests that are presented in Appendix A are included in this appendix. The displacement values that were modified are highlighted. The tables in this appendix include a column identifying the axial load ratio. This column was used to categorize columns as columns with high axial loads or low axial loads. The columns are also categorized based on their failure mode.

Appendix Table B.1 Flexural Failure Mode with low axial loads: Modified Database data

Test Number	Test Name	Axial Load Ratio	Flexural Cracking	Longitudinal Cracking	Shear Cracking	Onset of Spalling	Significant Concrete Spalling	Longitudinal Bar Buckling	Longitudinal Bar Fracture	Axial Capacity Loss	Lateral Capacity Loss
1	Gill et al. 1979, No. 1	0.26	3.0		5.0	11.0	22.5				
2	Gill et al. 1979, No. 2	0.21	3.4		8.0	8.0	17.0				
3	Gill et al. 1979, No. 3	0.42	1.5		7.0	7.0	14.0				
5	Ang et al. 1981, No. 3	0.38	3.5		10.0	10.0	20.0	50.0	50.0		
6	Ang et al. 1981, No. 4	0.21	7.0		18.0	19.0	19.8	58.0	58.0		
7	Soesianawati et al. 1986, No. 1	0.10	5.0		18.0	39.2	58.4	78.4	98.0	98.0	98.1
8	Soesianawati et al. 1986, No. 2	0.30	5.0		15.0	34.0	34.1	67.4	85.5		68.0
9	Soesianawati et al. 1986, No. 3	0.30	5.0	14.0	14.0	29.0	29.5	44.9			46.2
10	Soesianawati et al. 1986, No. 4	0.30	5.0		8.5	16.4	24.6	44.0			43.9
11	Zahn et al. 1986, No. 7	0.22	5.0	20.0	20.0	22.0		75.4			118.2
12	Zahn et al. 1986, No. 8	0.39	5.0	18.0	18.0	17.0		64.7			
18	Tanaka and Park 1990, No. 1	0.20	5.0	20.0		20.0	40.0	120.0			
19	Tanaka and Park 1990, No. 2	0.20	4.5	18.0		18.0	34.0	87.2			
20	Tanaka and Park 1990, No. 3	0.20	4.0	16.0		16.0	34.0	56.0			56.0
21	Tanaka and Park 1990, No. 4	0.20	4.0	16.0		16.0	32.0	80.0			
22	Tanaka and Park 1990, No. 5	0.10	5.5	22.0		22.0	46.0	73.8			
23	Tanaka and Park 1990, No. 6	0.10	4.8	19.0		19.0	32.0	67.2			
24	Tanaka and Park 1990, No. 7	0.30	4.8	19.0		19.0	29.0	82.4			
25	Tanaka and Park 1990, No. 8	0.30	3.3	13.0		13.0	25.0	78.0			
26	Park and Paulay 1990, No. 9	0.10	7.0	18.9				84.0			
32	Ohno and Nishioka 1984, L3	0.03									73.0
48	Kanda et al. 1988, 85STC-1	0.11									34.6
49	Kanda et al. 1988, 85STC-2	0.11									34.5
50	Kanda et al. 1988, 85STC-3	0.11									34.6
56	Muguruma et al. 1989, AL-1	0.40									21.4
66	Sakai et al. 1990, B1	0.35									10.3
67	Sakai et al. 1990, B2	0.35									20.1
68	Sakai et al. 1990, B3	0.35									10.1
69	Sakai et al. 1990, B4	0.35									10.1
70	Sakai et al. 1990, B5	0.35									9.5
71	Sakai et al. 1990, B6	0.35									10.1
72	Sakai et al. 1990, B7	0.35									5.1
89	Atalay and Penzien 1975, No. 2S1	0.09				20.3					

Table B.1 Continued

Test Number	Test Name	Axial Load Ratio	Flexural Cracking	Longitudinal Cracking	Shear Cracking	Onset of Spalling	Significant Concrete Spalling	Longitudinal Bar Buckling	Longitudinal Bar Fracture	Axial Capacity Loss	Lateral Capacity Loss
90	Atalay and Penzien 1975, No. 3S1	0.10				40.7					
91	Atalay and Penzien 1975, No. 4S1	0.10				19.0					
92	Atalay and Penzien 1975, No. 5S1	0.20				25.4					
93	Atalay and Penzien 1975, No. 6S1	0.18				30.5		40.6	40.7		
94	Atalay and Penzien 1975, No. 9	0.26				10.2					42.2
95	Atalay and Penzien 1975, No. 10	0.27				20.3					40.1
96	Atalay and Penzien 1975, No. 11	0.28				15.3					37.7
97	Atalay and Penzien 1975, No. 12	0.27				15.3					42.7
102	Azizinamini et al. 1988, NC-2	0.21				25.1					66.6
103	Azizinamini et al. 1988, NC-4	0.31				15.3					38.6
104	Saatcioglu and Ozcebe 1989, U1	0.00									48.7
105	Saatcioglu and Ozcebe 1989, U3	0.14									51.1
106	Saatcioglu and Ozcebe 1989, U4	0.15									89.9
107	Saatcioglu and Ozcebe 1989, U6	0.13									89.8
108	Saatcioglu and Ozcebe 1989, U7	0.13									88.0
109	Galeota et al. 1996, AA1	0.30									15.9
110	Galeota et al. 1996, AA2	0.30									17.2
111	Galeota et al. 1996, AA3	0.20									20.8
112	Galeota et al. 1996, AA4	0.20									16.0
113	Galeota et al. 1996, BA1	0.20									26.7
114	Galeota et al. 1996, BA2	0.30									36.4
115	Galeota et al. 1996, BA3	0.30									21.9
116	Galeota et al. 1996, BA4	0.20									41.0
117	Galeota et al. 1996, CA1	0.20									67.0
118	Galeota et al. 1996, CA2	0.30									53.5
119	Galeota et al. 1996, CA3	0.20									37.1
120	Galeota et al. 1996, CA4	0.30									40.5
122	Galeota et al. 1996, AB2	0.30									45.8
123	Galeota et al. 1996, AB3	0.30									42.7
124	Galeota et al. 1996, AB4	0.20									46.3
126	Galeota et al. 1996, BB1	0.20									58.0
127	Galeota et al. 1996, BB4	0.30									71.8
128	Galeota et al. 1996, BB4B	0.30									75.3

Table B.1 Continued

Test Number	Test Name	Axial Load Ratio	Flexural Cracking	Longitudinal Cracking	Shear Cracking	Onset of Spalling	Significant Concrete Spalling	Longitudinal Bar Buckling	Longitudinal Bar Fracture	Axial Capacity Loss	Lateral Capacity Loss
133	Wehbe et al. 1998, A1	0.10				40.0		122.0		163.0	122.1
134	Wehbe et al. 1998, A2	0.24				40.0		102.0		121.0	102.3
135	Wehbe et al. 1998, B1	0.09				46.0				185.0	160.8
136	Wehbe et al. 1998, B2	0.23						128.0		150.0	129.8
145	Xiao and Martirosyan 1998, HC4-8L19-T10-	0.10						45.0		47.0	47.7
146	Xiao and Martirosyan 1998, HC4-8L19-T10-	0.20						40.0			40.9
147	Xiao and Martirosyan 1998, HC4-8L16-T10-	0.10						37.0			37.6
148	Xiao and Martirosyan 1998, HC4-8L16-T10-	0.19						35.0			35.0
154	Sugano 1996, UC15L	0.35				1.3					20.4
155	Sugano 1996, UC20L	0.35				1.3					20.3
156	Nosho et al. 1996, No. 1	0.34				21.3	34.0		37.3		34.4
158	Bayrak and Sheikh 1996, AS-2HT	0.36				9.0		73.0			63.4
161	Bayrak and Sheikh 1996, AS-5HT	0.45				5.0		32.0			
162	Bayrak and Sheikh 1996, AS-6HT	0.46				8.0		56.0			55.7
163	Bayrak and Sheikh 1996, AS-7HT	0.45				4.0		34.0			23.1
164	Bayrak and Sheikh 1996, ES-8HT	0.47				7.0		29.7			25.0
165	Saatcioglu and Grira 1999, BG-1	0.43				32.9					
166	Saatcioglu and Grira 1999, BG-2	0.43				32.9		82.3			66.5
167	Saatcioglu and Grira 1999, BG-3	0.20				32.9					116.0
168	Saatcioglu and Grira 1999, BG-4	0.46				32.9		65.8			50.5
169	Saatcioglu and Grira 1999, BG-5	0.46				32.9		115.2			100.0
170	Saatcioglu and Grira 1999, BG-6	0.46				32.9					100.0
171	Saatcioglu and Grira 1999, BG-7	0.46				32.9					100.0
172	Saatcioglu and Grira 1999, BG-8	0.23				32.9		115.2			118.0
173	Saatcioglu and Grira 1999, BG-9	0.46				32.9		65.8			116.0
174	Saatcioglu and Grira 1999, BG-10	0.46				32.9					99.5
175	Matamoros et al. 1999,C10-05N	0.05									38.6
176	Matamoros et al. 1999,C10-05S	0.05									38.1
177	Matamoros et al. 1999,C10-10N	0.10									44.5
178	Matamoros et al. 1999,C10-10S	0.10									44.7
179	Matamoros et al. 1999,C10-20N	0.21									38.4
180	Matamoros et al. 1999,C10-20S	0.21									38.1
181	Matamoros et al. 1999,C5-00N	0.00									38.9

Table B.1 Continued

Test Number	Test Name	Axial Load Ratio	Flexural Cracking	Longitudinal Cracking	Shear Cracking	Onset of Spalling	Significant Concrete Spalling	Longitudinal Bar Buckling	Longitudinal Bar Fracture	Axial Capacity Loss	Lateral Capacity Loss
182	Matamoros et al. 1999,C5-00S	0.00									38.9
183	Matamoros et al. 1999,C5-20N	0.14									32.3
184	Matamoros et al. 1999,C5-20S	0.14									32.0
185	Matamoros et al. 1999,C5-40N	0.36									26.4
186	Matamoros et al. 1999,C5-40S	0.36									25.4
187	Mo and Wang 2000,C1-1	0.11				40.5	68.0				88.4
188	Mo and Wang 2000,C1-2	0.16				35.0	62.0		104.0		96.6
189	Mo and Wang 2000,C1-3	0.22				35.0	61.5		111.0		88.1
190	Mo and Wang 2000,C2-1	0.11				37.0	63.0		113.0		98.0
191	Mo and Wang 2000,C2-2	0.16				34.0	67.9		109.0		94.9
192	Mo and Wang 2000,C2-3	0.21				38.0	58.0		109.0		77.0
201	Thomsen and Wallace 1994, A1	0.00				35.8					
202	Thomsen and Wallace 1994, A3	0.20				14.9	14.9	47.8			20.2
203	Thomsen and Wallace 1994, B1	0.00				35.8					
204	Thomsen and Wallace 1994, B2	0.10				19.7	17.9				14.6
205	Thomsen and Wallace 1994, B3	0.20				11.9					13.8
206	Thomsen and Wallace 1994, C1	0.00				35.8					
207	Thomsen and Wallace 1994, C2	0.10				17.9	23.9				29.4
208	Thomsen and Wallace 1994, C3	0.20				13.0	14.9				18.5
209	Thomsen and Wallace 1994, D1	0.20				13.0	17.9	28.6	47.8		18.8
210	Thomsen and Wallace 1994, D2	0.20				11.9	17.9	29.0	47.8		11.9
211	Thomsen and Wallace 1994, D3	0.20				11.2	11.2	29.0	47.8		12.1
215	Paultre & Legeron, 2000, No. 1006015	0.14				34.0			182.0		182.3
216	Paultre & Legeron, 2000, No. 1006025	0.28				31.1			178.0		143.5
217	Paultre & Legeron, 2000, No. 1006040	0.39				27.4				126.0	63.2
218	Paultre & Legeron, 2000, No. 10013015	0.14				30.0			122.0		91.1
219	Paultre & Legeron, 2000, No. 10013025	0.26				28.8			75.5	92.5	47.5
220	Paultre & Legeron, 2000, No. 10013040	0.37				24.8				46.6	29.9
221	Paultre et al., 2001, No. 806040	0.40				26.5			208.3		174.4
222	Paultre et al., 2001, No. 1206040	0.41				24.7				122.1	122.1
223	Paultre et al., 2001, No. 1005540	0.35				26.4			143.9		98.0
224	Paultre et al., 2001, No. 1008040	0.37				28.5				108.0	52.6
227	Pujol 2002, No. 10-2-3N	0.09									21.9

Table B.1 Continued

Test Number	Test Name	Axial Load Ratio	Flexural Cracking	Longitudinal Cracking	Shear Cracking	Onset of Spalling	Significant Concrete Spalling	Longitudinal Bar Buckling	Longitudinal Bar Fracture	Axial Capacity Loss	Lateral Capacity Loss
228	Pujol 2002, No. 10-2-3S	0.09									20.9
229	Pujol 2002, No. 10-3-1.5N	0.09									27.9
230	Pujol 2002, No. 10-3-1.5S	0.09									28.8
231	Pujol 2002, No. 10-3-3N	0.10									21.5
232	Pujol 2002, No. 10-3-3S	0.10									21.6
233	Pujol 2002, No. 10-3-2.25N	0.10									21.0
234	Pujol 2002, No. 10-3-2.25S	0.10									22.1
237	Pujol 2002, No. 20-3-3N	0.16									22.9
238	Pujol 2002, No. 20-3-3S	0.16									23.0
239	Pujol 2002, No. 10-2-2.25N	0.08									22.0
240	Pujol 2002, No. 10-2-2.25S	0.08									21.7
241	Pujol 2002, No. 10-1-2.25N	0.08									22.1
242	Pujol 2002, No. 10-1-2.25S	0.08									21.5
243	Bechtoula, Kono, Arai and Watanabe, 2002	0.30									24.8
248	Takemura and Kawashima, 1997, Test 1 (JSCE-4)	0.03									43.7
249	Takemura and Kawashima, 1997, Test 2 (JSCE-5)	0.03									48.5
250	Takemura and Kawashima, 1997, Test 3 (JSCE-6)	0.03									74.2
251	Takemura and Kawashima, 1997, Test 4 (JSCE-7)	0.03									101.4
252	Takemura and Kawashima, 1997, Test 5 (JSCE-8)	0.03									84.5
254	Xiao & Yun 2002, No. FHC1-0.2	0.20						142.2			
255	Xiao & Yun 2002, No. FHC2-0.34	0.33						71.1			
256	Xiao & Yun 2002, No. FHC3-0.22	0.22						106.7			
257	Xiao & Yun 2002, No. FHC4-0.33	0.32						71.1			
258	Xiao & Yun 2002, No. FHC5-0.2	0.20						106.7			105.3
259	Xiao & Yun 2002, No. FHC6-0.2	0.20						106.7			
260	Bayrak & Sheikh, 2002, No. RS-9HT	0.34				17.0		98.4			85.0
263	Bayrak & Sheikh, 2002, No. RS-12HT	0.34				17.0		63.1			46.9
264	Bayrak & Sheikh, 2002, No. RS-13HT	0.35				13.0		68.6			56.2
265	Bayrak & Sheikh, 2002, No. RS-14HT	0.46				25.8		46.7			41.2
266	Bayrak & Sheikh, 2002, No. RS-15HT	0.36				31.7		88.9			69.3
267	Bayrak & Sheikh, 2002, No. RS-16HT	0.37				26.4		59.8			41.1
268	Bayrak & Sheikh, 2002, No. RS-17HT	0.34				22.2		80.2			62.1
271	Bayrak & Sheikh, 2002, No. RS-20HT	0.34				23.7		49.3			45.6

Table B.1 Continued

Test Number	Test Name	Axial Load Ratio	Flexural Cracking	Longitudinal Cracking	Shear Cracking	Onset of Spalling	Significant Concrete Spalling	Longitudinal Bar Buckling	Longitudinal Bar Fracture	Axial Capacity Loss	Lateral Capacity Loss
272	Bayrak & Sheikh, 2002, No. WRS-21HT	0.47				19.9		50.1			46.3
273	Bayrak & Sheikh, 2002, No. WRS-22HT	0.31				29.1		95.7			86.4
274	Bayrak & Sheikh, 2002, No. WRS-23HT	0.33				24.4		92.2			88.7
285	Saatcioglu and Ozcebe 1989, U2	0.16									42.0
286	Esaki, 1996 H-2-1/5	0.20									10.1
287	Esaki, 1996 HT-2-1/5	0.20									11.8
288	Esaki, 1996 H-2-1/3	0.33									8.0
289	Esaki, 1996 HT-2-1/3	0.33									10.0

Appendix Table B.2 Flexural Failure Mode with high axial loads: Modified Database data

Test Number	Test Name	Axial Load Ratio	Flexural Cracking	Longitudinal Cracking	Shear Cracking	Onset of Spalling	Significant Concrete Spalling	Longitudinal Bar Buckling	Longitudinal Bar Fracture	Axial Capacity Loss	Lateral Capacity Loss
4	Gill et al. 1979, No. 4	0.60	5.0			5.0	10.5				
13	Watson and Park 1989, No. 5	0.50	5.0	18.5		18.5					38.9
14	Watson and Park 1989, No. 6	0.50	5.0	18.5		18.5					25.2
15	Watson and Park 1989, No. 7	0.70	8.0	12.3		12.3					18.7
16	Watson and Park 1989, No. 8	0.70	8.0	12.3		12.3					17.2
17	Watson and Park 1989, No. 9	0.70	8.0	12.3		12.3					43.0
43	Zhou et al. 1987, No. 214-08	0.80									6.5
58	Muguruma et al. 1989, AL-2	0.63									10.9
151	Sugano 1996, UC10H	0.60				0.6					4.1
152	Sugano 1996, UC15H	0.60				0.7					8.2
153	Sugano 1996, UC20H	0.60				0.7					14.5
157	Bayrak and Sheikh 1996, ES-1HT	0.50				6.0		35.5			32.2
159	Bayrak and Sheikh 1996, AS-3HT	0.50				7.0		48.0			32.5
51	Bayrak and Sheikh 1996, AS-4HT	0.50				9.0		64.5			51.0
225	Paultre et al., 2001, No. 1005552	0.53				19.9				91.8	66.4
226	Paultre et al., 2001, No. 1006052	0.51				22.5				85.9	66.1
244	Bechtoula, Kono, Arai and Watanabe, 2002, D1N60	0.60									18.7
246	Bechtoula, Kono, Arai and Watanabe, 2002, L1N60	0.57									31.3
261	Bayrak & Sheikh, 2002, No. RS-10HT	0.50				12.5		65.9			42.2

Table B.2 Continued

Test Number	Test Name	Axial Load Ratio	Flexural Cracking	Longitudinal Cracking	Shear Cracking	Onset of Spalling	Significant Concrete Spalling	Longitudinal Bar Buckling	Longitudinal Bar Fracture	Axial Capacity Loss	Lateral Capacity Loss
262	Bayrak & Sheikh, 2002, No. RS-11HT	0.51				15.6		87.8			
269	Bayrak & Sheikh, 2002, No. RS-18HT	0.50				20.0		48.9			26.9
270	Bayrak & Sheikh, 2002, No. RS-19HT	0.53				13.8		93.5			50.9
275	Bayrak & Sheikh, 2002, No. WRS-24HT	0.50				17.5		65.6			33.4

Appendix C: Element Sub-Assemblage Information

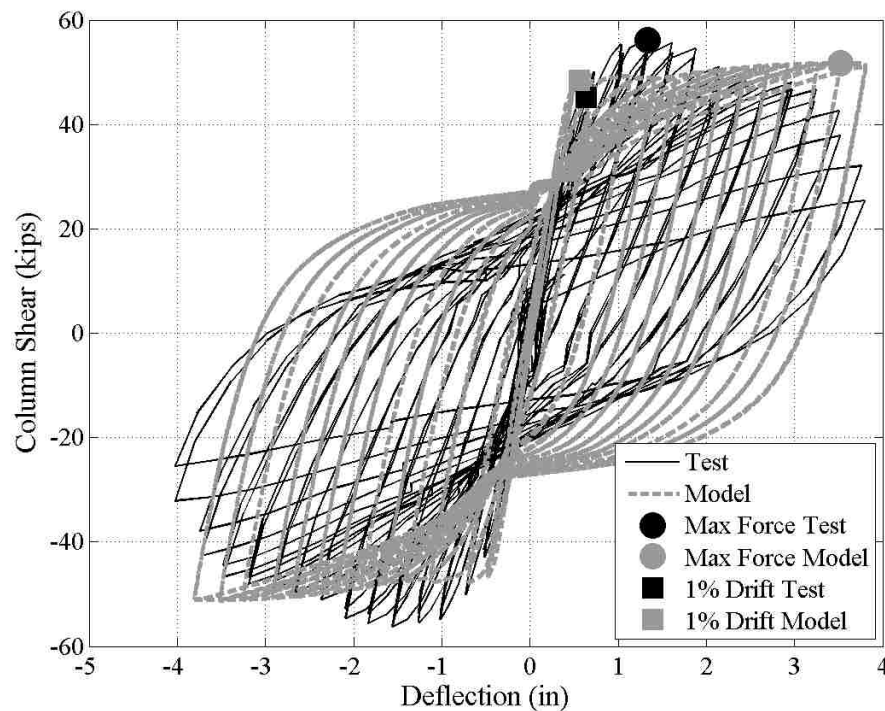
C.1 Introduction

This appendix contains plots for the simulations of the sub-assemblies modeled as well as a description of the experimental joint results used for validation purposes. Each column results plot compares the simulated response of a given specimen to the experimental response. The joints that the experimental load displacement data was available for are plotted with the simulated response. The joints that the experimental load displacement data was not available show the analytical data plotted next to an image of the experimental results.

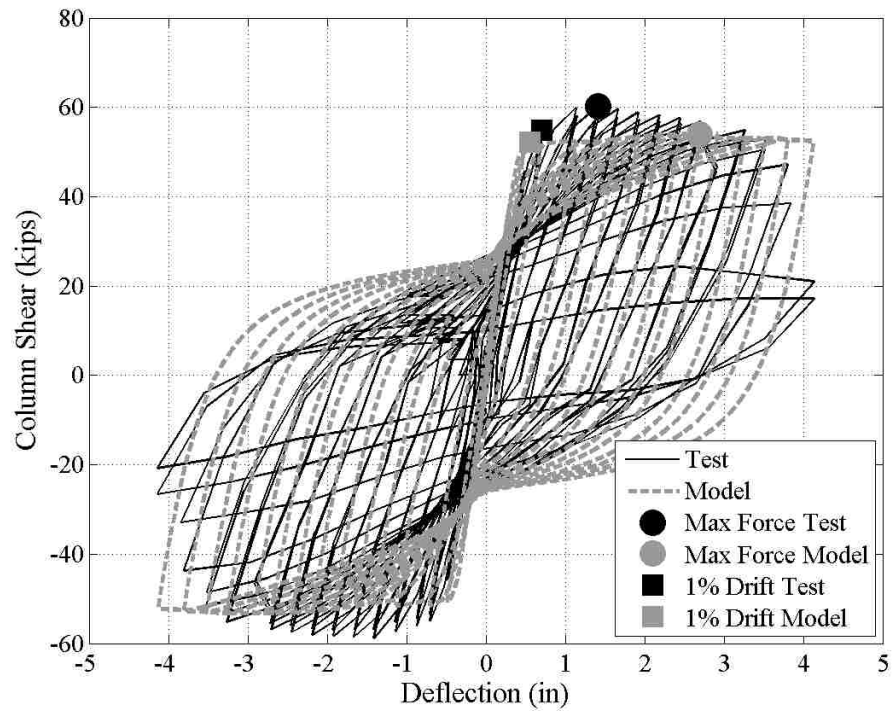
A more extensive discussion on the experimental behavior of the joints is accompanied by plots of the response of the beams and columns framing into the joint. This is included to show that the joint models captured degradation occurring in the joint region and degradation occurring in the beams and columns.

Experimental design data for each of the column specimens considered in this work can be found in the Database. The joint design data can be obtained in individual reports by Walker (2001), Alire (2002), Aycardi et al. (1992), and Pantelides et al. (2002) which are cited in the List of References.

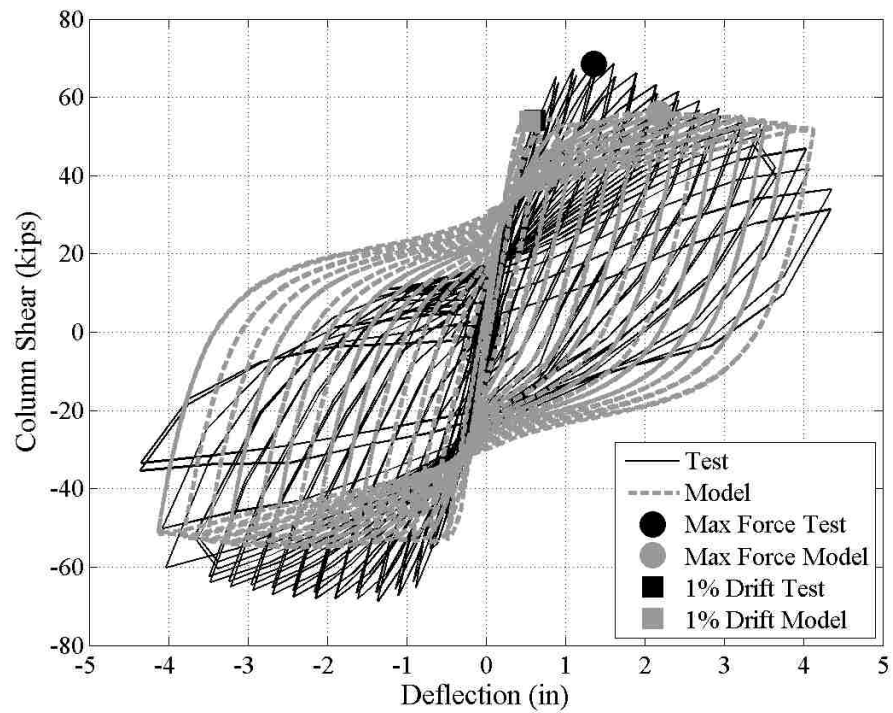
C.2 SMF Column Simulation Plots



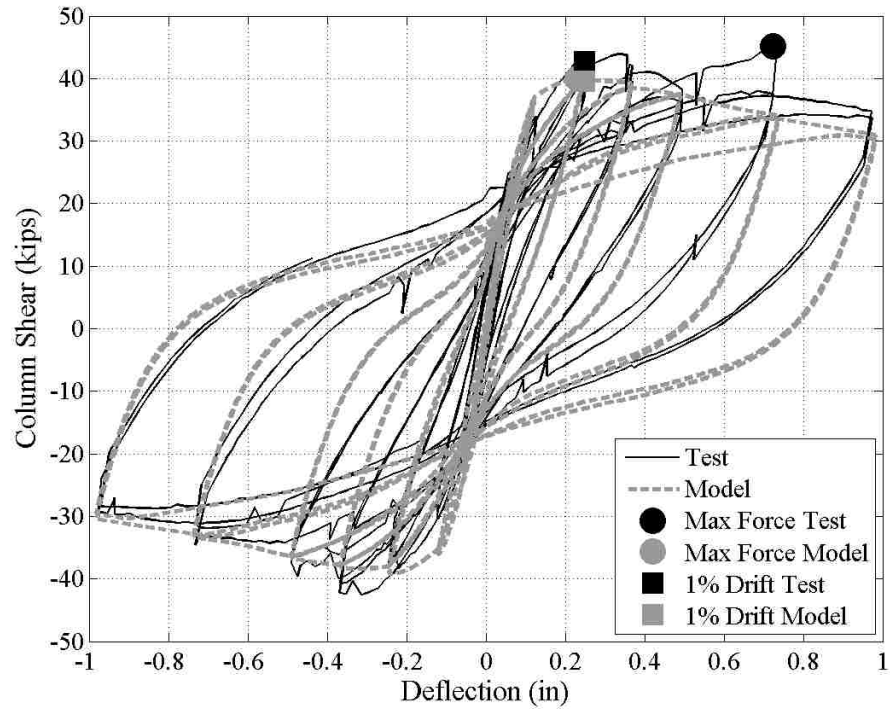
Appendix Figure C.1 Mo and Wang C1-1



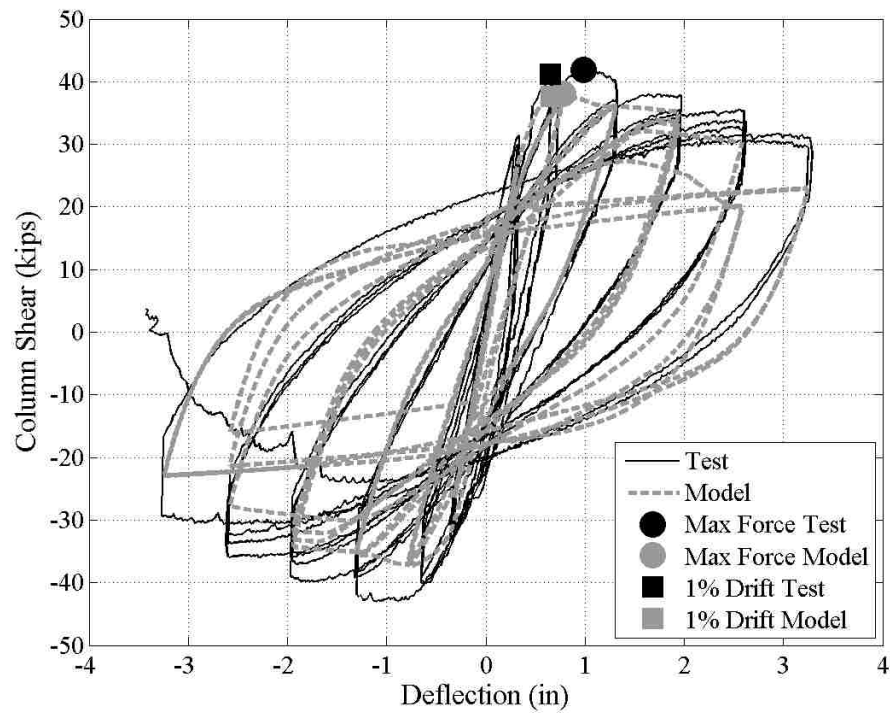
Appendix Figure C.2 Mo and Wang C1-2



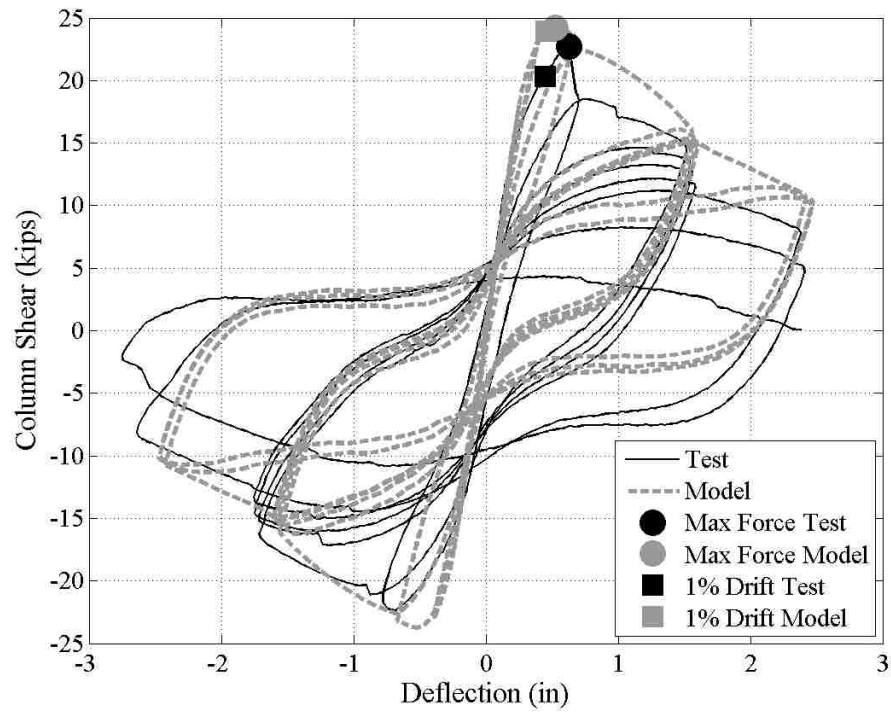
Appendix Figure C.3 Mo and Wang C1-3



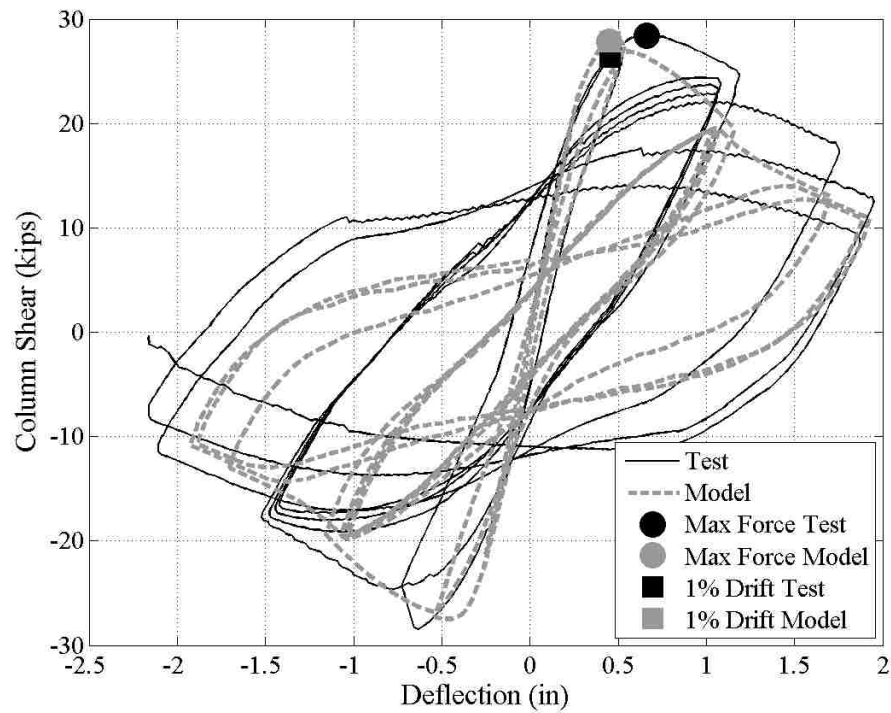
Appendix Figure C.4 Bechtoula et al. D1N30



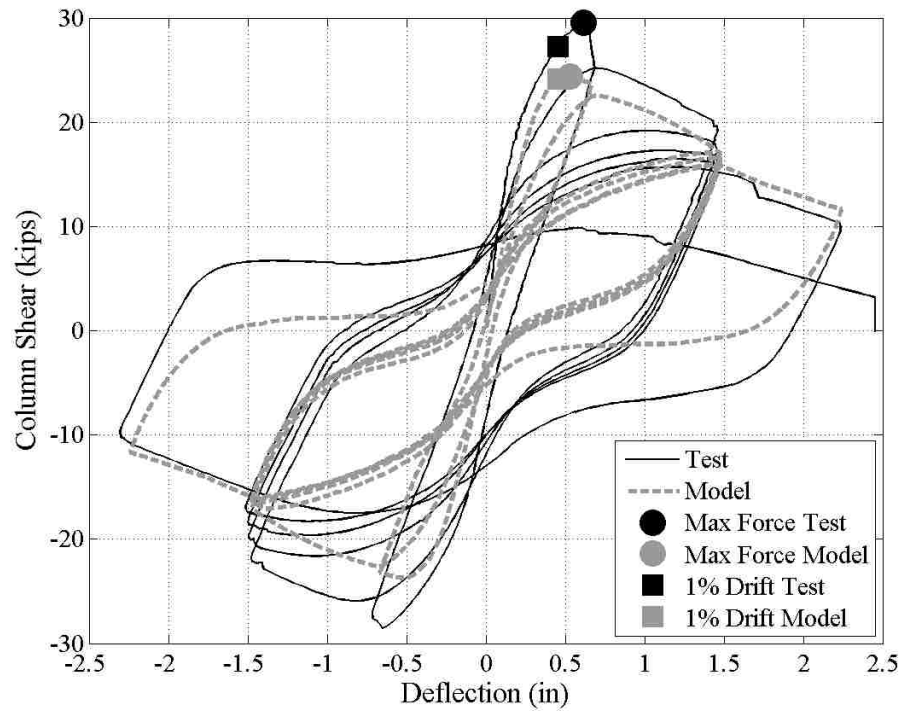
Appendix Figure C.5 Saatcioglu and Grira BG-2



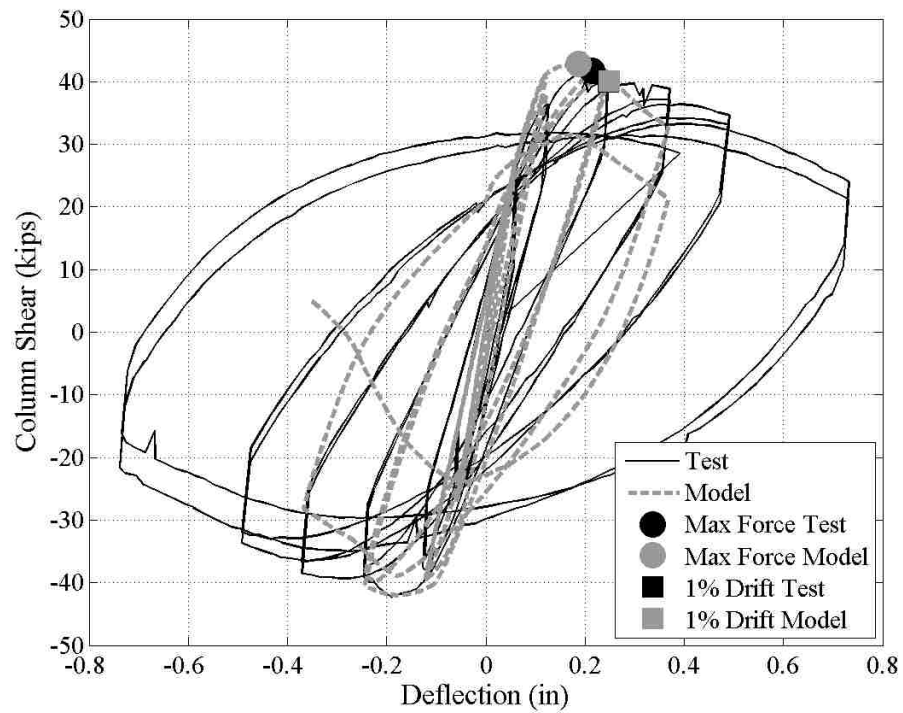
Appendix Figure C.6 Galeota et al. CA1



Appendix Figure C.7 Galeota et al. CA2

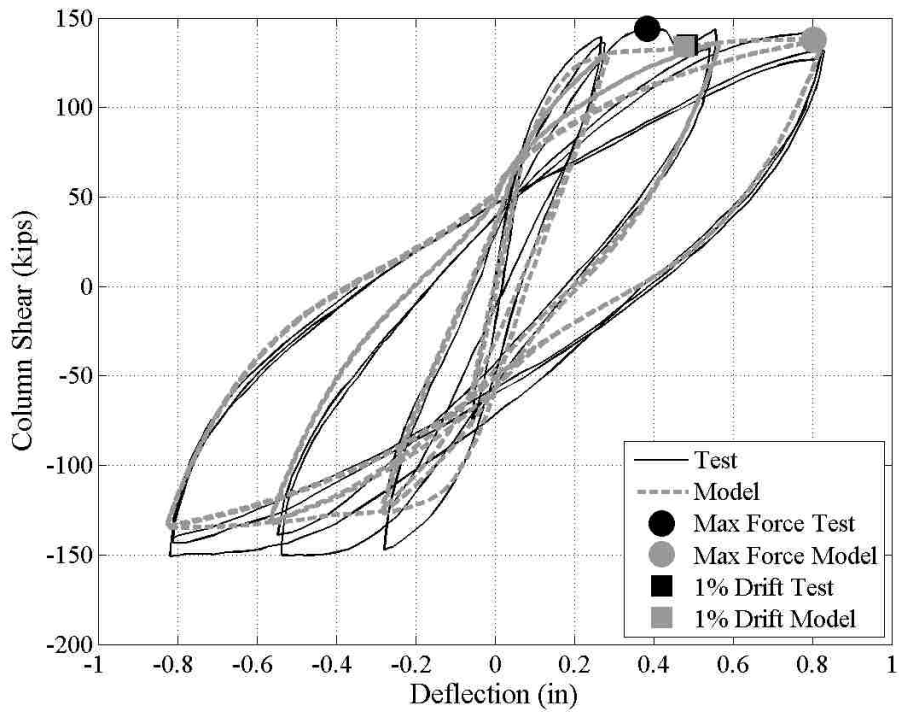


Appendix Figure C.8 Galeota et al. CA3

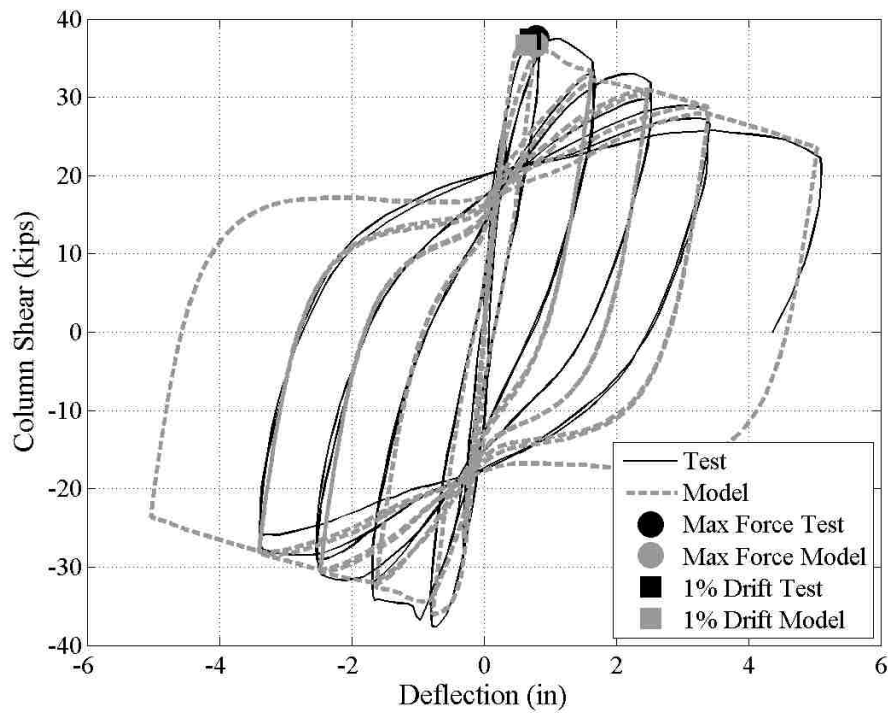


Appendix Figure C.9 Bechtoula et al. DIN60

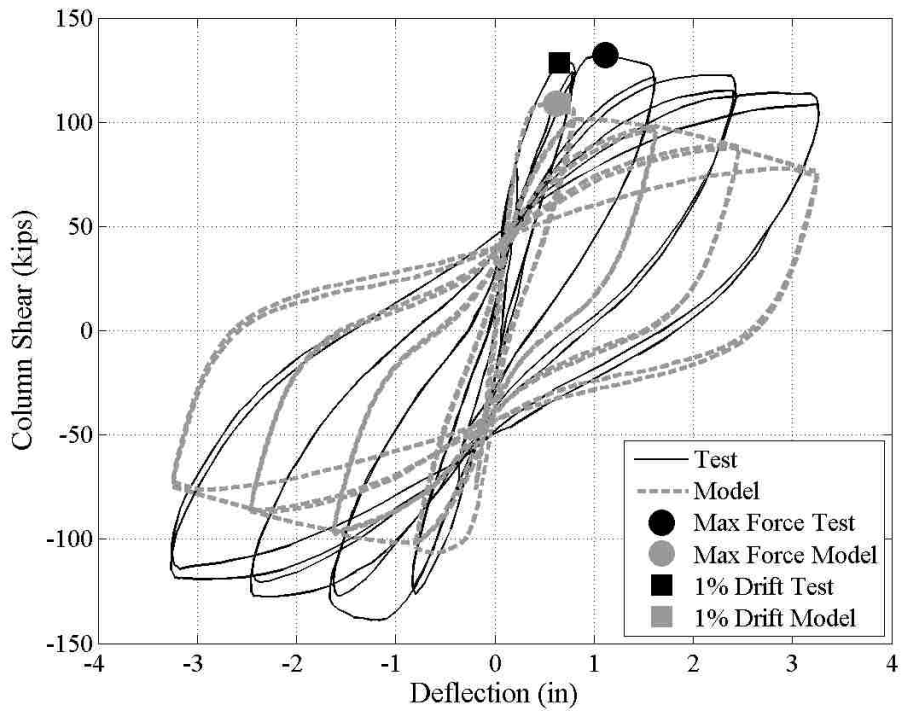
C.3 IMF Column Simulation Plots



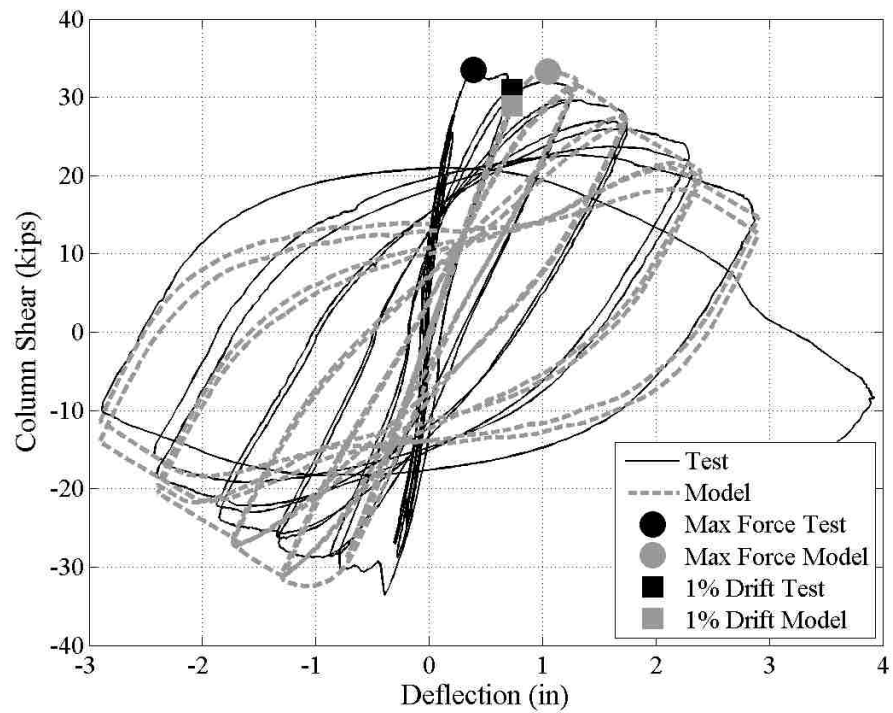
Appendix Figure C.10 Gill et al. 3



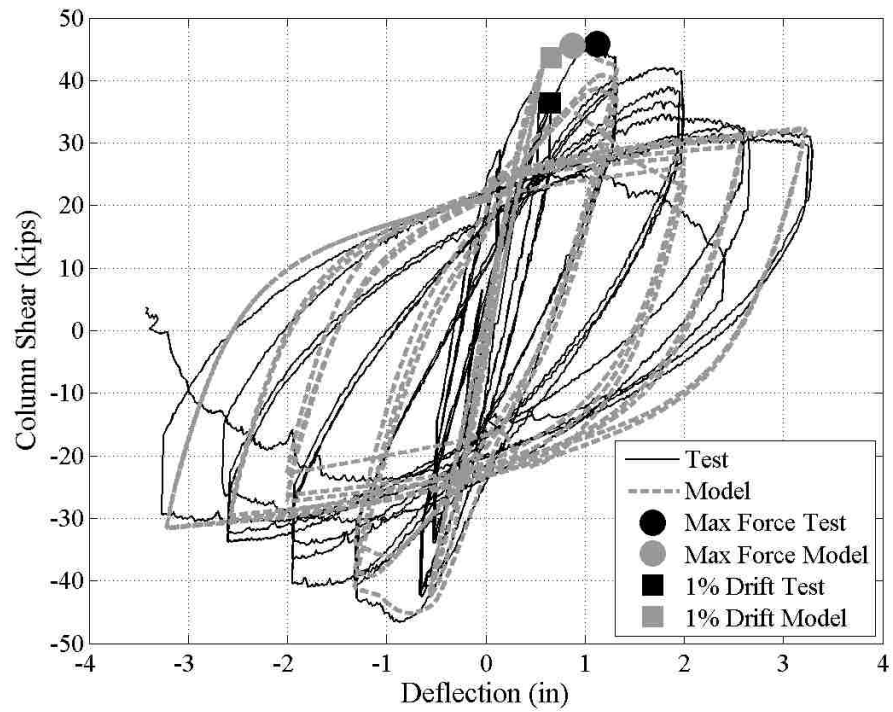
Appendix Figure C.11 Tanaka and Park 1



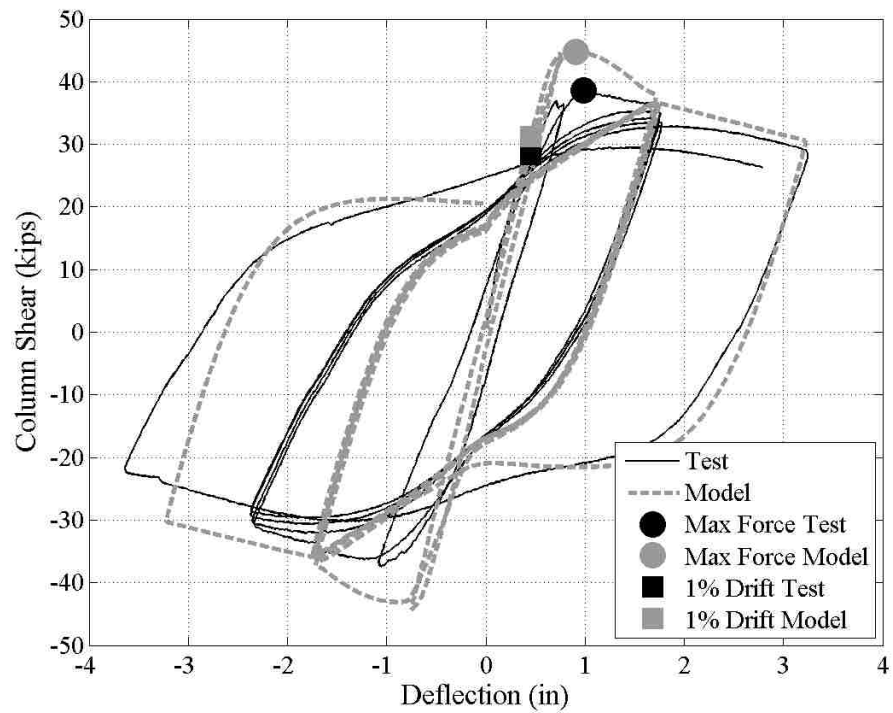
Appendix Figure C.12 Tanaka and Park 7



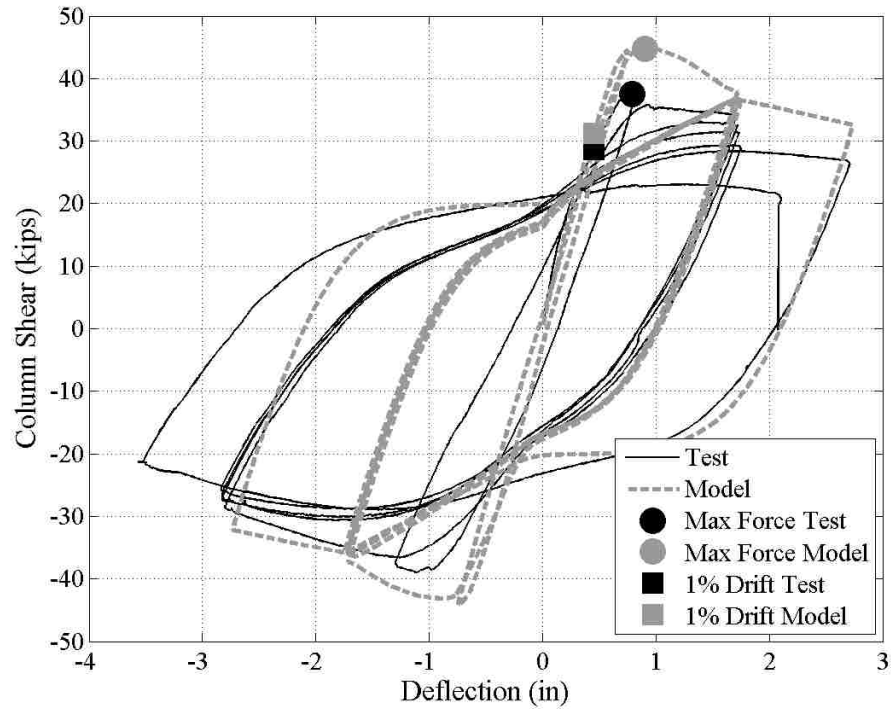
Appendix Figure C.13 Bayrak and Sheikh AS-2HT



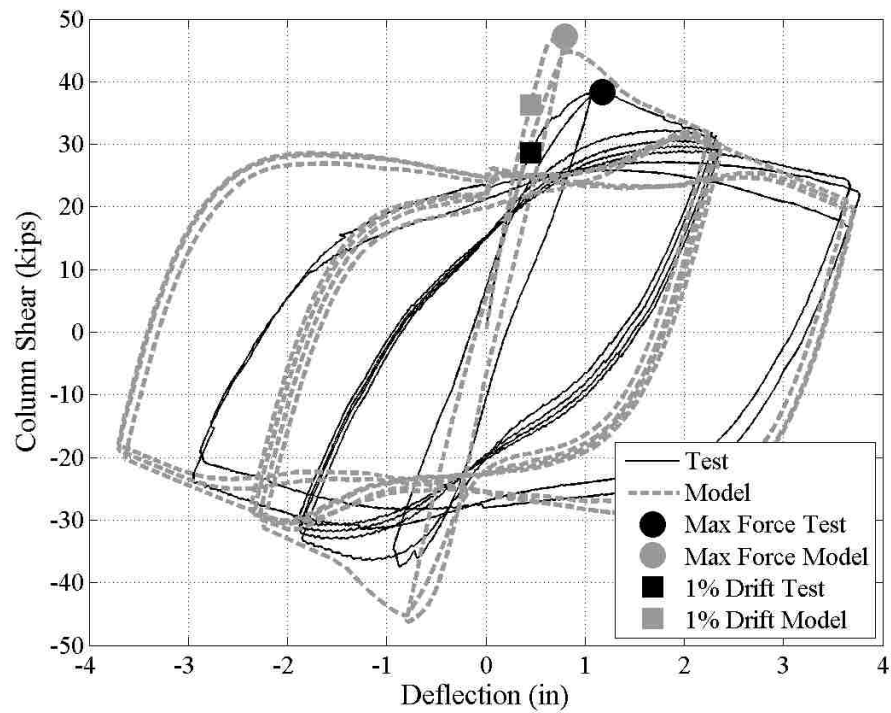
Appendix Figure C.14 Saatcioglu and Grira BG-4



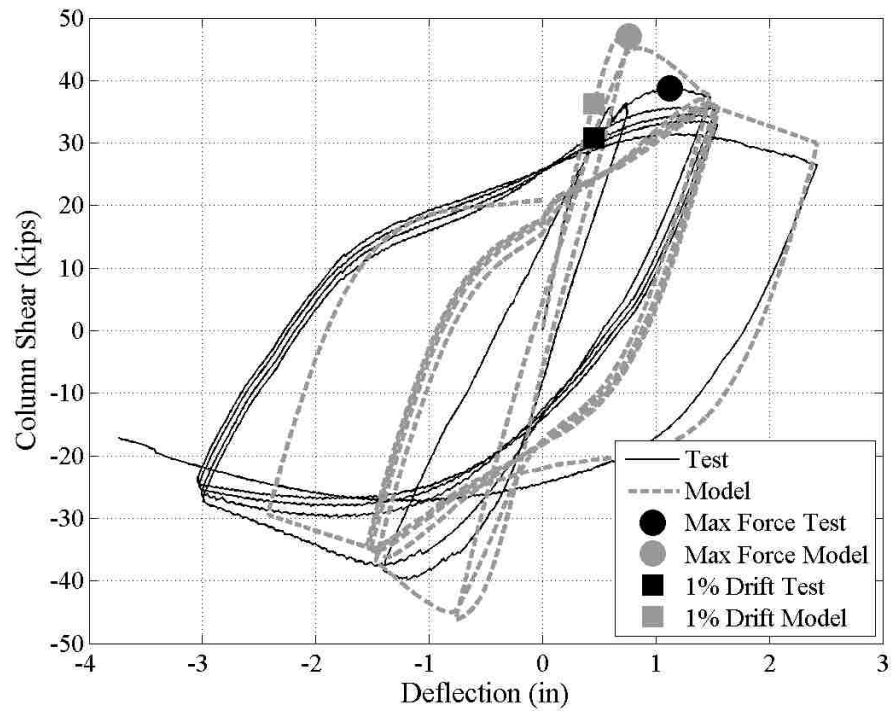
Appendix Figure C.15 Galeota et al. CB1



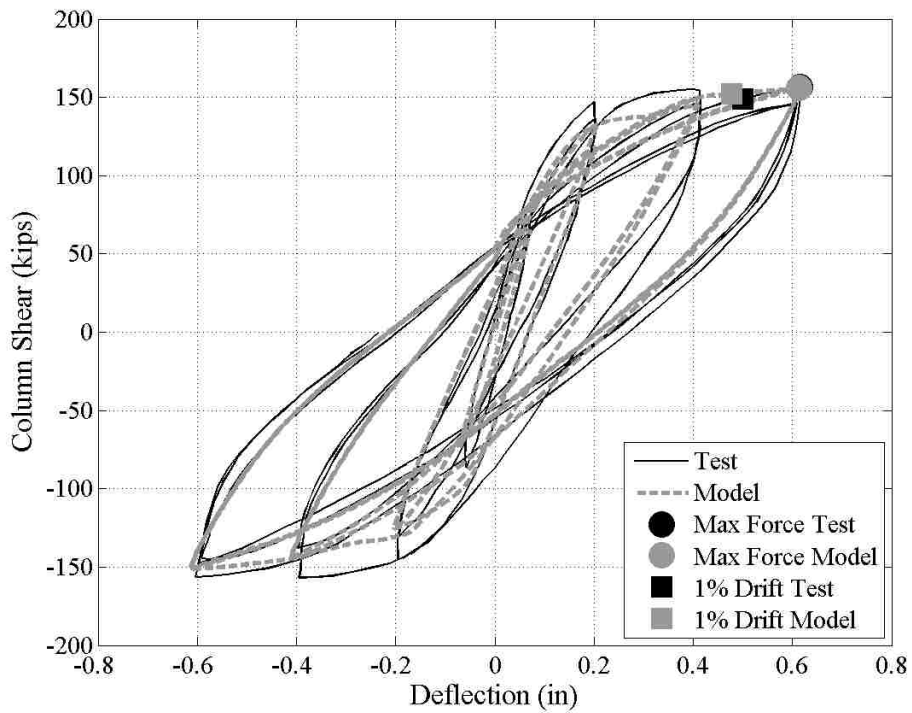
Appendix Figure C.16 Galeota et al. CB2



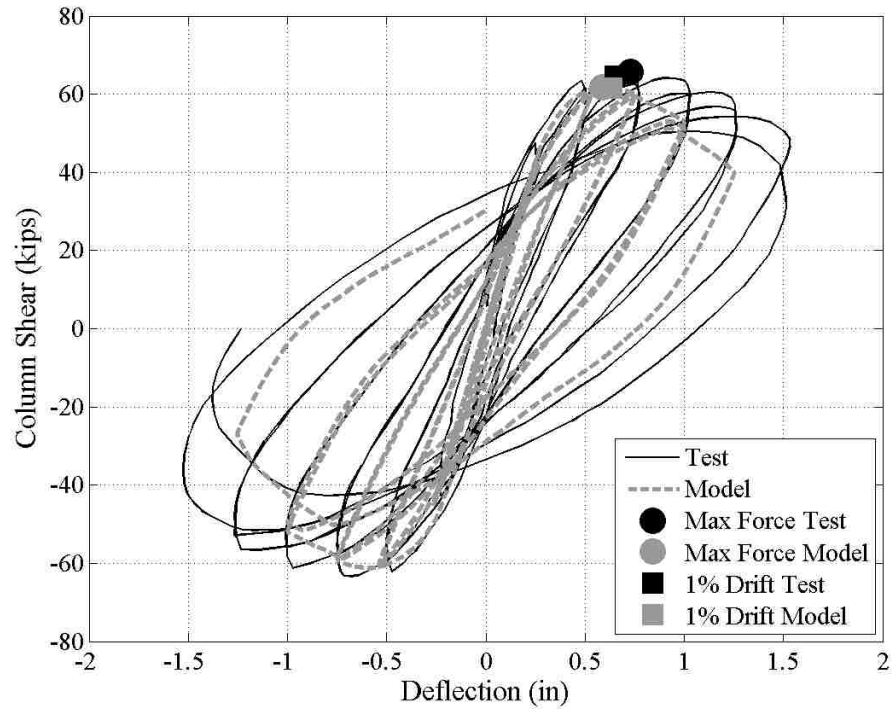
Appendix Figure C.17 Galeota et al. CB3



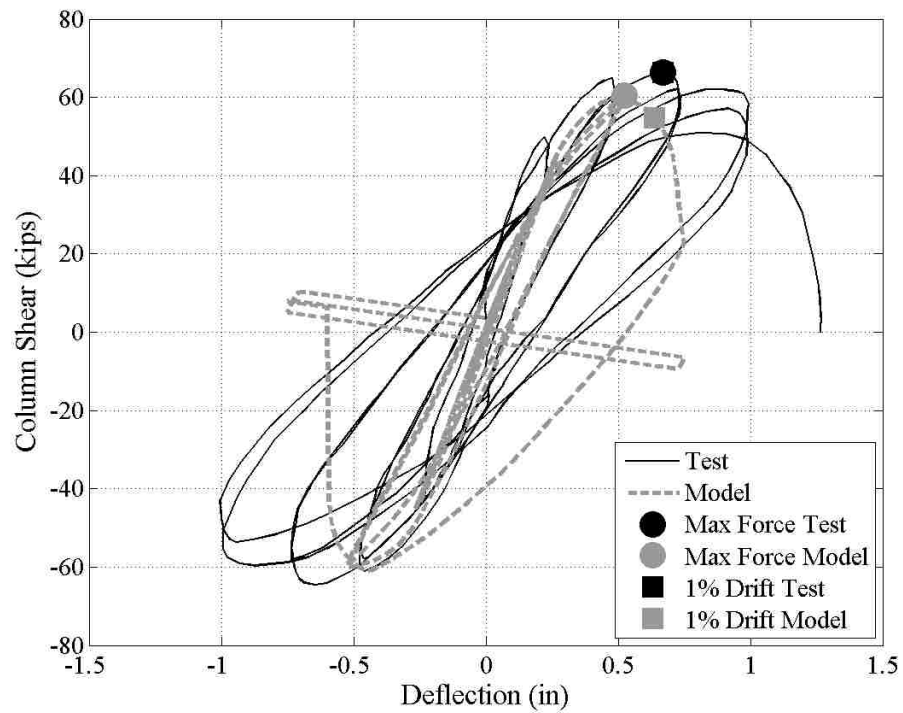
Appendix Figure C.18 Galeota et al. CB4



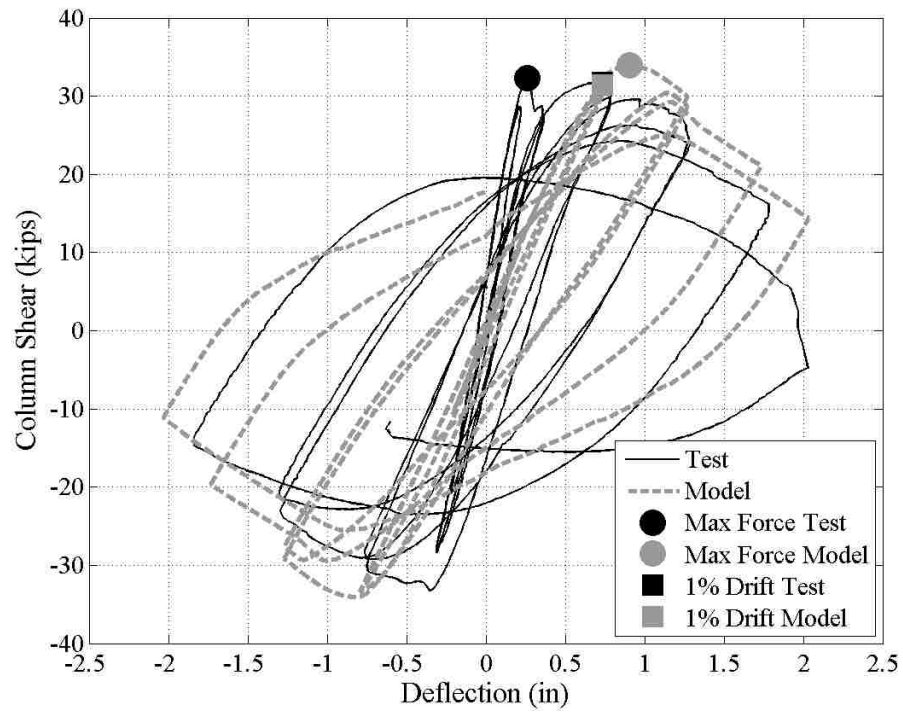
Appendix Figure C.19 Gill et al. 4



Appendix Figure C.20 Watson and Park 5

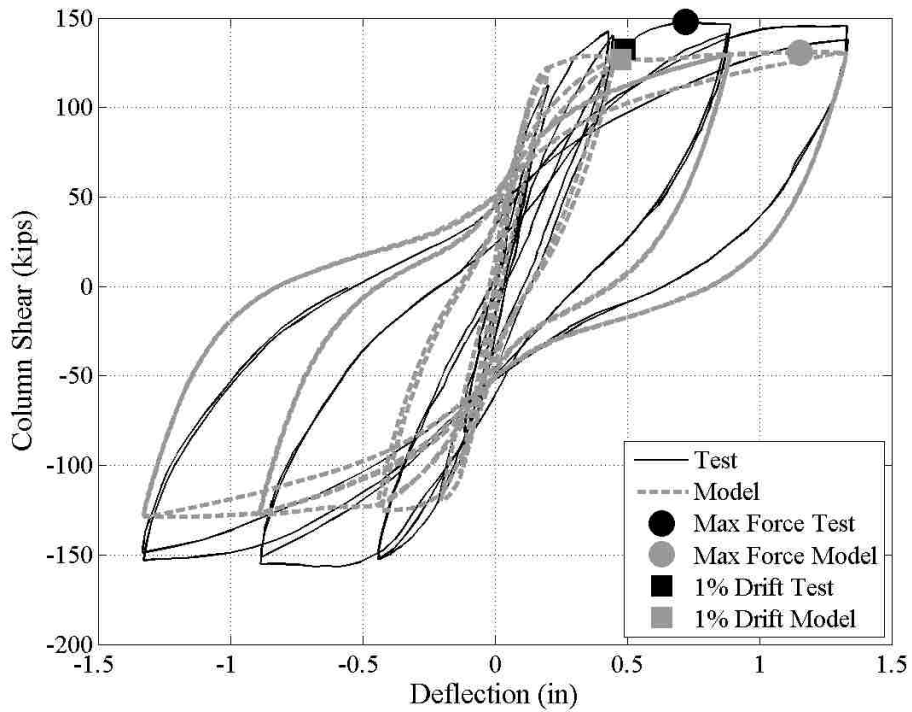


Appendix Figure C.21 Watson and Park 6

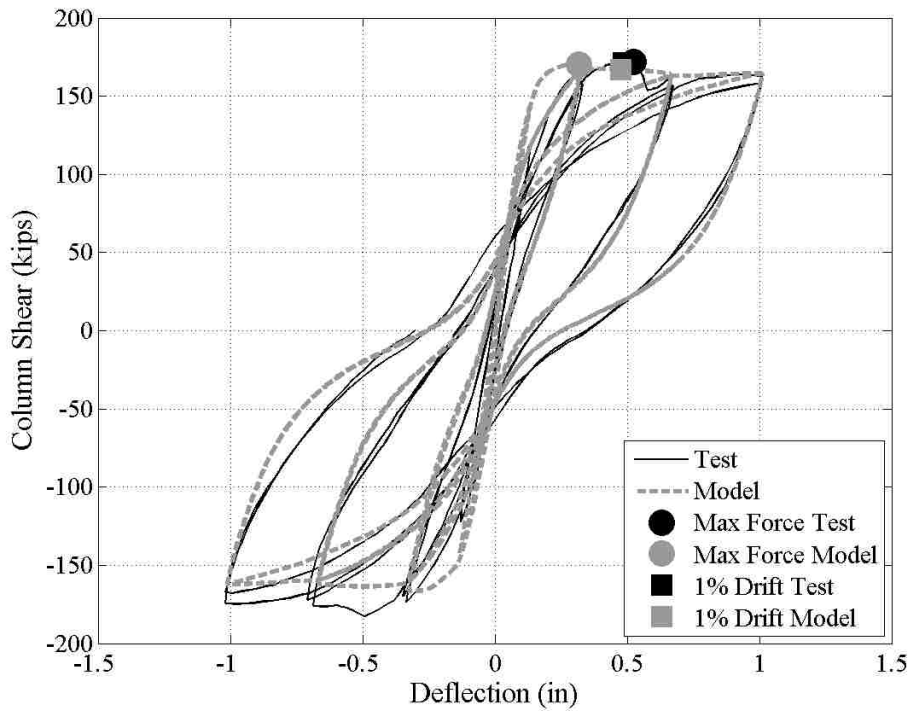


Appendix Figure C.22 Bayrak and Sheikh AS-3HT

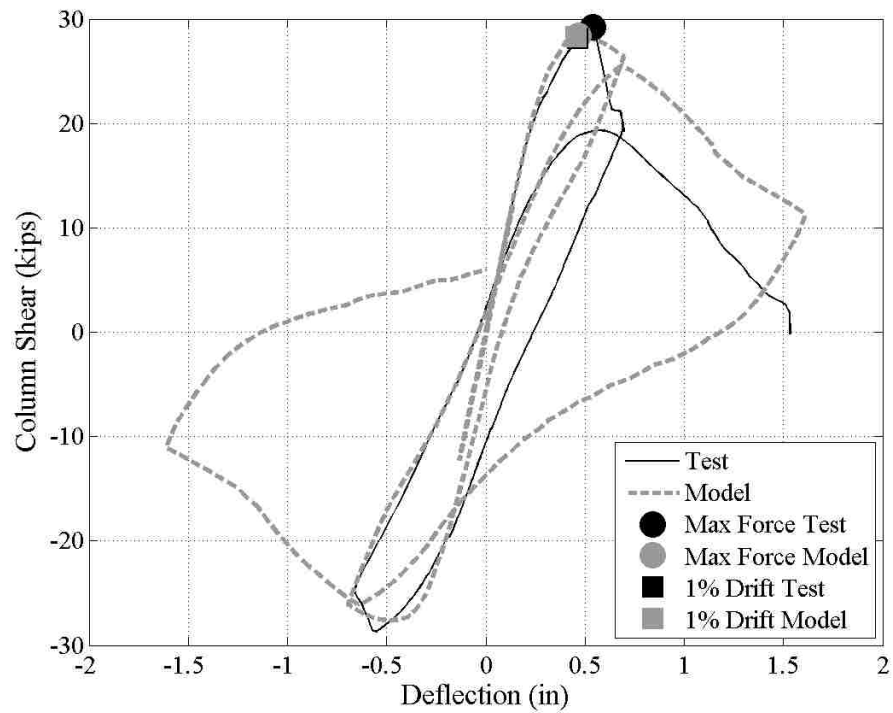
C.4 OMF Column Simulation Plots



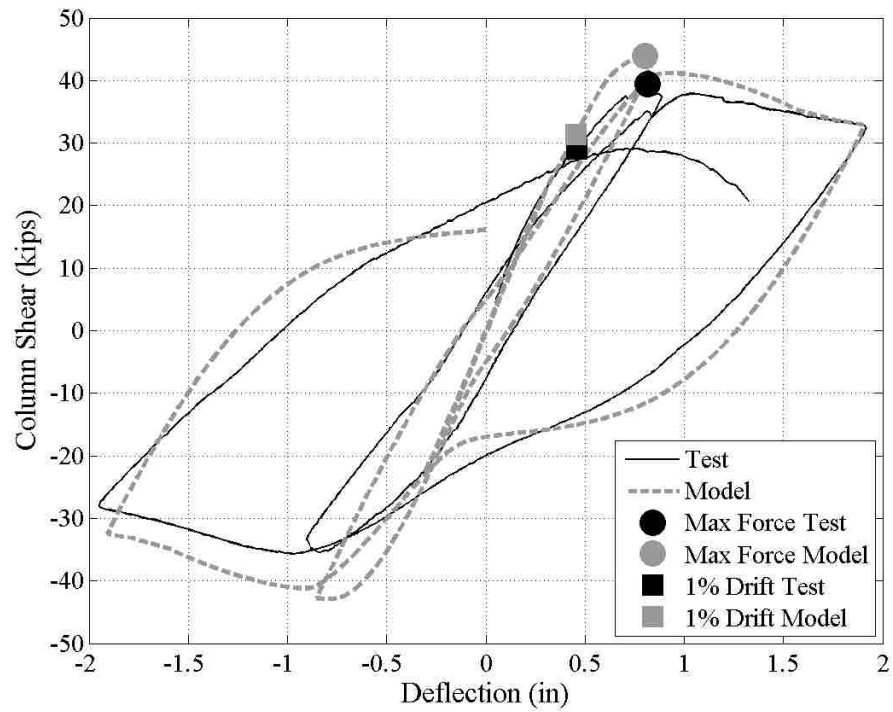
Appendix Figure C.23 Gill et al. 1



Appendix Figure C.24 Gill et al. 2

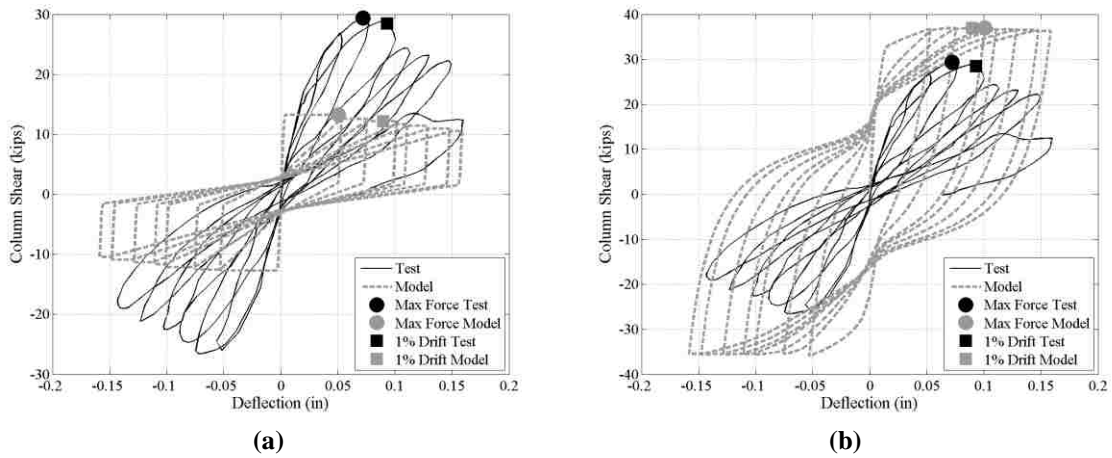


Appendix Figure C.25 Galeota et al. AA1

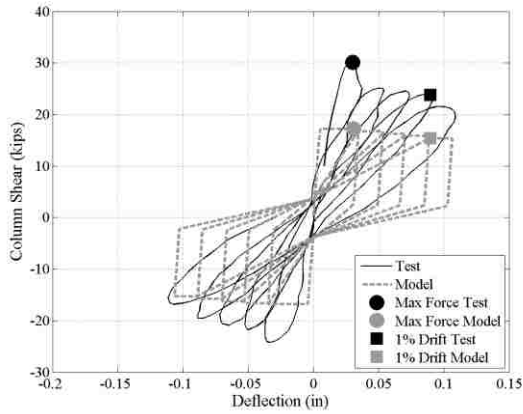


Appendix Figure C.26 Galeota et al. AB1

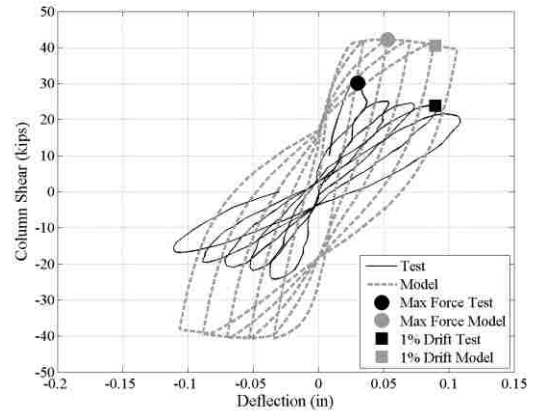
C.5 Shear Failure Simulation Plots



Appendix Figure C.27 Arakawa et al. OA2 (a) Shear (b) No Shear

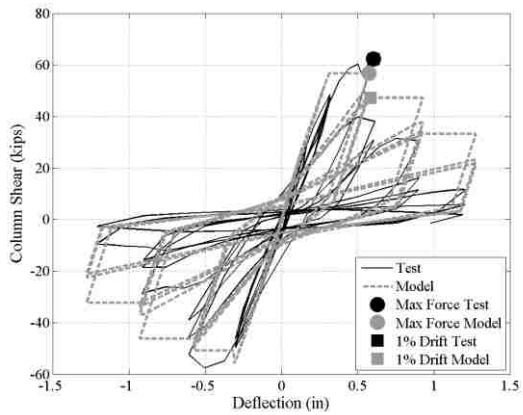


(a)

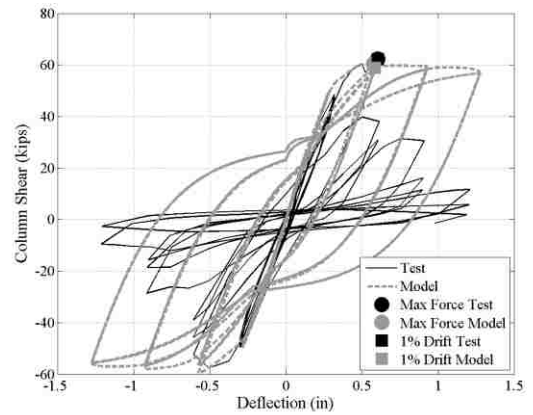


(b)

Appendix Figure C.28 Arakawa et al. OA5 (a) Shear (b) No Shear

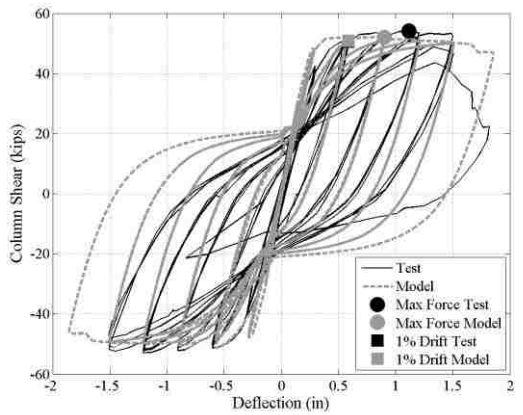


(a)

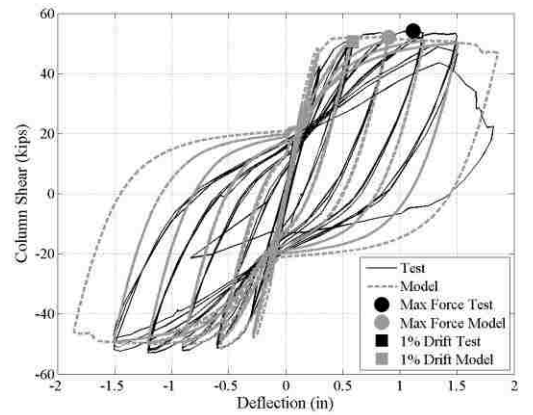


(b)

Appendix Figure C.29 Lynn et al. 3CLH18 (a) Shear (b) No Shear

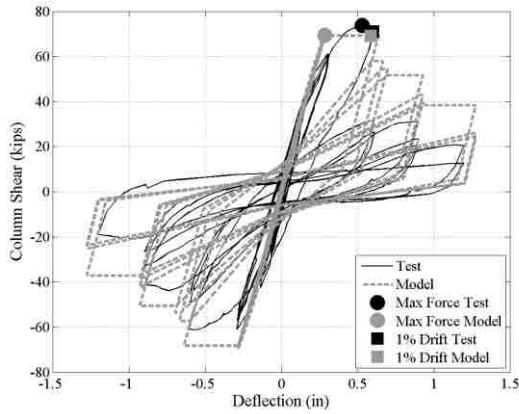


(a)

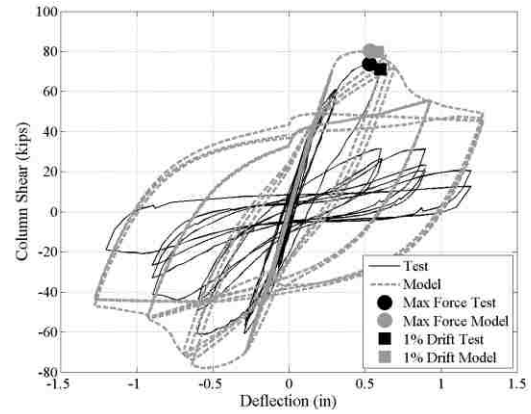


(b)

Appendix Figure C.30 Lynn et al. 2CLH18 (a) Shear (b) No Shear

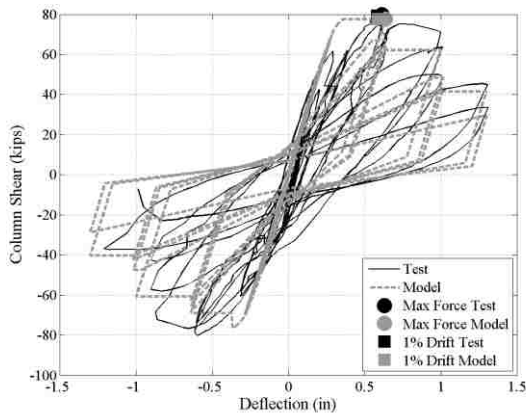


(a)

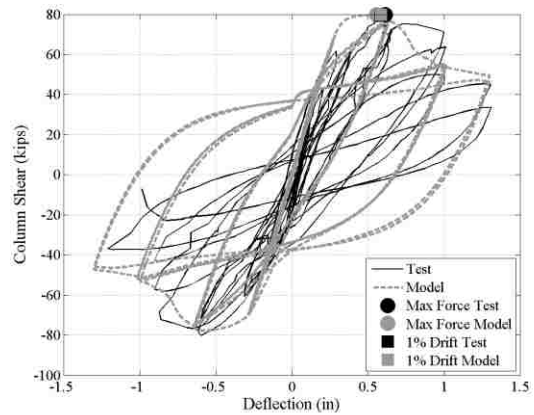


(b)

Appendix Figure C.31 Lynn et al. 3CMH18 (a) Shear (b) No Shear

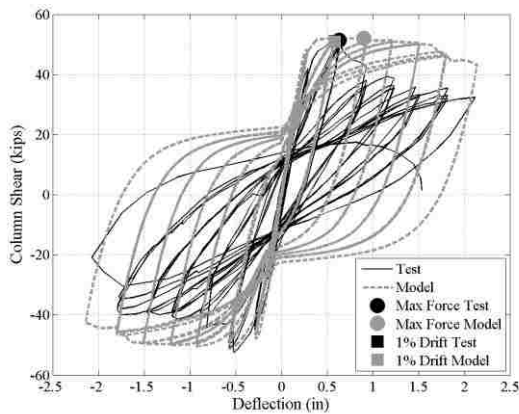


(a)

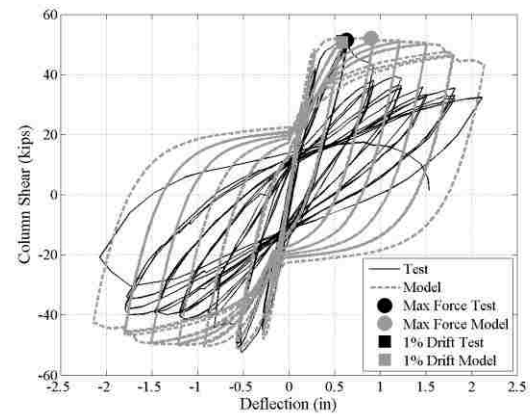


(b)

Appendix Figure C.32 Lynn et al. 3CMD12 (a) Shear (b) No Shear

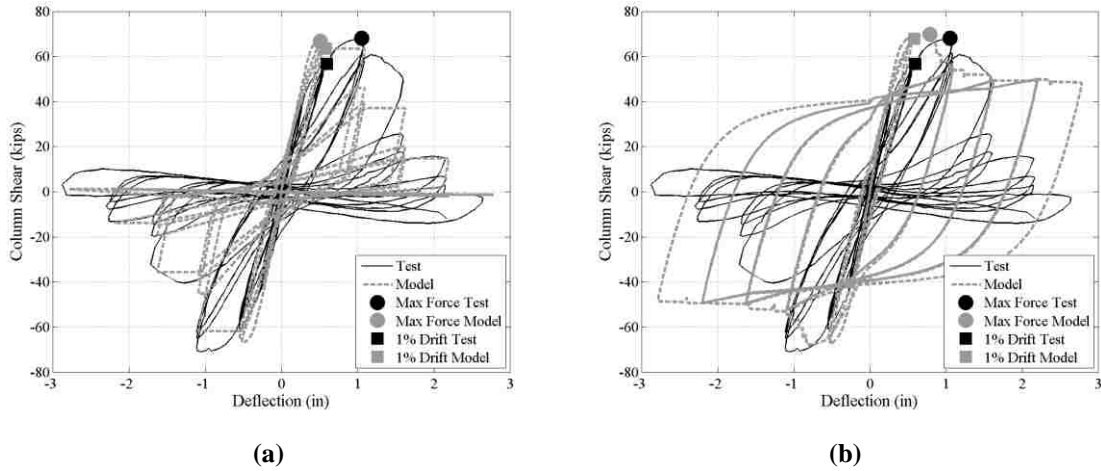


(a)



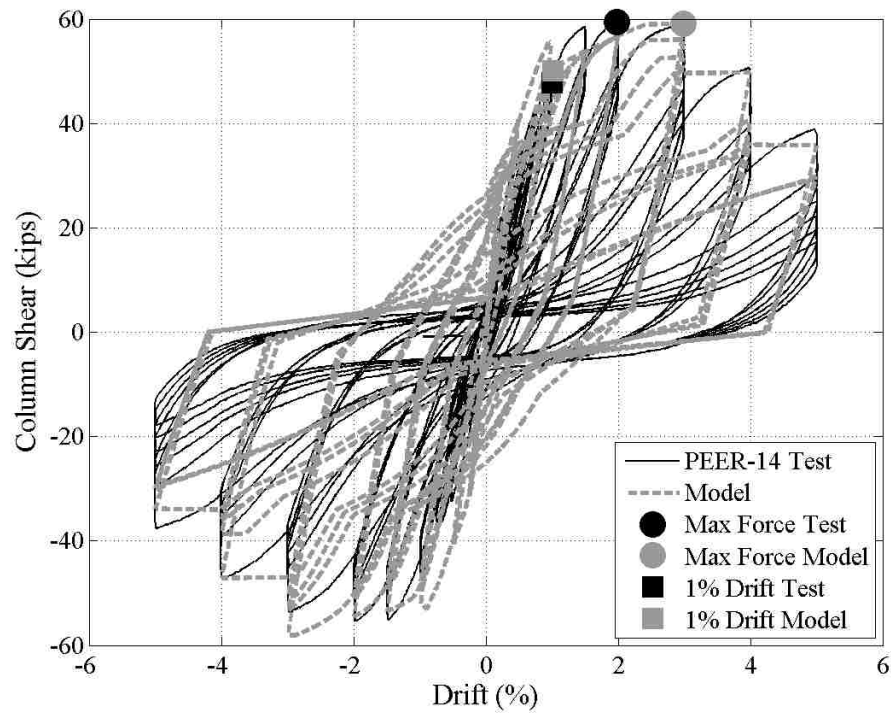
(b)

Appendix Figure C.33 Lynn et al. 2SLH18 (a) Shear (b) No Shear

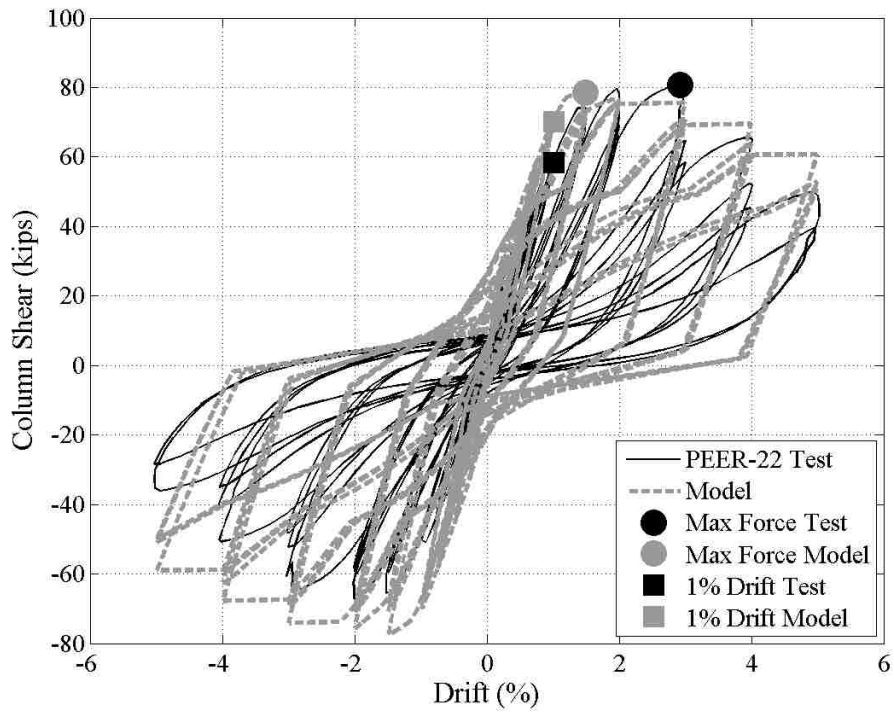


Appendix Figure C.34 Sezen and Moehle No. 1 (a) Shear (b) No Shear

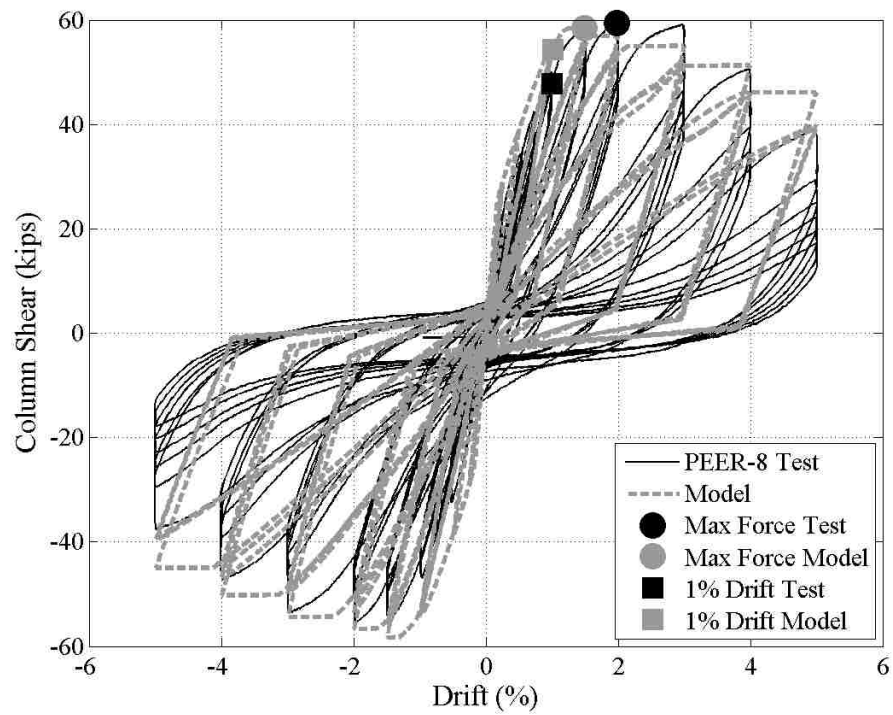
C.6 Older RC Interior Joint Simulation Plots



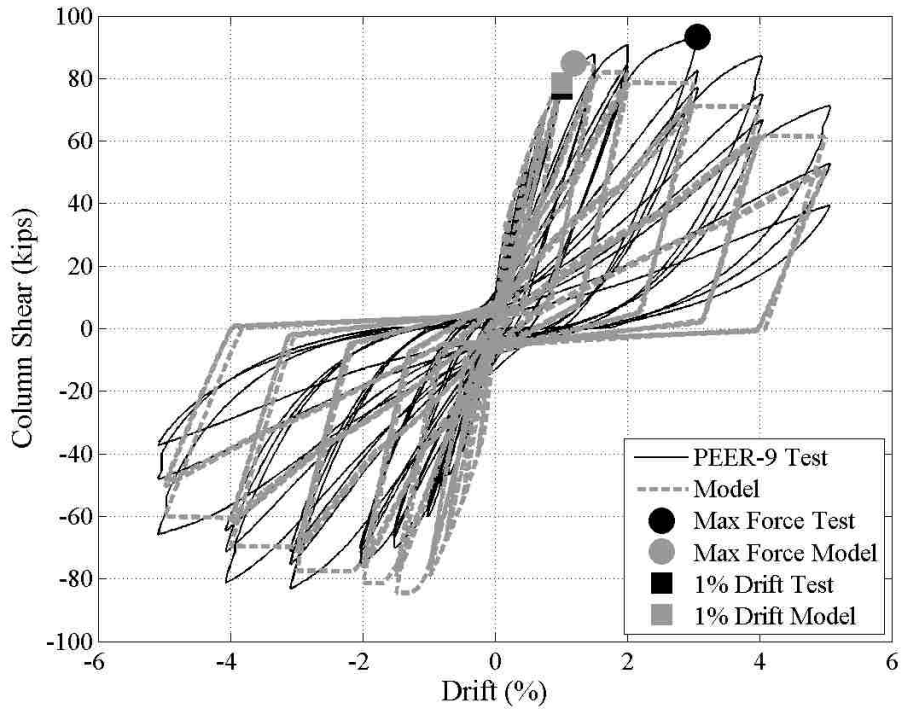
Appendix Figure C.35 Walker PEER14



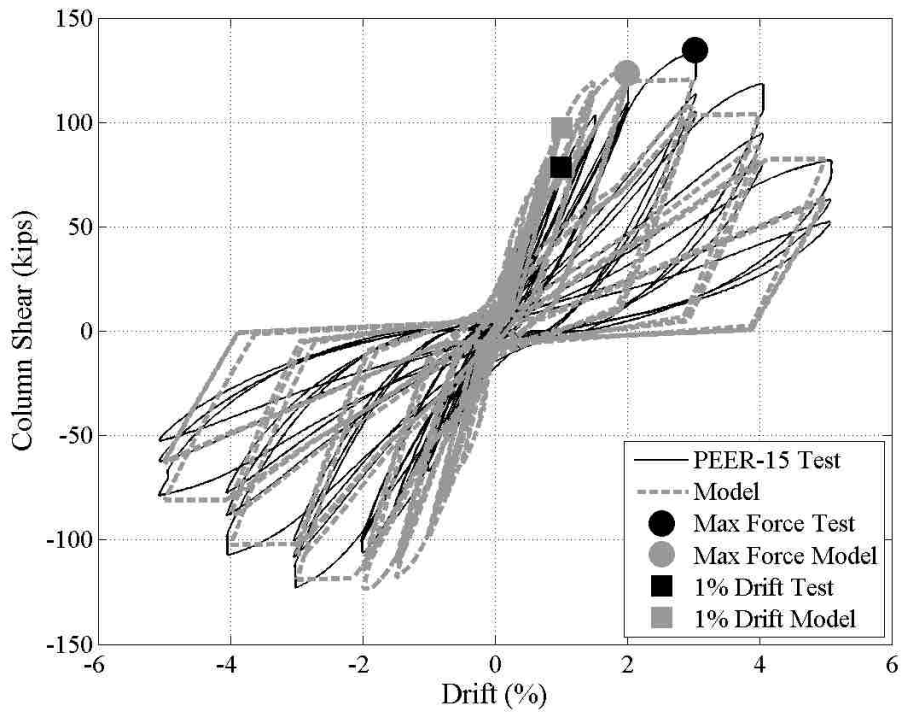
Appendix Figure C.36 Walker PEER22



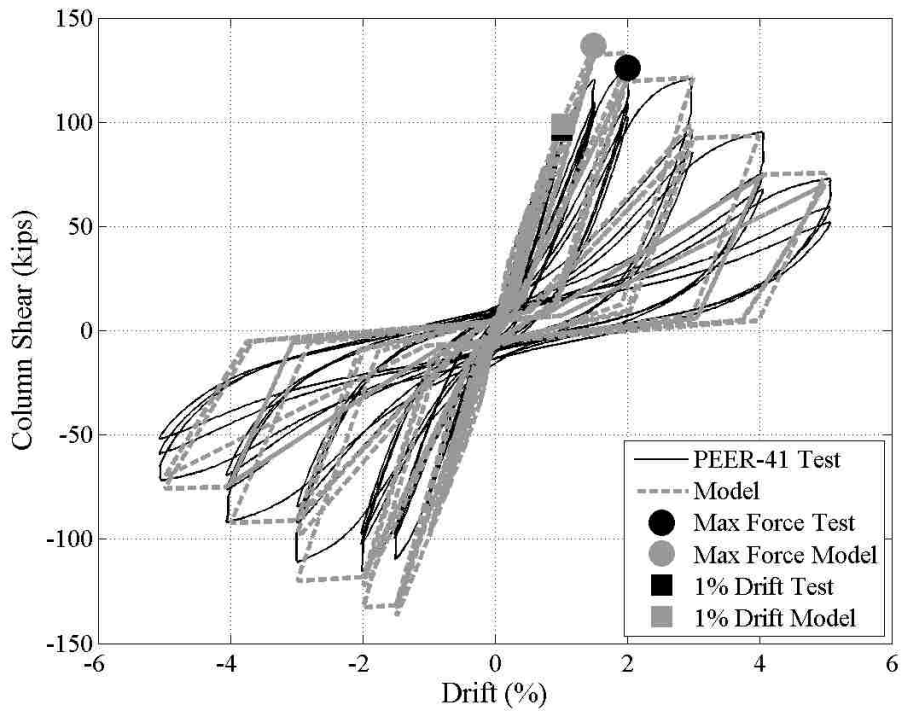
Appendix Figure C.37 Alire PEER8



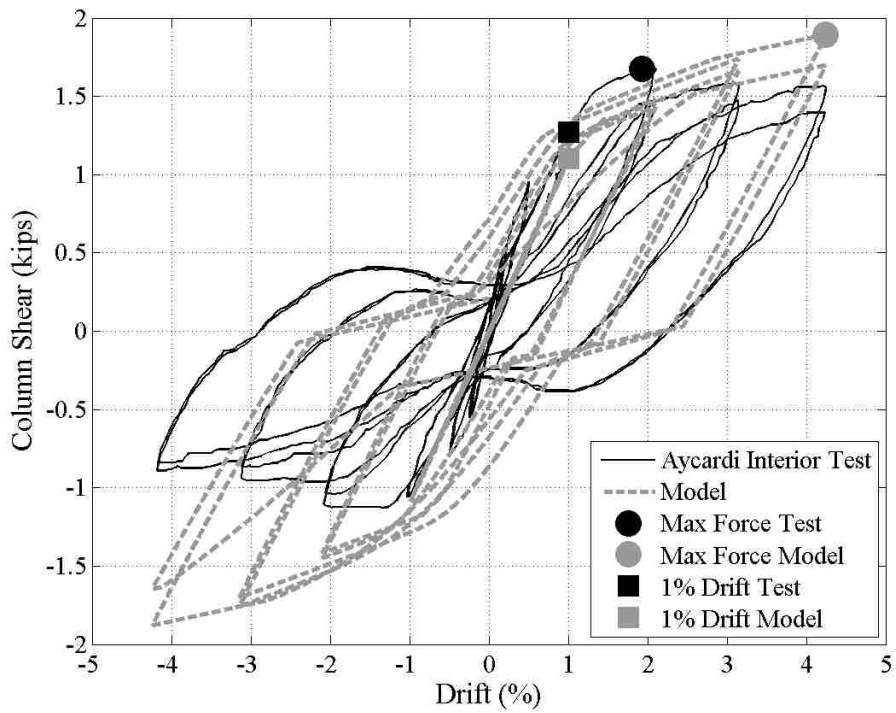
Appendix Figure C.38 Alire PEER9



Appendix Figure C.39 Alire PEER15

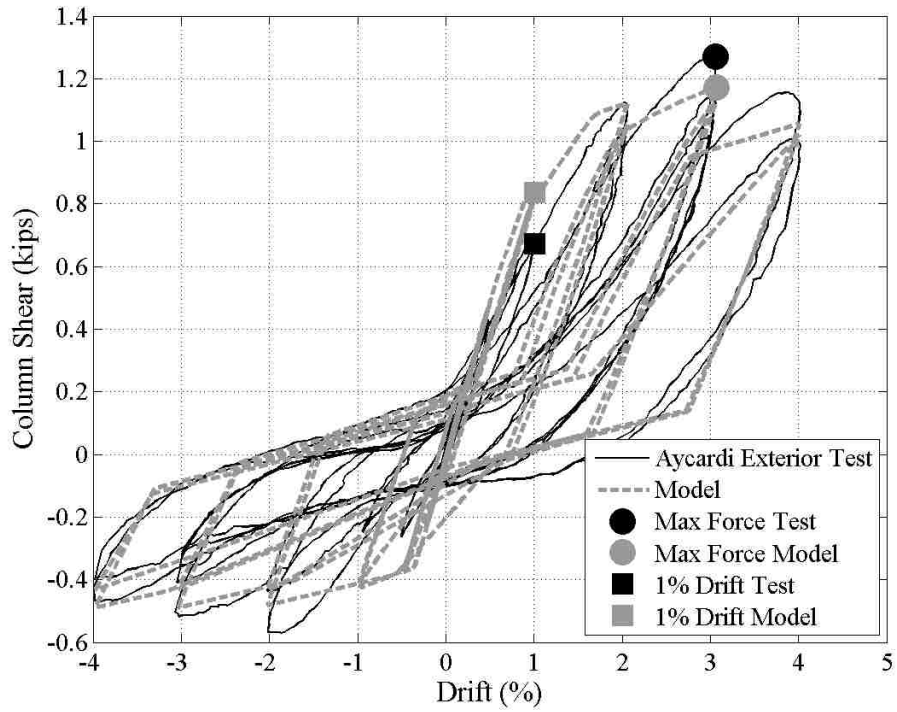


Appendix Figure C.40 Alire PEER41

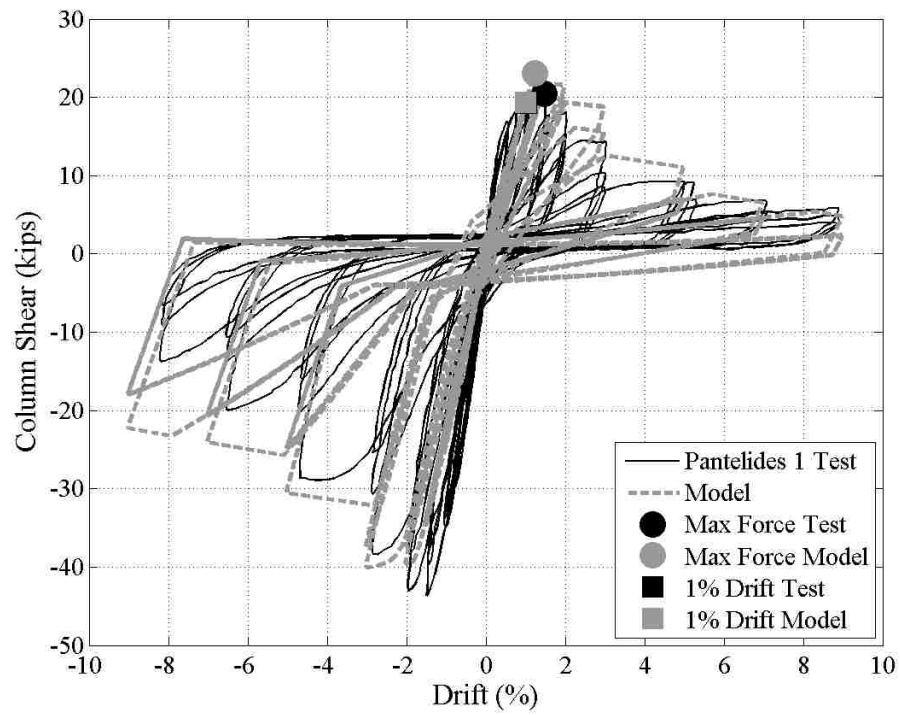


Appendix Figure C.41 Aycardi et al.

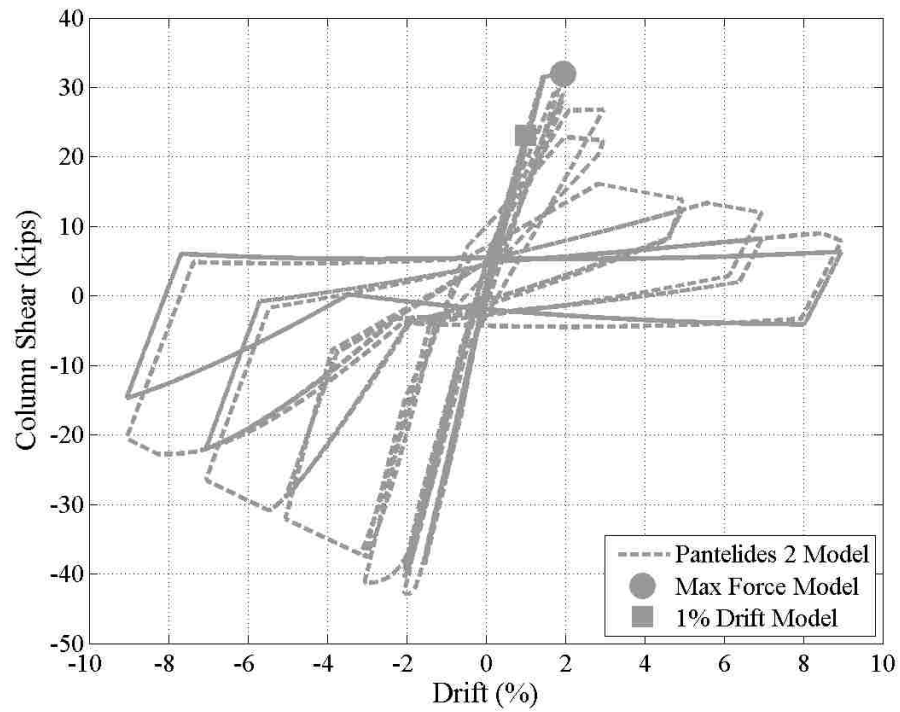
C.7 Older RC Exterior Joint Simulation Plots



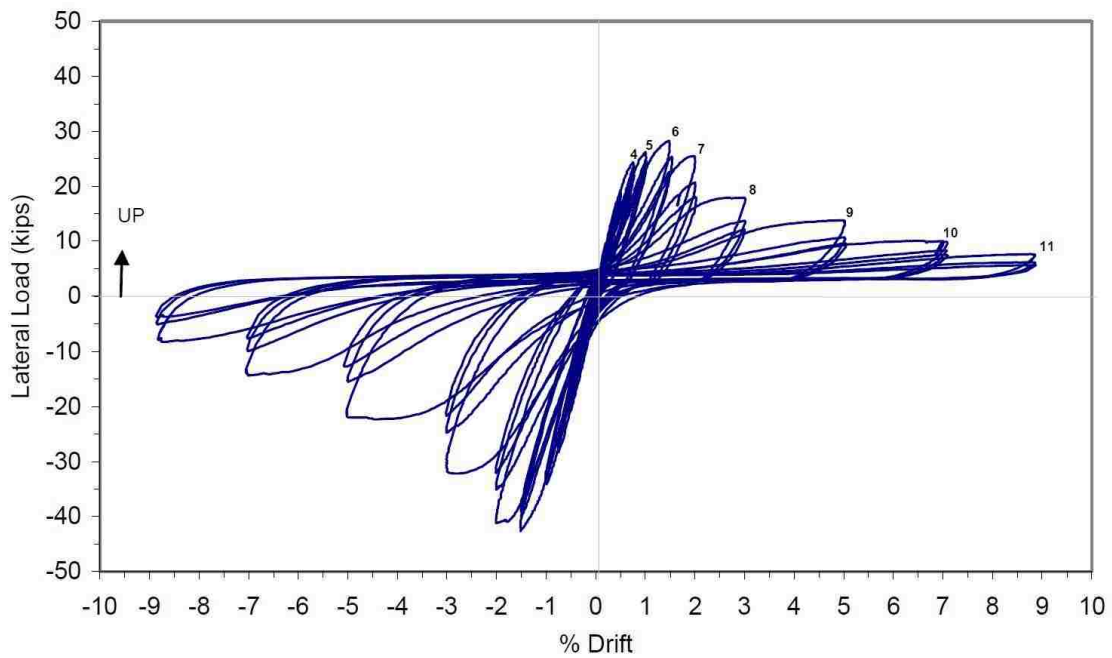
Appendix Figure C.42 Aycardi et al.



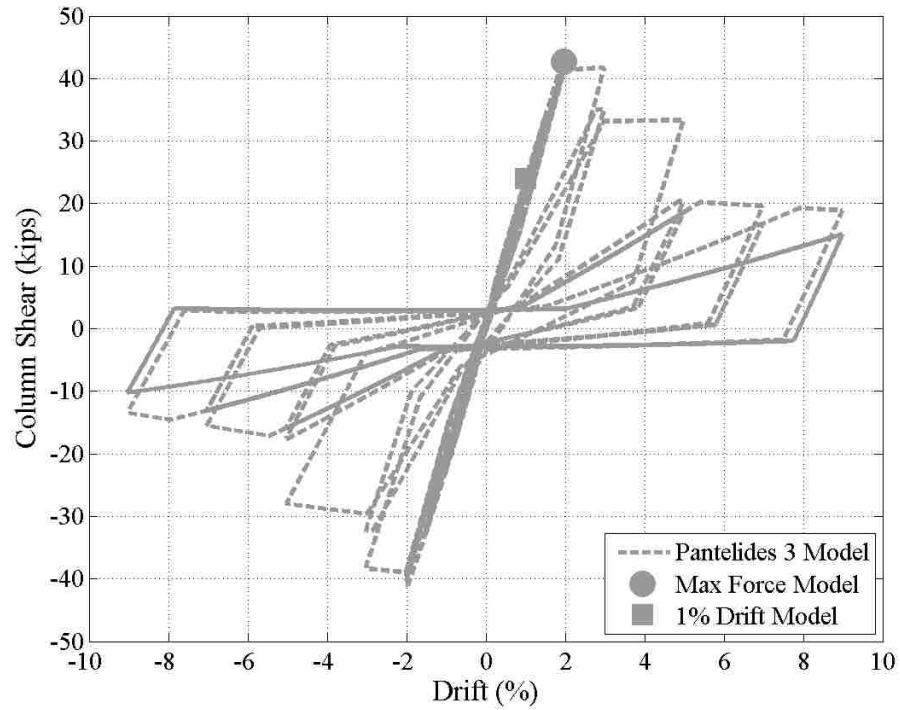
Appendix Figure C.43 Pantelides et al. 1



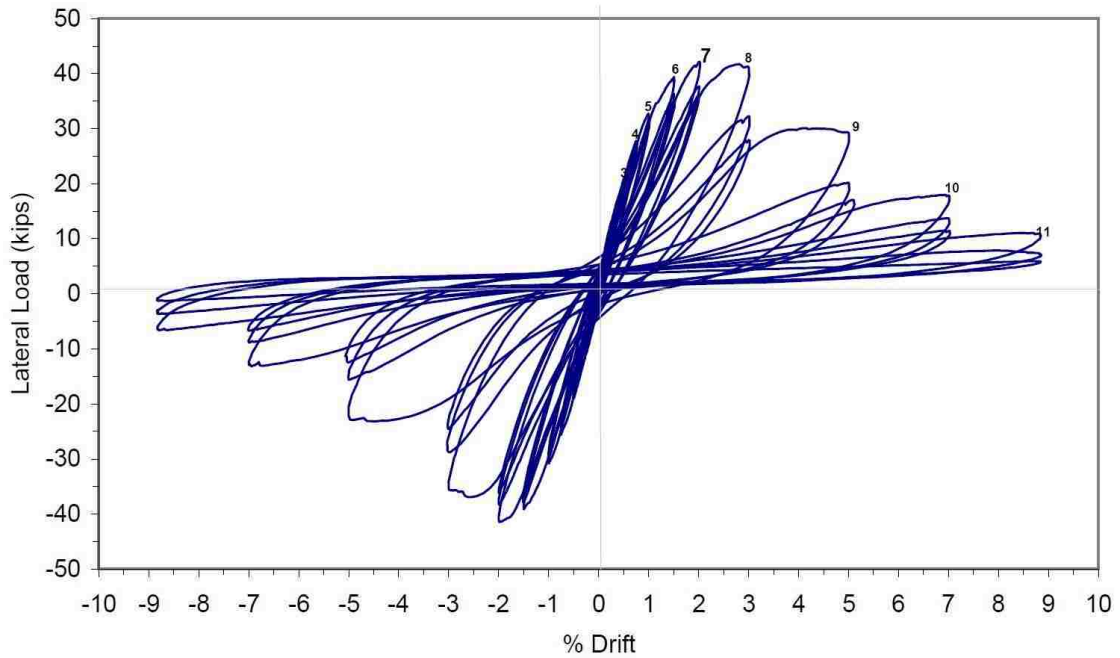
Appendix Figure C.44 Pantelides et al. 2: Model



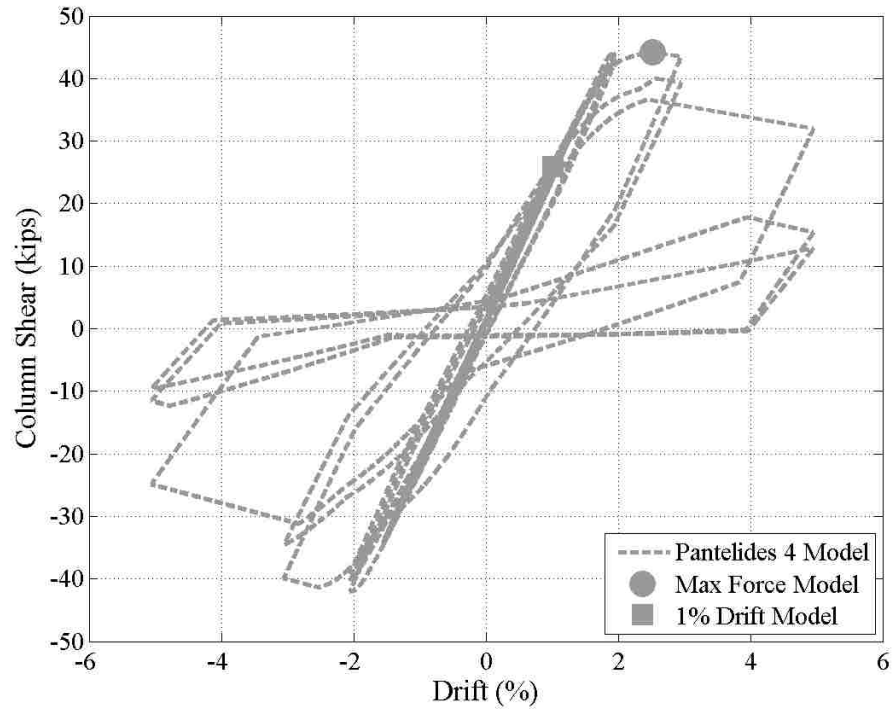
Appendix Figure C.45 Pantelides et al. 2: Experiment



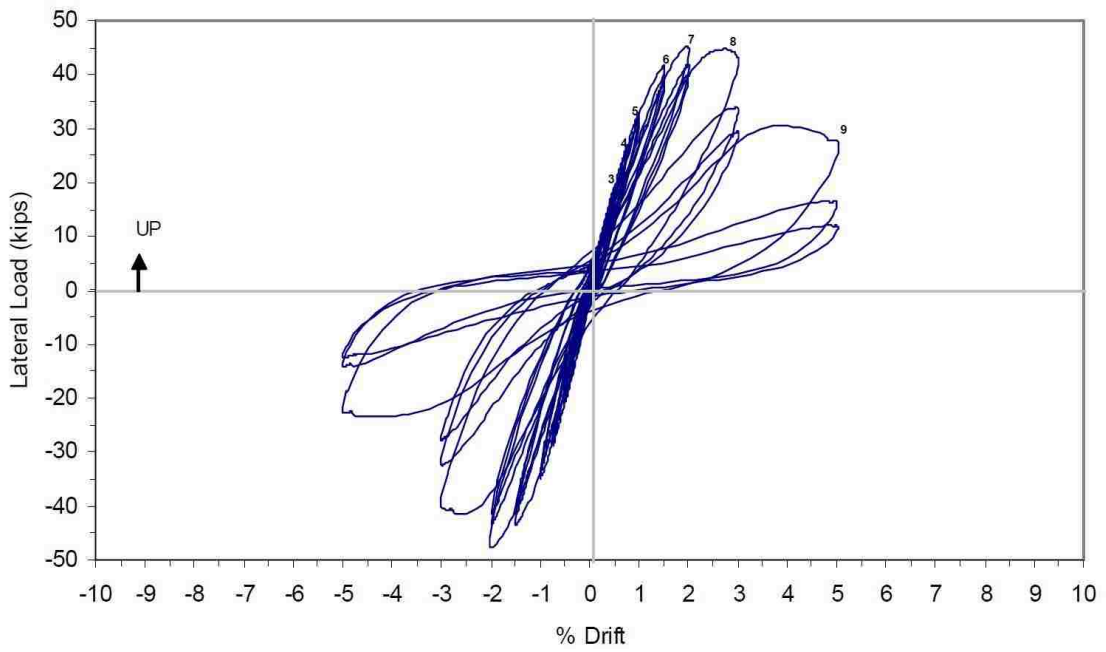
Appendix Figure C.46 Pantelides et al. 3: Model



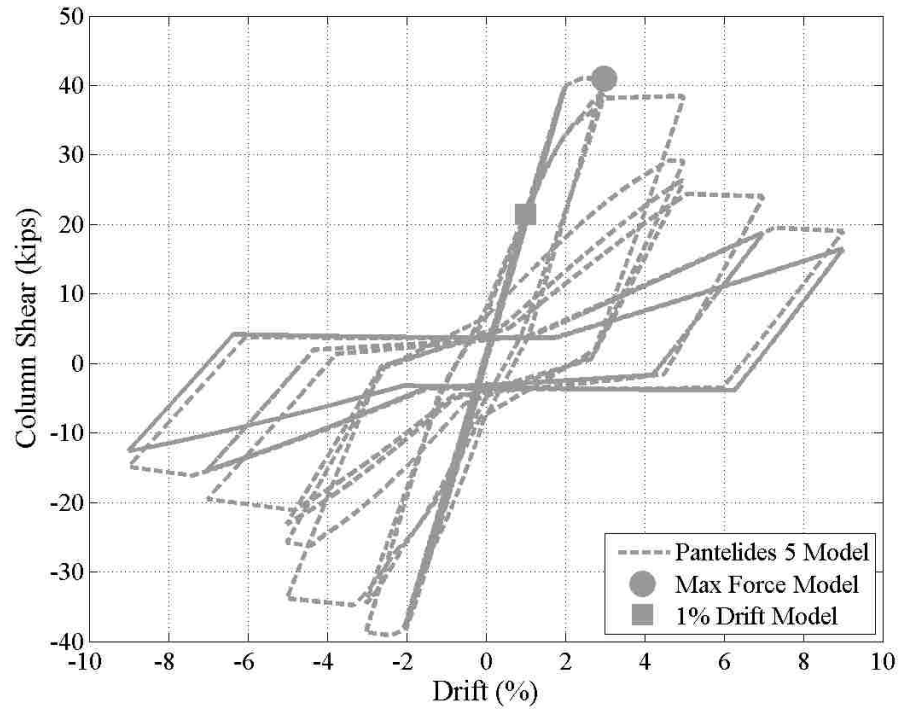
Appendix Figure C.47 Pantelides et al. 3: Experiment



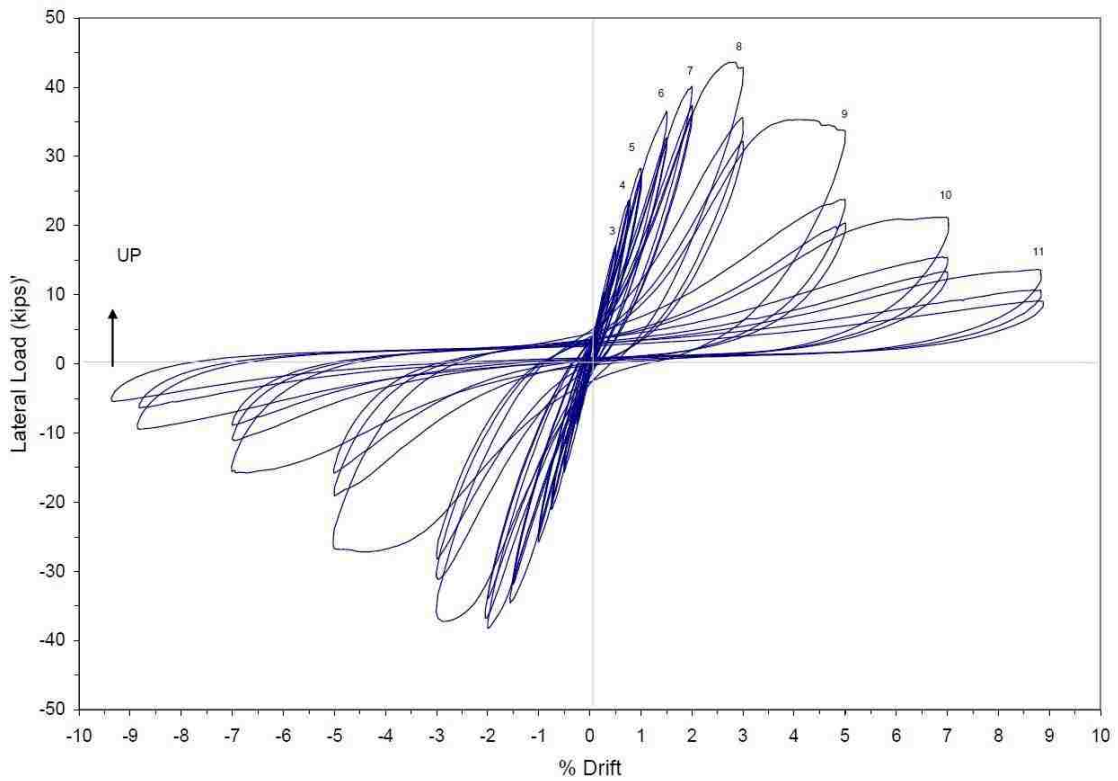
Appendix Figure C.48 Pantelides et al. 4: Model



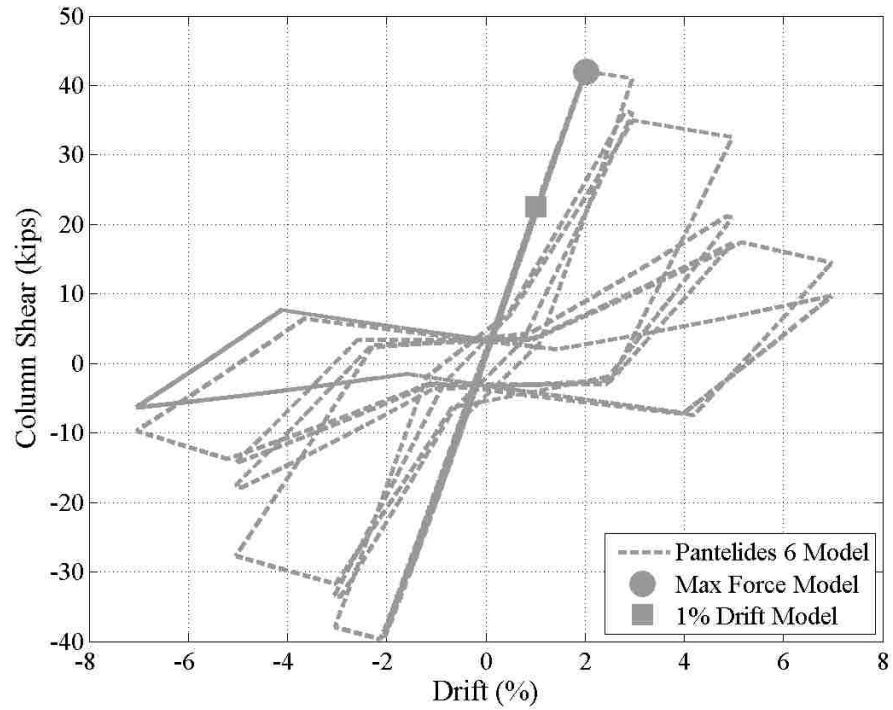
Appendix Figure C.49 Pantelides et al. 4: Experiment



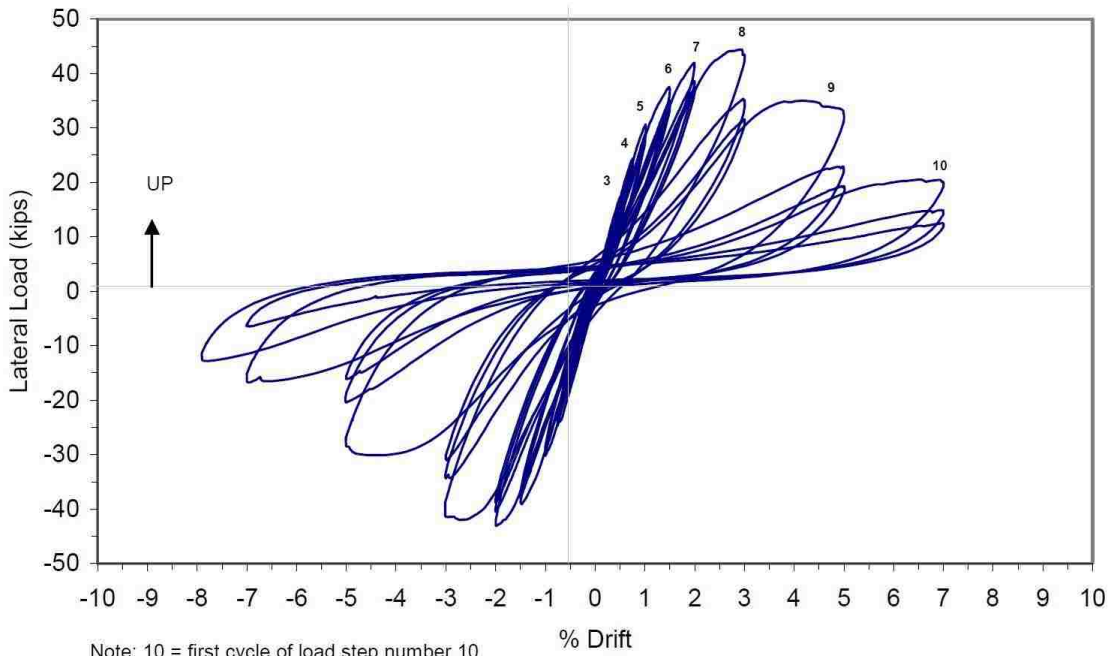
Appendix Figure C.50 Pantelides et al. 5: Model



Appendix Figure C.51 Pantelides et al. 5: Experiment



Appendix Figure C.52 Pantelides et al. 6: Model



Note: 10 = first cycle of load step number 10

Appendix Figure C.53 Pantelides et al. 6: Experiment

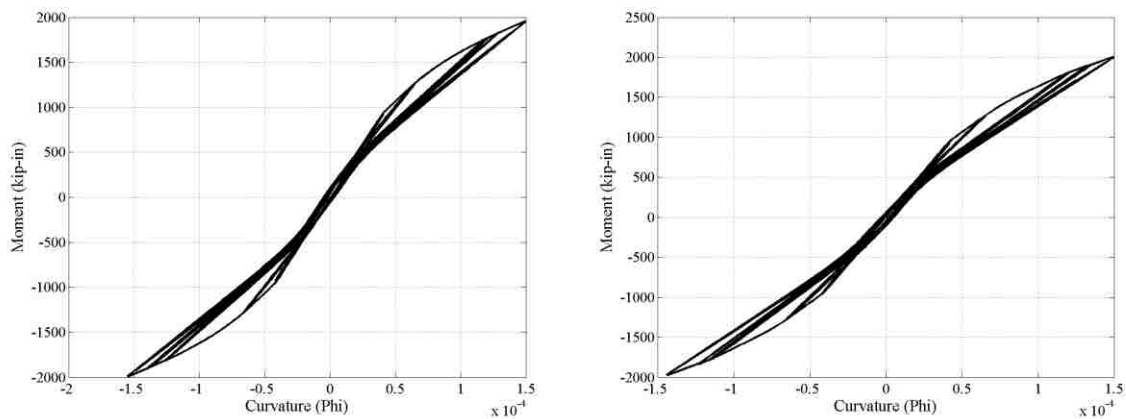
C.8 Joint Experimental Observations and Analysis Discussion

Interior Joints

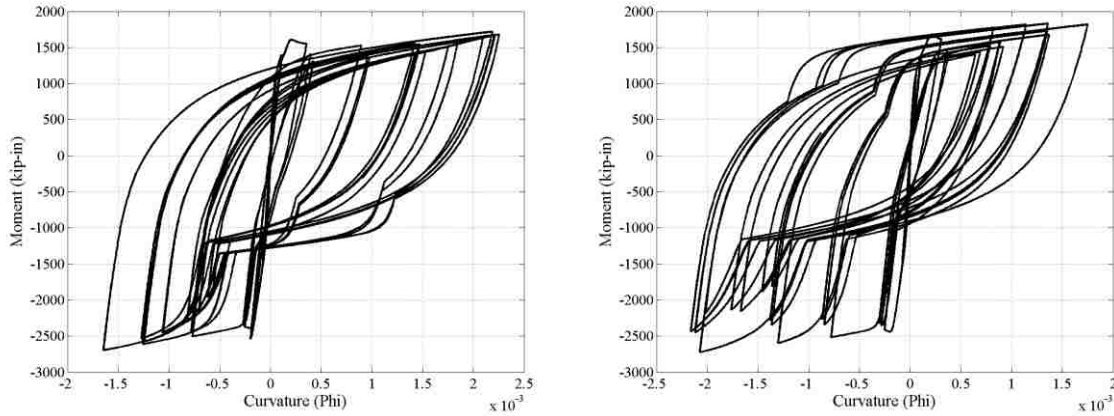
PEER 14 Experimental Damage Propagation

First cracks at the beam-column interface occurred during the first cycle to 0.25% drift. Initial joint cracking occurred at the 0.5% drift level. Positive loading caused the joint cracking. Limited additional joint cracking occurred during negative loading. No residual cracking at 0.5% drift levels. Beam cracks lengthened when the drift level was increased to 0.75%. Additional joint cracking occurred. Longitudinal beam reinforcement yielded at the 1% drift cycle. Concrete flaking was observed at the joint center. The cycle to 1.5% caused a significant reduction to the stiffness of the column shear-drift response. A photograph in the thesis (Walker 2001) shows the joint region after the drift cycles to 1.5%. No significant change to the damage occurred during the 2% drift cycles. At the end of the 3% drift cycles approximately 30% of the joint area had spalled. A photograph in the thesis shows the joint region after the 3% drift cycles. The 4% drift cycles caused exposure of 3 inches of the center longitudinal column bar at the joint's mid height. Spalling continued into the core of the joint as the three cycles at 4% drift were continued. A photograph was included in the thesis of the damage after the 4% drift cycles. At 5% drift the area and depth of spalling increased to the point which the side bars were exposed. Five cycles were carried out at 5% drift. This concluded the test. A photograph of the specimen was included after the 5% drift cycles. A figure in the thesis provides crack pattern diagrams for the joint to 3.0%. It is a good figure for assessing where damage is occurring.

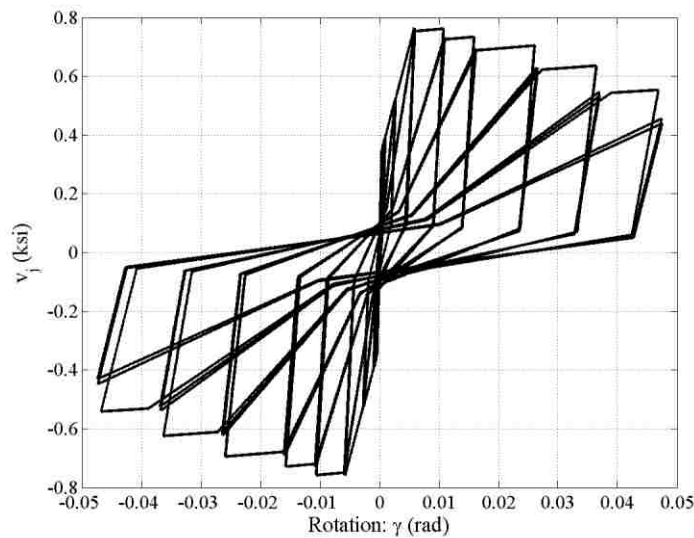
PEER 14 Modeling Observations



Appendix Figure C.54 Upper and Lower Column Moment-Curvature Response



Appendix Figure C.55 Left and Right Beam Moment-Curvature Response



Appendix Figure C.56 Joint Element Response: Joint Shear Stress-Rotation

PEER 14 Experiment vs. Analytical Model Comparison

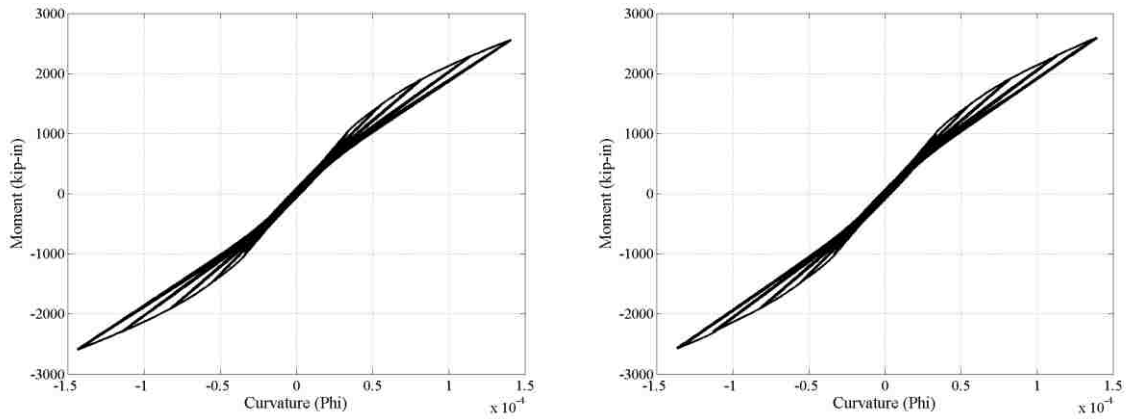
The model response matches the experimental damage. Both the beams and joint experienced inelastic action. The columns remained essentially elastic in both the experimental and analytical results.

PEER 22 Experimental Damage Propagation

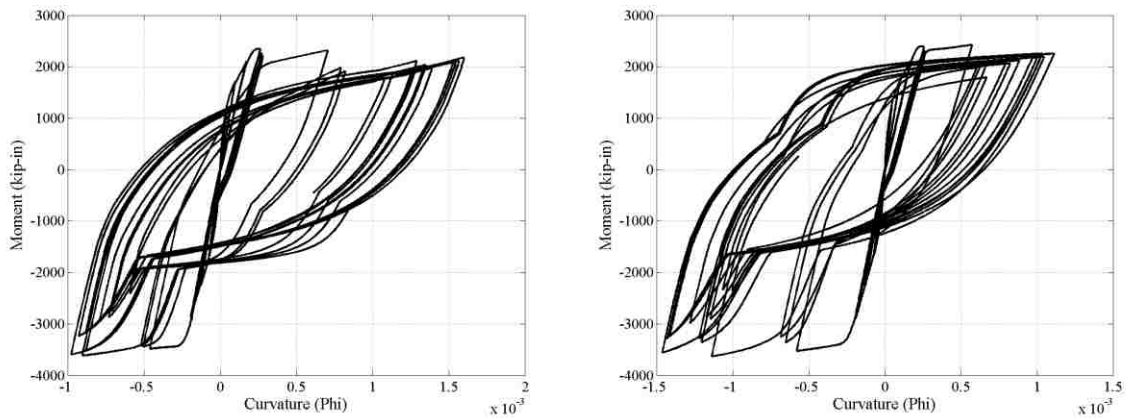
First cracks at the beam-column interface occurred during the first cycle to 0.25% drift. No joint cracks were observed. Initial diagonal joint cracking occurred at the 0.5% drift level. No residual cracking at 0.5% drift levels was observed. Additional beam cracks were observed. No significant increase in damage was observed during the 0.75% drift cycles. No residual cracking was observed. In the first cycle to 1.0% drift a column crack was observed. Joint cracks increased in number and width. At the 1.5% drift cycles minor joint spalling occurred. The longitudinal beam reinforcement yielded at first cycle to 1.5%. Cracking widened in the joint and the beams. A photograph was

included at this drift level. During the 2.0% cycles approximately 10% of the joint area had spalled. The joint crack widths increased while the beam cracking remained the same. A photograph was included showing damage at this drift level. Approximately 80% of the joint had spalled at the end of the 3% drift cycles. Nearly 4 inches of the column longitudinal steel was exposed. Crack widths in the beams remained the same and new damage was concentrated in the joint region. A photograph was included showing damage at this drift level. Corner column bars were exposed at drift cycles to 4%. Cycles to 5% caused buckling of the specimen and over a 20% reduction in lateral load-carrying capacity. This caused the test to be stopped. A photograph was included showing damage at this drift level.

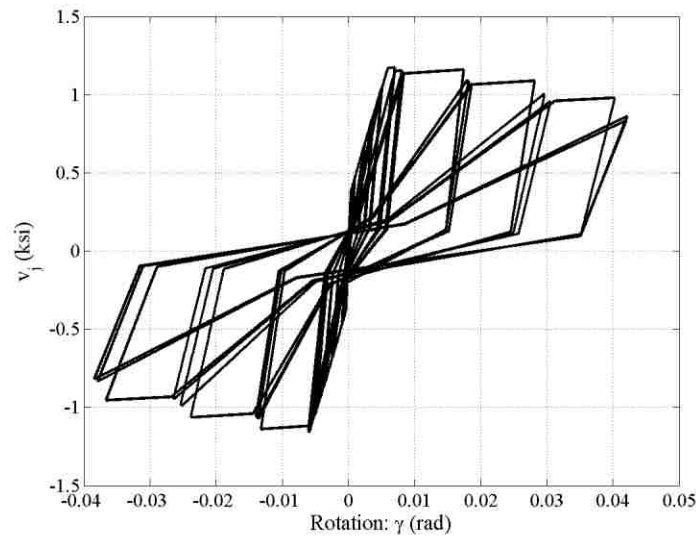
PEER 22 Modeling Observations



Appendix Figure C.57 Upper and Lower Column Moment-Curvature Response



Appendix Figure C.58 Left and Right Beam Moment-Curvature Response



Appendix Figure C.59 Joint Element Response: Joint Shear Stress-Rotation

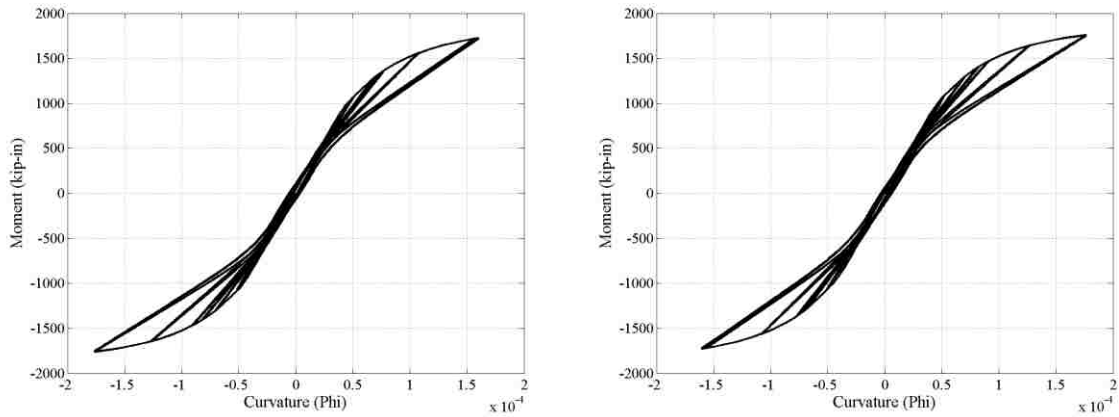
PEER 22 Experiment vs. Analytical Model Comparison

The model response matches the experimental damage. Both the beams and joint experienced inelastic action. The columns remained essentially elastic in both the experimental and analytical results.

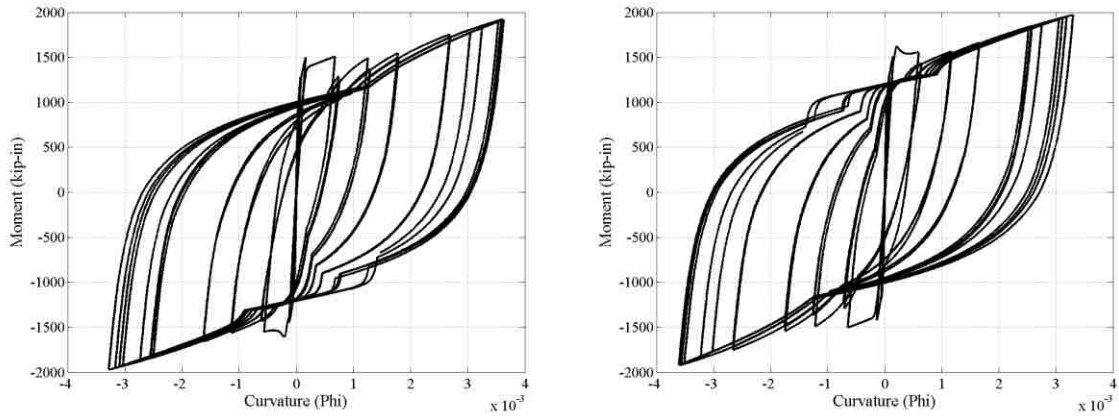
PEER 8 Experimental Damage Propagation

First cracks at the beam-column interface occurred during the first cycle to 0.25% drift. No joint cracks were observed. At 0.5% drift cracks continued to form around the joint region perimeter. Joint cracking did not occur to the center of the joint until the 2% drift cycles. It was determined that the absence of joint and column cracking meant the beams were hinging or the beam bars were slipping. The longitudinal beam reinforcement yielded at 0.42% drift as the displacement to the first 0.5% drift level was achieved. The extent of cracking did not change significantly after yielding occurred. Spalling occurred initially during the 3% drift cycle, and approximately 10% of the joint was visible at the end of the cycles at this drift. Spalling exposing the longitudinal column bars did not occur until 5% drift. This joint was designed to have beam hinges and little joint degradation. The column shear-drift response identified a ductile response in which the capacity reduction occurred in the beams.

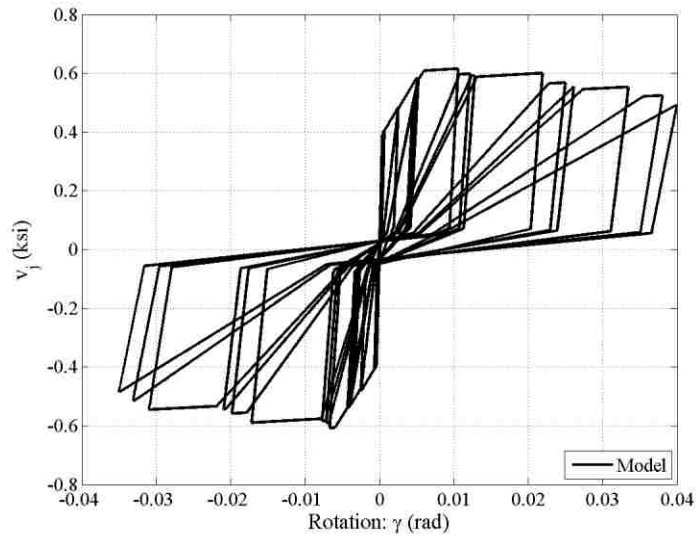
PEER 8 Modeling Observations



Appendix Figure C.60 Upper and Lower Column Moment-Curvature Response



Appendix Figure C.61 Left and Right Beam Moment-Curvature Response



Appendix Figure C.62 Joint Element Response: Joint Shear Stress-Rotation

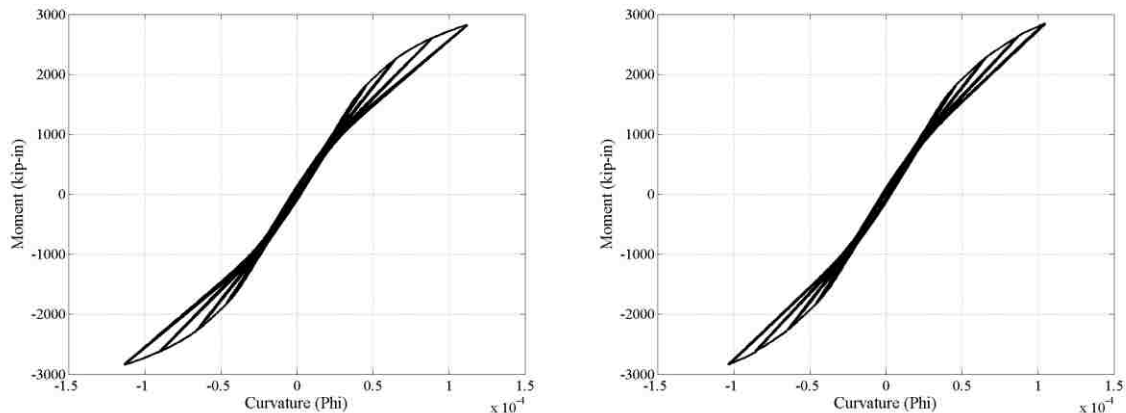
PEER 8 Experiment vs. Analytical Model Comparison

The model response is not as accurate for this specimen. The columns in the analytical model saw more inelastic action than what would be expected from the experimental damage identification. The experimental results identified a beam failure mechanism. There was significant inelastic action in both the beams and the joints in the experiment. The joint inelastic action occurred later in the experimental investigation for this test than in all the other tests. The model did capture more inelastic beam action. The moment curvature plots showed greater curvatures than in the other tests. The modeled joint rotations were near the same levels as the other modeled responses despite the experiment not reaching the same joint degradation. The model performed adequately and captured the degrading response of the experiment.

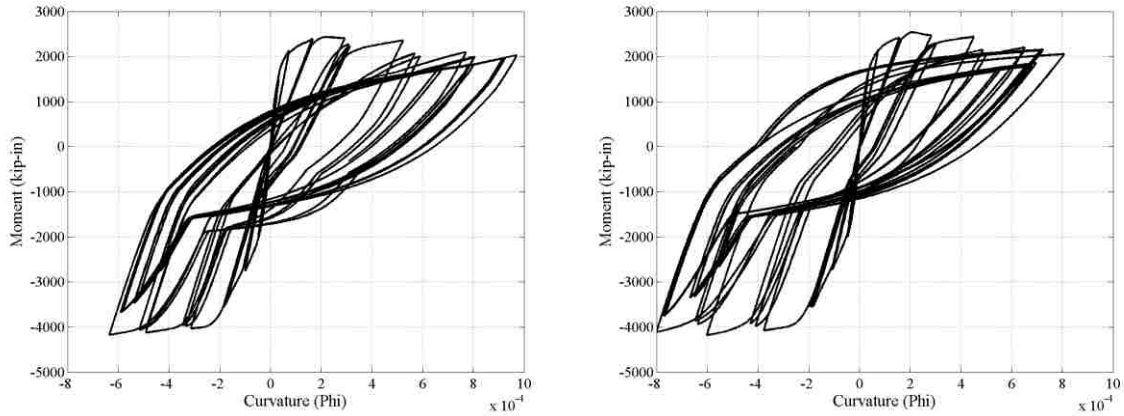
PEER 9 Experimental Damage Propagation

First cracks at the beam-column interface occurred during the first cycle to 0.25% drift. No joint cracks were observed. Diagonal joint cracking occurred at the 0.5% drift cycles. Joint and beam cracking increased at each increase in drift level to 1.5%. After the 1.5% drift level the joint cracking continued to increase, but the beam crack pattern remained constant. The longitudinal beam reinforcement yielded at the 1% drift level. The extent of cracking did not change significantly after yielding occurred. Initial spalling occurred at 2% drift cycles. The spalling progressed at each successive drift level. Spalling exposing column longitudinal steel occurred during the 3% drift cycles. Spalling extended through the joint at the end of the test and produced a void through the joint.

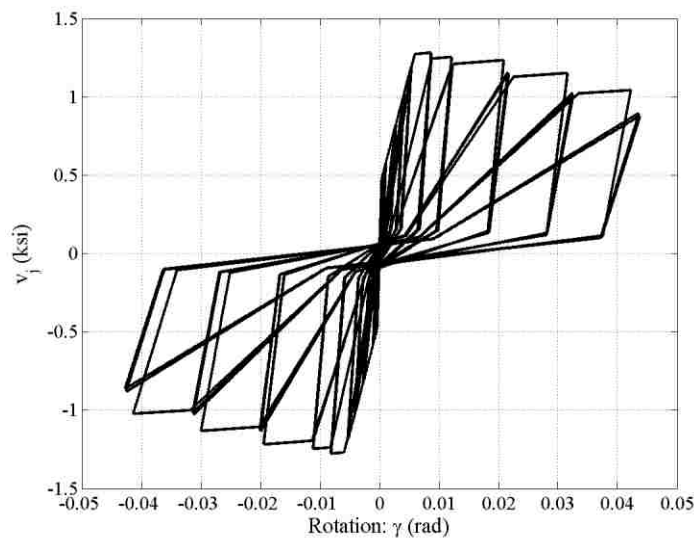
PEER 9 Modeling Observations



Appendix Figure C.63 Upper and Lower Column Moment-Curvature Response



Appendix Figure C.64 Left and Right Beam Moment-Curvature Response



Appendix Figure C.65 Joint Element Response: Joint Shear Stress-Rotation

PEER 9 Experiment vs. Analytical Model Comparison

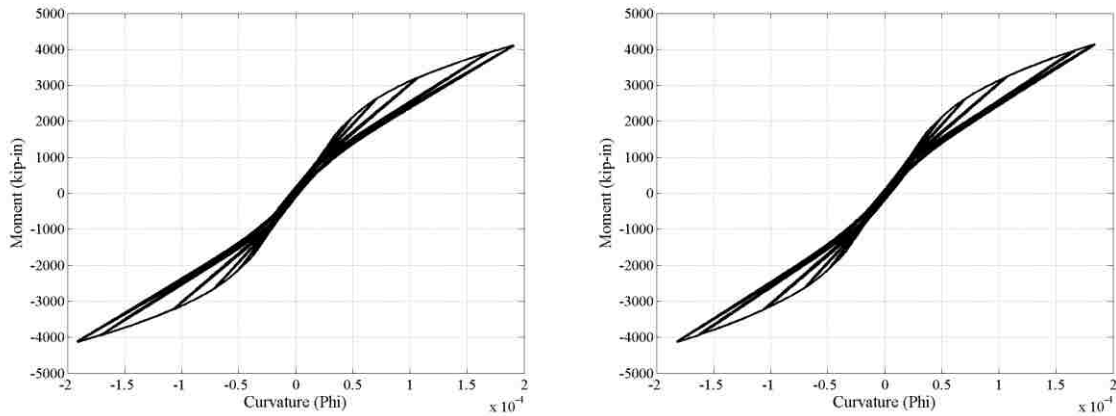
The model response does not match the experimental results. The modeled beam and joint response does seem to match the experimental damage progression. The experimental joint achieved significantly more strength than predicted by the model despite the component behavior. The columns remained mostly elastic in the model and matched the experimental behavior. The modeled beam response did not show as much plastic behavior as in the previous joints. There does not seem to be a clear explanation for the weak model at this time.

PEER 15 Experimental Damage Propagation

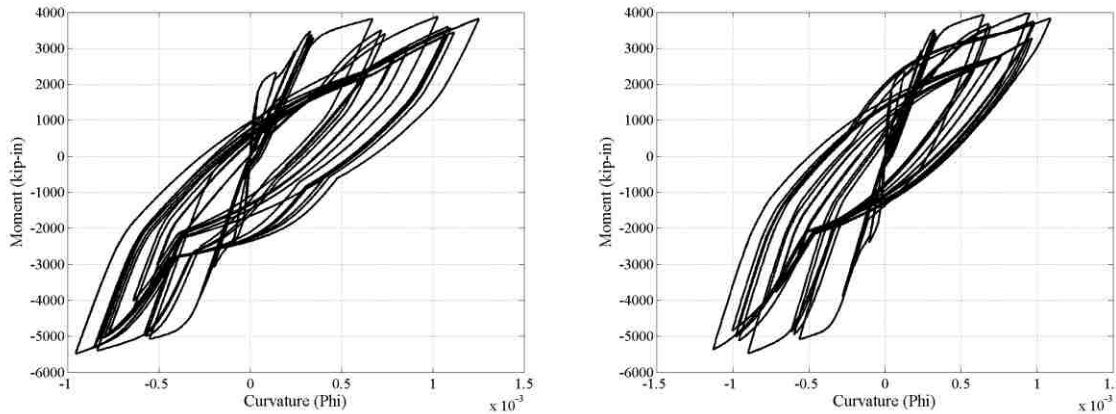
First cracks at the beam-column interface occurred during the first cycle to 0.25% drift. No joint cracks were observed. Diagonal joint cracking occurred at the 0.75% drift cycles. Joint and beam cracking increased at each increase in drift level to 1%. After the 1% drift level the joint cracking continued to increase, but the beam crack pattern remained constant. The longitudinal beam

reinforcement yielded at the 1.5% drift level. The extent of cracking did not change significantly after yielding occurred. Initial spalling occurred at 2% drift cycles. The spalling progressed at each successive drift level. Spalling exposing column longitudinal steel occurred during the 3% drift cycles. Spalling extended through the joint at the end of the test and produced a void through the joint.

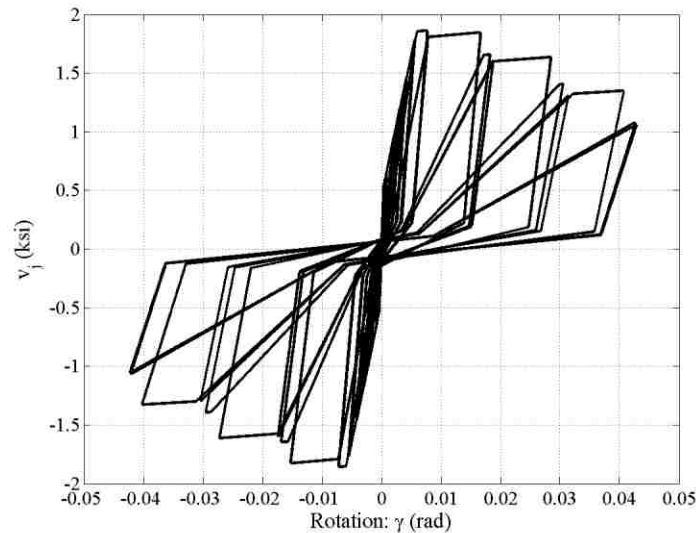
PEER 15 Modeling Observations



Appendix Figure C.66 Upper and Lower Column Moment-Curvature Response



Appendix Figure C.67 Left and Right Beam Moment-Curvature Response



Appendix Figure C.68 Joint Element Response: Joint Shear Stress-Rotation

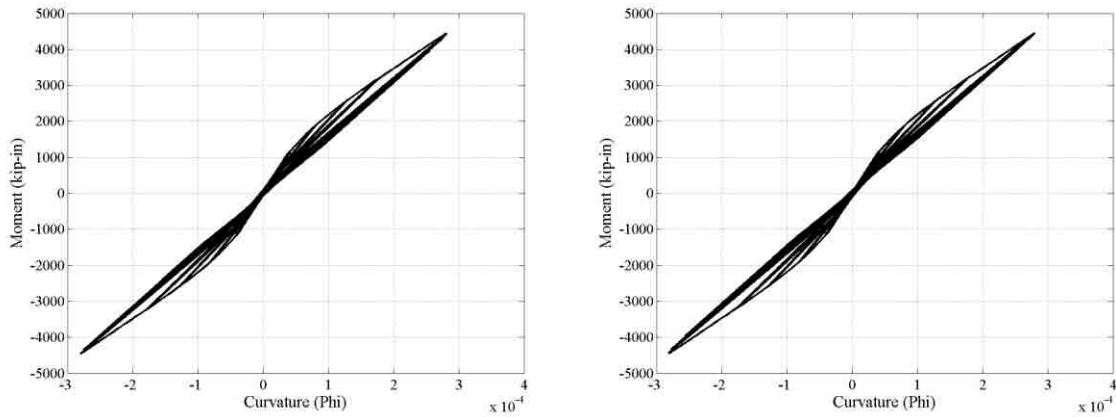
PEER 15 Experiment vs. Analytical Model Comparison

The model response matches the basic experimental joint response. The modeled beam and joint response matches the experimental damage progression. The columns remained mostly elastic but did reach slightly higher strain values in the model and matched the experimental behavior of very minor cracking. The modeled beam response did not show as much plastic behavior as in the previous joints. There does not seem to be a clear explanation for the weak model at this time.

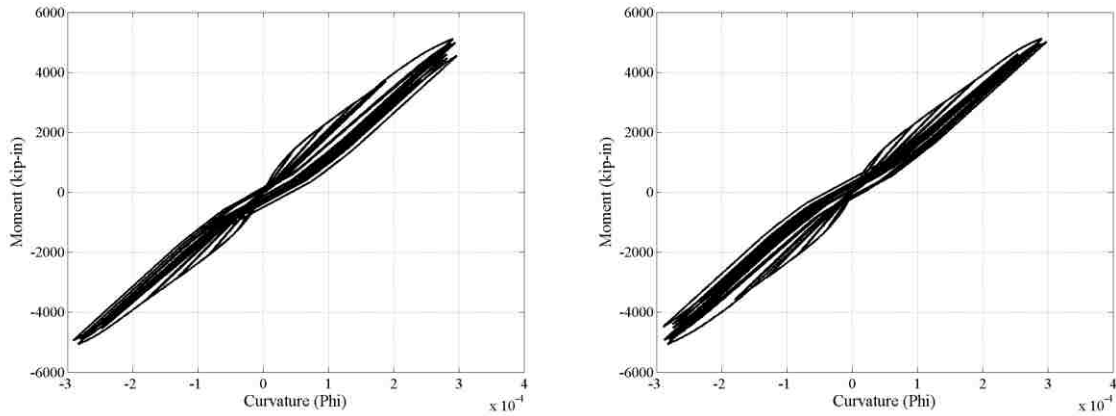
PEER 41 Experimental Damage Propagation

First cracks at the beam-column interface occurred during the first cycle to 0.25% drift. Diagonal joint cracking occurred at the 0.25% drift cycles. Joint and beam cracking increased at each increase in drift level to 0.75%. After the 0.75% drift level the joint cracking continued to increase, but the beam crack pattern remained constant. The longitudinal beam reinforcement did not yield until after significant concrete spalling had occurred at the 2% drift level. Initial spalling occurred at 1% drift cycles. Spalling exposing column longitudinal steel occurred during the 2% drift cycles. Spalling extended through the joint by the end of the 3% drift cycles and produced a void through the joint.

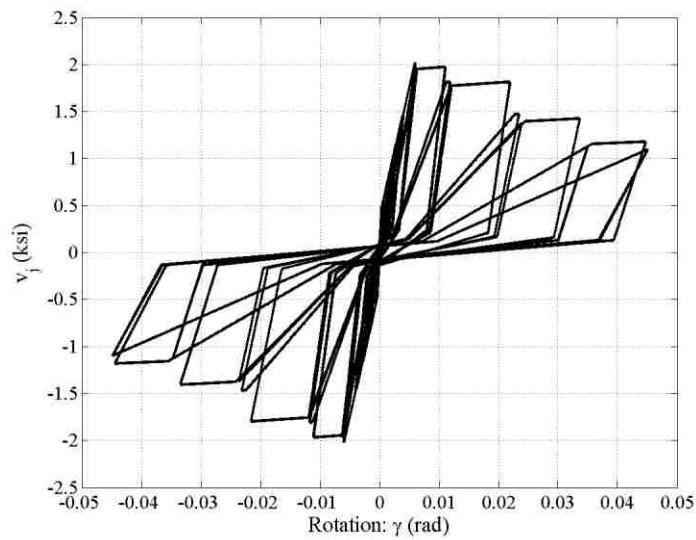
PEER 41 Modeling Observations



Appendix Figure C.69 Upper and Lower Column Moment-Curvature Response



Appendix Figure C.70 Left and Right Beam Moment-Curvature Response



Appendix Figure C.71 Joint Element Response: Joint Shear Stress-Rotation

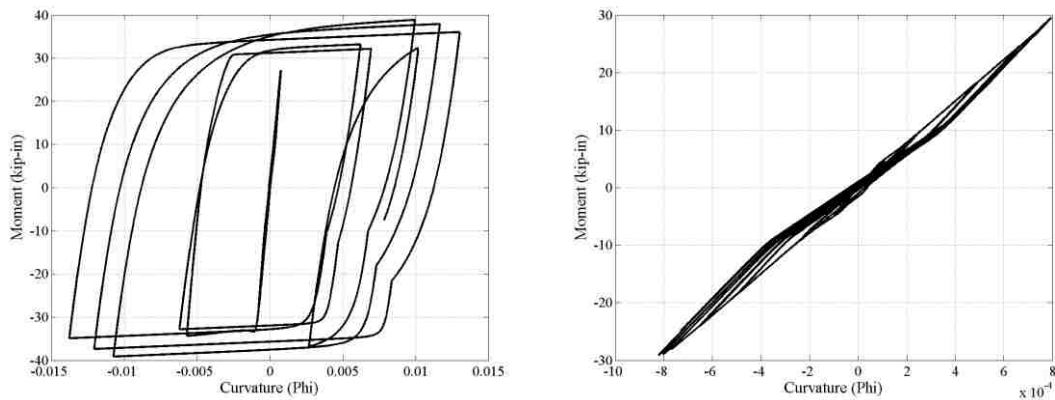
PEER 41 Experiment vs. Analytical Model Comparison

The model response matches the basic experimental joint response. The modeled beam and joint response matches the experimental damage progression. The photographed damage showed limited beam degradation and significant joint deterioration. The columns actually experienced cracking in the experiment and the model did show more inelastic action than in the previous models. The modeled beam response showed the least plastic action and matched the experimental observations.

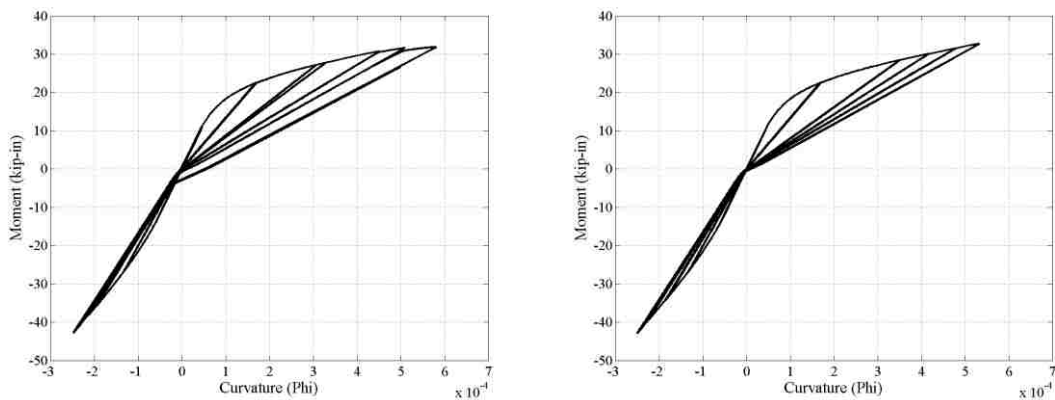
Aycardi Interior Joint Experimental Damage Propagation

Initial cracking occurred at the 2% drift cycles in the upper column. After the 3% drift cycles the flexural cracking in the upper column had increased and minor spalling had occurred. By the end of the 4% drift cycles only superficial cracking was evident in the beams and lower column. The upper column saw the majority of the damage. A weak column-strong beam mechanism was achieved in this test and essentially no joint damage occurred. Force-curvature plots for the beam and column elements indicated elastic response from all the elements except the upper column.

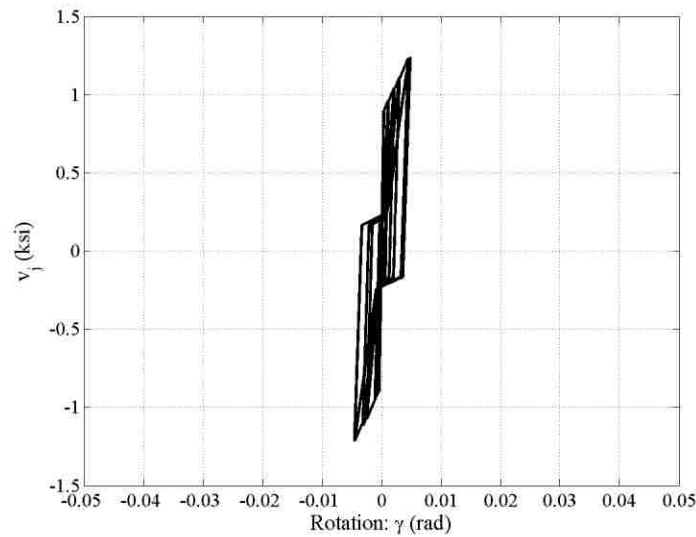
Aycardi Interior Joint Modeling Observations



Appendix Figure C.72 Upper and Lower Column Moment-Curvature Response



Appendix Figure C.73 Left and Right Beam Moment-Curvature Response



Appendix Figure C.74 Joint Element Response: Joint Shear Stress-Rotation

Aycardi Interior Experiment vs. Analytical Model Comparison

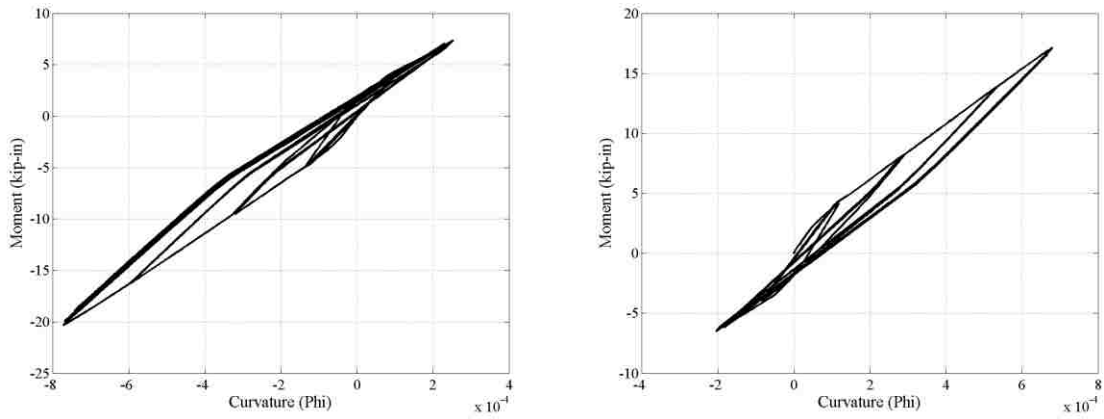
The model response matches the basic experimental joint response. The modeled beam and joint response matches the experimental damage progression. The photographed damage showed limited beam degradation and insignificant joint deterioration. The upper column saw nearly all the inelastic action in both the experiment and modeled behavior.

Exterior Joints

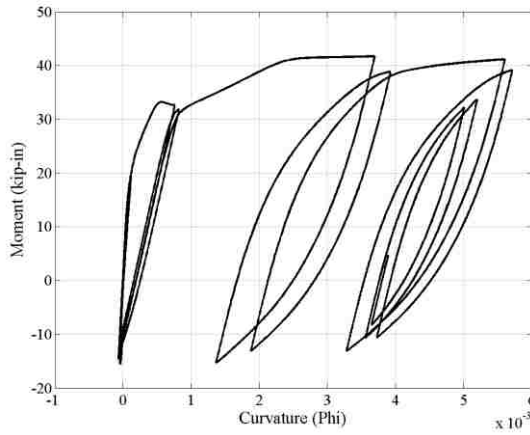
Aycardi Exterior Joint Experimental Damage Propagation

At the end of the 1% drift cycles cracking had occurred at the mid height of the upper column, at the column-beam interfaces, and at the transverse beam-slab interface. After completion of the 3% drift cycles spalling of the column corners had occurred. During the 4% drift cycles pull out of the bottom beam bars had occurred. Large cracks at the beam-column interface opened and closed. Concrete spalling and crushing was also evident in the lower column. The longitudinal reinforcement became exposed and joint damage was evident. The test program continued with 40 cycles at 4% drift and strength degradation did not continue. The beam and columns saw similar curvature demands and all the elements experienced inelastic action. The joint also experienced inelastic action according to the damage description, but the joint behavior was not monitored by experimental instrumentation.

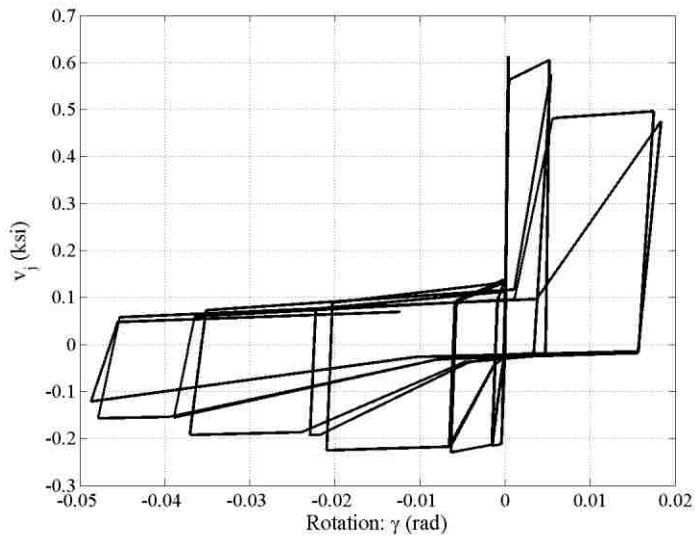
Aycardi Exterior Joint Modeling Observations



Appendix Figure C.75 Upper and Lower Column Moment-Curvature Response



Appendix Figure C.76 Beam Moment-Curvature Response



Appendix Figure C.77 Joint Element Response: Joint Shear Stress-Rotation

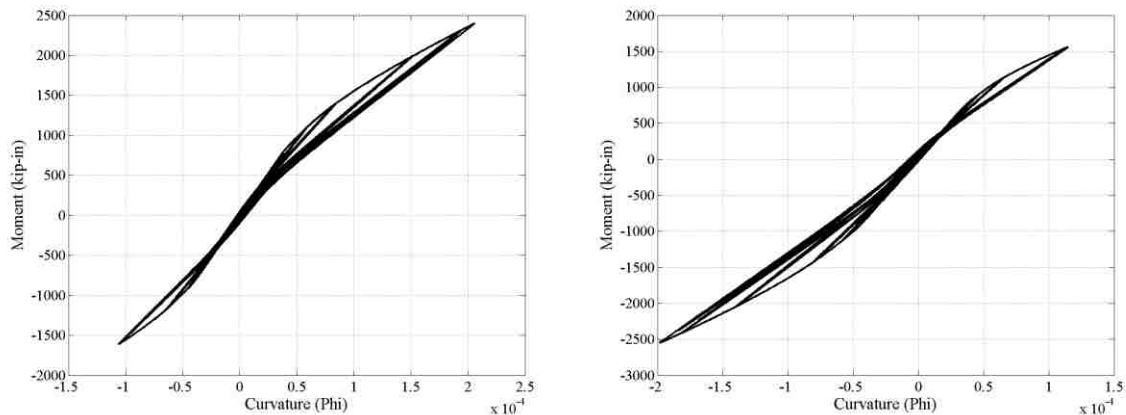
Aycardi Exterior Experiment vs. Analytical Model Comparison

The model response matches the experimental damage. The beam experienced the majority of the inelastic action. The joint behavior did not match the reported experimental behavior. The modeled columns remained primarily elastically as they did experimentally.

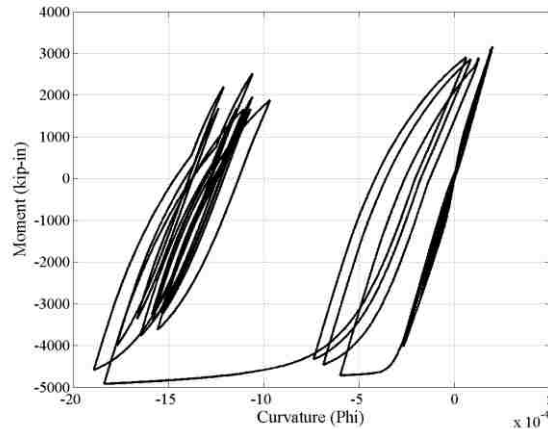
Pantelides 1 Experimental Damage Propagation

The inadequate bar anchorage was identified as the reason for the reduced load resistance in the upward displacement direction. The images from the report (Pantelides, et al. 2002) identify the lower beam bar anchorage zone as the failure point in the sub-assembly. Cracking began in the joint region near the beam at 1% drift and propagated towards the edge of the column. Spalling occurred at the bottom of the beam where it framed into the column at 2% drift. This occurred due to the inadequate embedment. A plot of joint shear stress versus joint shear strain was included. It indicated that inelastic action occurred in the joint region of the assemblage which was indicated by the damage.

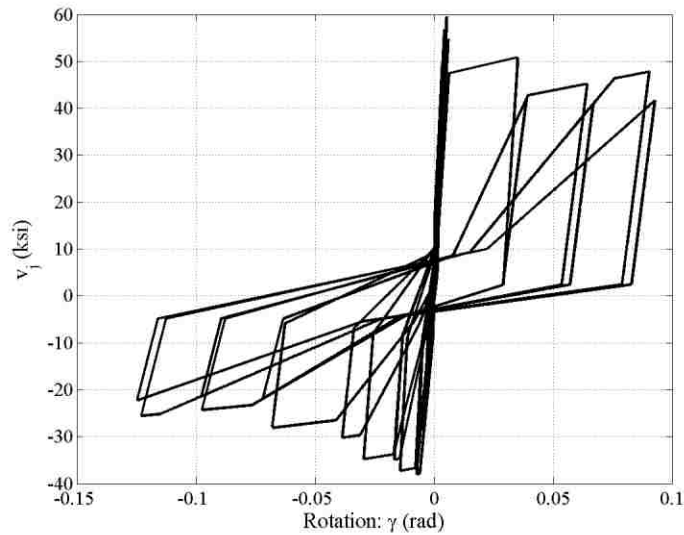
Pantelides 1 Modeling Observations



Appendix Figure C.78 Upper and Lower Column Moment-Curvature Response



Appendix Figure C.79 Beam Moment-Curvature Response



Appendix Figure C.80 Joint Element Response: Joint Shear Stress-Rotation

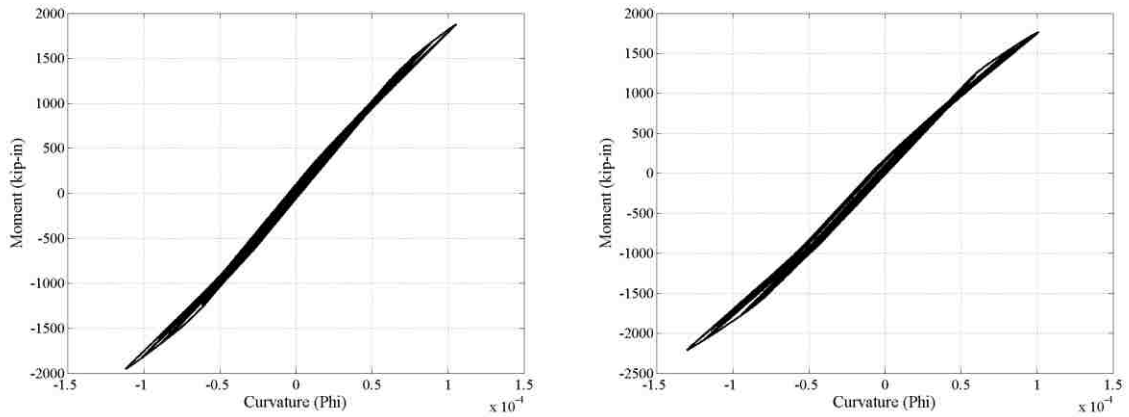
Pantelides 1 Experiment vs. Analytical Model Comparison

The model performed well for this experiment. There was very little damage in the columns except what was caused by bar pull out at the beam to lower column interface. The beam experienced inelastic action at the joint interface due to inadequate embedment. This also caused the joint to degrade.

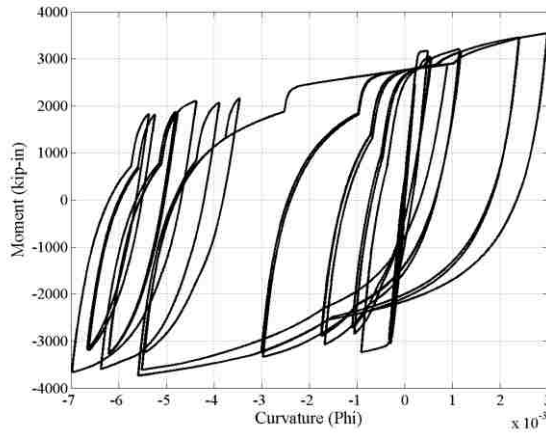
Pantelides 2 Experimental Damage Propagation

The images from the report identify the inadequate bar anchorage as the reason for the reduced load resistance in the upward displacement direction. The same damage progression occurred in this specimen as in Pantelides 1. The increased axial load was identified as the reason for an increased strength. Higher axial load was deemed beneficial in preventing the early bond slip of the bottom reinforcement. A plot of joint shear stress versus joint shear strain was not included due to LVDT failure.

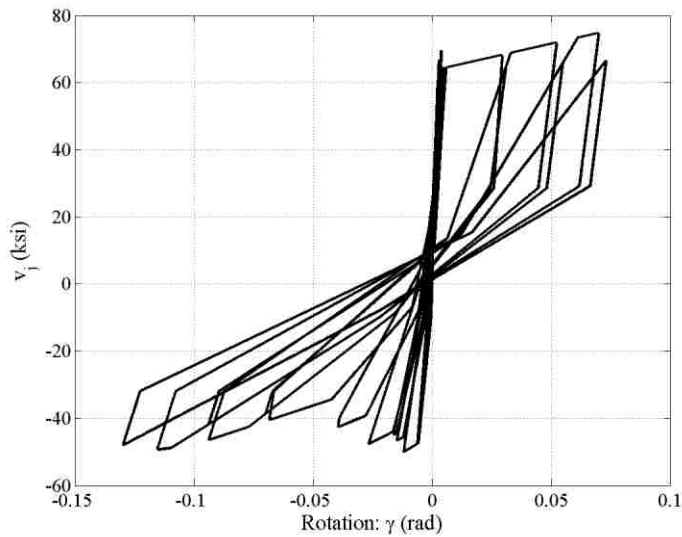
Pantelides 2 Modeling Observations



Appendix Figure C.81 Upper and Lower Column Moment-Curvature Response



Appendix Figure C.82 Beam Moment-Curvature Response



Appendix Figure C.83 Joint Element Response: Joint Shear Stress-Rotation

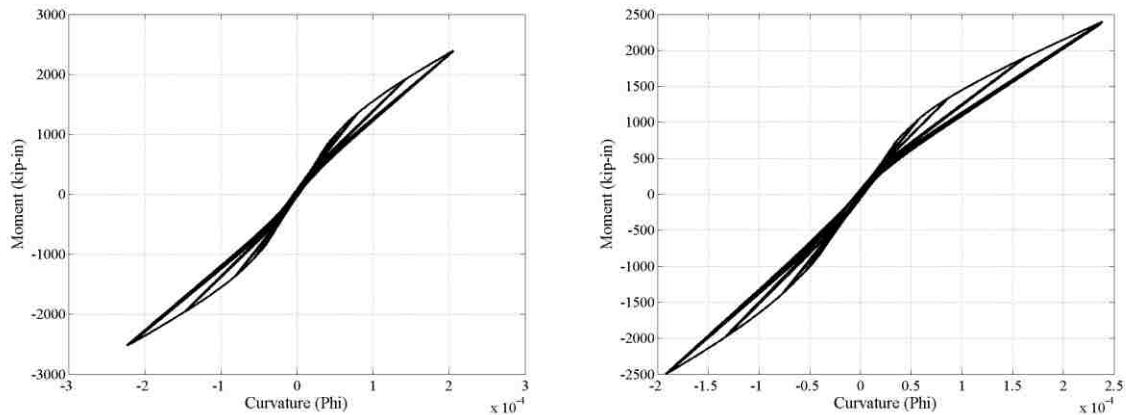
Pantelides 2 Experiment vs. Analytical Model Comparison

The model performed reasonably well for this experiment. There was very little damage in the columns except what was caused by bar pull out at the beam to lower column interface. The beam experienced inelastic action at the joint interface due to inadequate embedment. The increased axial load did seem to give the beam a better cyclic response than the first experiment. This also caused the joint degradation to be less severe. The joint performance in the downward push direction was significantly better due to the beam top bars adequate joint embedment providing tensile capacity.

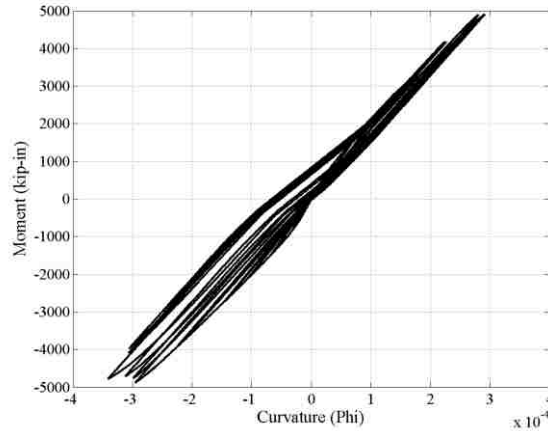
Pantelides 3 Experimental Damage Propagation

The loads in both the upward and downward directions were very similar signifying that the bottom bar embedment depth was adequate to develop the joint capacity. The images indicate cracking commencing in both the joint and beam at less than 1% drift. As the damage progressed, the cracking predominantly formed in the joint region. Spalling occurred at 5% drift in the joint region and became excessive prior to significant damage propagating to the beam or column. A plot of joint shear stress versus joint shear strain was included. It indicated that significant inelastic action occurred in the joint region of the assemblage which was indicated by the damage.

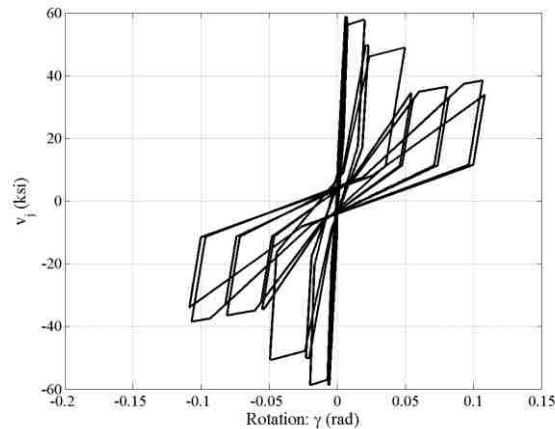
Pantelides 3 Modeling Observations



Appendix Figure C.84 Upper and Lower Column Moment-Curvature Response



Appendix Figure C.85 Beam Moment-Curvature Response



Appendix Figure C.86 Joint Element Response: Joint Shear Stress-Rotation

Pantelides 3 Experiment vs. Analytical Model Comparison

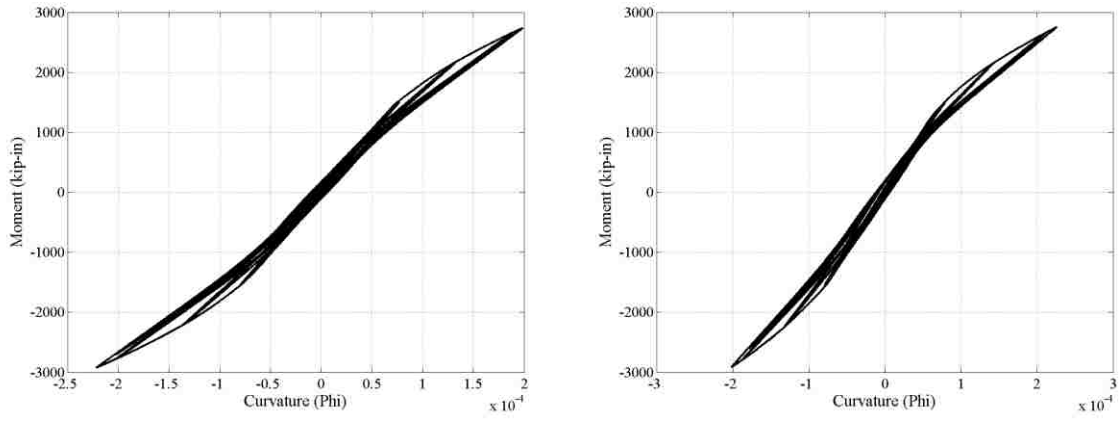
The model performed adequately. The columns and beam remained almost completely elastic. This doesn't match the exact performance of the experimental image set. The initial damage images appeared very similar to the two previous experiments, indicating more beam yielding should have occurred in the model. The joint behavior matches the experimental image set. The primary failure mechanism was joint failure. The joint stress-rotation plot shows significant degradation and an increased rotation from the previous models.

Pantelides 4 Experimental Damage Propagation

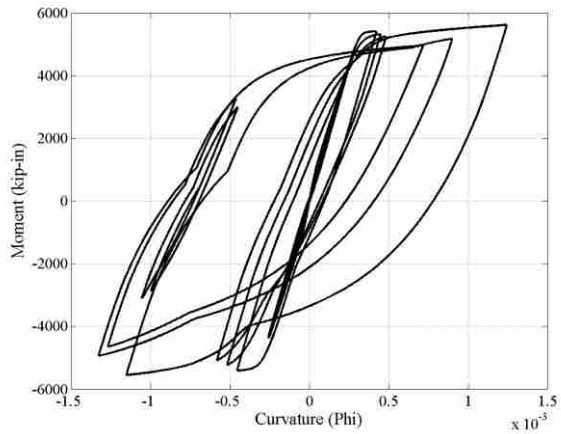
The loads in both the upward and downward directions were very similar signifying that the bottom bar embedment depth was adequate to develop the joint capacity. The images indicate cracking commencing in both the joint and beam at the same time at 1.5%. As the damage progressed the cracking predominantly formed in the joint region. Spalling occurred in the joint region at 5% and became excessive prior to significant damage propagating to the beam or column. A plot of joint

shear stress versus joint shear strain was included. It indicated that significant inelastic action occurred in the joint region of the assemblage.

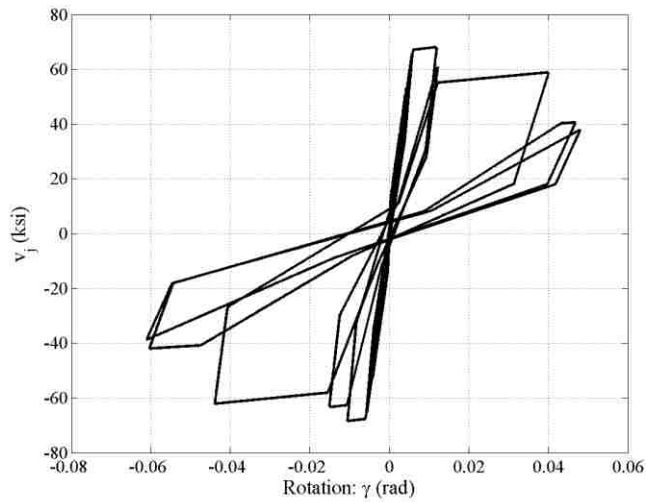
Pantelides 4 Modeling Observations



Appendix Figure C.87 Upper and Lower Column Moment-Curvature Response



Appendix Figure C.88 Beam Moment-Curvature Response



Appendix Figure C.89 Joint Element Response: Joint Shear Stress-Rotation

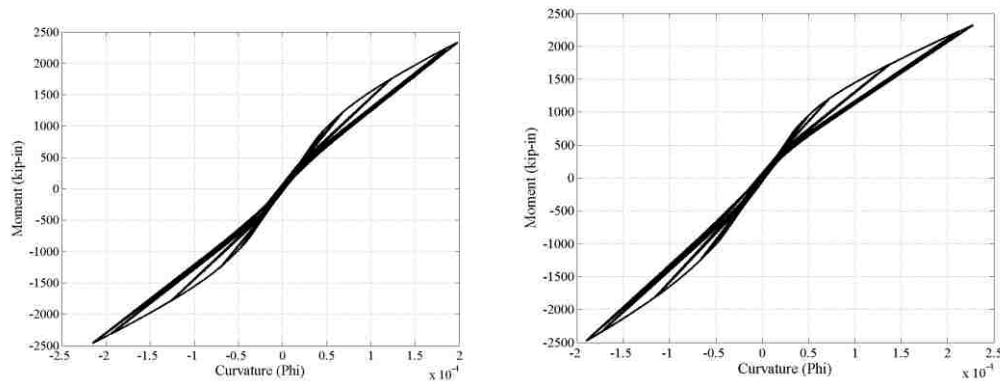
Pantelides 4 Experiment vs. Analytical Model Comparison

The model performed adequately. The columns remained almost completely elastic. The modeled beams behaved in a more inelastic manner than the experimental beams. The joint behavior matches the experimental image set. The primary failure mechanism was joint failure. The joint stress-rotation plot shows significant degradation, and due to the early failure the joint rotations did not reach the rotation level seen in the previous models.

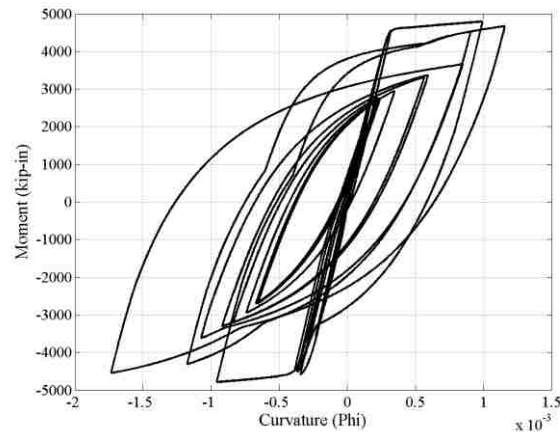
Pantelides 5 Experimental Damage Propagation

The loads in both the upward and downward directions were very similar signifying that the bottom bar embedment depth was adequate to develop the joint capacity. Cracking started in the joint region at 2%. The cracks were diagonal and turned into spalling at 5% drift. Severe spalling and large cracks developed and joint failure occurred. A plot of joint shear stress versus joint shear strain was included. It indicated that significant inelastic action occurred in the joint region of the assemblage.

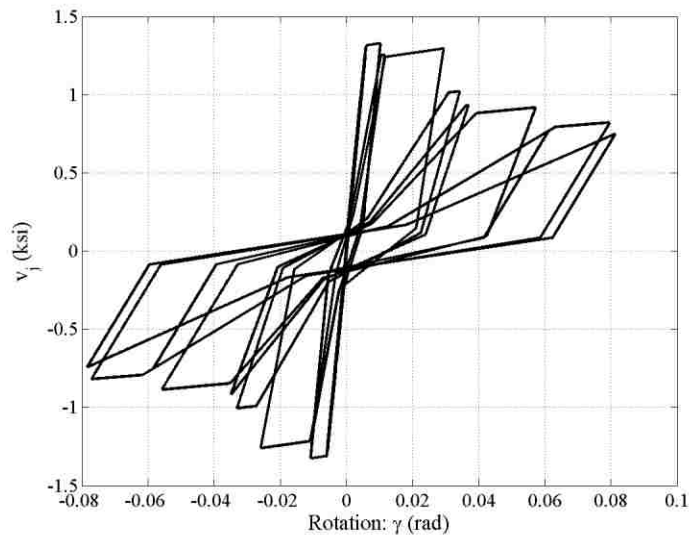
Pantelides 5 Modeling Observations



Appendix Figure C.90 Upper and Lower Column Moment-Curvature Response



Appendix Figure C.91 Beam Moment-Curvature Response



Appendix Figure C.92 Joint Element Response: Joint Shear Stress-Rotation

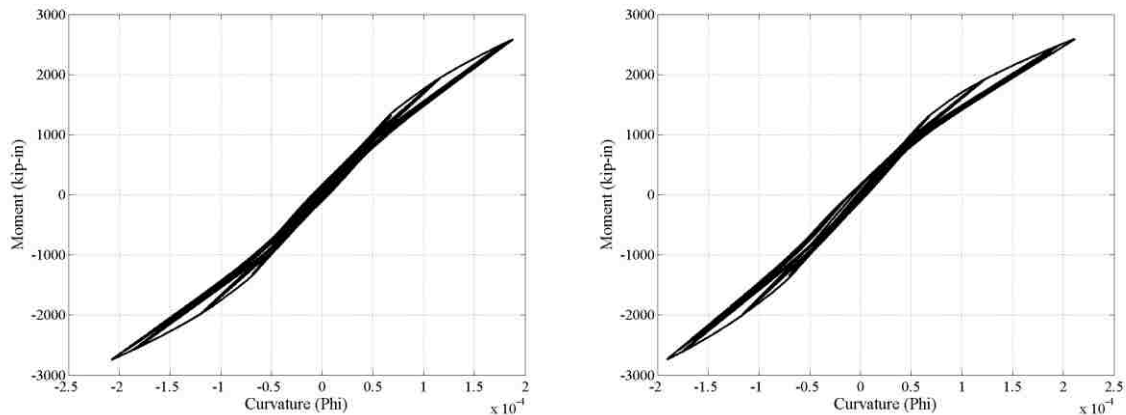
Pantelides 5 Experiment vs. Analytical Model Comparison

The model response matches the experimental damage.

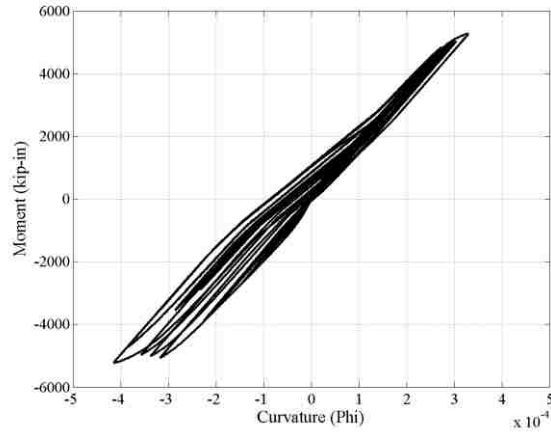
Pantelides 6 Experimental Damage Propagation

The loads in both the upward and downward directions were very similar signifying that the bottom bar embedment depth was adequate to develop the joint capacity. The images indicate cracking commencing at 2% drift in the joint. As the damage progressed the cracking predominantly formed in the joint region. Spalling occurred in the joint region at 5% drift and became excessive prior to significant damage propagating to the beam or column. A plot of joint shear stress versus joint shear strain was included. It indicated that significant inelastic action occurred in the joint region of the assemblage.

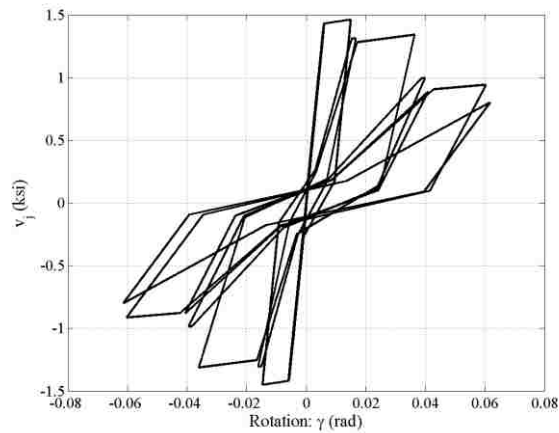
Pantelides 6 Modeling Observations



Appendix Figure C.93 Upper and Lower Column Moment-Curvature Response



Appendix Figure C.94 Beam Moment-Curvature Response



Appendix Figure C.95 Joint Element Response: Joint Shear Stress-Rotation

Pantelides 6 Experiment vs. Analytical Model Comparison

The model response matches the experimental damage.

Appendix D: Stanford Design Documentation

D.1 Introduction

This appendix provides the structural design details for each of the frames modeled and analyzed in Chapter 5. This appendix is a shorter reproduction of the work performed by Haselton (2006) and Liel (2008) for their PhD Dissertations. Haselton's and Liel's designs are obtained from the unpublished Appendix C and Appendix A of their respective Dissertations. Table D.1 lists the frames in the order that their documented designs will appear in this appendix.

Appendix Table D.1 Modeled frames

Report ID	Stanford Design ID	Stories	ACI Designation	Frame Type	Design Case	
SMF4-1.2-00 SMF4-1.2-0J	1003	4	SMF	Perimeter	Baseline	
SMF12-1.2-00 SMF12-1.2-0J	1013	12		Perimeter	Baseline	
SMF12-WS-00	New	12		Perimeter	WS	
OMF4-1.2-00 OMF4-1.2-0J OMF4-1.2-SJ	3004	4	OMF	Space	Baseline	
OMF4-0.8-00	New	4		Space	SCWB 0.8	
OMF4-2.0-00	New	4		Space	SCWB 2.0	
OMF12-1.2-00 OMF12-1.2-0J OMF12-1.2-SJ	3023	12		Space	Baseline	
OMF12-0.8-00	New	12		Space	SCWB 0.8	
OMF12-2.0-00	New	12		Space	SCWB 2.0	
OMF12-WS-00	New	12		Space	WS	
Legend and Notes:						
Baseline - Baseline design with SCWB of ≈ 1.2						
SCWB 0.8 - Strong-Column Weak-Beam ratio of 0.8						
SCWB 2.0 - Strong-Column Weak-Beam ratio of 2.0						
WS - Weak-story						

D.2 Process for Obtaining Designs not Completed by Haselton and Liel

The designs labeled New in the second column are modified designs. SMF12-WS-00 is a modification of Stanford Design ID 1013; OMF4-0.8-00 and OMF4-2.0-00 are modifications of Stanford Design ID 3004; and OMF12-0.8-00, OMF12-2.0-00, and OMF12-WS-00 are modifications of Stanford Design ID 3023.

D.2.1 Process for Obtaining Desired SCWB Ratios

To determine how to vary the SCWB Ratios in frames 3004 and 3023, Haselton's SMF designs were considered. Table D.2 shows the SMF designs with various SCWB Ratios that Haselton used in his thesis.

Appendix Table D.2 SMFs with varying strong-column weak-beam ratios

Strong-Column Weak-Beam Ratio	No. of Stories	Frame Type	Stanford Design ID
0.4	4	Space	2034
0.6			2025
0.8			2024
1.0			2023
1.2			1010
1.5			2005
2.0			2006
2.5			2007
3.0			2027
0.9			12
1.2	1013		
1.5	2055		
2.0	2056		
2.5	2057		
3.0	2058		

Table D.3 shows the frames used to determine a standard procedure to change to SCWB ratio for the OMFs used in Liel's Thesis.

Appendix Table D.3 SMFs used for OMF modification procedure

Strong-Column Weak-Beam Ratio	No. of Stories	Frame Type	Stanford Design ID
0.6	4	Space	2025
1.2			1010
2			2006
0.9	12	Perimeter	2060
1.2			1013
2			2056

Frame 1010 is designed to the code level SCWB. When comparing Frame 1010's design to Frame 2025's design the column sizes were reduced and the beam sizes were increased. Stronger

concrete was also specified to meet the joint shear force requirements. Frame 2006's design had the same size columns and beams. The only difference is the amount of reinforcement in the columns was increased.

Frame 1013 compared to Frame 2060 are identical except for the reinforcement in both the columns and beams. The beam reinforcement is increased and the column reinforcement is decreased in Frame 2060. Frame 2056's design has larger columns with more reinforcement in them. The Beams in Frame 2056's design are smaller than those in Frame 1013's design.

The SMF's all were designed using 4 ksi concrete so this parameter will remain constant in the modified designs. To reduce the baseline designs (Frames 3004 and 3023) SCWB ratio, it is recommended that the element sizes stay the same. Reducing the reinforcement ratio in the columns by 15% and increasing the beam reinforcement ratios by 5% changes the SCWB ratio from 1.2 to 0.9. These were the approximate percent changes used to change Frame 1013 to Frame 2060. To increase the baseline designs SCWB ratio the element sizes will stay the same. Increasing the reinforcement ratio in the columns by 45% and leaving the reinforcement ratio in the beams the same changes the SCWB ratio from 1.2 to 2.0. The 45% increase was the amount used to change Frame 1010 to Frame 2006.

D.2.1 Process for Obtaining Weak First Story

To determine how to produce a weak-story in the 12-story OMF, Haselton's SMF designs were considered. Table D.4 shows the SMF designs with various SCWB Ratios that Haselton used in his thesis.

Appendix Table D.4 SMFs used for OMF modification procedure

Design Case	No. of Stories	Frame Type	Stanford Design ID
Baseline	12	Space	1014
Weak-story (80%)			2068

Frame 1014 is designed to meet all ACI 318 code provisions. Haselton introduced a weak-story into Frame 2068 by increasing the reinforcement ratio of the columns above the first story by 45%. The first story column reinforcement ratios were also increased (by 15%) to meet code requirements. The beam reinforcement ratios remained the same in both designs. The same reinforcement ratio increases can be applied to the OMF 3023 to introduce a weak-story into that design.

D.3 Frame Design Information

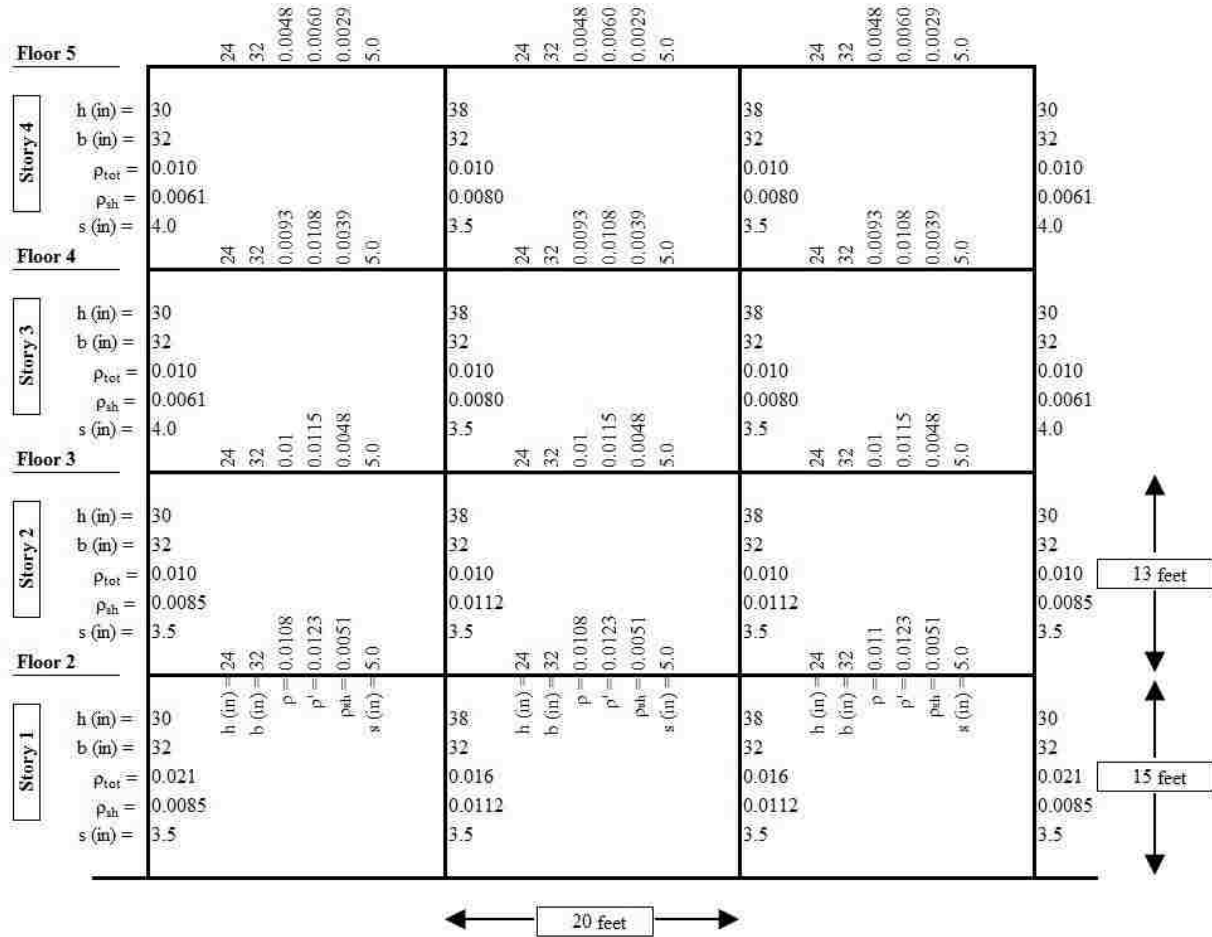
Report ID: SMF4-1.2-00, SMF4-1.2-0J

Stanford Design ID: 1003

Building Type: Special RC Frame, designed per 2003 IBC

Design Type: Baseline

Number of Stories: 4



Design base shear =		0.092	g,	386	k
f'_c beams =	5.0	ksi	f'_c , cols, lower =	7.0	ksi
f'_c , cols, upper =	5.0	ksi	f_y , rebar, nom. =	60	ksi

Report ID: SMF12-1.2-00,
SMF12-1.2-0J

Stanford Design ID: 1013

Building Type: Special RC
Frame, designed per 2003 IBC

Design Type: Baseline

Number of Stories: 12

Story	h (in)	b (in)	ρ_{int}	ρ_{ps}	s (in)	h (in)	b (in)	ρ_{int}	ρ_{ps}	s (in)	h (in)	b (in)	ρ_{int}	ρ_{ps}	s (in)
Floor 13	32	28	0.010	0.0033	3.5	32	28	0.010	0.0033	3.5	32	28	0.010	0.0033	3.5
Story 12	32	28	0.010	0.0035	3.5	32	28	0.010	0.0035	3.5	32	28	0.010	0.0035	3.5
Floor 12	32	28	0.010	0.0043	3.5	32	28	0.011	0.0043	3.5	32	28	0.011	0.0043	3.5
Story 11	32	28	0.010	0.0053	3.5	32	28	0.011	0.0053	3.5	32	28	0.011	0.0053	3.5
Floor 11	32	28	0.010	0.0065	3.5	32	28	0.013	0.0065	3.5	32	28	0.013	0.0065	3.5
Story 10	32	28	0.010	0.0086	3.5	32	28	0.013	0.0086	3.5	32	28	0.013	0.0086	3.5
Floor 10	32	28	0.010	0.0098	3.5	32	28	0.016	0.0098	3.5	32	28	0.016	0.0098	3.5
Story 9	32	28	0.011	0.0094	3.5	32	28	0.016	0.0094	3.5	32	28	0.016	0.0094	3.5
Floor 9	32	28	0.011	0.0094	3.5	32	28	0.016	0.0094	3.5	32	28	0.016	0.0094	3.5
Story 8	32	28	0.011	0.0094	3.5	32	28	0.016	0.0094	3.5	32	28	0.016	0.0094	3.5
Floor 8	32	28	0.013	0.0063	3.5	32	28	0.020	0.0063	3.5	32	28	0.020	0.0063	3.5
Story 7	32	28	0.014	0.0041	3.5	32	28	0.022	0.0041	3.5	32	28	0.022	0.0041	3.5
Floor 7	32	28	0.015	0.0044	3.5	32	28	0.022	0.0044	3.5	32	28	0.022	0.0044	3.5
Story 6	32	28	0.016	0.0045	3.5	32	28	0.022	0.0045	3.5	32	28	0.022	0.0045	3.5
Floor 6	32	28	0.017	0.0045	3.5	32	28	0.022	0.0045	3.5	32	28	0.022	0.0045	3.5
Story 5	32	28	0.017	0.0045	3.5	32	28	0.022	0.0045	3.5	32	28	0.022	0.0045	3.5
Floor 5	32	28	0.017	0.0045	3.5	32	28	0.022	0.0045	3.5	32	28	0.022	0.0045	3.5
Story 4	32	28	0.017	0.0045	3.5	32	28	0.022	0.0045	3.5	32	28	0.022	0.0045	3.5
Floor 4	32	28	0.017	0.0045	3.5	32	28	0.022	0.0045	3.5	32	28	0.022	0.0045	3.5
Story 3	32	28	0.017	0.0045	3.5	32	28	0.022	0.0045	3.5	32	28	0.022	0.0045	3.5
Floor 3	32	28	0.017	0.0045	3.5	32	28	0.022	0.0045	3.5	32	28	0.022	0.0045	3.5
Story 2	32	28	0.023	0.0045	3.5	32	28	0.022	0.0045	3.5	32	28	0.022	0.0045	3.5
Floor 2	32	28	0.023	0.0045	3.5	32	28	0.022	0.0045	3.5	32	28	0.022	0.0045	3.5

Design base shear =	0.044	ρ_c =	368	I_c	
f_c beams =	5.0	ksi	$f_{c,soth,lower}$ =	7.0	ksi
$f_{c,soth,upper}$ =	5.0	ksi	$f_{c,upper,com}$ =	60	ksi

Report ID: SMF12-WS-00

Stanford Design ID: NEW

Building Type: Special RC
Frame, designed per 2003 IBC

Design Type: Weak First
Story

Number of Stories: 12

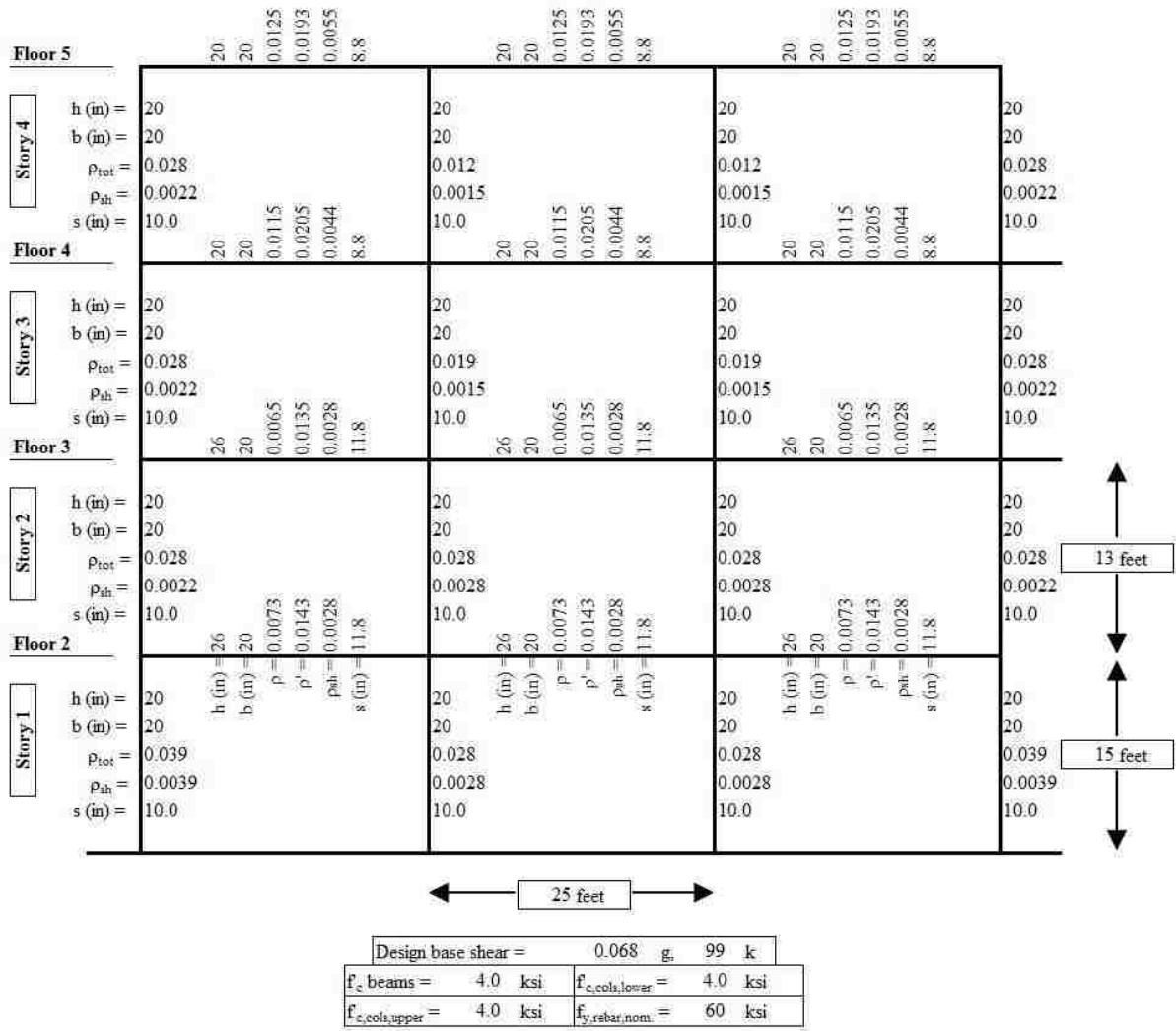
Story	h (in)	b (in)	ρ_{br}	ρ_{bc}	s (in)	h (in)	b (in)	ρ_{br}	ρ_{bc}	s (in)	h (in)	b (in)	ρ_{br}	ρ_{bc}	s (in)
Floor 13	32	28	0.015	0.0086	3.5	32	28	0.015	0.0086	3.5	32	28	0.015	0.0086	3.5
Story 12	32	28	0.015	0.0086	3.5	32	28	0.015	0.0086	3.5	32	28	0.015	0.0086	3.5
Floor 12	32	28	0.015	0.0086	3.5	32	28	0.015	0.0086	3.5	32	28	0.015	0.0086	3.5
Story 11	32	28	0.015	0.0086	3.5	32	28	0.015	0.0086	3.5	32	28	0.015	0.0086	3.5
Floor 11	32	28	0.015	0.0086	3.5	32	28	0.015	0.0086	3.5	32	28	0.015	0.0086	3.5
Story 10	32	28	0.015	0.0086	3.5	32	28	0.015	0.0086	3.5	32	28	0.015	0.0086	3.5
Floor 10	32	28	0.015	0.0086	3.5	32	28	0.015	0.0086	3.5	32	28	0.015	0.0086	3.5
Story 9	32	28	0.015	0.0086	3.5	32	28	0.015	0.0086	3.5	32	28	0.015	0.0086	3.5
Floor 9	32	28	0.015	0.0086	3.5	32	28	0.015	0.0086	3.5	32	28	0.015	0.0086	3.5
Story 8	32	28	0.015	0.0086	3.5	32	28	0.015	0.0086	3.5	32	28	0.015	0.0086	3.5
Floor 8	32	28	0.015	0.0086	3.5	32	28	0.015	0.0086	3.5	32	28	0.015	0.0086	3.5
Story 7	32	28	0.015	0.0086	3.5	32	28	0.015	0.0086	3.5	32	28	0.015	0.0086	3.5
Floor 7	32	28	0.015	0.0086	3.5	32	28	0.015	0.0086	3.5	32	28	0.015	0.0086	3.5
Story 6	32	28	0.015	0.0086	3.5	32	28	0.015	0.0086	3.5	32	28	0.015	0.0086	3.5
Floor 6	32	28	0.015	0.0086	3.5	32	28	0.015	0.0086	3.5	32	28	0.015	0.0086	3.5
Story 5	32	28	0.015	0.0086	3.5	32	28	0.015	0.0086	3.5	32	28	0.015	0.0086	3.5
Floor 5	32	28	0.015	0.0086	3.5	32	28	0.015	0.0086	3.5	32	28	0.015	0.0086	3.5
Story 4	32	28	0.015	0.0086	3.5	32	28	0.015	0.0086	3.5	32	28	0.015	0.0086	3.5
Floor 4	32	28	0.015	0.0086	3.5	32	28	0.015	0.0086	3.5	32	28	0.015	0.0086	3.5
Story 3	32	28	0.015	0.0086	3.5	32	28	0.015	0.0086	3.5	32	28	0.015	0.0086	3.5
Floor 3	32	28	0.015	0.0086	3.5	32	28	0.015	0.0086	3.5	32	28	0.015	0.0086	3.5
Story 2	32	28	0.015	0.0086	3.5	32	28	0.015	0.0086	3.5	32	28	0.015	0.0086	3.5
Floor 2	32	28	0.015	0.0086	3.5	32	28	0.015	0.0086	3.5	32	28	0.015	0.0086	3.5
Story 1	32	28	0.015	0.0086	3.5	32	28	0.015	0.0086	3.5	32	28	0.015	0.0086	3.5

20 feet

13 feet
15 feet

Design base shear =	0.044	ig. 368 k
f'_c beams =	5.0 ksi	f'_c colch, lower = 7.0 ksi
f'_c colch, upper =	5.0 ksi	f_y rebar, beam = 60 ksi

Report ID: OMF4-1.2-00, OMF4-1.2-0J, OMF4-1.2-SJ
 Stanford Design ID: 3004
 Building Type: RC Frame, designed per 1967 UBC
 Design Type: Baseline
 Number of Stories: 4



Report ID: OMF4-0.8-00
 Stanford Design ID: NEW
 Building Type: RC Frame, designed per 1967 UBC
 Design Type: SCWB 0.8
 Number of Stories: 4

Floor 5		20	20	0.0131	0.0203	0.0055	8.8	20	20	0.0131	0.0203	0.0055	8.8	20	20	0.0131	0.0203	0.0055	8.8
Story 4	h (in) =	20	20	20	20	20	20	20	20	20	20	20	20	20	20	20	20	20	20
	b (in) =	20	20	20	20	20	20	20	20	20	20	20	20	20	20	20	20	20	20
	ρ_{tot} =	0.024	0.010	0.010	0.024	0.010	0.010	0.024	0.010	0.010	0.010	0.024	0.010	0.010	0.010	0.024	0.010	0.010	0.024
	ρ_{sh} =	0.0022	0.0015	0.0015	0.0022	0.0015	0.0015	0.0022	0.0015	0.0015	0.0015	0.0022	0.0015	0.0015	0.0015	0.0022	0.0015	0.0015	0.0022
s (in) =	10.0	10.0	10.0	10.0	10.0	10.0	10.0	10.0	10.0	10.0	10.0	10.0	10.0	10.0	10.0	10.0	10.0	10.0	10.0
Floor 4		20	20	0.0121	0.0215	0.0044	8.8	20	20	0.0121	0.0215	0.0044	8.8	20	20	0.0121	0.0215	0.0044	8.8
Story 3	h (in) =	20	20	20	20	20	20	20	20	20	20	20	20	20	20	20	20	20	20
	b (in) =	20	20	20	20	20	20	20	20	20	20	20	20	20	20	20	20	20	20
	ρ_{tot} =	0.024	0.016	0.016	0.024	0.016	0.016	0.024	0.016	0.016	0.016	0.024	0.016	0.016	0.016	0.024	0.016	0.016	0.024
	ρ_{sh} =	0.0022	0.0015	0.0015	0.0022	0.0015	0.0015	0.0022	0.0015	0.0015	0.0015	0.0022	0.0015	0.0015	0.0015	0.0022	0.0015	0.0015	0.0022
s (in) =	10.0	10.0	10.0	10.0	10.0	10.0	10.0	10.0	10.0	10.0	10.0	10.0	10.0	10.0	10.0	10.0	10.0	10.0	10.0
Floor 3		26	20	0.0068	0.0142	0.0028	11.8	26	20	0.0068	0.0142	0.0028	11.8	26	20	0.0068	0.0142	0.0028	11.8
Story 2	h (in) =	20	20	20	20	20	20	20	20	20	20	20	20	20	20	20	20	20	20
	b (in) =	20	20	20	20	20	20	20	20	20	20	20	20	20	20	20	20	20	20
	ρ_{tot} =	0.024	0.024	0.024	0.024	0.024	0.024	0.024	0.024	0.024	0.024	0.024	0.024	0.024	0.024	0.024	0.024	0.024	0.024
	ρ_{sh} =	0.0022	0.0028	0.0028	0.0022	0.0028	0.0028	0.0022	0.0028	0.0028	0.0028	0.0022	0.0028	0.0028	0.0028	0.0022	0.0028	0.0028	0.0022
s (in) =	10.0	10.0	10.0	10.0	10.0	10.0	10.0	10.0	10.0	10.0	10.0	10.0	10.0	10.0	10.0	10.0	10.0	10.0	10.0
Floor 2		26	20	0.0077	0.0150	0.0028	11.8	26	20	0.0077	0.0150	0.0028	11.8	26	20	0.0077	0.0150	0.0028	11.8
Story 1	h (in) =	20	20	20	20	20	20	20	20	20	20	20	20	20	20	20	20	20	20
	b (in) =	20	20	20	20	20	20	20	20	20	20	20	20	20	20	20	20	20	20
	ρ_{tot} =	0.033	0.024	0.024	0.033	0.024	0.024	0.033	0.024	0.024	0.024	0.033	0.024	0.024	0.024	0.033	0.024	0.024	0.033
	ρ_{sh} =	0.0039	0.0028	0.0028	0.0039	0.0028	0.0028	0.0039	0.0028	0.0028	0.0028	0.0039	0.0028	0.0028	0.0028	0.0039	0.0028	0.0028	0.0039
s (in) =	10.0	10.0	10.0	10.0	10.0	10.0	10.0	10.0	10.0	10.0	10.0	10.0	10.0	10.0	10.0	10.0	10.0	10.0	10.0

25 feet

13 feet
15 feet

Design base shear = 0.068 g, 99 k	
f'_c beams = 4.0 ksi	f'_c , cols, lower = 4.0 ksi
f'_c , cols, upper = 4.0 ksi	f_y , rebar, nom. = 60 ksi

Report ID: OMF4-2.0-00
 Stanford Design ID: NEW
 Building Type: RC Frame, designed per 1967 UBC
 Design Type: SCWB 2.0
 Number of Stories: 4

	Floor 5				Floor 4				Floor 3				Floor 2				Floor 1				
Story 4	h (in) =	20	20	0.0125	0.0193	0.0055	20	20	0.0125	0.0193	0.0055	20	20	0.0125	0.0193	0.0055	20	20	0.0125	0.0193	0.0055
	b (in) =	20	20	0.0125	0.0193	0.0055	20	20	0.0125	0.0193	0.0055	20	20	0.0125	0.0193	0.0055	20	20	0.0125	0.0193	0.0055
	ρ_{tot} =	0.041	0.017	0.017	0.041	0.017	0.041	0.017	0.041	0.017	0.041	0.041	0.017	0.017	0.041	0.017	0.041	0.017	0.041	0.017	0.041
	ρ_{sh} =	0.0022	0.0015	0.0015	0.0022	0.0015	0.0022	0.0015	0.0022	0.0015	0.0022	0.0022	0.0015	0.0015	0.0022	0.0015	0.0022	0.0015	0.0022	0.0015	0.0022
	s (in) =	10.0	10.0	10.0	10.0	10.0	10.0	10.0	10.0	10.0	10.0	10.0	10.0	10.0	10.0	10.0	10.0	10.0	10.0	10.0	10.0
Story 3	h (in) =	20	20	0.0115	0.0205	0.0044	20	20	0.0115	0.0205	0.0044	20	20	0.0115	0.0205	0.0044	20	20	0.0115	0.0205	0.0044
	b (in) =	20	20	0.0115	0.0205	0.0044	20	20	0.0115	0.0205	0.0044	20	20	0.0115	0.0205	0.0044	20	20	0.0115	0.0205	0.0044
	ρ_{tot} =	0.041	0.028	0.028	0.041	0.028	0.041	0.028	0.041	0.028	0.041	0.041	0.028	0.028	0.041	0.028	0.041	0.028	0.041	0.028	0.041
	ρ_{sh} =	0.0022	0.0015	0.0015	0.0022	0.0015	0.0022	0.0015	0.0022	0.0015	0.0022	0.0022	0.0015	0.0015	0.0022	0.0015	0.0022	0.0015	0.0022	0.0015	0.0022
	s (in) =	10.0	10.0	10.0	10.0	10.0	10.0	10.0	10.0	10.0	10.0	10.0	10.0	10.0	10.0	10.0	10.0	10.0	10.0	10.0	10.0
Story 2	h (in) =	20	20	0.0065	0.0135	0.0028	20	20	0.0065	0.0135	0.0028	20	20	0.0065	0.0135	0.0028	20	20	0.0065	0.0135	0.0028
	b (in) =	20	20	0.0065	0.0135	0.0028	20	20	0.0065	0.0135	0.0028	20	20	0.0065	0.0135	0.0028	20	20	0.0065	0.0135	0.0028
	ρ_{tot} =	0.041	0.028	0.028	0.041	0.028	0.041	0.028	0.041	0.028	0.041	0.041	0.028	0.028	0.041	0.028	0.041	0.028	0.041	0.028	0.041
	ρ_{sh} =	0.0022	0.0015	0.0015	0.0022	0.0015	0.0022	0.0015	0.0022	0.0015	0.0022	0.0022	0.0015	0.0015	0.0022	0.0015	0.0022	0.0015	0.0022	0.0015	0.0022
	s (in) =	10.0	10.0	10.0	10.0	10.0	10.0	10.0	10.0	10.0	10.0	10.0	10.0	10.0	10.0	10.0	10.0	10.0	10.0	10.0	10.0
Story 1	h (in) =	20	20	0.0073	0.0143	0.0028	20	20	0.0073	0.0143	0.0028	20	20	0.0073	0.0143	0.0028	20	20	0.0073	0.0143	0.0028
	b (in) =	20	20	0.0073	0.0143	0.0028	20	20	0.0073	0.0143	0.0028	20	20	0.0073	0.0143	0.0028	20	20	0.0073	0.0143	0.0028
	ρ_{tot} =	0.057	0.041	0.041	0.057	0.041	0.057	0.041	0.041	0.057	0.041	0.057	0.041	0.041	0.057	0.041	0.057	0.041	0.041	0.057	0.041
	ρ_{sh} =	0.0039	0.0028	0.0028	0.0039	0.0028	0.0039	0.0028	0.0028	0.0039	0.0028	0.0039	0.0028	0.0028	0.0039	0.0028	0.0039	0.0028	0.0028	0.0039	0.0028
	s (in) =	10.0	10.0	10.0	10.0	10.0	10.0	10.0	10.0	10.0	10.0	10.0	10.0	10.0	10.0	10.0	10.0	10.0	10.0	10.0	10.0

25 feet

13 feet
15 feet

Design base shear = 0.068 g, 99 k	
f'_c beams = 4.0 ksi	f'_c cols, lower = 4.0 ksi
f'_c cols, upper = 4.0 ksi	f_y rebar, nom. = 60 ksi

Report ID: OMF12-1.2-00,
OMF12-1.2-0J,
OMF12-1.2-SJ

Stanford Design ID: 3023

Building Type: RC Frame,
designed per 1967 UBC

Design Type: Baseline

Number of Stories: 12

Floor	h (in)	b (in)	ρ_{sv}	ρ_{sh}	s (in)	h (in)	b (in)	ρ_{sv}	ρ_{sh}	s (in)	h (in)	b (in)	ρ_{sv}	ρ_{sh}	s (in)
Floor 13	26	26	0.0053	0.0066	0.0020	26	26	0.0053	0.0066	0.0020	26	26	0.0053	0.0066	0.0020
Story 12	h (in) = 26	b (in) = 26	$\rho_{sv} = 0.012$	$\rho_{sh} = 0.0095$	s (in) = 13.0	h (in) = 26	b (in) = 26	$\rho_{sv} = 0.010$	$\rho_{sh} = 0.0095$	s (in) = 13.0	h (in) = 26	b (in) = 26	$\rho_{sv} = 0.010$	$\rho_{sh} = 0.0095$	s (in) = 13.0
Floor 12	26	26	0.0047	0.0090	0.0020	26	26	0.0047	0.0090	0.0020	26	26	0.0047	0.0090	0.0020
Story 11	h (in) = 26	b (in) = 26	$\rho_{sv} = 0.012$	$\rho_{sh} = 0.0095$	s (in) = 13.0	h (in) = 26	b (in) = 26	$\rho_{sv} = 0.010$	$\rho_{sh} = 0.0095$	s (in) = 13.0	h (in) = 26	b (in) = 26	$\rho_{sv} = 0.010$	$\rho_{sh} = 0.0095$	s (in) = 13.0
Floor 11	26	26	0.0048	0.0105	0.0020	26	26	0.0048	0.0105	0.0020	26	26	0.0048	0.0105	0.0020
Story 10	h (in) = 26	b (in) = 26	$\rho_{sv} = 0.012$	$\rho_{sh} = 0.0095$	s (in) = 13.0	h (in) = 26	b (in) = 26	$\rho_{sv} = 0.010$	$\rho_{sh} = 0.0095$	s (in) = 13.0	h (in) = 26	b (in) = 26	$\rho_{sv} = 0.010$	$\rho_{sh} = 0.0095$	s (in) = 13.0
Floor 10	26	26	0.0048	0.0120	0.0020	26	26	0.0048	0.0120	0.0020	26	26	0.0048	0.0120	0.0020
Story 9	h (in) = 26	b (in) = 26	$\rho_{sv} = 0.015$	$\rho_{sh} = 0.0095$	s (in) = 13.0	h (in) = 26	b (in) = 26	$\rho_{sv} = 0.015$	$\rho_{sh} = 0.0095$	s (in) = 13.0	h (in) = 26	b (in) = 26	$\rho_{sv} = 0.015$	$\rho_{sh} = 0.0095$	s (in) = 13.0
Floor 9	26	26	0.005	0.013	0.0020	26	26	0.005	0.013	0.0020	26	26	0.005	0.013	0.0020
Story 8	h (in) = 26	b (in) = 26	$\rho_{sv} = 0.015$	$\rho_{sh} = 0.0095$	s (in) = 13.0	h (in) = 26	b (in) = 26	$\rho_{sv} = 0.015$	$\rho_{sh} = 0.0095$	s (in) = 13.0	h (in) = 26	b (in) = 26	$\rho_{sv} = 0.015$	$\rho_{sh} = 0.0095$	s (in) = 13.0
Floor 8	26	26	0.0052	0.0135	0.0020	26	26	0.0052	0.0135	0.0020	26	26	0.0052	0.0135	0.0020
Story 7	h (in) = 26	b (in) = 26	$\rho_{sv} = 0.021$	$\rho_{sh} = 0.0095$	s (in) = 13.0	h (in) = 26	b (in) = 26	$\rho_{sv} = 0.023$	$\rho_{sh} = 0.0095$	s (in) = 13.0	h (in) = 26	b (in) = 26	$\rho_{sv} = 0.023$	$\rho_{sh} = 0.0095$	s (in) = 13.0
Floor 7	32	26	0.0043	0.0105	0.0020	32	26	0.0043	0.0105	0.0020	32	26	0.0043	0.0105	0.0020
Story 6	h (in) = 26	b (in) = 26	$\rho_{sv} = 0.021$	$\rho_{sh} = 0.0090$	s (in) = 15.0	h (in) = 26	b (in) = 26	$\rho_{sv} = 0.023$	$\rho_{sh} = 0.0090$	s (in) = 15.0	h (in) = 26	b (in) = 26	$\rho_{sv} = 0.023$	$\rho_{sh} = 0.0090$	s (in) = 15.0
Floor 6	32	26	0.0045	0.0105	0.0021	32	26	0.0045	0.0105	0.0021	32	26	0.0045	0.0105	0.0021
Story 5	h (in) = 26	b (in) = 26	$\rho_{sv} = 0.021$	$\rho_{sh} = 0.0040$	s (in) = 15.0	h (in) = 26	b (in) = 26	$\rho_{sv} = 0.023$	$\rho_{sh} = 0.0040$	s (in) = 15.0	h (in) = 26	b (in) = 26	$\rho_{sv} = 0.023$	$\rho_{sh} = 0.0040$	s (in) = 15.0
Floor 5	32	26	0.0046	0.0105	0.0021	32	26	0.0046	0.0105	0.0021	32	26	0.0046	0.0105	0.0021
Story 4	h (in) = 26	b (in) = 26	$\rho_{sv} = 0.023$	$\rho_{sh} = 0.0040$	s (in) = 15.0	h (in) = 26	b (in) = 26	$\rho_{sv} = 0.025$	$\rho_{sh} = 0.0040$	s (in) = 15.0	h (in) = 26	b (in) = 26	$\rho_{sv} = 0.025$	$\rho_{sh} = 0.0040$	s (in) = 15.0
Floor 4	32	26	0.0048	0.0103	0.0031	32	26	0.0048	0.0103	0.0031	32	26	0.0048	0.0103	0.0031
Story 3	h (in) = 26	b (in) = 26	$\rho_{sv} = 0.023$	$\rho_{sh} = 0.0045$	s (in) = 10.0	h (in) = 26	b (in) = 26	$\rho_{sv} = 0.025$	$\rho_{sh} = 0.0045$	s (in) = 10.0	h (in) = 26	b (in) = 26	$\rho_{sv} = 0.025$	$\rho_{sh} = 0.0045$	s (in) = 10.0
Floor 3	32	26	0.0053	0.0105	0.0031	32	26	0.0053	0.0105	0.0031	32	26	0.0053	0.0105	0.0031
Story 2	h (in) = 26	b (in) = 26	$\rho_{sv} = 0.023$	$\rho_{sh} = 0.0045$	s (in) = 10.0	h (in) = 32	b (in) = 26	$\rho_{sv} = 0.025$	$\rho_{sh} = 0.0068$	s (in) = 9.0	h (in) = 32	b (in) = 26	$\rho_{sv} = 0.025$	$\rho_{sh} = 0.0068$	s (in) = 9.0
Floor 2	32	26	0.0058	0.0108	0.0021	32	26	0.0058	0.0108	0.0021	32	26	0.0058	0.0108	0.0021
Story 1	h (in) = 26	b (in) = 26	$\rho_{sv} = 0.040$	$\rho_{sh} = 0.0060$	s (in) = 10.0	h (in) = 32	b (in) = 26	$\rho_{sv} = 0.025$	$\rho_{sh} = 0.0068$	s (in) = 9.0	h (in) = 32	b (in) = 26	$\rho_{sv} = 0.025$	$\rho_{sh} = 0.0068$	s (in) = 9.0
Floor 1	32	26	0.0060	0.0060	0.0020	32	26	0.0060	0.0060	0.0020	32	26	0.0060	0.0060	0.0020

← 25 feet →

↑ 13 feet
↑ 15 feet

Design base shear =	0.053	g.	232	k	
f'_c beams =	4.0	ksi	f'_c col, lower =	4.0	ksi
f'_c col, upper =	4.0	ksi	f_y steel, nom. =	60	ksi

Report ID: OMF12-0.8-00

Stanford Design ID: NEW

Building Type: RC Frame,
designed per 1967 UBC

Design Type: SCWB 0.8

Number of Stories: 12

Floor	h (m)	b (in)	ρ_{ws}	ρ_{ws}	s (in)	h (m)	b (in)	ρ_{ws}	ρ_{ws}	s (in)	h (m)	b (in)	ρ_{ws}	ρ_{ws}	s (in)	h (m)	b (in)	ρ_{ws}	ρ_{ws}	s (in)
Floor 13	26	26	0.0056	0.0069	0.0020	26	26	0.0056	0.0069	0.0020	26	26	0.0056	0.0069	0.0020	26	26	0.0056	0.0069	0.0020
Story 12	h (m) = 26	b (in) = 26	$\rho_{ws} = 0.010$	$\rho_{ws} = 0.0095$	s (in) = 13.0	h (m) = 26	b (in) = 26	$\rho_{ws} = 0.009$	$\rho_{ws} = 0.0085$	s (in) = 13.0	h (m) = 26	b (in) = 26	$\rho_{ws} = 0.009$	$\rho_{ws} = 0.0085$	s (in) = 13.0	h (m) = 26	b (in) = 26	$\rho_{ws} = 0.009$	$\rho_{ws} = 0.0085$	s (in) = 13.0
Floor 12	26	26	0.0049	0.0095	0.0020	26	26	0.0049	0.0095	0.0020	26	26	0.0049	0.0095	0.0020	26	26	0.0049	0.0095	0.0020
Story 11	h (m) = 26	b (in) = 26	$\rho_{ws} = 0.010$	$\rho_{ws} = 0.0095$	s (in) = 13.0	h (m) = 26	b (in) = 26	$\rho_{ws} = 0.009$	$\rho_{ws} = 0.0085$	s (in) = 13.0	h (m) = 26	b (in) = 26	$\rho_{ws} = 0.009$	$\rho_{ws} = 0.0085$	s (in) = 13.0	h (m) = 26	b (in) = 26	$\rho_{ws} = 0.009$	$\rho_{ws} = 0.0085$	s (in) = 13.0
Floor 11	26	26	0.0050	0.0110	0.0020	26	26	0.0050	0.0110	0.0020	26	26	0.0050	0.0110	0.0020	26	26	0.0050	0.0110	0.0020
Story 10	h (m) = 26	b (in) = 26	$\rho_{ws} = 0.010$	$\rho_{ws} = 0.0095$	s (in) = 13.0	h (m) = 26	b (in) = 26	$\rho_{ws} = 0.009$	$\rho_{ws} = 0.0085$	s (in) = 13.0	h (m) = 26	b (in) = 26	$\rho_{ws} = 0.009$	$\rho_{ws} = 0.0085$	s (in) = 13.0	h (m) = 26	b (in) = 26	$\rho_{ws} = 0.009$	$\rho_{ws} = 0.0085$	s (in) = 13.0
Floor 10	26	26	0.0126	0.0020	7.5	26	26	0.0126	0.0020	7.5	26	26	0.0126	0.0020	7.5	26	26	0.0126	0.0020	7.5
Story 9	h (m) = 26	b (in) = 26	$\rho_{ws} = 0.013$	$\rho_{ws} = 0.0095$	s (in) = 13.0	h (m) = 26	b (in) = 26	$\rho_{ws} = 0.013$	$\rho_{ws} = 0.0095$	s (in) = 13.0	h (m) = 26	b (in) = 26	$\rho_{ws} = 0.013$	$\rho_{ws} = 0.0095$	s (in) = 13.0	h (m) = 26	b (in) = 26	$\rho_{ws} = 0.013$	$\rho_{ws} = 0.0095$	s (in) = 13.0
Floor 9	26	26	0.0053	0.0137	0.0020	26	26	0.0053	0.0137	0.0020	26	26	0.0053	0.0137	0.0020	26	26	0.0053	0.0137	0.0020
Story 8	h (m) = 26	b (in) = 26	$\rho_{ws} = 0.013$	$\rho_{ws} = 0.0095$	s (in) = 13.0	h (m) = 26	b (in) = 26	$\rho_{ws} = 0.013$	$\rho_{ws} = 0.0095$	s (in) = 13.0	h (m) = 26	b (in) = 26	$\rho_{ws} = 0.013$	$\rho_{ws} = 0.0095$	s (in) = 13.0	h (m) = 26	b (in) = 26	$\rho_{ws} = 0.013$	$\rho_{ws} = 0.0095$	s (in) = 13.0
Floor 8	26	26	0.0055	0.0142	0.0020	26	26	0.0055	0.0142	0.0020	26	26	0.0055	0.0142	0.0020	26	26	0.0055	0.0142	0.0020
Story 7	h (m) = 26	b (in) = 26	$\rho_{ws} = 0.018$	$\rho_{ws} = 0.0095$	s (in) = 13.0	h (m) = 26	b (in) = 26	$\rho_{ws} = 0.020$	$\rho_{ws} = 0.0045$	s (in) = 10.0	h (m) = 26	b (in) = 26	$\rho_{ws} = 0.020$	$\rho_{ws} = 0.0045$	s (in) = 10.0	h (m) = 26	b (in) = 26	$\rho_{ws} = 0.020$	$\rho_{ws} = 0.0045$	s (in) = 10.0
Floor 7	32	26	0.0045	0.0110	7.5	32	26	0.0045	0.0110	7.5	32	26	0.0045	0.0110	7.5	32	26	0.0045	0.0110	7.5
Story 6	h (m) = 26	b (in) = 26	$\rho_{ws} = 0.018$	$\rho_{ws} = 0.0090$	s (in) = 15.0	h (m) = 26	b (in) = 26	$\rho_{ws} = 0.020$	$\rho_{ws} = 0.0060$	s (in) = 10.0	h (m) = 26	b (in) = 26	$\rho_{ws} = 0.020$	$\rho_{ws} = 0.0060$	s (in) = 10.0	h (m) = 26	b (in) = 26	$\rho_{ws} = 0.020$	$\rho_{ws} = 0.0060$	s (in) = 10.0
Floor 6	32	26	0.0047	0.0110	14.5	32	26	0.0047	0.0110	14.5	32	26	0.0047	0.0110	14.5	32	26	0.0047	0.0110	14.5
Story 5	h (m) = 26	b (in) = 26	$\rho_{ws} = 0.018$	$\rho_{ws} = 0.0040$	s (in) = 15.0	h (m) = 26	b (in) = 26	$\rho_{ws} = 0.020$	$\rho_{ws} = 0.0060$	s (in) = 10.0	h (m) = 26	b (in) = 26	$\rho_{ws} = 0.020$	$\rho_{ws} = 0.0060$	s (in) = 10.0	h (m) = 26	b (in) = 26	$\rho_{ws} = 0.020$	$\rho_{ws} = 0.0060$	s (in) = 10.0
Floor 5	32	26	0.0048	0.0110	14.5	32	26	0.0048	0.0110	14.5	32	26	0.0048	0.0110	14.5	32	26	0.0048	0.0110	14.5
Story 4	h (m) = 26	b (in) = 26	$\rho_{ws} = 0.020$	$\rho_{ws} = 0.0040$	s (in) = 15.0	h (m) = 26	b (in) = 26	$\rho_{ws} = 0.021$	$\rho_{ws} = 0.0060$	s (in) = 10.0	h (m) = 26	b (in) = 26	$\rho_{ws} = 0.021$	$\rho_{ws} = 0.0060$	s (in) = 10.0	h (m) = 26	b (in) = 26	$\rho_{ws} = 0.021$	$\rho_{ws} = 0.0060$	s (in) = 10.0
Floor 4	32	26	0.0050	0.0108	14.5	32	26	0.0050	0.0108	14.5	32	26	0.0050	0.0108	14.5	32	26	0.0050	0.0108	14.5
Story 3	h (m) = 26	b (in) = 26	$\rho_{ws} = 0.020$	$\rho_{ws} = 0.0045$	s (in) = 10.0	h (m) = 26	b (in) = 26	$\rho_{ws} = 0.021$	$\rho_{ws} = 0.0067$	s (in) = 9.0	h (m) = 26	b (in) = 26	$\rho_{ws} = 0.021$	$\rho_{ws} = 0.0067$	s (in) = 9.0	h (m) = 26	b (in) = 26	$\rho_{ws} = 0.021$	$\rho_{ws} = 0.0067$	s (in) = 9.0
Floor 3	32	26	0.0056	0.0031	14.5	32	26	0.0056	0.0031	14.5	32	26	0.0056	0.0031	14.5	32	26	0.0056	0.0031	14.5
Story 2	h (m) = 26	b (in) = 26	$\rho_{ws} = 0.020$	$\rho_{ws} = 0.0045$	s (in) = 10.0	h (m) = 32	b (in) = 26	$\rho_{ws} = 0.021$	$\rho_{ws} = 0.0068$	s (in) = 9.0	h (m) = 32	b (in) = 26	$\rho_{ws} = 0.021$	$\rho_{ws} = 0.0068$	s (in) = 9.0	h (m) = 32	b (in) = 26	$\rho_{ws} = 0.021$	$\rho_{ws} = 0.0068$	s (in) = 9.0
Floor 2	32	26	0.0061	0.0113	14.5	32	26	0.0061	0.0113	14.5	32	26	0.0061	0.0113	14.5	32	26	0.0061	0.0113	14.5
Story 1	h (m) = 26	b (in) = 26	$\rho_{ws} = 0.034$	$\rho_{ws} = 0.0060$	s (in) = 10.0	h (m) = 32	b (in) = 26	$\rho_{ws} = 0.021$	$\rho_{ws} = 0.0068$	s (in) = 9.0	h (m) = 32	b (in) = 26	$\rho_{ws} = 0.021$	$\rho_{ws} = 0.0068$	s (in) = 9.0	h (m) = 32	b (in) = 26	$\rho_{ws} = 0.021$	$\rho_{ws} = 0.0068$	s (in) = 9.0

Design base shear =	0.053	g.	232	k
$F_{c,beams} = 4.0$ ksi	$F_{c,columns} = 4.0$ ksi	$F_{s,beams} = 60$ ksi	$F_{s,columns} = 60$ ksi	

Report ID: OMF12-2.0-00

Stanford Design ID: NEW

Building Type: RC Frame,
designed per 1967 UBC

Design Type: SCWB 2.0

Number of Stories: 12

Story	h (in)	b (in)	p_{net}	p_{pa}	s (in)	h (in)	b (in)	p_{net}	p_{pa}	s (in)	h (in)	b (in)	p_{net}	p_{pa}	s (in)
Floor 13	26	26	0.017	0.0085	13.0	26	26	0.015	0.0085	13.0	26	26	0.015	0.0085	13.0
Story 12	26	26	0.017	0.0085	13.0	26	26	0.015	0.0085	13.0	26	26	0.015	0.0085	13.0
Floor 12	26	26	0.017	0.0085	13.0	26	26	0.015	0.0085	13.0	26	26	0.015	0.0085	13.0
Story 11	26	26	0.017	0.0085	13.0	26	26	0.015	0.0085	13.0	26	26	0.015	0.0085	13.0
Floor 11	26	26	0.017	0.0085	13.0	26	26	0.015	0.0085	13.0	26	26	0.015	0.0085	13.0
Story 10	26	26	0.017	0.0085	13.0	26	26	0.015	0.0085	13.0	26	26	0.015	0.0085	13.0
Floor 10	26	26	0.017	0.0085	13.0	26	26	0.015	0.0085	13.0	26	26	0.015	0.0085	13.0
Story 9	26	26	0.022	0.0085	13.0	26	26	0.022	0.0085	13.0	26	26	0.022	0.0085	13.0
Floor 9	26	26	0.022	0.0085	13.0	26	26	0.022	0.0085	13.0	26	26	0.022	0.0085	13.0
Story 8	26	26	0.022	0.0085	13.0	26	26	0.022	0.0085	13.0	26	26	0.022	0.0085	13.0
Floor 8	26	26	0.022	0.0085	13.0	26	26	0.022	0.0085	13.0	26	26	0.022	0.0085	13.0
Story 7	26	26	0.030	0.0085	13.0	26	26	0.033	0.0085	10.0	26	26	0.033	0.0085	13.0
Floor 7	26	26	0.030	0.0085	13.0	26	26	0.033	0.0085	10.0	26	26	0.033	0.0085	13.0
Story 6	26	26	0.030	0.0085	13.0	26	26	0.033	0.0085	10.0	26	26	0.033	0.0085	13.0
Floor 6	26	26	0.030	0.0085	13.0	26	26	0.033	0.0085	10.0	26	26	0.033	0.0085	13.0
Story 5	26	26	0.030	0.0085	13.0	26	26	0.033	0.0085	10.0	26	26	0.033	0.0085	13.0
Floor 5	26	26	0.030	0.0085	13.0	26	26	0.033	0.0085	10.0	26	26	0.033	0.0085	13.0
Story 4	26	26	0.033	0.0085	15.0	26	26	0.036	0.0085	10.0	26	26	0.036	0.0085	15.0
Floor 4	26	26	0.033	0.0085	15.0	26	26	0.036	0.0085	10.0	26	26	0.036	0.0085	15.0
Story 3	26	26	0.033	0.0085	10.0	26	26	0.036	0.0085	9.0	26	26	0.036	0.0085	10.0
Floor 3	26	26	0.033	0.0085	10.0	26	26	0.036	0.0085	9.0	26	26	0.036	0.0085	10.0
Story 2	26	26	0.033	0.0085	10.0	32	32	0.036	0.0085	9.0	32	32	0.036	0.0085	10.0
Floor 2	26	26	0.033	0.0085	10.0	32	32	0.036	0.0085	9.0	32	32	0.036	0.0085	10.0
Story 1	26	26	0.058	0.0060	10.0	32	32	0.036	0.0068	9.0	32	32	0.036	0.0068	10.0
Floor 1	26	26	0.058	0.0060	10.0	32	32	0.036	0.0068	9.0	32	32	0.036	0.0068	10.0

Design base shear =	0.053	$g_c = 232$	k
F_c beams =	4.0	ksi	$f'_{c, column} = 4.0$ ksi
$f'_{c, column} =$	4.0	ksi	F_y rebar nom. = 60 ksi

Appendix E: Ground Motions

E.1 Introduction

The goal of the PEER report by Baker et al. (2011) was to develop a ground motion suite that could be used in a variety of applications. Structural and geotechnical systems at locations where the seismic hazard is dominated by mid to large magnitude crustal earthquakes at near to moderate distances could use the ground motion sets selected. The unique concept was that the ground motions are not intended to be site specific or structure specific. A wide variety of structural and geotechnical systems at a wide range of locations were considered, requiring standardized sets of ground motions to facilitate comparative evaluations in this research.

The differences between a broadband and site-specific set are worth mentioning. A broadband set has not been scaled, and there was no attempt to include or exclude velocity pulses from the selected motions. A site-specific set, on the other hand, consist of ground motions that have been scaled so their spectra closely match the target, and velocity pulses have been included in proportion to the expected likelihood of seeing velocity pulses for that particular site and ground motion intensity level.

A comprehensive comparison between this ground motion set and other standardized ground motion sets was also included in the report. The SAC ground motions, LMSR ground motions, and FEMA P695 ground motions were compared and a bulleted list of differences was provided for each set. Primary differences between the SAC ground motions are that the SAC set was selected in 1997 when there were far fewer available ground motions than in 2010. The SAC set is a smaller set of ground motions. The SAC set are for site specific purposes and have been pre scaled to satisfy NEHRP building code requirements. Primary differences between the LMSR ground motions are that the LMSR set only includes 20 motions. The LMSR set also has a narrower range of magnitudes and distances. Primary differences between the P695 ground motions are that the P695 set has fewer ground motions. The P695 ground motions have been pre-scaled and guidelines are provided for scaling tailored towards assessing median collapse capacity of a structure.

E.2 Ground Motions

The first 40 ground motions is labeled SET 1A and was intended to represent a moderately large broad-band ground motion at a small distance on a soil site. The second 40 ground motions were labeled SET 1B and were intended to represent a smaller broad-band earthquake at a moderate distance on a soil site. The third 40 ground motions were labeled SET 2 and were intended to

represent a moderately large broad-band ground motion at a small distance on a rock site. The following tables provide basic summary data for the selected ground motions.

Appendix Table E.1 SET 1A ground motions

Record Number	Earthquake Name	Year	Station	Magnitude	Closest Distance
1	Mammoth Lakes-01	1980	Long Valley Dam (Upr L Abut)	6.1	15.5
2	Chi-Chi, Taiwan	1999	CHY036	7.6	16.1
3	Cape Mendocino	1992	Rio Dell Overpass - FF	7.0	14.3
4	Imperial Valley-06	1979	Delta	6.5	22
5	Kocaeli, Turkey	1999	Yarimca	7.5	4.8
6	Imperial Valley-06	1979	Calipatria Fire Station	6.5	24.6
7	Chi-Chi, Taiwan	1999	CHY034	7.6	14.8
8	Chi-Chi, Taiwan	1999	NST	7.6	38.4
9	Kocaeli, Turkey	1999	Duzce	7.5	15.4
10	Trinidad	1980	Rio Dell Overpass, E Ground	7.2	-
11	Spitak, Armenia	1988	Gukasian	6.8	-
12	Loma Prieta	1989	Gilroy Array #4	6.9	14.3
13	Chi-Chi, Taiwan	1999	TCU060	7.6	8.5
14	Victoria, Mexico	1980	Chihuahua	6.3	19
15	Loma Prieta	1989	Fremont - Emerson Court	6.9	39.9
16	Chalfant Valley-02	1986	Zack Brothers Ranch	6.2	7.6
17	Chi-Chi, Taiwan	1999	TCU118	7.6	26.8
18	Denali, Alaska	2002	TAPS Pump Station #10	7.9	2.7
19	Imperial Valley-06	1979	El Centro Array #4	6.5	7.1
20	Big Bear-01	1992	San Bernardino - E & Hospitality	6.5	-
21	Landers	1992	Yermo Fire Station	7.3	23.6
22	Northridge-01	1994	Sylmar - Converter Sta	6.7	5.4
23	San Fernando	1971	LA - Hollywood Stor FF	6.6	22.8
24	N. Palm Springs	1986	Morongo Valley	6.1	12.1
25	Loma Prieta	1989	Hollister - South & Pine	6.9	27.9
26	Chi-Chi, Taiwan	1999	TCU055	7.6	6.4
27	Chi-Chi, Taiwan	1999	CHY025	7.6	19.1
28	Imperial Valley-06	1979	Brawley Airport	6.5	10.4
29	Chi-Chi, Taiwan	1999	CHY088	7.6	37.5
30	Duzce, Turkey	1999	Duzce	7.1	6.6
31	Chi-Chi, Taiwan	1999	TCU061	7.6	17.2
32	Loma Prieta	1989	Saratoga - Aloha Ave	6.9	8.5
33	Imperial Valley-02	1940	El Centro Array #9	7.0	6.1
34	Chi-Chi, Taiwan-03	1999	TCU123	6.2	31.8
35	Northridge-01	1994	Jensen Filter Plant	6.7	5.4
36	Chi-Chi, Taiwan-03	1999	CHY104	6.2	35.1
37	Loma Prieta	1989	Salinas - John & Work	6.9	32.8
38	Loma Prieta	1989	Coyote Lake Dam (Downst)	6.9	20.8
39	Chi-Chi, Taiwan	1999	CHY008	7.6	40.4
40	Chi-Chi, Taiwan-06	1999	TCU141	6.3	45.7

Appendix Table E.2 SET 1B ground motions

Record Number	Earthquake Name	Year	Station	Magnitude	Closest Distance
41	Big Bear-01	1992	Lake Cachulla	6.5	-
42	Big Bear-01	1992	Snow Creek	6.5	-
43	Loma Prieta	1989	Fremont - Emerson Court	6.9	39.9
44	Imperial Valley-06	1979	Superstition Mtn Camera	6.5	24.6
45	CA/Baja Border Area	2002	El Centro Array #7	5.3	-
46	Chalfant Valley-02	1986	Lake Crowley - Shehorn Res.	6.2	24.5
47	Northridge-01	1994	Elizabeth Lake	6.7	36.6
48	Northwest China-02	1997	Jiashi	5.9	-
49	Victoria, Mexico	1980	SAHOP Casa Flores	6.3	39.3
50	CA/Baja Border Area	2002	Calexico Fire Station	5.3	-
51	Whittier Narrows-01	1987	Norwalk - Imp Hwy, S Grnd	6.0	20.4
52	San Fernando	1971	Santa Felita Dam (Outlet)	6.6	24.9
53	Coalinga-01	1983	Parkfield - Stone Corral 3E	6.4	34.0
54	Imperial Valley-06	1979	Plaster City	6.5	30.3
55	El Alamo	1956	El Centro Array #9	6.8	-
56	Loma Prieta	1989	Fremont - Mission San Jose	6.9	39.5
57	N. Palm Springs	1986	San Jacinto - Valley Cemetery	6.1	31.0
58	Northridge-01	1994	Bell Gardens - Jaboneria	6.7	44.1
59	Chi-Chi, Taiwan-03	1999	CHY034	6.2	37.0
60	Morgan Hill	1984	Gilroy Array #2	6.2	13.7
61	CA/Baja Border Area	2002	Holtville Post Office	5.3	0.0
62	Morgan Hill	1984	San Juan Bautista, 24 Polk St	6.2	27.2
63	Livermore-01	1980	Tracy - Sewage Treatment Plant	5.8	-
64	Chi-Chi, Taiwan-03	1999	TCU145	6.2	48.5
65	N. Palm Springs	1986	Indio	6.1	35.6
66	Friuli, Italy-02	1976	Codroipo	5.9	41.4
67	Northridge-01	1994	Compton - Castlegate St	6.7	47.0
68	Morgan Hill	1984	Gilroy Array #7	6.2	12.1
69	Big Bear-01	1992	North Shore - Salton Sea Pk HQ	6.5	-
70	Big Bear-01	1992	Seal Beach - Office Bldg	6.5	-
71	Livermore-01	1980	San Ramon - Eastman Kodak	5.8	-
72	Coalinga-01	1983	Parkfield - Cholame 3W	6.4	45.7
73	Friuli, Italy-01	1976	Codroipo	6.5	33.4
74	Chi-Chi, Taiwan-03	1999	CHY047	6.2	46.2
75	Loma Prieta	1989	Dumbarton Bridge West End FF	6.9	35.5
76	Whittier Narrows-01	1987	West Covina - S Orange Ave	6.0	16.3
77	Mammoth Lakes-06	1980	Bishop - Paradise Lodge	5.9	-
78	Coalinga-01	1983	Parkfield - Fault Zone 16	6.4	27.7
79	Chi-Chi, Taiwan-06	1999	CHY036	6.3	46.2
80	Whittier Narrows-01	1987	Canoga Park - Topanga Can	6.0	49.0

Appendix Table E.3 SET 2 ground motions

Record Number	Earthquake Name	Year	Station	Magnitude	Closest Distance
81	San Fernando	1971	Lake Hughes #4	6.6	25.1
82	Loma Prieta	1989	Gilroy Array #6	6.9	18.3
83	Kocaeli, Turkey	1999	Izmit	7.5	7.2
84	Northridge-01	1994	LA - Wonderland Ave	6.7	20.3
85	Imperial Valley-06	1979	Cerro Prieto	6.5	15.2
86	Hector Mine	1999	Hector	7.1	11.7
87	San Fernando	1971	Pasadena - Old Seismo Lab	6.6	21.5
88	Duzce, Turkey	1999	Lamont 531	7.1	8.0
89	Hector Mine	1999	Heart Bar State Park	7.1	61.2
90	Chi-Chi, Taiwan	1999	TCU138	7.6	9.8
91	Chi-Chi, Taiwan-06	1999	TCU129	6.3	24.8
92	Coyote Lake	1979	Gilroy Array #6	5.7	3.1
93	Taiwan SMART1(45)	1983	SMART1 E02	7.3	-
94	Irpinia, Italy-01	1980	Bagnoli Irpinio	6.9	8.2
95	Loma Prieta	1989	San Jose - Santa Teresa Hills	6.9	14.7
96	Irpinia, Italy-01	1980	Bisaccia	6.9	21.3
97	Chi-Chi, Taiwan	1999	TCU045	7.6	26.0
98	Kocaeli, Turkey	1999	Gebze	7.5	10.9
99	Northridge-01	1994	Pacoima Dam (downstr)	6.7	7.0
100	Denali, Alaska	2002	Carlo (temp)	7.9	50.9
101	Helena, Montana-01	1935	Carroll College	6.0	-
102	Northridge-01	1994	Vasquez Rocks Park	6.7	23.6
103	Chi-Chi, Taiwan	1999	WNT	7.6	1.8
104	Loma Prieta	1989	Golden Gate Bridge	6.9	79.8
105	Loma Prieta	1989	UCSC	6.9	18.5
106	Victoria, Mexico	1980	Cerro Prieto	6.3	14.4
107	Northridge-01	1994	Santa Susana Ground	6.7	16.7
108	Loma Prieta	1989	Gilroy - Gavilan Coll.	6.9	10.0
109	Duzce, Turkey	1999	Mudurnu	7.1	34.3
110	Northridge-01	1994	Burbank - Howard Rd.	6.7	16.9
111	Chi-Chi, Taiwan-03	1999	TCU138	6.2	22.2
112	Chi-Chi, Taiwan-06	1999	TCU138	6.3	33.6
113	Loma Prieta	1989	UCSC Lick Observatory	6.9	18.4
114	Loma Prieta	1989	Gilroy Array #1	6.9	9.6
115	Northridge-01	1994	LA Dam	6.7	5.9
116	Northridge-01	1994	LA 00	6.7	19.1
117	Sitka, Alaska	1972	Sitka Observatory	7.7	34.6
118	Northridge-01	1994	LA - Chalon Rd	6.7	20.5
119	Loma Prieta	1989	Belmont - Envirotech	6.9	44.1
120	Chi-Chi, Taiwan	1999	TCU129	7.6	1.8

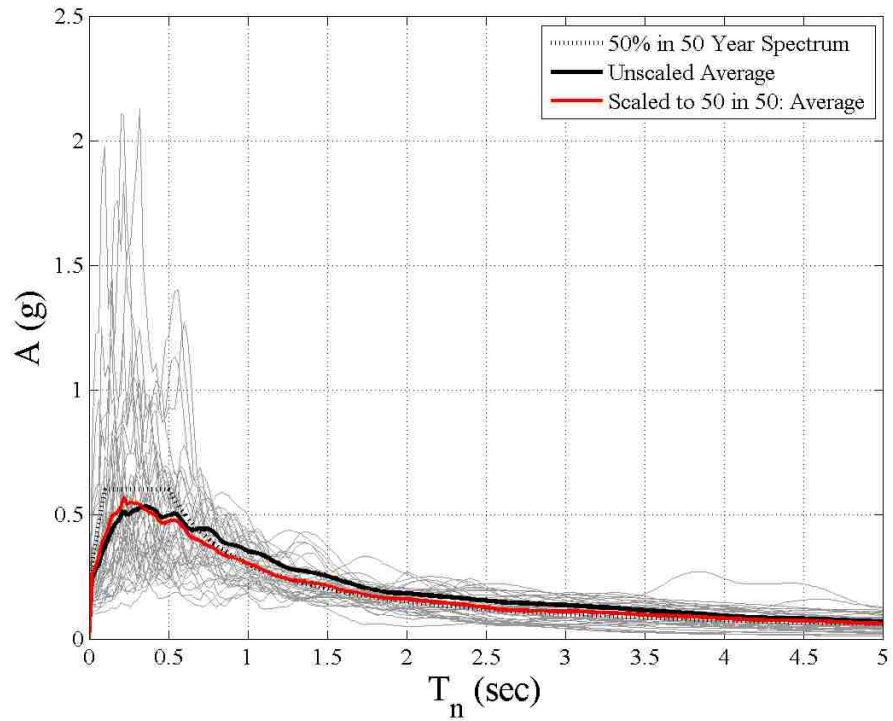
E.3 Ground Motion Scaling Factors

The scaling factors used to modify the original ground motion records are shown below. The 50% in 50 year event is intended to represent a weak ground motion. The 10% in 50 year event is

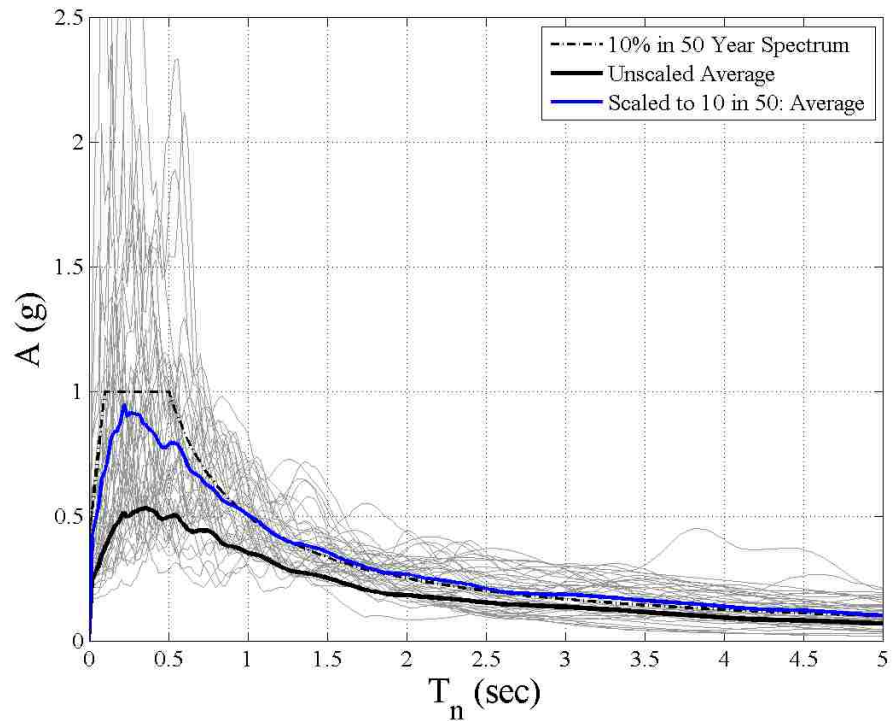
intended to represent a moderate ground motion. The 2% in 50 year event (MCE event) is intended to represent a severe ground motion. Figure E.1 to Figure E.9 show the scaled spectra that make up each set. The figures also show the un-scaled average and the scaled average spectra.

Appendix Table E.4 Scaling factors for ground motions

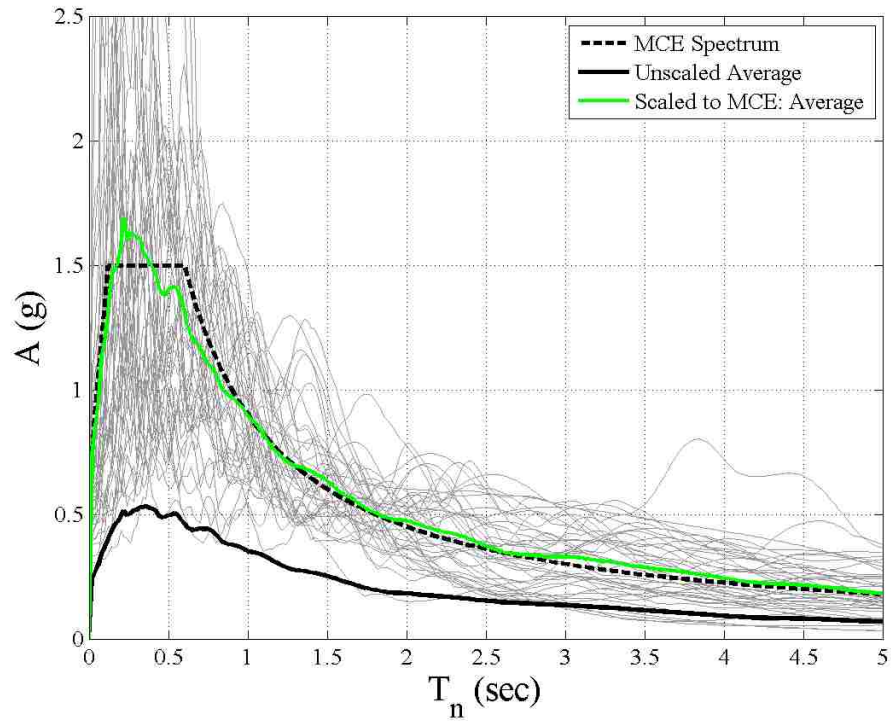
Set 1A				Set 1B				Set 2			
Record Number	50% in 50 Year: Scale Factors	10% in 50 Year: Scale Factors	MCE: Scale Factors	Record Number	50% in 50 Year: Scale Factors	10% in 50 Year: Scale Factors	MCE: Scale Factors	Record Number	50% in 50 Year: Scale Factors	10% in 50 Year: Scale Factors	MCE: Scale Factors
1	1.16	1.93	2.75	41	9.39	15.66	26.89	81	2.01	3.34	5.98
2	1.07	1.79	2.44	42	4.09	6.82	13.54	82	1.40	2.34	3.57
3	0.65	1.08	1.63	43	1.90	3.17	4.87	83	1.48	2.46	3.56
4	0.93	1.55	2.32	44	3.32	5.54	10.06	84	2.01	3.35	5.21
5	0.99	1.65	2.43	45	3.85	6.41	11.81	85	1.31	2.19	3.44
6	2.35	3.92	7.10	46	2.29	3.82	6.23	86	0.73	1.22	1.74
7	1.21	2.02	2.70	47	1.79	2.99	4.68	87	2.78	4.64	9.42
8	0.89	1.49	2.64	48	1.30	2.16	3.68	88	1.55	2.58	4.07
9	0.97	1.62	2.36	49	3.31	5.52	8.48	89	3.17	5.28	8.50
10	1.62	2.71	4.22	50	4.68	7.79	13.61	90	1.20	2.00	2.98
11	1.59	2.65	3.97	51	1.57	2.62	3.63	91	0.92	1.53	2.46
12	0.80	1.33	1.94	52	2.75	4.58	7.80	92	0.79	1.32	1.93
13	1.43	2.38	3.42	53	2.10	3.50	5.47	93	1.83	3.04	4.45
14	2.48	4.14	6.06	54	5.40	9.00	15.14	94	1.66	2.77	4.30
15	1.90	3.17	4.87	55	5.86	9.77	14.12	95	0.96	1.60	2.58
16	0.52	0.87	1.26	56	2.15	3.59	5.71	96	2.53	4.21	6.12
17	3.06	5.09	7.65	57	3.83	6.39	10.09	97	0.45	0.76	1.10
18	0.99	1.66	2.46	58	2.53	4.21	6.51	98	1.28	2.13	3.13
19	0.95	1.58	2.43	59	5.16	8.60	12.31	99	0.50	0.83	1.27
20	3.26	5.43	7.80	60	1.78	2.97	4.72	100	3.20	5.33	8.12
21	1.28	2.13	3.31	61	7.87	13.12	17.99	101	2.38	3.97	6.89
22	0.60	1.00	1.44	62	7.23	12.05	18.47	102	1.47	2.45	3.71
23	1.56	2.61	4.38	63	5.13	8.55	12.81	103	0.35	0.59	0.94
24	1.21	2.02	3.03	64	7.05	11.75	17.68	104	2.65	4.41	6.04
25	1.20	2.00	2.69	65	4.32	7.20	12.16	105	1.01	1.69	3.98
26	0.97	1.61	2.34	66	12.16	20.27	32.25	106	0.58	0.97	1.47
27	1.77	2.95	4.17	67	2.56	4.26	6.19	107	1.00	1.67	3.12
28	2.11	3.51	6.04	68	1.46	2.43	4.37	108	0.67	1.12	2.28
29	1.77	2.96	4.10	69	2.49	4.15	7.14	109	2.40	4.01	6.89
30	0.61	1.02	1.48	70	6.83	11.38	17.08	110	1.81	3.01	4.65
31	2.00	3.33	4.55	71	3.77	6.28	10.19	111	2.21	3.68	5.59
32	0.75	1.25	1.95	72	2.28	3.79	5.66	112	3.58	5.97	9.60
33	1.07	1.78	2.74	73	3.51	5.85	8.85	113	0.69	1.15	2.26
34	4.48	7.47	10.80	74	4.99	8.31	12.33	114	0.47	0.79	1.55
35	0.61	1.02	1.63	75	2.30	3.83	5.35	115	0.67	1.11	1.67
36	3.32	5.54	7.79	76	2.16	3.60	6.86	116	0.67	1.12	1.75
37	2.48	4.13	6.40	77	6.65	11.08	19.48	117	3.43	5.72	10.84
38	1.87	3.12	5.37	78	1.84	3.06	4.28	118	1.21	2.02	2.81
39	2.61	4.35	6.45	79	1.15	1.91	2.99	119	2.44	4.06	5.47
40	2.33	3.88	6.95	80	1.81	3.02	5.04	120	0.33	0.55	0.87



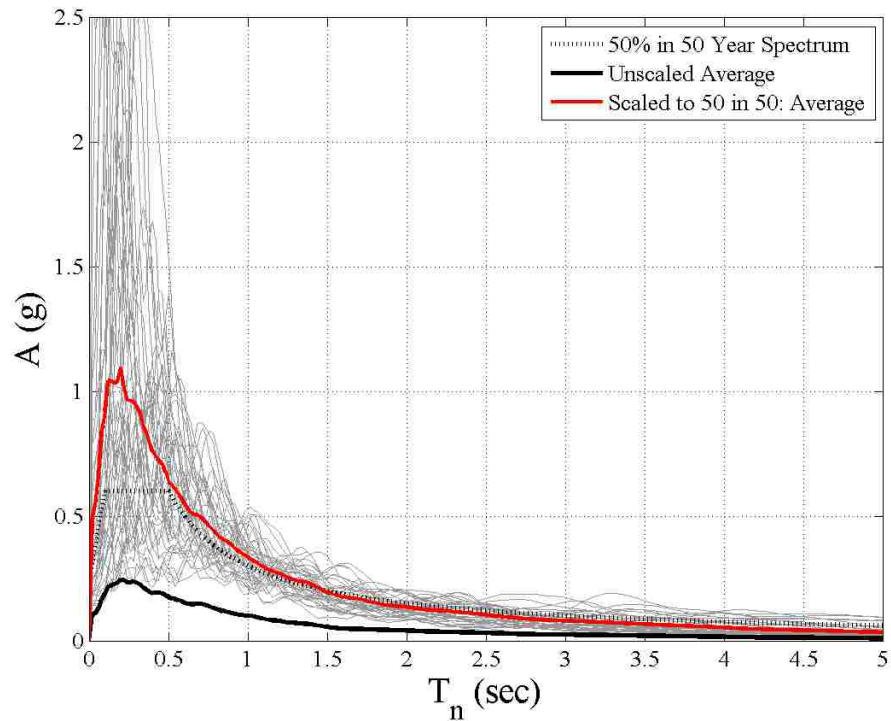
Appendix Figure E.1 SET 1A: 50% in 50 year scaling for 0.5 to 3.5 seconds



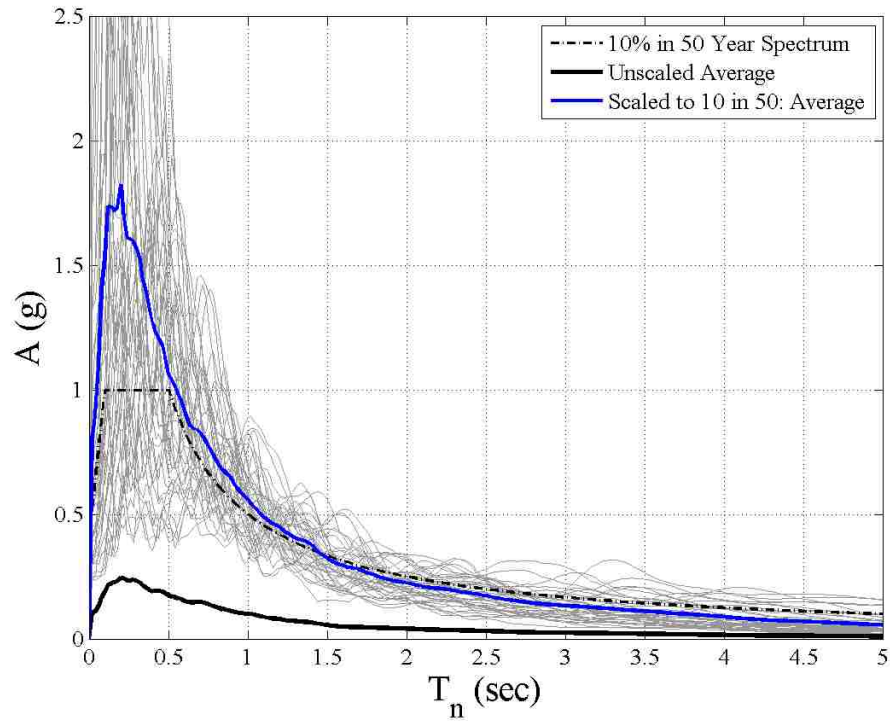
Appendix Figure E.2 SET 1A: 10% in 50 year scaling for 0.5 to 3.5 Seconds



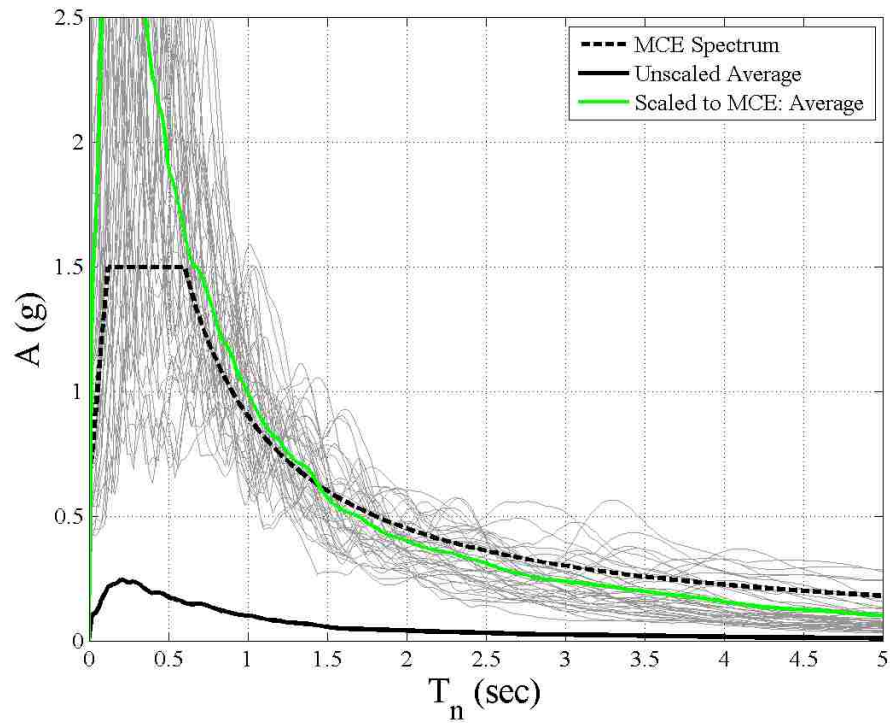
Appendix Figure E.3 SET 1A: 2% in 50 year scaling for 0.5 to 3.5 Seconds



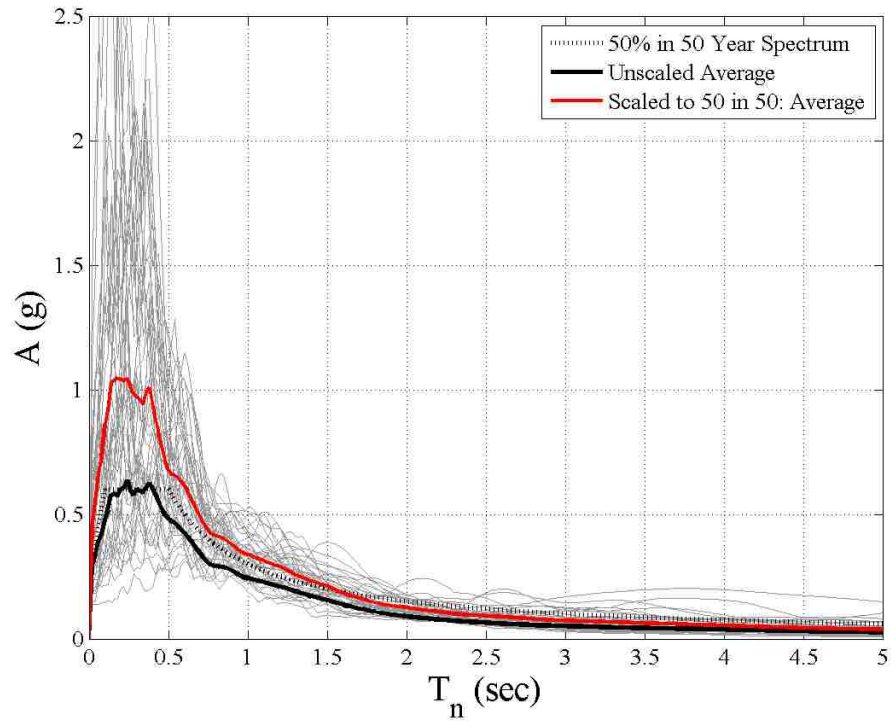
Appendix Figure E.4 SET 1B: 50% in 50 year scaling for 0.5 to 3.5 Seconds



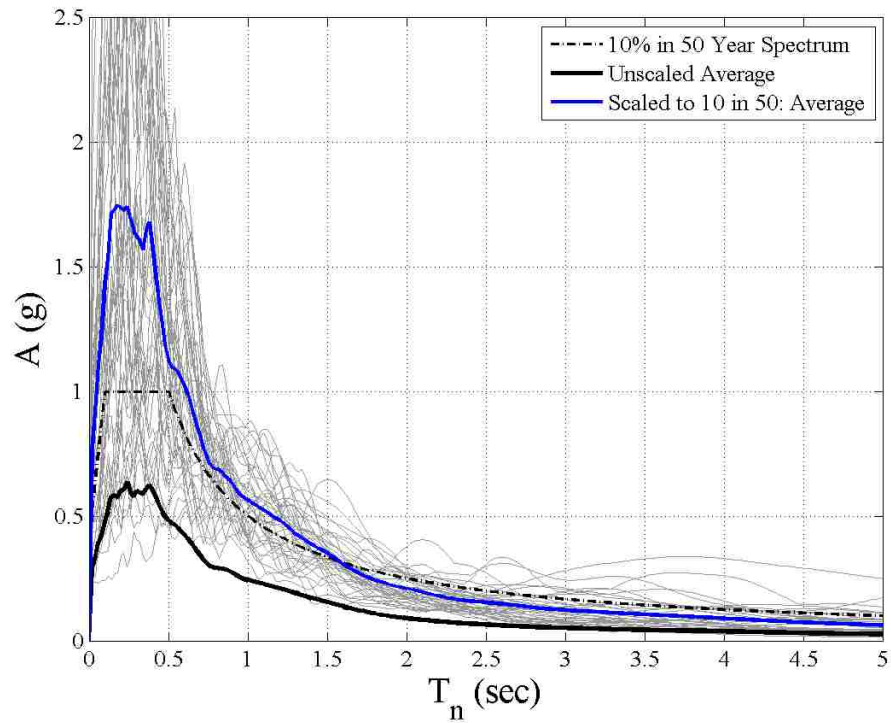
Appendix Figure E.5 SET 1B: 10% in 50 year scaling for 0.5 to 3.5 Seconds



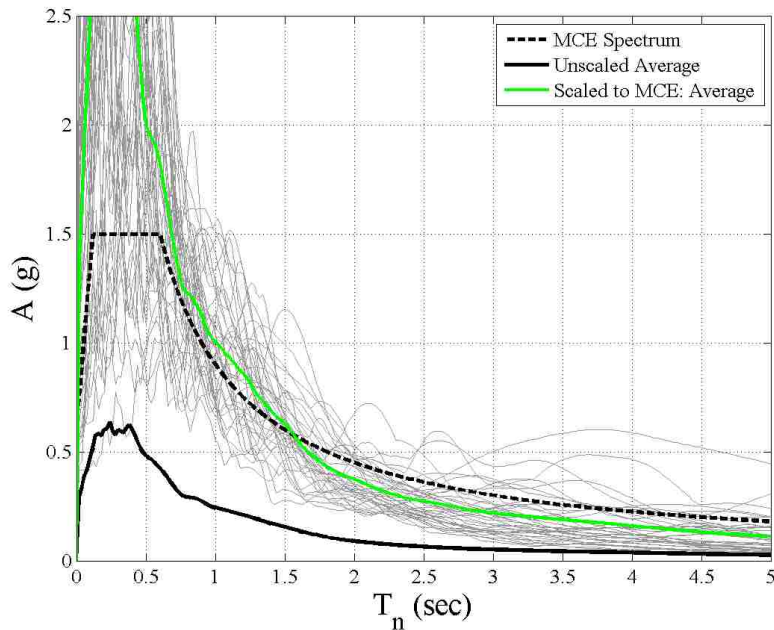
Appendix Figure E.6 SET 1B: 2% in 50 year scaling for 0.5 to 3.5 Seconds



Appendix Figure E.7 SET 2: 50% in 50 year scaling for 0.5 to 3.5 Seconds



Appendix Figure E.8 SET 2: 10% in 50 year scaling for 0.5 to 3.5 Seconds



Appendix Figure E.9 SET 2: 2% in 50 year scaling for 0.5 to 3.5 Seconds

E.4 Ground Motion Pairs

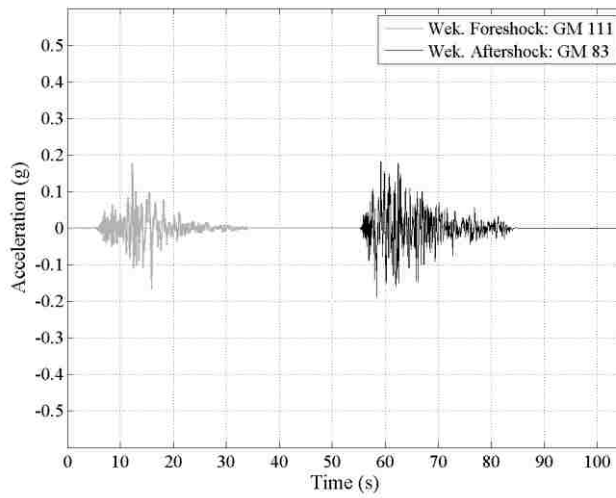
The 100 ground motion pairs are shown in Table E.6. The order that they appear in the table is how MATLAB created the array. Following the table are plots of all nine combinations of the GM 111 – GM 83 ground motion pair. These plots are presented so the ground motions that have been scaled to different site specific hazard levels can be compared. Table E.5 shows the factors used to scale the ground motions presented in Figures E.10 – E.18. The labels in Table E.5 and Figures E.10 – E.18 correspond to the 50% in 50 year event (Wek. : Weak), 10% in 50 year event (Mod. : Moderate), and 2% in 50 year event (Sev. : Severe).

Appendix Table E.5 Foreshock-Aftershock pairs

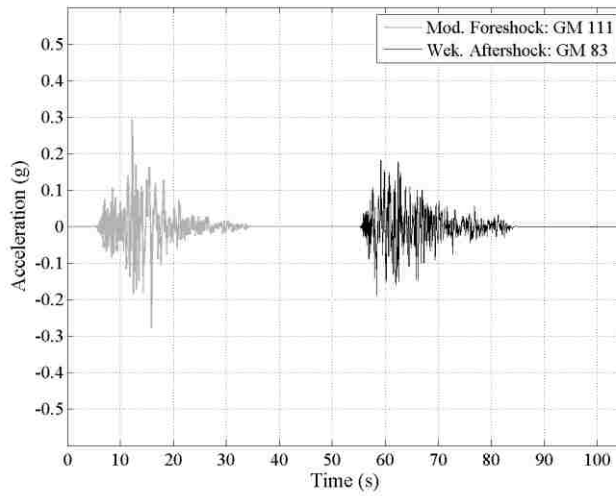
	Scaling Factors		
	Wek.	Mod.	Sev.
GM 111	2.21	3.68	5.59
GM 83	1.48	2.46	3.56

Appendix Table E.6 Foreshock-Aftershock pairs

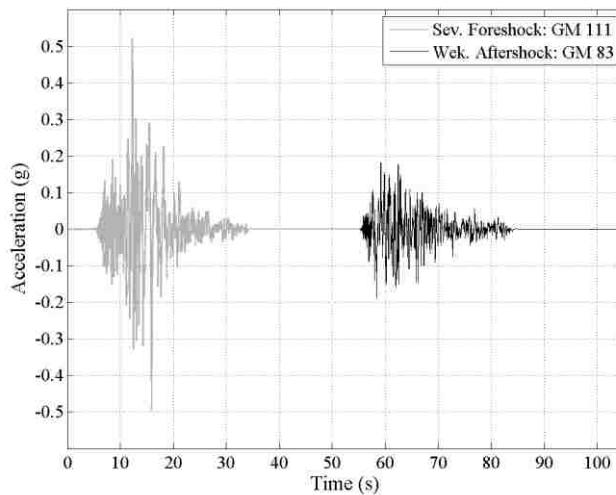
Foreshock	Aftershock	Foreshock	Aftershock	Foreshock	Aftershock	Foreshock	Aftershock
98	20	91	105	34	51	42	21
109	96	90	11	82	6	24	78
16	38	48	48	79	109	31	88
110	64	79	32	20	114	74	78
76	20	21	97	15	59	57	55
12	73	85	52	60	59	43	66
34	32	4	110	116	41	100	36
66	79	34	22	41	109	71	90
115	83	6	32	71	45	66	23
116	90	12	18	27	14	111	83
19	55	99	17	91	94	35	23
117	11	84	105	31	47	91	45
115	28	39	70	61	30	91	76
59	110	115	66	84	49	46	94
97	19	5	18	107	12	69	10
18	100	53	103	116	16	10	112
51	65	46	75	66	114	7	94
110	120	92	43	17	115	64	59
96	10	96	62	18	70	94	53
116	54	23	49	31	8	113	54
79	13	59	10	101	29	16	37
5	116	54	29	31	43	69	62
102	1	78	15	98	99	57	62
113	93	86	23	30	2	2	99
82	99	91	29	112	6	41	96



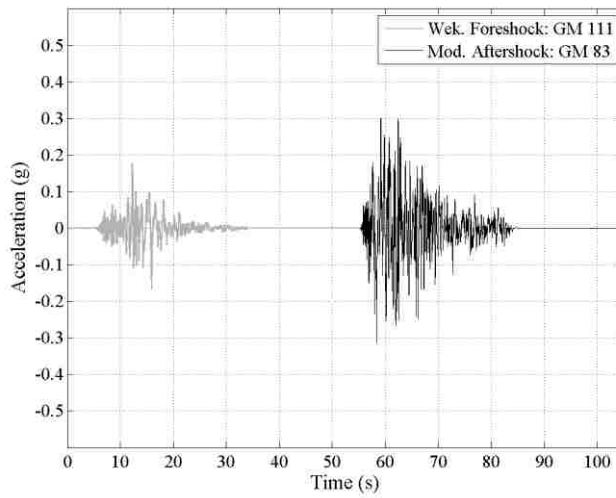
Appendix Figure E.10 Weak – Weak records for GM 111 – GM 83 pair



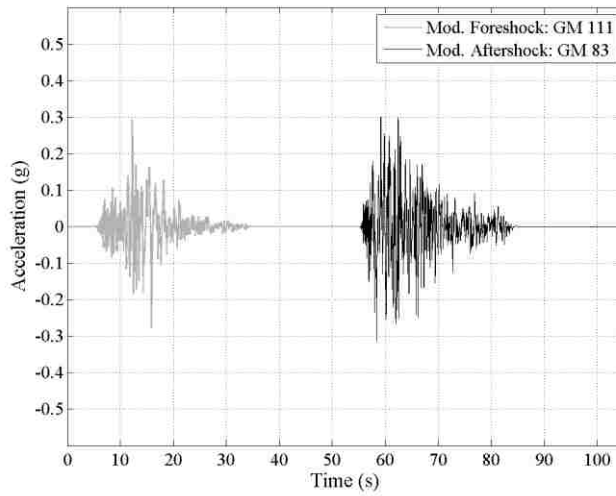
Appendix Figure E.11 Moderate – Weak records for GM 111 – GM 83 pair



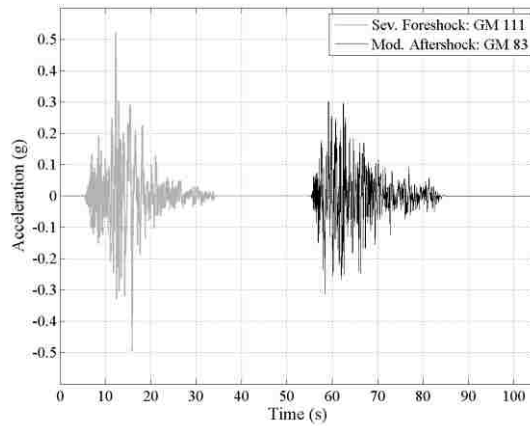
Appendix Figure E.12 Severe – Weak records for GM 111 – GM 83 pair



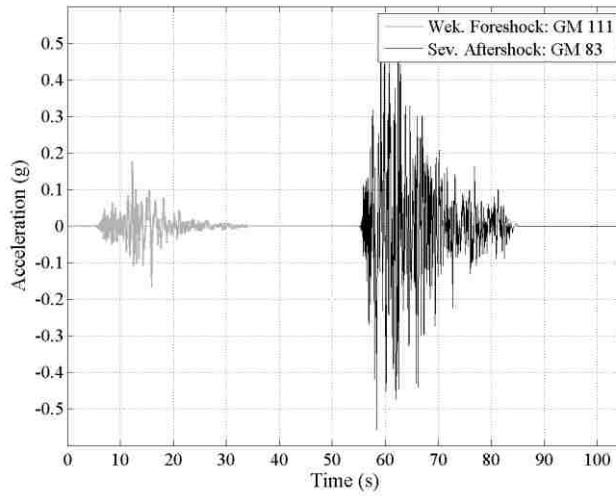
Appendix Figure E.13 Weak – Moderate records for GM 111 – GM 83 pair



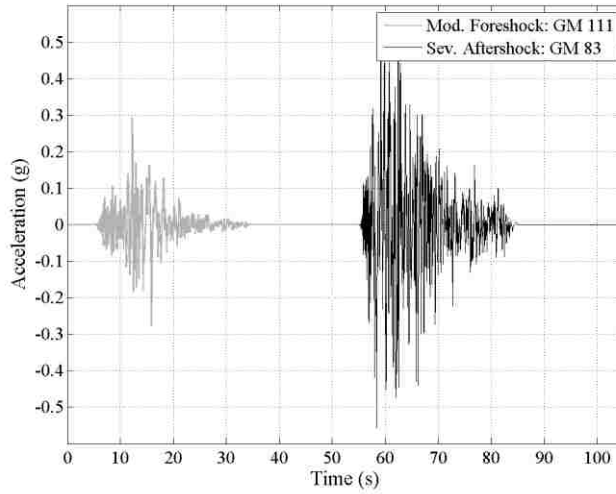
Appendix Figure E.14 Moderate – Moderate records for GM 111 – GM 83 pair



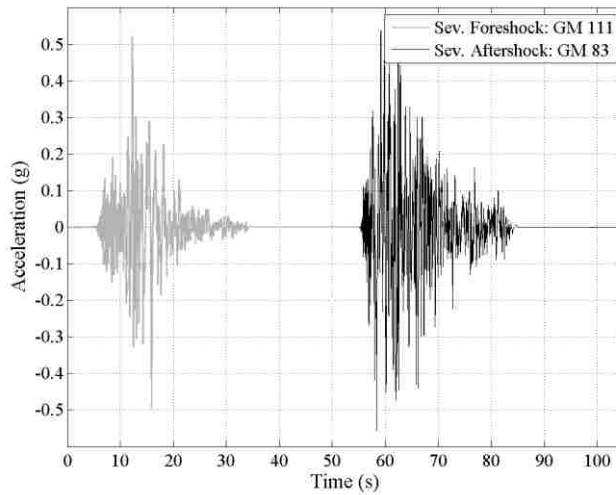
Appendix Figure E.15 Severe – Moderate records for GM 111 – GM 83 pair



Appendix Figure E.16 Weak – Severe records for GM 111 – GM 83 pair



Appendix Figure E.17 Moderate – Severe records for GM 111 – GM 83 pair



Appendix Figure E.18 Severe – Severe records for GM 111 – GM 83 pair

Appendix F: Building Pushover Data

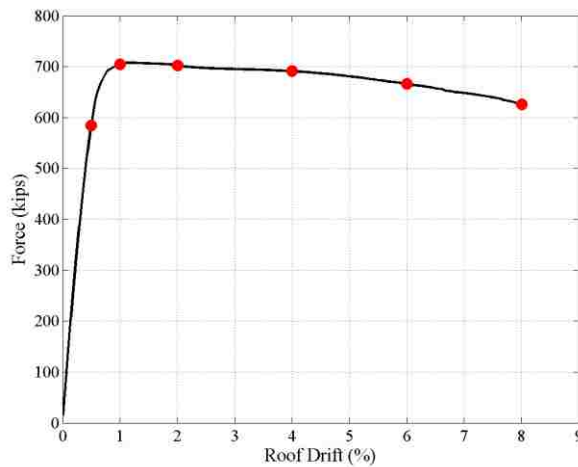
F.1 Introduction

The results of the pushover analyses are presented in this appendix. The data explanation is presented in the following figure.

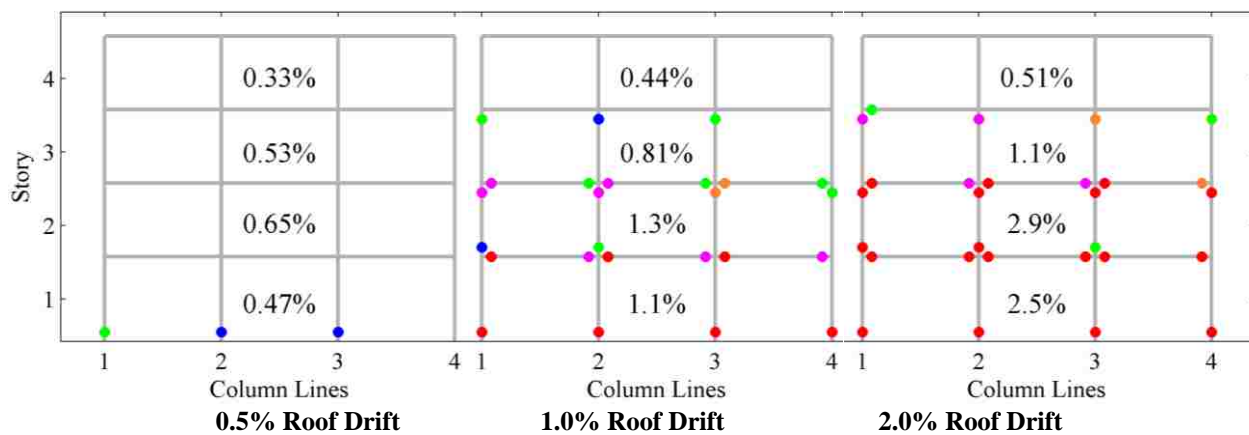


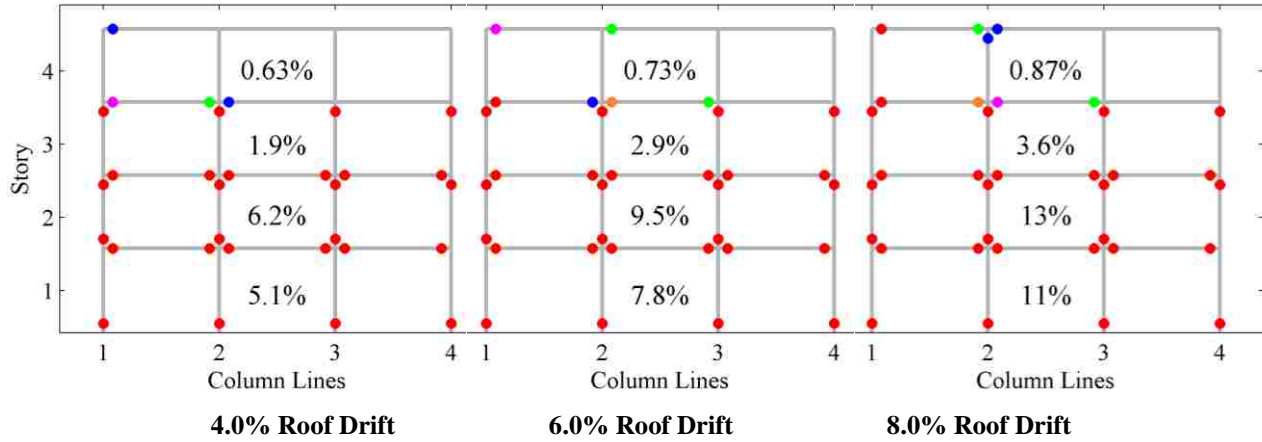
Appendix Figure F.1 Ductility demand legend for pushover results

Frame ID SMF4-1.2-00



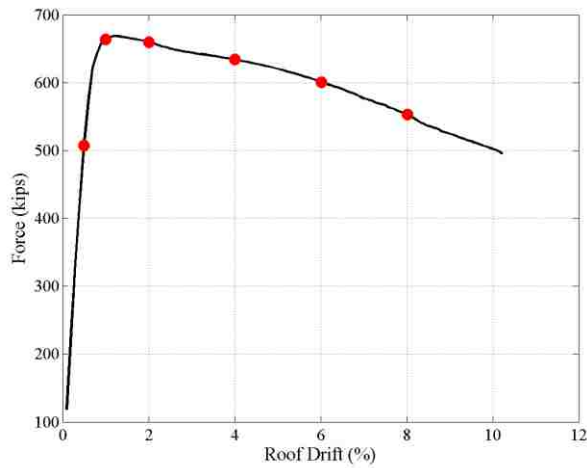
Appendix Figure F.2 SMF4-1.2-00: Pushover Curve with Curvature Ductility Points



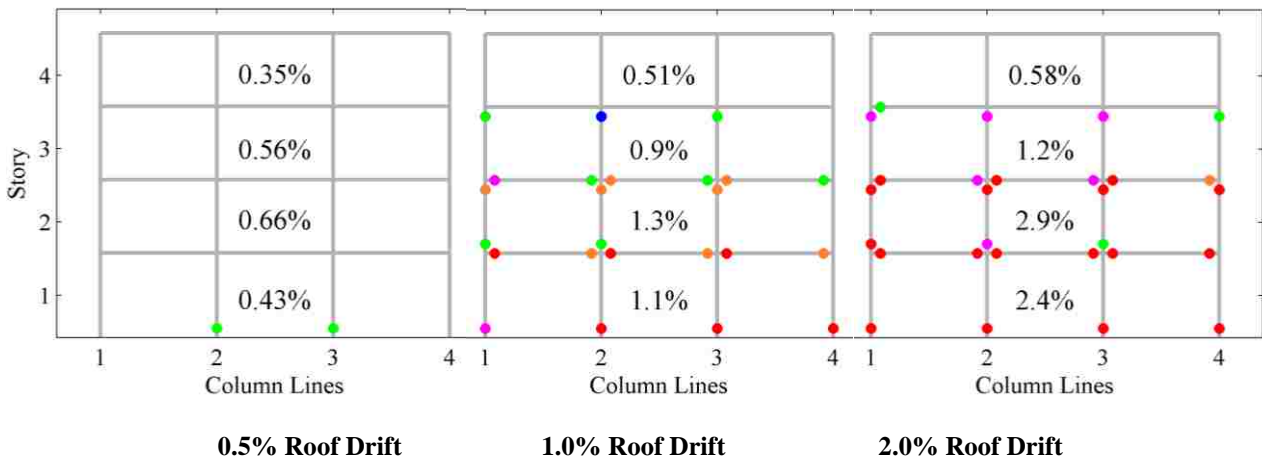


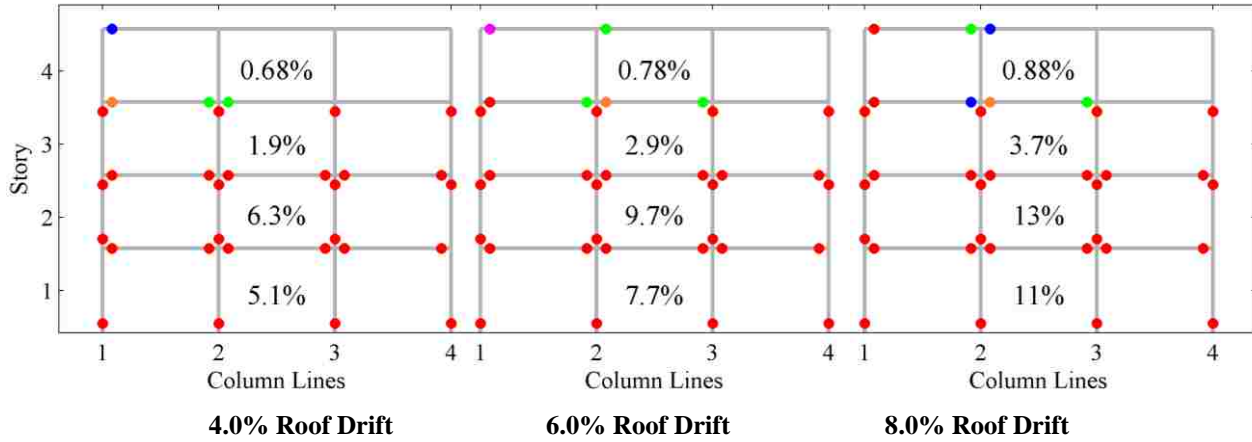
Appendix Figure F.3 SMF4-1.2-00: Drift and Curvature Ductility Plots

Frame ID SMF4-1.2-0J



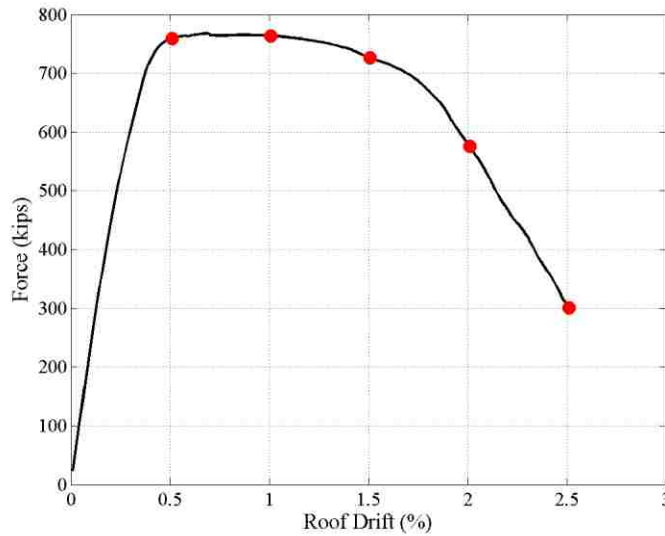
Appendix Figure F.4 SMF4-1.2-0J: Pushover Curve with Curvature Ductility Points



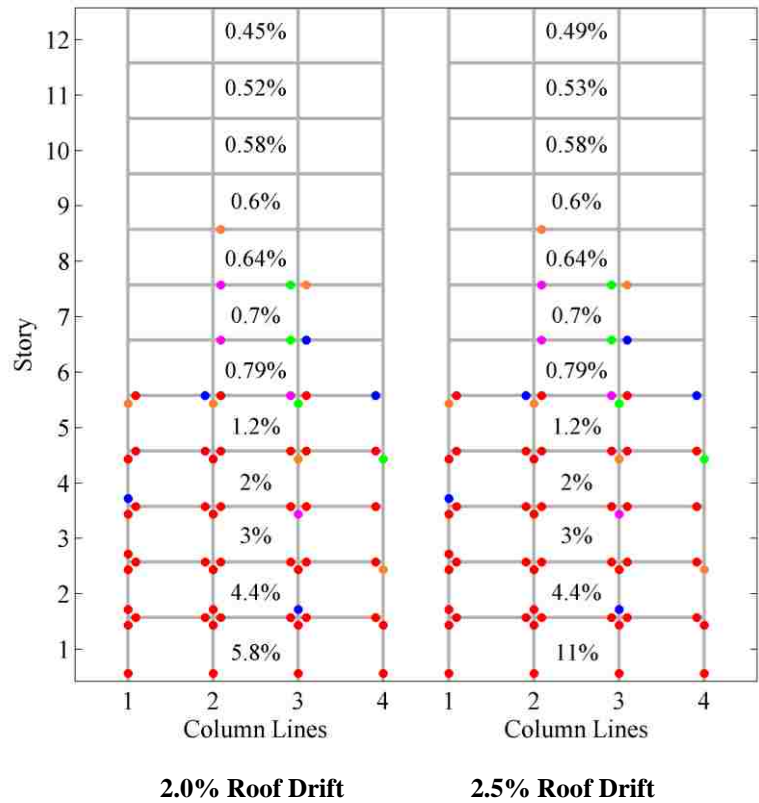
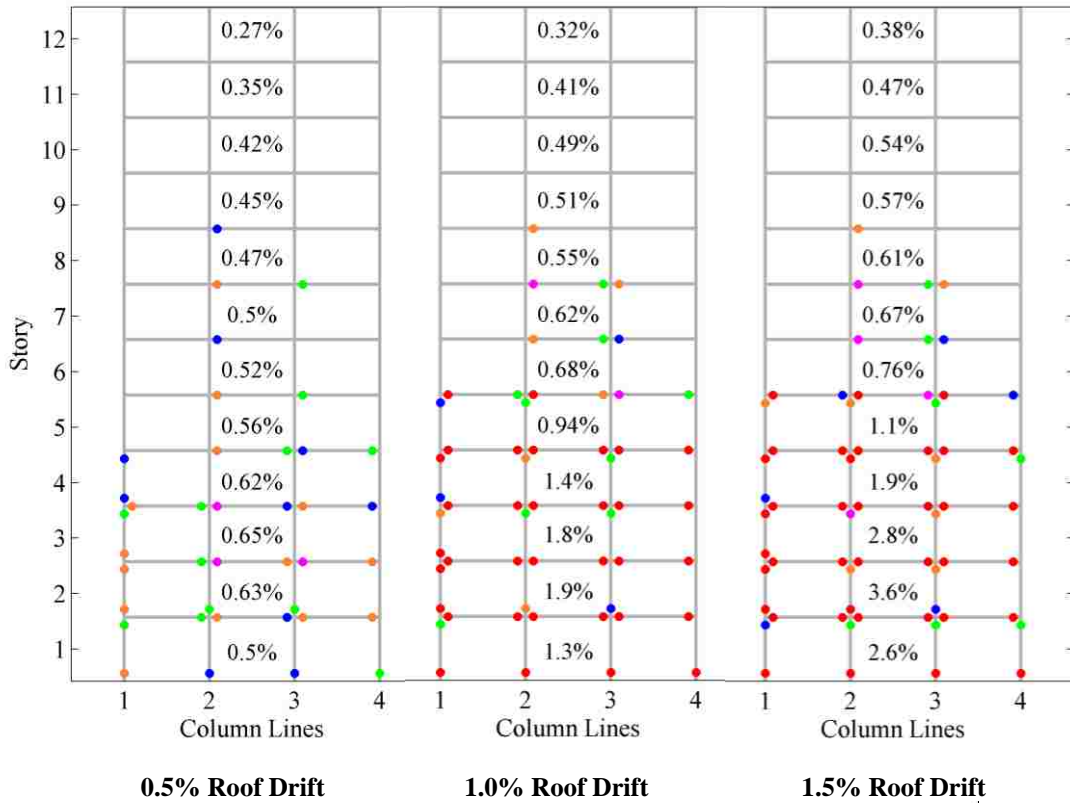


Appendix Figure F.5 SMF4-1.2-0J: Drift and Curvature Ductility Plots

Frame ID SMF12-1.2-00

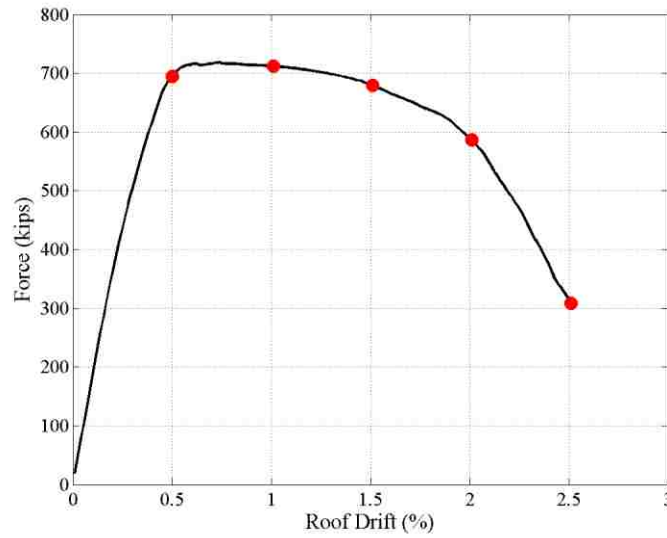


Appendix Figure F.6 SMF12-1.2-00: Pushover Curve with Curvature Ductility Points

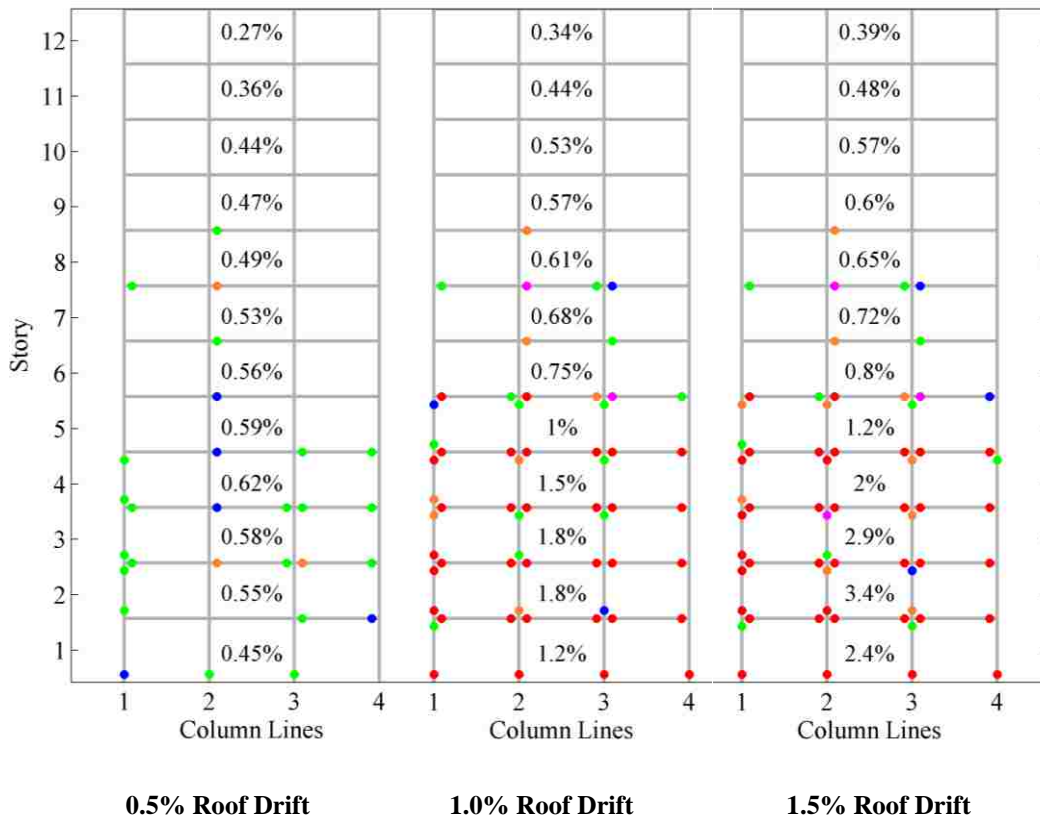


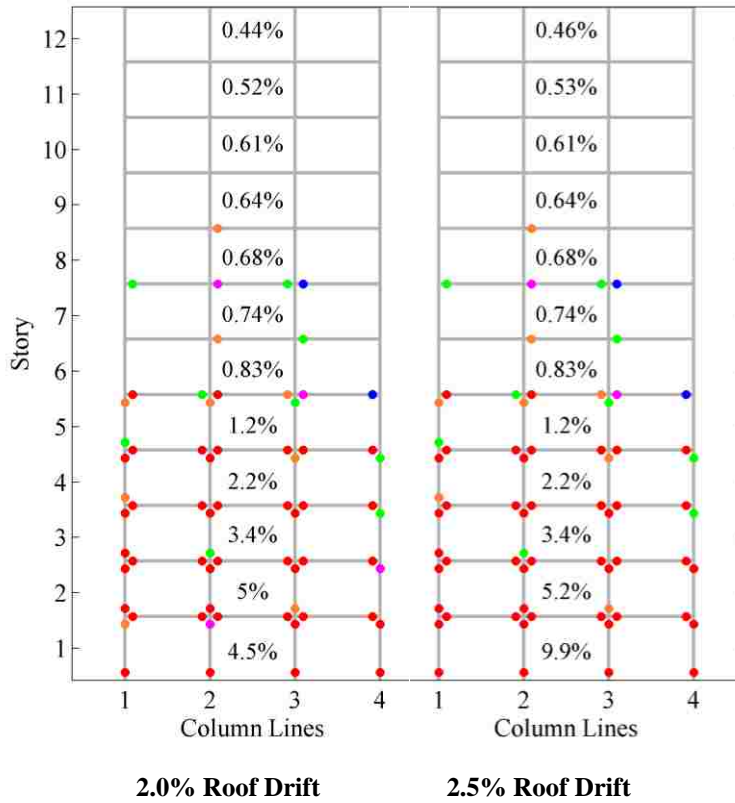
Appendix Figure F.7 SMF12-1.2-00: Drift and Curvature Ductility Plots

Frame ID SMF12-1.2-0J



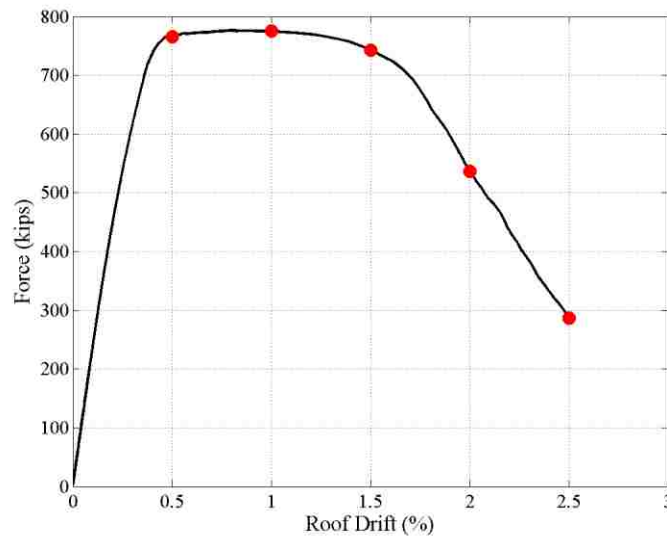
Appendix Figure F.8 SMF12-1.2-0J: Pushover Curve with Curvature Ductility Points



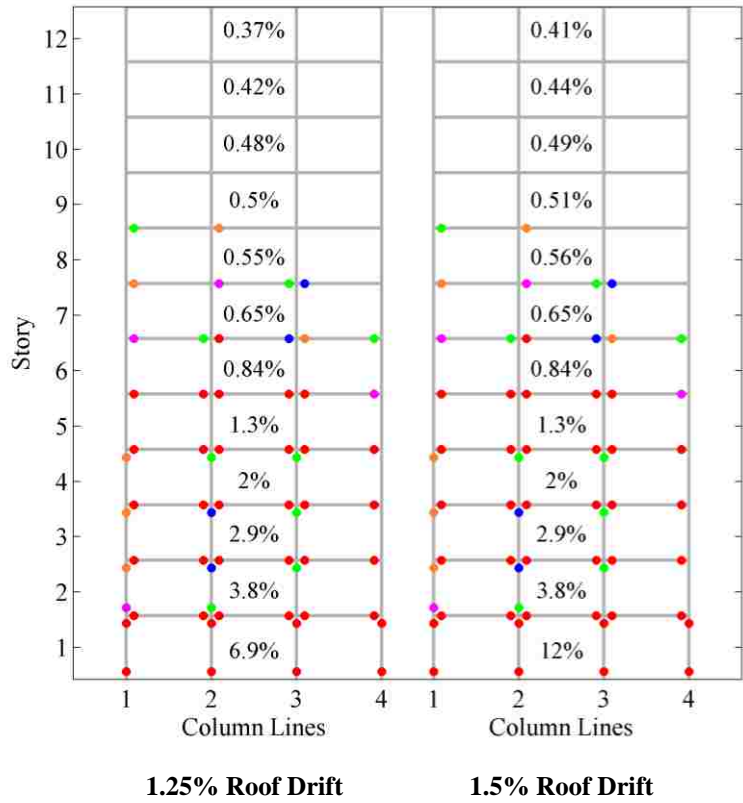
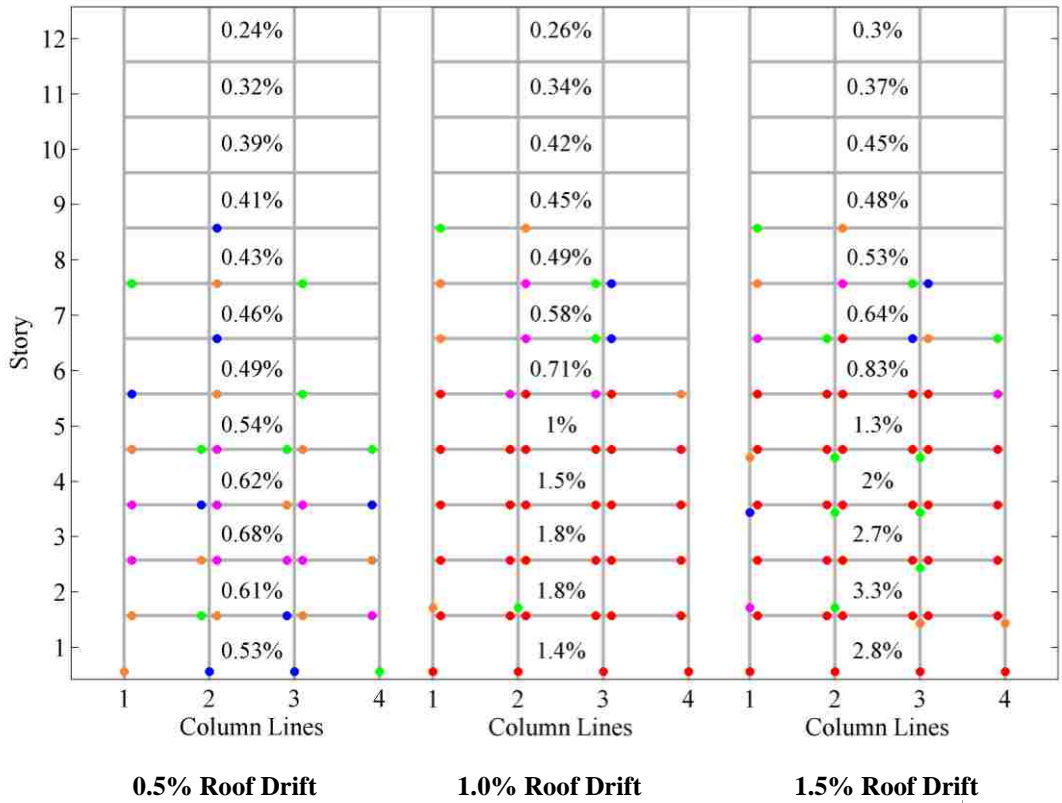


Appendix Figure F.9 SMF12-1.2-0J: Drift and Curvature Ductility Plots

Frame ID SMF12-P-1.2-WS-00

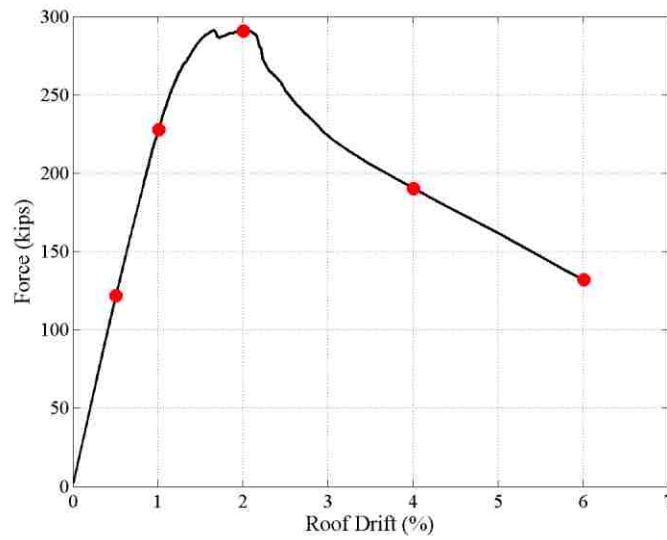


Appendix Figure F.10 SMF12-WS-00: Pushover Curve with Curvature Ductility Points

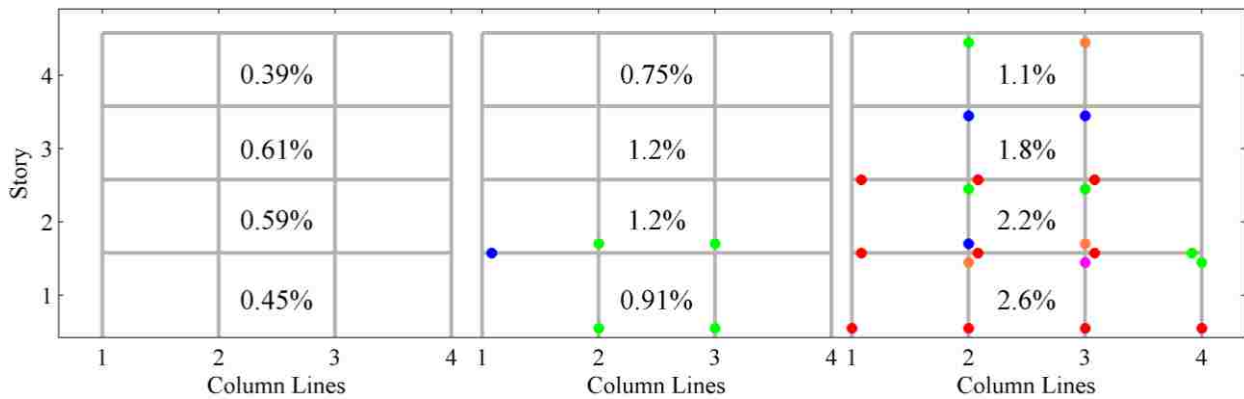


Appendix Figure F.11 SMF12-WS-00: Drift and Curvature Ductility Plots

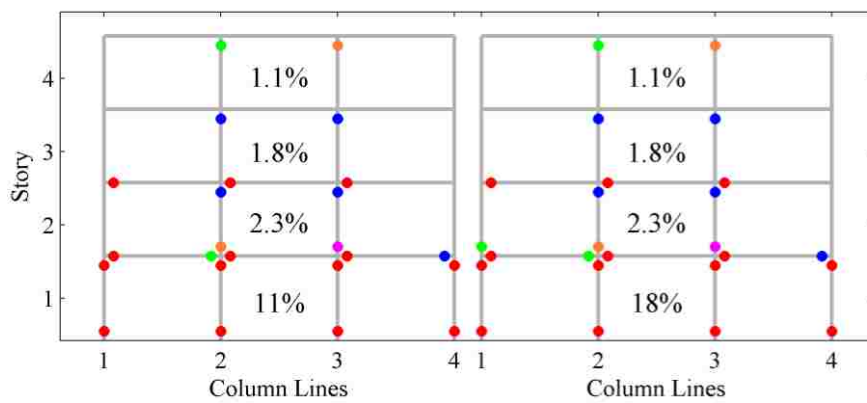
Frame ID OMF4-1.2-00



Appendix Figure F.12 OMF4-1.2-00: Pushover Curve with Curvature Ductility Points



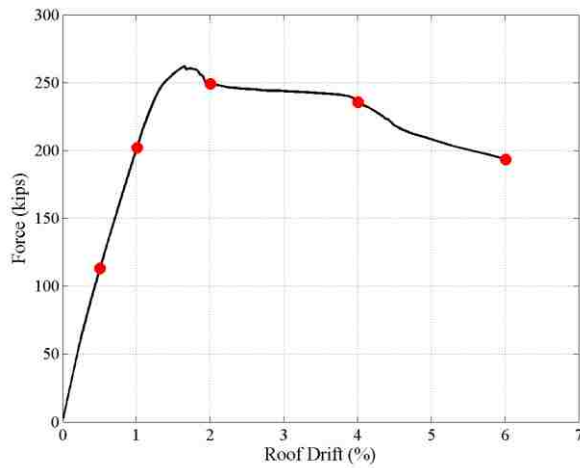
0.5% Roof Drift 1.0% Roof Drift 2.0% Roof Drift



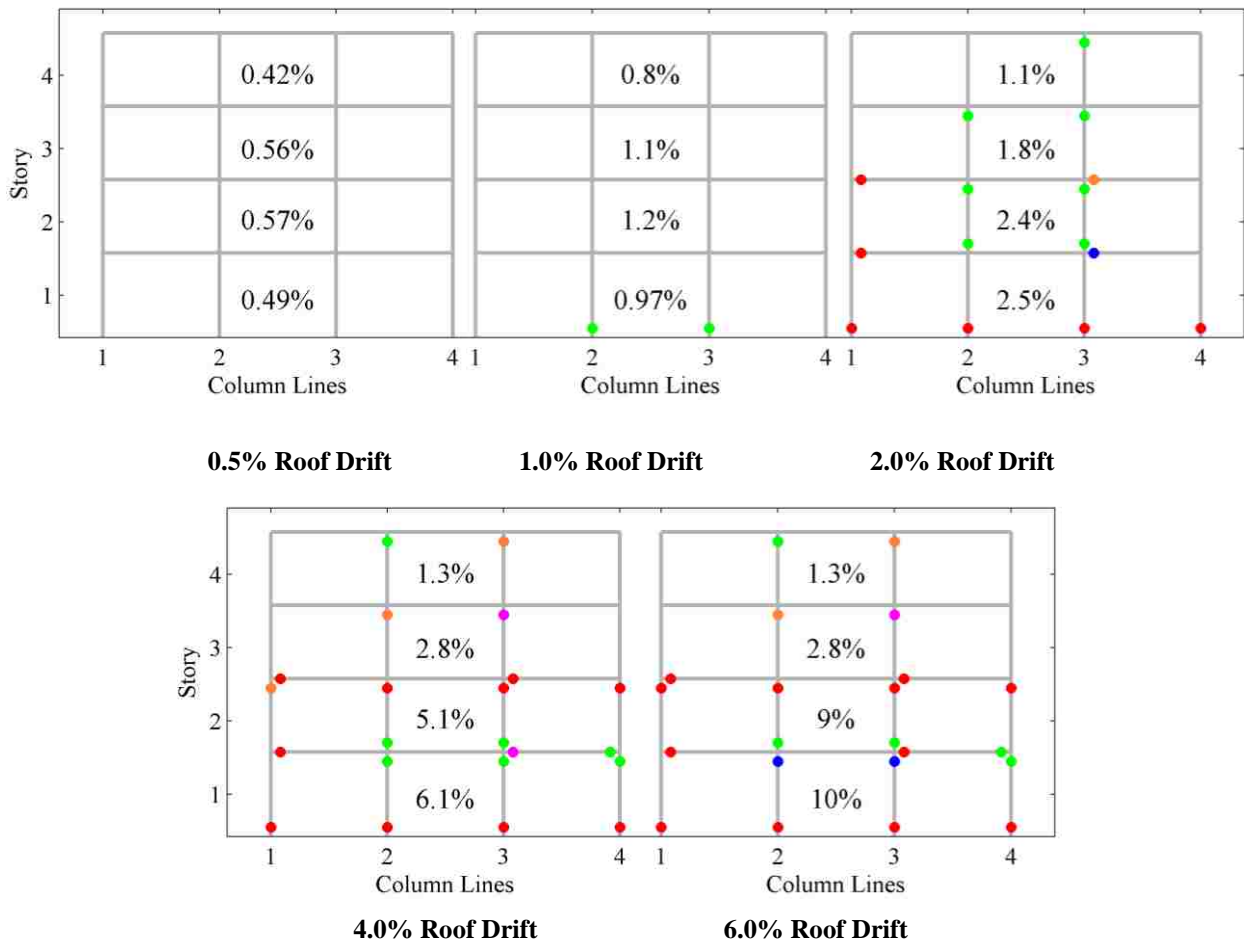
4.0% Roof Drift 6.0% Roof Drift

Appendix Figure F.13 OMF4-1.2-00: Drift and Curvature Ductility Plots

Frame ID OMF4-1.2-0J

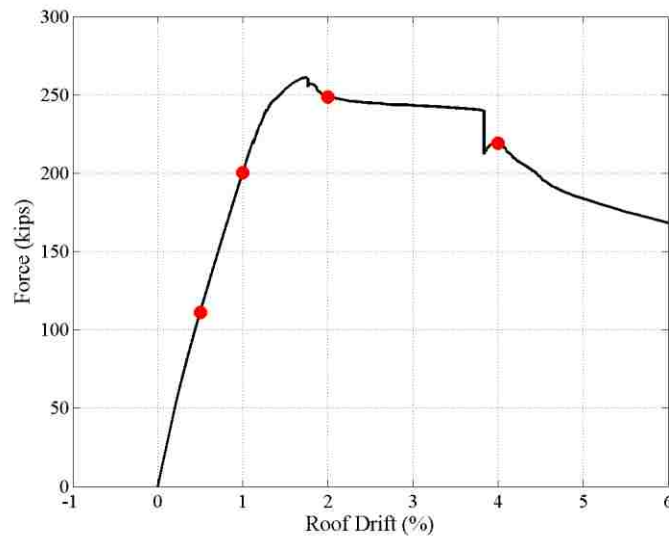


Appendix Figure F.14 OMF4-1.2-0J: Pushover Curve with Curvature Ductility Points

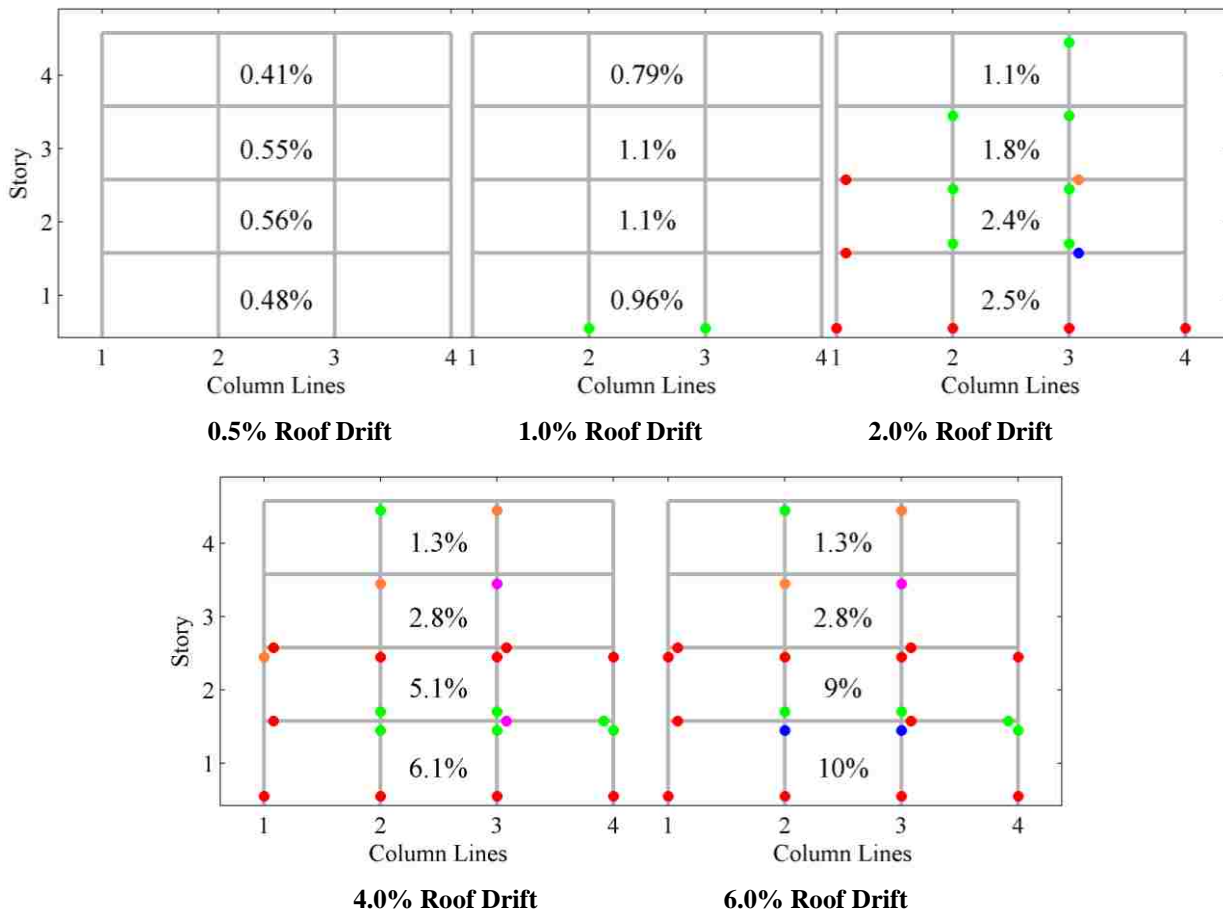


Appendix Figure F.15 OMF4-1.2-0J: Drift and Curvature Ductility Plots

Frame ID OMF4-1.2-SJ

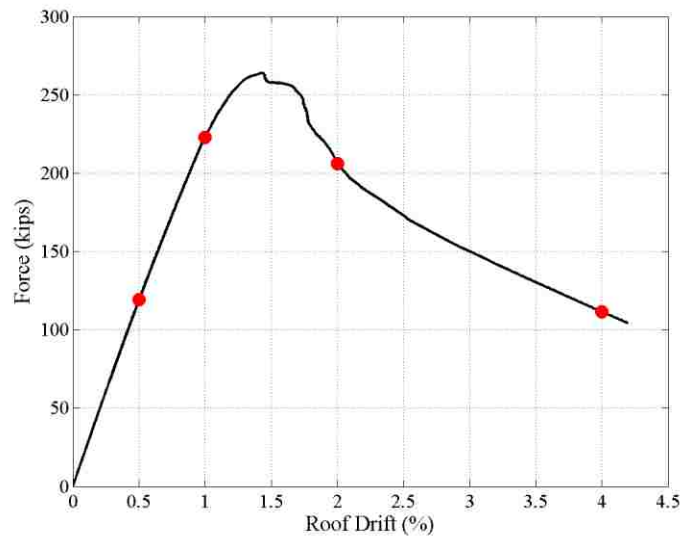


Appendix Figure F.16 OMF4-1.2-SJ: Pushover Curve with Curvature Ductility Points

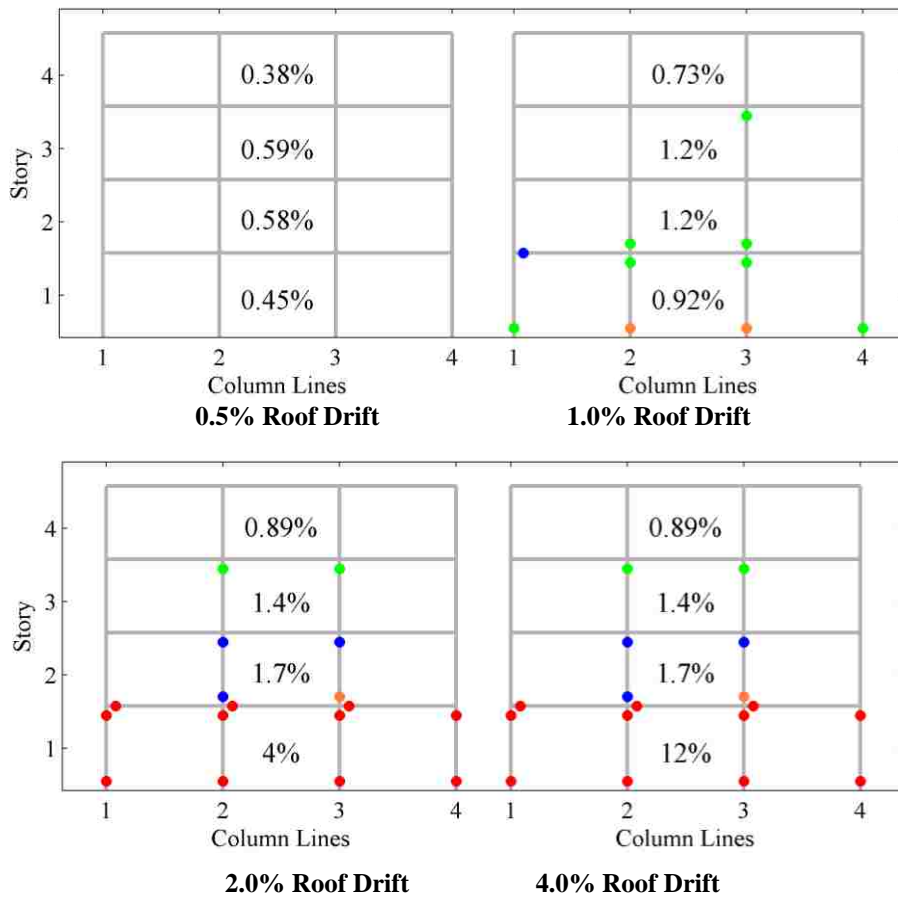


Appendix Figure F.17 OMF4-1.2-SJ: Drift and Curvature Ductility Plots

Frame ID OMF4-0.8-00

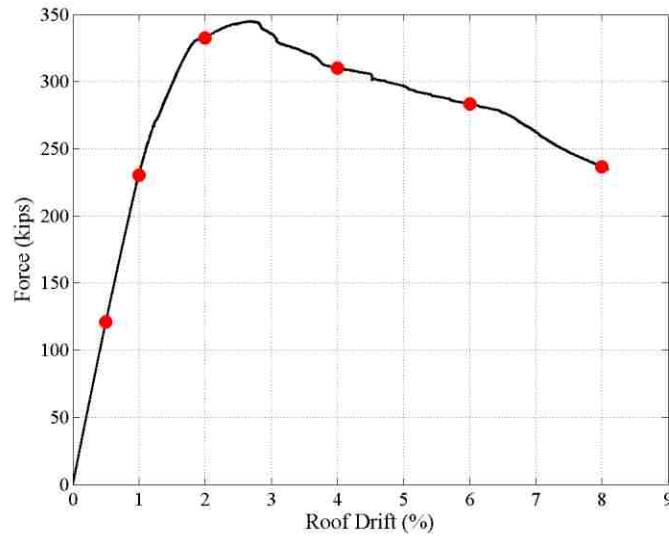


Appendix Figure F.18 OMF4-0.8-00: Pushover Curve with Curvature Ductility Points

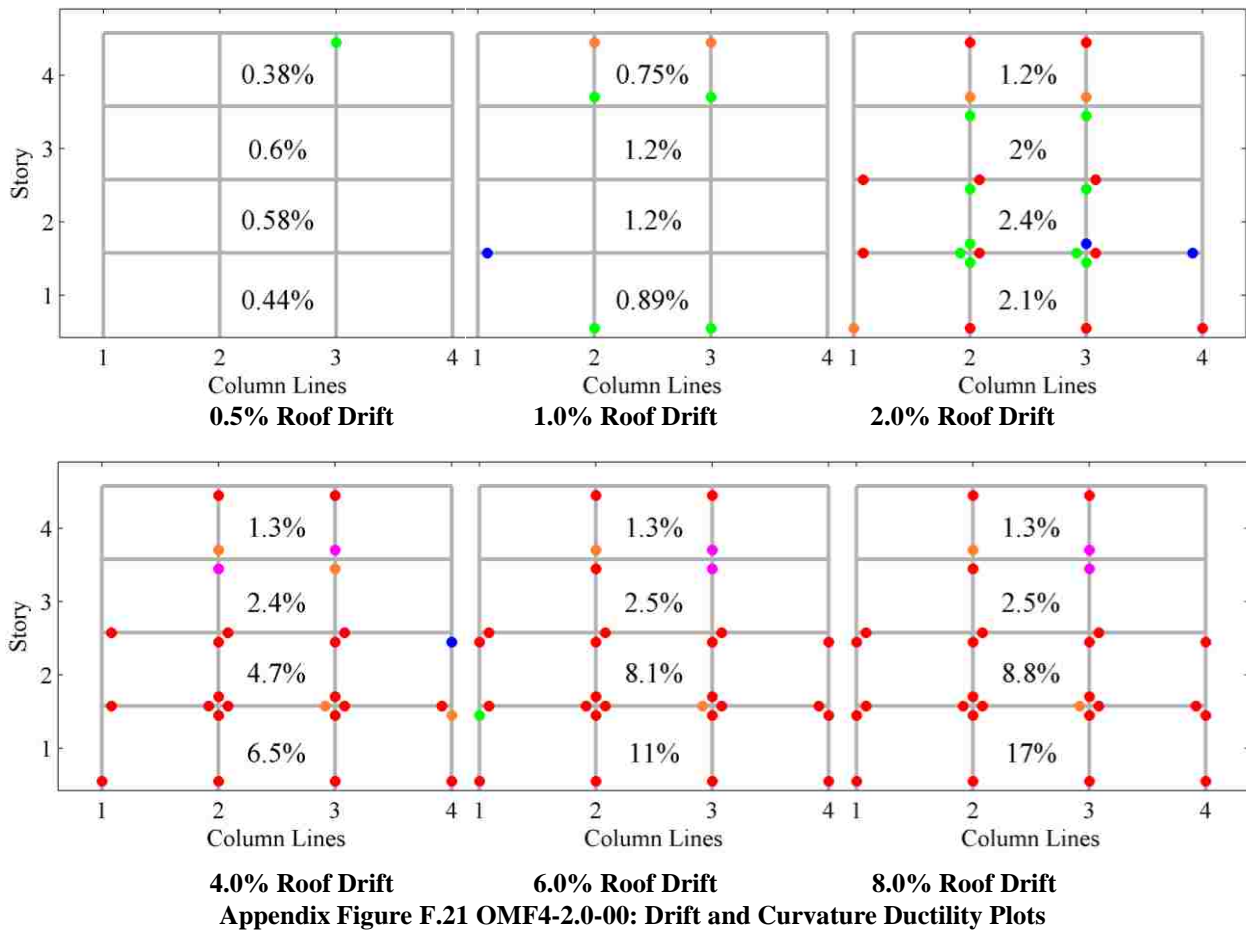


Appendix Figure F.19 OMF4-0.8-00: Drift and Curvature Ductility Plots

Frame ID OMF4-2.0-00

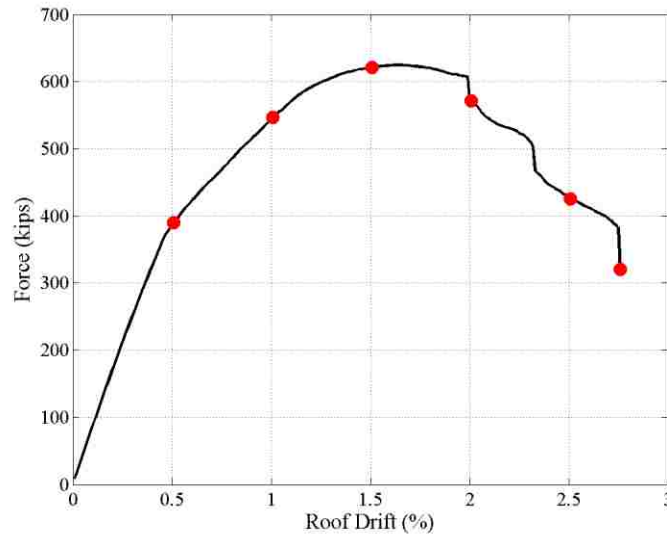


Appendix Figure F.20 OMF4-2.0-00: Pushover Curve with Curvature Ductility Points

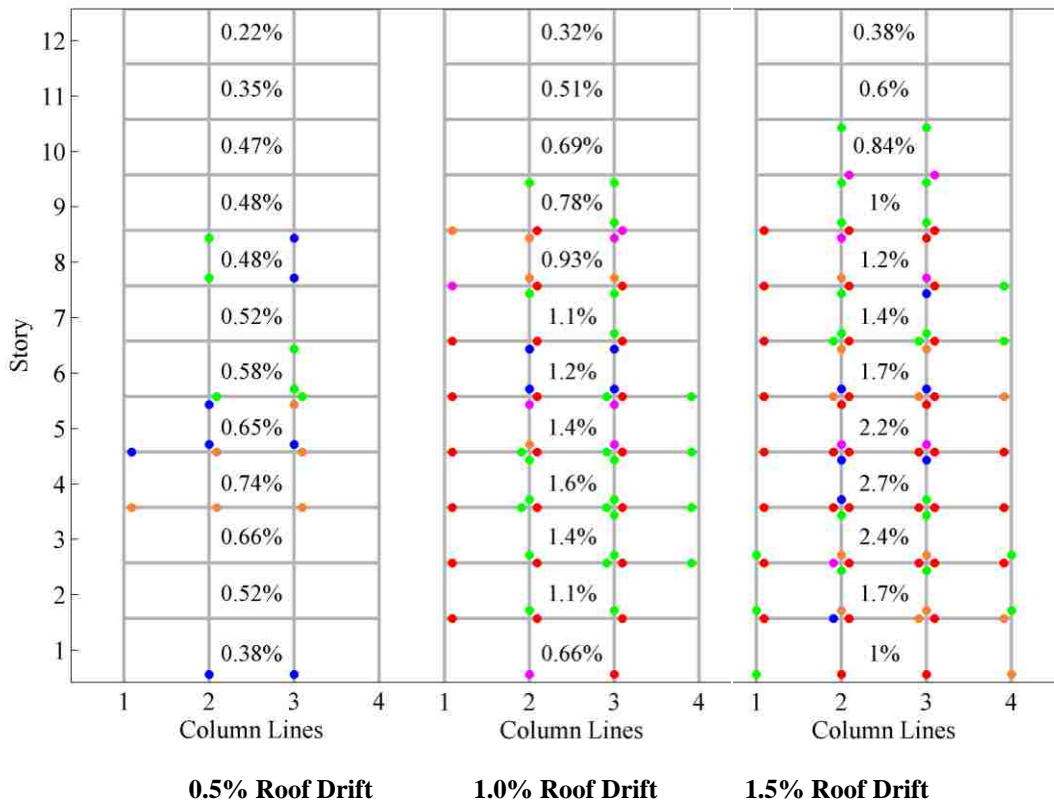


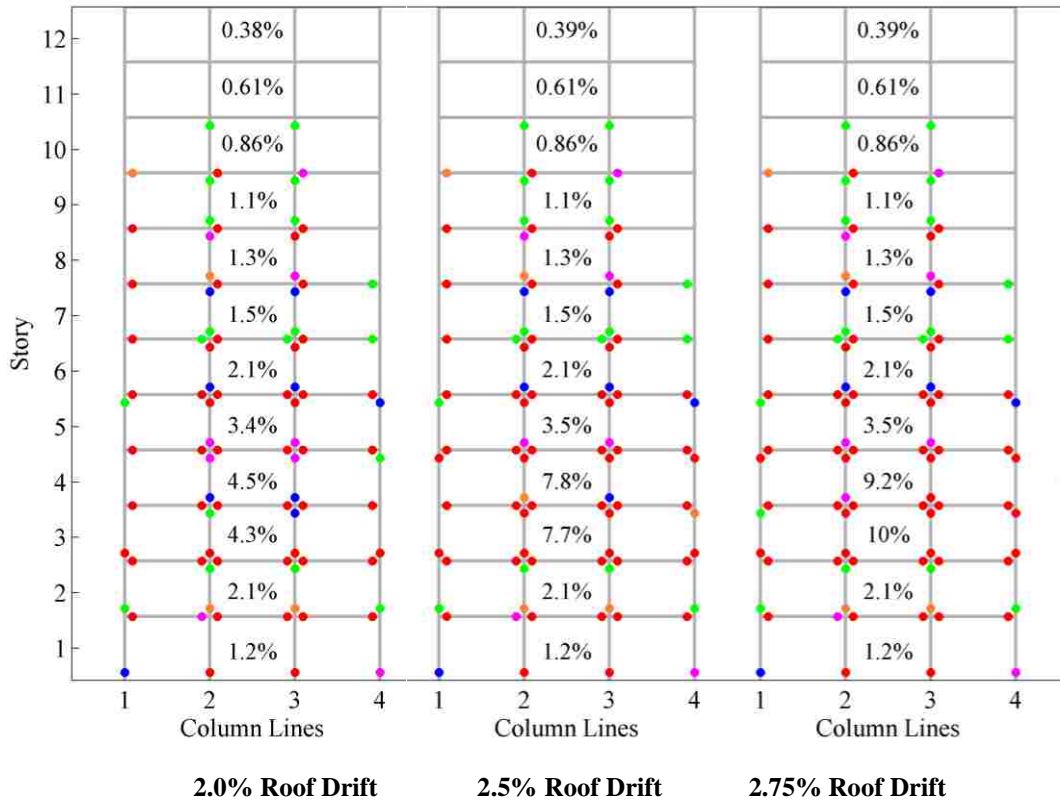
Appendix Figure F.21 OMF4-2.0-00: Drift and Curvature Ductility Plots

Frame ID OMF12-1.2-00



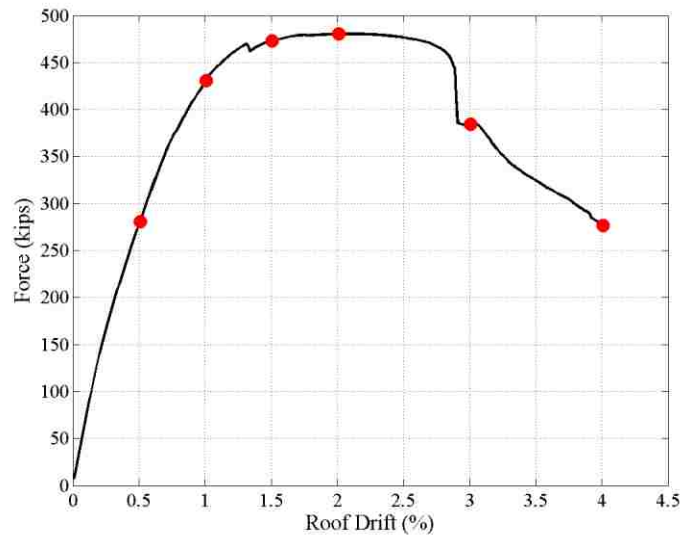
Appendix Figure F.22 OMF12-1.2-00: Pushover Curve with Curvature Ductility Points



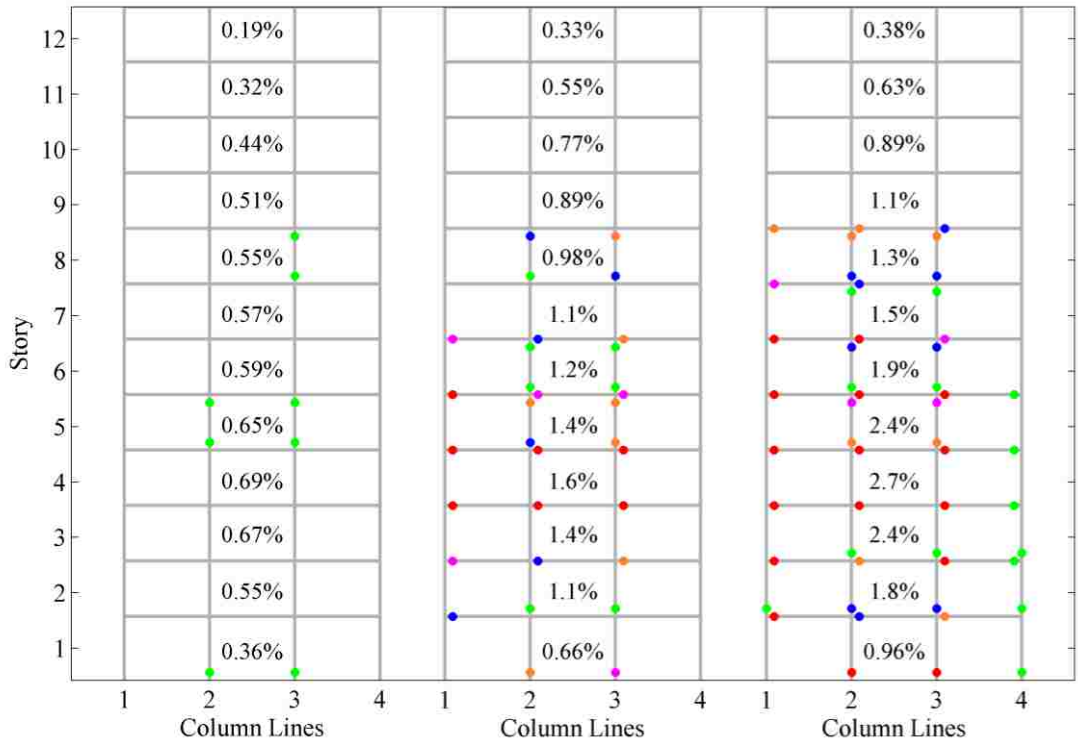


Appendix Figure F.23 OMF12-1.2-00: Drift and Curvature Ductility Plots

Frame ID OMF12-1.2-0J



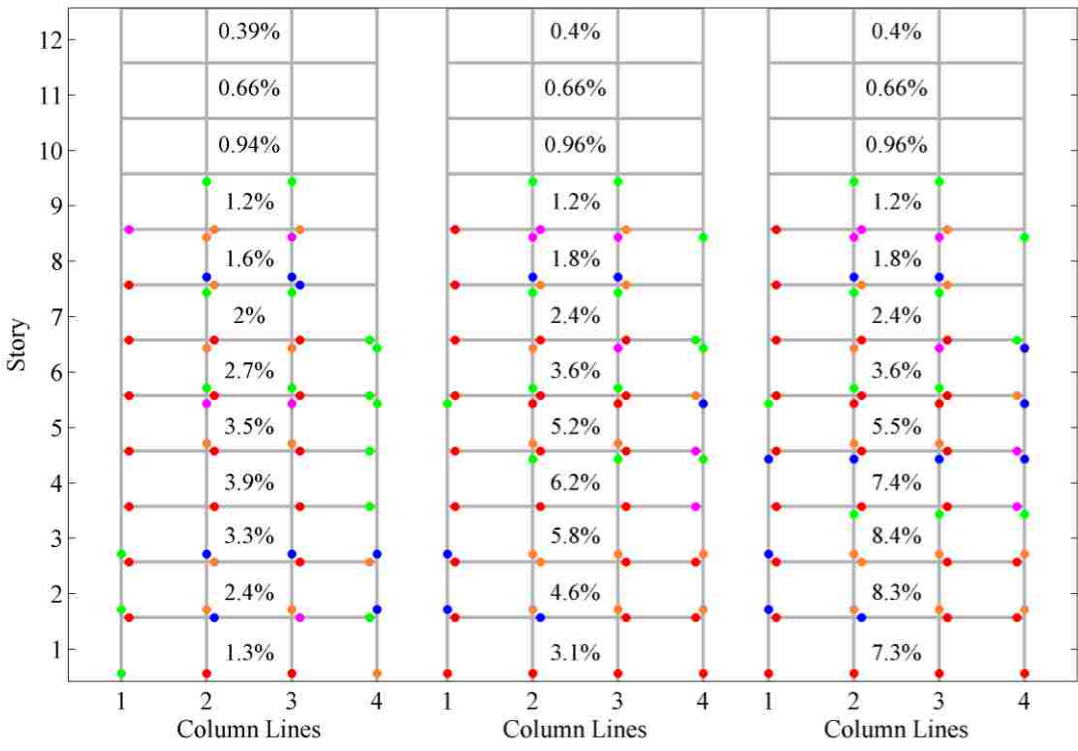
Appendix Figure F.24 OMF12-1.2-0J: Pushover Curve with Curvature Ductility Points



0.5% Roof Drift

1.0% Roof Drift

1.5% Roof Drift



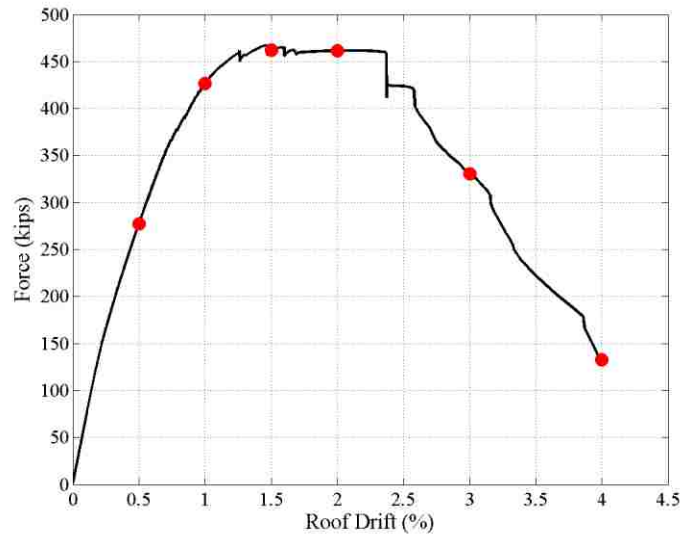
2.0% Roof Drift

3.0% Roof Drift

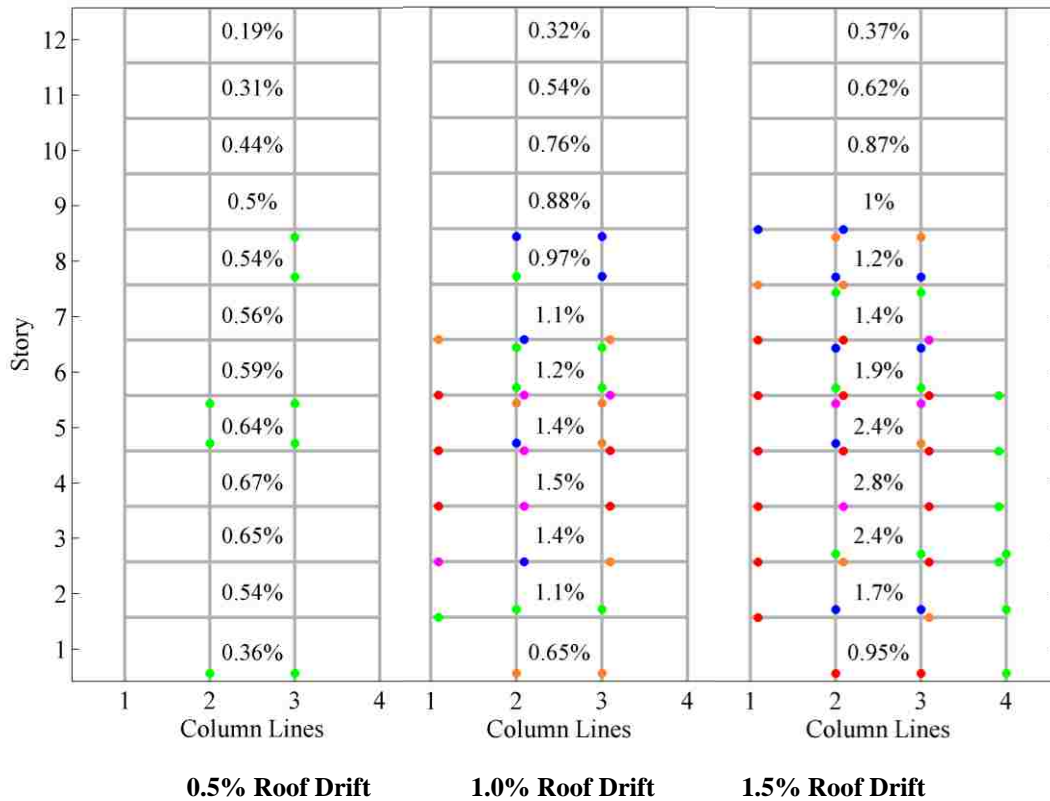
4.0% Roof Drift

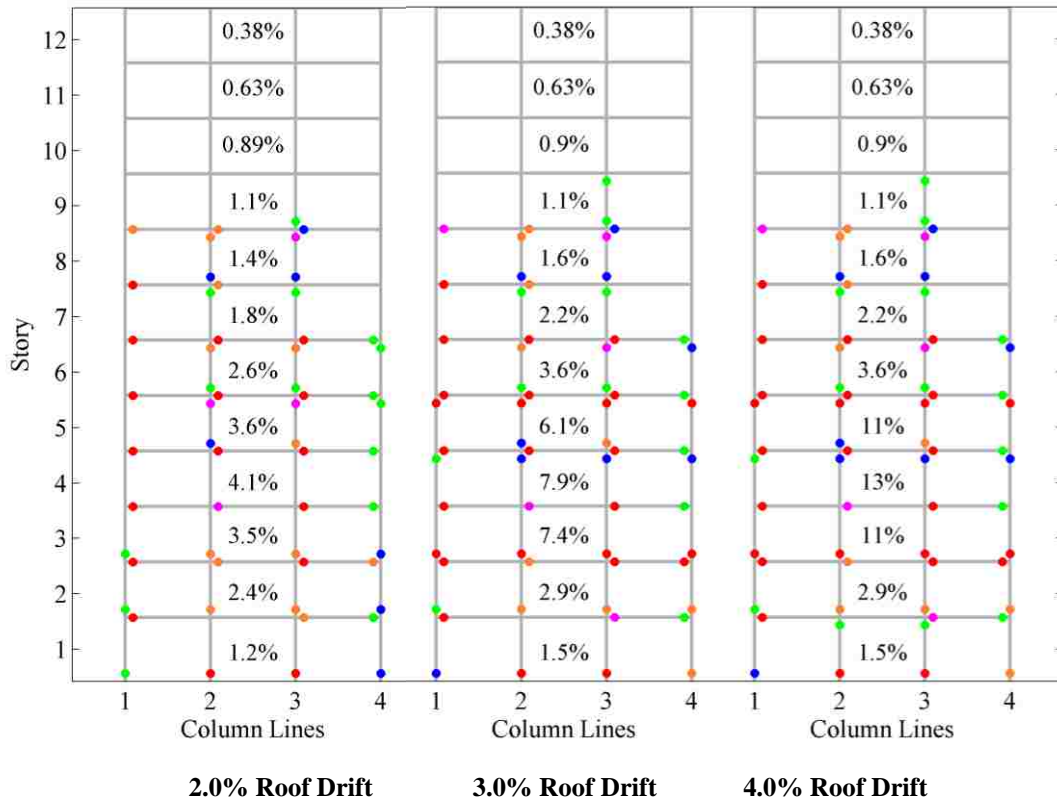
Appendix Figure F.25 OMF12-1.2-0J: Drift and Curvature Ductility Plots

Frame ID OMF12-1.2-SJ



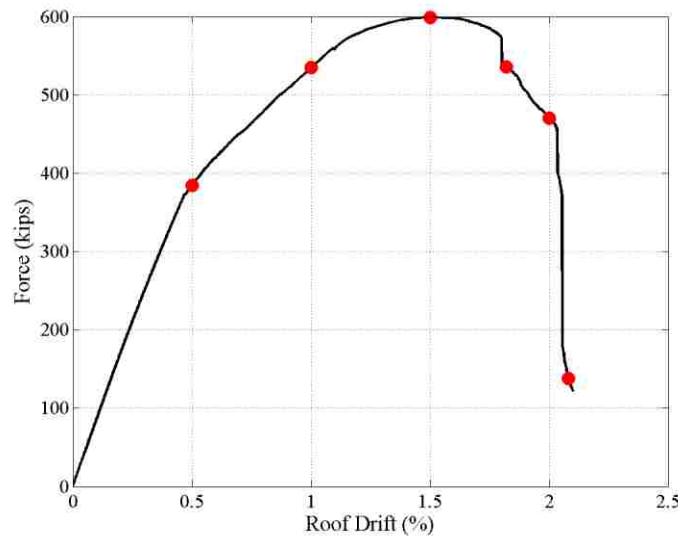
Appendix Figure F.26 OMF12-1.2-SJ: Pushover Curve with Curvature Ductility Points



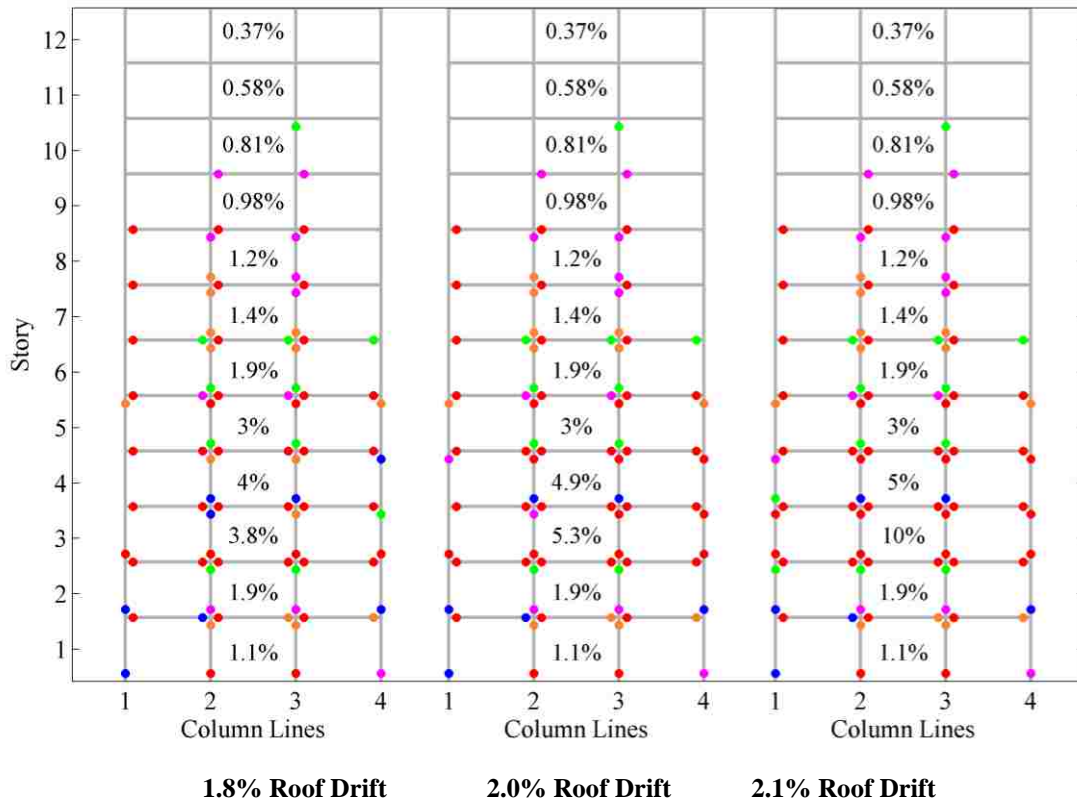
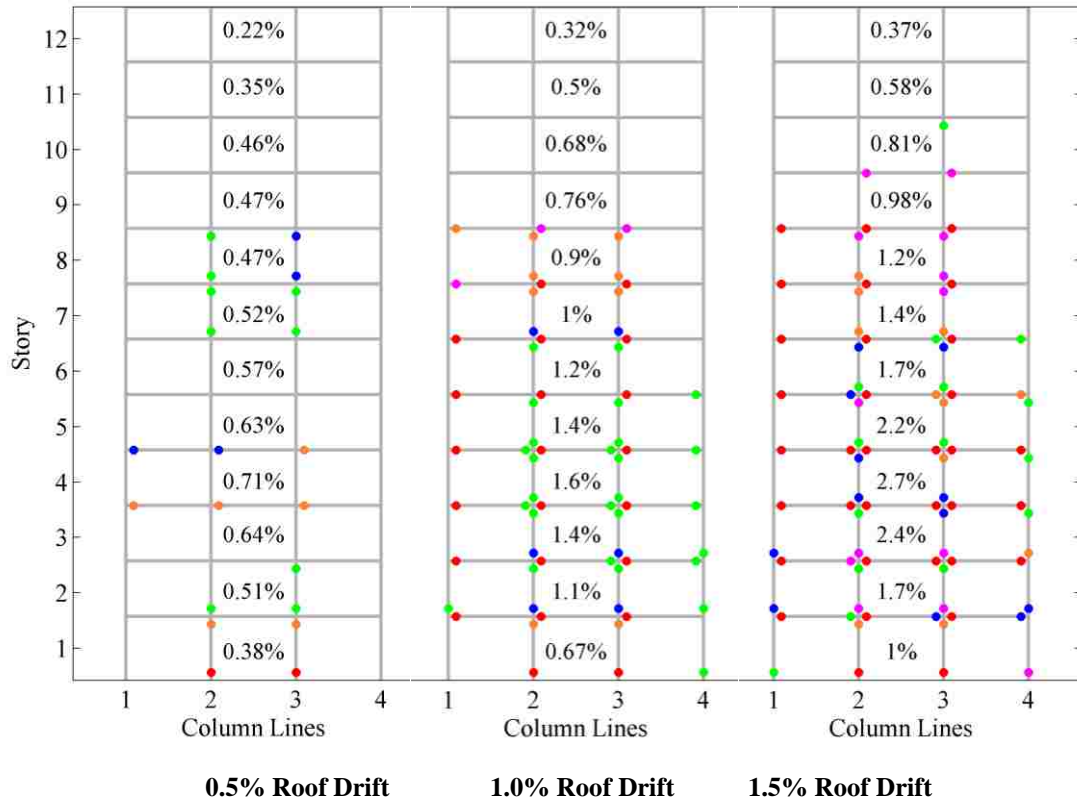


Appendix Figure F.27 OMF12-1.2-SJ: Drift and Curvature Ductility Plots

Frame ID OMF12-0.8-00

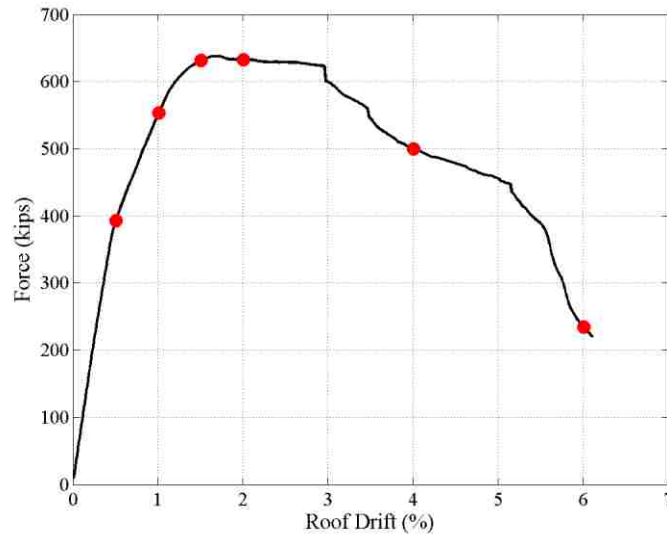


Appendix Figure F.28 OMF12-0.8-00: Pushover Curve with Curvature Ductility Points

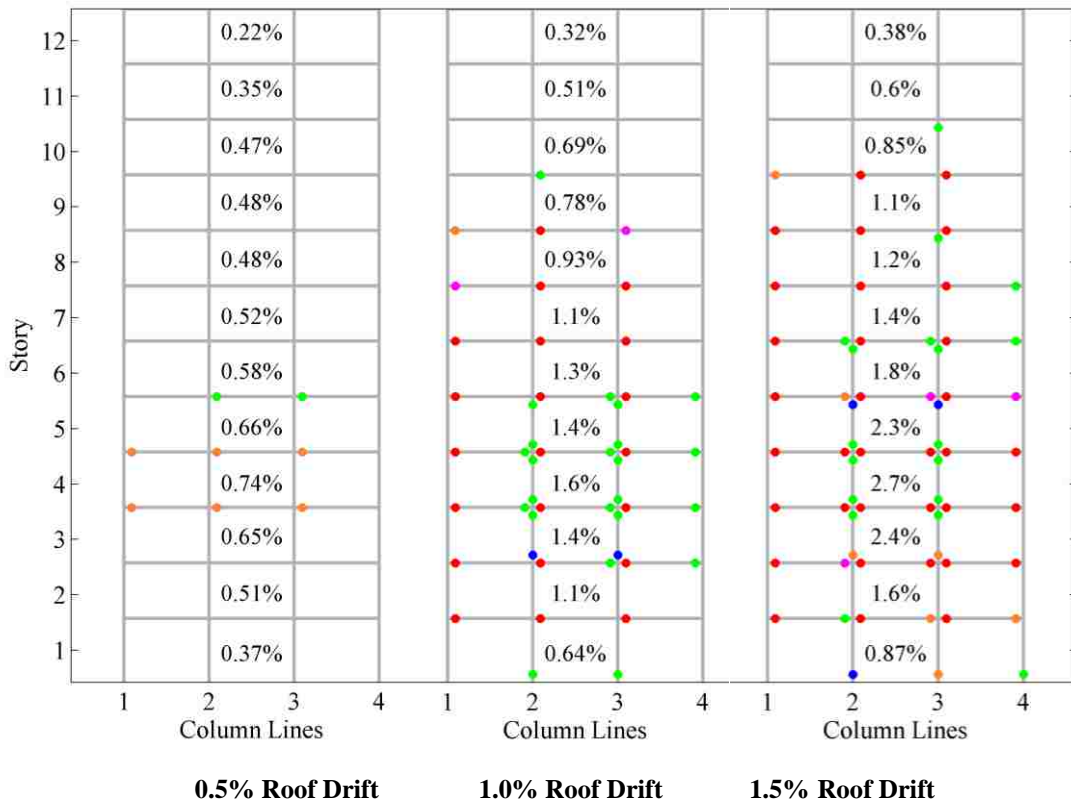


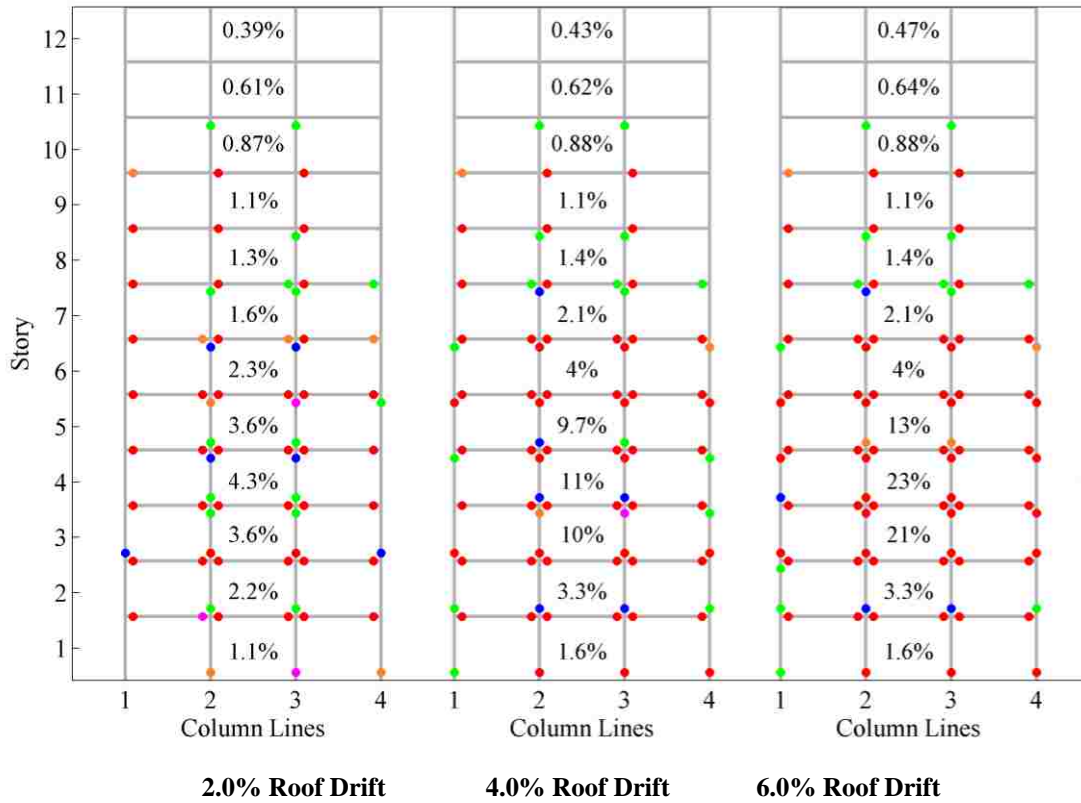
Appendix Figure F.29 OMF12-0.8-00: Drift and Curvature Ductility Plots

Frame ID OMF12-2.0-00



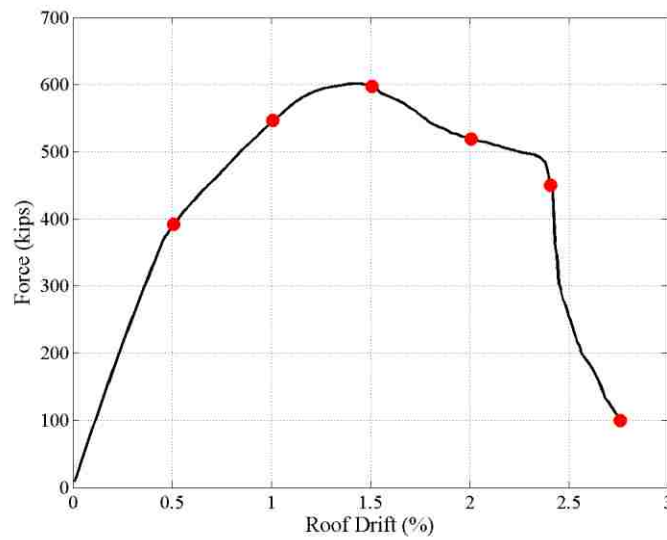
Appendix Figure F.30 OMF12-2.0-00: Pushover Curve with Curvature Ductility Points



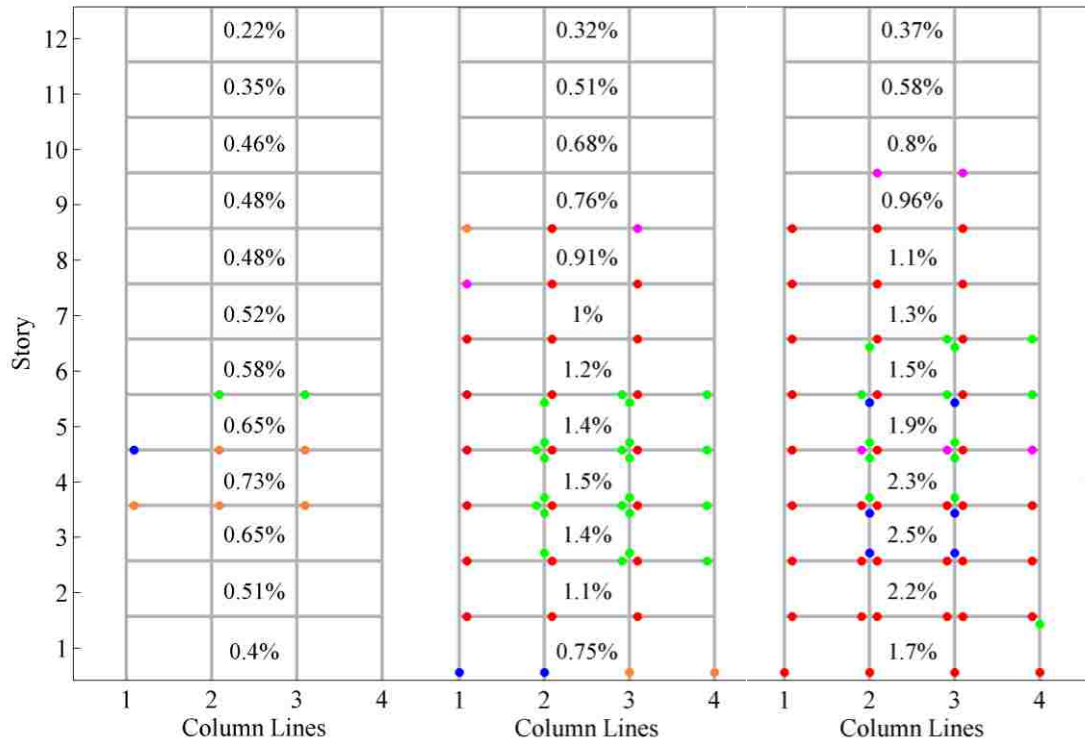


Appendix Figure F.31 OMF12-2.0-00: Drift and Curvature Ductility Plots

Frame ID OMF12-WS-00



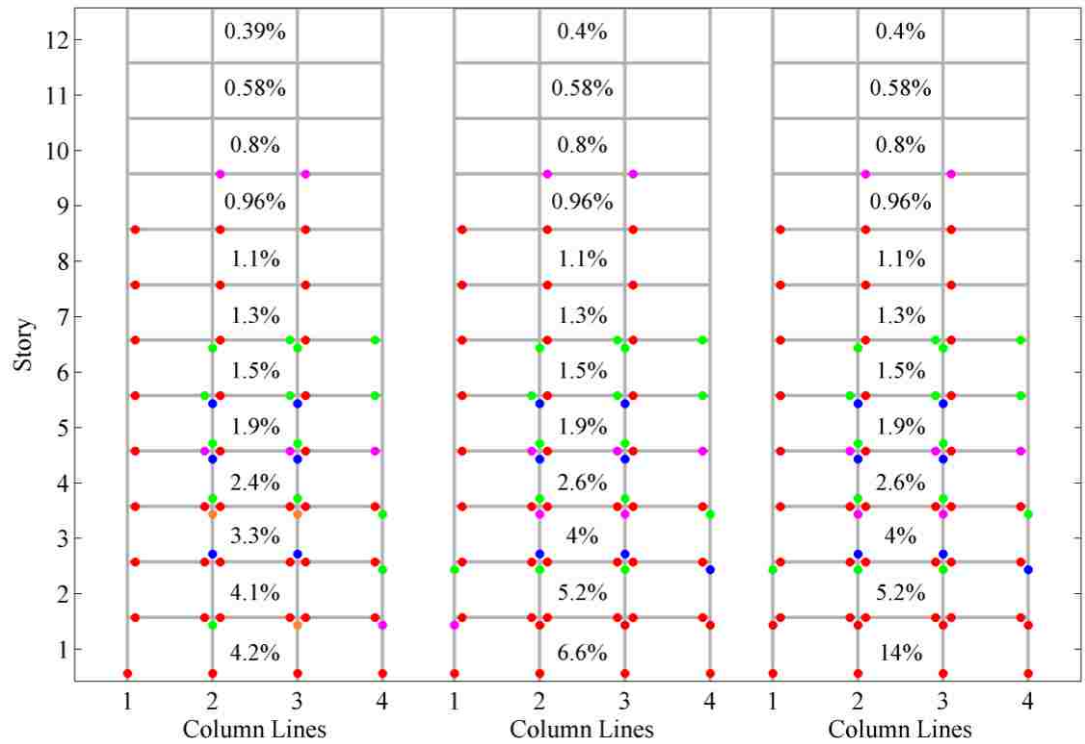
Appendix Figure F.32 OMF12-WS-00: Pushover Curve with Curvature Ductility Points



0.5% Roof Drift

1.0% Roof Drift

1.5% Roof Drift



2.0% Roof Drift

2.4% Roof Drift

2.75% Roof Drift

Appendix Figure F.33 WS: Drift and Curvature Ductility Plots

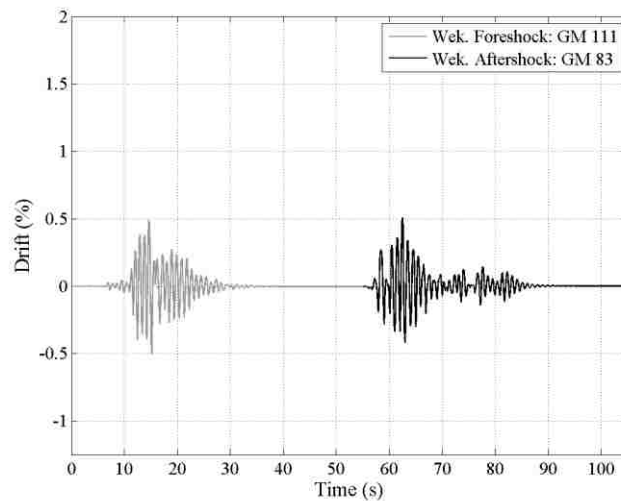
Appendix G: Cyclic Analysis Data

G.1 Introduction

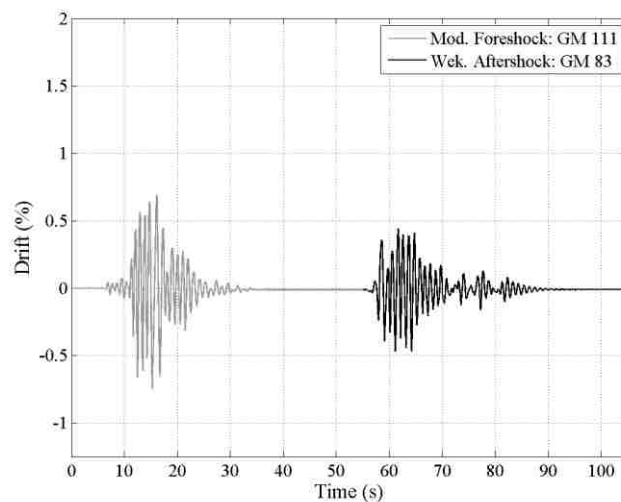
The results of the dynamic analyses are presented in this appendix.

G.2 Roof Drift Response

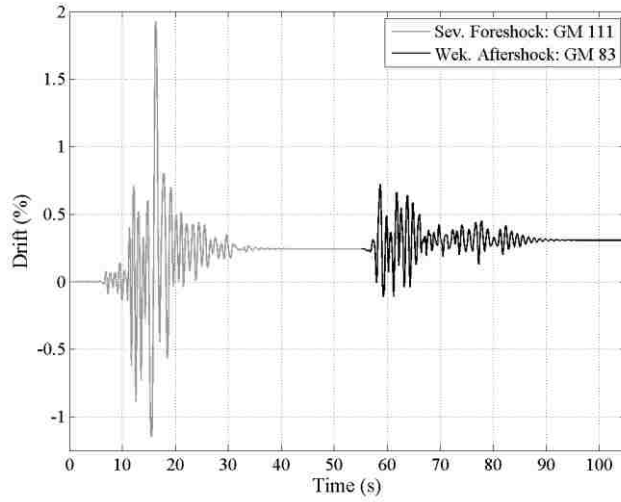
A set of roof drift responses from the 12 combinations of ground motions is presented in Appendix Figure G.1 through Appendix Figure G.9. The labels in Appendix Figure G.1 through Appendix Figure G.9 correspond to the 50% in 50 year event (Wek. : Weak), 10% in 50 year event (Mod. : Moderate), and 2% in 50 year event (Sev. : Severe). The response is presented for SMF4-1.2-00.



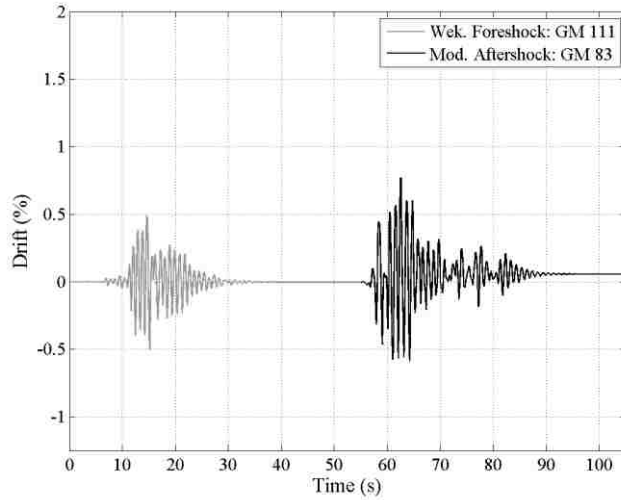
Appendix Figure G.1 Weak – Weak roof drift response



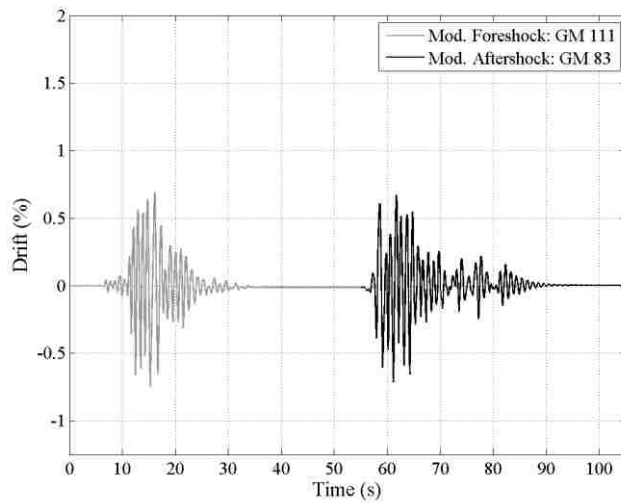
Appendix Figure G.2 Moderate – Weak roof drift response



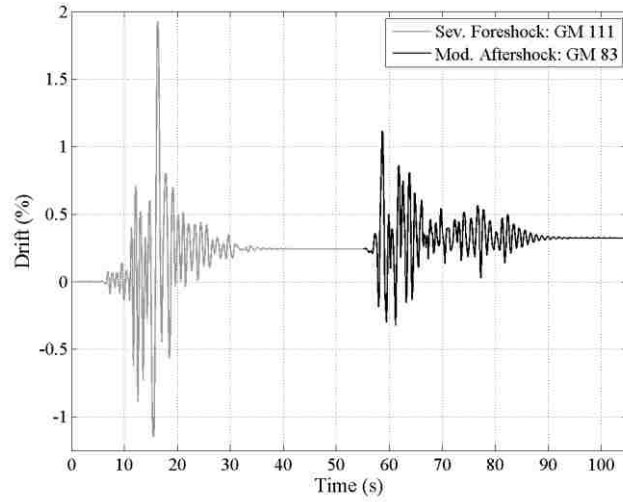
Appendix Figure G.3 Severe – Weak roof drift response



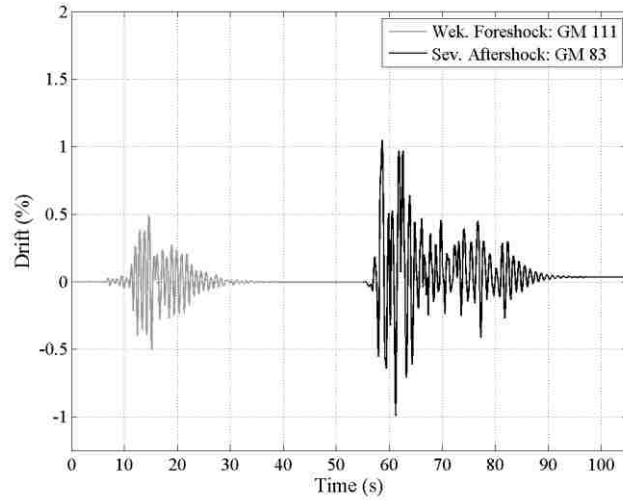
Appendix Figure G.4 Weak – Moderate roof drift response



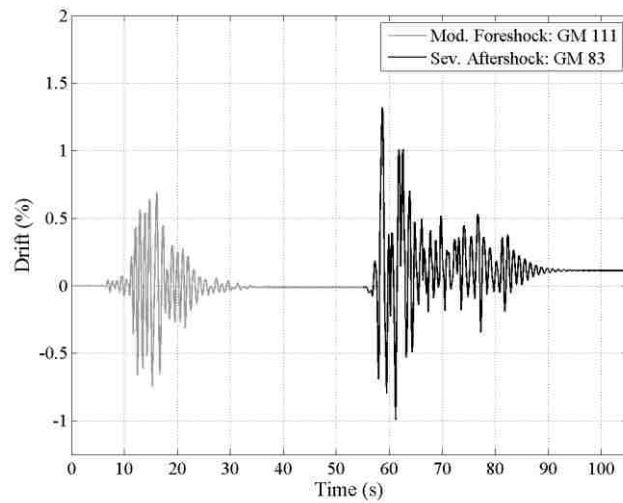
Appendix Figure G.5 Moderate – Moderate roof drift response



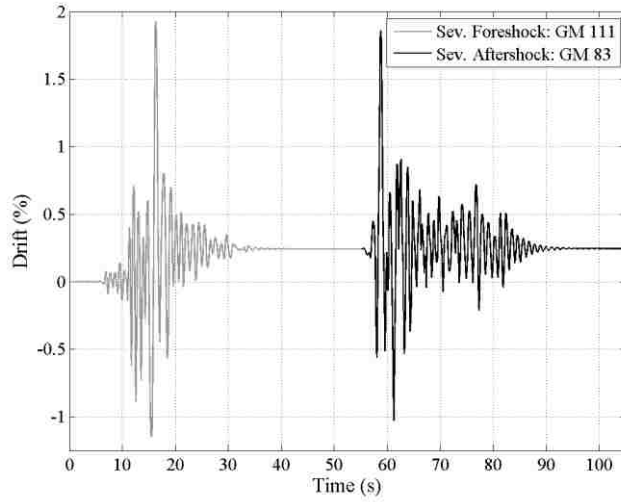
Appendix Figure G.6 Severe – Moderate roof drift response



Appendix Figure G.7 Weak – Severe roof drift response



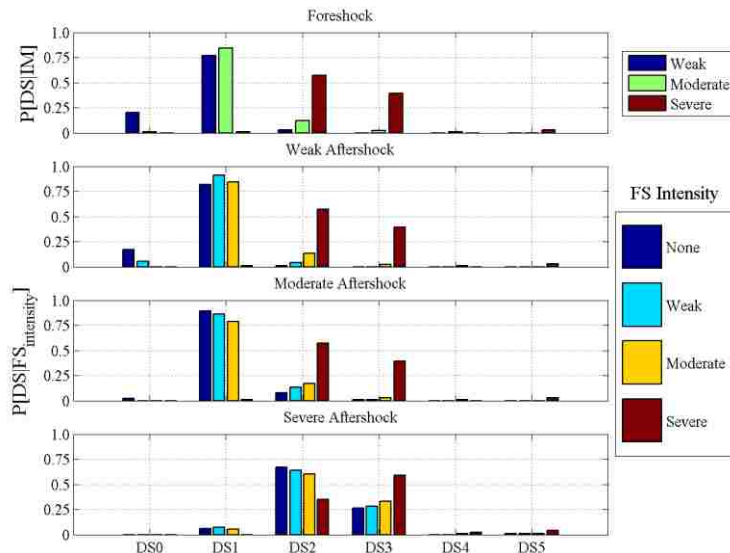
Appendix Figure G.8 Moderate – Severe roof drift response



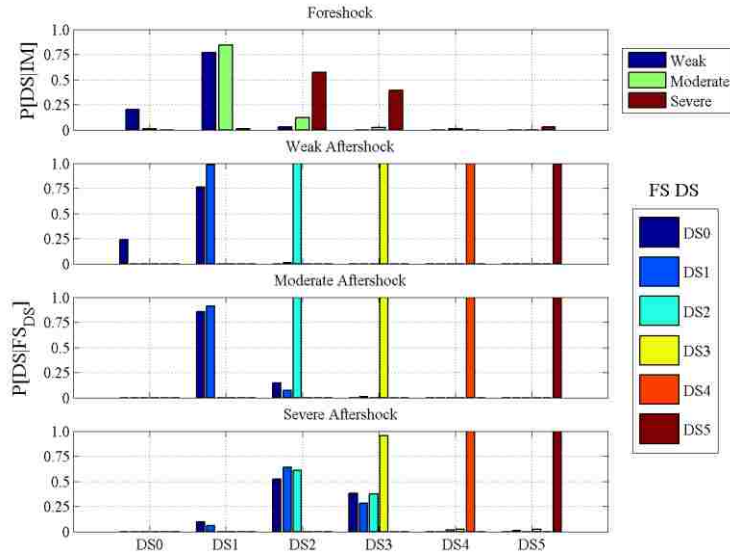
Appendix Figure G.9 Severe – Severe roof drift response

G.3 Probabilities for Frames

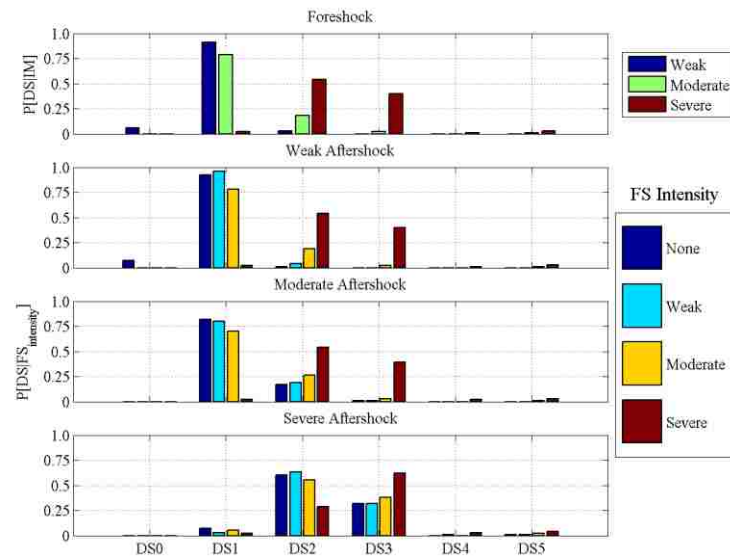
The results presented in Chapter 5 are supplemented by the following plots for each frame.



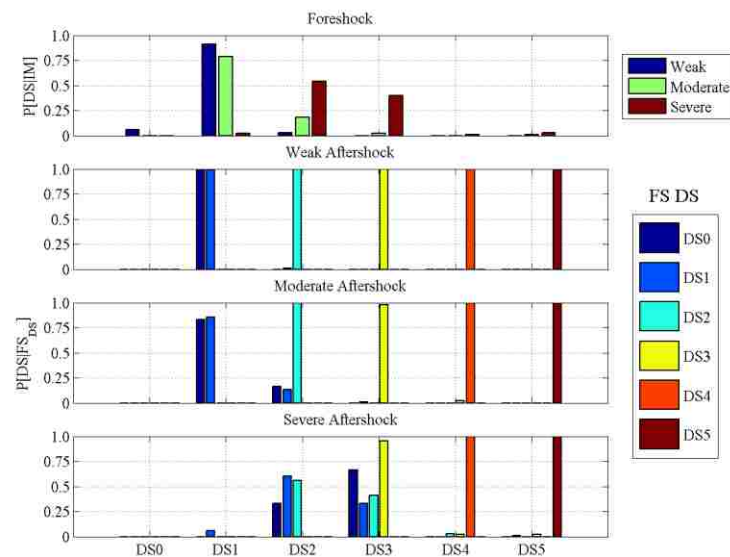
Appendix Figure G.10 SMF4-1.2-00 probability of DS given the FS intensity



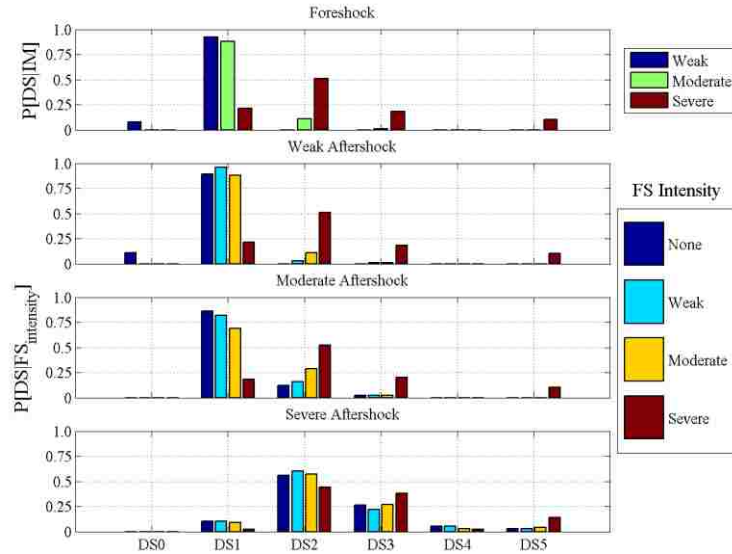
Appendix Figure G.11 SMF4-1.2-00 probability of DS given the FS DS



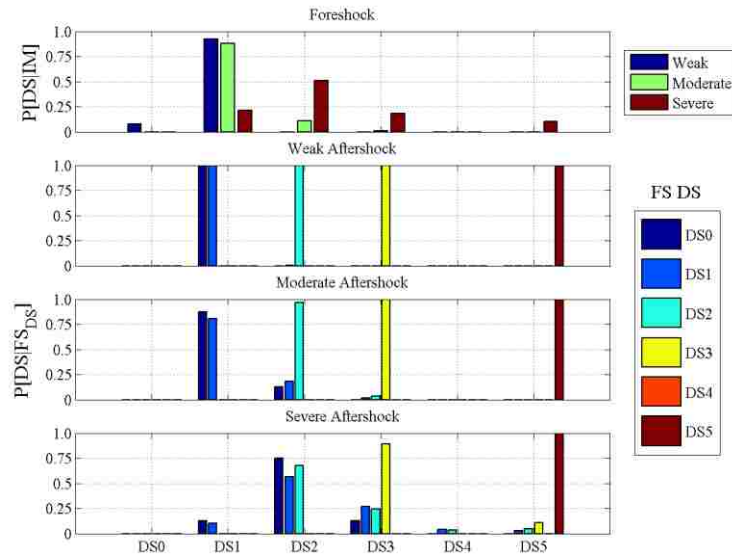
Appendix Figure G.12 SMF4-1.2-0J probability of DS given the FS intensity



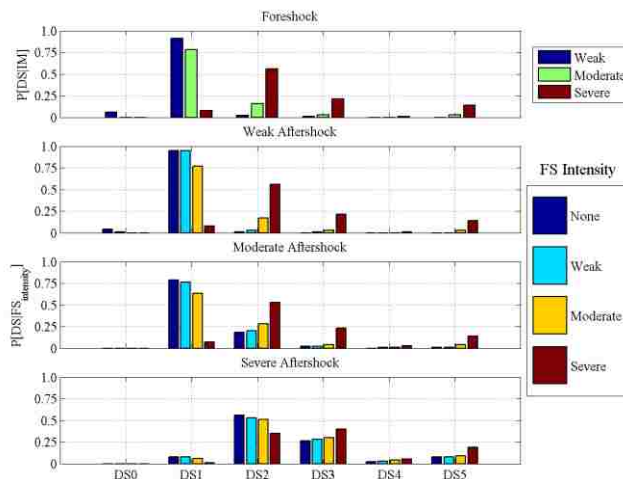
Appendix Figure G.13 SMF4-1.2-0J probability of DS given the FS DS



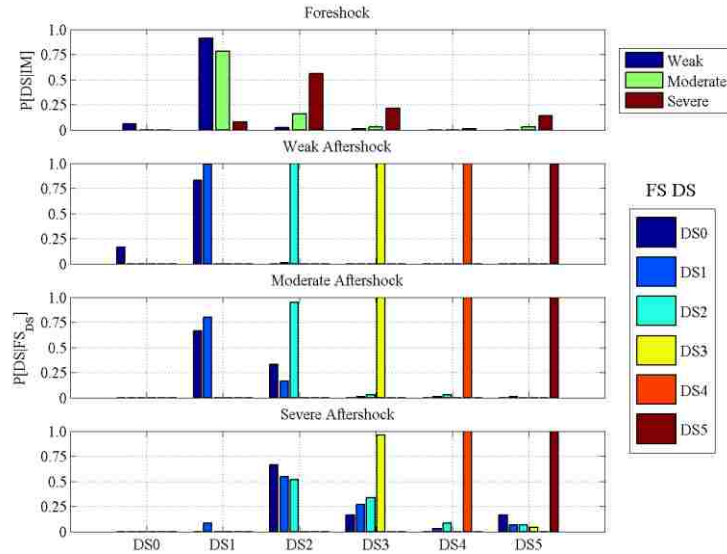
Appendix Figure G.14 SMF12-1.2-00 probability of DS given the FS intensity



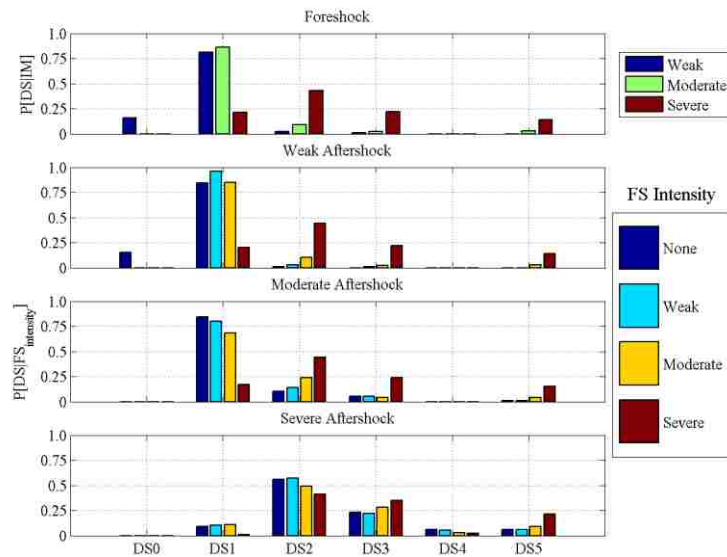
Appendix Figure G.15 SMF12-1.2-00 probability of DS given the FS DS



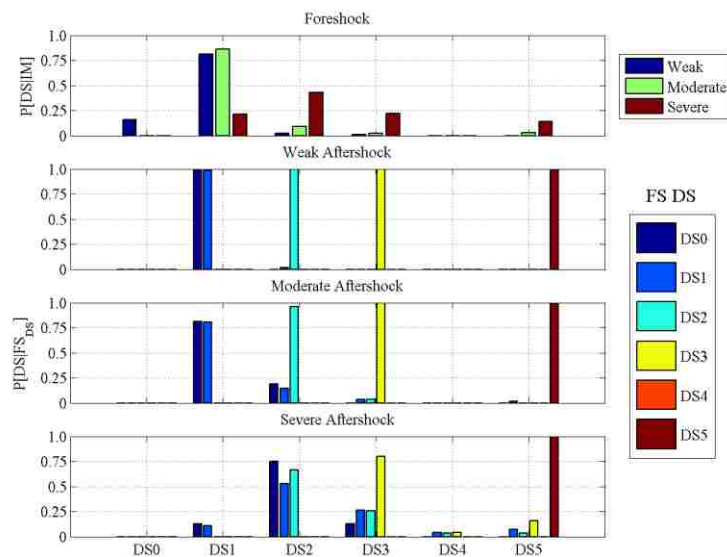
Appendix Figure G.16 SMF12-1.2-0J probability of DS given the FS intensity



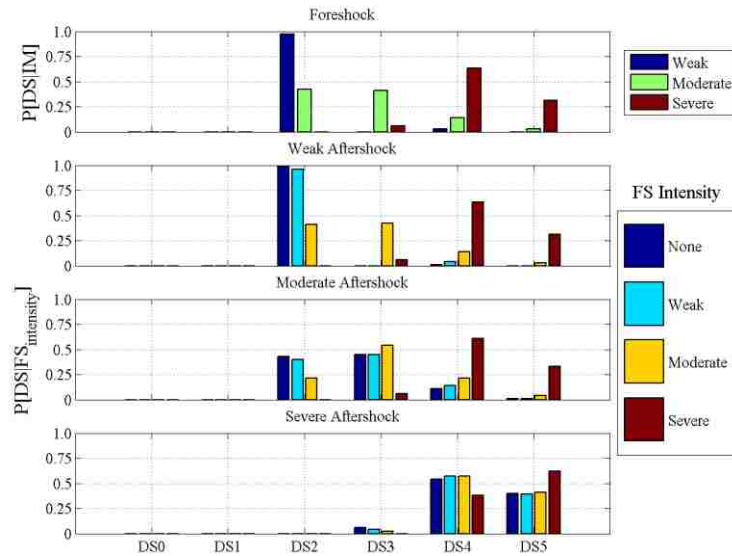
Appendix Figure G.17 SMF12-1.2-0J probability of DS given the FS DS



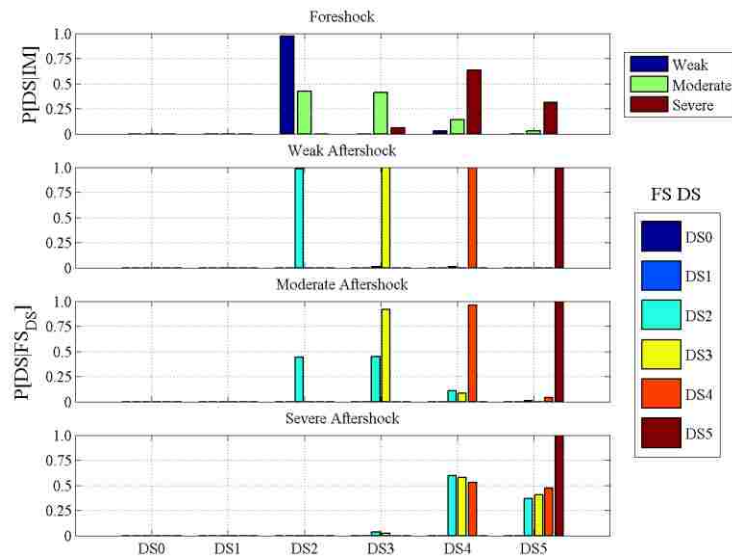
Appendix Figure G.18 SMF12-WS-00 probability of DS given the FS intensity



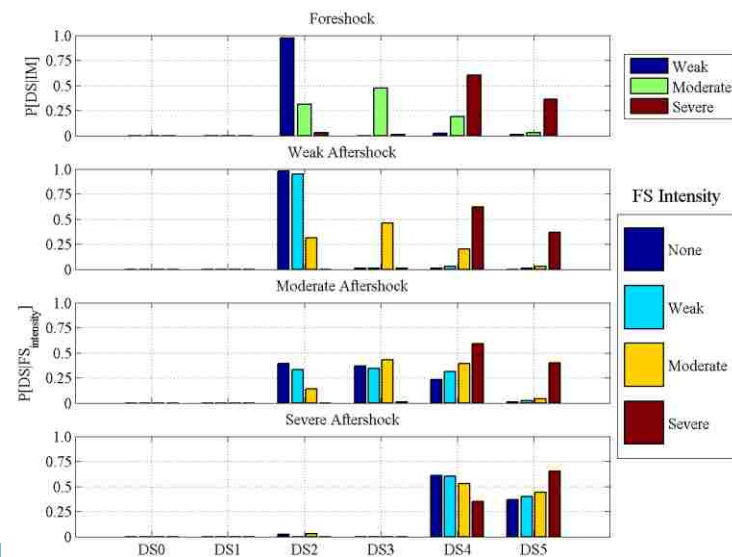
Appendix Figure G.19 SMF12-WS-00 probability of DS given the FS DS



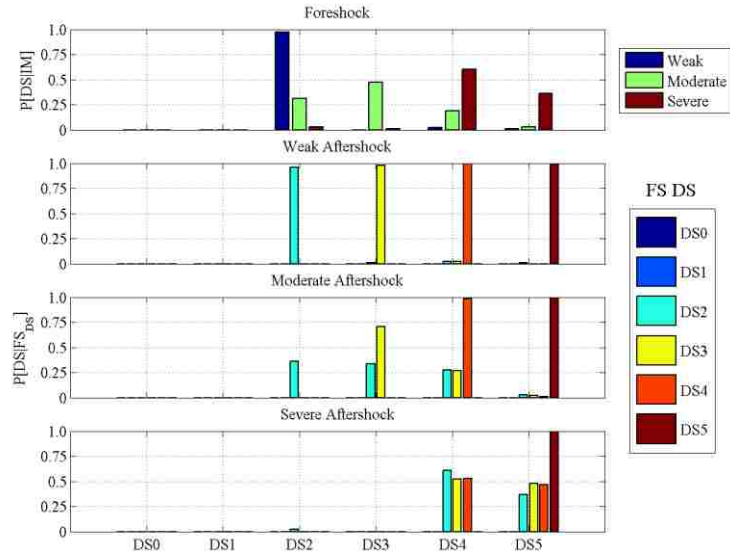
Appendix Figure G.20 OMF4-1.2-00 probability of DS given the FS intensity



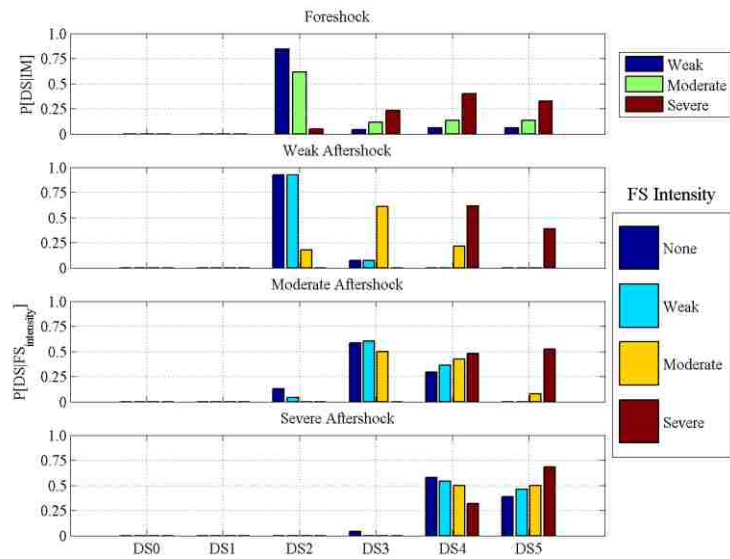
Appendix Figure G.21 OMF4-1.2-00 probability of DS given the FS DS



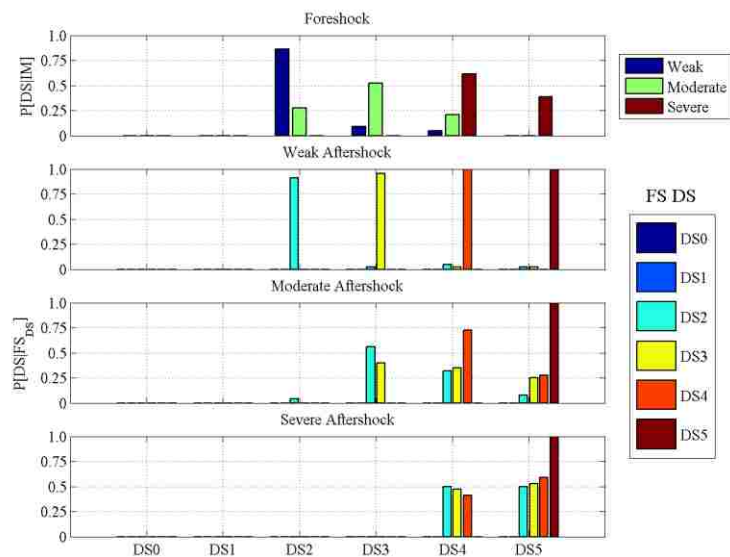
Appendix Figure G.22 OMF4-1.2-0J probability of DS given the FS intensity



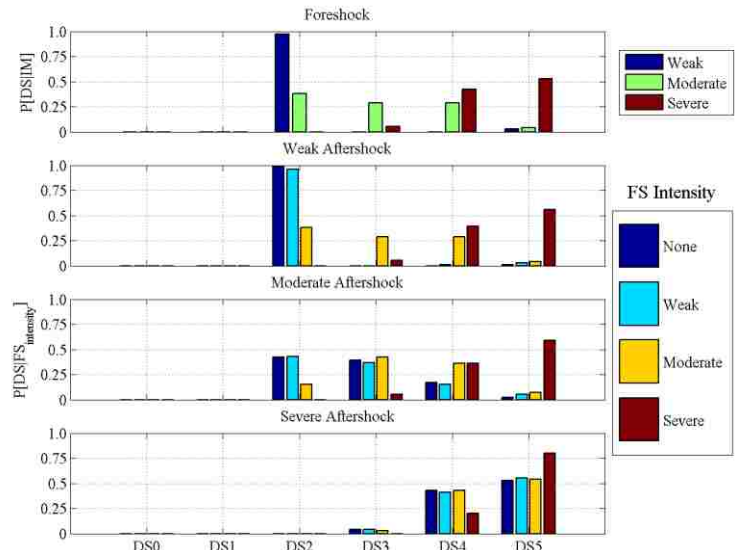
Appendix Figure G.23 OMF4-1.2-0J probability of DS given the FS DS



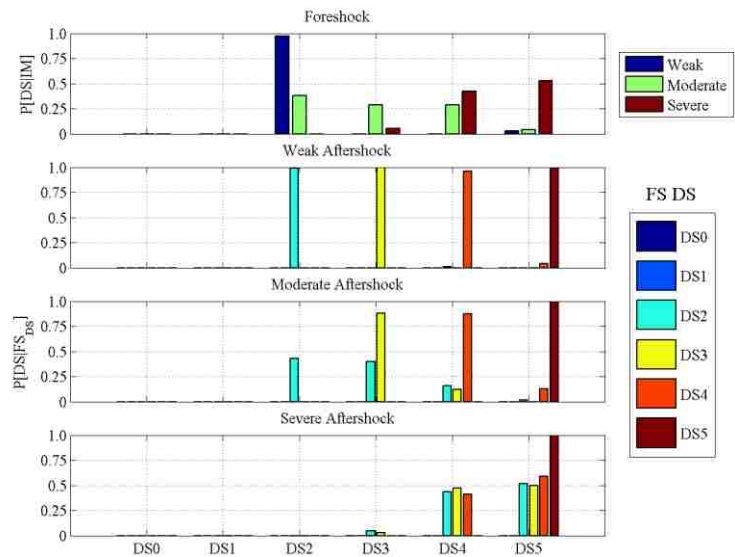
Appendix Figure G.24 OMF4-1.2-SJ probability of DS given the FS intensity



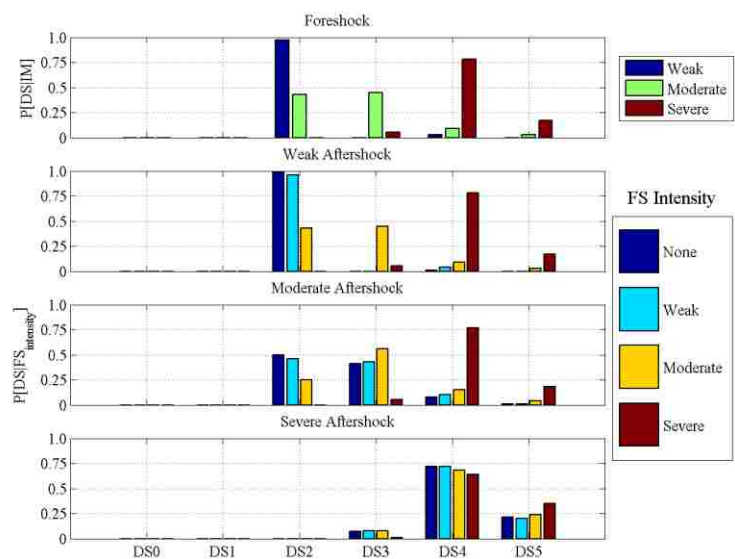
Appendix Figure G.25 OMF4-1.2-SJ probability of DS given the FS DS



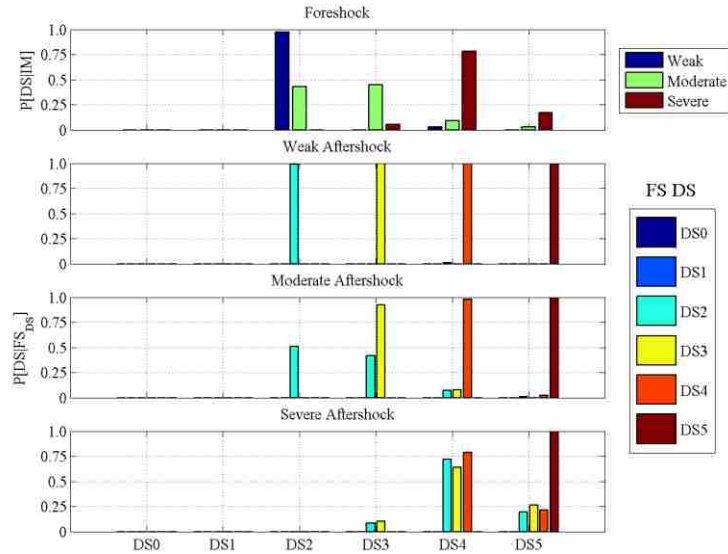
Appendix Figure G.26 OMF4-0.8-00 probability of DS given the FS intensity



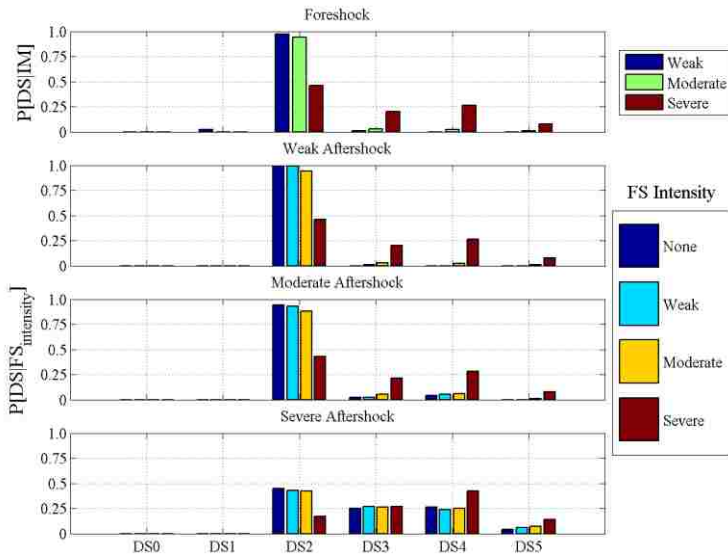
Appendix Figure G.27 OMF4-0.8-00 probability of DS given the FS DS



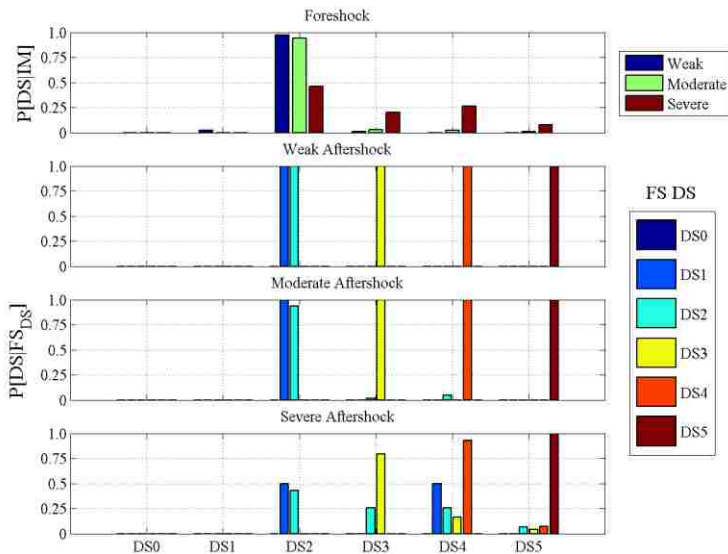
Appendix Figure G.28 OMF4-2.0-00 probability of DS given the FS intensity



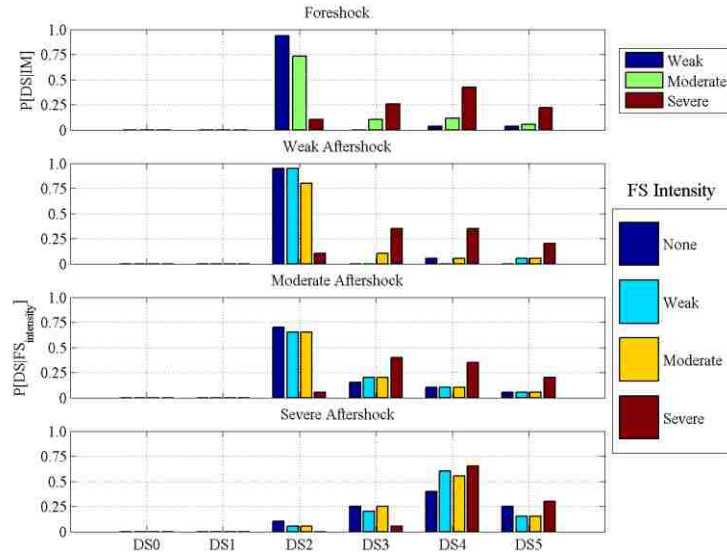
Appendix Figure G.29 OMF4-2.0-00 probability of DS given the FS DS



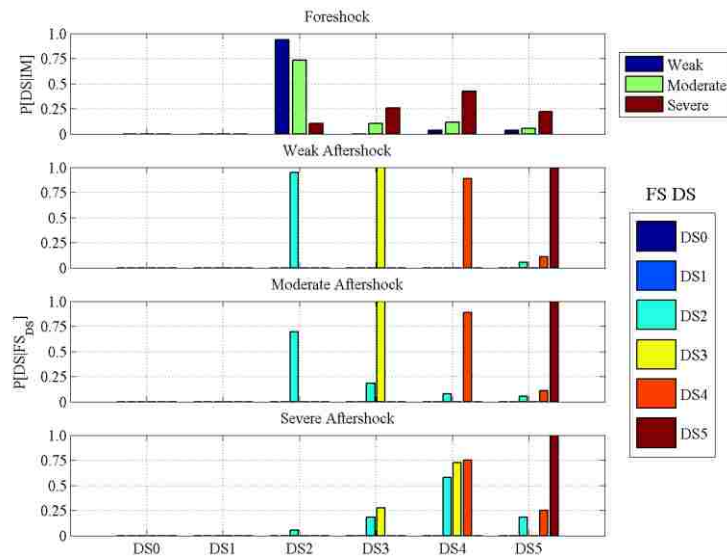
Appendix Figure G.30 OMF12-1.2-00 probability of DS given the FS intensity



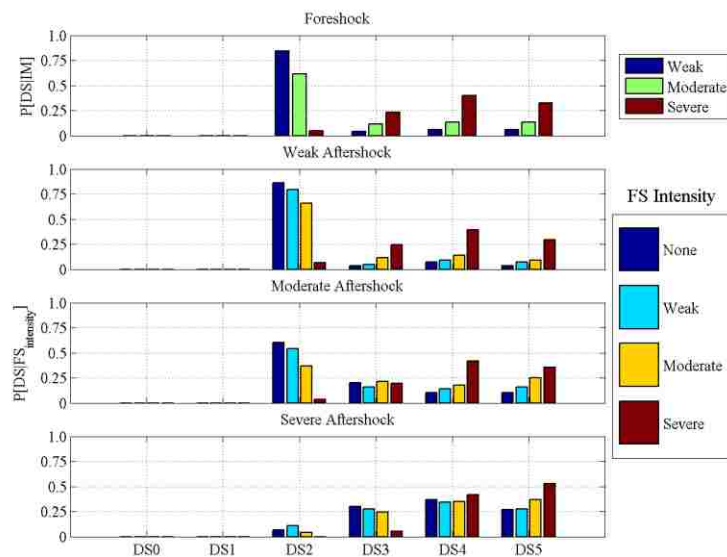
Appendix Figure G.31 OMF12-1.2-00 probability of DS given the FS DS



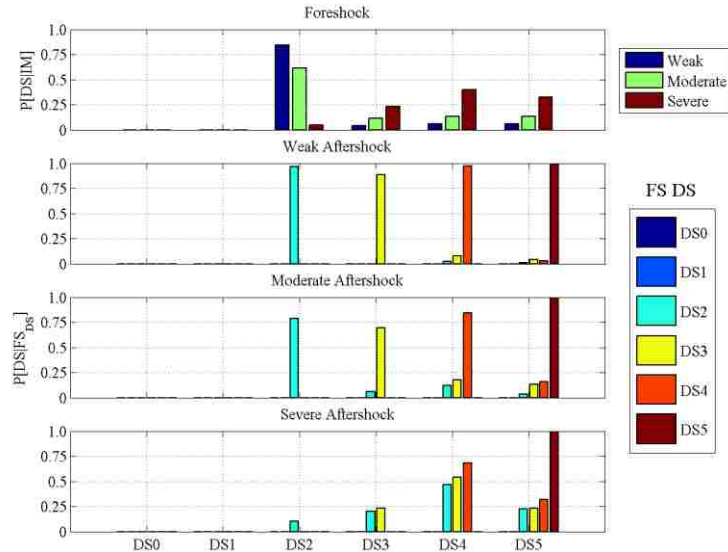
Appendix Figure G.32 OMF12-1.2-0J probability of DS given the FS intensity



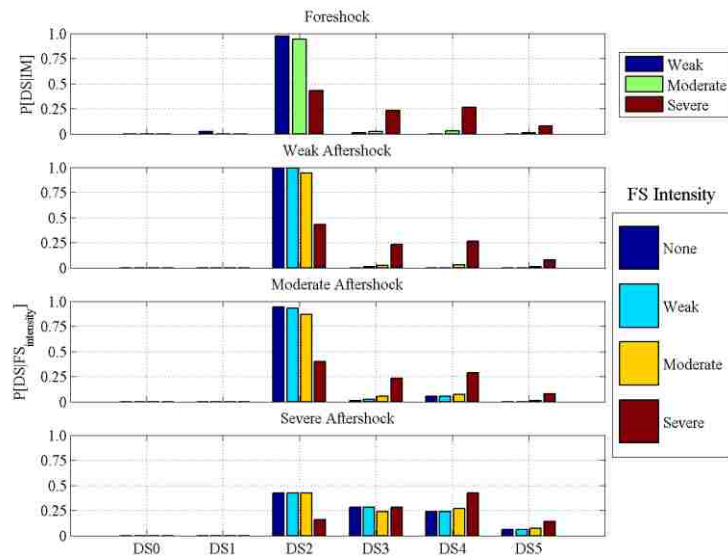
Appendix Figure G.33 OMF12-1.2-0J probability of DS given the FS DS



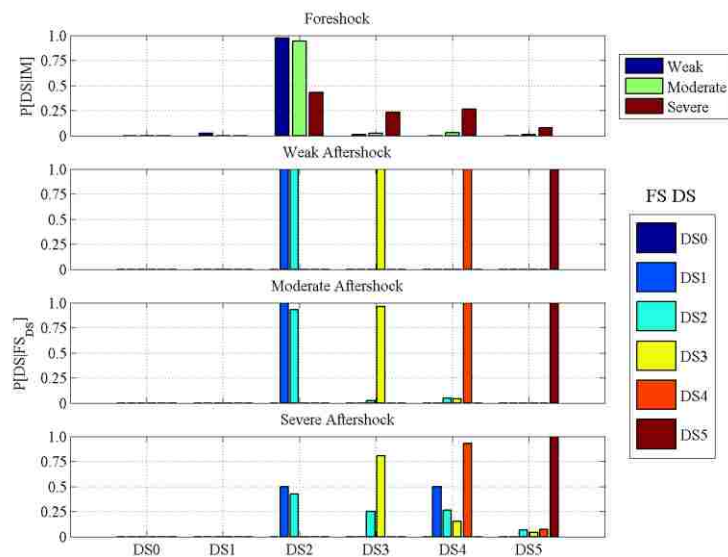
Appendix Figure G.34 OMF12-1.2-SJ probability of DS given the FS intensity



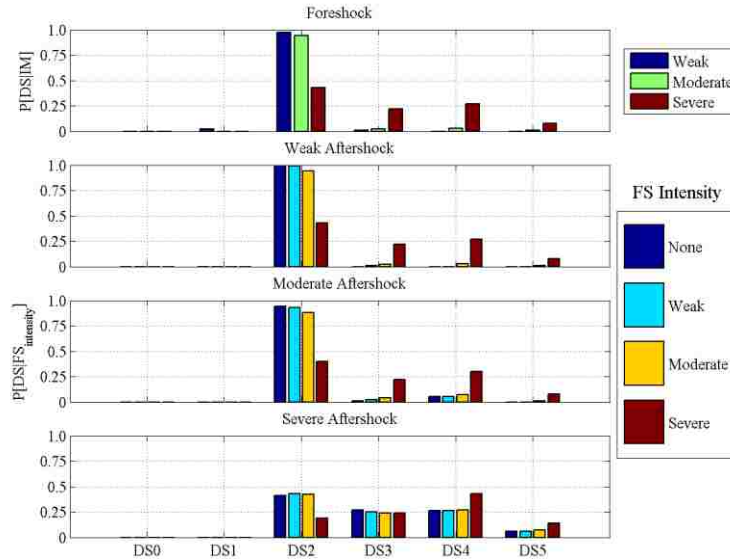
Appendix Figure G.35 OMF12-1.2-SJ probability of DS given the FS DS



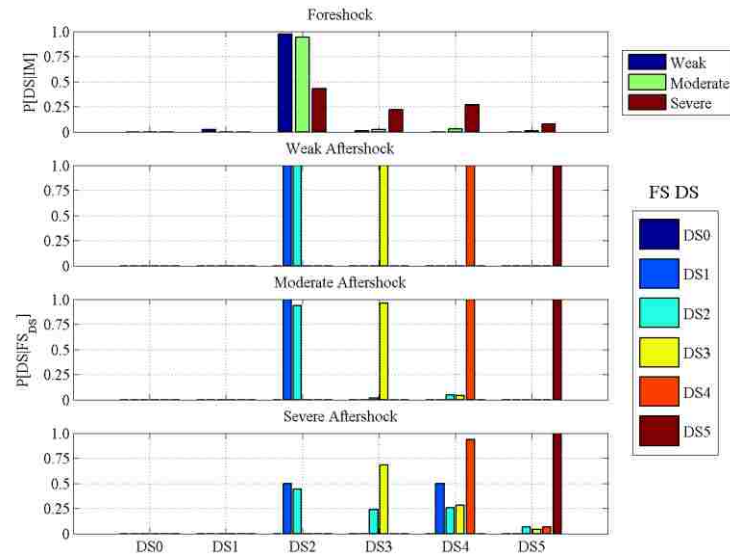
Appendix Figure G.36 OMF12-0.8-00 probability of DS given the FS intensity



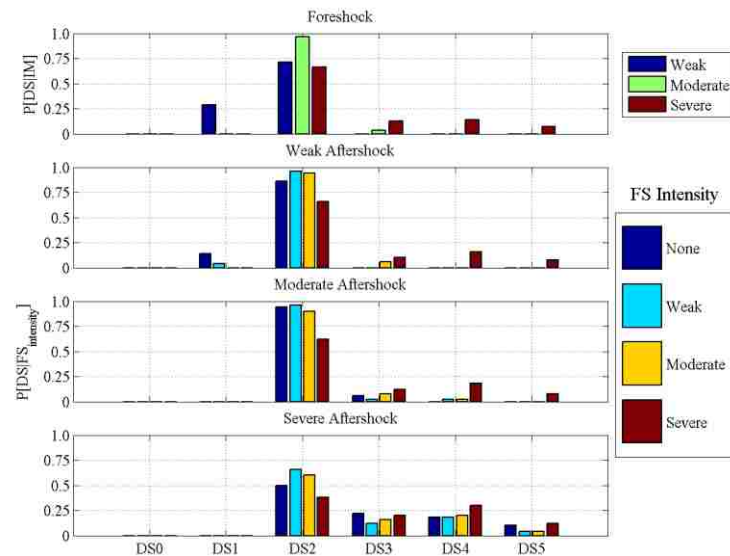
Appendix Figure G.37 OMF12-0.8-00 probability of DS given the FS DS



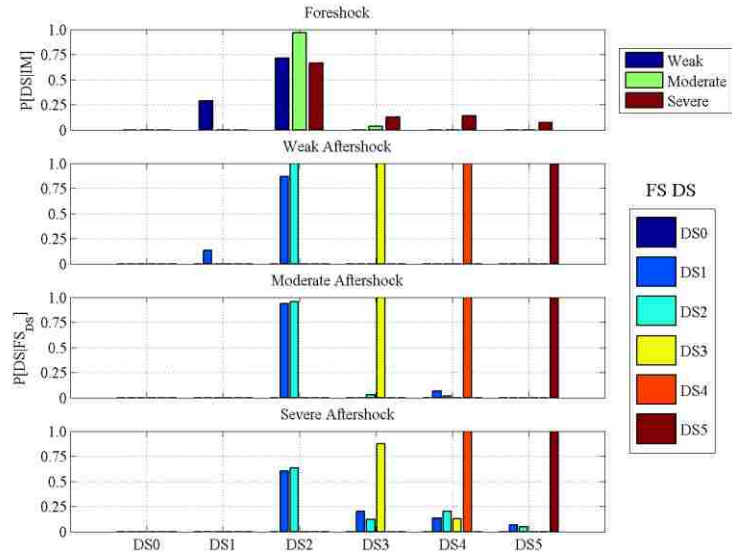
Appendix Figure G.38 OMF12-2.0-00 probability of DS given the FS intensity



Appendix Figure G.39 OMF12-2.0-00 probability of DS given the FS DS



Appendix Figure G.40 OMF12-WS-00 probability of DS given the FS intensity



Appendix Figure G.41 OMF12-WS-00 probability of DS given the FS DS

Appendix H: Additional Database Data

H.1 Introduction

The results of a load-displacement assessment identifying stiffness values from the Database are presented in this appendix. The initial unloading stiffness and unloading stiffness at each identified damage state were identified and pulled from the data in the same way the residual drift data was identified in Section 3.7. Unloading stiffness were determined by computing the slopes of the lines between the maximum drifts and residual drifts. Secant stiffness for each recorded damage state were also taken from the Database. The secant stiffness were determined by taking the slope between the peaks at which the damage states occurred and the origin.

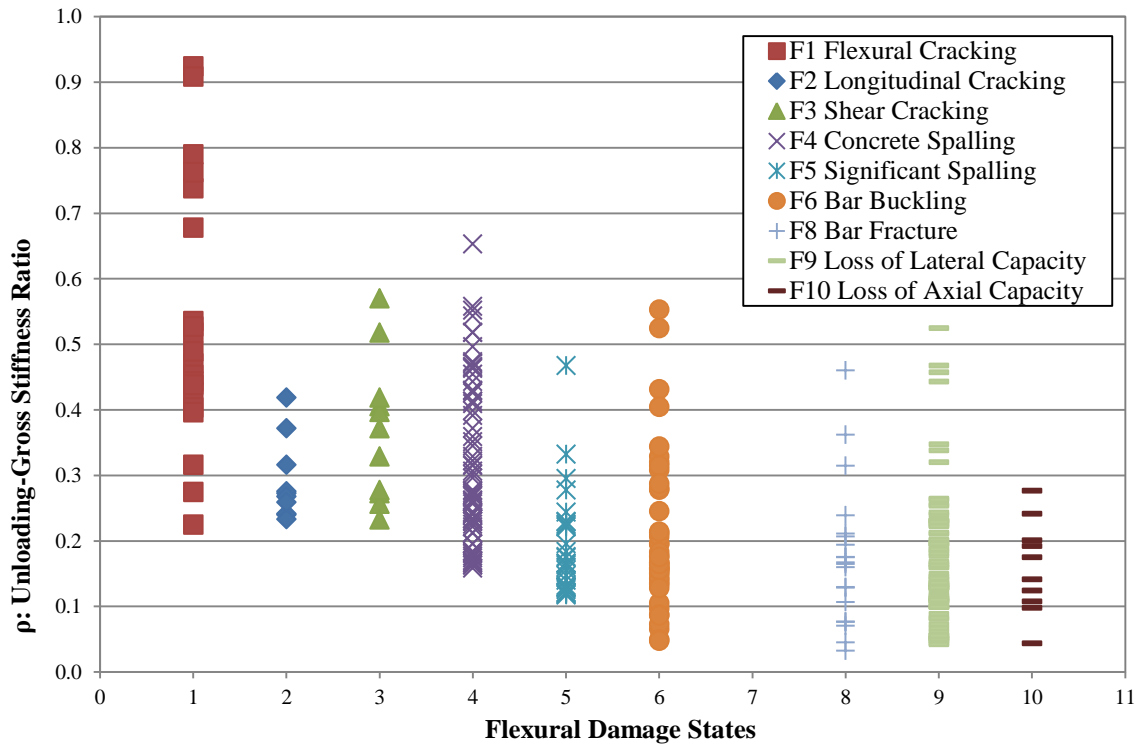
H.2 Unloading Stiffness Results

Modeling the hysteretic behavior of reinforced concrete columns under lateral deformations has been the focus of multiple research efforts. Ibarra et al. (2005) proposed simple hysteretic models that included strength and stiffness deterioration. It is important that hysteretic models can capture all the contributions to the degrading behavior of structural components. The Database provides an ideal source for validating the unloading stiffness rates of RC columns.

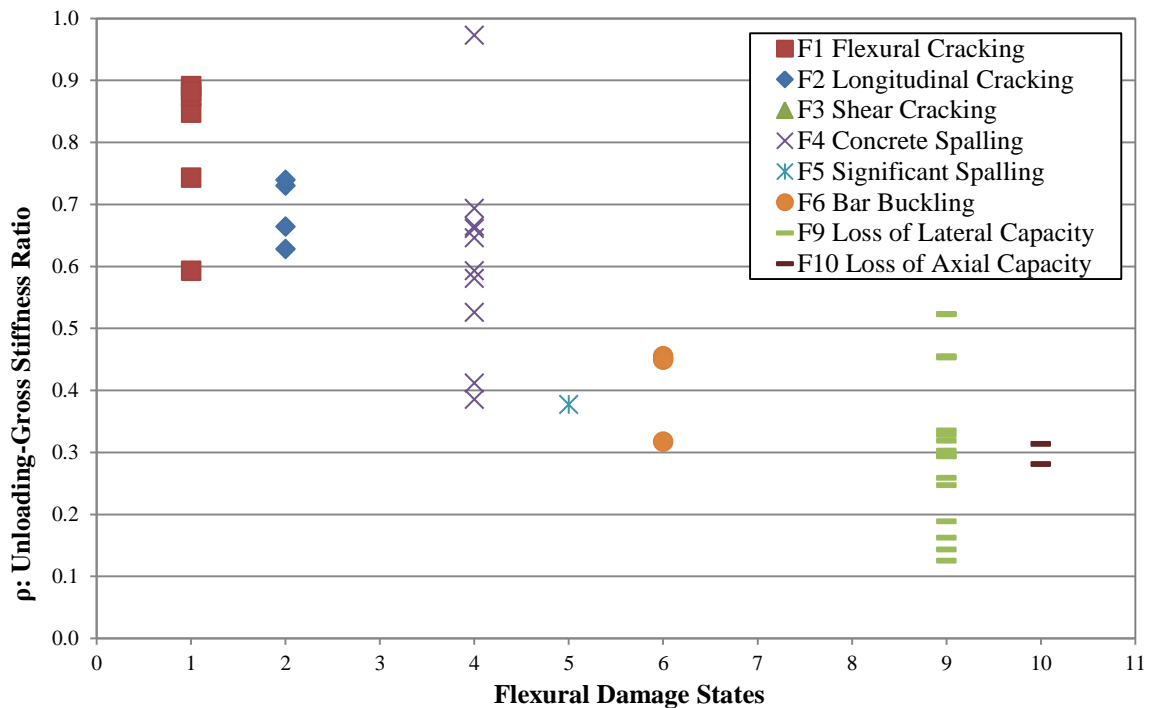
The unloading-gross stiffness ratio, ρ , is a measure of the amplitude of the unloading stiffness, EI_U , to the gross stiffness, EI_{gross} . The unloading stiffness was taken as the slope of the line connecting the peak drift with the corresponding residual drift at zero load. The gross stiffness was determined by computing the slope of the line connecting the first peak to the origin. In equation form the ratio is as follows:

$$\rho = \frac{EI_U}{EI_{gross}}$$

Appendix Figure H.1 and Appendix Figure H.2 present the unloading-gross stiffness ratio data plotted against the corresponding damage states for columns with low and high axial loads respectively.



Appendix Figure H.1 Unloading-Gross Stiffness Ratio vs. Flexural Damage States for columns with low axial loads



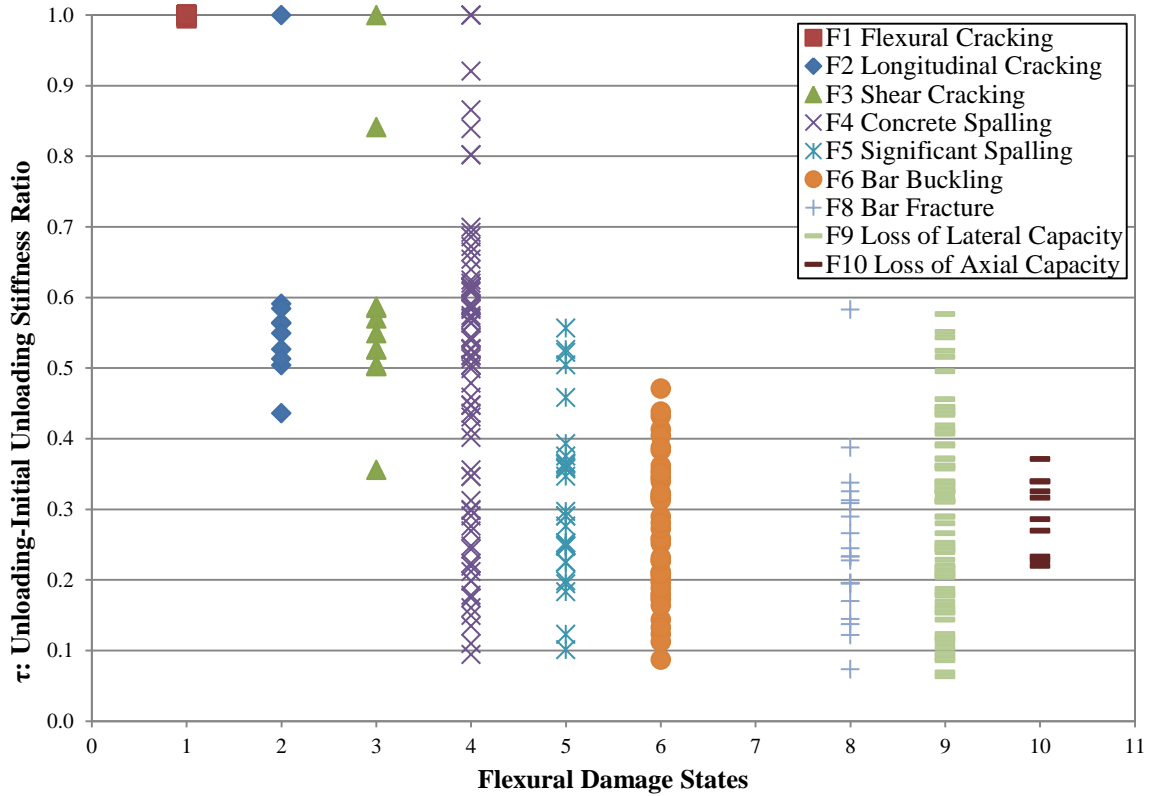
Appendix Figure H.2 Unloading-Gross Stiffness Ratio vs. Flexural Damage States for columns with high axial loads

The unloading-initial unloading stiffness ratio, τ , is a measure of the amplitude of the unloading stiffness, EI_U , to the initial unloading stiffness, EI_{IU} . The initial unloading stiffness is the slope of the line

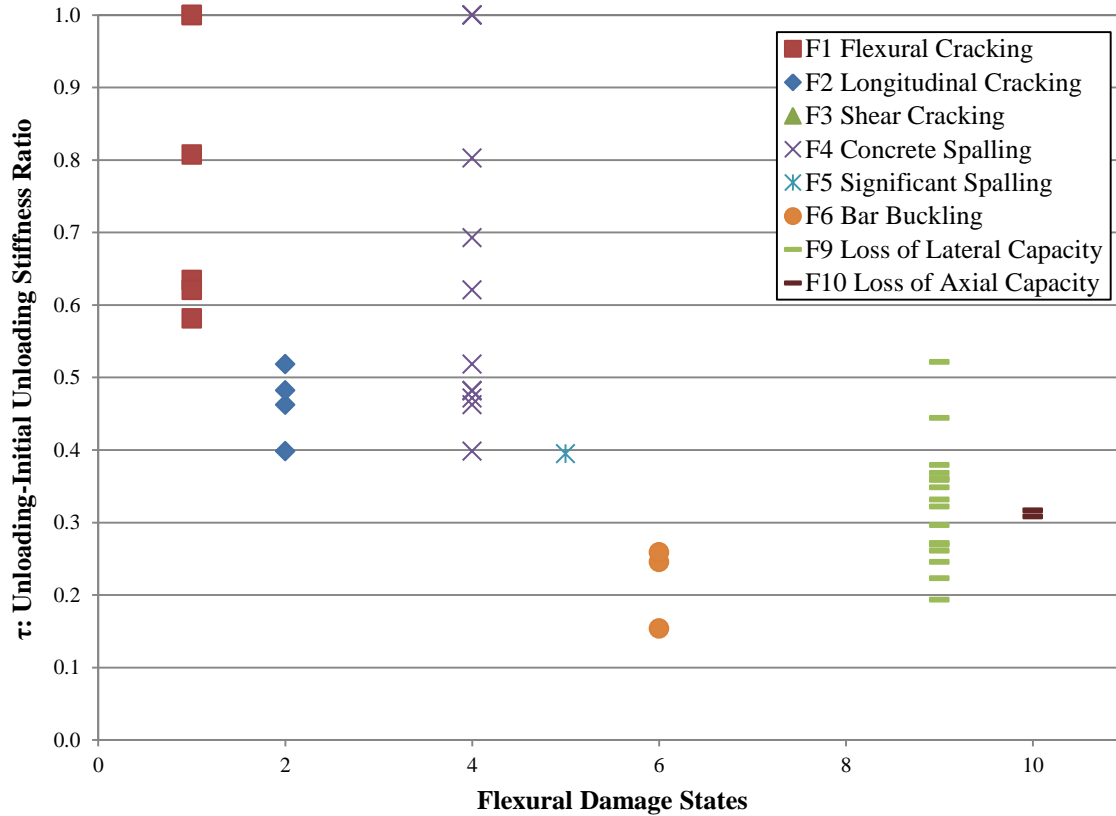
connecting the first peak in the load-displacement history to the corresponding residual drift observed at the end of the first loading cycle. In equation form the ratio is as follows:

$$\tau = \frac{EI_U}{EI_{IU}}$$

Appendix Figure H.3 and Appendix Figure H.4 present the unloading stiffness ratio data plotted against the corresponding damage states for columns with low and high axial loads respectively.



Appendix Figure H.3 Unloading-Initial Unloading Stiffness Ratios vs. Flexural Damage States for columns with low axial loads



Appendix Figure H.4 Unloading-Initial Unloading Stiffness Ratios vs. Flexural Damage States for columns with high axial loads

The median values for the unloading stiffness ratios are presented in Appendix Table H.1 along with the coefficients of variation.

Appendix Table H.1 Unloading stiffness data

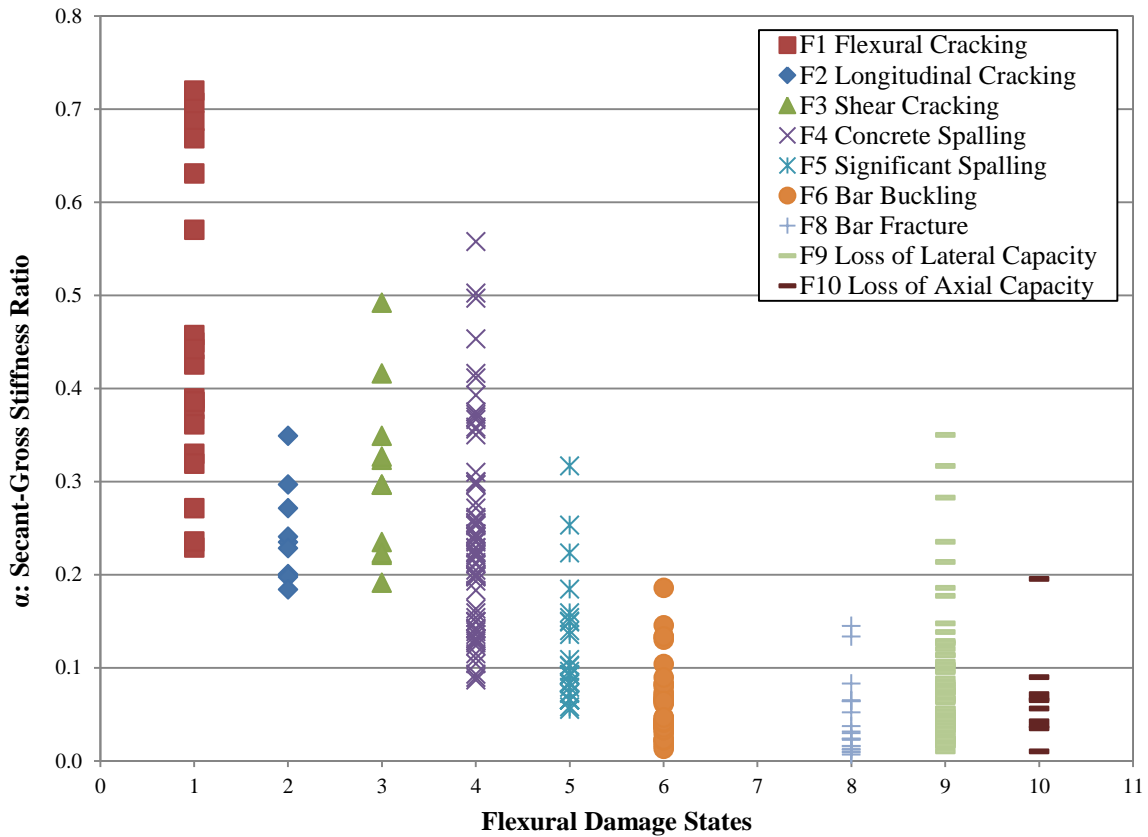
Flexure Damage States	ρ : Unloading-Gross Stiffness Ratio				τ : Unloading-Initial Unloading Stiffness Ratio			
	Low Axial Load		High Axial Load		Low Axial Load		High Axial Load	
	Median	COV	Median	COV	Median	COV	Median	COV
F1 Flexural Cracking	48%	0.37	86%	0.15	100%	0.00	72%	0.25
F2 Longitudinal Cracking	27%	0.25	50%	0.26	56%	0.25	47%	0.11
F3 Shear Cracking	37%	0.29			55%	0.30		
F4 Concrete Spalling	27%	0.39	65%	0.44	52%	0.45	57%	0.35
F5 Significant Spalling	17%	0.41	38%		29%	0.37	39%	
F6 Bar Buckling	17%	0.56	45%	0.19	26%	0.36	25%	0.26
F8 Bar Fracture	17%	0.61			23%	0.45		
F9 Loss of Lateral Capacity	14%	0.59	30%	0.41	29%	0.45	33%	0.26
F10 Loss of Axial Capacity	14%	0.43	30%	0.08	29%	0.26	31%	0.02

H.3 Secant Stiffness Result

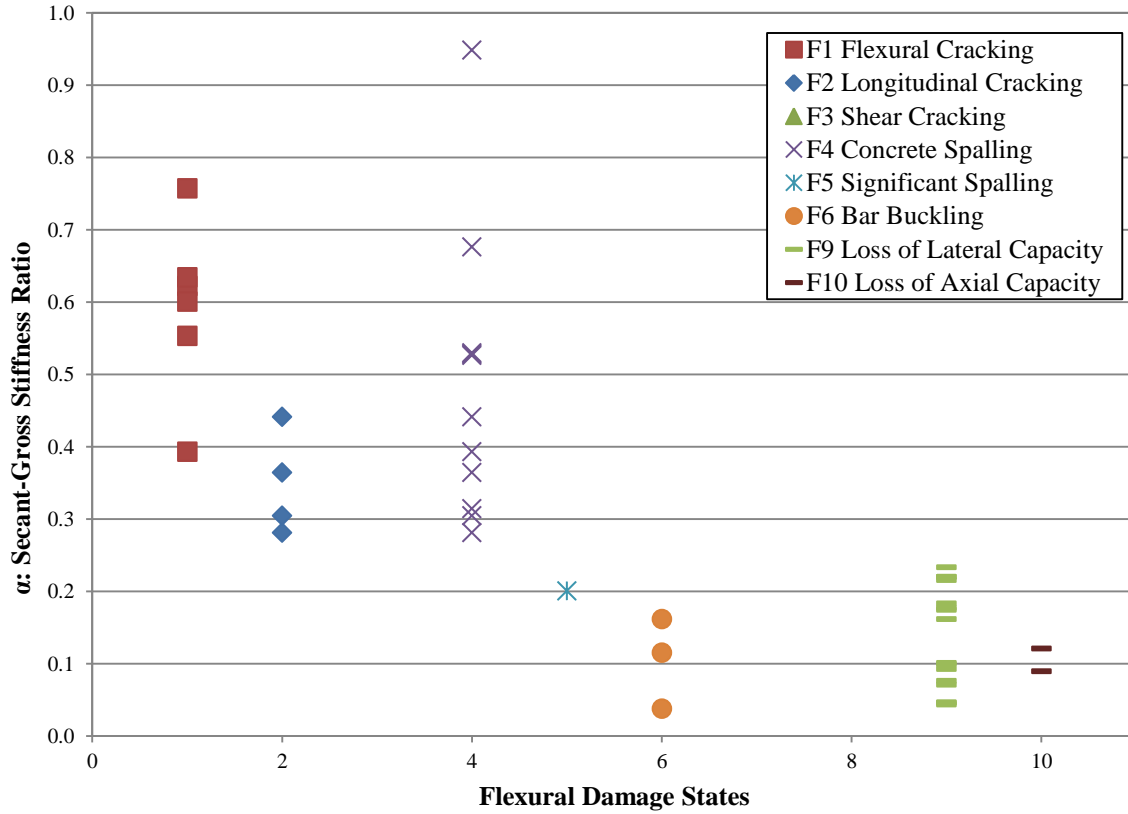
The secant-gross stiffness ratio, α , is a measure of the amplitude of the secant stiffness, EI_s , to the gross stiffness, EI_{gross} . The secant stiffness were determined by taking the slope between the peaks at which the damage states occurred and the origin. In equation form it is as follows:

$$\alpha = \frac{EI_s}{EI_{gross}}$$

Appendix Figure H.5 and Appendix Figure H.6 present the secant stiffness ratio data plotted against the corresponding damage states for columns with low and high axial loads respectively.



Appendix Figure H.5 Secant-Gross Stiffness Ratios vs. Flexural Damage States for columns with low axial loads

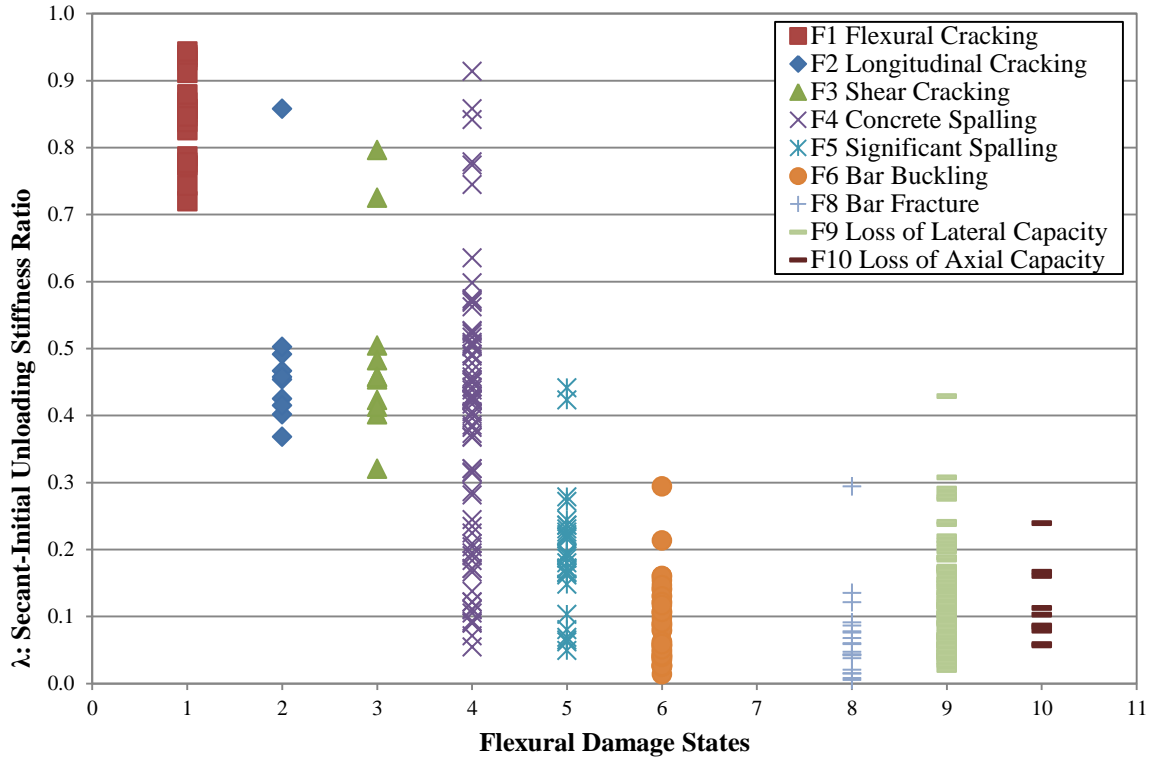


Appendix Figure H.6 Secant-Gross Stiffness Ratios vs. Flexural Damage States for columns with high axial loads

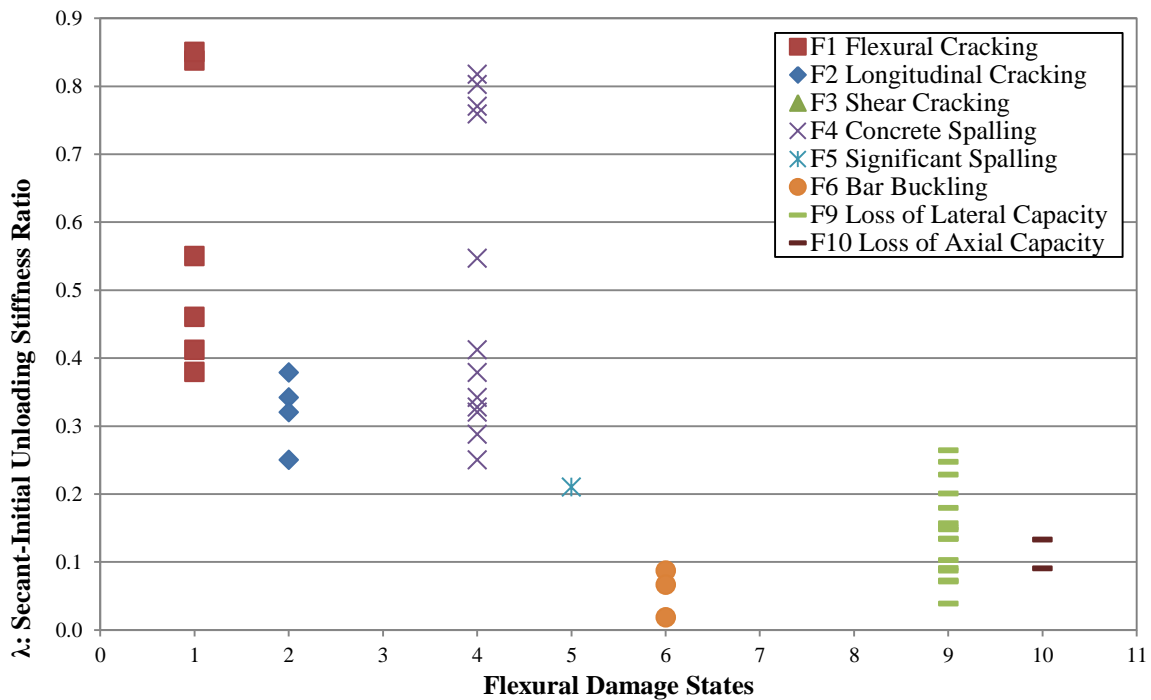
The secant-initial unloading stiffness ratio, λ , is a measure of the amplitude of the secant stiffness, EI_s , to the initial unloading stiffness, EI_{IU} . In equation form it is as follows:

$$\lambda = \frac{EI_s}{EI_{IU}}$$

Appendix Figure H.7 and Appendix Figure H.8 present the secant stiffness ratio data plotted against the corresponding damage states for columns with low and high axial loads respectively.



Appendix Figure H.7 Secant-Initial Unloading Stiffness Ratios vs. Flexural Damage States for columns with low axial loads



Appendix Figure H.8 Secant-Initial Unloading Stiffness Ratios vs. Flexural Damage States for columns with high axial loads

The median values for the secant stiffness ratios are presented in Appendix Table H.2 along with the coefficients of variation.

Appendix Table H.2 Secant stiffness data

Flexure Damage States	α : Secant-Gross Stiffness Ratio				λ : Secant-Initial Unloading Stiffness Ratio			
	Low Axial Load		High Axial Load		Low Axial Load		High Axial Load	
	Median	COV	Median	COV	Median	COV	Median	COV
F1 Flexural Cracking	41%	0.35	61%	0.20	86%	0.09	51%	0.36
F2 Longitudinal Cracking	23%	0.26	33%	0.21	45%	0.27	33%	0.17
F3 Shear Cracking	30%	0.29			46%	0.29		
F4 Concrete Spalling	23%	0.44	48%	0.59	42%	0.51	40%	0.45
F5 Significant Spalling	9%	0.54	20%		19%	0.47	21%	
F6 Bar Buckling	4%	0.64	12%	0.60	8%	0.66	7%	0.62
F8 Bar Fracture	3%	0.93			5%	0.95		
F9 Loss of Lateral Capacity	5%	0.87	13%	0.52	11%	0.62	14%	0.46
F10 Loss of Axial Capacity	6%	0.79	11%	0.21	9%	0.57	11%	0.27